



**You have downloaded a document from
RE-BUS
repository of the University of Silesia in Katowice**

Title: FCC-ee : the Lepton Collider : Future Circular Collider Conceptual Design Report Volume 2

Author: A. Abada, M. Abbrescia, S. S. Abdus Salam, I. Abdyukhanov, J. Abelleira Fernandez, A. Abramov, Bartosz Dziewit, Wojciech Flieger, Janusz Gluza, Krzysztof Grzanka, Karol Kołodziej, Magdalena Kordiaczyńska, Seweryn Kowalski, Szymon Puławski, Tord Riemann + 1353 The FCC Collaboration

Citation style: Abada A., Abbrescia M., Abdus Salam S. S., Abdyukhanov I., Abelleira Fernandez J., Abramov A., Dziewit Bartosz, Flieger Wojciech, Gluza Janusz, Grzanka Krzysztof, Kołodziej Karol, Kordiaczyńska Magdalena, Kowalski Seweryn, Puławski Szymon, Riemann Tord + 1353 The FCC Collaboration. (2019). FCC-ee : the Lepton Collider : Future Circular Collider Conceptual Design Report Volume 2. "The European Physical Journal Special Topics" (Vol. 228, iss. 2 (2019), s. 261-623), doi 10.1140/epjst/e2019-900045-4



Uznanie autorstwa - Licencja ta pozwala na kopiowanie, zmienianie, rozprowadzanie, przedstawianie i wykonywanie utworu jedynie pod warunkiem oznaczenia autorstwa.



UNIwersYTET ŚLĄSKI
W KATOWICACH



Biblioteka
Uniwersytetu Śląskiego



Ministerstwo Nauki
i Szkolnictwa Wyższego

FCC-ee: The Lepton Collider

Future Circular Collider Conceptual Design Report Volume 2

A. Abada³², M. Abbrescia^{117,257}, S.S. AbdusSalam²¹⁸, I. Abdyukhanov¹⁶, J. Abelleira Fernandez¹⁴², A. Abramov²⁰⁴, M. Aburaia²⁸⁴, A.O. Acar²³⁸, P.R. Adzic²⁸⁷, P. Agrawal⁷⁹, J.A. Aguilar-Saavedra⁴⁶, J.J. Aguilera-Verdugo¹⁰⁶, M. Aiba¹⁹¹, I. Aichinger⁶⁴, G. Aielli^{134,272}, A. Akay²³⁸, A. Akhundov⁴⁵, H. Aksakal¹⁴⁵, J.L. Albacete⁴⁶, S. Albergo^{120,260}, A. Alekou³¹¹, M. Aleksa⁶⁴, R. Aleksan³⁹, R.M. Alemany Fernandez⁶⁴, Y. Alexahin⁷⁰, R.G. Alía⁶⁴, S. Alioli¹²⁶, N. Alipour Tehrani⁶⁴, B.C. Allanach²⁹⁸, P.P. Allport²⁹⁰, M. Altinli^{112,62}, W. Altmannshofer²⁹⁷, G. Ambrosio⁷⁰, D. Amorim⁶⁴, O. Amstutz¹⁶¹, L. Anderlini^{123,262}, A. Andreazza^{127,266}, M. Andreini⁶⁴, A. Andriatis¹⁶⁷, C. Andris¹⁶⁵, A. Andronic³⁴⁴, M. Angelucci¹¹⁵, F. Antinori^{129,267}, S.A. Antipov⁶⁴, M. Antonelli¹¹⁵, M. Antonello^{127,264}, P. Antonioli¹¹⁸, S. Antusch²⁸⁶, F. Anulli^{133,271}, L. Apolinário¹⁵⁸, G. Apollinari⁷⁰, A. Apollonio⁶⁴, D. Appellö³⁵⁰, R.B. Appleby^{311,301}, A. Apyan⁷⁰, A. Apyan¹, A. Arbey³³⁵, A. Arbuzov¹⁷, G. Arduini⁶⁴, V. Ari⁹, S. Arias^{66,309}, N. Armesto¹⁰⁸, R. Arnaldi^{136,274}, S.A. Arsenyev⁶⁴, M. Arzeo⁶⁴, S. Asai²³⁶, E. Aslanides³¹, R.W. Aßmann⁴⁹, D. Astapovych²²⁸, M. Atanasov⁶⁴, S. Atieh⁶⁴, D. Attie³⁹, B. Auchmann⁶⁴, A. Audurier^{119,259}, S. Aull⁶⁴, S. Aumon⁶⁴, S. Aune³⁹, F. Avino⁶⁴, G. Avrillaud⁸³, G. Aydın¹⁷³, A. Azatov^{214,137}, G. Azuelos²⁴¹, P. Azzi^{129,267}, O. Azzolini¹¹⁶, P. Azzurri^{132,215}, N. Bacchetta^{129,267}, E. Bacchiocchi²⁶⁶, H. Bachacou³⁹, Y.W. Baek⁷⁴, V. Baglin⁶⁴, Y. Bai³³¹, S. Baird⁶⁴, M.J. Baker³³³, M.J. Baldwin¹⁶⁷, A.H. Ball⁶⁴, A. Ballarín⁶⁴, S. Banerjee⁵⁴, D.P. Barber^{49,316}, D. Barducci^{214,137}, P. Barjhoux³, D. Barna¹⁷², G.G. Barnaföldi¹⁷², M.J. Barnes⁶⁴, A. Barr¹⁹⁰, J. Barranco García⁵⁶, J. Barreiro Guimarães da Costa⁹⁷, W. Bartmann⁶⁴, V. Baryshevsky⁹⁵, E. Barzi⁷⁰, S.A. Bass⁵³, A. Bastianin²⁶⁶, B. Baudouy³⁹, F. Bauer³⁹, M. Bauer⁵⁴, T. Baumgartner²³², I. Bautista-Guzmán¹⁵, C. Bayındır^{82,19}, F. Beaudette³², F. Bedeschi^{132,215}, M. Béguin⁶⁴, I. Bellafont⁶, L. Bellagamba^{118,258}, N. Bellegarde⁶⁴, E. Belli^{133,271,208}, E. Bellingeri⁴³, F. Bellini⁶⁴, G. Bellomo^{127,266}, S. Belomestnykh⁷⁰, G. Bencivenni¹¹⁵, M. Benedikt^{64,a}, G. Bernardi³², J. Bernardi²³², C. Bernet^{32,335}, J.M. Bernhardt³, C. Bernini⁴³, C. Berriaud³⁹, A. Bertarelli⁶⁴, S. Bertolucci^{118,258}, M.I. Besana¹⁹¹, M. Besançon³⁹, O. Beznosov³¹⁶, P. Bhat⁷⁰, C. Bhat⁷⁰, M.E. Biagini¹¹⁵, J.-L. Biarrotte³², A. Bibet Chevalier²⁷, E.R. Bielert³⁰⁴, M. Biglietti^{135,273}, G.M. Bilei^{131,270}, B. Bilki³⁰⁵, C. Biscari⁶, F. Bishara^{49,190}, O.R. Blanco-García¹¹⁵, F.R. Blázquez⁶⁴, F. Blekman³⁴⁰, A. Blondel³⁰³, J. Blümlein⁴⁹, T. Boccali^{132,215}, R. Boels⁸⁴, S.A. Bogacz²³⁷, A. Bogomyagkov²³, O. Boine-Frankenheim²²⁸, M.J. Boland³²¹, S. Bologna²⁹¹, O. Bolukbasi¹¹², M. Bomben³², S. Bondarenko¹⁷, M. Bonvini^{133,271}, E. Boos²²¹, B. Bordini⁶⁴, F. Bordry⁶⁴, G. Borghello^{64,275}, L. Borgonovi^{118,258}, S. Borowka⁶⁴, D. Bortoletto¹⁹⁰, D. Boscherini^{118,258}, M. Boscolo¹¹⁵, S. Boselli^{130,269}, R.R. Bosley²⁹⁰, F. Bossu³², C. Botta⁶⁴, L. Bottura⁶⁴, R. Boughezal¹¹, D. Boutin³⁹, G. Bovone⁴³, I. Božović Jelisavčić³³⁹, A. Bozbey²³⁸, C. Bozzi^{122,261}, D. Bozzini⁶⁴, V. Braccini⁴³, S. Braibant-Giacomelli^{118,258}, J. Bramante^{200,193}, P. Braun-Munzinger⁷⁷, J.A. Briffa³¹⁰, D. Britzger¹⁶⁹, S.J. Brodsky²²⁵, J.J. Brooke²⁹¹, R. Bruce⁶⁴,

P. Brückman De Renstrom⁹⁹, E. Bruna^{136,274}, O. Brüning⁶⁴, O. Brunner⁶⁴, K. Brunner¹⁷², P. Bruzzone⁵⁶, X. Buffat⁶⁴, E. Bulyak¹⁸¹, F. Burkart⁶⁴, H. Burkhardt⁶⁴, J.-P. Burnet⁶⁴, F. Butin⁶⁴, D. Buttazzo^{132,215}, A. Butterworth⁶⁴, M. Caccia^{127,264}, Y. Cai²²⁵, B. Caiffi^{124,263}, V. Cairo²²⁵, O. Cakir⁹, R. Calaga⁶⁴, S. Calatroni⁶⁴, G. Calderini³², G. Calderola¹¹⁶, A. Caliskan⁷⁸, D. Calvet^{30,281}, M. Calviani⁶⁴, J.M. Camalich¹⁰², P. Camarri^{134,272}, M. Campanelli²⁸³, T. Camporesi⁶⁴, A.C. Canbay⁹, A. Canepa⁷⁰, E. Cantergiani⁸³, D. Cantore-Cavalli^{127,266}, M. Capeans⁶⁴, R. Cardarelli^{134,272}, U. Cardella¹⁶¹, A. Cardini¹¹⁹, C.M. Carloni Calame^{130,269}, F. Carra⁶⁴, S. Carra^{127,266}, A. Carvalho¹⁵⁸, S. Casalbuoni¹⁴⁶, J. Casas⁶, M. Cascella²⁸³, P. Castelnovo²⁶⁶, G. Castorina^{133,271}, G. Catalano²⁶⁶, V. Cavasinni^{132,215}, E. Cazzato²⁸⁶, E. Cennini⁶⁴, A. Cerrì³²⁷, F. Cerutti⁶⁴, J. Cervantes⁶⁴, I. Chaikovska³², J. Chakraborty⁸⁷, M. Chala⁵⁴, M. Chamizo-Llatas²⁰, H. Chanal³⁰, D. Chanal²⁷, S. Chance³², A. Chancé³⁹, P. Charitos⁶⁴, J. Charles³¹, T.K. Charles³¹⁴, S. Chattopadhyay¹⁸⁶, R. Chehab¹⁵³, S.V. Chekanov¹¹, N. Chen¹⁷⁴, A. Chernoded²²¹, V. Chetvertkova⁷⁷, L. Chevalier³⁹, G. Chiarelli^{132,215}, G. Chiarello^{133,271,208}, M. Chiesa¹⁴⁴, P. Chiggiato⁶⁴, J.T. Childers¹¹, A. Chmieleńska^{64,56}, A. Cholakian^{167,79}, P. Chomaz³⁹, M. Chorowski³⁴⁶, W. Chou⁹⁷, M. Chruszcz⁹⁹, E. Chyhyrynets¹¹⁶, G. Cibirnetto^{122,261}, A.K. Ciftci¹⁴⁰, R. Ciftci⁵⁸, R. Cimino¹¹⁵, M. Ciuchini^{135,273}, P.J. Clark³⁰¹, Y. Coadou^{31,25,4}, M. Cobal^{137,275}, A. Coccaro¹²⁴, J. Cogan^{32,31}, E. Cogneras²⁹, F. Collamati^{133,271}, C. Colldelram⁶, P. Collier⁶⁴, J. Collot^{32,282}, R. Contino²¹⁵, F. Conventi¹²⁸, C.T.A. Cook⁶⁴, L. Cooley^{177,10}, G. Corcella^{115,116}, A.S. Cornell³²⁸, G.H. Corral³⁵, H. Correia-Rodrigues⁶⁴, F. Costanza³², P. Costa Pinto⁶⁴, F. Couderc³⁹, J. Coupard⁶⁴, N. Craig²⁹⁶, I. Crespo Garrido³³⁴, A. Crivellin¹⁹¹, J.F. Croteau⁸³, M. Crouch⁶⁴, E. Cruz Alaniz¹⁴², B. Curé⁶⁴, J. Curti¹⁶⁷, D. Curtin³²⁹, M. Czech⁶⁴, C. Dachauer¹⁶¹, R.T. D'Agnolo²²⁵, M. Daibo⁷³, A. Dainese^{129,267}, B. Dalena³⁹, A. Daljevec⁶⁴, W. Dallapiazza⁸⁵, L. D'Aloia Schwartzentruber²⁶, M. Dam¹⁸⁴, G. D'Ambrosio¹²⁸, S.P. Das²⁴⁹, S. DasBakshi⁸⁷, W. da Silva³², G.G. da Silveira²⁵¹, V. D'Auria⁵⁶, S. D'Auria²⁶⁶, A. David⁶⁴, T. Davidek⁶⁸, A. Deandrea^{32,335}, J. de Blas^{129,267}, C.J. Debono³¹⁰, S. De Curtis^{123,262}, N. De Filippis^{117,257}, D. de Florian¹⁰⁹, S. Deghaye⁶⁴, S.J. de Jong^{175,94}, C. Del Bo²⁶⁶, V. Del Duca^{136,274}, D. Delikaris⁶⁴, F. Deliot³⁹, A. Dell'Acqua⁶⁴, L. Delle Rose^{123,262}, M. Delmastro¹⁵², E. De Lucia¹¹⁵, M. Demarteau¹¹, D. Denegri³⁹, L. Deniau⁶⁴, D. Denisov⁷⁰, H. Denizli², A. Denner³³², D. d'Enterria⁶⁴, G. de Rijk⁶⁴, A. De Roeck⁶⁴, F. Derue³², O. Deschamps³², S. Descotes-Genon³², P.S.B. Dev³⁴¹, J.B. de Vivie de Régie³², R.K. Dewanjee¹⁷⁸, A. Di Ciaccio^{134,272}, A. Di Cicco¹¹⁵, B.M. Dillon¹⁰¹, B. Di Micco^{135,273}, P. Di Nezza¹¹⁵, S. Di Vita^{127,266}, A. Doblhammer²³², A. Dominjon¹⁵², M. D'Onofrio³⁰⁸, F. Dordei⁶⁴, A. Drago¹¹⁵, P. Draper³⁰⁴, Z. Drasal⁶⁸, M. Drewes¹⁴⁷, L. Duarte²⁴⁸, I. Dubovyk⁸⁴, P. Duda³⁴⁶, A. Dudarev⁶⁴, L. Dudko²²¹, D. Duellmann⁶⁴, M. Dünser⁶⁴, T. du Pree¹⁷⁵, M. Durante³⁹, H. Duran Yildiz⁹, S. Dutta²²⁴, F. Duval⁶⁴, J.M. Duval⁴⁰, Y. Dydyshka⁵⁵, B. Dziewit³²⁴, S. Eisenhardt³⁰¹, M. Eisterer²³², T. Ekelof³³⁶, D. El Khechen⁶⁴, S.A. Ellis²²⁵, J. Ellis¹⁴⁹, J.A. Ellison³¹⁶, K. Elsener⁶⁴, M. Elsing⁶⁴, Y. Enari²³⁶, C. Englert²¹⁰, H. Eriksson¹⁶⁴, K.J. Eskola³⁰⁶, L.S. Esposito⁶⁴, O. Etischen⁹, E. Etzion²³³, P. Fabbriatore^{124,263}, A. Falkowski³², A. Falou¹⁵³, J. Faltova⁶⁸, J. Fan²¹, L. Fanò^{131,270}, A. Farilla^{135,273}, R. Farinelli^{122,261}, S. Farinon^{124,263}, D.A. Faroughy¹⁰¹, S.D. Fartoukh⁶⁴, A. Faus-Golfe³², W.J. Fawcett²⁹⁸, G. Felici¹¹⁵, L. Felsberger¹⁶³, C. Ferdeghini⁴², A.M. Fernandez Navarro³⁴, A. Fernández-Téllez¹⁵, J. Ferradas Troitino^{64,303}, G. Ferrara^{127,266}, R. Ferrari^{130,269}, L. Ferreira⁶⁴, P. Ferreira da Silva⁶⁴, G. Ferrera^{266,126}, F. Ferro^{124,263}, M. Fiascaris⁶⁴, S. Fiorendi¹²⁶, C. Fiorio²⁶⁶, O. Fischer^{286,146}, E. Fischer⁷⁷, W. Flieger³²⁴, M. Florio²⁶⁶, D. Fomesu⁶⁴, E. Fontanesi^{118,258}, N. Foppiani⁷⁹,

K. Foraz⁶⁴, D. Forkel-Wirth⁶⁴, S. Forte²⁶⁶, M. Fouaidy⁸⁹, D. Fournier³²,
 T. Fowler⁶⁴, J. Fox²²⁶, P. Francavilla^{132,215}, R. Franceschini^{135,273}, S. Franchino²⁷⁷,
 E. Franco^{133,271}, A. Freitas¹⁹⁶, B. Fuks¹⁵⁶, K. Furukawa⁸¹, S.V. Furuseth⁵⁶,
 E. Gabrielli^{137,275}, A. Gaddi⁶⁴, M. Galanti³¹⁹, E. Gallo⁴⁹, S. Ganjour³⁹, J. Gao¹⁹¹,
 J. Gao⁹⁷, V. Garcia Diaz¹¹⁶, M. García Pérez⁶⁴, L. García Tabarés³⁴, C. Garion⁶⁴,
 M.V. Garzelli^{276,280}, I. Garzia^{122,261}, S.M. Gascon-Shotkin^{32,335}, G. Gaudio^{130,269},
 P. Gay^{32,30}, S.-F. Ge^{292,236}, T. Gehrmann³³³, M.H. Genest^{32,282}, R. Gerard⁶⁴,
 F. Gerigk⁶⁴, H. Gerwig⁶⁴, P. Giacomelli^{118,258}, S. Giagu^{133,271}, E. Gianfelice-
 Wendt⁷⁰, F. Gianotti⁶⁴, F. Giffoni^{266,28}, S.S. Gilardoni⁶⁴, M. Gil Costa³⁴,
 M. Giovannetti¹¹⁵, M. Giovannozzi⁶⁴, P. Giubellino^{136,77}, G.F. Giudice⁶⁴,
 A. Giunta²⁵⁴, L.K. Gladilin²²¹, S. Glukhov²³, J. Gluza³²⁴, G. Gobbi⁶⁴,
 B. Goddard⁶⁴, F. Goertz¹⁶⁸, T. Golling³⁰³, V.P. Goncalves²⁵², D. Goncalves
 Netto³⁵¹, R. Gonçalo¹⁵⁸, L.A. Gonzalez Gomez¹¹⁵, S. Gorgi Zadeh³²⁰, G. Gorine⁵⁶,
 E. Gorini^{125,256}, S.A. Gourlay¹⁶⁰, L. Gouskos²⁹⁶, F. Grancagnolo^{125,265},
 A. Grassellino⁷⁰, A. Grau¹⁴⁶, E. Graverini³³³, H.M. Gray¹⁶⁰, M. Greco^{135,273},
 M. Greco^{135,273}, J.-L. Grenard⁶⁴, O. Grimm⁵⁹, C. Grojean⁴⁹, V.A. Gromov¹⁴³,
 J.F. Grosse-Oetringhaus⁶⁴, A. Grudiev⁶⁴, K. Grzanka³²⁴, J. Gu¹⁴¹,
 D. Guadagnoli¹⁵², V. Guidi^{122,261}, S. Guiducci¹¹⁵, G. Guillermo Canton³⁵,
 Y.O. Günaydin¹⁴⁵, R. Gupta²⁰, R.S. Gupta⁵⁴, J. Gutierrez⁸⁸, J. Gutleber⁶⁴,
 C. Guyot³⁹, V. Guzey¹⁹⁴, C. Gwenlan¹⁹⁰, C. Haberstroh²³⁰, B. Hacışahinoğlu¹¹²,
 B. Haerer⁶⁴, K. Hahn¹⁸⁷, T. Hahn³⁴³, A. Hammad²⁸⁶, C. Han²³⁶, M. Hance²⁹⁷,
 A. Hannah²¹¹, P.C. Harris¹⁶⁷, C. Hati^{30,281}, S. Haug²⁸⁹, J. Hauptman¹¹⁰,
 V. Haurylavets⁹⁵, H.-J. He²¹⁹, A. Hegglin^{220,217}, B. Hegner²⁰, K. Heinemann³¹⁶,
 S. Heinemeyer¹⁰⁵, C. Helsens⁶⁴, A. Henriques⁶⁴, A. Henriques⁶⁴, P. Hernandez¹⁰⁴,
 R.J. Hernández-Pinto²⁴⁵, J. Hernandez-Sanchez¹⁵, T. Herzig⁹⁸, I. Hiekkänen¹⁶⁴,
 W. Hillert²⁷⁶, T. Hoehn²³¹, M. Hofer²³², W. Höfle⁶⁴, F. Holdener²²⁰,
 S. Holleis²³², B. Holzer⁶⁴, D.K. Hong¹⁹⁹, C.G. Honorato¹⁵, S.C. Hopkins⁶⁴,
 J. Hrdinka⁶⁴, F. Hug¹⁴¹, B. Humann²³², H. Humer¹², T. Hurth¹⁴¹, A. Hutton²³⁷,
 G. Iacobucci³⁰³, N. Ibarrola⁶⁴, L. Iconomidou-Fayard³², K. Ilyina-Brunner⁶⁴,
 J. Incandela²⁹⁶, A. Infantino⁶⁴, V. Ippolito^{133,271}, M. Ishino²³⁶, R. Islam⁸⁶,
 H. Ita⁷, A. Ivanovs²⁰³, S. Iwamoto²⁶⁷, A. Iyer¹²⁸, S. Izquierdo Bermudez⁶⁴,
 S. Jadach⁹⁹, D.O. Jamin¹⁰⁰, P. Janot⁶⁴, P. Jarry³⁹, A. Jeff^{64,36}, P. Jenny¹⁶⁵,
 E. Jensen⁶⁴, M. Jensen⁶⁶, X. Jiang²⁷⁹, J.M. Jiménez⁶⁴, M.A. Jones⁶⁴,
 O.R. Jones⁶⁴, J.M. Jowett⁶⁴, S. Jung²¹⁶, W. Kaabi³², M. Kado^{64,133,271},
 K. Kahle⁶⁴, L. Kalinovskaya⁵⁵, J. Kalinowski³³⁰, J.F. Kamenik¹⁰¹, K. Kannike¹⁷⁸,
 S.O. Kara^{9,185}, H. Karadeniz⁷⁵, V. Karavantzias⁶⁴, I. Karpov⁶⁴, S. Kartal¹¹²,
 A. Karyukhin⁹³, V. Kashikhin⁷⁰, J. Katharina Behr⁴⁹, U. Kaya^{238,9}, J. Keintzel²³²,
 P.A. Keinz³³⁸, K. Keppel¹¹⁶, R. Kersevan⁶⁴, K. Kershaw⁶⁴, H. Khanpour^{209,323},
 S. Khatibi^{209,48}, M. Khatiri Yanehsari²⁰⁹, V.V. Khoze⁵⁴, J. Kieseler⁶⁴, A. Kilic²⁴⁴,
 A. Kilpinen¹⁶⁴, Y.-K. Kim²⁹⁹, D.W. Kim⁷⁴, U. Klein³⁰⁸, M. Klein³⁰⁸, F. Kling²⁹⁴,
 N. Klinkenberg^{64,67}, S. Klöppel²³⁰, M. Klute¹⁶⁷, V.I. Klyukhin²²¹, M. Knecht^{32,31},
 B. Kniehl⁸⁴, F. Kocak²⁴⁴, C. Koeberl¹⁸³, A.M. Kolano⁶⁴, A. Kollegger²⁸⁴,
 K. Kołodziej³²⁴, A.A. Kolomiets¹⁴³, J. Komppula⁶⁴, I. Koop²³, P. Koppenburg¹⁷⁵,
 M. Koratzinos¹⁶⁷, M. Kordiaczyńska³²⁴, M. Korjik⁹⁵, O. Kortner³⁴³, P. Kostka³⁰⁸,
 W. Kotlarski²³⁰, C. Kotnig⁶⁴, T. Köttig⁶⁴, A.V. Kotwal⁵³, A.D. Kovalenko¹⁴³,
 S. Kowalski³²⁴, J. Kozaczuk³⁰⁴, G.A. Kozlov¹⁴³, S.S. Kozub¹⁴³, A.M. Krainer⁶⁴,
 T. Kramer⁶⁴, M. Krämer²⁰², M. Krammer⁶⁴, A.A. Krasnov²³, F. Krauss⁵⁴,
 K. Kravalis²⁰³, L. Kretschmar³³⁸, R.M. Kriske¹⁶⁷, H. Kritscher¹⁸³, P. Krkotic⁶,
 H. Kroha¹⁶⁹, M. Kucharczyk⁹⁹, S. Kuday¹¹¹, A. Kuendig¹⁶¹, G. Kuhlmann⁷¹,
 A. Kulesza³⁴⁴, M. Kumar⁵⁶, M. Kumar³²⁸, A. Kusina⁹⁹, S. Kuttimalai²²⁵,
 M. Kuze²³⁹, T. Kwon²¹⁶, F. Lackner⁶⁴, M. Lackner²⁸⁴, E. La Francesca^{115,271},
 M. Laine²⁸⁹, G. Lamanna¹⁵², S. La Mendola⁶⁴, E. Lançon²⁰, G. Landsberg²¹,
 P. Langacker⁹⁰, C. Lange⁶⁴, A. Langner⁶⁴, A.J. Lankford²⁹⁴, J.P. Lansberg³²,

- T. Lari¹²⁶, P.J. Laycock³⁰⁸, P. Lebrun⁶⁵, A. Lechner⁶⁴, K. Lee²¹⁶, S. Lee^{24,151}, R. Lee²³, T. Lefevre⁶⁴, P. Le Guen⁶⁴, T. Lehtinen²⁰¹, S.B. Leith²⁷⁹, P. Lenzi^{123,262}, E. Leogrande⁶⁴, C. Leonidopoulos²⁹⁸, I. Leon-Monzon²⁴⁵, G. Lerner⁶⁴, O. Leroy^{32,31}, T. Lesiak⁹⁹, P. Lévai¹⁷², A. Leveratto⁴³, E. Levichev²³, G. Li⁹⁷, S. Li²¹⁹, R. Li³⁴⁹, D. Liberati⁴¹, M. Liepe⁴⁴, D.A. Lissauer²⁰, Z. Liu³¹², A. Lobko⁹⁵, E. Locci³⁹, E. Logothetis Agaliotis^{64,182}, M.P. Lombardo^{123,262}, A.J. Long³¹⁵, C. Lorin³⁹, R. Losito⁶⁴, A. Louzguiti⁶⁴, I. Low¹¹, D. Lucchesi^{129,267}, M.T. Lucchini¹⁹⁷, A. Luciani⁶¹, M. Lueckhof²⁷⁶, A.J.G. Lunt⁶⁴, M. Luzum²⁵⁰, D.A. Lyubintsev¹⁴³, M. Maggiora^{136,274}, N. Magnin⁶⁴, M.A. Mahmoud⁶⁹, F. Mahmoudi^{32,335}, J. Maitre²⁷, V. Makarenko⁹⁵, A. Malagoli⁴³, J. Malclès³⁹, L. Malgeri⁶⁴, P.J. Mallon³⁹, F. Maltoni¹⁴⁷, S. Malvezzi¹²⁶, O.B. Malyshev²¹¹, G. Mancinelli^{32,31}, P. Mandrik⁹³, P. Manfrinetti^{263,43}, M. Mangano⁶⁴, P. Manil³⁹, M. Mannelli⁶⁴, G. Marchiori^{32,154}, F. Marhauser²³⁷, V. Mariani^{131,270}, V. Marinozzi^{127,266}, S. Mariotto^{127,266}, P. Marquard⁵⁰, C. Marquet³², T. Marriott-Dodginton⁶⁴, R. Martin⁶⁴, O. Martin¹⁷⁰, J. Martin Camalich^{102,247}, T. Martinez³⁴, H. Martinez Bruzual^{130,269}, M.I. Martínez-Hernández¹⁵, D.E. Martins²⁵³, S. Marzani^{124,263}, D. Marzocca¹³⁷, L. Marzola¹⁷⁸, S. Masciocchi^{77,277}, I. Masina^{122,261}, A. Massimiliano¹²⁷, A. Massironi⁶⁴, T. Masubuchi²³⁶, V.A. Matveev¹⁴³, M.A. Mazzoni¹³³, M. McCullough⁶⁴, P.A. McIntosh²¹¹, P. Meade²²⁷, L. Medina²⁴⁶, A. Meier¹⁶¹, J. Meignan⁶⁴, B. Mele^{133,271}, J.G. Mendes Saraiva¹⁵⁸, F. Menez²⁷, M. Mentink⁶⁴, E. Meoni^{255,121}, P. Meridiani^{127,266}, M. Merk¹⁷⁵, P. Mermoud³⁰³, V. Mertens⁶⁴, L. Mether⁵⁶, E. Métral⁶⁴, M. Migliorati^{133,271}, A. Milanese⁶⁴, C. Milardi¹¹⁵, G. Milhano¹⁵⁸, B.L. Militsyn²¹¹, F. Millet²⁸², I. Minashvili^{143,139}, J.V. Minervini¹⁶⁷, L.S. Miralles⁶⁴, D. Mirarchi⁶⁴, S. Mishima⁸¹, D.P. Missiaen⁶⁴, G. Mitselmakher³⁰², T. Mitsuhashi⁸¹, J. Mnich⁴⁹, M. Mohammadi Najafabadi²⁰⁹, R.N. Mohapatra³¹², N. Mokhov⁷⁰, J.G. Molson⁶⁴, R. Monge⁶, C. Montag²⁰, G. Montagna^{130,269}, S. Monteil^{32,30}, G. Montenero¹⁹¹, E. Montesinos⁶⁴, F. Moortgat⁶⁴, N. Morange¹⁵³, G. Morello¹¹⁵, M. Moreno Llácer⁶⁴, M. Moretti^{122,261}, S. Moretti²¹², A.K. Morley⁶⁴, A. Moros²³², I. Morozov²³, V. Morretta²⁶⁶, M. Morrone⁶⁴, A. Mostacci^{133,271}, S. Muanza^{32,31}, N. Muchnoi²³, M. Mühlegger¹⁶¹, M. Mulder¹⁷⁵, M. Mulders⁶⁴, B. Müller^{53,20}, F. Müller⁹⁸, A.-S. Müller¹⁴⁶, J. Munilla³⁴, M.J. Murray³⁰⁷, Y. Muttoni⁶⁴, S. Myers⁶⁴, M. Mylonas⁶⁴, J. Nachtman³⁰⁵, T. Nakamoto⁸¹, M. Nardecchia⁶⁴, G. Nardini³²⁵, P. Nason¹²⁶, Z. Nergiz²³⁸, A.V. Nesterenko¹⁴³, A. Nettsträter⁷¹, C. Neubüser⁶⁴, J. Neundorff⁴⁹, F. Niccoli⁶⁴, O. Nicosini^{130,269}, Y. Nie⁶⁴, U. Niedermayer²²⁸, J. Niedziela⁶⁴, A. Niemi⁶⁴, S.A. Nikitin²³, A. Nisati^{133,271}, J.M. No¹⁰⁵, M. Nonis⁶⁴, Y. Nosochkov²²⁵, M. Novák¹⁷², A. Novikhatski²²⁵, J.M. O'Callaghan²⁷⁸, C. Ochando¹⁵⁷, S. Ogur¹⁹, K. Ohmi⁸¹, K. Oide⁶⁴, V.A. Okorokov¹⁸⁰, Y. Okumura²³⁶, C. Oleari¹²⁶, F.I. Olness²²³, Y. Oneil³⁰⁵, M. Ortino²³², J. Osborne⁶⁴, P. Osland²⁸⁸, T. Otto⁶⁴, K.Y. Oyulmaz², A. Ozansoy⁹, V. Özcan¹⁹, K. Özdemir¹⁹⁵, C.E. Pagliarone^{114,52,112}, H.F. Pais da Silva⁶⁴, E. Palmieri¹¹⁶, L. Palumbo^{133,271}, A. Pampaloni^{124,263}, R.-Q. Pan³⁴⁸, M. Panareo^{125,265}, O. Panella^{131,270}, G. Panico²⁶², G. Panizzo^{137,275}, A.A. Pankov⁷⁶, V. Pantsyrny¹⁶, C.G. Papadopoulos¹⁷⁶, A. Papaefstathiou¹⁷⁵, Y. Papaphilippou⁶⁴, M.A. Parker²⁹⁸, V. Parma⁶⁴, M. Pasquali⁶⁴, S.K. Patra⁸⁷, R. Patterson⁴⁴, H. Paukkunen³⁰⁶, F. Pauss⁵⁹, S. Peggs²⁰, J.-P. Penttinen²⁰¹, G. Peón⁶⁴, E.E. Perepelkin¹⁴³, E. Perez⁶⁴, J.C. Perez⁶⁴, G. Perez³⁴², F. Pérez⁶, E. Perez Codina⁶⁴, J. Perez Morales³⁴, M. Perfilov²²¹, H. Pernegger⁶⁴, M. Peruzzi⁶⁴, C. Pes³⁹, K. Peters⁴⁹, S. Petracca¹¹³, F. Petriello¹⁸⁷, L. Pezzotti^{130,269}, S. Pfeiffer²³², F. Piccinini^{130,269}, T. Pieloni⁵⁶, M. Pierini⁶⁴, H. Pikhartova²⁰⁴, G. Pikurs²⁰³, E. Pilicer²⁴⁴, P. Piminov²³, C. Pira¹¹⁶, R. Pittau⁴⁶, W. Płaczek¹⁶⁶, M. Plagge^{64,189}, T. Plehn²⁷⁷, M.-A. Pleier²⁰, M. Płoskoń¹⁶⁰, M. Podeur³²⁶, H. Podlech⁹¹,

T. Podzorny⁶⁴, L. Poggioli³², A. Poiron⁵⁷, G. Polesello^{130,269}, M. Poli Lener¹¹⁵,
 A. Polini^{118,258}, J. Polinski³⁴⁶, S.M. Polozov¹⁸⁰, L. Ponce⁶⁴, M. Pont⁶,
 L. Pontecorvo^{133,271}, T. Portaluri⁵⁹, K. Potamianos⁴⁹, C. Prasse⁷¹, M. Prausa⁷,
 A. Preinerstorfer¹², E. Premat²⁶, T. Price²⁹⁰, M. Primavera¹²⁵, F. Prino^{136,274},
 M. Prioli¹²⁷, J. Proudfoot¹¹, A. Provino⁴³, T. Pugnati³⁹, N. Pukhaeva¹⁴³,
 S. Puławski³²⁴, D. Pulikowski^{64,345}, G. Punzi^{132,215}, M. Putti²⁶³, A. Pyarelal²⁸⁵,
 H. Quack²³⁰, M. Quispe⁶, A. Racioppi¹⁷⁸, H. Rafique³¹¹, V. Raginel⁷⁷,
 M. Raidal¹⁷⁸, N.S. Ramírez-Uribe¹⁰³, M.J. Ramsey-Musolf³¹³, R. Rata⁶⁴,
 P. Ratoff³⁷, F. Ravotti⁶⁴, P. Rebello Teles³³, M. Reboud¹⁵², S. Redaelli⁶⁴,
 E. Renner²³², A.E. Renteria-Olivo¹⁰⁴, M. Rescigno^{133,271}, J. Reuter⁴⁹,
 A. Ribon⁶⁴, A.M. Ricci^{124,263}, W. Riegler⁶⁴, S. Riemann⁵⁰, B. Riemann²²⁹,
 T. Riemann³²⁴, J.M. Rifflet³⁹, R.A. Rimmer²³⁷, R. Rinaldesi⁶⁴, L. Rinolfi⁶⁴,
 O. Rios Rubiras⁶⁴, T. Risselada⁶⁴, A. Rivetti^{136,274}, L. Rivkin¹⁹¹, T. Rizzo²²⁵,
 T. Robens²⁰⁵, F. Robert²⁶, A.J. Robson³⁰³, E. Rochepault³⁹, C. Roda^{132,215},
 G. Rodrigo¹⁰⁶, M. Rodríguez-Cahuantzi¹⁵, C. Rogan³⁰⁷, M. Roig³, S. Rojas-
 Torres²⁴⁵, J. Rojo¹⁷⁵, G. Rolandi^{132,215}, G. Rolando^{64,191}, P. Roloff⁶⁴,
 A. Romanenko⁷⁰, A. Romanov⁸⁸, F. Roncarolo⁶⁴, A. Rosado Sanchez¹⁵,
 G. Rosaz⁶⁴, L. Rossi^{64,266}, A. Rossi^{131,270}, R. Rossmanith^{49,146}, B. Rousset⁴⁰,
 C. Royon³⁰⁷, X. Ruan³²⁸, I. Ruehl⁶⁴, V. Ruhlmann-Kleider³⁹, R. Ruiz⁵⁴,
 L. Rumyantsev^{55,222}, R. Ruprecht¹⁴⁶, A.I. Ryazanov¹⁷⁹, A. Saba⁴³, R. Sadykov⁵⁵,
 D. Saez de Jauregui¹⁴⁶, M. Sahin³³⁷, B. Sailer²², M. Saito²³⁶, F. Sala⁴⁹,
 G.P. Salam¹⁹⁰, J. Salfeld-Nebgen¹⁹⁷, C.A. Salgado¹⁰⁸, S. Salini²⁶⁶, J.M. Sallèse⁵⁶,
 T. Salmi²⁰¹, A. Salzburger⁶⁴, O.A. Sampayo¹⁰⁷, S. Sanfilippo¹⁹¹, J. Santiago⁴⁶,
 E. Santopinto¹²⁴, R. Santoro^{127,264}, A. Sanz Ull⁶⁰, X. Sarasola¹⁹¹, I.H. Sarpün⁵,
 M. Sauvain¹⁵⁹, S. Savelyeva²³⁰, R. Sawada²³⁶, G.F.R. Sborlini^{45,109}, A. Schaffer³²,
 M. Schaumann⁶⁴, M. Schenk⁶⁴, C. Scheuerlein⁶⁴, I. Schienbein¹⁵⁵, K. Schlenga²²,
 H. Schmickler⁶⁴, R. Schmidt^{64,228}, D. Schoerling⁶⁴, T. Schöerner-Sadenius⁴⁹,
 A. Schoning²⁰⁶, M. Schott¹⁹⁸, D. Schulte⁶⁴, P. Schwaller¹⁴¹, C. Schwanenberger⁴⁹,
 P. Schwemling³⁹, N. Schweg⁶⁴, L. Scibile⁶⁴, A. Sciuto^{120,260}, E. Scomparin^{136,274},
 C. Sebastiani^{133,271}, B. Seeber^{303,213}, M. Segreti³⁹, P. Selva¹⁶¹, M. Selvaggi⁶⁴,
 C. Senatore³⁰³, A. Senol², L. Serin³², M. Serluca¹⁵², N. Serra³³³, A. Seryi¹⁴²,
 L. Sestini^{129,267}, A. Sfyrila³⁰³, M. Shaposhnikov⁵⁶, E. Shaposhnikova⁶⁴,
 B.Y. Sharkov¹⁴³, D. Shatilov²³, J. Shelton³⁰⁴, V. Shiltsev⁷⁰, I.P. Shipsey¹⁹⁰,
 G.D. Shirkov¹⁴³, A. Shivaji^{130,269}, D. Shwartz²³, T. Sian^{311,301,211}, S. Sidorov¹⁹¹,
 L. Silvestrini^{133,271}, N. Simand²⁷, F. Simon¹⁶⁹, B.K. Singh¹³, A. Siódmok⁹⁹,
 Y. Sirois³², E. Sirtori²⁸, R. Sirvinskaite^{211,162}, B. Sitar³⁸, T. Sjöstrand³⁰⁹,
 P. Skands¹⁷¹, E. Skordis^{64,308}, K. Skovpen³⁴⁰, M. Skrzypek⁹⁹, E. Slade¹⁹⁰,
 P. Slavich¹⁵⁶, R. Slovak⁶⁸, V. Smaluk²⁰, V. Smirnov²²¹, W. Snoeys⁶⁴,
 L. Soffi⁴⁴, P. Sollander⁶⁴, O. Solovyanov⁹³, H.K. Soltveit²⁷⁷, H. Song²⁸⁵,
 P. Sopicki⁹⁹, M. Sorbi^{127,266}, L. Spallino¹¹⁵, M. Spannowsky⁵⁴, B. Spataro^{133,271},
 P. Sphicas⁶⁴, H. Spiesberger¹⁹⁸, P. Spiller⁷⁷, M. Spira¹⁹¹, T. Srivastava⁸⁷,
 J. Stachel²⁷⁷, A. Stakia⁶⁴, J.L. Stanyard⁶⁴, E. Starchenko¹⁷⁹, A.Y. Starikov¹⁴³,
 A.M. Staśto²³⁵, M. Statera^{127,266}, R. Steerenberg⁶⁴, J. Steggemann⁶⁴,
 A. Stenvall²⁰¹, F. Stivanello¹¹⁶, D. Stöckinger²³⁰, L.S. Stoel⁶⁴, M. Stöger-
 Pollach²³², B. Strauss^{47,96}, M. Stuart⁶⁴, G. Stupakov²²⁵, S. Su²⁸⁵, A. Sublet⁶⁴,
 K. Sugita⁷⁷, L. Sulak¹⁸, M.K. Sullivan²²⁵, S. Sultansoy²³⁸, T. Sumida¹⁵⁰,
 K. Suzuki⁸¹, G. Sylva⁴³, M.J. Syphers¹⁸⁶, A. Sznajder²⁵¹, M. Taborelli⁶⁴,
 N.A. Tahir⁷⁷, M. Takeuchi²³⁶, E. Tal Hod²³³, C. Tambasco⁵⁶, J. Tanaka²³⁶,
 K. Tang¹⁶⁷, I. Tapan²⁴⁴, S. Taroni³¹⁷, G.F. Tartarelli^{127,266}, G. Tassielli^{125,265},
 L. Taviani⁶⁴, T.M. Taylor⁶⁴, G.N. Taylor³¹⁴, A.M. Teixeira^{32,30}, G. Tejeda-
 Muñoz¹⁵, V.I. Telnov^{23,188}, R. Tenchini^{132,215}, H.H.J. ten Kate⁶⁴, K. Terashi²³⁶,
 A. Tesi^{123,262}, M. Testa¹¹⁵, C. Tetrel²⁷, D. Teytelman⁵¹, J. Thaler¹⁶⁷,
 A. Thamm⁶⁴, S. Thomas²⁰⁷, M.T. Tiirakari⁶⁴, V. Tikhomirov⁹⁵, D. Tikhonov⁸⁰,

H. Timko⁶⁴, V. Tisserand^{32,30}, L.M. Tkachenko¹⁴³, J. Tkaczuk^{282,40}, J.P. Tock⁶⁴, B. Todd⁶⁴, E. Todesco⁶⁴, R. Tomás García⁶⁴, D. Tommasini⁶⁴, G. Tonelli^{132,215}, F. Toral³⁴, T. Torims²⁰³, R. Torre⁶⁴, Z. Townsend⁶⁴, R. Trant⁶⁴, D. Treille⁶⁴, L. Trentadue^{126,268}, A. Tricoli²⁰, A. Tricomi^{120,260}, W. Trischuk³²⁹, I.S. Tropin⁷⁰, B. Tuchming³⁹, A.A. Tudora⁶⁴, B. Turbiarz⁹⁹, I. Turk Cakir⁷⁵, M. Turri²⁶⁶, T. Tydecks⁶⁴, J. Usovitsch²⁴⁰, J. Uythoven⁶⁴, R. Vaglio⁴³, A. Valassi⁶⁴, F. Valchkova⁶⁴, M.A. Valdivia García²⁴⁶, P. Valente^{127,266}, R.U. Valente²⁷¹, A.-M. Valente-Feliciano²³⁷, G. Valentino³¹⁰, L. Vale Silva³²⁷, J.M. Valet²⁷, R. Valizadeh²¹¹, J.W.F. Valle¹⁰⁶, S. Vallecorsa⁷⁴, G. Vallone¹⁶⁰, M. van Leeuwen¹⁷⁵, U.H. van Rienen³²⁰, L. van Riesen-Haupt¹⁴², M. Varasteh⁶⁴, L. Vecchi⁵⁶, P. Vadrine³⁹, G. Velev⁷⁰, R. Veness⁶⁴, A. Ventura^{125,256}, W. Venturini Delsolaro⁶⁴, M. Verducci^{135,273}, C.B. Verhaaren²⁹³, C. Vernieri⁷⁰, A.P. Verweij⁶⁴, O. Verwilligen^{117,257}, O. Viazlo⁶⁴, A. Vicini^{127,266}, G. Viehhauser¹⁹⁰, N. Vignaroli^{129,267}, M. Vignolo⁴³, A. Vitrano³⁹, I. Vivarelli³²⁷, S. Vlachos¹⁸², M. Vogel²⁷⁹, D.M. Vogt³²⁶, V. Völkl⁹², P. Volkov²²¹, G. Volpini^{127,266}, J. von Ahnen⁴⁹, G. Vorotnikov²²¹, G.G. Voutsinas⁶⁴, V. Vysotsky⁸, U. Wagner⁶⁴, R. Wallny⁵⁹, L.-T. Wang²⁹⁹, R. Wang¹¹, K. Wang³⁴⁷, B.F.L. Ward^{14,343}, T.P. Watson¹³⁸, N.K. Watson²⁹⁰, Z. Was⁹⁹, C. Weiland¹⁹⁶, S. Weinzierl¹⁹⁸, C.P. Welsch³⁰⁸, J. Wenninger⁶⁴, M. Widorski⁶⁴, U.A. Wiedemann⁶⁴, H.-U. Wienands¹¹, G. Wilkinson¹⁹⁰, P.H. Williams²¹¹, A. Winter²⁹⁰, A. Wohlfahrt⁷¹, T. Wojtoń⁹⁹, D. Wollmann⁶⁴, J. Womersley⁶⁶, D. Woog⁶⁴, X. Wu³⁰³, A. Wulzer^{129,267}, M.K. Yanehsari²⁰⁹, G. Yang¹⁴⁸, H.J. Yang^{219,243}, W.-M. Yao¹⁶⁰, E. Yazgan⁹⁷, V. Yermolchik⁹⁵, A. Yilmaz¹¹², A. Yilmaz⁷⁵, H.-D. Yoo²¹⁶, S.A. Yost²³⁴, T. You²⁹⁸, C. Young²²⁵, T.-T. Yu³¹⁸, F. Yu¹⁴¹, A. Zaborowska⁶⁴, S.G. Zadeh³²⁰, M. Zahnd⁵⁷, M. Zanetti^{129,267}, L. Zanutto¹¹⁶, L. Zawiejski⁹⁹, P. Zeiler⁶³, M. Zerlauth⁶⁴, S.M. Zernov⁷², G. Zevi Dell Porta²⁹⁵, Z. Zhang³², Y. Zhang³⁴¹, C. Zhang¹⁹², H. Zhang⁹⁷, Z. Zhao³²², Y.-M. Zhong¹⁸, J. Zhou^{130,269}, D. Zhou⁸¹, P. Zhuang²⁴², G. Zick³, F. Zimmermann⁶⁴, J. Zinn-Justin³⁹, L. Zivkovic²⁸⁷, A.V. Zlobin⁷⁰, M. Zobov¹¹⁵, J. Zupan³⁰⁰, J. Zurita¹⁴⁶, and the FCC Collaboration³⁵²

¹ A.I. Alikhanyan National Science Laboratory (YerPhi), Yerevan, Armenia

² Abant Izzet Baysal University (AIBU), Bolu, Turkey

³ Air Liquide Advanced Technologies (ALAT), Sassenage, France

⁴ Aix-Marseille Université (AMU), Marseille, France

⁵ Akdeniz University (UAKDENIZ), Antalya, Turkey

⁶ ALBA Synchrotron – Consorcio para la Construcción, Equipamiento y Explotación del Laboratorio de Luz Sincrotrón, Cerdanyola del Vallès (CELLS-ALBA), Cerdanyola del Vallès, Spain

⁷ Albert-Ludwigs-Universität Freiburg (UFreiburg), Freiburg, Germany

⁸ All-Russian Scientific Research and Development Cable Institute (VNIKP), Moscow, Russia

⁹ Ankara University (Ankara U), Tandogan, Ankara, Turkey

¹⁰ Applied Superconductivity Center (ASC), Tallahassee, FL, USA

¹¹ Argonne National Laboratory (ANL), Argonne, IL, USA

¹² Austrian Institute of Technology (AIT), Vienna, Austria

¹³ Banaras Hindu University (BHU), Varanasi, India

¹⁴ Baylor University (Baylor), Waco, TX, USA

¹⁵ Benemérita Universidad Autónoma de Puebla (BUAP), Puebla, Mexico

¹⁶ Bochvar Institute of Inorganic Materials (VNIINM), Moscow, Russia

¹⁷ Bogoliubov Laboratory of Theoretical Physics (BLTP JINR), Dubna, Russia

¹⁸ Boston University (BU), Boston, MA, USA

¹⁹ Boğaziçi University (BOUN), Istanbul, Turkey

- ²⁰ Brookhaven National Laboratory (BNL), Upton, NY, USA
- ²¹ Brown University (Brown), Providence, RI, USA
- ²² BRUKER EST (Bruker), Hanau, Germany
- ²³ Budker Institute of Nuclear Physics (BINP), Novosibirsk, Russia
- ²⁴ Center for High Energy Physics (CHEP), Daegu, Republic of Korea
- ²⁵ Centre de Physique des Particules de Marseille (CPPM), Marseille, France
- ²⁶ Centre d'Etudes des Tunnels (CETU), Bron, France
- ²⁷ Centre d'études et d'expertise sur les risques, l'environnement, la mobilité et l'aménagement (CEREMA), Lyon, France
- ²⁸ Centre for Industrial Studies (CSIL), Milan, Italy
- ²⁹ Centre National de la Recherche Scientifique (CNRS), Aubière, France
- ³⁰ Centre National de la Recherche Scientifique (CNRS/IN2P3), Clermont-Ferrand, France
- ³¹ Centre National de la Recherche Scientifique (CNRS), Marseille, France
- ³² Centre National de la Recherche Scientifique (CNRS), Paris, France
- ³³ Centro Brasileiro de Pesquisas Físicas (CBPF), Rio de Janeiro, Brazil
- ³⁴ Centro de Investigaciones Energéticas, Medioambientales y Tecnológicas (CIEMAT), Madrid, Spain
- ³⁵ Centro de Investigacion y de Estudios Avanzados (CINVESTAV), Meridia, Mexico
- ³⁶ Cockcroft Institute (CI Daresbury), Daresbury, UK
- ³⁷ Cockcroft Institute (CI Lancaster), Lancaster, UK
- ³⁸ Comenius University (CU), Bratislava, Slovakia
- ³⁹ Commissariat à l'énergie atomique et aux énergies alternatives – Institut de Recherche sur les lois Fondamentales de l'Univers Saclay (CEA/DSM/Irfu Saclay), Gif-sur-Yvette, France
- ⁴⁰ Commissariat à l'énergie atomique et aux énergies alternatives – Institut Nanosciences et Cryogénie (CEA), Grenoble, France
- ⁴¹ Consiglio Nazionale delle Ricerche (CNR), Milan, Italy
- ⁴² Consiglio Nazionale delle Ricerche – Superconducting and other Innovative materials and devices institute (CNR-SPIN), Genoa, Italy
- ⁴³ Consiglio Nazionale delle Ricerche – Superconducting and other Innovative materials and devices institute (CNR-SPIN), Naples, Italy
- ⁴⁴ Cornell University (Cornell), Ithaca, NY, USA
- ⁴⁵ Departamento de Física Teórica, Universidad de València (UV), València, Spain
- ⁴⁶ Departamento de Física Teórica y del Cosmos and CAFPE, Universidad de Granada (UGR), Granada, Spain
- ⁴⁷ Department of Energy (DoE), Washington, DC, USA
- ⁴⁸ Department of Physics, University of Tehran (UT), Tehran, Iran
- ⁴⁹ Deutsches Elektronen Synchrotron (DESY), Hamburg, Germany
- ⁵⁰ Deutsches Elektronen Synchrotron (DESY ZEUP), Zeuthen, Germany
- ⁵¹ Dimtel, Inc. (Dimtel), San Jose, CA, USA
- ⁵² Dipartimento di Ingegneria Civile e Meccanica, Università degli Studi di Cassino e del Lazio Meridionale (DICEM), Cassino, Italy
- ⁵³ Duke University (DU), Durham, NC, USA
- ⁵⁴ Durham University, Institute for Particle Physics Phenomenology (IPPP), Durham, UK
- ⁵⁵ Dzhelepov Laboratory of Nuclear Problems (DLNP JINR), Dubna, Russia
- ⁵⁶ Ecole polytechnique fédérale de Lausanne (EPFL), Lausanne, Switzerland
- ⁵⁷ Ecotec Environnement SA (Ecotec), Geneva, Switzerland
- ⁵⁸ Ege University (EgeU), Izmir, Turkey
- ⁵⁹ Eidgenössische Technische Hochschule Zürich (ETHZ), Zürich, Switzerland
- ⁶⁰ Eindhoven University of Technology (TU/e), Eindhoven, The Netherlands
- ⁶¹ Elle Marmi SARL (EM), Carrara, Italy
- ⁶² Eskişehir Technical University (ESTU), Istanbul, Turkey
- ⁶³ Esslingen University of Applied Sciences (HS Esslingen), Göppingen, Germany
- ⁶⁴ European Organization for Nuclear Research (CERN), Geneva, Switzerland
- ⁶⁵ European Scientific Institute (ESI), Archamps, France

- ⁶⁶ European Spallation Source (ESS), Lund, Sweden
- ⁶⁷ Fachhochschule Südwestfalen (FH-SWF), Gelsenkirchen, Germany
- ⁶⁸ Faculty of Mathematics and Physics, Charles University Prague (CU), Prague, Czech Republic
- ⁶⁹ Fayoum University (FU), El-Fayoum, Egypt
- ⁷⁰ Fermi National Accelerator Laboratory (FNAL), Batavia, IL, USA
- ⁷¹ Fraunhofer-Institut für Materialfluss und Logistik (FIML), Dortmund, Germany
- ⁷² Fuel Company of Rosatom TVEL (TVEL), Moscow, Russia
- ⁷³ Fujikura Ltd. (Fujikura), Sakura City, Japan
- ⁷⁴ Gangneung-Wonju National University (GWNU), Gangneung-Wonju, Republic of Korea
- ⁷⁵ Giresun University (Giresun), Giresun, Turkey
- ⁷⁶ Gomel State Technical University (GSTU), Gomel, Belarus
- ⁷⁷ GSI Helmholtz Zentrum für Schwerionenforschung (GSI), Darmstadt, Germany
- ⁷⁸ Gümüşhane University (Gumushane), Gümüşhane, Turkey
- ⁷⁹ Harvard University (Harvard), Cambridge, MA, USA
- ⁸⁰ Helmholtz-Zentrum Berlin (HZB), Berlin, Germany
- ⁸¹ High Energy Accelerator Research Organization (KEK), Tsukuba, Japan
- ⁸² Işık University (Isikun), Istanbul, Turkey
- ⁸³ I-Cube Research (I-Cube), Toulouse, France
- ⁸⁴ II. Institut für Theoretische Physik, Universität Hamburg (UNITH), Hamburg, Germany
- ⁸⁵ ILF Consulting Engineers (ILF), Zürich, Switzerland
- ⁸⁶ Indian Institute of Technology Guwahati (IITG), Guwahati, India
- ⁸⁷ Indian Institute of Technology Kanpur (IITK), Kanpur, Uttar Pradesh, India
- ⁸⁸ Institut de Ciència de Materials de Barcelona (ICMAB-CSIC), Barcelona, Spain
- ⁸⁹ Institut de Physique Nucléaire d'Orsay (CNRS/IN2P3/IPNO), Orsay, France
- ⁹⁰ Institute for Advanced Study (IAS), Princeton, NJ, USA
- ⁹¹ Institute for Applied Physics, Goethe University (IAP), Frankfurt, Germany
- ⁹² Institute for Astro and Particle Physics, University of Innsbruck (UIBK), Innsbruck, Austria
- ⁹³ Institute for High Energy Physics of NRC "Kurchatov Institute" (IHEP), Protvino, Russia
- ⁹⁴ Institute for Mathematics, Astrophysics and Particle Physics, Radboud University (IMAPP), Nijmegen, The Netherlands
- ⁹⁵ Institute for Nuclear Problems of Belarusian State University (INP BSU), Minsk, Belarus
- ⁹⁶ Institute of Electrical and Electronic Engineers (IEEE), Piscataway, NJ, USA
- ⁹⁷ Institute of High Energy Physics, Chinese Academy of Science, Beijing (IHEP CAS), Beijing, P.R. China
- ⁹⁸ Institute of Machine Components, University of Stuttgart (IMA), Stuttgart, Germany
- ⁹⁹ Institute of Nuclear Physics Polish Academy of Sciences (IFJ PAN), Krakow, Poland
- ¹⁰⁰ Institute of Physics, Academia Sinica (AS), Taipei, Taiwan
- ¹⁰¹ Institut Jožef Stefan (IJS), Ljubljana, Slovenia
- ¹⁰² Instituto de Astrofísica de Canarias (IAC), La Laguna, Spain
- ¹⁰³ Instituto de Física Corpuscular (CSIC-UV), Paterna, Spain
- ¹⁰⁴ Instituto de Física Corpuscular (CSIC-UV), València, Spain
- ¹⁰⁵ Instituto de Física Teórica, Universidad Autónoma de Madrid (IFT-UAM), Madrid, Spain
- ¹⁰⁶ Instituto de Física, Universitat de València (CSIC), València, Spain
- ¹⁰⁷ Instituto de Investigaciones Físicas de Mar del Plata (IFIMAR), Mar del Plata, Argentina
- ¹⁰⁸ Instituto Galego de Física de Altas Enxerxías, Universidade de Santiago de Compostela (IGFAE), Santiago de Compostela, Spain
- ¹⁰⁹ International Center for Advanced Studies, Universidad Nacional de San Martín (ICAS-UNSAM), San Martín, Argentina
- ¹¹⁰ Iowa State University (ISU), Ames, IA, USA

- ¹¹¹ Istanbul Aydin University (IAU), Istanbul, Turkey
- ¹¹² Istanbul University (IÜ), Istanbul, Turkey
- ¹¹³ Istituto Nazionale di Fisica Nucleare, Gruppo Collegato di Salerno – Sezione di Napoli (INFN SA), Salerno, Italy
- ¹¹⁴ Istituto Nazionale di Fisica Nucleare, Laboratori Nazionali del Gran Sasso (INFN LNGS), Assergi (L'Aquila), Italy
- ¹¹⁵ Istituto Nazionale di Fisica Nucleare, Laboratori Nazionali di Frascati (INFN LNF), Frascati, Italy
- ¹¹⁶ Istituto Nazionale di Fisica Nucleare, Laboratori Nazionali di Legnaro (INFN LNLN), Legnaro, Italy
- ¹¹⁷ Istituto Nazionale di Fisica Nucleare Sezione di Bari (INFN BA), Bari, Italy
- ¹¹⁸ Istituto Nazionale di Fisica Nucleare, Sezione di Bologna (INFN BO), Bologna, Italy
- ¹¹⁹ Istituto Nazionale di Fisica Nucleare, Sezione di Cagliari (INFN CA), Cagliari, Italy
- ¹²⁰ Istituto Nazionale di Fisica Nucleare, Sezione di Catania (INFN CT), Catania, Italy
- ¹²¹ Istituto Nazionale di Fisica Nucleare, Sezione di Cosenza (INFN CS), Cosenza, Italy
- ¹²² Istituto Nazionale di Fisica Nucleare, Sezione di Ferrara (INFN FE), Ferrara, Italy
- ¹²³ Istituto Nazionale di Fisica Nucleare, Sezione di Firenze (INFN FI), Florence, Italy
- ¹²⁴ Istituto Nazionale di Fisica Nucleare, Sezione di Genova (INFN GE), Genoa, Italy
- ¹²⁵ Istituto Nazionale di Fisica Nucleare, Sezione di Lecce (INFN LE), Lecce, Italy
- ¹²⁶ Istituto Nazionale di Fisica Nucleare, Sezione di Milano Bicocca (INFN MIB), Milan, Italy
- ¹²⁷ Istituto Nazionale di Fisica Nucleare, Sezione di Milano (INFN MI), Milan, Italy
- ¹²⁸ Istituto Nazionale di Fisica Nucleare, Sezione di Napoli (INFN NA), Naples, Italy
- ¹²⁹ Istituto Nazionale di Fisica Nucleare, Sezione di Padova (INFN PD), Padua, Italy
- ¹³⁰ Istituto Nazionale di Fisica Nucleare, Sezione di Pavia (INFN PV), Pavia, Italy
- ¹³¹ Istituto Nazionale di Fisica Nucleare, Sezione di Perugia (INFN PG), Perugia, Italy
- ¹³² Istituto Nazionale di Fisica Nucleare, Sezione di Pisa, Università di Pisa (INFN PI), Pisa, Italy
- ¹³³ Istituto Nazionale di Fisica Nucleare, Sezione di Roma 1 (INFN Roma 1), Rome, Italy
- ¹³⁴ Istituto Nazionale di Fisica Nucleare, Sezione di Roma Tor Vergata (INFN Roma 2), Rome, Italy
- ¹³⁵ Istituto Nazionale di Fisica Nucleare, Sezione di Roma Tre (INFN Roma 3), Rome, Italy
- ¹³⁶ Istituto Nazionale di Fisica Nucleare, Sezione di Torino (INFN TO), Turin, Italy
- ¹³⁷ Istituto Nazionale di Fisica Nucleare, Sezione di Trieste (INFN TS), Trieste, Italy
- ¹³⁸ ITER (ITER), Cadarache, France
- ¹³⁹ Ivane Javakhishvili T'bilisi State University (TSU), T'bilisi, Georgia
- ¹⁴⁰ Izmir University of Economics (IUE), Izmir, Turkey
- ¹⁴¹ Johannes-Gutenberg-Universität (JGU), Mainz, Germany
- ¹⁴² John Adams Institute for Accelerator Science, The Chancellor, Masters and Scholars of the University of Oxford (JAI), Oxford, UK
- ¹⁴³ Joint Institute for Nuclear Research (JINR), Dubna, Russia
- ¹⁴⁴ Julius-Maximilians-Universität Würzburg (UWUERZBURG), Würzburg, Germany
- ¹⁴⁵ Kahramanmaraş Sutcu Imam University (KSU), Kahramanmaraş, Turkey
- ¹⁴⁶ Karlsruher Institut für Technologie (KIT), Karlsruhe, Germany
- ¹⁴⁷ Katholieke Universiteit Leuven Research & Development (LRD), Louvain, Belgium
- ¹⁴⁸ Key Laboratory of Theoretical Physics, Chinese Academy of Science (SKLTP ITP CAS), Beijing, P.R. China
- ¹⁴⁹ King's College London (KCL), London, UK
- ¹⁵⁰ Kyoto University (Kyodai), Kyoto, Japan
- ¹⁵¹ Kyungpook National University (KNU), Sankyuk-dong, Republic of Korea
- ¹⁵² Laboratoire d'Annecy-Le-Vieux de Physique des Particules (CNRS/IN2P3/LAPP), Annecy, France
- ¹⁵³ Laboratoire de l'Accélérateur Linéaire, Université de Paris Sud (CNRS/IN2P3/UPSUD/LAL), Orsay, France
- ¹⁵⁴ Laboratoire de Physique Nucléaire et de Hautes Energies (LPNHE), Paris, France

- ¹⁵⁵ Laboratoire de Physique Subatomique et de Cosmologie Grenoble (LPSC), Grenoble, France
- ¹⁵⁶ Laboratoire de Physique Théorique et Hautes Energies (CNRS/Sorbonne/LPTHE), Paris, France
- ¹⁵⁷ Laboratoire Leprince-Ringuet, Ecole Polytechnique (LLR), Palaiseau, France
- ¹⁵⁸ Laboratório de Instrumentação e Física Experimental de Partículas (LIP), Lisbon, Portugal
- ¹⁵⁹ Latitude Durable (LD), Geneva, Switzerland
- ¹⁶⁰ Lawrence Berkeley National Laboratory (LBNL), Berkeley, CA, USA
- ¹⁶¹ Linde Kryotechnik AG (Linde), Pfungen, Switzerland
- ¹⁶² Loughborough University (LBoro), Loughborough, UK
- ¹⁶³ Ludwig Maximilians University of Munich (LMU), Munich, Germany
- ¹⁶⁴ Luvata Pori Oy (Luvata), Pori, Finland
- ¹⁶⁵ MAN Energy Solutions Schweiz AG (MAN ES), Zürich, Switzerland
- ¹⁶⁶ Marian Smoluchowski Institute of Physics, Jagiellonian University (UJ), Kraków, Poland
- ¹⁶⁷ Massachusetts Institute of Technology (MIT), Cambridge, MA, USA
- ¹⁶⁸ Max-Planck-Institut für Kernphysik (MPIK), Heidelberg, Germany
- ¹⁶⁹ Max-Planck-Institut für Physik (MPP), Munich, Germany
- ¹⁷⁰ Ministère de l'Europe et des Affaires étrangères (MEAE), Paris, France
- ¹⁷¹ Monash University (Monash), Melbourne, Australia
- ¹⁷² MTA Wigner Research Centre for Physics (Wigner), Budapest, Hungary
- ¹⁷³ Mustafa Kemal Üniversitesi (MKU), Hatay, Turkey
- ¹⁷⁴ Nankai University (NKU), Tianjin, P.R. China
- ¹⁷⁵ Nationaal instituut voor subatomaire fysica (NIKHEF), Amsterdam, The Netherlands
- ¹⁷⁶ National Centre for Scientific Research Demokritos (NCSR), Athens, Greece
- ¹⁷⁷ National High Magnetic Field Laboratory, Florida State University (MagLab), Tallahassee, FL, USA
- ¹⁷⁸ National Institute of Chemical Physics and Biophysics (NICPB), Tallin, Estonia
- ¹⁷⁹ National Research Center Kurchatov Institute (NRCKI), Moscow, Russia
- ¹⁸⁰ National Research Nuclear University MEPhI (MEPhI), Moscow, Russia
- ¹⁸¹ National Science Centre Kharkov Institute of Physics and Technology (KIPT), Kharkov, Ukraine
- ¹⁸² National Technical University of Athens (NTUA), Athens, Greece
- ¹⁸³ Naturhistorisches Museum Wien (NHM), Vienna, Austria
- ¹⁸⁴ Niels Bohr Institute, Copenhagen University (NBI), Copenhagen, Denmark
- ¹⁸⁵ Nigde Ömer Halisdemir University (OHU), Nigde, Turkey
- ¹⁸⁶ Northern Illinois University (NIU), DeKalb, IL, USA
- ¹⁸⁷ Northwestern University (NU), Evanston, IL, USA
- ¹⁸⁸ Novosibirsk State University (NSU), Novosibirsk, Russia
- ¹⁸⁹ Otto-von-Guericke-Universität Magdeburg (OVGU), Magdeburg, Germany
- ¹⁹⁰ Oxford University (UOXF), Oxford, UK
- ¹⁹¹ Paul Scherrer Institute (PSI), Villigen, Switzerland
- ¹⁹² Peking University (PU), Beijing, P.R. China
- ¹⁹³ Perimeter Institute for Theoretical Physics (PI), Waterloo, Canada
- ¹⁹⁴ Petersburg Nuclear Physics Institute, NRC "Kurchatov Institute" (PNPI), Gatchina, Russia
- ¹⁹⁵ Piri Reis University (PRU), Istanbul, Turkey
- ¹⁹⁶ Pittsburgh Particle physics, Astrophysics & Cosmology Center and Department of Physics & Astronomy, University of Pittsburgh (PITT PACC), Pittsburgh, PA, USA
- ¹⁹⁷ Princeton University (PU), Princeton, NJ, USA
- ¹⁹⁸ PRISMA Cluster of Excellence, Inst. für Physik, Johannes-Gutenberg-Universität (PRISMA), Mainz, Germany
- ¹⁹⁹ Pusan National University (PNU), Busan, Republic of Korea
- ²⁰⁰ Queen's University (Queens U), Kingston, Canada
- ²⁰¹ RAMENTOR Oy (RAMENTOR), Tampere, Finland

- 202 Rheinisch-Westfälische Technische Hochschule Aachen (RWTH), Aachen, Germany
- 203 Riga Technical University (RTU), Riga, Latvia
- 204 Royal Holloway University (RHUL), London, UK
- 205 Ruder Boskovic Institute (RBI), Zagreb, Croatia
- 206 Ruprecht Karls Universität Heidelberg (RKU), Heidelberg, Germany
- 207 Rutgers, The State University of New Jersey (RU), Piscataway, NJ, USA
- 208 Sapienza Università di Roma (UNIROMA1), Rome, Italy
- 209 School of Particles and Accelerators, Institute for Research in Fundamental Sciences (IPM), Tehran, Iran
- 210 School of Physics and Astronomy, University of Glasgow (SUPA), Glasgow, UK
- 211 Science and Technology Facilities Council, Daresbury Laboratory (STFC DL), Warrington, UK
- 212 Science and Technology Facilities Council, Appleton Laboratory (STFC RAL), Rutherford, Didcot, UK
- 213 scMetrology SARL (scMetrology), Geneva, Switzerland
- 214 Scuola Int. Superiore di Studi Avanzati di Trieste (SISSA), Trieste, Italy
- 215 Scuola Normale Superiore (SNS), Pisa, Italy
- 216 Seoul National University (SNU), Seoul, Republic of Korea
- 217 Sevanplan und Wurm Schweiz AG (WURM), Winterthur, Switzerland
- 218 Shahid Beheshti University (SBUT), Tehran, Iran
- 219 Shanghai Jiao Tong University (SJTU), Shanghai, P.R. China
- 220 Shirokuma GmbH (Shirokuma), Wetzikon, Switzerland
- 221 Skobeltsyn Institute of Nuclear Physics, Lomonosov Moscow State University (SINP MSU), Moscow, Russia
- 222 Southern Federal University (SFU), Rostov-on-Don, Russia
- 223 Southern Methodist University (SMU), Dallas, TX, USA
- 224 Sri Guru Tegh Bahadur Khalsa College, University of Delhi (SGTB Khalsa College), New Delhi, India
- 225 Stanford National Accelerator Center (SLAC), Menlo Park, CA, USA
- 226 Stanford University (SU), Stanford, CA, USA
- 227 Stony Brook University (SBU), Stony Brook, NY, USA
- 228 Technische Universität Darmstadt (TU Darmstadt), Darmstadt, Germany
- 229 Technische Universität Dortmund (TU Dortmund), Dortmund, Germany
- 230 Technische Universität Dresden (TU Dresden), Dresden, Germany
- 231 Technische Universität Graz (TU Graz), Graz, Austria
- 232 Technische Universität Wien (TU Wien), Vienna, Austria
- 233 Tel Aviv University (TAU), Tel Aviv, Israel
- 234 The Citadel, The Military College of South Carolina (Citadel), Charleston, SC, USA
- 235 The Pennsylvania State University (PSU), University Park, PA, USA
- 236 The University of Tokyo (Todai), Tokyo, Japan
- 237 Thomas Jefferson National Accelerator Facility (JLab), Newport News, VA, USA
- 238 TOBB University of Economics and Technology (TOBB ETU), Ankara, Turkey
- 239 Tokyo Institute of Technology (Tokyo Tech), Tokyo, Japan
- 240 Trinity College Dublin (TCD), Dublin, Ireland
- 241 Tri-University Meson Facility (TRIUMF), Vancouver, Canada
- 242 Tsinghua University (THU), Beijing, P.R. China
- 243 Tsung-Dao Lee Institute (TDLI), Shanghai, P.R. China
- 244 Uludag University (ULUÜ), Bursa, Turkey
- 245 Universidad Autónoma de Sinaloa (UAS), Culiacán, Mexico
- 246 Universidad de Guanajuato (UGTO), Guanajuato, Mexico
- 247 Universidad de La Laguna (ULL), La Laguna, Spain
- 248 Universidad de la República (Udelar), Montevideo, Uruguay
- 249 Universidad de los Andes (Uniandes), Bogotá, Colombia
- 250 Universidade de São Paulo (USP), São Paulo, Brazil
- 251 Universidade do Estado do Rio de Janeiro (UERJ), Rio de Janeiro, Brazil

- 252 Universidade Federal de Pelotas (UFPel), Pelotas, Brazil
- 253 Universidade Federal de Rio de Janeiro (UFRJ), Rio de Janeiro, Brazil
- 254 Università degli Studi Roma Tre – Centro Ricerche Economiche e Sociali Manlio Rossi-Doria (EDIRC), Rome, Italy
- 255 Università della Calabria (UNICAL), Arcavacata, Italy
- 256 Università del Salento (UNISALENTO), Lecce, Italy
- 257 Università di Bari (UNIBA), Bari, Italy
- 258 Università di Bologna (UNIBO), Bologna, Italy
- 259 Università di Cagliari (UNICA), Cagliari, Italy
- 260 Università di Catania (UNICT), Catania, Italy
- 261 Università di Ferrara (UNIFE), Ferrara, Italy
- 262 Università di Firenze (UNIFI), Florence, Italy
- 263 Università di Genova (UNIGE), Genoa, Italy
- 264 Università di Insubria (UNINSUBRIA), Milan, Italy
- 265 Università di Lecce (UNILE), Lecce, Italy
- 266 Università di Milano (UNIMI), Milan, Italy
- 267 Università di Padova (UNIPD), Padua, Italy
- 268 Università di Parma (UNIPR), Parma, Italy
- 269 Università di Pavia (UNIPV), Pavia, Italy
- 270 Università di Perugia (UNIPG), Perugia, Italy
- 271 Università di Roma Sapienza (UNIROMA1), Rome, Italy
- 272 Università di Roma Tor Vergata (UNIROMA2), Rome, Italy
- 273 Università di Roma Tre (UNIROMA3), Rome, Italy
- 274 Università di Torino (UNITO), Turin, Italy
- 275 Università di Udine (UNIUD), Udine, Italy
- 276 Universität Hamburg (UHH), Hamburg, Germany
- 277 Universität Heidelberg (HEI), Heidelberg, Germany
- 278 Universitat Politècnica de Catalunya (UPC), Barcelona, Spain
- 279 Universität Siegen (U Siegen), Siegen, Germany
- 280 Universität Tübingen (TU), Tübingen, Germany
- 281 Université Clermont Auvergne (UCA), Aubière, France
- 282 Université Grenoble Alpes (UGA), Grenoble, France
- 283 University College London (UCL), London, UK
- 284 University of Applied Sciences Technikum Wien (UAS TW), Vienna, Austria
- 285 University of Arizona (UA), Tucson, AZ, USA
- 286 University of Basel (UNIBAS), Basel, Switzerland
- 287 University of Belgrade (UB), Belgrade, Serbia
- 288 University of Bergen (UiB), Bergen, Norway
- 289 University of Bern (UNIBE), Bern, Switzerland
- 290 University of Birmingham (UBIRM), Birmingham, UK
- 291 University of Bristol (UOB), Bristol, UK
- 292 University of California Berkeley (UCB), Berkeley, CA, USA
- 293 Davis (UCD), University of California, Davis, CA, USA
- 294 Irvine (UCI), University of California, Irvine, CA, USA
- 295 San Diego (UCSD), University of California, San Diego, CA, USA
- 296 University of California Santa Barbara (UCSB), Santa Barbara, CA, USA
- 297 University of California Santa Cruz (UCSC), Santa Cruz, CA, USA
- 298 University of Cambridge (CAM), Cambridge, UK
- 299 University of Chicago (UCHI), Chicago, IL, USA
- 300 University of Cincinnati (UC), Cincinnati, OH, USA
- 301 University of Edinburgh (ED), Edinburgh, UK
- 302 University of Florida (UF), Gainesville, FL, USA
- 303 University of Geneva (UniGE), Geneva, Switzerland
- 304 University of Illinois at Urbana Champaign (UIUC), Urbana Champaign, IL, USA
- 305 University of Iowa (UIowa), Iowa City, IA, USA

- 306 University of Jyväskylä (JYU), Jyväskylä, Finland
- 307 University of Kansas (KU), Lawrence, KS, USA
- 308 University of Liverpool (ULIV), Liverpool, UK
- 309 University of Lund (ULU), Lund, Sweden
- 310 University of Malta (UM), Msida, Malta
- 311 University of Manchester (UMAN), Manchester, UK
- 312 University of Maryland (UMD), College Park, MD, USA
- 313 University of Massachusetts-Amherst (UMass), Amherst, MA, USA
- 314 University of Melbourne (UniMelb), Melbourne, Australia
- 315 University of Michigan (UMich), Ann Arbor, MI, USA
- 316 University of New Mexico (NMU), Albuquerque, NM, USA
- 317 University of Notre Dame du Lac (ND), South Bend, IA, USA
- 318 University of Oregon (UO), Eugene, OR, USA
- 319 University of Rochester (Rochester), Rochester, NY, USA
- 320 University of Rostock (U Rostock), Rostock, Germany
- 321 University of Saskatchewan (USASK), Saskatoon, Canada
- 322 University of Science and Technology of China (USTC), Hefei, P.R. China
- 323 University of Science and Technology of Mazandaran (USTM), Behshahr, Iran
- 324 University of Silesia (USKAT), Katowice, Poland
- 325 University of Stavanger (UiS), Stavanger, Norway
- 326 University of Stuttgart (USTUTT), Stuttgart, Germany
- 327 University of Sussex (US), Brighton, UK
- 328 University of the Witwatersrand (WITS), Johannesburg, South Africa
- 329 University of Toronto (UToronto), Toronto, Canada
- 330 University of Warsaw (UW), Warszawa, Poland
- 331 University of Wisconsin-Madison (WISC), Madison, WI, USA
- 332 University of Würzburg (U Würzburg), Würzburg, Germany
- 333 University of Zürich (UZH), Zürich, Switzerland
- 334 University Rey Juan Carlos (URJC), Madrid, Spain
- 335 Univ. Lyon 1, CNRS/IN2P3, Institut de Physique Nucléaire de Lyon (CNRS/IN2P3/IPNL), Lyon, France
- 336 Uppsala University (UU), Uppsala, Sweden
- 337 Usak University (Usak), Usak, Turkey
- 338 Vienna University of Economics and Business (WU), Vienna, Austria
- 339 Vinca Institute of Nuclear Sciences (Vinca), Belgrade, Serbia
- 340 Vrije Universiteit Brussel (VUB), Brussels, Belgium
- 341 Washington University (WUSTL), St. Louis, MO, USA
- 342 Weizmann Institute (Weizmann), Rehovot, Israel
- 343 Max-Planck-Institut für Physik (MPP), Werner-Heisenberg-Institut, Munich, Germany
- 344 Westfälische Wilhelms-Universität Münster (WWU), Münster, Germany
- 345 West Pomeranian University of Technology (ZUT), Szczecin, Poland
- 346 Wrocław University of Science and Technology (PWR), Wrocław, Poland
- 347 Wuhan University of Technology (WHUT), Wuhan, P.R. China
- 348 Department of Physic (ZIMP), Zhejiang Institute of Modern Physics, Hangzhou, P.R. China
- 349 Zhejiang University (ZJU), Hangzhou, P.R. China
- 350 University of Colorado Boulder (CU Boulder), Boulder, CO, USA
- 351 Pittsburgh University (PITT), Pittsburgh, USA
- 352 fcc.secretariat@cern.ch

Received 20 December 2018

Published online 10 June 2019

Abstract. In response to the 2013 Update of the European Strategy for Particle Physics, the Future Circular Collider (FCC) study was launched, as an international collaboration hosted by CERN. This study covers a highest-luminosity high-energy lepton collider (FCC-ee) and an energy-frontier hadron collider (FCC-hh), which could, successively, be installed in the same 100 km tunnel. The scientific capabilities of the integrated FCC programme would serve the worldwide community throughout the 21st century. The FCC study also investigates an LHC energy upgrade, using FCC-hh technology. This document constitutes the second volume of the FCC Conceptual Design Report, devoted to the electron-positron collider FCC-ee. After summarizing the physics discovery opportunities, it presents the accelerator design, performance reach, a staged operation scenario, the underlying technologies, civil engineering, technical infrastructure, and an implementation plan. FCC-ee can be built with today's technology. Most of the FCC-ee infrastructure could be reused for FCC-hh. Combining concepts from past and present lepton colliders and adding a few novel elements, the FCC-ee design promises outstandingly high luminosity. This will make the FCC-ee a unique precision instrument to study the heaviest known particles (Z, W and H bosons and the top quark), offering great direct and indirect sensitivity to new physics.

^a e-mail: Michael.Benedikt@cern.ch

Preface

The 2013 Update of the European Strategy for Particle Physics (ESPPU) [1] stated, inter alia, that “... *Europe needs to be in a position to propose an ambitious post-LHC accelerator project at CERN by the time of the next Strategy update*” and that “*CERN should undertake design studies for accelerator projects in a global context, with emphasis on proton-proton and electron-positron high-energy frontier machines. These design studies should be coupled to a vigorous accelerator R&D programme, including high-field magnets and high-gradient accelerating structures, in collaboration with national institutes, laboratories and universities worldwide*”.

In response to this recommendation, the Future Circular Collider (FCC) study was launched [2] as a world-wide international collaboration under the auspices of the European Committee for Future Accelerators (ECFA). The FCC study was mandated to deliver a Conceptual Design Report (CDR) in time for the following update of the European Strategy for Particle Physics.

European studies of post-LHC circular energy-frontier accelerators at CERN had actually started a few years earlier, in 2010–2013, for both hadron [3–5] and lepton colliders [6–8], at the time called HE-LHC/VHE-LHC and LEP3/DLEP/TLEP, respectively. In response to the 2013 ESPPU, in early 2014 these efforts were combined and expanded into the FCC study.

The 2013 ESPPU recognised the importance of electron-positron colliders for the precise measurement of the properties of the Higgs boson. Since its inception, the international FCC collaboration has worked on delivering the conceptual design for a staged e^+e^- collider (FCC-ee) that would allow detailed studies of the heaviest known particles (Z, W and H bosons and the top quark) and offer great direct and indirect sensitivity to new physics.

Five years of intense work and a steadily growing international collaboration have resulted in the present Conceptual Design Report, consisting of four volumes covering the physics opportunities, technical challenges, cost and schedule of several different circular colliders, some of which could be part of an integrated programme extending until the end of the 21st century.

Geneva, December 2018



Rolf Heuer
CERN Director-General 2009–2015



Fabiola Gianotti
CERN Director-General since 2016

Contents

1	Physics discovery potential	290
1.1	Overview	290
1.2	Precision electroweak measurements	293
1.2.1	Current situation	293
1.2.2	Opportunities at the Z pole	295
1.2.3	Opportunities at the $W^+ W^-$ and $t\bar{t}$ threshold	298
1.2.4	Additional opportunities	300
1.2.5	Global electroweak Fit	301
1.3	The Higgs boson	303
1.3.1	Absolute coupling determination from the Higgs branching fractions	303
1.3.2	Additional opportunities	306
1.4	Discovery potential for new physics	309
1.4.1	Generic constraints on effective interactions from precision measurements	309
1.4.2	Sensitivity to new physics predicted in specific BSM models	313
1.5	Requirements	320
1.5.1	Collider	320
1.5.2	Detectors	322
1.5.3	Theory	323
2	Collider design and performance	324
2.1	Requirements and design considerations	324
2.2	Layout and key parameters	324
2.2.1	Layout	324
2.2.2	Beam parameter optimisation	326
2.3	Design challenges and approaches	330
2.3.1	Synchrotron radiation	330
2.3.2	Tapering	331
2.3.3	Dynamic aperture, beam lifetime, top-up injection	331
2.3.4	Low emittance tuning and optics correction	331
2.4	Optics design and beam dynamics	333
2.4.1	Lattices	333
2.4.2	Interaction region	335
2.4.3	RF section and other straight sections	337
2.4.4	Dynamic aperture	338
2.4.5	Tolerances and optics tuning	342
2.4.6	Improving dynamic and momentum aperture using PSO and machine learning	343
2.5	Machine detector interface	346
2.5.1	Overall layout of the interaction region	346
2.5.2	Magnet systems	349
2.5.3	Luminometer	350
2.5.4	Synchrotron radiation	350
2.5.5	Beamstrahlung, radiative bhabha scattering	352
2.6	Collective effects	353
2.6.1	Introduction	353
2.6.2	Impedance budget	353
2.6.3	Resistive wall impedance	353
2.6.4	RF cavities and tapers	353
2.6.5	Synchrotron radiation absorbers	354
2.6.6	Collimators	354

2.6.7	Beam position monitors	355
2.6.8	RF shielding	355
2.6.9	Overall impedance budget	356
2.6.10	Single bunch instabilities	356
2.6.11	Microwave instability	357
2.6.12	Transverse mode-coupling instability	359
2.6.13	Multi-bunch instabilities	359
2.6.14	Bunch-by-bunch feedback	360
2.6.15	Interaction region impedance budget	362
2.6.16	Electron cloud	363
2.6.17	Fast beam-ion instability	366
2.7	Energy calibration and polarisation	368
2.8	Injection and extraction	374
2.8.1	Top-up injection	374
2.8.2	Extraction and beam dump	376
2.9	Operation and performance	376
2.9.1	Efficiency	376
2.9.2	Physics goals	376
2.9.3	Estimated annual performance	377
2.9.4	Radiofrequency system staging	378
2.9.5	Luminosity parameters and operation plan	379
2.9.6	Benchmarking against performance of past and present colliders	379
2.10	Running at other energies	385
2.10.1	s -channel H Production	385
2.10.2	Higher collision energy	387
3	Collider technical systems	387
3.1	Introduction	387
3.2	Main magnet system	387
3.2.1	Introduction	387
3.2.2	Main dipole magnets	388
3.2.3	Main quadrupole magnets	390
3.2.4	Main sextupole magnets	393
3.2.5	Main magnet powering	393
3.2.6	Interaction region and final focus quadrupoles	395
3.2.7	Final-focus quadrupoles	396
3.2.8	Final-focus sextupoles	398
3.2.9	Polarisation wigglers	398
3.2.10	Magnets for the booster	400
3.3	Vacuum system and electron-cloud mitigation	401
3.3.1	Introduction	401
3.3.2	Arc vacuum system	401
3.3.3	Interaction-region vacuum system	405
3.3.4	Local beam-pipe shielding	406
3.4	Radiofrequency system	408
3.4.1	Overview	408
3.4.2	Superconducting cavities	411
3.4.3	Powering	412
3.4.4	Feedback	414
3.4.5	Low-level RF	414
3.4.6	Staging	414
3.4.7	Beam-cavity interaction and beam dynamics issues	416
3.5	Beam transfer systems	417
3.5.1	Introduction	418

3.5.2	Injection system	418
3.5.3	Beam abort system	421
3.5.4	Parameter tables	422
3.6	Beam diagnostics requirements and concepts	422
3.6.1	Beam position monitoring	425
3.6.2	Beam size monitoring	425
3.6.3	Bunch length monitoring	426
3.6.4	Beam current and intensity measurements	426
3.6.5	Beam loss monitoring	427
3.6.6	Topics for further study	427
3.7	Combined polarimeter and spectrometer	427
3.8	Halo collimators	432
3.9	Machine protection	432
3.9.1	Architecture and powering of magnet circuits	432
3.9.2	Magnet protection and energy extraction	432
3.9.3	Beam protection concepts	433
3.10	Controls requirements and concepts	433
3.11	Radiation environment	435
3.11.1	Reference radiation levels	435
3.11.2	Radiation hardness	436
3.11.3	Radiation-hard technology trends	437
4	Civil engineering	439
4.1	Requirements and design considerations	439
4.2	Layout and placement	439
4.2.1	Layout	439
4.2.2	Placement	440
4.2.3	Necessary site investigations	442
4.3	Underground structures	443
4.3.1	Tunnels	443
4.3.2	Shafts	445
4.3.3	Alcoves	446
4.3.4	Experiment caverns	446
4.3.5	Service caverns	446
4.3.6	Junction caverns	447
4.4	Surface sites	447
4.4.1	Experiment surface sites	447
4.4.2	Technical surface sites	447
4.4.3	Access roads	448
5	Technical infrastructure	448
5.1	Requirements and design considerations	448
5.2	Piped utilities	448
5.2.1	Introduction	448
5.2.2	Water cooling	449
5.2.3	Operational parameters	450
5.2.4	Chilled water	451
5.2.5	Drinking water	452
5.2.6	Fire fighting network	452
5.2.7	Reject water	452
5.2.8	Compressed air	453
5.3	Heating, ventilation, air conditioning	453
5.3.1	Overall design concept	453
5.3.2	Interior conditions	453
5.3.3	Ventilation of underground areas	453

5.3.4	Machine tunnel	454
5.3.5	Experiment caverns	455
5.3.6	Other areas	455
5.3.7	Operating modes	455
5.3.8	Working parameters	456
5.3.9	Ventilation of surface buildings	457
5.3.10	Safety	457
5.4	Electricity distribution	458
5.4.1	Conceptual layout	458
5.4.2	Source of electrical energy	458
5.4.3	Transmission network topology	458
5.4.4	Distribution network topology	460
5.4.5	Power quality and transient voltage dip mitigation	460
5.5	Emergency power	462
5.6	Cryogenic system	464
5.6.1	Overview	464
5.6.2	Functions and constraints	464
5.6.3	Layout and architecture	465
5.6.4	Temperature levels	466
5.6.5	Heat loads	467
5.6.6	Cooling scheme and cryogenic distribution	467
5.6.7	Cryogenic plants	468
5.6.8	Cryogen inventory and storage	469
5.7	Equipment transport and handling	469
5.7.1	Underground vehicles	469
5.7.2	Overhead cranes	470
5.7.3	Lifts	472
5.8	Personnel transport	473
5.8.1	Transport for emergency services	473
5.9	Geodesy, survey and alignment	474
5.9.1	Introduction	474
5.9.2	Alignment tolerances	474
5.9.3	Geodesy	475
5.9.4	Metrological aspects	475
5.9.5	Alignment of accelerator components	476
5.9.6	Interaction regions and collimator areas	477
5.9.7	Experiments	477
5.10	Communications, computing and data services	477
5.11	Safety and access management systems	481
6	Injector complex	482
6.1	Injector overview	482
6.2	Electron gun	484
6.3	Linac	484
6.4	Linac at 20 GeV	487
6.5	Positron source and capture system	488
6.6	Damping ring	490
6.7	Bunch compressors	492
6.8	Pre-booster	493
6.9	Booster	494
6.10	Transfer lines	496
7	Experiment environment and detector designs	497
7.1	Experiment environment	497
7.1.1	Synchrotron radiation	497

7.1.2	Pair-production background	499
7.2	Luminometer	499
7.2.1	Design	500
7.2.2	Acceptance and luminosity measurement	502
7.2.3	Electromagnetic focussing of bhabha electrons	503
7.2.4	Machine and beam-induced backgrounds in the luminometer	503
7.3	The CLD detector design	504
7.3.1	CLD tracking system	504
7.3.2	Backgrounds in the CLD tracking system	506
7.3.3	CLD calorimetry	507
7.3.4	CLD Muon system	507
7.4	IDEA detector concept	508
7.4.1	IDEA vertex detector	508
7.4.2	IDEA drift chamber	509
7.4.3	IDEA tracking system performance	510
7.4.4	Backgrounds in the IDEA tracking system	510
7.4.5	IDEA preshower detector	511
7.4.6	IDEA dual-readout calorimeter	512
7.4.7	IDEA muon system	513
7.5	Detector magnet systems	513
7.5.1	The CLD detector magnet	513
7.5.2	The IDEA Detector Magnet	513
7.6	Constraints on readout systems	515
7.7	Infrastructure requirements	516
8	Safety	517
8.1	Safety policy and regulatory framework	517
8.1.1	Legal context of CERN	517
8.1.2	Hazard register and safety performance based design	517
8.2	Occupational health and safety	518
8.2.1	Fire hazard	518
8.2.2	Oxygen deficiency	520
8.3	Radiation protection	520
8.3.1	Particle beam operation	521
8.3.2	Activation of solids	521
8.3.3	Activated or contaminated liquids	522
8.3.4	Activated or radioactive gases and radioactive aerosols	522
9	Energy efficiency	522
9.1	Requirements and design considerations	522
9.2	Power requirements	523
9.3	Energy management and saving	525
9.4	Waste heat recovery	526
10	Environment	528
10.1	Requirements and approach considerations	528
10.1.1	Legal context	528
10.1.2	Environmental compatibility management concept	529
10.2	Environmental impact	530
10.2.1	Radiological impact	530
10.2.2	Conventional impact	531
10.3	Waste management	532
10.3.1	Radioactive waste management	532
10.3.2	Conventional waste management	533
11	Education, economy and society	534
11.1	Implementation with the host states	534

11.1.1 Overview	534
11.1.2 France	536
11.1.3 Switzerland	538
11.2 Socio-economic opportunities	539
11.2.1 Introduction and motivation	539
11.2.2 The value of training	540
11.2.3 Opportunities for industries and technological spillover	541
11.2.4 Cultural effects	544
11.2.5 Impact potential	546
12 Strategic research and development	547
12.1 Introduction	547
12.2 High efficiency radiofrequency power sources	548
12.3 High efficiency superconducting radiofrequency cavities	549
12.4 Energy storage and release R&D	551
12.5 Efficient power distribution infrastructure	553
12.6 Efficient use of excavation materials	555
Appendix A: Theoretical physics computations	559
Appendix B: Uncertainties	561
B.1 Accelerator and technologies	561
B.2 Implementation	564
Appendix C: Communities	567
Appendix D: Timeline	570
Appendix E: Costs	571
E.1 Construction costs	571
E.2 Operation costs	571

Executive summary

Overview

Particle physics has arrived at an important moment in its history. The discovery of the 125 GeV Higgs boson completes the matrix of particles and interactions that has constituted the “Standard Model” for several decades. This model is a consistent and predictive theory, which has so far proven successful at describing all phenomena accessible to collider experiments. On the other hand, several experimental facts require the extension of the Standard Model and explanations are needed for observations such as the domination of matter over antimatter, the evidence for dark matter and the non-zero neutrino masses. Theoretical issues that need to be addressed include the hierarchy problem, the neutrality of the Universe, the stability of the Higgs boson mass upon quantum corrections and the strong CP problem.

This report contains the description of a novel research infrastructure based on a highest-luminosity energy frontier electron-positron collider (FCC-ee) to address the open questions of modern physics. It will be a general precision instrument for the continued in-depth exploration of nature at the smallest scales, optimised to study with high precision the Z, W, Higgs and top particles, with samples of 5×10^{12} Z bosons, 10^8 W pairs, 10^6 Higgs bosons and 10^6 top quark pairs. The FCC-ee offers unprecedented sensitivity to signs of new physics, appearing in the form of small deviations from the Standard Model, of forbidden decay processes, or of production of new particles with very small couplings.

This collider will be implemented in stages, successively spanning the entire energy range from the Z pole over the WW threshold and HZ production peak

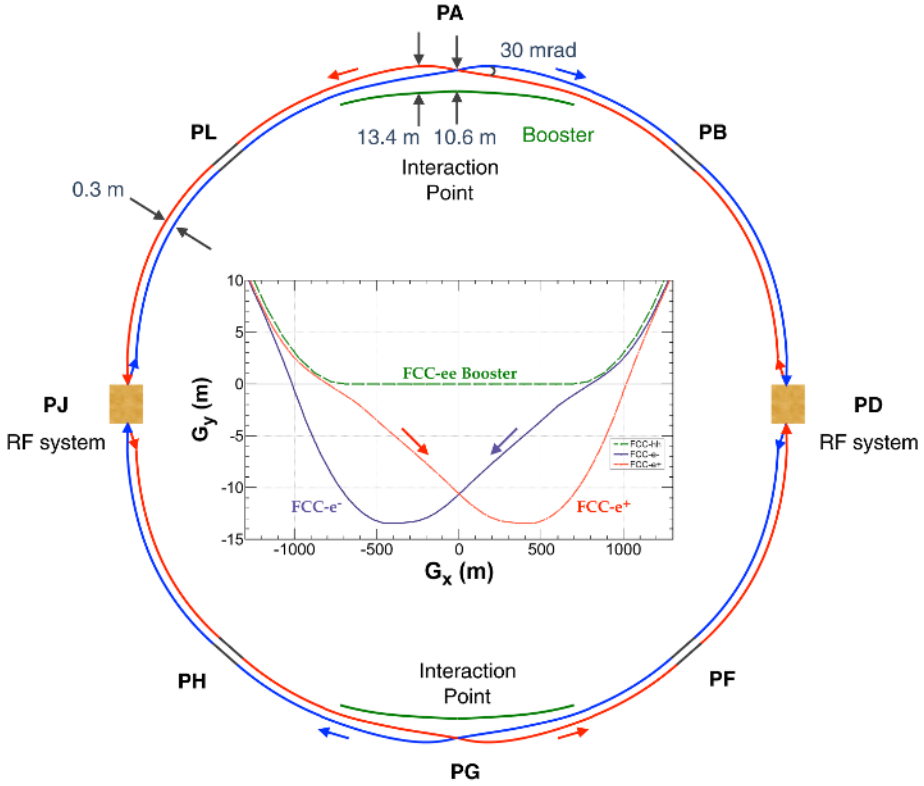


Fig. 1. Overall layout of the FCC-ee with a zoomed view of the trajectories across interaction point G. The FCC-ee rings are placed 1 m outside the FCC-hh footprint (used for the booster and indicated in green colour in the figure) in the arc. In the arc the e^+ and e^- rings are horizontally separated by 30 cm. The main booster follows the footprint of the FCC-hh collider ring. The interaction points are shifted by 10.6 m towards the outside of FCC-hh. The beam trajectories toward the IP are straighter than the outgoing ones in order to reduce the synchrotron radiation at the IP.

to the $t\bar{t}$ threshold and above. Most of the infrastructure (e.g. underground structures, surface sites, electrical distribution, cooling & ventilation, RF systems) can be directly reused for a subsequent highest-energy hadron collider (described in the FCC Conceptual Design Report volume 3). The complex will thus serve the world-wide particle-physics community in a highly synergetic and cost-effective manner throughout the 21st century.

The European Strategy for Particle Physics (ESPP) 2013 update stated “*To stay at the forefront of particle physics, Europe needs to be in a position to propose an ambitious post-LHC accelerator project at CERN by the time of the next Strategy update*”. The FCC study has implemented the ESPP recommendation by developing a long-term vision for an “*accelerator project in a global context*”. This document describes the detailed design and preparation of a construction project for a post-LHC circular lepton collider “*in collaboration with national institutes, laboratories and universities worldwide*”, and enhanced by a strong participation of industrial partners. A coordinated preparation effort can now be based on a core of an ever-growing consortium of already more than 135 institutes world-wide.

Table 1. Machine parameters of the FCC-ee for different beam energies.

	Z	WW	ZH	tt	
Circumference (km)			97.756		
Bending radius (km)			10.760		
Free length to IP l^* (m)			2.2		
Solenoid field at IP (T)			2.0		
Full crossing angle at IP θ (mrad)			30		
SR power/beam (MW)			50		
Beam energy (GeV)	45.6	80	120	175	182.5
Beam current (mA)	1390	147	29	6.4	5.4
Bunches/beam	16 640	2000	328	59	48
Average bunch spacing (ns)	19.6	163	994	2763	3396
Bunch population (10^{11})	1.7	1.5	1.8	2.2	2.3
Horizontal emittance ε_x (nm)	0.27	0.84	0.63	1.34	1.46
Vertical emittance ε_y (pm)	1.0	1.7	1.3	2.7	2.9
Horizontal β_x^* (m)	0.15	0.2	0.3	1.0	
Vertical β_y^* (mm)	0.8	1.0	1.0	1.6	
Energy spread (SR/BS) σ_δ (%)	0.038/0.132	0.066/0.131	0.099/0.165	0.144/0.186	0.150/0.192
Bunch length (SR/BS) σ_z (mm)	3.5/12.1	3.0/6.0	3.15/5.3	2.01/2.62	1.97/2.54
Piwinski angle (SR/BS) ϕ	8.2/28.5	3.5/7.0	3.4/5.8	0.8/1.1	0.8/1.0
Energy loss/turn (GeV)	0.036	0.34	1.72	7.8	9.2
RF frequency (MHz)	400			400/800	
RF voltage (GV)	0.1	0.75	2.0	4.0/5.4	4.0/6.9
Longitudinal damping time (turns)	1273	236	70.3	23.1	20.4
Energy acceptance (DA) (%)	± 1.3	± 1.3	± 1.7	$-2.8 + 2.4$	
Polarisation time t_p (min)	15000	900	120	18.0	14.6
Luminosity/IP ($10^{34}/\text{cm}^2\text{s}$)	230	28	8.5	1.8	1.55
Beam-beam ξ_x/ξ_y	0.004/0.133	0.010/0.113	0.016/0.118	0.097/0.128	0.099/0.126
Beam lifetime by rad. Bhabha scattering (min)	68	59	38	40	39
Actual lifetime incl. beam-strahlung (min)	>200	>200	18	24	18

Notes. For $t\bar{t}$ operation a common RF system is used.

Accelerator

The FCC-ee accelerator design provides a high luminosity at each of many different collision energies, between 88 and 365 GeV, while satisfying several stringent constraints. Apart from a ± 1.2 km-long section around each interaction point (IP), the machine follows the layout of the 97.75 km circumference hadron collider [9]. The present design houses two interaction points. The synchrotron radiation power is limited to 50 MW per beam at all energies.

Machine design and layout

For a collision energy of 365 GeV, as required for $t\bar{t}$ operation, the cost-optimised circumference is about 100 km [10]. The FCC-ee is designed as a double ring collider, like the KEKB and PEP-II B factories. The double-ring configuration allows a large number of bunches (Fig. 1 shows the layout). The two beam lines cross at two interaction points (IPs) with a horizontal crossing angle of 30 mrad. Profiting from the crossing angle, a crab waist collision scheme [11,12] is adopted, which enables an extremely small vertical beta function β_y^* at the IP (about 50 times smaller than at LEP) and a high beam-beam tune shift. This novel collision scheme has been successfully used at DAΦNE since 2008/09. The critical energy of the synchrotron radiation of the incoming beams towards the IP is kept below 100 keV at all beam energies. A common lattice is used for all beam energies, except for a small rearrangement in the RF section for the $t\bar{t}$ mode. The betatron tune, phase advance in the arc cell, final focus optics and the configuration of the sextupoles are set to the optimum at each energy by changing the strengths of the magnets. The two experiments are situated in points A and G. The length of the free area around the IP (ℓ^*) and the strength of the detector solenoid are kept constant at 2.2 m and 2 T, respectively, for all energies. A “tapering” scheme scales the strengths of all magnets, apart from the solenoids, according to the local beam energy, taking into account the energy loss due to synchrotron radiation. Two RF sections per ring are placed in the straight sections at points D and J. The RF cavities will be common to e^+ and e^- in the case of $t\bar{t}$.

Parameters

The FCC-ee machine parameters are compiled in Table 1. The beam current varies greatly between the Z pole and the $t\bar{t}$ threshold. The current is adjusted primarily by changing the number of bunches. In present electron storage rings, the equilibrium beam parameters are determined by synchrotron radiation (SR) generated in the dipoles of the collider arcs. For the FCC-ee, the energy spread and the beam lifetime are also affected by beamstrahlung (BS), which is a special type of synchrotron radiation, emitted during the collision due to the field of the opposite bunch.

Injection

A top-up injection scheme maintains the stored beam current and the luminosity at the highest level throughout the physics run. Without top-up injection the integrated luminosity would be more than an order of magnitude lower. It is, therefore, necessary to install a booster synchrotron in the collider tunnel.

Injection into the top-up booster takes place at 20 GeV, similar to injection into LEP. The layout of the pre-injector complex resembles the KEKB/SuperKEKB injector. For the FCC-ee, it consists of a 6 GeV normal-conducting S-band linac, a prebooster (possibly the SPS) which accelerates the electron and positron beams from 6 to 20 GeV, a positron source, where 4.46 GeV electrons from the linac are sent onto a hybrid target with flux concentrator, and a small positron damping ring. The linac will accelerate 1 or 2 bunches per pulse at a repetition rate of 100 or 200 Hz. The complete filling for Z running is the most demanding with respect to the number of bunches, bunch intensity and therefore injector flux. It requires a linac bunch intensity of 2×10^{10} particles for both species. The positron rate required is similar to the rates at SuperKEKB and the SLC. Alternative injector scenarios could include a longer 20 GeV linac, without any pre-booster, or a recirculating SC linac.

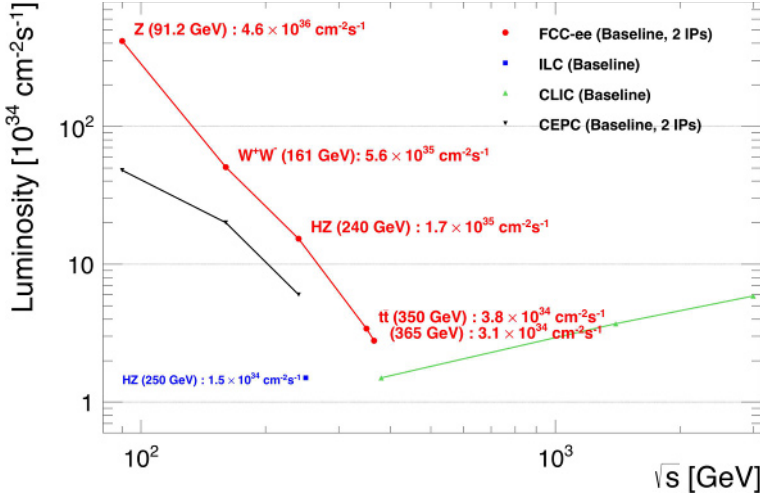


Fig. 2. Baseline luminosities expected to be delivered (summed over all interaction points) as a function of the centre-of-mass energy \sqrt{s} , at each of the four worldwide e^+e^- collider projects: ILC (blue square), CLIC (green upward triangles), CEPC (black downward triangles), and FCC-ee (red dots), drawn with a 10% safety margin. The FCC-ee performance data are taken from this volume, the latest incarnation of the CEPC parameters is inferred from [20], and the linear collider luminosities are taken from [15,17].

Performance

As a result of the renewed worldwide interest for e^+e^- physics and the pertaining discovery potential since the observation of the Higgs boson at the LHC, the FCC is not alone in its quest. Today four e^+e^- collider designs are contemplated to study the properties of the Higgs boson and other standard model (SM) particles with an unprecedented precision: the International Linear Collider (ILC [13]) project with a centre-of-mass energy of 250 GeV [14,15]; the Compact Linear Collider (CLIC [16]), whose lowest centre-of-mass energy point was reduced from 500 to 380 GeV [17]; the Circular Electron Positron Collider (CEPC [18–20]), in a 100 km tunnel in China, with centre-of-mass energies from 90 to 250 GeV; and the Future e^+e^- Circular Collider in a new ~ 100 km tunnel at CERN (FCC-ee, formerly called TLEP [8,21]). The baseline luminosities expected to be delivered at the ILC, CLIC, CEPC, and FCC-ee centre-of-mass energies are illustrated in Figure 2.

The expected integrated luminosities and operation phases at each energy are illustrated in Figure 3. The FCC-ee delivers the highest rates in a clean, well-defined, and precisely predictable environment, at the Z pole (91 GeV), at the WW threshold (161 GeV), as a Higgs factory (240 GeV), and around the $t\bar{t}$ threshold (340–365 GeV), to two interaction points. Thanks to the availability of transverse polarisation up to over 80 GeV beam energy, it also provides high precision centre-of-mass energy calibration at the 100 keV level at the Z and W energies, a unique feature of circular colliders. The FCC-ee is, therefore, genuinely best suited to offer extreme statistical precision and experimental accuracy for the measurements of the standard model particle properties, it opens windows to detect new rare processes, and it furnishes opportunities to observe tiny violations of established symmetries.

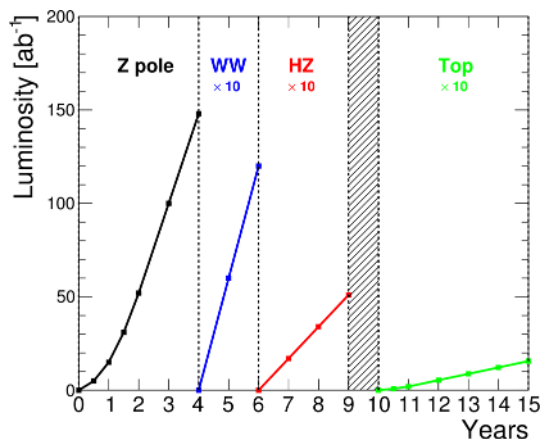


Fig. 3. Operation model for the FCC-ee, resulting from the five year conceptual design study, showing the integrated luminosity at the Z pole (black), the WW threshold (blue), the Higgs factory (red), and the top-pair threshold (green) as a function of time. The hatched area indicates the shutdown time needed to prepare the collider for the highest energy runs.

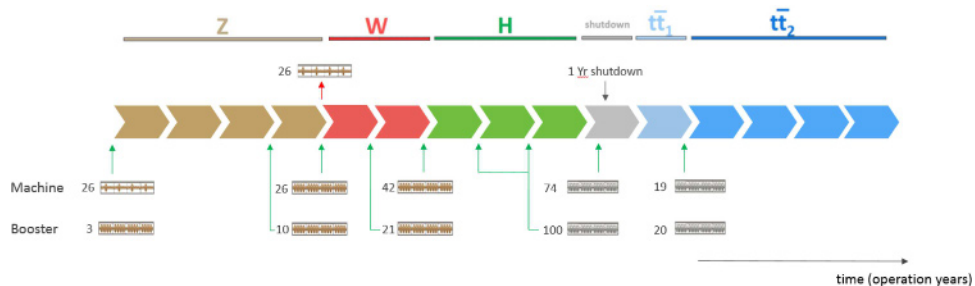


Fig. 4. FCC-ee operation time line. The bottom part indicates the number of cryomodules to be installed in the collider and booster, respectively, during the various winter shutdown periods; also see [22].

Technical systems

Table 1 reveals that the FCC-ee machine faces quite different requirements in its various modes of operation. For example, on the Z pole FCC-ee is an Ampere-class storage ring, like PEP-II, KEKB and DAΦNE, with a high beam current, but a low RF voltage, of order 0.1 GV. For the $t\bar{t}$ mode, the beam current is only a few mA, as for the former LEP2, while an RF voltage above 10 GV is required. In both cases a total of 100 MW RF power must be constantly supplied to the two circulating beams.

Three sets of RF cavities are proposed to cover all operation modes for the FCC-ee collider rings and booster. (1) For the high intensity operation (Z, FCC-hh) 400 MHz mono-cell cavities (4 per cryomodule) based on Nb/Cu thin-film technology at 4.5 K; (2) for higher energy (W, H, $t\bar{t}$) 400 MHz four-cell cavities (4 per cryomodule) again based on Nb/Cu technology at 4.5 K, and (3), finally for the $t\bar{t}$ machine a complement of 800 MHz five-cell cavities (again 4 per cryomodule) based on bulk Nb at 2 K. The installation sequence (Fig. 4) is comparable to that of LEP, where about 30 cryomodules were installed per shutdown.

A high overall energy efficiency is achieved through a combination of different technical and operational measures, for example, by using advanced RF

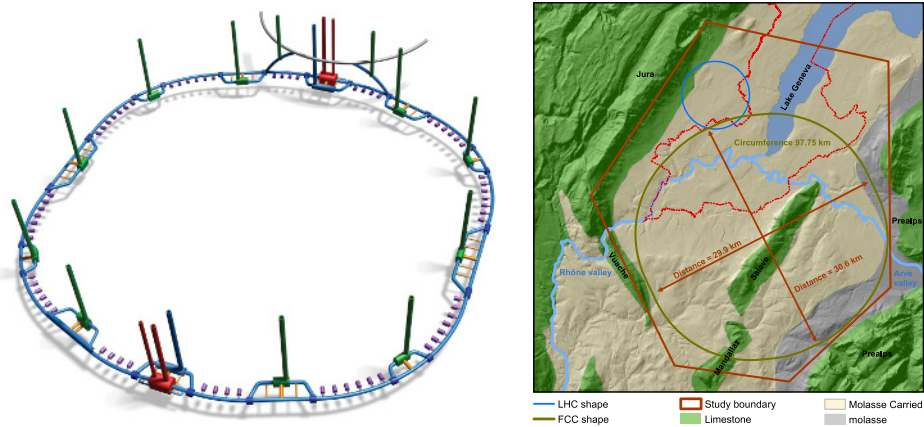


Fig. 5. Left: 3D, not-to-scale schematic of the underground structures. Right: study boundary (red polygon), showing the main topographical and geological structures, LHC (blue line) and FCC tunnel trace (brown line).

power sources [23] and novel low-power twin aperture magnets [24], and by top-up injection.

Civil engineering

The principal structure of the FCC-ee collider is a quasi-circular tunnel composed of arc segments interleaved with straight sections with 5.5 m diameter and a circumference of 97.75 km. Approximately 8 km of bypass tunnels, 18 shafts, 14 large caverns and 12 new surface sites are also planned. On the left, Figure 5 shows a 3D, not-to-scale schematic of the underground structures. The chosen layout satisfies the requirements of the FCC-ee and the FCC-hh machine.

Many different considerations played a role in choosing a suitable position for the machine. The underground structures should be located as much as possible in the sedimentary rock of the Geneva basin, known as Molasse (which provides good conditions for tunneling) avoiding the limestone of the nearby Jura. Another aim was to limit the depth of the tunnel and shafts to control the overburden pressure on the underground structures and to limit the lengths of service infrastructures (cables, ducts, pipes). These requirements, along with the need to connect to the existing accelerator chain through new beam transfer lines, led to the definition of the study boundary, within the Jura range to the north-west, the Vuache mountain to the south-west and the Pre-Alps to the south-east and east. An additional boundary is placed to the north due to the increasing depth of Lake Geneva (see Fig. 5 right).

In order to evaluate different layouts and positions within the boundary area, a software tool incorporating a 3D geological model was developed and used. The tunnel will be constructed with a slope of 0.2% in a single plane, in part to optimise for the geology intersected by the tunnel and the shaft depths and in part to implement a gravity drainage system. It is anticipated that the majority of the machine tunnel will be constructed using tunnel boring machines. One sector passing through limestone will be mined. For the excavations, different lining designs have been developed corresponding to the rock condition.

The study was based on geological data from previous projects and data available from national services. Based on this information, the civil engineering project is considered feasible, both in terms of technology and project risk control. Dedicated

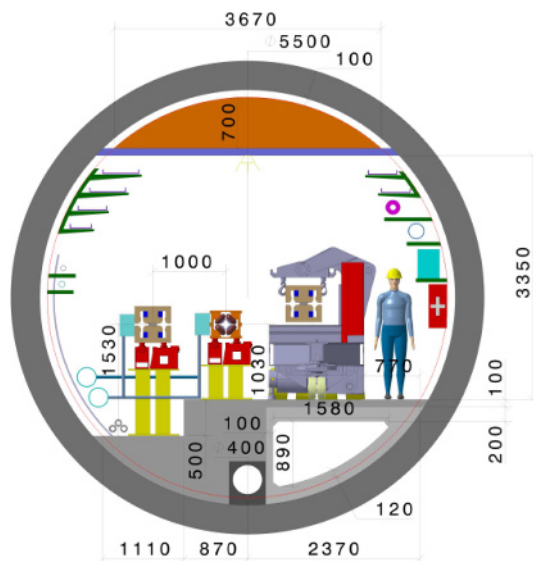


Fig. 6. Machine tunnel cross section in a regular arc with machine elements, services and transport equipment.

ground and site investigations are required during the early stage of a preparatory phase to confirm the findings and to provide a comprehensive technical basis for an optimised placement and as preparation for project planning and implementation processes.

For the access points and their associated surface structures, the focus was identifying possible locations which are feasible from socio-urbanistic and environmental perspectives. The construction methods, and hence the technical feasibility of construction, were studied and are deemed achievable.

A 5.5m internal diameter tunnel is required to house all necessary equipment for the machine, while providing sufficient space for transport. The chosen diameter is also compatible with the FCC-hh requirements. Figure 6 shows the cross section of the tunnel in a typical arc segment, with air supply and smoke extraction ducts integrated into the civil engineering design, the collider and the booster ring as well as the other services required.

Detector considerations

Circular colliders have the advantage of delivering collisions to multiple interaction points. Several experimental collaborations will therefore be called to study and optimise different detector designs for the FCC-ee. On one hand, the planned performance of these detectors for heavy-flavour tagging, for particle identification, for tracking and particle-flow reconstruction, and for lepton, jet, missing energy and angular resolution, need to match the physics programme and the statistical precision offered by the FCC-ee. On the other hand, the detectors must satisfy the constraints imposed by machine performance and interaction region layout: the occupancy from beam-induced background needs to be minimised; the interaction rates (up to 100 kHz at the Z pole) put strict constraints on the event size and readout speed; due to the beam crossing angle, the detector solenoid magnetic field is limited to 2 T to avoid a significant impact on the luminosity; the accurate measurement of the significant centre-of-mass energy spread (90 MeV at the Z pole, 500 MeV at the highest FCC-ee energies) requires an angular resolution better than 100 μ rad for

muons; the luminometer must be situated only 1 m away from the interaction point, but still provide a precision better than 10^{-4} on the luminosity; etc.

Two general-purpose detector concepts have been studied and optimised for this conceptual design report: (i) CLD, a consolidated option based on the detector design developed for CLIC, with a silicon tracker and a 3D-imaging highly-granular calorimeter, surrounded by a conventional superconducting solenoid coil; and (ii) IDEA, a bolder, possibly more cost-effective, design, with a short-drift wire chamber and a dual-readout calorimeter, interleaved by a thin, low-mass superconducting solenoid coil. This particular choice has been motivated by the wish to explore the technology and cost spectrum. With these two examples, it was demonstrated that detectors satisfying the requirements are feasible. This choice is of course not unique. While the optimisation of these two concepts will continue, other concepts must be explored and might actually prove to be better adapted to the FCC-ee physics programme.

Cost and schedule

The construction cost for FCC-ee amounts to 10 500 million CHF for the Z, W and H working points including all civil engineering works. All particle accelerator related investments amount to 3100 million CHF or 30% of the total cost and the staged implementation distributes these costs over a decade long operation phase. Civil engineering accounts for 51% (5400 million CHF). The capital cost for the technical infrastructure is 2000 million CHF. Both, civil engineering and general technical infrastructures can be fully reused for a subsequent hadron collider (FCC-hh). The operation costs are expected to remain within limits, since the electricity consumption is not a cost driver and the evolution from LEP to LHC operation today shows a steady decrease in the efforts needed to operate, maintain and repair the equipment. The cost-benefit analysis of the LHC/HL-LHC programme reveals that a research infrastructure project of such a scale and investment volume has the potential to pay back in terms of socio-economic value creation throughout its lifetime.

The FCC-ee programme will commence with a preparatory phase of 8 years, followed by the construction phase (all civil and technical infrastructure, machines and detectors including commissioning) lasting 10 years. A duration of 15 years is projected for the subsequent operation of the FCC-ee facility, to complete the currently envisaged physics programme. This makes a total of nearly 35 years for construction and operation of FCC-ee.

Outlook

The technology for constructing a high-energy, highest-luminosity circular lepton collider exists today. The FCC-ee concept comprises a high-efficiency, superconducting radiofrequency system, a power-saving twin-aperture magnet system, a continuous top-up injection scheme for stable operation and maximum integrated luminosity. Combined with an energy staging scheme, the FCC-ee represents the most efficient and most sustainable route for executing the research required to discover signs of new physics beyond the Standard Model. The step-wise energy increase of the FCC-ee does not require any additional civil engineering activities.

Strategic R&D for FCC-ee aims at minimising construction cost and energy consumption, while maximising the socio-economic impact. It will mitigate residual technology-related risks and ensure that industry can benefit from an acceptable economic utility. Concerning the implementation, a preparatory phase of about

eight years is both necessary and adequate to establish the project governing and organisational structures, building the international machine and experiment consortia, developing a territorial implementation plan in agreement with the host states' requirements, optimising the disposal of land and underground volumes and preparing the civil engineering project. Such a large-scale, international fundamental research infrastructure, tightly involving industrial partners and providing training at all education levels, will be a strong motor of economic and societal development in all participating nations.

The FCC study has implemented a set of actions towards a coherent vision for the world-wide high-energy and particle physics community, providing a collaborative framework for topically complementary and geographically well-balanced contributions. This conceptual design report lays the foundation for a subsequent infrastructure preparatory and technical design phase.

1 Physics discovery potential

1.1 Overview

“There is a strong scientific case for an electron-positron collider, complementary to the LHC, that can study the properties of the Higgs boson and other particles with unprecedented precision and whose energy can be upgraded.” [25]

This strategic guideline from the 2013 update of the European Strategy for Particle Physics (ESPP 2013) unambiguously defines the high standards to be met by the future e^+e^- collider, quite possibly the next high-energy collider to be built. Since its inception, the FCC-ee study has aimed at delivering the e^+e^- collider conceptual design that best complies with this guideline, and consequently offers, in a cost-effective fashion, the broadest physics discovery potential and the most ambitious perspectives for future developments.

As a result of the renewed worldwide interest for e^+e^- physics and the pertaining discovery potential since the observation of the Higgs boson at the LHC, the FCC is not alone in this quest. In the absence of convincing hints for physics beyond the standard model (BSM) in the LHC data so far, the situation has significantly evolved since 2013, so that today no fewer than four e^+e^- collider designs are contemplated to study the properties of the Higgs boson and other standard model (SM) particles with an unprecedented precision:

- the International Linear Collider (ILC [13]) project, for which the above guideline was originally tailored, now focusses on studying the Higgs boson with a centre-of-mass energy of 250 GeV [14,15];
- the Compact Linear Collider (CLIC [16]), whose lowest centre-of-mass energy point was reduced from 500 to 380 GeV [17], in order to better study the Higgs boson and the top quark;
- the Circular Electron Positron Collider (CEPC [18–20]), in a 100 km tunnel in China, able to study the Z, the W, and the Higgs boson, with centre-of-mass energies from 90 to 250 GeV;
- the Future e^+e^- Circular Collider in a new ~ 100 km tunnel at CERN (FCC-ee, formerly called TLEP [8,21]), which can study the entire electroweak (EW) sector (Z and W bosons, Higgs boson, top quark) with centre-of-mass energies between 88 and 365 GeV.

The baseline luminosities expected to be delivered at the ILC, CLIC, CEPC, and FCC-ee centre-of-mass energies are illustrated in Figure 1.1.

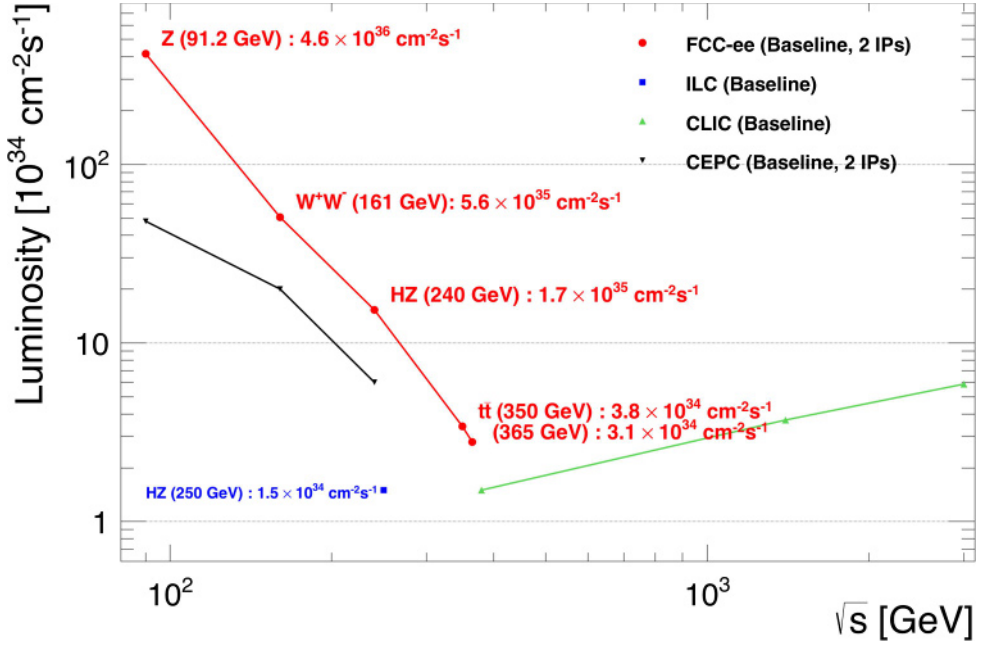


Fig. 1.1. Baseline luminosities expected to be delivered (summed overall interaction points) as a function of the centre-of-mass energy \sqrt{s} , at each of the four worldwide e^+e^- collider projects: ILC (blue square), CLIC (green upward triangles), CEPC (black downward triangles), and FCC-ee (red dots), drawn with a 10% safety margin. The FCC-ee performance data are taken from Section 2, the latest CEPC parameters are taken from [20], and the linear collider luminosities are taken from [15,17].

The FCC-ee delivers the highest rates in a clean, well-defined, and precisely predictable environment, at the Z pole (91 GeV), at the WW threshold (161 GeV), as a Higgs factory (240 GeV), and around the $t\bar{t}$ threshold (340–365 GeV), to several interaction points. It also provides high precision centre-of-mass energy calibration at the 100 keV level at the Z and WW energies, a feature unique to circular colliders¹. The FCC-ee is therefore genuinely best suited to offer extreme statistical precision and experimental accuracy for the measurements of the standard model particle properties, it opens windows to detect new rare processes, and it furnishes opportunities to observe tiny violations of established symmetries.

Historically, such precise measurements or subtle observations have been precursors for the discovery of new phenomena and new particles, and for a deeper understanding of fundamental physics. These historical precedents have also shown the important role played by lower-energy precision measurements when establishing road-maps for higher-energy machines. In the second half of the 1970s, precision measurements of neutral currents led scientists to infer the existence of the W and Z bosons, as well as the values of their masses, from which the dimensions of the LEP tunnel were determined. The W and Z were then observed in the early 1980's at the

¹ A circular e^+e^- Higgs factory, LEP3, had also been proposed in the LHC tunnel back in 2011 [21,26]. With respect to the FCC-ee, the LEP3 facility would have had the advantage of reusing existing infrastructure, at the severe expense of a much reduced sensitivity to new phenomena, with (i) a luminosity smaller by a factor 4–5 at the Z, WW, and Higgs operation points; (ii) the impossibility of a precise energy calibration at the WW threshold; (iii) the inability to measure the top-quark properties; and (iv) the lack of a vibrant perspective for subsequent energy-frontier exploration in the same tunnel.

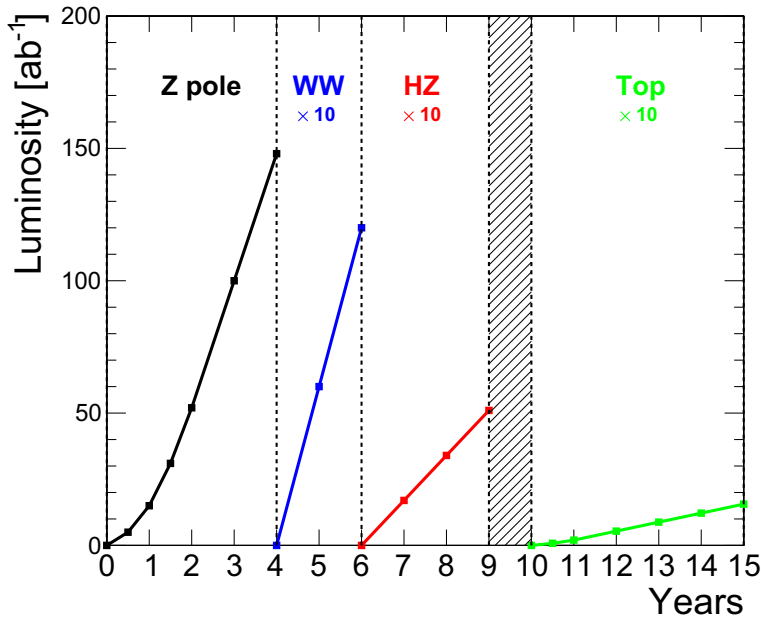


Fig. 1.2. Operation model for the FCC-ee, as a result of the five-year conceptual design study, showing the integrated luminosity at the Z pole (black), the WW threshold (blue), the Higgs factory (red), and the top-pair threshold (green) as a function of time. The hatched area indicates the shutdown time needed to prepare the collider for the highest energy runs.

CERN SpS collider with masses in the predicted range. Subsequently, as described in more detail in Section 1.2, the CERN LEP e^+e^- collider measured the properties of the Z and W bosons with high precision in the 1990's [27,28]. These precise measurements could determine in a definitive way the number of light, active neutrinos, as well as allow inferring the mass of the so far unseen top quark, which was soon observed at the Tevatron within the predicted mass range. With m_{top} fixed by the Tevatron measurement, the ensemble of precision measurements at LEP/SLC, at the Tevatron, and from low energy inputs led in turn to a $\pm 30\%$ accurate prediction for the mass of the Higgs boson, which was observed in 2012 at the LHC within the predicted mass range. It is important to note that these predictions were based on the Standard Model with no additional particle content with respect to that known today.

With the Higgs boson discovery, the standard model seems complete and its predictions have no more flexibility beyond the uncertainties in the theoretical calculations and in the input parameters. Several experimental facts, however, reveal without any doubt that new phenomena must exist: non-baryonic dark matter; the cosmological baryon-antibaryon asymmetry; the finite albeit extremely small neutrino masses, etc., are all evidence for physics beyond the standard model. The agreement between the predicted and observed W, top and Higgs masses, and the null result of experiments at colliders so far, are an indication that either the new physics scale is too high and/or the pertaining couplings are too small. Any new hint would be a major discovery, whether it is the observation of a new particle, a new so-far unobserved phenomenon, or a non-trivial deviation from the standard model predictions.

As a result, the next accelerator project must allow the broadest possible field of research. This is the case for the FCC. To begin with, the FCC-ee would measure the Z, W, Higgs, and top properties in e^+e^- collisions, either for the first time

or with orders of magnitude increases in precision, thereby giving access to either much higher scales or much smaller couplings. The FCC-ee is the most powerful of all proposed e^+e^- colliders at the electroweak (EW) scale – all things being equal, in particular the duration of operation (Fig. 1.2). The FCC-ee proposes a broad, multifaceted exploration to

1. measure a comprehensive set of electroweak and Higgs observables with high precision,
2. tightly constrain a large number of the parameters of the standard model,
3. unveil small but significant deviations with respect to the standard model predictions,
4. observe rare new processes or particles, beyond the standard model expectations,

and, therefore, maximise opportunities for major fundamental discoveries. The FCC-ee also meets the last part of the ESPP 2013 guideline (“[. . .] and whose energy can be upgraded”) in the most ambitious manner, as the FCC-ee tunnel is designed to subsequently host the FCC-hh, a hadron collider with a centre-of-mass energy of 100 TeV. Combined with the FCC-ee measurements, the FCC-hh physics reach at the energy and precision frontiers is likely to be unbeatable. The multiple synergies between the FCC-ee and FCC-hh physics opportunities are discussed in Vol. 1 of this Conceptual Design Report.

The primary goal of the FCC-ee design study was to demonstrate the feasibility of the accelerator. This goal has been successfully met, confirming and even exceeding the original luminosity expectations (Figs. 1.1 and 1.2). Great confidence can be given in the integration of the detectors at the collision points, and in the ability to reach the beam energy calibration targets. The exploration of the physics capabilities is still at a preliminary stage. Nevertheless the studies presented in the next sections provide a flavour of the extraordinary physics potential of the FCC-ee.

1.2 Precision electroweak measurements

Since the early work by Veltman [29], it has been known that the electroweak quantum corrections are sensitive to particles with electroweak couplings and with masses much higher than accessible directly with the centre-of-mass energies available. The case of the top quark and Higgs boson were particularly interesting: despite their high masses, their effect would indeed not decouple. Further studies in the late 1980s led to the realisation that these quantum corrections could be separated into blocks with different sensitivities. Accurate measurements of these observables thus become sensitive to the possible presence of further particles coupled to the SM interactions in a broader sense. The FCC-ee enables precision measurements of the Z, the W, the Higgs boson and the top quark properties, together with those of input parameters to the standard model, such as the electromagnetic and strong coupling constants at the Z mass scale, thereby providing sensitivity to new particles with masses of up to 10–70 TeV.

1.2.1 Current situation

As briefly mentioned above, the Z lineshape parameters (the Z mass m_Z , the Z width Γ_Z , and the peak cross section σ^0) fitted to the per-mil precision measurements of fermion pair production cross sections at and around the Z pole [27] performed at LEP, were sensitive to the yet unobserved top quark and to a lesser extent to the putative Higgs boson, as illustrated in the Feynman diagrams of Figure 1.3.

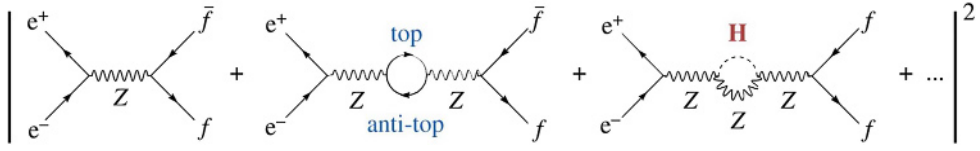


Fig. 1.3. Schematic representation of the perturbative expansion for calculating the cross section for e^+e^- annihilation into a pair of leptons or quarks (denoted f , for fermions); the representative higher order diagrams involving quantum loops with a top quark or a Higgs boson are indicated.

Similarly, the measurements of fermion pair asymmetries allow the determination of the effective weak mixing angle $\sin^2 \theta_W^{\text{eff}}$, the value of which is predicted in the SM from the relation:

$$\sin^2 \theta_W^{\text{eff}} \cos^2 \theta_W^{\text{eff}} = \frac{\pi \alpha_{\text{QED}}(m_Z^2)}{\sqrt{2} G_F m_Z^2} \times (1 + \Delta\kappa), \quad (1.1)$$

where $\alpha_{\text{QED}}(m_Z^2)$ is the electromagnetic coupling constant evaluated at the Z pole, G_F is the Fermi constant, and $\Delta\kappa$ is a small correction factor that depends on the top quark and Higgs boson masses via the graphs displayed in Figure 1.3. The magnitude of the second graph of Figure 1.3 is proportional to the square of the top quark mass. It is much larger than that of the third one, proportional to $\log(m_H/m_Z)$, and amounts to about ten times the LEP measurement accuracy. As a consequence, LEP was able to predict the mass of the top quark within the SM (assuming that no other particle but the Higgs boson would impact the radiative corrections) [27]:

$$m_{\text{top}}^{\text{SM}} = 173_{-10}^{+13} \text{ GeV}. \quad (1.2)$$

The W boson mass is in turn predicted within the SM from the relation:

$$m_W^{\text{SM}} = \left[\frac{\pi \alpha_{\text{QED}}(m_Z^2)}{\sqrt{2} G_F \sin^2 \theta_W^{\text{eff}}} \times \frac{1}{1 - \Delta r} \right]^{\frac{1}{2}}, \quad (1.3)$$

where Δr is yet another small correction factor that depends on m_{top} and m_H . Numerically, the W mass was predicted from the LEP measurements at the Z pole with a remarkable precision (including the above uncertainty on the top quark mass and the absence of knowledge of the Higgs boson at the time) [27]:

$$m_W^{\text{SM}} = 80.362_{-0.031}^{+0.032} \text{ GeV}. \quad (1.4)$$

By increasing its centre-of-mass energy to above the W^+W^- production threshold, LEP did measure the W mass directly, in agreement with equation (1.4) and with a similar precision [28]. The Tevatron later improved this precision by about a factor two [30], and observed for the first time the top quark [31,32], at the mass predicted by LEP (Eq. (1.2)) in the context of the standard model *and nothing else*. Today, the W boson and top quark masses are directly measured with the following accuracies [33]:

$$m_W^{\text{direct}} = 80.379 \pm 0.012 \text{ GeV}, \quad (1.5)$$

$$m_{\text{top}}^{\text{direct}} = 173.3 \pm 0.4(\text{exp}) \pm 0.5(\text{theory}) \text{ GeV}. \quad (1.6)$$

The direct measurements of m_W and m_{top} were then used to determine the magnitude of the second graph of Figure 1.3, and made the third graph become the

dominant unknown term of the perturbative expansion. As a consequence, the LEP and Tevatron measurements were able to infer the existence of a Higgs boson and to predict its mass within the SM:

$$m_{\text{H}}^{\text{SM}} = 98_{-21}^{+25} \text{ GeV}. \quad (1.7)$$

The LHC observed the production of the Higgs boson in 2012 for the first time, at a mass well compatible with this prediction in the context of the standard model *and nothing else*. The current overall situation of the standard model fit to the precision measurements available to date is summarised in Figure 1.4. The fit prediction for the W mass and the weak mixing angle [34] within the SM, namely

$$\begin{aligned} m_{\text{W}} &= 80.3584 \pm 0.0055_{m_{\text{top}}} \pm 0.0025_{m_{\text{Z}}} \pm 0.0018_{\alpha_{\text{QED}}} \\ &\quad \pm 0.0020_{\alpha_{\text{S}}} \pm 0.0001_{m_{\text{H}}} \pm 0.0040_{\text{theory}} \text{ GeV} \\ &= 80.358 \pm 0.008_{\text{total}} \text{ GeV}, \\ \sin^2 \theta_{\text{W}}^{\text{eff}} &= 0.231488 \pm 0.000029_{m_{\text{top}}} \pm 0.000015_{m_{\text{Z}}} \pm 0.000035_{\alpha_{\text{QED}}} \\ &\quad \pm 0.000010_{\alpha_{\text{S}}} \pm 0.000001_{m_{\text{H}}} \pm 0.000047_{\text{theory}} \\ &= 0.23149 \pm 0.00007_{\text{total}}, \end{aligned} \quad (1.8)$$

are also very compatible with the world average of their direct measurements within current uncertainties:

$$m_{\text{W}} = 80.379 \pm 0.012 \text{ GeV}, \text{ and } \sin^2 \theta_{\text{W}}^{\text{eff}} = 0.23153 \pm 0.00016. \quad (1.9)$$

1.2.2 Opportunities at the Z pole

Electroweakly-coupled new physics would appear either as additional/different contributions to the perturbative expansion of the electroweak observable predictions, similar to those shown in Figure 1.3, or as modifications of the tree-level couplings to leptons and quarks. From the agreement between the predictions and the direct measurements, it follows that the effect of new physics, if any, must be smaller than the current uncertainties. The next significant step in this quest is therefore to drastically reduce these uncertainties, typically by one order of magnitude or more. In this section, it is assumed that theoretical uncertainties can be brought, by the calculation of missing QED, EW and QCD higher orders within the standard model *and nothing else*, to a level similar to, or smaller than, that of the experimental uncertainties. This issue is addressed briefly in Section 1.5. Numerically, the FCC-ee is able to deliver about 10^5 times the luminosity that was produced by LEP at the Z pole, i.e. typically $1.5 \times 10^{11} \text{ Z} \rightarrow \mu^+ \mu^-$ or $\tau^+ \tau^-$ decays and 3×10^{12} hadronic Z decays. Measurements with a statistical uncertainty up to 300 times smaller than at LEP (from a few per mil to 10^{-5}) are therefore at hand.

Forward-backward and polarisation asymmetries at the Z pole are a powerful experimental tool to measure $\sin^2 \theta_{\text{W}}^{\text{eff}}$, which regulates the difference between the right-handed and left-handed fermion couplings to the Z. With unpolarised incoming beams, the amount of Z polarisation at production is

$$\mathcal{A}_e = \frac{g_{\text{L,e}}^2 - g_{\text{R,e}}^2}{g_{\text{L,e}}^2 + g_{\text{R,e}}^2} \frac{2v_e/a_e}{1 + (v_e/a_e)^2}, \text{ with } v_e/a_e \equiv 1 - 4 \sin^2 \theta_{\text{W}}^{\text{eff}}, \quad (1.10)$$

by definition of the effective weak mixing angle $\sin^2 \theta_{\text{W}}^{\text{eff}}$. The resulting forward-backward asymmetry at the Z pole amounts to $A_{\text{FB}}^{\text{ff}} = \frac{3}{4} \mathcal{A}_e \mathcal{A}_f$. The experimental

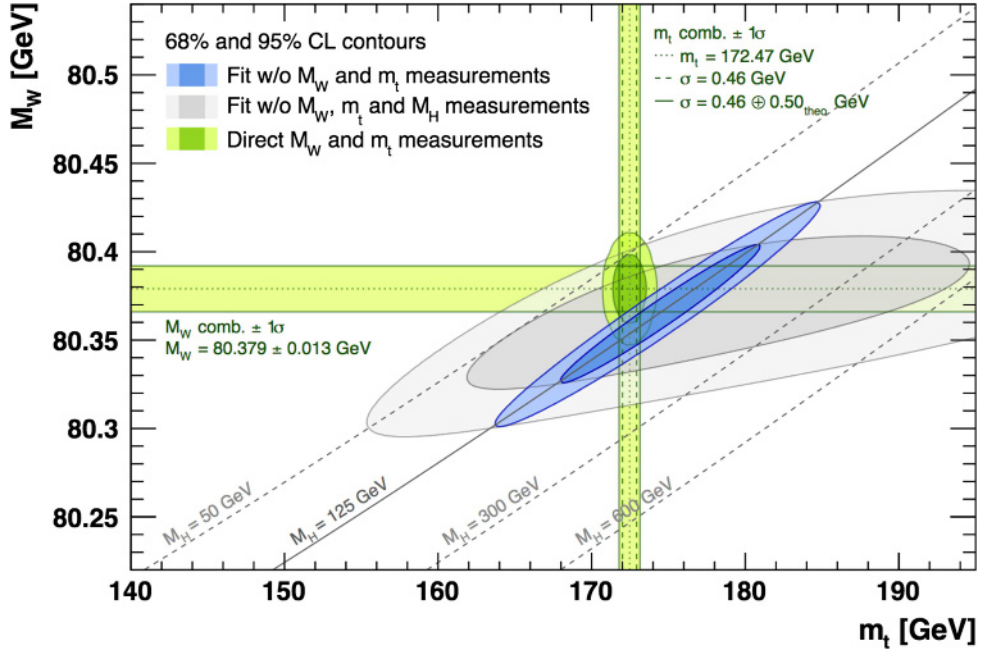


Fig. 1.4. From reference [35]: Contours of 68% and 95% confidence level obtained from fits of the standard model to the precision measurements available to date, in the (m_{top}, m_W) plane. The grey area is the result of the fit without the direct measurements of the W, top, and Higgs masses, while the narrower blue area includes the Higgs boson mass measurement at the LHC. The horizontal and vertical green bands and the combined green area indicate the 1σ regions of the m_W and m_{top} measurements (world averages).

control of the longitudinal polarisation of each of the beams can be made with the foreseen polarimeter (Sect. 2.7) with great accuracy.

From the experimental point of view, the $e^+e^- \rightarrow Z \rightarrow \mu^+ \mu^-$ process is a golden channel for an accurate measurement of $A_{\text{FB}}^{\mu\mu}$. The dominant source of experimental uncertainty arises from the knowledge of the centre-of-mass energy. Indeed, in the vicinity of the Z pole, $A_{\text{FB}}^{\mu\mu}$ exhibits a strong \sqrt{s} dependence

$$A_{\text{FB}}^{\mu\mu}(s) \simeq \frac{3}{4} A_e A_\mu \times \left[1 + \frac{8\pi\sqrt{2}\alpha_{\text{QED}}(s)}{m_Z^2 G_F (1 - 4\sin^2\theta_W^{\text{eff}})^2} \frac{s - m_Z^2}{2s} \right], \quad (1.11)$$

caused by the off-peak interference between the Z and the photon exchange in the process $e^+e^- \rightarrow \mu^+ \mu^-$. As suggested in Section 2.7, a continuous measurement with resonant depolarisation of non-colliding bunches should allow a reduction of this uncertainty to below 0.1 MeV. The resulting uncertainty on $A_{\text{FB}}^{\mu\mu}$ amounts to 9×10^{-6} (a factor three larger than the statistical uncertainty), which propagates to an uncertainty on $\sin^2\theta_W^{\text{eff}}$ of 6×10^{-6} . Among the other asymmetries to be measured at the FCC-ee, the τ polarisation asymmetry in the $\tau \rightarrow \pi\nu\tau$ decay mode provides a similarly accurate determination of $\sin^2\theta_W^{\text{eff}}$, with a considerably reduced \sqrt{s} dependence. In addition, the scattering angle dependence of the τ polarisation asymmetry provides an individual determination of both A_e and A_τ , which allows, in combination with the $A_{\text{FB}}^{\mu\mu}$ and the three leptonic partial width measurements, the vector and axial couplings of each lepton species to be determined. Similarly, heavy-quark forward-backward asymmetries (for b quarks, c quarks and, possibly s quarks) together with the corresponding Z decay partial widths and the precise knowledge of

A_e from the τ polarisation, provide individual measurements of heavy-quark vector and axial couplings.

An experimental precision better than 5×10^{-6} is therefore a robust target for the measurement of $\sin^2 \theta_W^{\text{eff}}$ at the FCC-ee, corresponding to more than a thirty-fold improvement with respect to the current precision of 1.6×10^{-4} (Eq. (1.9)). Individual measurements of leptonic and heavy quark couplings are achievable, with a factor of several hundred improvement on statistical errors and, with the help of detectors providing better particle identification and vertexing, by up to two orders of magnitude on systematic uncertainties.

For this accuracy to be instrumental in constraining new physics, the parametric uncertainties of the $\sin^2 \theta_W^{\text{eff}}$ SM prediction (Eq. (1.8)) need to be brought to a similar level. The largest parametric uncertainty on the prediction, 3.5×10^{-5} , arises from the limited knowledge of the electromagnetic coupling constant evaluated at the Z mass scale. It is hoped that this figure can be reduced by a factor of two to three with a better determination of the hadronic vacuum polarisation, in part with future low-energy e^+e^- data and in part with the use of perturbative QCD [36]. The large luminosity offered by the FCC-ee allows a direct determination of $\alpha_{\text{QED}}(m_Z^2)$ to be contemplated [37], from the slope of the muon forward-backward asymmetry as a function of the centre-of-mass energy in the vicinity of the Z pole (Eq. (1.11)). As displayed in Figure 1.5, the statistical uncertainty of this measurement is minimum just below ($\sqrt{s} = 87.9$ GeV) and just above ($\sqrt{s} = 94.3$ GeV) the Z pole. It is shown in reference [37] that the experimental precision on α_{QED} can be improved by a factor 3–4 with 40 ab^{-1} at each of these two points. Because most systematic uncertainties are common to both points and almost perfectly cancel in the slope determination, the experimental uncertainty is statistics dominated as long as the centre-of-mass energy spread (90 MeV at the Z pole) can be determined to a relative accuracy better than 1%, which is deemed achievable at the FCC-ee every few minutes [38]. More studies are needed to understand if the $\alpha_{\text{QED}}(m_Z^2)$ determination can profit from the centre-of-mass energy dependence of other asymmetries.

An experimental relative accuracy of 3×10^{-5} on $\alpha_{\text{QED}}(m_Z^2)$ can be achieved at the FCC-ee, from the measurement of the muon forward-backward asymmetry with 40 ab^{-1} of centre-of-mass energies ~ 3 GeV below and ~ 3 GeV above the Z pole. The corresponding parametric uncertainties on the $\sin^2 \theta_W^{\text{eff}}$ and m_W SM predictions are accordingly reduced from 3.5×10^{-5} and 1.8 MeV to 9×10^{-6} and 0.5 MeV, respectively.

The next parametric uncertainty to address at the Z pole is that arising from the Z mass. The Z mass and width were determined at LEP from the line shape scan to be $m_Z = 91187.5 \pm 2.1$ MeV and $\Gamma_Z = 2495.2 \pm 2.3$ MeV, with data taken mostly at $\sqrt{s} = 89.4, 91.2$, and 93 GeV. The statistical errors of 1.2 MeV and 2 MeV would be reduced below 5 keV and 8 keV at the FCC-ee, with data taken at 87.9, 91.2, and 93.9 GeV. In both cases, the systematic uncertainty was dominated at LEP by the error pertaining to the beam energy calibration (1.7 MeV, and 1.2 MeV). With a precision of 0.1 MeV on the centre-of-mass energy (Sect. 2.7) and the centre-of-mass energy spread [38] at the FCC-ee, the uncertainty on m_Z improves accordingly. A similar improvement is expected for the Z width if the point-to-point relative accuracy on the integrated luminosity is reduced to 5×10^{-5} (Sect. 7).

Overall experimental uncertainties of 0.1 MeV or better are achievable for the Z mass and width measurements at the FCC-ee. The corresponding parametric uncertainties on the $\sin^2 \theta_W^{\text{eff}}$ and m_W SM predictions are accordingly reduced to 6×10^{-7} and 0.12 MeV, respectively.

The third and final parametric uncertainty to address at the Z pole comes from the knowledge of the strong coupling constant $\alpha_s(m_Z^2)$. The ratio R_ℓ of the Z hadronic

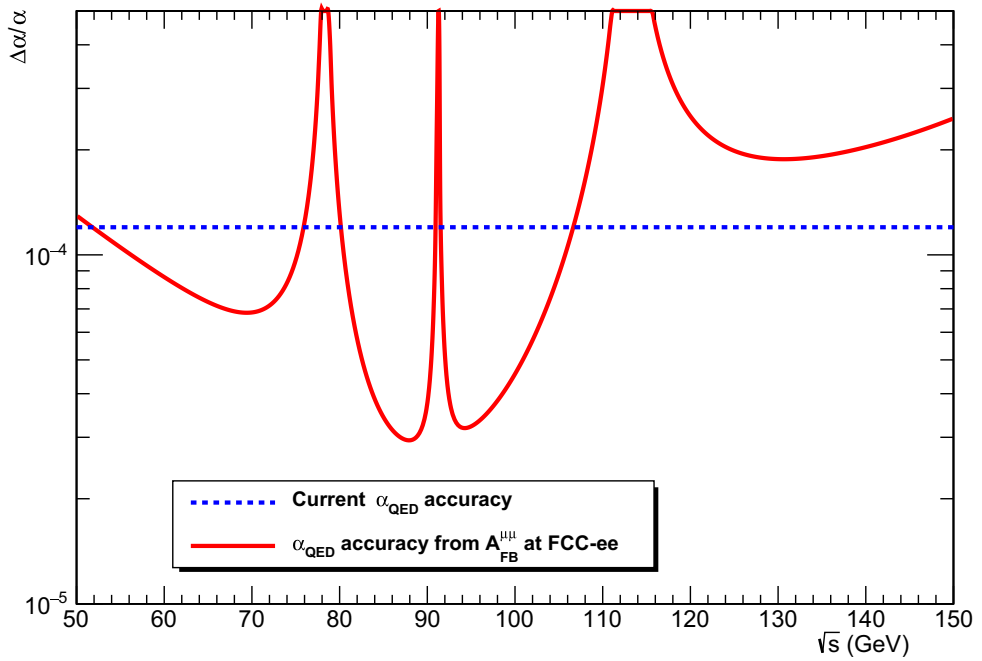


Fig. 1.5. Relative statistical accuracy of the α_{QED} determination from the muon forward-backward asymmetry at the FCC-ee, as a function of the centre-of-mass energy. The integrated luminosity is assumed to be 40 ab^{-1} below and above the Z pole, and to follow the profile of Figure 1.2 for other centre-of-mass energies. The dashed blue line shows the current uncertainty.

width to the Z leptonic width, $R_\ell = 20.767 \pm 0.025$, has been used, at LEP, for the determination of the strong coupling constant, which yielded $\alpha_s(m_Z^2) = 0.1196 \pm 0.0028 \text{ (exp)} \pm 0.0009 \text{ (theory)}$. The experimental uncertainty was dominated by the statistics of the Z leptonic decays and therefore a combination of the three lepton species – with the assumption of lepton universality – was required. At the FCC-ee, the statistical uncertainty is negligible and the measurement of R_μ , yielding an experimental precision of 0.001 from the knowledge of the detector acceptance, suffices. The experimental uncertainty on $\alpha_s(m_Z^2)$ shrinks accordingly to 0.00015, as illustrated in Figure 1.6. A similar figure can be obtained from the measurements of the hadronic and leptonic decay branching ratio of the W boson [39], copiously produced with the FCC-ee running at larger centre-of-mass energies.

An absolute (relative) uncertainty of 0.001 (5×10^{-5}) on the ratio of the Z hadronic-to-leptonic partial widths (R_ℓ) is well within the reach of the FCC-ee. The same relative uncertainty is expected for the ratios of the Z leptonic widths, which allows a stringent test of lepton universality. The overall uncertainty on $\alpha_s(m_Z^2)$ obtained from R_ℓ drops by more than an order of magnitude. The corresponding parametric uncertainties on the SM predictions of $\sin^2 \theta_W^{\text{eff}}$ and m_W are accordingly reduced to 10^{-6} and 0.2 MeV, respectively.

1.2.3 Opportunities at the $W^+ W^-$ and $t\bar{t}$ threshold

The safest and most sensitive way to determine the W boson and top quark masses and widths is to measure the sharp increase of the $e^+e^- \rightarrow W^+W^-$ and $e^+e^- \rightarrow t\bar{t}$ cross sections at the production thresholds, at centre-of-mass energies around twice

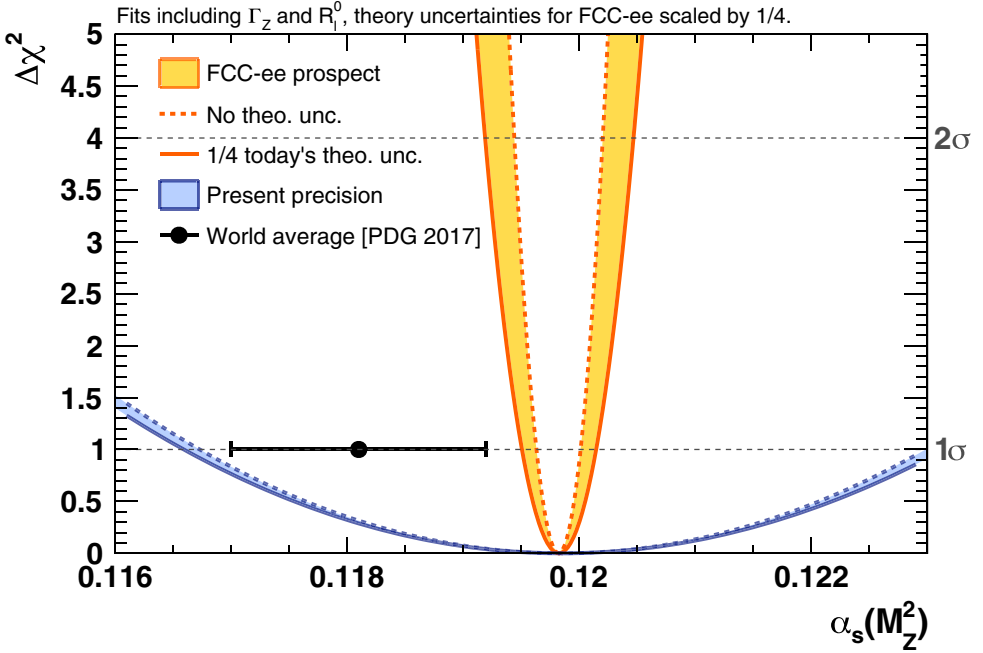


Fig. 1.6. Precision on α_s derived from the electroweak fit today (blue band from [35]) and expected at the FCC-ee (yellow band, without theoretical uncertainties and with the current theoretical uncertainties divided by a factor of four). All fits were performed with the GFit software (<http://cern.ch/gfitter/Software/index.html>).

the W and top masses (Fig. 1.7). In both cases, the mass can be best determined at a quasi-fixed point where the cross section dependence on the width vanishes: $\sqrt{s} \simeq 162.5$ GeV for m_W and 342.5 GeV for m_{top} . The cross section sensitivity to the width is maximum at $\sqrt{s} \simeq 157.5$ GeV for Γ_W , and 344 GeV for Γ_{top} .

With 12 ab^{-1} equally shared between 157.5 and 162.5 GeV, a simultaneous fit of the W mass and width to the $e^+e^- \rightarrow W^+W^-$ cross-section measurements yields a precision of 0.5 MeV on m_W and 1.2 MeV on Γ_W . Lest the measurements be limited by systematic uncertainties, the following conditions need to be met. The centre-of-mass energies must be measured with a precision of 0.5 MeV. The point-to-point variation of the detector acceptance (including that of the luminometer) and the WW cross section prediction must be controlled within a few 10^{-4} . Finally, the background must be known at the few per-mil level. These conditions are less stringent than the requirements at the Z pole – where the centre-of-mass energies must be measured to 0.1 MeV or better and the point-to-point variations of the luminometer acceptance must be controlled to 5×10^{-5} , etc. In addition, the backgrounds can be controlled by an additional energy point below the W pair production threshold.

An experimental precision of 0.5 (1.2) MeV for the W mass (width) is within reach at the FCC-ee, with 12 ab^{-1} accumulated at the W pair production threshold.

The situation is slightly different for the top quark. A multipoint scan in a 4 GeV window will be needed for the top mass determination, because m_{top} might not be known to better than ± 1 GeV from the theoretical interpretation of the hadron collider measurements. In addition, the $t\bar{t}$ cross section depends on the top Yukawa coupling, arising from the Higgs boson exchange at the $t\bar{t}$ vertex (Sect. 1.3.2). This dependence can be fitted away with supplementary data at centre-of-mass energies slightly above the $t\bar{t}$ threshold. The non- $t\bar{t}$ background, on the other hand,

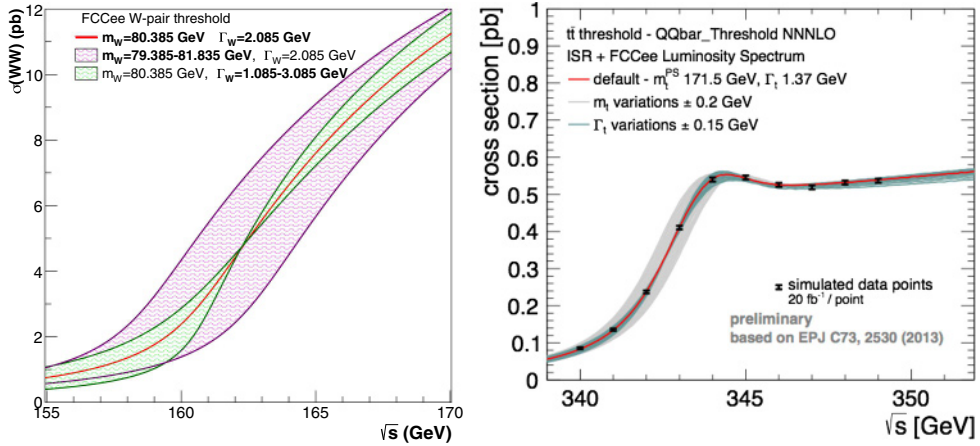


Fig. 1.7. Production cross section of W boson (left) and top-quark pairs (right) in the vicinity of the production thresholds, with different values of the masses and widths. In the left panel, the pink and green bands include variations of the W mass and width by ± 1 GeV. In the right panel, the grey and green bands include variations of the top-quark mass and width by ± 0.2 and ± 0.15 GeV. The dots with error bars indicate the result of a 10-point energy scan in steps of 1 GeV, with 0.02 ab^{-1} per point.

needs to be evaluated from data at centre-of mass energies slightly below the $t\bar{t}$ threshold.

With a luminosity of 25 fb^{-1} recorded at eight different centre-of-mass energies (340, 341, 341.5, 342, 343, 343.5, 344, and 345 GeV), the top-quark mass and width can be determined with statistical precisions of $\pm 17 \text{ MeV}$ and $\pm 45 \text{ MeV}$, respectively. The uncertainty on the mass improves to less than 10 MeV if the width is fixed to its SM value. Each of the centre-of-mass energies can be measured with a precision smaller than 10 MeV from the final state reconstruction [40] of $e^+e^- \rightarrow W^+W^-$, ZZ , and $Z\gamma$ events and from the knowledge of the W and Z masses, which causes a 3 MeV uncertainty on the top-quark mass. Today, the theory uncertainty due to missing higher orders in QCD is at the 40 MeV level for the mass and the width.

An uncertainty of 17 (45) MeV is achievable for the top-quark mass (width) measurement at the FCC-ee, with 0.2 ab^{-1} accumulated around the $t\bar{t}$ threshold. The corresponding parametric uncertainties on the SM predictions of $\sin^2 \theta_W^{\text{eff}}$ and m_W are accordingly reduced to 6×10^{-7} and 0.11 MeV, respectively.

It is only once all above measurements are performed that the total parametric uncertainty on the W mass and on $\sin^2 \theta_W^{\text{eff}}$ predictions (0.6 MeV and 10^{-5} , respectively), dominated by the in-situ precision on $\alpha_{\text{QED}}(m_Z^2)$, can match the uncertainty on their direct determination (0.5 MeV and 5×10^{-6} , respectively). At the time of writing, the FCC-ee is the only future collider project that plans to realise this tour-de-force, a prerequisite for an optimal sensitivity to new physics beyond the standard model (Sect. 1.4.1).

1.2.4 Additional opportunities

The measurement of the Z decay width into invisible states is of great interest as it constitutes a direct test of the unitarity of the neutrino mixing matrix – or of the existence of right-handed quasi-sterile neutrinos, as pointed out in reference [41]. At LEP, it was mostly measured at the Z pole from the peak hadronic cross section to

be, when expressed in number of active neutrinos, $N_\nu = 2.984 \pm 0.008$. The measurement of the peak hadronic cross-section at the Z pole is dominated by systematic uncertainties, related, on one hand, to the theoretical prediction of the low-angle Bhabha-scattering cross section (used for the integrated luminosity determination), and to the absolute integrated luminosity experimental determination, on the other. At the FCC-ee, a realistic target for this systematics-limited uncertainty is bounded from below to 0.001, based on ongoing progress with the theoretical calculations and experimental technology.

At larger centre-of-mass energies, the use of radiative return to the Z [42], $e^+e^- \rightarrow Z\gamma$, is likely to offer a more accurate measurement of the number of neutrinos. Indeed, this process provides a clean photon-tagged sample of on-shell Z bosons, with which the Z properties can be measured. From the WW threshold scan alone, the cross section of about 5 pb [43–46] ensures that fifty million $Z\gamma$ events are produced with a $Z \rightarrow \nu\bar{\nu}$ decay and a high-energy photon in the detector acceptance. The 25×10^6 $Z\gamma$ events with leptonic decays, in turn, provide a direct measurement of the ratio $\Gamma_Z^{\text{inv}}/\Gamma_Z^{\text{lept}}$, in which uncertainties associated with absolute luminosity and photon detection efficiency cancel. The 150 million $Z\gamma$ events with either hadronic or leptonic Z decays will also provide a cross check of the systematic uncertainties and backgrounds related to the QED predictions for the energy and angular distributions of the high energy photon. The invisible Z width will thus be measured with a dominant statistical error corresponding to 0.001 neutrino family. Data at higher energies contribute to further reduce this uncertainty by about 20%. A somewhat lower centre-of-mass energy, for example $\sqrt{s} = 125$ GeV – with both a larger luminosity and a larger $Z\gamma$ cross section and potentially useful for Higgs boson studies (Sect. 1.3.2) – would be even more appropriate for this important measurement.

The FCC-ee has the potential to deliver a measurement of the Z invisible width with an overall, statistics-dominated, uncertainty smaller than 0.0008 of a SM neutrino partial width.

A complete set of electroweak precision measurements also requires the precise determination of the electroweak couplings of the top quark, which may carry enhanced sensitivity to new physics. It is shown in reference [47] that the polarisation of the top quark arising from its parity-violating couplings to the Z in the process $e^+e^- \rightarrow t\bar{t}$ allows a simultaneous measurement of these couplings without incoming beam polarisation, and with an optimal centre-of-mass energy of 365 GeV. With one million $t\bar{t}$ events (corresponding to an integrated luminosity of 1.5 ab^{-1} at $\sqrt{s} = 365$ GeV), the vector and axial top-quark couplings to the Z can be measured with a precision of 0.5% and 1.5%, respectively, from an analysis of the angular and energy distributions of the leptons (e, μ) coming from the top-quark semi-leptonic decays. The production cross section needs to be predicted with a couple of per-cent precision in order not to dominate the coupling uncertainties.

A per-cent level precision can be reached on the vector and axial couplings of the top quark to the Z boson at the FCC-ee, with 1.5 ab^{-1} at $\sqrt{s} = 365$ GeV.

1.2.5 Global electroweak Fit

Once the W boson and the top-quark masses are measured with precisions of a few tenths and a few tens of MeV, respectively, and with the measurement of the Higgs boson mass at the LHC (to be further improved at the FCC-ee), the SM prediction of a number of observables sensitive to electroweak radiative corrections become absolute with no remaining additional parameters. Any deviation will be a demonstration of the existence of new, weakly interacting particle(s). As just discussed, the FCC-ee offers the opportunity to measure such quantities with precisions between

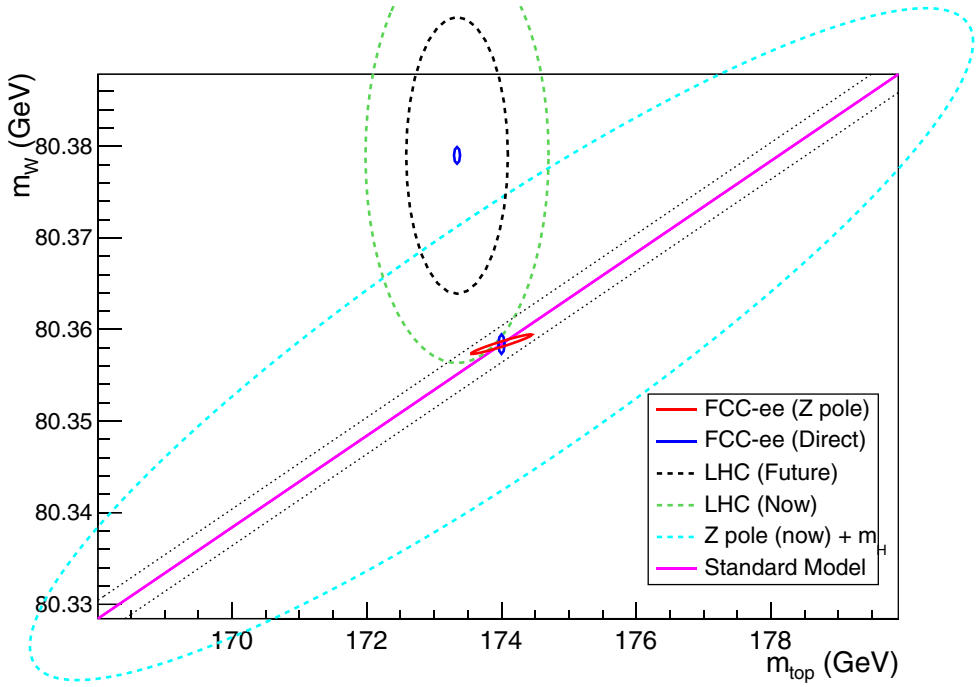


Fig. 1.8. Contours of 68% confidence level obtained as in Figure 1.4 from fits of the standard model to the electroweak precision measurements offered by the FCC-ee, under the assumption that all relevant theory uncertainties can be reduced to match the experimental uncertainties, in the (m_{top}, m_W) plane. All fits were performed with the GFitter software (<http://cern.ch/gfitter/Software/index.html>). The red ellipse is obtained from the FCC-ee measurements at the Z pole, while the blue ellipses arise from the FCC-ee direct measurements of the W and top masses. One of the two blue ellipses is centred around the central values measured today, the other is central around the values predicted by the standard model (pink line) for $m_H = 125.09$ GeV. The two dotted lines around the standard model prediction illustrate the uncertainty from the Z mass measurement if it were not improved at the FCC-ee. The green ellipse corresponds to the current W and top mass uncertainties from the Tevatron and the LHC, as in Figure 1.4. The potential future improvements from the LHC are illustrated by the black dashed ellipse. The cyan ellipse corresponds to the dark blue 68% CL contour of Figure 1.4 that includes all current Z pole measurements and the current Higgs boson mass measurement at the LHC.

one and two orders of magnitude better than the present status. The theoretical prediction of these quantities with a matching precision is an incredible challenge, but the genuine ability of these tests of the completeness of the standard model to discover new weakly-interacting particles beyond those already known is a fundamental motivation to take it up and bring it to a satisfactory conclusion.

As an illustration, the SM can be fitted to all the electroweak precision observables measured at the FCC-ee but the m_W and m_{top} direct measurements. The result as obtained with the GFitter program [34], under the assumption that all relevant theory uncertainties can be reduced to match the experimental uncertainties, is displayed in Figure 1.8 as 68% CL contours in the (m_{top}, m_W) plane. This fit is compared to the direct m_W and m_{top} measurements at the W^+W^- and the $t\bar{t}$ thresholds. A comparison with the precisions obtained with the current data at lepton and hadron colliders, as well as with LHC projections, is also shown.

1.3 The Higgs boson

Owing to its recent observation at the LHC, the Higgs boson is the least understood of all particles in the standard model. Accurate and model-independent measurements of its properties are in order to unravel its profile and to better understand the role it played/will play in the history of the universe. The LHC and its high-luminosity upgrade will provide insights into the Higgs boson couplings to the SM gauge bosons and to the heaviest SM fermions (t , b , τ , μ). A precision that is qualitatively up to the 5% level will be achieved, under a number of model-dependent assumptions, in particular on the Higgs boson decays that cannot be accessed directly at hadron colliders. Interactions between the Higgs boson and other new particles at a higher energy scale Λ typically modify the Higgs boson couplings to SM particles (denoted g_{HXX} for the coupling of the Higgs boson to particle X), either at tree level or via quantum corrections. Coupling deviations $\delta g_{\text{HXX}}/g_{\text{HXX}}$ with respect to their SM predictions are in general smaller than 5% for $\Lambda = 1 \text{ TeV}$, with a dependence that is inversely proportional to Λ^2 .

1.3.1 Absolute coupling determination from the Higgs branching fractions

From the previous argument, a sub-percent accuracy on a given coupling measurement would be needed to access the 10 TeV energy scale, and maybe to exceed it by an analysis of the deviation pattern among all couplings. Similarly, quantum corrections to Higgs couplings are at the level of a few % in the SM. The quantum nature of the Higgs boson can therefore only be tested if the measurement of its properties is pushed well below this level of precision, to a few per mil or better.

An experimental sample of at least one million Higgs bosons has to be produced and analysed to potentially reach this statistical precision. Production at e^+e^- colliders proceeds mainly via the Higgsstrahlung process $e^+e^- \rightarrow \text{HZ}$ and WW fusion $e^+e^- \rightarrow (\text{WW} \rightarrow \text{H})\nu\bar{\nu}$. The cross sections are displayed in Figure 1.9 as a function of the centre-of-mass energy. The total cross section presents a maximum at $\sqrt{s} = 260 \text{ GeV}$, but the event rate per unit of time is largest at 240 GeV, as a consequence of the specific circular-collider luminosity profile. As the cross section amounts to 200 fb at this energy, the production of one million events requires an integrated luminosity of at least 5 ab^{-1} at $\sqrt{s} = 240 \text{ GeV}$. This sample, dominated by HZ events, is usefully complemented with 1.5 ab^{-1} luminosity collected at $\sqrt{s} = 365 \text{ GeV}$ by about 180 000 HZ events and 45 000 WW-fusion events.

At $\sqrt{s} = 240 \text{ GeV}$, the determination of Higgs boson couplings follows the strategy described in references [8,48], with an improved analysis that exploits the superior performance of the CLD detector design (Sect. 7). The total Higgs production cross section is determined from counting $e^+e^- \rightarrow \text{HZ}$ events tagged with a leptonic Z decay, $Z \rightarrow \ell^+\ell^-$, independently of the Higgs boson decay. An example of such an event is displayed in Figure 1.10 (left). The mass m_{Recoil} of the system recoiling against the lepton pair is calculated with precision from the lepton momenta and the total energy-momentum conservation: $m_{\text{Recoil}}^2 = s + m_Z^2 - 2\sqrt{s}(E_{\ell^+} + E_{\ell^-})$, so that HZ events have m_{Recoil} equal to the Higgs boson mass and can be easily counted from the accumulation around m_{H} . Their number allows the HZ cross section, σ_{HZ} , to be precisely determined in a model-independent fashion. This precision cross-section measurement alone is a powerful probe of the quantum nature of the Higgs boson. Under the assumption that the coupling structure is identical in form to the SM, this cross section is proportional to the square of the Higgs boson coupling to the Z, g_{HZZ} .

Building upon this powerful measurement, the Higgs boson width can then be inferred by counting the number of HZ events in which the Higgs boson decays into a

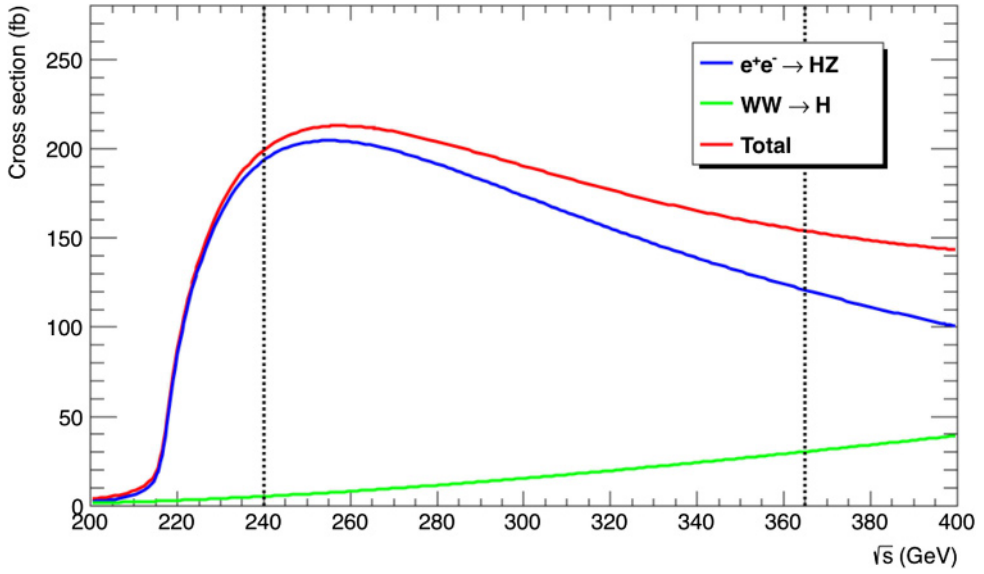


Fig. 1.9. The Higgs boson production cross section as a function of the centre-of-mass energy in unpolarised e^+e^- collisions. The blue and green curves stand for the Higgsstrahlung and WW fusion processes, respectively, and the red curve displays the total production cross section. The vertical dashed lines indicate the centre-of-mass energies of choice at the FCC-ee for the measurement of the Higgs boson properties.

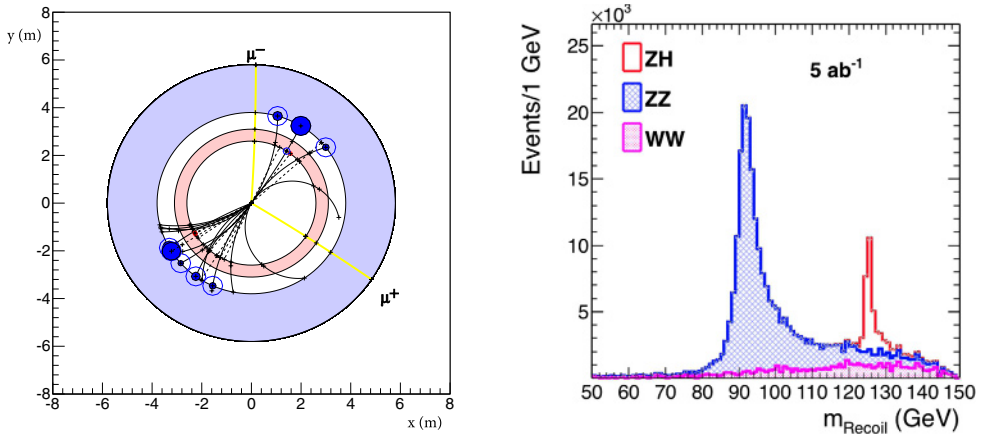


Fig. 1.10. Left: a schematic view, transverse to the detector axis, of an $e^+e^- \rightarrow HZ$ event with $Z \rightarrow \mu^+\mu^-$ and with the Higgs boson decaying hadronically. The two muons from the Z decay μ^\pm are indicated. Right: distribution of the mass recoiling against the muon pair, determined from the total energy-momentum conservation, with an integrated luminosity of 5 ab^{-1} and the CLD detector design. The peak around 125 GeV (in red) consists of HZ events. The rest of the distribution (in blue and pink) originates from ZZ and WW production.

Table 1.1. Relative statistical uncertainty on $\sigma_{\text{HZ}} \times \text{BR}(\text{H} \rightarrow \text{XX})$ and $\sigma_{\nu\bar{\nu}\text{H}} \times \text{BR}(\text{H} \rightarrow \text{XX})$, as expected from the FCC-ee data, obtained from a fast simulation of the CLD detector and consolidated with extrapolations from full simulations of similar linear-collider detectors (SiD and CLIC).

\sqrt{s} (GeV)	240		365	
Luminosity (ab^{-1})	5		1.5	
$\delta(\sigma\text{BR})/\sigma\text{BR}$ (%)	HZ	$\nu\bar{\nu}\text{H}$	HZ	$\nu\bar{\nu}\text{H}$
$\text{H} \rightarrow \text{any}$	± 0.5		± 0.9	
$\text{H} \rightarrow \text{b}\bar{\text{b}}$	± 0.3	± 3.1	± 0.5	± 0.9
$\text{H} \rightarrow \text{c}\bar{\text{c}}$	± 2.2		± 6.5	± 10
$\text{H} \rightarrow \text{gg}$	± 1.9		± 3.5	± 4.5
$\text{H} \rightarrow \text{W}^+\text{W}^-$	± 1.2		± 2.6	± 3.0
$\text{H} \rightarrow \text{ZZ}$	± 4.4		± 12	± 10
$\text{H} \rightarrow \tau\tau$	± 0.9		± 1.8	± 8
$\text{H} \rightarrow \gamma\gamma$	± 9.0		± 18	± 22
$\text{H} \rightarrow \mu^+\mu^-$	± 19		± 40	
$\text{H} \rightarrow \text{invisible}$	< 0.3		< 0.6	

Notes. All numbers indicate 68% CL intervals, except for the 95% CL sensitivity in the last line. The accuracies expected with 5 ab^{-1} at 240 GeV are given in the middle column, and those expected with 1.5 ab^{-1} at $\sqrt{s} = 365 \text{ GeV}$ are displayed in the last column.

pair of Z bosons. Under the same coupling assumption, this number is proportional to the ratio $\sigma_{\text{HZ}} \times \Gamma(\text{H} \rightarrow \text{ZZ})/\Gamma_{\text{H}}$, hence to $g_{\text{HZZ}}^4/\Gamma_{\text{H}}$. The measurement of g_{HZZ} described above thus allows Γ_{H} to be extracted. The numbers of events with exclusive decays of the Higgs boson into $\text{b}\bar{\text{b}}$, $\text{c}\bar{\text{c}}$, gg , $\tau^+\tau^-$, $\mu^+\mu^-$, W^+W^- , $\gamma\gamma$, $\text{Z}\gamma$, and invisible Higgs boson decays (tagged with the presence of just one Z boson and missing mass in the event) measure $\sigma_{\text{HZ}} \times \Gamma(\text{H} \rightarrow \text{XX})/\Gamma_{\text{H}}$ with precisions indicated in Table 1.1.

With σ_{HZ} and Γ_{H} known, the numbers of events are proportional to the square of the g_{HXX} coupling involved. A significantly improved measurement of Γ_{H} and of g_{HWW} can be achieved from the WW-fusion process at $\sqrt{s} = 365 \text{ GeV}$. In practice, the width and the couplings are determined with a global fit in the κ framework, which closely follows the logic of reference [50]. The results of this fit are summarised in Table 1.2 and are compared to the same fit applied to HL-LHC projections [51] and to those of other e^+e^- colliders [52–54] exploring the 240–380 GeV centre-of-mass energy range.

In addition to the unique electroweak precision measurement programme presented in Section 1.2, the FCC-ee also provides the best model-independent precisions for all couplings accessible from Higgs boson decays, among the e^+e^- collider projects at the EW scale. With larger luminosities delivered to several detectors at several centre-of-mass energies (240, 350, and 365 GeV), the FCC-ee improves over the model-dependent HL-LHC precisions by an order of magnitude for all non-rare decays. With a sub-per-cent precision for all these decays, the FCC-ee is therefore able to test the quantum nature of the Higgs boson. The FCC-ee also determines the Higgs boson width with a precision of 1.6%, which in turn allows the HL-LHC measurements to be interpreted in a model-independent way as well. Other e^+e^- colliders at the EW scale are limited by the precision with which the HZ or the WW fusion cross sections can be measured, i.e. by the luminosity delivered either at 240–250 GeV, or at 365–380 GeV, or both.

Table 1.2. Precision determined in the κ framework for the Higgs boson couplings and total decay width, as expected from the FCC-ee data, and compared to those from HL-LHC and other e^+e^- colliders exploring the 240–380 GeV centre-of-mass energy range.

Collider	HL-LHC	ILC ₂₅₀	CLIC ₃₈₀	LEP3 ₂₄₀	CEPC ₂₅₀	FCC-ee ₂₄₀₊₃₆₅		
Lumi (ab ⁻¹)	3	2	1	3	5	5 ₂₄₀	+1.5 ₃₆₅	+ HL-LHC
Years	25	15	8	6	7	3	+4	
$\delta\Gamma_{\text{H}}/\Gamma_{\text{H}}$ (%)	SM	3.6	4.7	3.6	2.8	2.7	1.3	1.1
$\delta g_{\text{HZZ}}/g_{\text{HZZ}}$ (%)	1.5	0.3	0.60	0.32	0.25	0.2	0.17	0.16
$\delta g_{\text{HWW}}/g_{\text{HWW}}$ (%)	1.7	1.7	1.0	1.7	1.4	1.3	0.43	0.40
$\delta g_{\text{Hbb}}/g_{\text{Hbb}}$ (%)	3.7	1.7	2.1	1.8	1.3	1.3	0.61	0.56
$\delta g_{\text{Hcc}}/g_{\text{Hcc}}$ (%)	SM	2.3	4.4	2.3	2.2	1.7	1.21	1.18
$\delta g_{\text{Hgg}}/g_{\text{Hgg}}$ (%)	2.5	2.2	2.6	2.1	1.5	1.6	1.01	0.90
$\delta g_{\text{HTT}}/g_{\text{HTT}}$ (%)	1.9	1.9	3.1	1.9	1.5	1.4	0.74	0.67
$\delta g_{\text{H}\mu\mu}/g_{\text{H}\mu\mu}$ (%)	4.3	14.1	n.a.	12	8.7	10.1	9.0	3.8
$\delta g_{\text{H}\gamma\gamma}/g_{\text{H}\gamma\gamma}$ (%)	1.8	6.4	n.a.	6.1	3.7	4.8	3.9	1.3
$\delta g_{\text{Htt}}/g_{\text{Htt}}$ (%)	3.4	–	–	–	–	–	–	3.1
BR _{EXO} (%)	SM	<1.7	<2.1	<1.6	<1.2	<1.2	< 1.0	< 1.0

Notes. All numbers indicate 68% CL sensitivities, except for the last line which gives the 95% CL sensitivity on the “exotic” branching fraction, accounting for final states that cannot be tagged as SM decays. The FCC-ee accuracies are subdivided into three categories: the first sub-column gives the results of the model-independent fit expected with 5 ab⁻¹ at 240 GeV, the second sub-column in bold – directly comparable to the other collider fits – includes the additional 1.5 ab⁻¹ at \sqrt{s} = 365 GeV, and the last sub-column shows the result of the combined fit with HL-LHC. The fit to the HL-LHC projections alone (first column) requires two additional assumptions to be made: here, the branching ratios into $c\bar{c}$ and into exotic particles are set to their SM values. These HL-LHC estimates use the latest ATLAS/CMS projected sensitivities [49].

1.3.2 Additional opportunities

Several Higgs boson couplings are not directly accessible from its decays, because the masses involved, and therefore the decay branching ratios, are too small to allow for an observation within 10⁶ events – as is the case for the couplings to the particles of the first SM family: electron, up quark, down quark – or because the masses involved are too large for the decay to be kinematically open – as is the case for the top-quark Yukawa coupling and for the Higgs boson self coupling. Traditionally, bounds on the top Yukawa and Higgs cubic couplings are extracted from the (inclusive and/or differential) measurement of the $t\bar{t}H$ and HH production cross sections, which require significantly higher centre-of-mass energy, either in e^+e^- or in proton–proton collisions. The $t\bar{t}H$ production has already been detected at the LHC with a significance larger than 5 σ by both the ATLAS [55] and CMS [56] collaborations, corresponding to a combined precision of the order of 20% on the cross section and which constitutes the first observation of the top-quark Yukawa coupling.

The Higgs self coupling

The determination of the Higgs self-interactions is of primary importance. They characterise the Higgs potential, whose structure is intimately connected to the naturalness problem and to the question of the (meta)stability of the EW vacuum. Moreover, they control the properties of the electroweak phase transition,

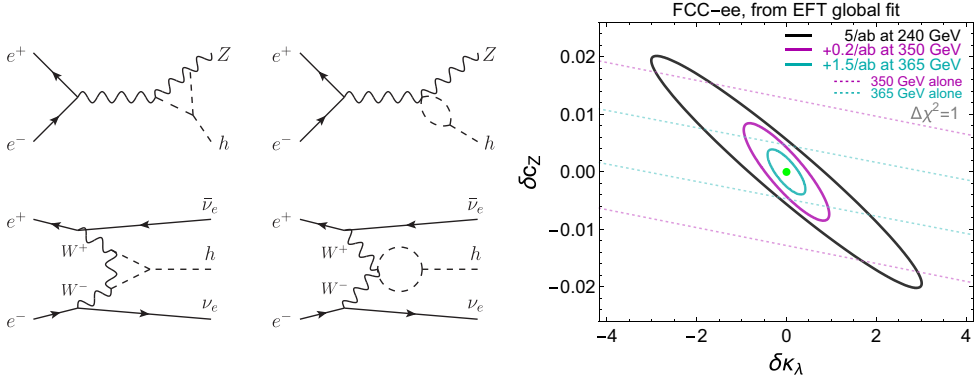


Fig. 1.11. Left, from reference [61]: sample Feynman diagrams illustrating the effects of the Higgs trilinear self-coupling on single Higgs process at next-to-leading order. Right: FCC-ee precision in the simultaneous determination of the Higgs trilinear self-coupling and the HZZ/HWW coupling, at 240 GeV (black ellipse), 350 GeV (purple dashed), 365 GeV (green dashed), and by combining data at 240 and 350 GeV (purple ellipse), and at 240, 350, and 365 GeV (green ellipse).

determining its possible relevance for baryogenesis. Sizeable deviations in the Higgs self-couplings are expected in several BSM scenarios, including for instance Higgs portal models or theories with Higgs compositeness. They however remain intangible at the LHC: at present, the trilinear Higgs coupling is loosely constrained at the $\mathcal{O}(10)$ level, and the HL-LHC program will only test it with an $\mathcal{O}(1)$ accuracy. The prospects for extracting the quadrilinear Higgs self-coupling are even less promising.

At the energy frontier, only the FCC-hh has the potential to reach a precision of the order of $\pm 5\%$ in the determination of the trilinear Higgs coupling, in combination with the precise Higgs decay branching ratio and top-quark electroweak coupling measurements from the FCC-ee. The highest-energy e^+e^- colliders (beyond 1 TeV) are limited to a precision of about $\pm 10\text{--}15\%$ [53,57], and so is the high-energy upgrade of the LHC [58]. At lower energies (15 years at 250 GeV and 12 years at 500 GeV), the ILC would reach a 3σ sensitivity to the trilinear Higgs coupling [59], corresponding to a precision of about $\pm 30\%$. With the large luminosity delivered at 240 and 365 GeV, however, the FCC-ee has privileged sensitivity to the trilinear coupling by measuring its centre-of-mass-energy-dependent effects at the quantum level on single Higgs observables [60], such as the HZ and the $\nu\bar{\nu}H$ production cross sections, representative diagrams of which are displayed in Figure 1.11 (left). Robust and model-independent bounds can be obtained [61,62] through a global (Higgs and EW) fit that includes the Higgs self-coupling κ_λ and the coupling to SM gauge bosons c_Z . When all centre-of-mass energies are included in the fit, a precision of $\pm 42\%$ can be achieved on κ_λ (Fig. 1.11, right), reduced to $\pm 34\%$ in combination with HL-LHC, and to $\pm 12\%$ when only κ_λ is allowed to vary. No meaningful constraint is obtained on κ_λ with only a single centre-of-mass energy. The FCC-ee precision EW measurements at lower energies (Sect. 1.2) are equally important to fix extra parameters that would otherwise enter the global Higgs fit and open flat directions that cannot be resolved.

The top Yukawa coupling

The precise determination of the top Yukawa coupling to $\pm 5\%$ is often used as another argument for e^+e^- collisions at a centre-of-mass energy of 500 GeV or above. This coupling will, however, be determined with a similar or better precision already by the HL-LHC ($\pm 3.4\%$, model dependent), and constrained to $\pm 3.1\%$ through a combined model-independent fit with FCC-ee data (Tab. 1.2). The FCC-ee also has access to this coupling on its own, through its effect at quantum level on the $t\bar{t}$ cross section just above production threshold, $\sqrt{s} = 350$ GeV. Here too, the FCC-ee measurements at lower energies are important to fix the value of the strong coupling constant α_s (Sect. 1.2.2). This precise measurement allows the QCD effects to be disentangled from those of the top Yukawa coupling at the $t\bar{t}$ vertex. A precision of $\pm 10\%$ is achievable at the FCC-ee on the top Yukawa coupling. A very high energy machine, such as the FCC-hh, has the potential to reach a precision better than $\pm 1\%$ with the measurement of the ratio of the $t\bar{t}H$ to the $t\bar{t}Z$ cross sections, when combined with the top EW couplings precisely measured at the FCC-ee (Sect. 1.2.4).

The Electron Yukawa coupling

The measurement of the electron Yukawa coupling is challenging due to the smallness of the electron mass. If, for a variety of reasons, the overall FCC schedule called for a prolongation of the FCC-ee operations, a few additional years spent at centre-of-mass energy in the immediate vicinity of the Higgs boson pole mass, $\sqrt{s} \simeq 125.09$ GeV, would be an interesting option. At this energy, the resonant production of the Higgs boson in the s channel, $e^+e^- \rightarrow H$, has a tree-level cross section of 1.64 fb, reduced to 0.6 fb when initial-state radiation is included, and to 0.3 fb if the centre-of-mass energy spread were equal to the Higgs boson width of 4.2 MeV [63].

A much larger spread, typically of the order of 100 MeV, is expected when the machine parameters are tuned to deliver the maximal luminosity, rendering the resonant Higgs production virtually invisible. The energy spread can be reduced with mono-chromatisation schemes [64], at the expense of a similar luminosity reduction. It is estimated that 2 (7) ab^{-1} can be delivered in one year of running at $\sqrt{s} \simeq 125.09$ GeV with a centre-of-mass energy spread of 6 (10) MeV. From a preliminary cut-and-count study in ten different Higgs decay channels, the resonant Higgs boson production is expected to yield a significance of 0.4σ within a year in both scenarios, allowing an upper limit to be set on the electron Yukawa coupling to 2.5 times the SM value. The SM sensitivity can be reached in five years [65].

The FCC-ee therefore offers a unique opportunity to set stringent upper bounds on the electron Yukawa coupling. These bounds are of prime importance when it comes to interpreting electron electric dipole measurements setting constraints on new physics. The bounds on top CP violating couplings given in reference [66], for example, are invalidated if the electron Yukawa coupling is neither fixed to its SM value nor constrained independently.

CP studies

By probing the coupling of the Higgs boson to weak gauge bosons the LHC established that the spin-parity quantum numbers of the Higgs boson are consistent with $J^{PC} = 0^{++}$ [67,68]. The data leave room, however, for significant CP violation in the interactions of the Higgs boson. New physics at the TeV scale could result in a small pseudoscalar contribution that is more significant in the couplings to fermions

than in those to gauge bosons. The large $H \rightarrow \tau^+\tau^-$ sample provided by the FCC-ee offers a unique handle to deepen the understanding of the CP properties of the Higgs boson by measuring the CP phase Δ of the $H\tau\tau$ coupling, which determines the mixing angle between the scalar and pseudoscalar contribution in the $H \rightarrow \tau^+\tau^-$ decay. In the subsequent decays $\tau^\pm \rightarrow \rho^\pm \nu_\tau \rightarrow \pi^\pm \pi^0 \nu_\tau$, the relative orientation of the two charged pions contains information on the CP phase Δ . About 1000 HZ events with $H \rightarrow \tau^+\tau^- \rightarrow \rho^+\rho^-\nu_\tau\bar{\nu}_\tau$ are expected in 5 ab^{-1} at $\sqrt{s} = 240\text{ GeV}$. With this sample, the FCC-ee can measure Δ with a precision of about 10° , if the τ decays can be fully reconstructed.

1.4 Discovery potential for new physics

1.4.1 Generic constraints on effective interactions from precision measurements

Effective field theories (EFT) provide a general framework for well-defined experimental probes of BSM physics at high energies, if the mass of the new particles is significantly above the energy scale of the processes of interest. In this so-called SMEFT, the effective interactions are built from the SM particles under the assumption that the Higgs boson belongs to an $SU(2)_L$ doublet and the interactions respect Lorentz symmetry and SM gauge invariance. An infinite set of operators satisfy these conditions. These operators capture the possible effects of microscopic substructure and can be ordered according to their canonical mass dimensions in an effective Lagrangian:

$$\mathcal{L}_{\text{Eff}} = \sum_{d=4}^{\infty} \frac{1}{\Lambda^{d-4}} \mathcal{L}_d = \mathcal{L}_{\text{SM}} + \frac{1}{\Lambda} \mathcal{L}_5 + \frac{1}{\Lambda^2} \mathcal{L}_6 + \dots, \quad \mathcal{L}_d = \sum_i C_i \mathcal{O}_i. \quad (1.12)$$

In equation (1.12), the EFT cut off is denoted by Λ , each \mathcal{L}_d contains operators \mathcal{O}_i of mass dimension d , and the leading order term $\mathcal{L}_4 \equiv \mathcal{L}_{\text{SM}}$ is the SM Lagrangian. The new physics effects are encoded in the values of the Wilson coefficients C_i of each higher-dimensional operator. These operators can be related to specific models by integrating out the heavy degrees of freedom of the high-energy theory [69–72]. The observable effects of an operator of dimension d are suppressed by $(E/\Lambda)^{d-4}$, where $E \ll \Lambda$ is the typical energy of the process, in general \sqrt{s} , or the Higgs vacuum expectation value. Therefore, the leading new physics contributions are expected to be given by dimension-six operators. (The only operator in \mathcal{L}_5 , the main effect of which is to generate Majorana neutrino masses, is irrelevant for the analysis presented here.) A complete basis of dimension-six operators, consistent with independent conservation of baryon and lepton number was first presented in reference [73]. It contains 59 types of dimension-six operators, for a total of 2499 operators if the flavour indices are taken into account.

The FCC-ee measurements of electroweak precision observables (EWPO) and of Higgs boson observables, summarised in Sections 1.2 and 1.3, give rise to enhanced sensitivity to the presence of these operators and hence new physics. The most representative set chosen for this study includes the following ten operators entering EWPO in the basis of reference [73]:

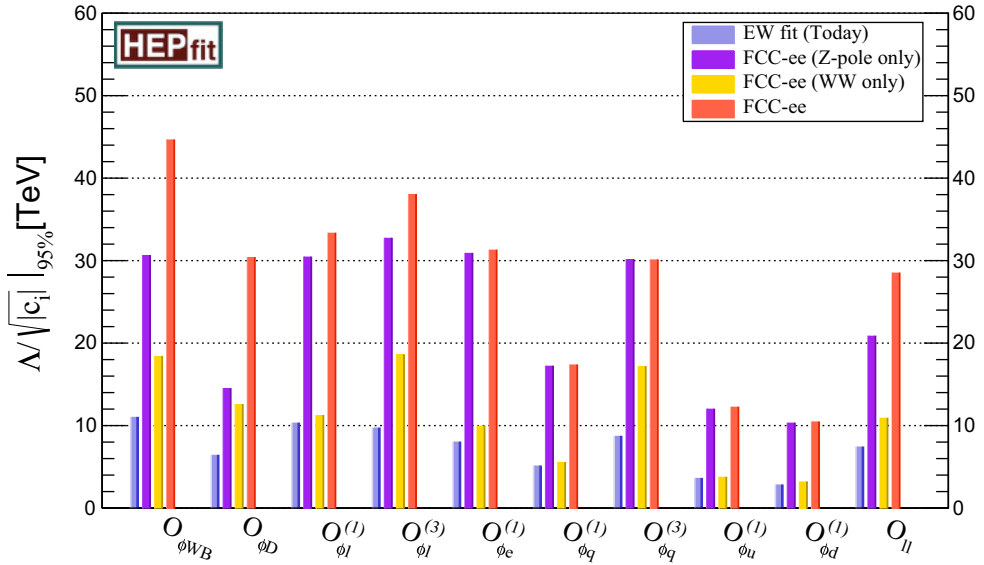


Fig. 1.12. Expected improvement of the current EW constraints from the SMEFT fit of the FCC-ee Z-pole data only (Z lineshape, partial decay widths, and asymmetries), the FCC-ee measurements at the WW threshold only (W mass, width and the invisible Z width), as well as the whole set of EWPO at the FCC-ee.

$$\begin{aligned}
 \mathcal{O}_{\phi D} &= |\phi^\dagger D^\mu \phi|^2, & \mathcal{O}_{\phi WB} &= (\phi^\dagger \sigma_a \phi) W_{\mu\nu}^a B^{\mu\nu}, \\
 \mathcal{O}_{\phi\psi}^{(1)} &= (\phi^\dagger \overleftrightarrow{D}_\mu \phi) (\bar{\psi}^i \gamma^\mu \psi^i), & \mathcal{O}_{\phi F}^{(3)} &= (\phi^\dagger \overleftrightarrow{D}_\mu^a \phi) (\bar{F}^i \gamma^\mu \sigma_a F^i), & \mathcal{O}_{ll} &= (\bar{l} \gamma_\mu l) (\bar{l} \gamma^\mu l),
 \end{aligned} \tag{1.13}$$

where ϕ is the scalar doublet, ψ runs overall the 5 types of SM fermion multiplets, while F only refers to the 2 types of SM left-handed fermion doublets. A closer scrutiny of the operator $\mathcal{O}_{\phi D}$ helps in gaining intuitive understanding of how these operators give rise to observable effects: when the Higgs vacuum expectation value is inserted into this operator, an additional contribution to the W/Z mass splitting is generated, beyond the usual SM prediction. Some of the above operators, as well as additional interactions absent in EWPO, enter Higgs boson observables, such as

$$\begin{aligned}
 \mathcal{O}_{\phi G} &= \phi^\dagger \phi G_{\mu\nu}^A G^{A\mu\nu}, & \mathcal{O}_{\phi W} &= \phi^\dagger \phi W_{\mu\nu}^a W^{a\mu\nu}, & \mathcal{O}_{\phi B} &= \phi^\dagger \phi B_{\mu\nu} B^{\mu\nu}, \\
 \mathcal{O}_{\phi\Box} &= (\phi^\dagger \phi) \Box (\phi^\dagger \phi), & \mathcal{O}_{\mu\phi} &= (\phi^\dagger \phi) (\bar{l}^2 \phi \mu), & \mathcal{O}_{\tau\phi} &= (\phi^\dagger \phi) (\bar{l}^3 \phi \tau), \\
 \mathcal{O}_{b\phi} &= (\phi^\dagger \phi) (\bar{q}^3 \phi b), & \mathcal{O}_{c\phi} &= (\phi^\dagger \phi) (\bar{q}^2 \phi c).
 \end{aligned} \tag{1.14}$$

For clarity and simplicity, the expected sensitivities to the above-mentioned dimension-six operators are estimated with a fit in which only one operator is present at a time. While these results are technically not model-independent, they still serve to illustrate the expected sensitivity improvement of future experimental data.

The projected sensitivity to new physics obtained from the FCC-ee electroweak precision measurements is illustrated in Figure 1.12. These results assume that the intrinsic uncertainty of SM theory calculations will be reduced according to the conservative projections of reference [74]. The improvement of the SM parametric

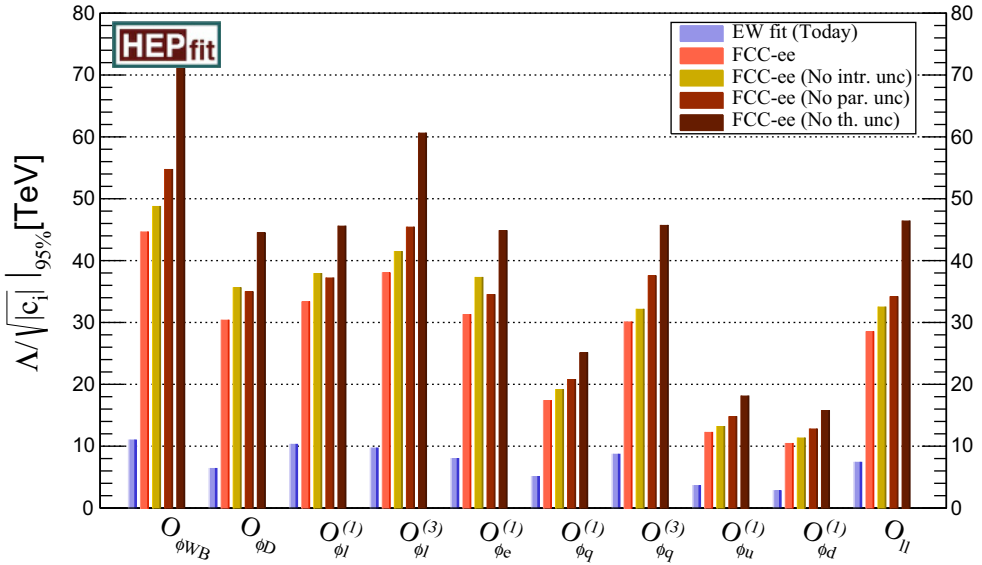


Fig. 1.13. Comparison of sensitivities from the SMEFT fit of the full FCC-ee set of EWPO, using the future SM theory uncertainties and those neglecting either the intrinsic errors, the parametric ones, or both.

uncertainties due to the more precise measurements of the SM inputs at the FCC-ee is also taken into account, together with the expected advance in the determination of the strong coupling constant from lattice calculations. The sensitivities to the ratios C_i/Λ^2 are reported as the 95% probability bounds on the *interaction* scale, $\Lambda/\sqrt{C_i}$, associated to each operator. This interaction scale must not be confused with the mass scale of new particles, in the same way as the Fermi constant $G_F^{-1/2}$ does not represent the scale where new degrees of freedom, i.e. the W boson, enter in the electroweak theory.

These bounds are compared to the results obtained from current electroweak precision data [75,76]. In general, an overall improvement of over one order of magnitude is expected in the sensitivity to C_i/Λ^2 . Not surprisingly, an even stronger constraining power could be achieved if theory uncertainties were further reduced, as shown in Figure 1.13.

Figure 1.14 shows similar results for the case of a fit to the precise measurements of the Higgs boson observables. The corresponding limits on the interaction scale are compared to those from current LHC data [77]. The overall sensitivity to C_i/Λ^2 can be, again, as large as ~ 20 times that of current data and up to 5–10 times that expected after the HL-LHC. The experimental uncertainties for the Higgs boson measurements are expected to be similar to or larger than those from SM calculations. More FCC-ee data would therefore allow the sensitivity to be improved even further, in some cases. Finally, Figure 1.15 compares both EWPO and Higgs boson constraints and shows also the resulting bounds obtained with the combination of both sets of observables. In these simplified fits to each interaction individually, the EWPO and Higgs boson constraints are very much complementary.

These fits must be used carefully when translated into specific scenarios, as they are not fully model-independent. The results, however, clearly demonstrate the important step that the FCC-ee physics programme represents with respect to any

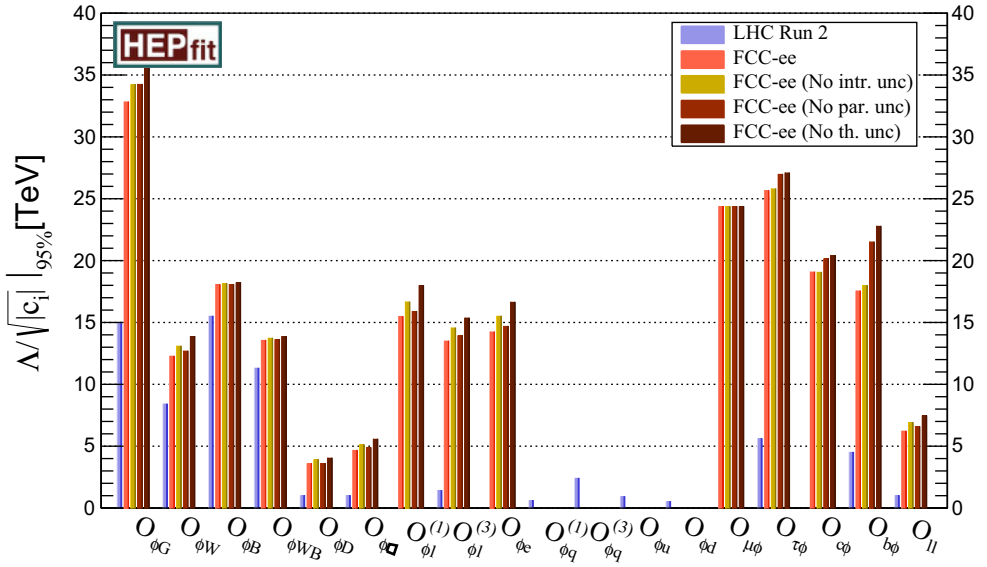


Fig. 1.14. FCC-ee Higgs constraints on the different EFT interactions in equations (1.13) and (1.14), compared to the current LHC Run 2 results. The impact of the different types of SM theory uncertainties are also shown (neglecting intrinsic, parametric and both uncertainties, respectively).

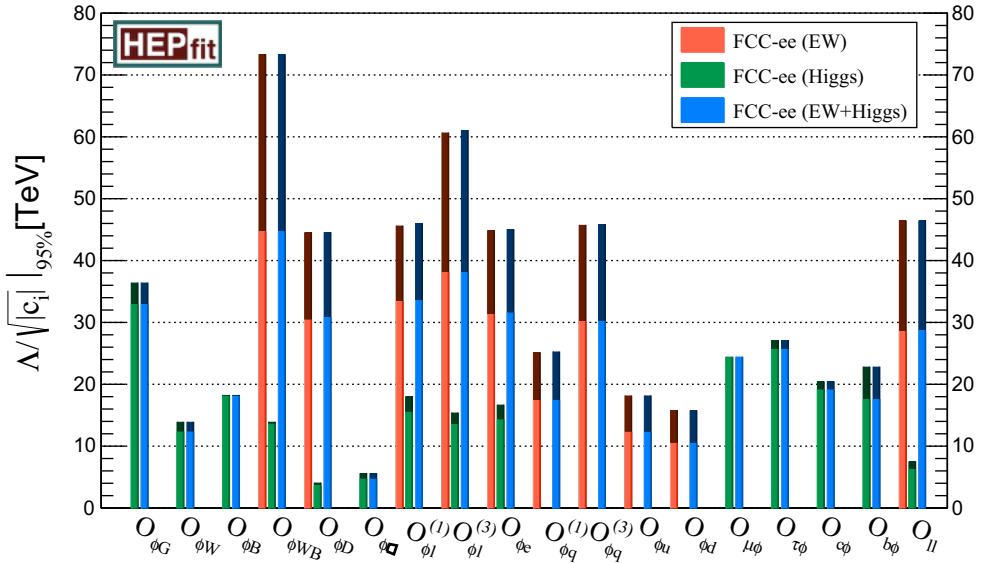


Fig. 1.15. Comparison of the separate EW and Higgs constraints, as well as the results combining both in a global SMEFT fit. Darker shades of each color indicate the results neglecting all SM theory uncertainties.

existing experiments, in terms of the potential for comprehensive precision studies of the electroweak sector.

1.4.2 Sensitivity to new physics predicted in specific BSM models

The fits presented in Section 1.4.1 are generic in that they make no specific assumption about the underlying BSM theory, except that its energy scale must be large with respect to the centre-of-mass energy. More specific extensions of the standard model have been proposed to explain the current agreement between observations at colliders and SM predictions, on the one hand, and the growing experimental evidence for new phenomena (non-baryonic dark matter, small neutrino masses, baryon asymmetry of the universe, ...), on the other. These extensions predict either very small deviations from standard model predictions in EWPO and Higgs precision measurements, or the existence of new light or heavy particles, or both, which could be tested at the FCC-ee. In particular, a multitude of Z decays that are predicted to be rare or forbidden in the SM can be studied or searched for in the 5×10^{12} events produced at the Z pole. In this section, the unique sensitivity of the FCC-ee to a selected but representative set of BSM models or situations is reviewed.

Right-handed neutrinos

Neutrino oscillations demonstrate that neutrinos have mass [78]. As such, they provide laboratory evidence for physics beyond the renormalisable interactions of the SM. Understanding the origin of neutrino masses would open the way to a deeper understanding of particle masses, as well as possible solutions to outstanding issues in particle physics such as the origin of the baryon asymmetry in the universe or of dark matter. A minimal and natural way to account for the observed smallness of neutrino masses is the existence of non-renormalisable Majorana neutrino mass terms, which can arise due to heavy right-handed neutrinos with Majorana mass terms [79–84]. For these reasons, in the discussion of future projects, experimental sensitivity to right-handed neutrinos (also named “sterile neutrinos”) has become one of the benchmarks for discovery potential. Right-handed neutrinos lead to a rich variety of signatures at the FCC-ee, from their impact on precision measurements to the possible observation of right-handed neutrino decays.

It has been argued that in some scenarios the right-handed neutrino mass scale M can have a common origin with the electroweak scale [85–88]. The limit $M \rightarrow 0$ gives rise to an approximate $B - L$ symmetry, thus it is technically natural for M to be small. Reviews of how comparatively light right-handed neutrinos can address the fundamental puzzles of the baryon asymmetry of the universe and dark matter can be found in references [89–104]. Model classes that allow for a low scale see-saw are known as “inverse see-saw models” [79,80,105,106], and “linear see-saw models” [81,83,107–113], and are consistent with “minimal flavour violation” [84, 114]. A recent review of the collider phenomenology of neutrino mass models can be found in reference [115].

Right-handed neutrinos impact precision measurements through mixing with their left-handed counterparts, with angle Θ . After diagonalisation one has heavy and light mass eigenstates. The light neutrinos states, while remaining mostly left-handed, acquire a small sterile component yielding an apparent violation of the unitarity of the PMNS matrix [116]. The PMNS non-unitarity alters the couplings

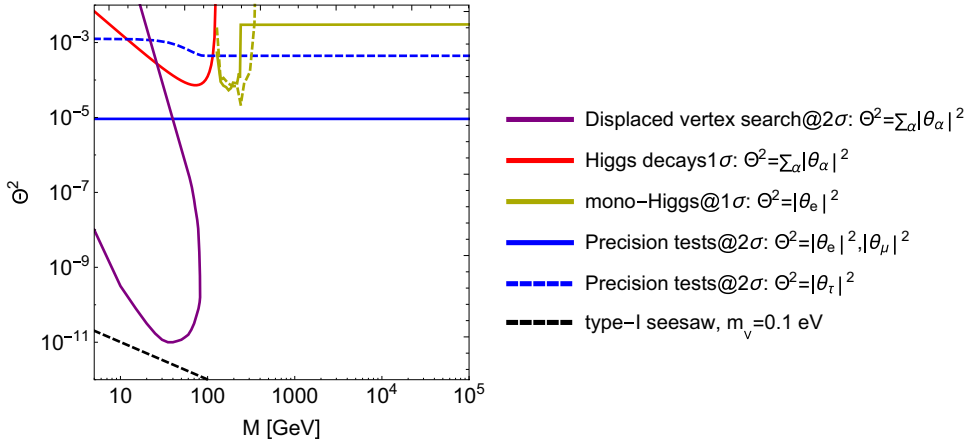


Fig. 1.16. Sensitivities of the different signatures to the active-sterile mixing angle Θ and sterile neutrino mass M at the FCC-ee, from reference [124]. In addition to the main signatures described in the text, the sensitivities from Higgs decays and mono-Higgs production is also shown.

of the light neutrinos to the weak currents, thereby systematically shifting all the observables in which neutrinos are involved [117–123] and leading to a very specific pattern of deviations from the SM.

The single most important observable is the Fermi constant G_F , which is measured very precisely in muon decays $\mu \rightarrow e \nu_\mu \nu_e$, while being an input parameter for the electroweak precision observables. In the FCC-ee era, with many of these observables measured at the 10^{-5} precision level or better, a reduction of the neutrino coupling of that magnitude will be visible. Other observables that can be measured with great precision to test the PMNS matrix (non)unitarity include the charged current branching ratios, in particular $\tau \rightarrow \ell \nu_\ell \nu_\tau$ and $W \rightarrow \ell \nu_\ell$, rare lepton-flavour-violating processes ($\ell \rightarrow \ell' \gamma$, $\ell \rightarrow 3 \ell'$), as well as weak cross sections for processes like $e^+e^- \rightarrow HZ$, ZZ , and W^+W^- . For example, with 1.5×10^{11} tau lepton pairs produced, the tau leptonic branching ratios should be measurable to a relative precision of better than 10^{-5} . Based on reference [117], the sensitivity from the FCC-ee precision measurements in the plane (Θ^2, M) is shown by the horizontal blue lines in Figure 1.16. Two points should be noted. Firstly, the combination of lepton universality and the available EWPO will allow separate access to the three lepton flavour mixing angles. Secondly, the sensitivity to heavy neutrinos from precision measurements extends well beyond 100 TeV; this is a particular example of BSM physics for which decoupling is not at work.

Heavy neutrinos N with masses M below m_Z and active-sterile mixing Θ below the present constraints [125] naturally have long lifetimes ($\simeq 3 [\text{cm}] / |\Theta|^2 (M [\text{GeV}])^6$), which can give rise to visible displaced secondary vertices in the detector, especially when the decay is semi-leptonic: $N \rightarrow \ell q \bar{q}$. Searches for heavy neutrino decays with detached vertices are most efficient during the Z pole run due to the larger luminosity and production cross section from $Z \rightarrow \nu N$ decays. These searches [126–128] can reach sensitivities to active-sterile mixing parameters $|\Theta|^2$ down to and below $\sim 10^{-11}$, as shown by the purple line in Figure 1.16, and by the orange line in the left panel of Figure 1.17. The search benefits from the suppression of the SM background due to the displaced vertex of the heavy neutrino decay. The small beam pipe radius and the clean experimental conditions are additional advantages.

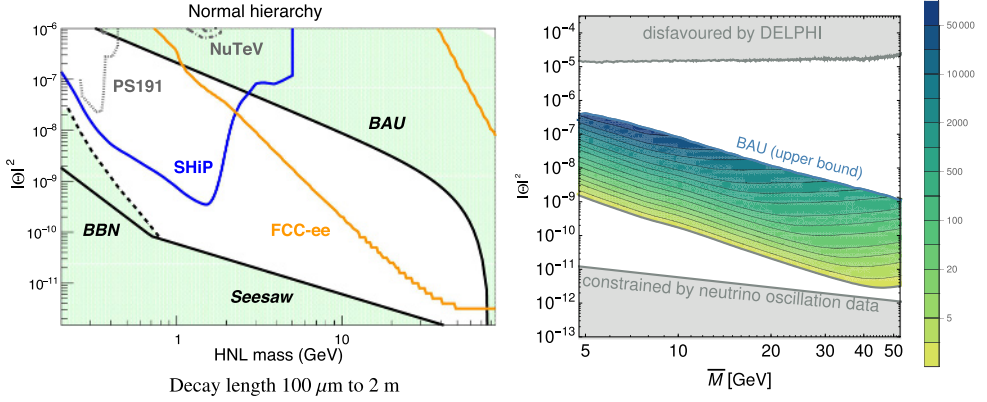


Fig. 1.17. Left: the region of sensitivity to the right-handed neutrinos as a function of their mixing angle Θ with active neutrinos and their mass M , in the displaced vertex search, put in perspective with the lower energy searches in neutrino beams or beam dump experiments (from Ref. [126], updated for the CDR FCC-ee conditions), and with theoretical constraints. Right: detail of the parameter space showing by colour code the number of events expected at the FCC-ee within the parameter space (thick black line) consistent with the leptogenesis hypothesis (from Ref. [129]); constraints from the DELPHI searches [125] and from neutrino oscillation data are shown. In both plots, normal mass ordering is assumed.

The sensitivity could be improved to some extent by a larger tracking volume, but the dominant factor remains the huge luminosity at the Z pole. The right panel of Figure 1.17 indicates the number of events that would be observed as a function of M and $|\Theta|^2$. In some regions of the parameter space, several hundred signal events are expected to be observed, which would allow a first determination of the mass and lifetime of the right-handed neutrino and establish its relative decay rate into the three lepton flavours. This discovery, which would be made early in the life of the FCC-ee, would certainly have an impact on both detector design and motivation for FCC-hh, for which (i) dedicated displaced vertex triggers would be necessary; and (ii) the right-handed neutrinos would be produced most abundantly in W leptonic decays, thereby giving access to both initial and final state lepton charge and flavour.

Hidden sector

The evidence for the existence of dark matter is highly suggestive and has motivated innumerable searches for particle interactions of dark matter. The paucity of signals in searches for standard WIMP dark matter candidates, combined with an evolving theoretical perspective that increasingly takes inspiration from the visible sector features, has revealed that the nature of the dark sector could be much more complex than previously thought. The Higgs and Z-boson are unique as they are the only massive neutral bosons in the standard model. They are therefore prime candidates for probing the dark sector as they may decay readily to new light neutral fields beyond the SM. If these fields decay back into SM states, they could provide a unique window into the dark sector.

Furthermore, a variety of evidence for physics beyond the SM points to new sectors that may have new light states. One popular class of models that offers an explanation for the insensitivity of the weak scale to new high energy physics scales in nature is known by the moniker of “neutral naturalness”. (The “Twin

Higgs” [130] is the first incarnation of this idea.) This name originates from the fact that the particles that protect the Higgs boson mass from large quantum corrections are neutral. Furthermore, these models also often require, structurally, that some of the new particles are light and could thus show up in rare decays of the Higgs boson. Further motivation for the possibility of new neutral “hidden” sectors arises in many models of electroweak baryogenesis, in which the nature of the electroweak phase transition is modified to become strongly first order as the result of new neutral fields interacting with the Higgs boson.

Due to the cleanliness of the detection environment and the large samples of Z and Higgs bosons available at the FCC-ee, non-standard decays, facilitated through the production of new hidden sector particles, could be probed down to very small branching ratios. In Figure 1.18 the results of two dedicated studies of exotic Z and Higgs-boson decays [131,132] are shown, where the decays occur through the production of new hidden sector particles. For both bosons, the reach in probing such hidden sectors at the FCC-ee would far surpass that attainable at the HL-LHC, with the constraints in both cases comparable to the rare decay constraints usually delivered in lower energy hadron physics at the intensity frontier.

Composite Higgs models

All the measurements in the Higgs sector so far are aligned with the SM predictions. Yet, it is not known whether at small distances the Higgs boson is a fundamental scalar field, or a composite bound state like all the other scalar particles observed thus far. Composite Higgs models are the particle physics version of the BCS theory of superconductivity. They also solve the hierarchy problem of the standard model owing to compositeness form factors taming the divergent growth of the Higgs boson mass upon quantum effects. Furthermore, the measured Higgs boson mass could well be consistent with the fact that such a (now composite) object arises as a pseudo Nambu-Goldstone Boson (pNGB) from a particular coset of a global symmetry breaking [133,134]. Models with a Higgs state as a pNGB generally also predict modifications of its couplings to both bosons and fermions of the SM, hence the measurement of these quantities, at either a hadronic or a leptonic collider, represents a powerful way to test its possible non-fundamental nature [135]. In addition to deviations in the Higgs couplings, composite Higgs models also predict vector resonances at a scale of a few TeV; heavy vector-like fermionic top partners that could mix with the top quarks and induce some sizeable deviations in the EW couplings of the top quark; and heavy vector-like top partners with exotic charges that could be searched for directly, for instance in same-sign di-lepton channels. The synergy and complementarity between these direct and indirect signatures have been discussed in the literature [136,137].

Concrete phenomenological studies for FCC-ee have been carried out considering an explicit four-dimensional model which realises this idea of Higgs compositeness (4DCHM) [138]. This model features new neutral massive gauge bosons, hereafter denoted by $Z'_{2,3}$, with mass larger than ~ 3 TeV that could escape detection at the LHC owing to the small Z'_i couplings to both light quarks and leptons [139], combined with possibly very large widths of the Z'_i states. Such additional EW gauge bosons would however enter the $e^+e^- \rightarrow t\bar{t}$ cross Section [140], in a twofold way. On the one hand, their presence can be felt through mixing effects with the Z state of the SM that would modify the $Zt\bar{t}$ and the $Z\ell^+\ell^-$ couplings. On the other hand, new Feynman diagram topologies with the propagation of such $Z'_{2,3}$ states would also enter top-pair production and appear as effective $\gamma t\bar{t}$ coupling modifications. The

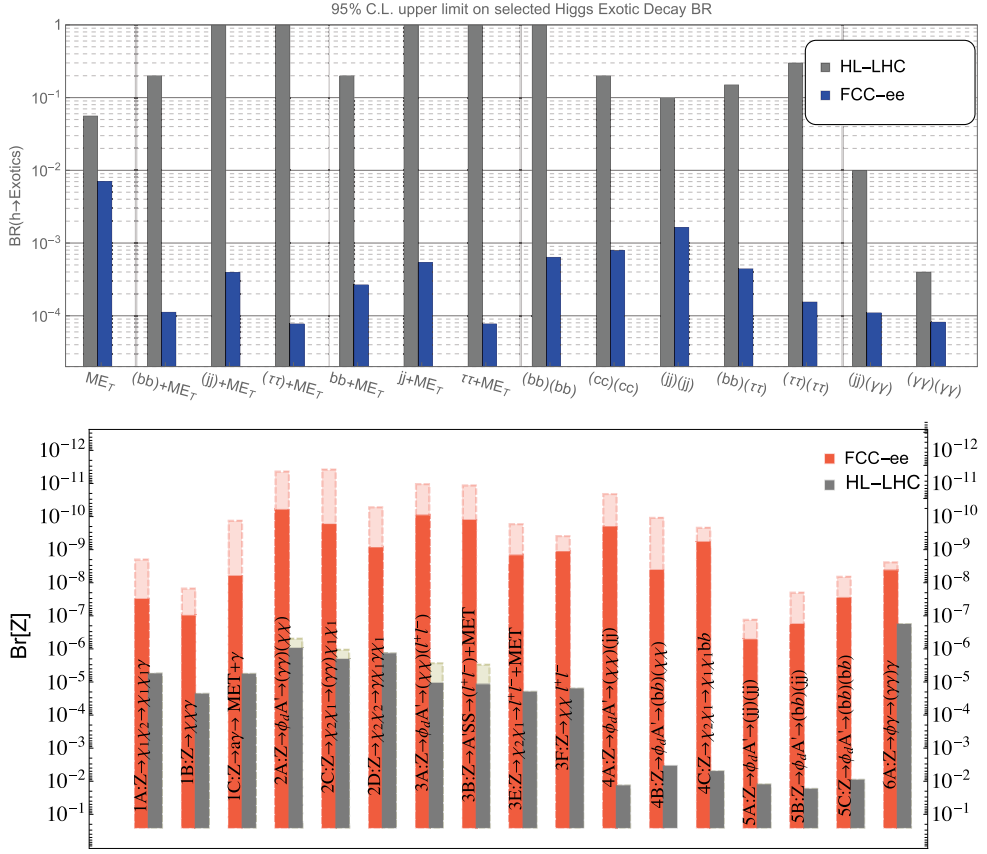


Fig. 1.18. Expected upper limits on the branching ratios for the exotic decays of the Higgs boson (top) and Z boson (bottom) that can be accessed at FCC-ee, including decays involving dark matter. These figures are taken from [131,132]. The large and experimentally clean samples of these bosons allow for the discovery of exotic decays even for very small exotic branching ratios. For exotic Z decays expected limits for the worst- and best-case scenario are shown.

modification of the $Z\ell^+\ell^-$ couplings would also affect other processes, specifically $e^+e^- \rightarrow \mu^+\mu^-$.

To evaluate the sensitivity of the FCC-ee to these models, a benchmark point A was identified to evade the latest projected bounds of the HL-LHC searches for Z' gauge bosons and to be compatible with current EWPO measurements, by the following choice of 4DCHM gauge sector parameters: the compositeness scale f is set to 1.6 TeV, and the strong gauge coupling g^* to 1.8 [138]. With these parameters, the Z' masses amount to $m_{Z'_2} = 2.98$ TeV and $m_{Z'_3} = 3.07$ TeV, and their widths are all of the order of 20–30% of their masses. As shown in Figure 1.19, the large statistics offered by the FCC-ee would reveal significant deviations in almost all observables mentioned above with respect to the SM: top-quark left and right couplings to the Z (4σ), effective top couplings to the photons (8σ), Higgs boson couplings to the Z boson and to the b quark (13σ), or $e^+e^- \rightarrow \mu^+\mu^-$ cross sections above the Z pole ($>20\sigma$). With such a pattern of significance, these measurements in principle allow the model parameters to be accurately fit. For example, the Z' masses would be predicted with a precision of 50 GeV (2%), the scale f with a precision of 130 GeV

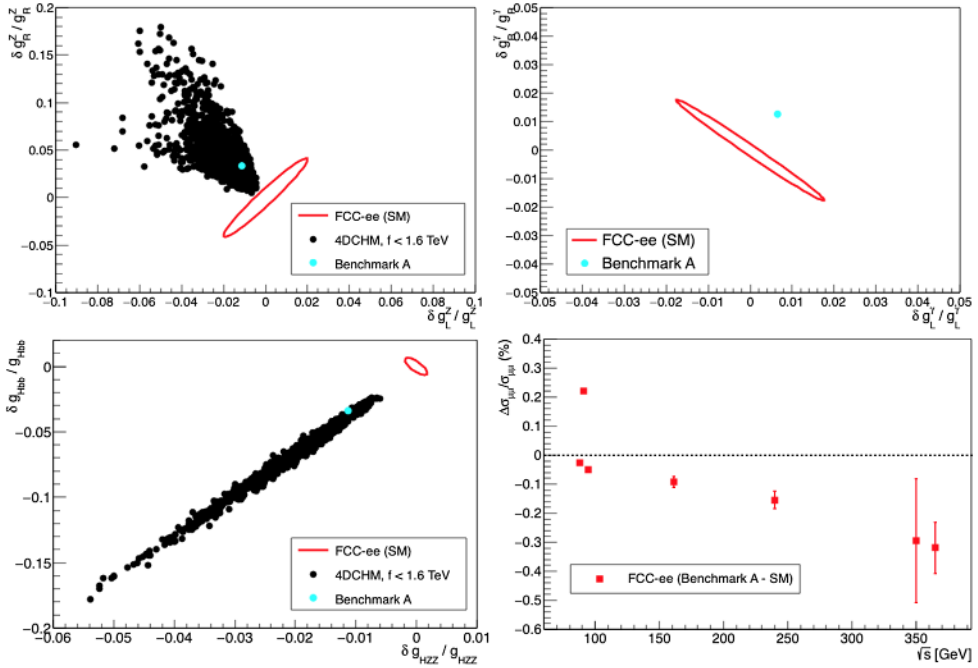


Fig. 1.19. Predicted deviations of the top-quark left and right couplings to the Z (top left) and effective couplings to the photon (top right), of the Higgs boson couplings to the Z boson and the b quark (bottom left), and of the dimuon cross section as a function of the centre-of-mass energy (bottom right) for the 4DCHM benchmark point A (represented by a cyan marker in the first three graphs) with respect to the SM, centred at (0,0) in the first three graphs, and at 0 in the fourth. The FCC-ee measurement uncertainties are displayed either as red ellipses or as error bars. The black markers in the top-left and bottom-left plots show the deviations predicted by other 4DCHM parameter sets, with $f \leq 1.6$ TeV.

(8%), and the coupling constant g^* with a precision of 0.14 (8%) with the sole $\mu^+\mu^-$ observables.

Lepton flavour violating Z decays

The observation of flavour-violating Z decays, e.g. $Z \rightarrow e\mu$, $\mu\tau$, or $e\tau$, would provide indisputable evidence for physics beyond the SM. These decays are forbidden in the SM by the GIM mechanism [141] and their branching fractions are still predicted to be extremely small (below 10^{-50}) when the SM is minimally extended to incorporate flavour violation in the neutral lepton sector (LFV) induced by the leptonic mass mixing matrix [142]. Sizeable rates for these LFV $Z \rightarrow \ell_1^\mp \ell_2^\pm$ processes could, hence, reflect the existence of new particles such as right-handed neutrinos. The search for LFV Z decays is also complementary to the direct search for heavy neutral leptons.

A phenomenological study [143] addresses the potential for the FCC-ee to probe the existence of sterile neutral fermions in the light of the improved determination of neutrino oscillations parameters, the new bounds on low-energy LFV observables, as well as cosmological bounds. This work also addresses the complementarity of these searches with the current and foreseeable precision of similar searches at lower energy experiments. The best sensitivity to observe or constrain LFV in the $e\mu$ sector is then obtained by the experiments based on the muon-electron conversion

in nuclei [144]. In contrast, the study of the decays $Z \rightarrow e\tau$ and $Z \rightarrow \mu\tau$ provides an invaluable and unique insight into the connection to the third generation.

The current limits on the branching ratios of charged lepton flavour violating Z decays were established by the LEP experiments [145–147]. More recently, the ATLAS experiment improved the bound for $e\mu$ final states [148]. Typical upper limits on the branching fractions are at the level of 10^{-5} – 10^{-6} . The production at FCC-ee of 5×10^{12} Z decays provides improved limits by several orders of magnitude and probes BSM physics scenarios for branching fractions down to 10^{-9} [149].

Electroweak Penguins in b-quark transitions

The production of all species of heavy flavours in a sample of 10^{12} $Z \rightarrow b\bar{b}$ events, with a large boost as in the LHCb experiment, makes the FCC-ee a natural home for precision flavour physics. Processes involving a quark transition $b \rightarrow s\ell^+\ell^-$ (ℓ denotes here an electron or a muon) are currently receiving substantial phenomenological [150–153] and experimental [154–156] interest. The departures from the SM predictions observed in these studies question, in particular, the lepton universality in quark-based transitions and may even suggest BSM physics with new gauge bosons or leptoquarks. Should these deviations be confirmed, observables involving the third generation charged lepton τ may enhance the evidence and shed new light on the new physics involved. In this respect, the $B_s \rightarrow \tau^+\tau^-$ and $\bar{B}^0 \rightarrow K^{*0}(892)\tau^+\tau^-$ decays are obvious candidates to study. The presence of neutrinos in the final states makes the experimental reconstruction of these decays particularly challenging at hadron colliders. At the FCC-ee, however, the excellent knowledge of the decay vertices of multi-hadronic τ decays allows the kinematics of these decays to be fully and unambiguously reconstructed. Identification of the different hadron species in the tracking system of the detector would be an additional advantage to further reduce the background.

About 1000 events with a reconstructed $\bar{B}^0 \rightarrow K^{*0}(892)\tau^+\tau^-$ decay are expected at the FCC-ee, which opens the way to measuring the angular properties of the decay [157] and, therefore, to a much refined characterisation of the potentially underlying new physics. Figure 1.20 displays the reconstructed B^0 mass distribution of simulated SM signal and background events in a sample of 5×10^{12} Z decays in the CLD detector design. The signal purity and yield obtained at the FCC-ee are unequalled at any current or foreseeable collider and would increase in a correlated manner with any improvement to the charge-particle track impact parameter resolution.

Other unique opportunities in flavour physics

The study of the two rare decays above has shown that the statistics available at a high-luminosity Z factory, complemented by state-of-the-art detector performance, can allow their potential measurement at unequalled precision. They can also serve as a benchmark to open the way to other physics observables in quark and lepton sectors. The loop-induced leptonic decays $B_{d,s} \rightarrow e^+e^-$, $\mu^+\mu^-$, and $\tau^+\tau^-$ provide SM candles and are sensitive to several realisations of BSM physics. The observation of $B_s \rightarrow \tau^+\tau^-$ would be invaluable in this respect and, with 100 000 events expected, is reachable at the FCC-ee. The charged-current-mediated leptonic decays $B_{u,c} \rightarrow \mu\nu\mu$ or $\tau\nu\tau$ offer the possibility to determine the CKM elements $|V_{ub}|$ $|V_{cb}|$ with mild theoretical uncertainties. The CP violation in mixing can be measured through semileptonic asymmetries, as yet unobserved, but the FCC-ee sensitivity is

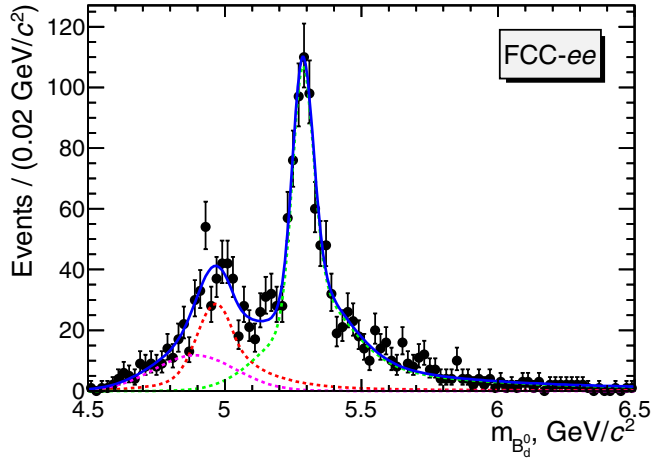


Fig. 1.20. Invariant mass of $\bar{B}^0 \rightarrow K^{*0}(892) \tau^+ \tau^-$ reconstructed candidates (dots with error bars). In the selected events, the τ particles decay into three prongs $\tau^- \rightarrow \pi^- \pi^+ \pi^- \nu_\tau$ allowing the τ decay tertiary vertex to be reconstructed. The primary vertex (Z vertex) is reconstructed from primary charged particle tracks, and the secondary vertex (\bar{B}^0 vertex) is reconstructed with the $K^*(892)$ daughter particles ($K^*(892) \rightarrow K^+ \pi^-$). The dominant sources of backgrounds included in the analysed sample, namely $\bar{B}_s \rightarrow D_s^+ D_s^- K^{*0}(892)$ and $\bar{B}^0 \rightarrow D_s^+ \bar{K}^{*0}(892) \tau^- \bar{\nu}_\tau$, are modelled by the red and pink probability density functions (p.d.f.), respectively. The signal p.d.f. is displayed with the green curve.

close to their SM predictions. The cleanliness of the e^+e^- experimental environment will benefit the study of B_s , B_c and b baryons, the decay modes involving neutral particles in the final state (π_0 , K_S , η , η' , ν), as well as the many-body fully hadronic b -hadron decays. The harvest of CP-eigenstates in several b -hadron decays will allow the CP-violating weak phases to be comprehensively measured.

1.5 Requirements

1.5.1 Collider

In 2013, the European Strategy for Particle Physics (ESPP) unambiguously recognised the importance of an electron-positron collider able to measure the properties of the Higgs boson and other particles with an unprecedented accuracy. In order to significantly increase the sensitivity to new physics of these measurements, such an e^+e^- factory must deliver integrated luminosities at centre-of-mass energies from around the Z pole to above the $t\bar{t}$ threshold such that the statistical precision of most electroweak and Higgs observable measurements improves by one to two orders of magnitude.

The minimum data samples needed to achieve this ambitious goal correspond to:

1. An integrated luminosity of at least 30 ab^{-1} at $\sqrt{s} \simeq 88$ and 94 GeV for the measurement of the electromagnetic coupling constant at the Z mass scale. These data are also useful for the determination of the Z decay width.
2. An integrated luminosity of at least 100 ab^{-1} at $\sqrt{s} \simeq m_Z \simeq 91.2 \text{ GeV}$ in particular, for the measurement of the effective weak mixing angle and for the search for, or study of, rare decays. These data are also important for the determination of the Z mass and of the strong coupling constant at the Z mass scale.

3. An integrated luminosity of at least 10 ab^{-1} around the W^+W^- production threshold, for the measurement of the W mass and decay width, evenly shared between $\sqrt{s} \simeq 157.5$ and 162.5 GeV . These data are also important for the determination of the number of neutrino species and an independent measurement of the strong coupling constant.
4. An integrated luminosity of at least 5 ab^{-1} at $\sqrt{s} = 240 \text{ GeV}$, for the measurements of the Higgs boson couplings from its decays branching fraction and the total HZ production cross section.
5. An integrated luminosity of about 0.2 ab^{-1} in a 5-GeV -wide window around the $t\bar{t}$ threshold, typically shared among eight centre-of-mass energy points from ~ 340 to $\sim 345 \text{ GeV}$, for the measurement of the top-quark mass, decay width, and Yukawa coupling to the Higgs boson.
6. An integrated luminosity of at least 1.5 ab^{-1} above the $t\bar{t}$ threshold, $\sqrt{s} \simeq 365 \text{ GeV}$, for the measurement of the top electroweak couplings. These data also provide a threefold improvement of the Higgs boson decay width accuracy with respect to the sole data at $\sqrt{s} = 240 \text{ GeV}$, which in turn, significantly constrains the Higgs boson couplings.

Over the whole period, the collider design must be compatible with operating at the Z pole every now and then to accumulate a few 10^7 Z decays in less than a day, for detector calibration purposes. (This important feature, used repeatedly during the second phase of LEP, cannot be proposed with current linear collider designs.)

The unprecedented precision measurements achievable with these data in the electroweak, Higgs and top sectors are complementary and altogether sensitive to new physics scales up to 70 TeV . The Z factory run with 5×10^{12} Z can discover dark-matter candidate particles which couple with a strength down to as little as 10^{-11} of the weak coupling. Furthermore, with the synergetic runs at 240 and 365 GeV in combination with HL-LHC, the top Yukawa coupling will be known with a precision at the $\pm 3\%$ level, and the trilinear Higgs self coupling to $\pm 34\%$.

At this stage of the study, it appears that once the desired luminosity is accumulated at each of these energies, the potential gain in the precision of the Higgs boson and other particle properties is not enough (if any) to justify an upgrade to larger centre-of-mass energies, e.g. $\sqrt{s} = 500 \text{ GeV}$, especially with the perspective of a 100 TeV proton-proton collider operating later in the same tunnel. (Of course, the appearance at the LHC of some threshold for new physics accessible in e^+e^- collisions above 365 GeV may change the picture entirely.) On the other hand, many of the measurements offered by the FCC-ee between the Z pole and a maximum energy of 365 GeV , above the $t\bar{t}$ threshold, would still be limited by statistical uncertainties and would continue to improve with higher luminosity.

It can be argued that experiments might wish to study the Higgs boson as a priority, rather than devoting the first six years at the Z pole and the WW threshold. There is indeed no fundamental obstacle to run first at $\sqrt{s} = 240 \text{ GeV}$, should it be felt compelling by the community. From the point-of-view of the machine installation and evolution, however, the proposed staging plan results from the most natural, efficient, economic, and logical operation model. From the scientific point-of-view, changing the order of the energy points would not change the overall outcome of the programme. Also, the perceived urgency of the Higgs precision measurements might well be not as incisive after 15 years of measurements at the LHC and the HL-LHC as it is today. Moreover, the EFT analysis reveals that the EW precision measurements at the FCC-ee have sensitivity to heavy new physics that is higher than, albeit complementary to, the Higgs precision measurements, and therefore offers no decisive arguments in favour of a different operation model.

While the twofold symmetry of the current tunnel design (arguably tailored for the FCC-hh) limits the number of e^+e^- interaction points to two, a fourfold symmetry would open the possibility to profit from four interaction points (as was checked for LEP3 in the LEP tunnel) and therefore roughly double the total integrated luminosity collected in a given amount of time. A striking illustration is that of the trilinear Higgs self coupling [158]. With four IPs, two years at the Z pole and one year at the WW threshold would suffice to get the same integrated luminosity as after six years with two IPs (with the additional benefit of an earlier start of the Higgs precision measurement phase). The saved years and the four detectors could be optimally used to accumulate about 12 ab^{-1} at 240 GeV and 5.5 ab^{-1} at 365 GeV. The larger data sample would yield a measurement of the Higgs self coupling with a precision of $\pm 25\%$, reduced to $\pm 21\%$ in combination with the HL-LHC, and to $\pm 9\%$ if only the Higgs self-coupling is allowed to vary. The first 5σ demonstration of the existence – or, equivalently, the discovery – of this coupling is therefore within reach at the FCC-ee. The already strong scientific case of the FCC-ee is much stronger with four IPs instead of two. While the rest of this study is conservatively presented with two IPs only, more work will be devoted in the near future to investigate this interesting configuration.

A feature unique to circular e^+e^- colliders is the possibility to use transverse polarisation of the incoming beams as a tool for precision beam energy calibration. A precision of the order of 100 keV on the centre-of-mass energy is a high-priority target at the Z pole and at the W pair threshold, for absolute measurements of the Z and W masses with the promised accuracies. Measurements of the beam energy and of the beam energy spread are also compulsory for the determination of most EWPOs, which show a strong dependence on these two quantities. On the other hand, the study demonstrated that longitudinal polarisation of the incoming beams provides no information that cannot be obtained otherwise with the large FCC-ee luminosity. Electroweak observables accessible with longitudinal polarisation can be measured with a similar accuracy from either unpolarised asymmetries [159] or by using the measurable polarisation of weakly decaying final state particles such as the top quark [47] and the τ lepton.

Finally, a unique possibility of the FCC-ee is operate at $\sqrt{s} \simeq m_H \simeq 125 \text{ GeV}$, with moderate centre-of-mass energy monochromatisation. The study showed that, for such a mode of operation, a data sample corresponding to an integrated luminosity of at least 10 ab^{-1} would be a valuable addition to constrain the Yukawa coupling of the electron to the Higgs boson. These data would also allow the precision of the number of neutrino species to be improved by a factor two with respect to the same amount of data at the W pair threshold.

1.5.2 Detectors

As mentioned above, circular colliders have the advantage of delivering collisions to multiple interaction points, which allow different detector designs to be studied and optimised. On the one hand, the planned performance of heavy-flavour tagging, of particle identification, of tracking and particle-flow reconstruction, and of lepton, jet, missing energy and angular resolution, need to match the physics programme and the statistical precision offered by the FCC-ee. On the other hand, the detectors must satisfy the constraints imposed by machine performance and interaction region layout: the occupancy from beam-induced background needs to be minimised; the interaction rates (up to 100 kHz at the Z pole) put strict constraints on the event size and readout speed; due to the beam crossing angle, the detector solenoid magnetic field is limited to 2 T to confine its impact on the luminosity; the accurate

measurement of the significant centre-of-mass energy spread (90 MeV at the Z pole, 500 MeV at the highest FCC-ee energies) requires an angular resolution better than $100\,\mu\text{rad}$ for muons; the luminometer must be situated only 1 m away from the interaction point, but still provide a precision better than 10^{-4} on the luminosity; etc.

Two detector concepts have been studied and optimised for the FCC-ee, and are briefly presented in Section 7: (i) CLD, a consolidated option based on the detector design developed for CLIC, with a silicon tracker and a 3D-imaging highly-granular calorimeter; and (ii) IDEA, a bolder, possibly more cost-effective, design, with a short-drift wire chamber and a dual-readout calorimeter. It was demonstrated that detectors satisfying the requirements are feasible.

The particular choice of detectors, motivated by the wish to explore the technology and cost spectrum, is of course not unique. The optimisation of these two concepts must continue, but other concepts might actually prove to be better adapted to the FCC-ee physics programme and need to be studied in the near future in order to move towards timely FCC-ee detector proposals. At the same time, a more concrete study of systematic uncertainties must be done to match the statistical precision available.

1.5.3 Theory

The opportunities offered by the FCC-ee luminosities at centre-of-mass energies ranging from around the Z pole to above the $t\bar{t}$ threshold allow improvements of between one and two orders of magnitude on the experimental accuracy of most electroweak and Higgs precision observable measurements, with respect to the achievements of previous e^+e^- and hadron colliders.

To fully capitalise upon these high precision measurements by testing the predictions of the Standard Model, it is necessary that theoretical uncertainties will be subdominant to experimental uncertainties. A dedicated study of the future of precision SM calculations has been undertaken [160]. A group consisting of nearly 30 theoreticians interested in the project has been formed for this purpose. A first proposal for training and study with precision calculations is included in the R&D part of this report (Appendix A). It comprises a five-year initial plan, but further continuation is being discussed. The results of [160] are summarised as follows.

At the electroweak scale it is estimated that for the precision electroweak pseudo-observables m_W , $\sin^2\theta_W^{\text{eff}}$, Γ_Z , R_b , and R_ℓ , projected intrinsic errors arising due to uncalculated higher order perturbative corrections will be comparable to experimental errors at the time of FCC-ee running. The same is true for the parametric errors arising due to uncertainties in the SM input parameters. For the Higgs factory operation, all relevant intrinsic errors can be reduced to less than the anticipated experimental sensitivity. Parametric errors are expected to be subdominant when compared to experimental errors. The exception is the case of Higgs boson decays to charm and bottom quarks, where the parametric errors due to the quark-mass uncertainty in the inputs can still be at the same level as the expected experimental precision.

The complexity of the task ahead in minimising theoretical errors is similar to that of the computations required for the HL-LHC data and the necessary tools have been identified [161]. These studies demand focussed investment and support by the community in order to reach the necessary level of development. With this investment, it is estimated that all main obstacles can be overcome in the course of the preparations, before the actual operation of the accelerator.

2 Collider design and performance

2.1 Requirements and design considerations

The FCC-ee lepton collider is designed to provide e^+e^- collisions with centre-of-mass energies from 88 to 365 GeV. The centre-of-mass operating points with most physics interest are around 91 GeV (Z pole), 160 GeV (W^\pm pair-production threshold), 240 GeV (ZH production) and 340–365 GeV ($t\bar{t}$ threshold and above). The machine should accommodate at least two experiments operated simultaneously and deliver peak luminosities above $1 \times 10^{34} \text{ cm}^{-2} \text{ s}^{-1}$ per experiment at the $t\bar{t}$ threshold and the highest ever luminosities at lower energies.

The layout of the FCC-ee collider follows the layout of the FCC-hh hadron collider infrastructure, which has been developed with a view to its integration with the existing CERN accelerator complex as injector facility. As is the case for the hadron collider, beam with adequate quality can be provided by an upgrade of the existing injector complex. Alternatively, a dedicated optimised injector could be built. Care has been taken to ensure easy implementation of transfer lines from the SPS to the future collider tunnel.

2.2 Layout and key parameters

2.2.1 Layout

The design goal is to maximise the luminosity for each energy under the following constraints:

- Apart from $\pm 1.2 \text{ km}$ around each interaction point (IP), the machine should follow the layout of the 97.75 km circumference hadron collider [9].
- There should be two interaction points, located in the straight sections at PA and PG as shown in Figure 2.1.
- Synchrotron radiation power should be limited to 50 MW/beam at all energies.

Figure 2.1 shows the layout of the FCC-ee together with FCC-hh. For FCC-ee, the design principles are

- A double ring collider.
- A horizontal crossing angle of 30 mrad at the IP, with the crab waist collision scheme [11,12].
- The critical energy of the synchrotron radiation of the incoming beams towards the IP is kept below 100 keV at all beam energies.
- A common lattice for all energies, except for a small rearrangement in the RF section for the $t\bar{t}$ mode. The betatron tune, phase advance in the arc cell, final focus optics and the configuration of the sextupoles are set to the optimum at each energy by changing the strengths of the magnets.
- The length of the free area around the IP (ℓ^*) and the strength of the detector solenoid are kept constant at 2.2 m and 2 T, respectively, for all energies.
- A “tapering” scheme, which scales the strengths of all magnets, apart from the solenoids, according to the local beam energy, taking into account the energy loss due to synchrotron radiation.
- Two RF sections per ring placed in the straight sections at PD and PJ. The RF cavities will be common to e^+ and e^- in the case of $t\bar{t}$.
- A top-up injection scheme to maintain the stored beam current and the luminosity at the highest level throughout the physics run. It is therefore necessary to have a booster synchrotron in the collider tunnel. The integrated luminosity will be

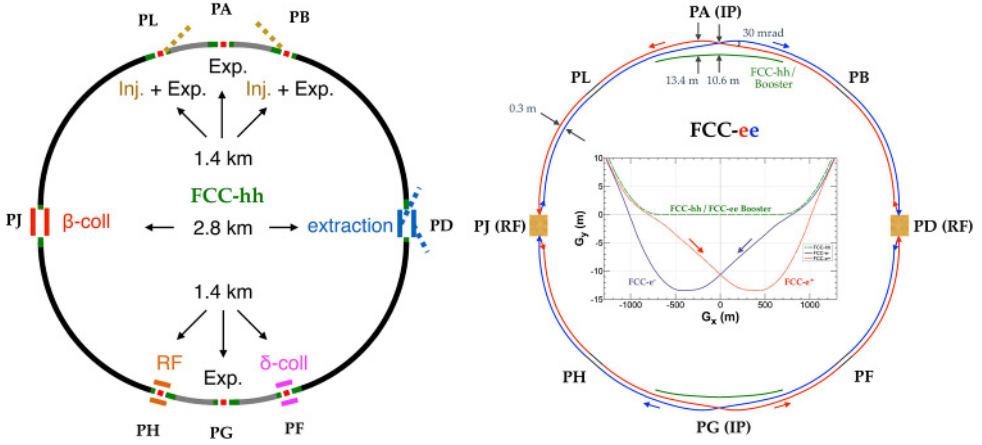


Fig. 2.1. The layouts of FCC-hh (left), FCC-ee (right), and a zoomed view of the trajectories across interaction point PG (right middle). The FCC-ee rings are placed 1 m outside the FCC-hh footprint in the arc. In the arc the e^+ and e^- rings are horizontally separated by 30 cm. The main booster follows the footprint of the hadron collider. The interaction points are shifted by 10.6 m towards the outside of FCC-hh layout. The beams coming toward the interaction points are straighter than the outgoing ones in order to reduce the synchrotron radiation at the IP.

reduced by more than an order without the top-up, due to ramping ($\sim 1/2$), reduction of the beam-beam parameter ($\sim 1/2 - 1/4$), lower beam current ($\sim 1/2$) at a lower injection energy, loss of stability of the machine ($\sim 1/2$), etc.

The FCC-ee inherits two important aspects from the previous generations of e^+e^- circular colliders. At and above the $t\bar{t}$ threshold, the FCC-ee will encounter strong synchrotron radiation with the associated rapid damping. This situation is reminiscent of earlier high-energy colliders, especially LEP2. By contrast, at the Z pole, FCC-ee will operate with much less damping, but with a high beam current and a large number of bunches. This mode of operation mode was successfully established by several high-intensity colliders, such as the two B factories and DAΦNE.

There are two reasons for choosing a double-ring collider. Firstly, at low energies, especially at Z, more than 16 000 bunches must be stored to achieve the desired luminosity. This is only possible by avoiding parasitic collisions with a double-ring collider. Secondly, at the highest energy $t\bar{t}$, although the optimum number of bunches reduces to ~ 30 , the double ring scheme is still necessary to allow “tapering” [162]. The local energy of the beam deviates by up to $\pm 1.2\%$ between the entrance and the exit of the RF sections, with the result that the orbit deviation due to the horizontal dispersion in the arc and the associated optical distortion becomes intolerable. The optics may even fall into an unstable region. The tapering scheme restores the ideal orbit and optics almost completely. In the case of a single ring, the tapering scheme cannot be applied to the e^+e^- beams simultaneously.

The number of IPs is restricted by the current layout choice for the straight sections in the FCC-hh. The straight sections around PD and PJ do not have large caverns for detectors. The intermediate straight sections at PB, PF, PH and PL are placed asymmetrically in the arcs and are not a suitable location for the FCC-ee RF cavities. Therefore, with this twofold ring symmetry, two IPs are the only solution for the FCC-ee. (It has, however, been demonstrated that four IPs would be possible for a ring of four-fold symmetry.) The resulting beam optics [162] have a complete

periodicity of two. The beam lines for e^+ and e^- have a mirror symmetry with respect to the line connecting the two IPs and the beam optics are identical.

The crab waist scheme [11,163,164] is essential to boost the luminosity by more than four orders of magnitude at Z, compared to previous colliders. This scheme gives a very small beam size at the IP together with a large crossing angle and small emittances, without exciting harmful synchrotron-betatron resonances associated with the crossing angle [164]. This scheme simply needs a pair of static sextupole magnets at both sides of the IP. These sextupoles are incorporated in the local chromatic correction system (LCCS) [162]. The effect of the crab waist is produced by reducing the strengths of some sextupoles in the LCCS, so there is no need for special hardware. The optimum parameters with the crab waist scheme including β^* s, bunch intensity, bunch length, etc., are obtained by the procedures described in the next section. The optimisation takes into account beamstrahlung – synchrotron radiation caused by the coherent EM field of the opposite bunch [164–168] – and various other beam-beam effects.

The layout around the IP including the crossing angle, the strengths of solenoids and beam pipes are common for all energies. The polarity as well as the strengths of final quadrupoles change according to the beam energy and optimum focusing.

2.2.2 Beam parameter optimisation

One of the main factors determining collider performance is the beam-beam interaction, which at high energies can gain an extra dimension due to beamstrahlung. FCC-ee will be the first collider where beamstrahlung plays a significant role in the beam dynamics. Only half of the ring with one IP will be discussed in this section, because the other half will behave in the same way due to symmetry. To avoid confusion, the half-ring tunes will be marked by the superscript*.

The luminosity per IP for flat beams ($\sigma_x \gg \sigma_y$) can be written as:

$$L = \frac{\gamma}{2er_e} \cdot \frac{I_{\text{tot}}\xi_y}{\beta_y^*} \cdot R_{\text{HG}}, \quad (2.1)$$

where I_{tot} is the total beam current which is in this case determined by the synchrotron radiation power limit of 50 MW per beam. Therefore L can only be increased by making the vertical beam-beam parameter ξ_y larger and β_y^* smaller while keeping the hour-glass factor R_{HG} reasonably large. The latter depends only on L_i/β_y^* ratio, where L_i is the length of interaction area which in turn depends on the bunch length σ_z and Piwinski angle ϕ :

$$\phi = \frac{\sigma_z}{\sigma_x} \tan\left(\frac{\theta}{2}\right), \quad (2.2)$$

$$L_i = \frac{\sigma_z}{\sqrt{1+\phi^2}} \xrightarrow[\phi \gg 1, \theta \ll 1]{\quad} \frac{2\sigma_x}{\theta}, \quad (2.3)$$

here θ is the full crossing angle, see Figure 2.2. The beam-beam parameters for $\theta \neq 0$ become [169]:

$$\xi_x = \frac{N_p r_e}{2\pi\gamma} \cdot \frac{\beta_x^*}{\sigma_x^2(1+\phi^2)} \xrightarrow[\phi \gg 1, \theta \ll 1]{\quad} \frac{N_p r_e}{\pi\gamma} \cdot \frac{2\beta_x^*}{(\sigma_z\theta)^2}, \quad (2.4a)$$

$$\xi_y = \frac{N_p r_e}{2\pi\gamma} \cdot \frac{\beta_y^*}{\sigma_x\sigma_y\sqrt{1+\phi^2}} \xrightarrow[\phi \gg 1, \theta \ll 1]{\quad} \frac{N_p r_e}{\pi\gamma} \cdot \frac{1}{\sigma_z\theta} \sqrt{\frac{\beta_y^*}{\varepsilon_y}}, \quad (2.4b)$$

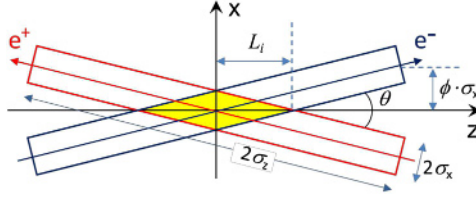


Fig. 2.2. Sketch of collisions with a large Piwinski angle.

where N_p is the number of particles per bunch. Note that $\xi_x \propto 1/\varepsilon_x$ (in head-on collision) transforms to $\xi_x \propto \beta_x^*/\sigma_z^2$ when $\phi \gg 1$, and ξ_y dependence on σ_x vanishes.

In the following, the main parameters that need to be optimised are listed:

- The vertical emittance should be as small as possible, but there are two restrictions: $\varepsilon_y \geq 0.002 \cdot \varepsilon_x$ and $\varepsilon_y \geq 1$ pm.
- At Z there is some contribution to ε_y (0.2–0.3 pm) coming from the detector solenoids. It follows that ε_x should also be minimised, but there is no gain by reducing it below 0.4 nm.
- An important parameter for the luminosity is β_y^* , whose minimum value is 0.8 mm and which is limited by the dynamic aperture.
- It is assumed that ξ_y can be easily controlled by N_p , which implies that the number of bunches is adjusted to keep I_{tot} unchanged.
- Finally, it should be noted that β_x^* , the RF voltage (which determines the bunch length and the synchrotron tune), and the betatron tunes are relatively free parameters.

Optimisation at the Z pole

Since the FCC-ee is designed for a wide range of beam energies, parameter optimisation looks different at various energies. To find the good working points at the lowest energies (44–47 GeV), a scan of betatron tunes was performed in a simplified model: linear lattice, and weak-strong beam-beam simulations (without coherent instabilities). The results are presented in Figure 2.3. Since $\xi_x \ll \xi_y$, the footprint looks like a narrow vertical strip, with the bottom edge resting on the working point. Particles with small vertical betatron amplitudes have maximum tune shifts and are in the upper part of the footprint, so that the strong resonances of Figure 2.3, such as $Q_x^* + 2Q_y^* = n$, come closer. Thus the good region is reduced to the red triangular area bounded by the main coupling resonance $Q_x^* - Q_y^* = n$, sextupole resonance $Q_x^* + 2Q_y^* = n$, and half-integer resonance $2Q_x^* = 1$ with its synchrotron satellites. All other higher-order coupling resonances are suppressed by the crab waist and, therefore, not visible. As seen from the plot, the range of permissible Q_x for large ξ_y is bounded on the right by 0.57–0.58.

At the Z pole and the WW threshold, the main problems associated with the beam-beam interaction come from the two new phenomena found in beam-beam simulations: coherent synchrotron-betatron (x – z) instability [170–172] and 3D flip-flop [172], the latter occurring only in the presence of beamstrahlung. Both instabilities are bound with the horizontal synchro-betatron resonances, satellites of half-integer. In any case, it is necessary to move away from low-order resonances, so Q_x^* is chosen close to the upper limit (thus $Q_{x,y}$ move further away from the integer, which facilitates tuning of linear optics). Another requirement is that ξ_x must be substantially less than the distance between neighbouring satellites, which is equal to the synchrotron tune Q_s^* . In other words, it is necessary to reduce the ratio ξ_x/Q_s^* .

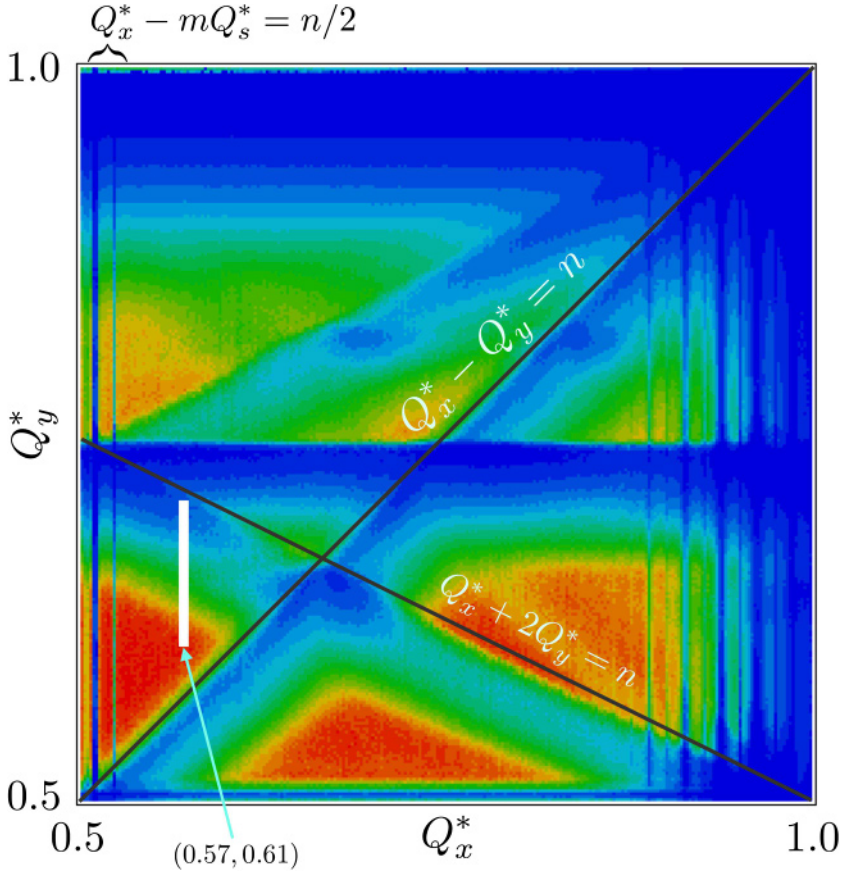


Fig. 2.3. Luminosity at Z as a function of betatron tunes. The colour scale from zero (blue) to $2.3 \times 10^{36} \text{ cm}^{-2} \text{ s}^{-1}$ (red). The white narrow rectangle above (0.57, 0.61) shows the footprint due to the beam-beam interaction. A few synchrotron-betatron resonance lines $Q_x^* - mQ_s^* = n/2$ are seen.

The first step is to reduce β_x^* . However, because of the absence of local horizontal chromaticity correction in the interaction region, attempts to make β_x^* too small lead to a decrease in the energy acceptance. β_x^* can be reduced to 15 cm at Z, but this is not enough to suppress the instabilities. The next step is to reduce ξ_x for a given β_x^* , whilst trying to keep ξ_y unchanged. This can only be done by increasing σ_z . The most efficient way is to increase the momentum compaction factor α_p , because not only does ξ_x decrease (due to larger σ_z) but also Q_s^* grows. In addition, larger α_p raises the threshold of microwave instability to an acceptable level. The only drawback of this approach is that the horizontal emittance ε_x grows with the power of $3/2$ with respect to α_p . For the luminosity, ε_x is not so important by itself, but ε_y should be small and it is normally proportional to ε_x . However, the horizontal emittance at Z with small α_p and FODO arc cells with $90^\circ/90^\circ$ phase advances is small – less than 90 pm. Therefore, even a threefold increase still allows achieving the design vertical emittance $\varepsilon_y = 1$ pm. Thus, the FCC-ee features a lattice where doubling of α_p is achieved by reducing the phase advance per FODO cell in the arcs to $60^\circ/60^\circ$, see Section 2.4.1.

Turning to the dependence on RF voltage: $\sigma_z \propto 1/\sqrt{V_{\text{RF}}}$, $Q_s^* \propto \sqrt{V_{\text{RF}}}$. The requirement to keep ξ_y unchanged means that N_p/σ_z is held constant. Therefore, if

V_{RF} is lowered, ξ_x decreases inversely with σ_z (and not with the square of the inverse bunch length, as it might have seemed at first glance). As a result, ξ_x/Q_s^* does not change, but by lowering Q_s^* the order of synchro-betatron resonances located in the vicinity of working point is increased. For this reason V_{RF} is made small and one can find betatron tunes where neither instability manifests itself. For example, the working point is located between high order synchrotron-betatron resonances $2Q_x^* - 10Q_s^* = 1$ and $2Q_x^* - 12Q_s^* = 1$.

At low energies beamstrahlung leads to a significant increase in the energy spread and, correspondingly, the bunch lengthening. If N_p is large enough to achieve high ξ_y , then σ_z becomes several times larger; in this case it scales as $\sigma_z \propto \sqrt{N_p}$. Accordingly, ξ_y and luminosity also grow $\propto \sqrt{N_p}$ while ξ_x remains constant. This means that increasing N_p does not reach the instability threshold, but only increase the energy spread. In general, N_p can be limited by several factors: ξ_y , beam lifetime (depends on the energy spread and energy acceptance), and the impedances. The result is close to all these limits, which corresponds to a full exploitation of the available margins.

Optimisation at the WW threshold

As the energy increases to ~ 80 GeV, σ_x grows due to the synchrotron radiation and the bunch lengthening due to the beamstrahlung decreases, therefore the Piwinski angle drops. In addition, the damping decrement grows with γ^3 . All this leads to an increase in the instability threshold. For example, at W^\pm it is already possible to work in a lattice with small momentum compaction. However, there is one more important requirement: in order to obtain a resonant depolarisation, which is necessary for the energy calibration, the synchrotron tune Q_s^* must be larger than 0.025 (see Sect. 2.7). To achieve such a Q_s^* value, the momentum compaction has to be increased. Therefore, the same $60^\circ/60^\circ$ lattice was chosen as for Z. Furthermore, the RF voltage must be increased to 750 MV, so the only window for a good working point can be found between $2Q_x^* - 4Q_s^* = 1$ and $2Q_x^* - 6Q_s^* = 1$. In order that instabilities do not arise near these resonances, $\beta_x^* \leq 20$ cm is required. Here it should be noted that with increasing energy, obtaining small beta functions becomes more difficult as this leads to a reduction in the dynamic aperture and momentum acceptance. Consequently, β_y^* was increased to 1 mm. To obtain the higher V_{RF} required, the single-cell cavities used at Z will be replaced by multi-cell ones, whose capacity to damp the higher order modes (HOM) is limited. An important consequence is that the number of bunches should not be smaller than 2000 and, therefore, the luminosity at W^\pm is limited by this factor.

The possibility of increasing Q_s^* further to 0.0375 at W^\pm was also considered, in accordance with the desire to improve the conditions for resonant depolarisation. In this case Q_x^* falls between low order resonances $2Q_x^* - 2Q_s^* = 1$ and $2Q_x^* - 4Q_s^* = 1$. To avoid coherent instabilities it is necessary to reduce β_x^* to 15 cm. The momentum acceptance drops accordingly and, as a consequence, luminosity decreases. On the other hand, the number of bunches for this option is larger (2500), though they are shorter. This option is not worse for HOM and the luminosity is about the same as for 2000 bunches with $Q_s^* = 0.025$. However, obtaining $Q_s^* = 0.0375$ would require twice the RF voltage V_{RF} and, thereby, a revised RF staging scenario. Therefore, the current baseline is $Q_s^* = 0.025$.

Optimisation at the ZH cross-section maximum

Polarisation is not an issue at a beam energy of 120 GeV (ZH production) and the optimum parameters are selected as follows:

1. The $90^\circ/90^\circ$ lattice, which provides naturally smaller emittances.
2. The RF voltage is made as small as possible, but adjusted so that the RF acceptance (bucket height) is larger than the energy acceptance due to dynamic aperture, resulting in $Q_s^* \approx 0.018$.
3. Q_x^* is selected in the range of 0.56–0.58 with the condition that $Q_x^* \approx 0.5 + Q_s^* \cdot (m+0.5)$ in order to be separated from the low-order synchro-betatron resonances and $Q_y^* = Q_x^* + (0.03\text{--}0.04)$.
4. A β_x^* at which the coherent instabilities disappear is then sought; in this case, 30 cm is enough.
5. With the given ε_x and β_x^* , the length of interaction area $L_i \approx 0.9$ mm, and this defines the optimum β_y^* . However, obtaining small β_y^* at higher energies is more difficult, so 1 mm was chosen.
6. The lattice optimisation was performed for the selected β^* in order to maximise the dynamic aperture and energy acceptance.
7. A fine scan of betatron tunes was performed to choose the working point more precisely.
8. Then quasi-strong-strong beam-beam simulations were performed with an asymmetry of 3% in the bunch currents (3% is determined by the required beam lifetime and the injection cycle time). At energies W^\pm , ZH, and $t\bar{t}$, single high-energy beamstrahlung photons become important and impose a limit on N_p . The bunch population is scanned, while the restriction is the lifetime of the weak (less populated) bunch. The maximum N_p and luminosity are determined in this way.

Optimisation at the $t\bar{t}$ threshold and above

At the $t\bar{t}$ production (beam energy from 170 to 182.5 GeV) the coherent instabilities are suppressed by very strong damping, but another problem becomes dominant: the lifetime limitation by single high-energy beamstrahlung photons [168]. Thus, in contrast to low energies, β_x^* should be increased in order to make σ_x larger and thereby weaken the beamstrahlung. With increased σ_x , $L_i \approx 1.8$ mm is obtained, and β_y^* should be about the same (or slightly smaller). It should be noted that an increase in ε_x is not profitable since a small ε_y is needed for high luminosity, so the $90^\circ/90^\circ$ lattice is used.

2.3 Design challenges and approaches

Based on combinations of existing technologies for e^+e^- circular colliders developed through the last half century, the FCC-ee will achieve the best ever luminosities at each energy. Although some components need final touches to their design or prototyping in the phase after the CDR, the fundamental feasibility of their construction has already been proven in other colliders and storage rings.

2.3.1 Synchrotron radiation

The synchrotron radiation (SR) is a key feature for any e^+e^- storage ring. It is worth comparing the characteristics of FCC-ee with those of LEP2, the highest energy e^+e^- ring ever operated and PEP-II high energy ring, one of the e^+e^- colliders with the highest beam current (see Tab. 2.2).

While the total radiation power is higher than that of LEP2 by a factor of 4, the critical energy and the energy loss per arc length are only 20% and 10% higher,

respectively. The power dissipation per arc length is less than 1/4 of that at PEP-II. The level of synchrotron radiation can therefore be handled by existing technology.

Another aspect of the SR is the radiation towards the detector at the IP. This issue is addressed by the beam optics around the IP which limits the critical energy of the SR photons from the dipoles upstream of the IP to below 100 keV [162], from ~ 480 m from the IP. The highest critical energy of photons experienced at LEP2 was 83 keV at ~ 270 m from the IP [174]. Thus the criterion for FCC-ee sounds reasonable. The suppression of the SR towards the IP is achieved by asymmetric beam optics around the IP. The detailed analysis of the effect of SR for the detector is given in Section 2.5.

2.3.2 Tapering

The tapering method is essential to maintain the beam orbit and the optics at the design values with the high synchrotron radiation loss around the ring, especially at $t\bar{t}$. Here it is assumed that all dipoles and quadrupoles have independent trim windings to facilitate the tapering [162]. Sextupoles are paired more or less locally and have independent power supplies. The magnitude of the trims reaches $\pm 1.2\%$ near the RF cavities. These trim windings are also useful for the correction of the orbit and the beam optics. While most of the dipoles and quadrupoles use the “twin aperture” scheme described below, trim windings can be installed independently for the two beams.

2.3.3 Dynamic aperture, beam lifetime, top-up injection

The FCC-ee will be the first circular collider where beamstrahlung dominates the luminosity performance. Thus the first requirement is that the collider optics must have sufficiently large dynamic momentum acceptance to hold a particle that loses its energy in a single photon emission due to beamstrahlung. The second requirement arises because beamstrahlung also increases the equilibrium momentum spread of the beam by multiple random emissions of photons, therefore the dynamic momentum aperture must ensure the quantum lifetime [175]. Generally speaking, at higher energy such as $t\bar{t}$, the first effect is more critical than the second one.

The dynamic aperture must be large enough to capture the injected beam for the top-up injection. There are at least two schemes: off-axis-on-momentum and on-axis-off-momentum injections. They need transverse on-momentum or off-momentum dynamic apertures, respectively. The dynamic aperture of the optics that has been designed is sufficient for both injection schemes at all energies [176].

There are two major processes which determine the beam lifetime. One is the radiative Bhabha scattering at the IP, which is proportional to the luminosity divided by the number of particles stored in the ring. The other is the lifetime given by the beamstrahlung and the dynamic momentum acceptance. The latter depends on the optimisation of the beam parameters as discussed in the previous section. The resulting lifetime, as shown in Table 2.1, matches the capacity of the injector. The injection must be done with a “bootstrap” procedure, in which the imbalance of the charges of both beams is kept within a certain relative difference, i.e. $\pm 5\%$ at Z and $\pm 3\%$ at higher energies, as described in the previous section.

2.3.4 Low emittance tuning and optics correction

To maintain the vertical emittance ε_y below the design criteria is also necessary to reach the higher luminosity, as well as being important to ensure beam polarisation

Table 2.1. Machine parameters of the FCC-ee for different beam energies.

	Z	WW	ZH	tt	
Circumference (km)			97.756		
Bending radius (km)			10.760		
Free length to IP ℓ^* (m)			2.2		
Solenoid field at IP (T)			2.0		
Full crossing angle at IP θ (mrad)			30		
SR power / beam (MW)			50		
Beam energy (GeV)	45.6	80	120	175	182.5
Beam current (mA)	1390	147	29	6.4	5.4
Bunches / beam	16640	2000	328	59	48
Average bunch spacing (ns)	19.6	163	994	2763 ^a	3396 ^a
Bunch population (10^{11})	1.7	1.5	1.8	2.2	2.3
Horizontal emittance ε_x (nm)	0.27	0.84	0.63	1.34	1.46
Vertical emittance ε_y (pm)	1.0	1.7	1.3	2.7	2.9
Arc cell phase advances (deg)	60/60		90/90		
Momentum compaction α_p (10^{-6})	14.8		7.3		
Arc sextupole families	208		292		
Horizontal β_x^* (m)	0.15	0.2	0.3	1.0	
Vertical β_y^* (mm)	0.8	1.0	1.0	1.6	
Horizontal size at IP σ_x^* (μm)	6.4	13.0	13.7	36.7	38.2
Vertical size at IP σ_y^* (nm)	28	41	36	66	68
Energy spread (SR/BS) σ_δ (%)	0.038/0.132	0.066/0.131	0.099/0.165	0.144/0.186	0.150/0.192
Bunch length (SR/BS) σ_z (mm)	3.5/12.1	3.0/6.0	3.15/5.3	2.01/2.62	1.97/2.54
Piwinski angle (SR/BS) ϕ	8.2/28.5	3.5/7.0	3.4/5.8	0.8/1.1	0.8/1.0
Length of interaction area L_i (mm)	0.42	0.85	0.90	1.8	1.8
Hourglass factor R_{HG}	0.95	0.89	0.88	0.84	0.84
Crab sextupole strength ^b (%)	97	87	80	40	40
Energy loss / turn (GeV)	0.036	0.34	1.72	7.8	9.2
RF frequency (MHz)	400			400 / 800	
RF voltage (GV)	0.1	0.75	2.0	4.0 / 5.4	4.0 / 6.9
Synchrotron tune Q_s	0.0250	0.0506	0.0358	0.0818	0.0872
Longitudinal damping time (turns)	1273	236	70.3	23.1	20.4
RF bucket height (%)	1.9	3.5	2.3	3.36	3.36
Energy acceptance (DA) (%)	± 1.3	± 1.3	± 1.7	$-2.8 + 2.4$	

Notes. ^(a) A half ring is filled with the common RF scheme. ^(b) Relative to the geometrical strength $k_2 = (\theta_x \beta_y^* \beta_{y,\text{sext}})^{-1} \sqrt{\beta_x^* / \beta_{x,\text{sext}}}$.

Table 2.1. (Continued.)

	Z	WW	ZH	t\bar{t}	
Polarisation time t_p (min)	15000	900	120	18.0	14.6
Luminosity / IP ($10^{34}/\text{cm}^2\text{s}$)	230	28	8.5	1.8	1.55
Horizontal tune Q_x	269.139	269.124	389.129	389.108	
Vertical tune Q_y	269.219	269.199	389.199	389.175	
Beam-beam ξ_x/ξ_y	0.004/0.133	0.010/0.113	0.016/0.118	0.097/0.128	0.099/0.126
Allowable e^+e^- charge asymmetry (%)	± 5	± 3			
Lifetime by rad. Bhabha scattering (min)	68	59	38	40	39
Actual lifetime due to beamstrahlung (min)	> 200	> 200	18	24	18

Table 2.2. Comparison of synchrotron radiation between FCC-ee, LEP2 [173], and PEP-II [173] at their highest energies.

		FCC-ee	LEP2	PEP-II (high energy ring)
Highest beam energy (GeV)		182.5	104.6	9.0
Bending radius (km)		10.760	2.584	0.167
Synchrotron radiation loss per turn (GeV)		9.05	4.07	0.0034
Critical energy in the arc dipole (MeV)		1.06	0.83	0.0082
Beam current / species (mA)		5.5	3	1960
Radiation power per beam (MW)		50	12.2	6.8
Total radiation power per arc length (kW/m)		1.2	1.1	5.5

at Z and W^\pm . It is assumed that the emittance ratio is $\varepsilon_y/\varepsilon_x \geq 0.2\%$ and that $\varepsilon_y \geq 1$ pm at all energies. The latter condition is important since the vertical emittance generated by the fringe field of the solenoids together with the crossing angle reaches 0.2 pm at Z, where the effect is the largest.

The tuning scheme described later uses skew quadrupole fields generated by trim windings on arc sextupoles to control the vertical emittance generated by the misalignments in the arc. The x – y coupling and dispersion can be measured using beam position monitors (BPMs) at each quadrupole in either a turn-by-turn or multi-turn mode. The method resembles those developed at other colliders such as LHC and B factories, as well as those used at light sources. The misalignment tolerances and the precision of the diagnostics is comparable to those that have been achieved in the aforementioned machines. Special care will be needed for the error correction of the final focus quadrupoles and the local chromaticity section, where the β functions assume high values of up to 6 km.

The correction of the beam optics including the β -functions and horizontal dispersion will be important for both the low emittance tuning and the dynamic aperture. The trim windings on all of the quadrupoles equipped for tapering will also be used for optics corrections.

2.4 Optics design and beam dynamics

2.4.1 Lattices

The beam optics was established for the baseline in 2016 [162], then further revised [177,178] so as to include several modifications such as $60^\circ/60^\circ$ phase advance at

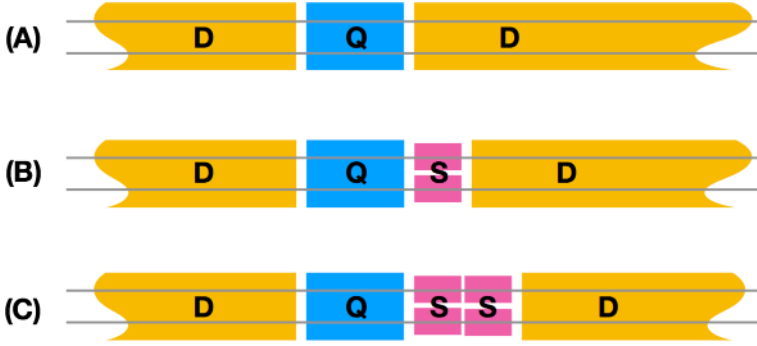


Fig. 2.5. Three magnet arrangements around a quadrupole. D: twin-aperture dipole, Q: twin-aperture quadrupole. S: single-aperture sextupole. (A) no sextupole, (B) single aperture, singlet sextupole only for $60^\circ/60^\circ$, (C) single aperture, doublet sextupole for either $60^\circ/60^\circ$ or $90^\circ/90^\circ$. In case (C) for $60^\circ/60^\circ$, only the part of the doublet next to the quadrupole is powered. As a result, three dipole lengths are needed to maintain a constant distance between quadrupoles.

damping partition, but the resulting momentum spread is not suitable for polarisation and this option has therefore been rejected.

Non-interleaved families of sextupole pairs, with a $-I$ transformation between sextupoles [180], are placed in the FODO cells. As the phase advance is different between high and low energies, the locations of the usable sextupoles depend on the mode of operation. There are three types of the arrangement of a sextupole around a quadrupole as shown in Figure 2.5: no sextupole, a singlet sextupole, and a doublet sextupole. Whilst a doublet is used at higher energies, only one of the two sextupoles is used at lower energies, if the optics requires a sextupole field at that location. A singlet sextupole is installed where a sextupole is only needed at the lower energy. To achieve a better dipole packing factor where possible, the spaces not needed for a sextupole are filled with dipoles. Thus, there are three dipole lengths but with the same bending radius. The resulting lattice has a super period of 35 FODO cells as shown in Figure 2.6. Within the super period, the β -functions are almost periodic in each cell, since the focusing due to dipoles is weak. On the other hand, the horizontal dispersion has a modulation within a super period. Studies of the effect of such a modulation on the dynamic aperture have so far not shown any negative effect. All sextupole pairs are independently powered. There are 294 and 208 independent pairs per half ring for $90^\circ/90^\circ$ and $60^\circ/60^\circ$, respectively. The non-interleaved scheme of sextupoles has been applied at B-factories and successfully operated for more than 15 years [181,182]. At KEKB, the number of pairs was 52 per ring.

2.4.2 Interaction region

One of the beam optics challenges for the collider is providing an adequate dynamic aperture with small β -functions down to $\beta_{x,y}^* = (0.15\text{ m}, 0.8\text{ mm})$ at the interaction point, for operation on the Z pole. Although these values are still higher than those in modern B factories [183], the associated vertical chromaticity around the IP is comparable, since the distance, ℓ^* , from the face of the final quadrupole magnet to the IP is longer than those in the B factories. Also, especially at the $t\bar{t}$ energy, the beamstrahlung caused by the collisions requires a very wide momentum acceptance of $-2.8\% + 2.4\%$. The transverse on-momentum dynamic aperture must be larger than $\sim 12\sigma_x$ to enable top-up injection in the horizontal plane.

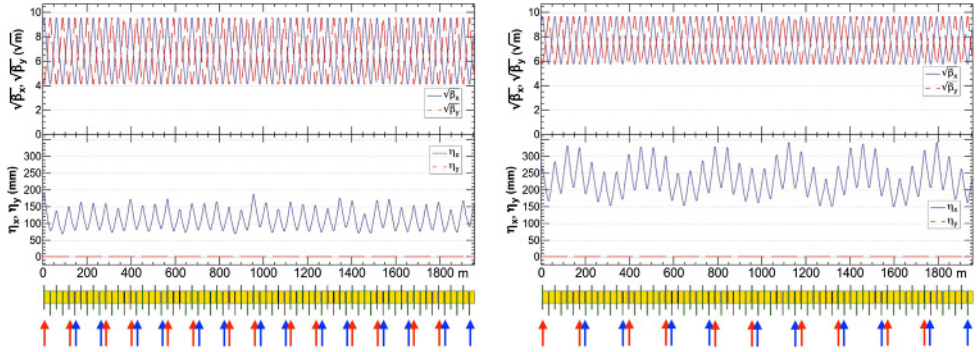


Fig. 2.6. The beam optics of the arc super cell of FCC-ee, for two phase advances. Left: $90^\circ/90^\circ$ (for ZH and $t\bar{t}$) right: $60^\circ/60^\circ$ (for Z and WW). The upper and lower rows show $\sqrt{\beta_{x,y}}$ and dispersions, respectively. The locations of the focusing and defocusing sextupoles, SF and SD, are indicated by red and blue arrows, respectively, for each phase advance. Every two sextupoles are paired with a $-I$ transformation between them.

Figure 2.7 shows the optics in the interaction region (IR) for $t\bar{t}$. It has a local chromaticity correction system (LCCS) only in the vertical plane at each side of the IP. The sextupole magnet pairs for the LCCS have one at each side of the IP and only the inner ones at (b,c) have non-zero horizontal dispersion [184]. The outer ones at (a,d) perform two functions: cancelling the geometrical nonlinearity of the inner ones and generating the crab waist at the IP; in order to accomplish the second function the (a,d) phase advance from the IP is chosen as $\Delta\psi_{x,y} = (2\pi, 2.5\pi)$, as described in [162]. The incorporation of the crab sextupoles into the LCCS saves space and reduces the number of optical components. The optimum magnitude of the sextupole depends on the luminosity optimisation. As the crab sextupoles are dispersion-free [184], they can be adjusted to any ratio up to the “full crab waist” without causing unnecessary side effects.

The beam lines in the interaction region are separate for the two beams and there are no common quadrupoles in the IR. As a baseline ℓ^* is chosen to be 2.2 m [185], which is sufficient for two independent final quadrupoles with a 30 mrad crossing angle. The detector solenoids are common to the two beams and their effects are compensated locally with counter solenoids, which cancel the $\int B_z dz$ between the IP and the faces of the final quadrupole, as shown in Figure 2.8. The vertical orbit, vertical dispersion, and $x-y$ couplings do not leak out for any off-momentum particles. The vertical emittance increases due to the fringe field of the compensating solenoid combined with the horizontal crossing angle. The increase becomes largest at the Z energy as the solenoid field is independent of the beam energy. The increase of the vertical emittance is below 0.4 pm for 2 IPs. A realistic profile of B_z shown in Section 2.5.

The optimised $\beta_{x,y}^*$ discussed in Section 2.2 is smaller at lower beam energies. To reduce β_x^* at the Z from $\beta_{x,y}^* = (1 \text{ m}, 1.6 \text{ mm})$ at $t\bar{t}$ to $(0.15 \text{ m}, 0.8 \text{ mm})$ at Z, the vertical focusing quadrupole in the final focus which is closest to the IP (known as QC1), which is located at $\ell^* = 2.2 \text{ m}$ from the IP, is split into three pieces. The polarities and the strengths of these pieces depend on the beam energy. For instance, all three pieces provide vertical focusing at $t\bar{t}$, and only the first piece provides vertical focusing while the remaining two focus horizontally at Z. The field strengths are limited to the same value, 100 T/m, at all beam energies. With this triple splitting, the centre of focusing for each plane moves closer towards the IP at the Z, which reduces the increment of the chromaticity for the smaller β^* . Comparing

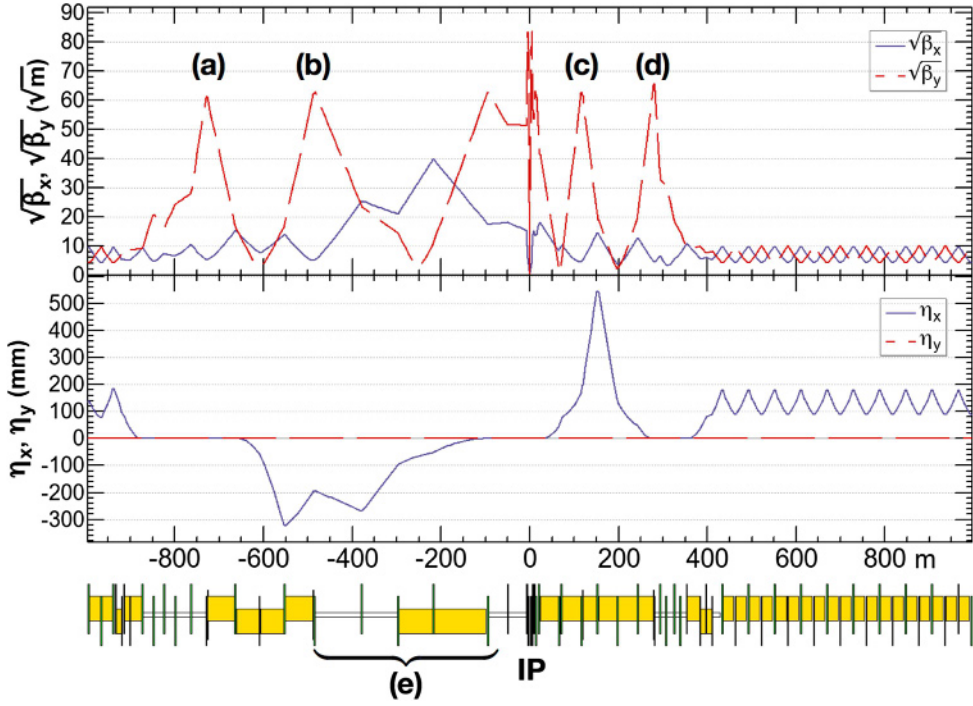


Fig. 2.7. The beam optics of the FCC-ee IR for $t\bar{t}$. Upper and lower rows show $\sqrt{\beta_{x,y}}$ and dispersions, respectively. The beam passes from the left to the right. The optics is asymmetric to suppress the synchrotron radiation toward the IP. Dipoles are indicated by yellow boxes; those in region (e) have a critical energy of the SR photon below 100 keV at the $t\bar{t}$. Sextupoles for the LCCS are located at (a–d), and sextupoles at (a,d) play the role of crab sextupoles.

left and right of Figure 2.8, it can be seen that the beam sizes at Z through this region are still smaller than those at $t\bar{t}$. The peak value of β_y is almost unchanged even though β_y^* is reduced by a factor of 2. The peak of β_x at Z is about 3 times higher, while β_x^* becomes 1/6 of the value at $t\bar{t}$.

The critical energy of SR photons from the dipoles up to 500 m upstream of the IP is set below 100 keV at $t\bar{t}$. There are no dipole magnets upstream of the IP for up to 100 m.

2.4.3 RF section and other straight sections

Figure 2.9 shows the beam optics for the half ring for $t\bar{t}$. The RF sections are located in the long straight sections around PJ and PD as shown in Figure 2.1. At $t\bar{t}$, an acceleration voltage of ~ 5.3 GV per section is needed; As a result, the length of the RF installation for the collider will be about 1 km (with a similar length for the top-up booster). At the $t\bar{t}$ energy, both beams pass through a common RF section. A combination of electrostatic separators and a dipole magnets deflects only the outgoing beam so as to avoid any SR shining towards the RF cavities. In this running mode, the quadrupoles within the RF section are common to both beams, but they are still compatible with the overall tapering scheme, if their strengths are symmetrical about the mid-point of the RF section.

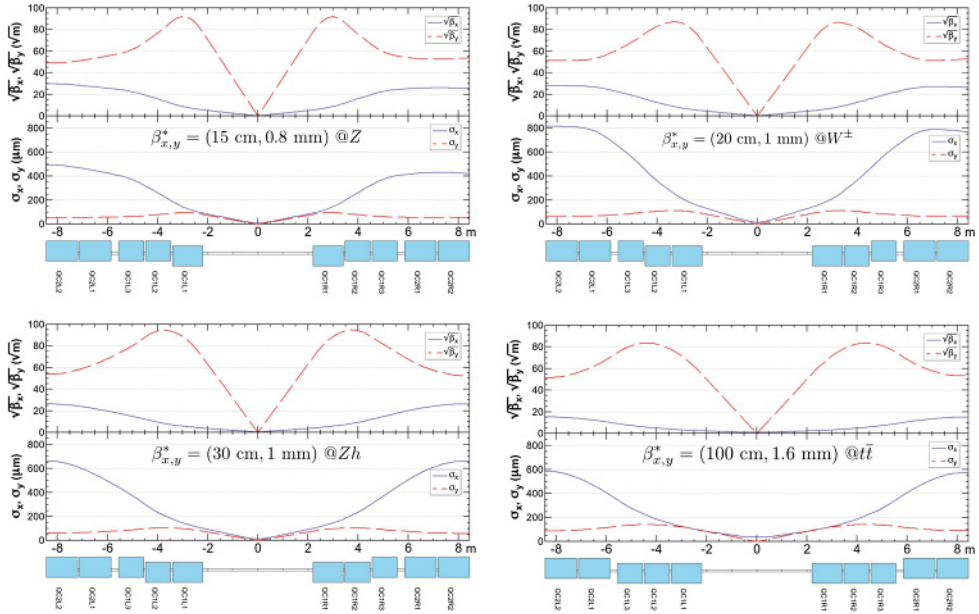


Fig. 2.8. The $\sqrt{\beta_{x,y}}$ and beam sizes around the IP at Z (upper left), WW (upper right), ZH (lower left), and $t\bar{t}$ (lower right). The beam sizes assume the equilibrium emittances listed in Table 2.1. The final quadrupoles QC1(L/R) are longitudinally split into three slices. While all slices of QC1 are vertically focussing at $t\bar{t}$, only the first ones are at Z. Note that the inner radius of the beam pipe through these quadrupoles is larger than 15 mm.

The staging of the RF system adds cavity modules step by step as the energy increases, starting at Z up to $t\bar{t}$. The beam line in the RF section needs minimal modification as more modules are installed. Most of the RF cavities and cryomodules are reused at the various stages. Figure 2.10 depicts the tunnel cross section with the installed RF system.

The straight section (a) in Figure 2.9 has space for a spectrometer which will use inverse Compton scattering from a laser to measure the beam energy and the polarisation. This section has a free space of 100 m immediately after the dispersion suppressor dipole at the entrance of the inner ring and therefore the beam optics is different to that of (b).

The remaining straight sections will be used for injection, beam dump and collimation.

2.4.4 Dynamic aperture

The dynamic aperture (DA) has been estimated using the computer code SAD [186], taking into account the effects listed in Table 2.3. The synchrotron radiation from the dipoles improves the aperture, especially at $t\bar{t}$, due to the strong damping, whereas the radiation loss in the quadrupoles for particles with large betatron amplitudes reduces the dynamic aperture. This is due to the synchrotron motion induced by the radiation loss as described in reference [162]. This effect is most noticeable in the horizontal arc quadrupoles; therefore, the length of the arc quadrupoles must be sufficiently long. The final focus quadrupole has another effect resulting from the SR which makes the transverse damping unstable. The vertical motion for a

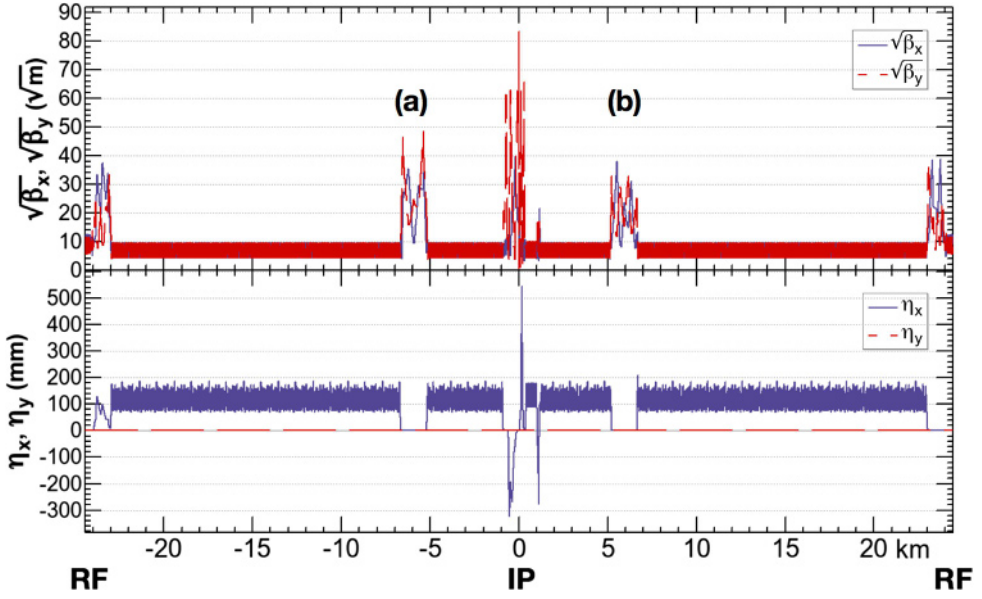


Fig. 2.9. The beam optics of the FCC-ee half ring for $t\bar{t}$. Upper/lower plots show $\sqrt{\beta_{x,y}}$ and horizontal/vertical dispersions, respectively. These plots start and end in the middle of the RF sections, and the IP is located at the centre. Sections marked by (a,b) correspond to the intermediate straight sections PB, PF, PH, PL in Figure 2.1.

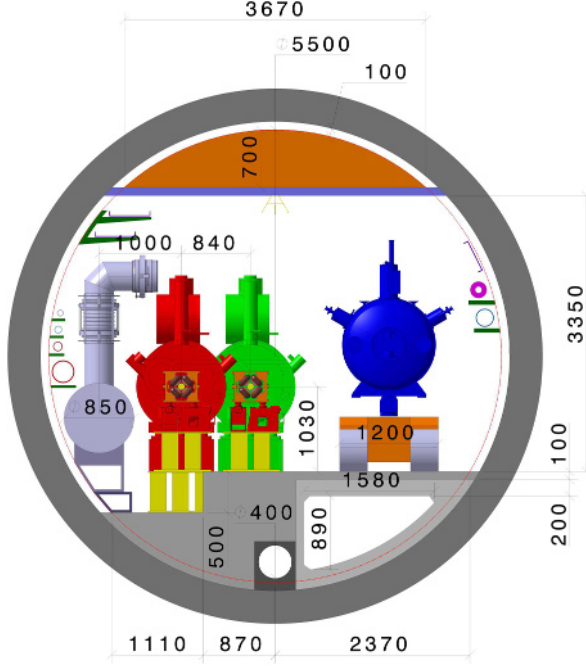


Fig. 2.10. Tunnel cross section with radiofrequency equipment installed (collider main ring in red and booster ring in green). An RF unit being installed is shown in blue. The grey equipment represents the cryogenic distribution line.

Table 2.3. Effects taken into account during the optimisation of the dynamic aperture.

Effect	Significance
Synchrotron motion	Essential
Radiation loss in dipoles	Essential – improves the aperture, esp. at ZH and $t\bar{t}$
Radiation loss in quadrupoles	Essential – reduces the aperture
Radiation loss in sextupoles	Minimal
Tapering	Essential
Crab waist	Transverse aperture is reduced by $\sim 20\%$ for 100% strength
Maxwellian fringes [187]	Small
Kinematic terms	Small

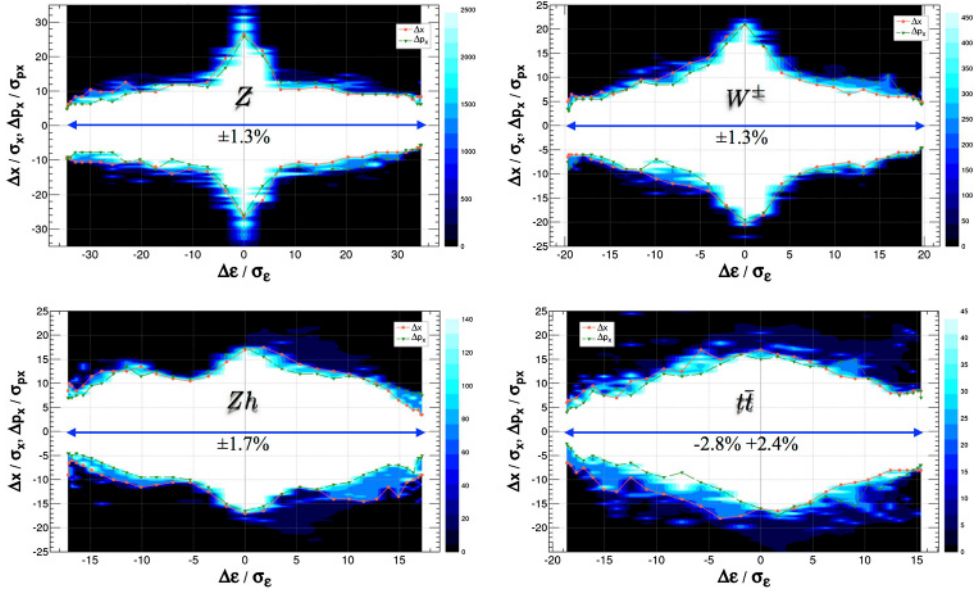


Fig. 2.11. Dynamic apertures in z – x plane after sextupole optimisation with particle tracking for each energy. The initial vertical amplitude for the tracking is always set to $J_y/J_x = \varepsilon_y/\varepsilon_x$. The number of turns corresponds to about 2 longitudinal damping times. The resulting momentum acceptances are consistent with the luminosity optimisation shown in Table 2.1. Effects in Table 2.3 are taken into account. The momentum acceptance at $t\bar{t}$ is “asymmetric” to match the distribution with beamstrahlung.

$\beta_y^* = 0.8$ mm at Z is unstable for $\Delta y \gtrsim 30\sigma_y$ due to the large β_y and the strong field gradient in the quadrupole.

The DA has been optimised by particle tracking with a downhill simplex method scripted within SAD and varying the sextupole settings. All the effects listed in Table 2.3 were included in the optimisation. The goal of optimisation is to determine a weighted area covered by the initial conditions in the z – x plane, detailed in reference [162]. The results are shown in Figure 2.11. The transverse apertures in the x – y plane, shown in Figure 2.12, are evaluated after the optimisation for the z – x plane.

The resulting DA satisfies the requirements for both beamstrahlung and top-up injection, including field errors and misalignments [188]. The optimisation was done for each energy. The number of initial conditions that can be studied is limited by the computing resources available. A larger number is always better, but when n_z

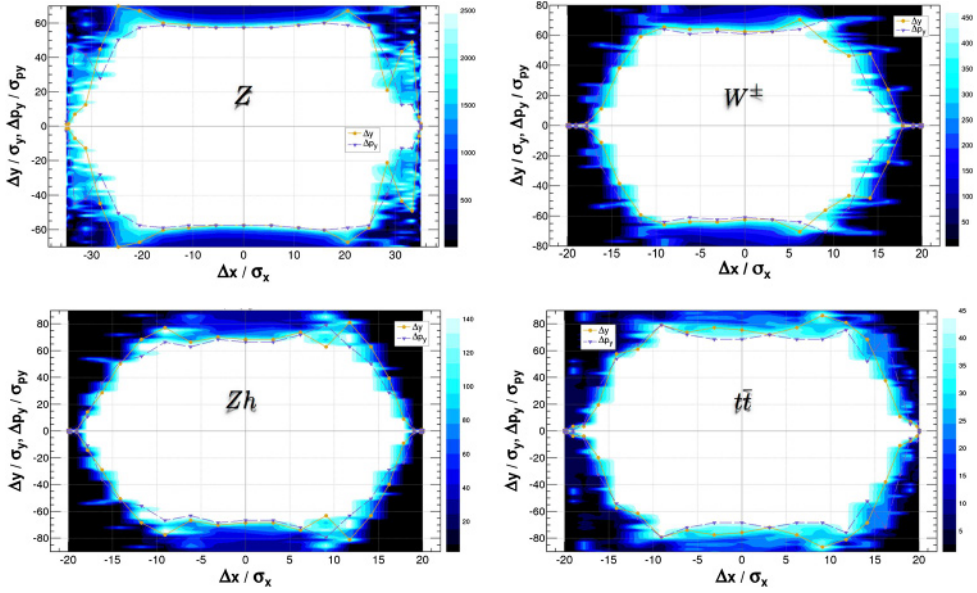


Fig. 2.12. On-momentum transverse dynamic apertures after an optimisation of sextupoles at each energy. The initial momentum offset is set to 0. All the effects of Table 2.3 were taken into account.

and the number of revolutions from Figure 2.11 were doubled, the resulting change in the DA was tiny.

So far all sextupole pairs have been used independently in the optimisation, thus the degree of freedom for the optimisation is 296 for ZH and $t\bar{t}$, and 210 for Z and WW, respectively, including the sextupoles for the local chromatic correction. The super period periodicity of 2 for the ring is kept. It has not been verified whether the large number of sextupole families is really necessary.

The purpose of a wide momentum acceptance is to re-capture the particles which emit a beamstrahlung photon at the IP. Since the primary energy change is always negative, the momentum acceptance can be wider on the negative side and somewhat narrower on the positive side. The acceptance on the positive side can be determined by the damping and the diffusion during a synchrotron motion half cycle thus:

$$A_+ \approx -A_- \exp(-\alpha_z/2Q_s) + 3\sigma_{\delta,BS} \sqrt{1 - \exp(-\alpha_z/Q_s)} , \quad (2.5)$$

where α_z , Q_s , $\sigma_{\delta,BS}$ are the longitudinal damping rate per turn, the synchrotron tune and the equilibrium momentum spread including the beamstrahlung, respectively. The size of the diffusion has been set at 3σ . At $t\bar{t}$ if $A_- = -2.8\%$, then $A_+ = +2.4\%$, as shown in Table 2.1. The optimisation of the DA at $t\bar{t}$ has been done for such an asymmetric momentum acceptance. Since this effect is weak at lower energies, symmetric acceptances have been applied.

A number of effects are not included in the optimisation process, mainly due to their stochastic nature, which will need a large number of samples to simulate. Table 2.5 lists such effects, which are evaluated separately after the optimisation. Among them, the quantum fluctuation should have significant effects and the radiation fluctuation of the SR in the lattice should be simulated together with the beamstrahlung, since they have comparable magnitudes.

Table 2.4. On-momentum transverse dynamic and physical apertures at each energy.

Energy	Dynamic		Physical	
	$\Delta x/\sigma_x$	$\Delta y/\sigma_y$	$\Delta x/\sigma_x$	$\Delta y/\sigma_y$
Z	± 35	± 58	± 37	± 170
WW	± 22	± 55	± 23	± 133
ZH	± 18	± 67	± 34	± 144
$t\bar{t}$	± 19	± 70	± 43	± 107

Notes. The narrowest physical aperture is given by the beam pipe of the final quadrupole with 15 mm inner radius as shown in Figure 2.8. All effects in Table 2.3 were included for the DA.

Table 2.5. Effects evaluated separately after the optimisation of DA.

Effect	Significance at $t\bar{t}$
Detector and compensation solenoids	Minimal, if locally compensated at the IP
Beam-beam effect with beamstrahlung	Overall beam lifetime satisfies the requirement (strong-weak model)
Radiation fluctuation	Essential , evaluated together with beamstrahlung
Multipoles of final quadrupoles	Minimal for the proposed design of the magnets
Multipoles of other magnets	Minimal for the proposed design of the magnets
Misalignments of magnets with corrections	Essential

2.4.5 Tolerances and optics tuning

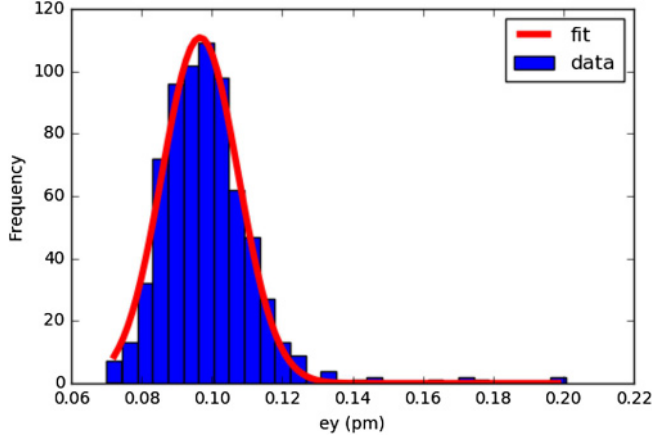
The low emittance budget and the small β^* at the interaction point define error tolerances and tuning requirements. Magnet misalignments and other optics errors generate spurious vertical dispersion (which can amount to several hundred meters without any correction applied) and betatron coupling, both of which compromise the target emittances, in particular at high energy. Several correction methods and algorithms were developed in order to achieve emittances close to their design values.

Horizontal correctors were installed at every focusing quadrupole and vertical correctors at every defocusing quadrupole. Beam position monitors (BPM) were placed at each quadrupole, including the final quadrupole doublets next to the IPs. Skew quadrupole correctors combined with a trim quadrupole are placed at each sextupole in order to correct the beta-beat and to rematch the horizontal dispersion. Special skew quadrupoles were installed in the interaction region to compensate the possible tilt of the final-doublet quadrupoles. The effect of dipole tilts will be included in the next phase of the study.

The vertical dispersion distortion was first corrected with orbit correctors via the dispersion free steering method [189] and then with skew quadrupoles with the help of response matrices. The linear coupling was corrected by adjusting the linear coupling resonance driving term parameters, as tested at the ESRF [190]. Trim quadrupoles were used to rematch the phase advances between the BPMs, again using response matrices. Satisfactory results for the misalignment tolerance were found when the magnets were misaligned as defined in Table 2.6. For example, when the correction algorithm was applied to 1000 error seeds, 70% of the cases converged (see Fig. 2.13), with the following results for the

Table 2.6. Tolerance for arc quadrupoles, sextupoles and quadrupoles of the IPs.

Magnet type	Hor. displacement Δx μm	Vert. displacement Δy μm	Tilt $\Delta\theta$ μrad
Arc quadrupoles	100	100	100
Sextupoles	100	100	0
IP quadrupoles	50	50	50

**Fig. 2.13.** Statistical distribution of the vertical emittance after applying the correction algorithm, for 700 different (converged) seeds with input random misalignments according to Table 2.6.

emittances:

$$\begin{aligned}
 \epsilon_y &= 0.10 \pm 0.013 \text{ pm}, \\
 \epsilon_x &= 1.52 \pm 0.01 \text{ nm}, \\
 \epsilon_y/\epsilon_x &= 0.0065\%.
 \end{aligned}$$

Efforts are going on to reduce the number of dipole correctors, e.g. by using trim windings on sextupoles, to include additional machine errors such as the roll angle of dipoles, to improve the algorithm for a better conversion.

2.4.6 Improving dynamic and momentum aperture using PSO and machine learning

Dynamic and momentum aperture optimisation using PSO

Applying particle swarm optimisation (PSO) in accelerator physics to improve machine parameters is a worthwhile method for coping with the increasingly large number of degrees of freedom to be optimised. With an existing machine it is possible to optimise the sextupole setting by improving dynamic aperture through lifetime optimisation using PSO [191].

A particle swarm optimiser is an evolutionary algorithm with both cognitive and “social” components, originally influenced by bird flocking behaviour [192]. PSO can be employed to improve dynamic and momentum aperture of FCC with its high number of degrees of freedom.

In the case of FCC-ee, the number of degrees of freedom may be reduced by keeping the proposed $-I$ transform between sextupole pairs, and additionally maintaining the periodicity of the machine after each half-turn. Doing so, 294° of freedom

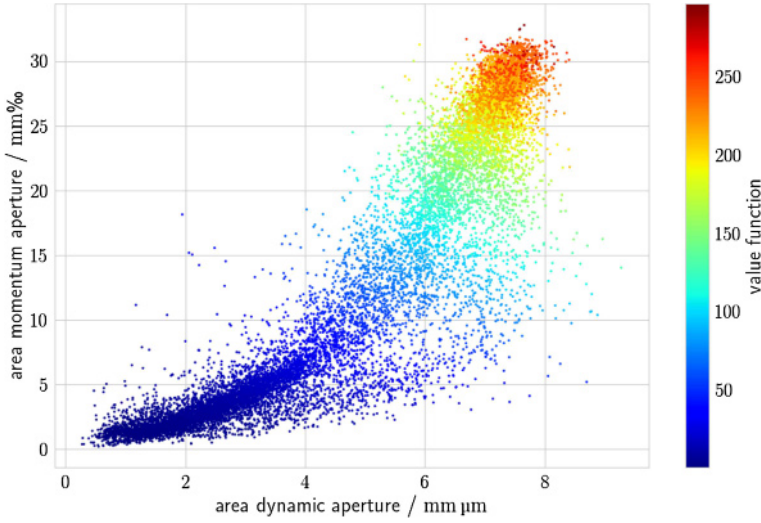


Fig. 2.14. Value function as a function of area of momentum aperture and area of dynamic aperture for all solutions of the PSO algorithm.

are left. This number is clearly still out of range for brute force scanning; evolutionary algorithms like PSO are better suited to handle the optimisation.

The optimiser improves the objective function(s) over time by iteratively adjusting position and speed of the candidate solutions (particles) in search space:

$$\mathbf{x}_{n+1} = \mathbf{x}_n + \mathbf{v}_{n+1}, \quad (2.6)$$

$$\mathbf{v}_{n+1} = \omega \mathbf{v}_n + c_r r_1 (\mathbf{x}_{p\text{-best}} - \mathbf{x}_n) + c_s r_2 (\mathbf{x}_{g\text{-best}} - \mathbf{x}_n). \quad (2.7)$$

Here, \mathbf{x} is the position in search space, which in this scenario would be a vector containing the individual sextupole strengths, and \mathbf{v} is the velocity (change of position per generation) of the individual particle in search space. Additionally, $\mathbf{x}_{p\text{-best}}$ is the position where the individual particle has best performed in its history, and $\mathbf{x}_{g\text{-best}}$, is the global best position known so far. The velocity for the next generation \mathbf{v}_{n+1} therefore depends on

- the initial velocity \mathbf{v}_n , weighted by the factor ω , describing the rigidity of movement;
- the individual particles personal best solution $\mathbf{x}_{p\text{-best}}$, weighted by the cognitive factor c_c ; and
- the global best solution $\mathbf{x}_{g\text{-best}}$, weighted by the social factor c_s .

Based on tracking dynamic and momentum aperture for different candidate solutions, candidates are assigned a score (value function in Fig. 2.14) which makes them more or less successful in their impact on the population. With the way the value function is set, the algorithm may be steered towards favouring one objective over another (e.g. favouring area of momentum aperture over area of dynamic aperture).

The particles are initialised with the sum of a vector containing the reference sextupole setting and a random vector, with maximum change in k_2 per sextupole of 0.01 m^{-2} . The solution presented here is found in the 17th generation. It yields an improvement of the area of momentum aperture of 18.0% compared to the reference lattice.

In Figure 2.16, the change of k_2 between the optimised solution and the reference solution is presented. Although at first glance the solution appears to be as arbitrary

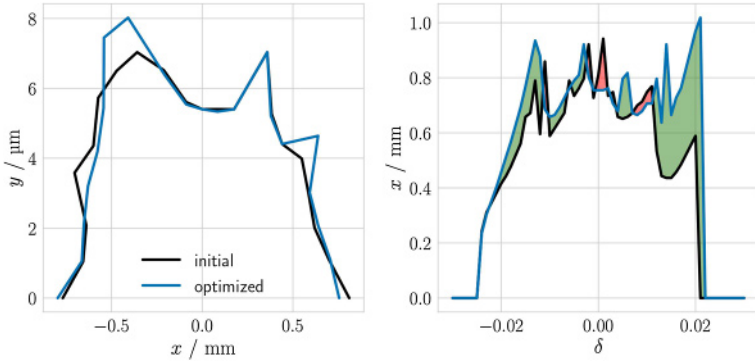


Fig. 2.15. Dynamic aperture (left) and momentum aperture (right) for reference lattice (black) and optimised lattice (blue). The area of dynamic aperture is improved by 3.1% while the area of momentum aperture is increased by 18.0%.

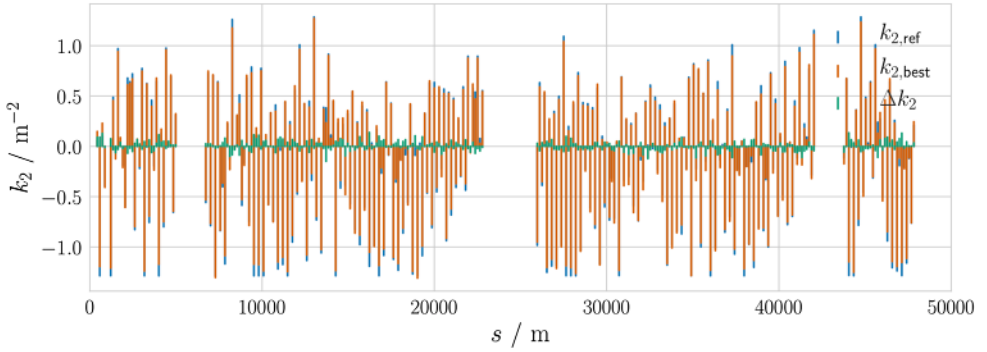


Fig. 2.16. Change in sextupole strengths (green) between optimised solution (red) and reference solution (blue) for one half ring.

as the reference setting, when looking closely at the peak sextupole strengths a difference can be observed: the peak sextupole strengths appear to have been reduced by the optimiser compared to the reference setting.

Prospects of employing machine learning concepts for PSO

As a side effect of the optimisation process, the dynamic aperture and momentum acceptance were determined for a large number of sextupole settings (Fig. 2.14). These settings can be used to train an artificial neural network (NN) predicting the off-momentum dynamic aperture for different sextupole settings. With such a model, the optimisation process can be significantly accelerated since time consuming particle tracking can be avoided.

As a proof of principle, an NN containing an input layer, three hidden layers, and an output layer has been tested. As input, the NN takes the 298 sextupole strengths including final focus. The hidden layers all accept 300 input values and produce 300 output values. The output layer is the 61 horizontal apertures for different energy deviations ranging from -3% to 3% in steps of 0.1% . First results indicate reasonably good agreement between the predictions from the trained model and the actual data, for a test data set withheld from training, as is illustrated in Figure 2.17.

However, for large energy deviations, the trained model fails to reproduce tracked apertures. Since the training data set contains only small apertures for large energy

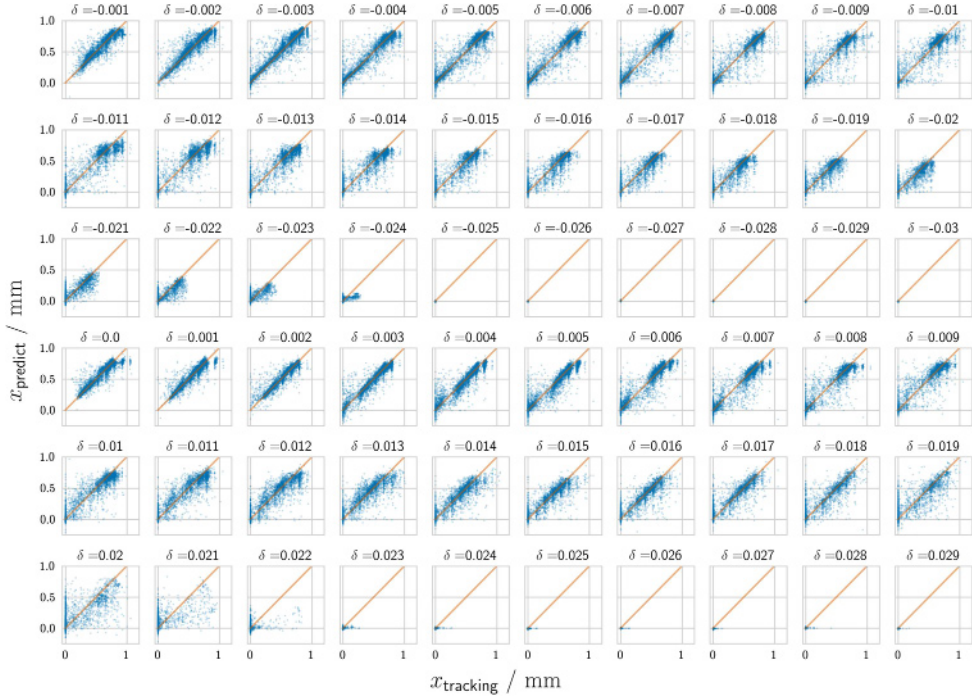


Fig. 2.17. Aperture predictions for different energy deviations from a trained NN model together with true values from particle tracking, for a test data set, which has been withheld from training.

deviations, the model will assume that any combination of sextupole strengths must lead to small apertures for large energy deviations.

Nevertheless, the trained model itself can be used in a PSO algorithm, performing the formerly time consuming step of determining the aperture in a matter of milliseconds. Doing so, the model can be used to enhance aperture for energy deviations in a range where the training data set already found a considerable aperture. By testing promising candidates through tracking, the training data set (and the model) may be continuously enhanced with respect to large energy deviation apertures.

Thus, a shortcut in optimising dynamic aperture can be provided. Furthermore, it is possible to evaluate different objective functions, e. g. favoring particular shapes of aperture, based on the trained model. In addition, analysis of the trained model might provide insight into which sextupoles have less impact on dynamic aperture compared to others, in order to mainly use them for chromaticity correction.

In a future application, machine learning can be used to optimise the repopulating step in PSO. By intervening in the evolution process through selecting high potential candidates whilst maintaining diversity, the optimisation process can be significantly enhanced as has been shown in the light source community [193].

2.5 Machine detector interface

2.5.1 Overall layout of the interaction region

The combined requirements of the detector and accelerator at the collision point make the interaction region one of the more challenging parts of the overall design.

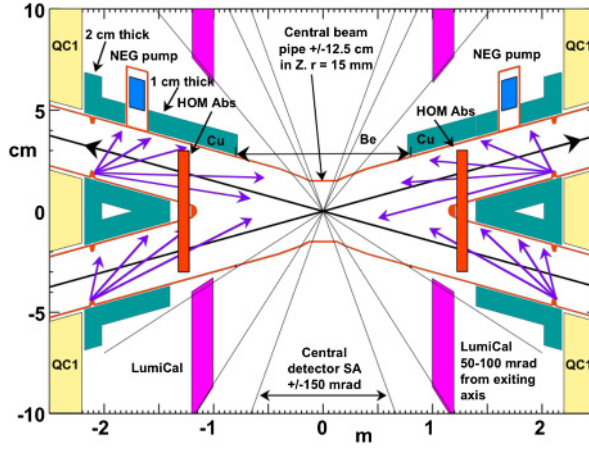


Fig. 2.18. x - z view of the FCC-ee interaction region layout for ± 2.5 m from the interaction point. Note the different horizontal (m) and vertical (cm) scales.

The challenge is to maximise performance in terms of integrated luminosity whilst maintaining the related background at a tolerable level for the experiments and this includes minimising synchrotron radiation. The IR has a flexible design to allow running at different energies and the optics scales with the energy which means that a common layout can be used for all energies.

To reach the target luminosity of $2 \times 10^{36} \text{ cm}^{-2} \text{ s}^{-1}$ at the Z pole it is necessary to use the crab-waist collision scheme and at the same time keep the beam current below the limit determined by the SR. The main guideline for the IR optics has been to keep the SR backgrounds acceptable for the detector. The process has been guided by experience from LEP2. There, the highest local critical energy was 72 keV for photons emitted 260 m from the IP [174]. Consequently, the main guideline in the FCC-ee IR design has been to keep critical energies from bending magnets up to 500 m from the interaction point (IP) below 100 keV for the incoming beam and to have the first dipoles located at least 100 m from the IP. An additional goal for the optics design that comes from considerations of synchrotron radiation, is to keep all critical energies around the ring below ~ 1 MeV in order to minimise neutron production. An asymmetric IR optics has been designed to meet these goals for the critical energy in the presence of crossing angles as large as 30 mrad, which are required by the crab-waist scheme. The asymmetry allows the beams to come from the inner rings towards the IP. After the IP, the beams are bend more strongly to merge back to the outer ring as shown in Figure 2.1.

The transverse distance between the IP and the FCC-hh beamline is 10.6 m. Outside the IR, the FCC-ee and FCC-hh trajectories are on the same orbit but an enlarged tunnel is necessary over ~ 1.2 km on either side of the IP, in order to satisfy the requirement for the SR.

An expanded horizontal view of the IR layout is shown in Figure 2.18, for the region ± 2.5 m around the IP. As is shown in the figure, the interaction region is symmetric and the two beam pipes are merged together close to the IP. The distance between the IP and the entrance of the first quadrupole ℓ^* is 2.2 m.

The aperture of the vacuum beam pipe, which is circular and has a constant radius of 15 mm, is indicated by red colour in Figure 2.18. The first final focus quadrupole “QC1” is shown in yellow. Synchrotron-radiation mask tips which intercept SR scattered particles are also shown in the plot; the horizontal masks are located just in front of QC1, at 2.1 m from the IP. The horizontal aperture at these

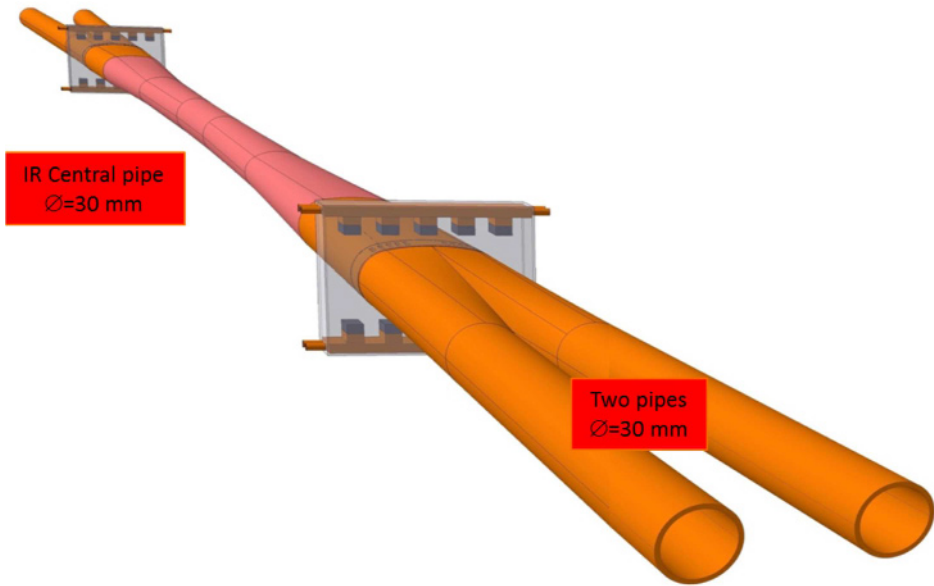


Fig. 2.19. 3D view of the interaction region (IR) vacuum chamber in the region where two beam pipes merge. On both sides of the interaction point, higher order mode (HOM) absorbers are placed.

mask tips is 12 mm. Section 2.5.4 describes in more detail how the synchrotron radiation is handled. The luminosity monitor, shown in magenta, is placed longitudinally between 1.074 and 1.19 m from the IP. The luminosity monitor is described in Section 2.5.3.

To reduce multiple scattering towards the luminosity monitor, the vacuum chamber located within ± 0.9 m from the IP will be made from beryllium, followed by a copper vacuum chamber throughout the final focus doublet. The vacuum chamber inside the superconducting final focus is at ambient temperature. The central vacuum chamber will also have a $5\text{ }\mu\text{m}$ gold coating to shield the detector and luminosity monitor from scattered synchrotron radiation photons. Outside the vacuum chamber, between the luminosity monitor window and QC1, 1 cm of tantalum (or some other high Z material such as lead or tungsten) shielding (the blue-green objects in Fig. 2.18) will be installed to protect the detectors. It has been confirmed by a full GEANT4 [194] simulation of the sub-detectors (see Sect. 7.1) that this high- Z material shielding is necessary and sufficient, especially at the $t\bar{t}$ energy.

The geometry of the beam pipe in the IR is constant and smooth. Particular care is taken for the region where the two separate beam pipes merge. This region, shown on the left in Figure 2.19, was designed using CST [195] and HFSS [196] with CAD to correctly analyse electro-magnetic fields in the IR. These studies show that the cut-off frequency of electro-magnetic fields generated or trapped in the IR is at a safe value. HOM absorbers have also been studied following the PEP-II experience [197]. The right plot of Figure 2.19 shows the vacuum chamber in the IR with a sketch of the HOM absorbers. A detailed analysis of this study is presented in Section 2.6.15. The HOM absorber design includes a water cooling system to avoid heating. The beam pipes through the IR will be at room temperature and will be water (or liquid) cooled.

2.5.2 Magnet systems

The magnetic elements required in the vicinity of the IP are the main detector solenoid and the final focus quadrupoles. The main detector solenoid is a cylinder with half-length 4 m and a diameter of around 3.8 m with a peak field strength of 2 T (see Sect. 7.1 for more details). The value of 2 T was chosen as a good compromise between physics performance and the requirement for the vertical emittance to be in the pm region. Due to the crab-waist design, the first final focus quadrupole, QC1, is inside the main detector solenoid. Further requirements can be formulated as follows:

1. Leave adequate space for the detectors: in the present design magnetic elements reach angles of up to ± 100 mrad. The luminosity counter sits unobstructed in front of all magnetic elements.
2. In order to minimise emittance blow-up due to coupling between transverse planes, the integrated field seen by the electrons and positrons crossing the IP should vanish. Field compensation should be better than 1% to avoid any noticeable increase in emittance (if the compensation is off by 0.1% then the resulting vertical emittance blow up would be 0.1 pm per IP – the effect is quadratic).
3. Vertical emittance blow-up due to fringe fields in the vicinity of the IP should be significantly smaller than the nominal emittance budget. Particular attention is given to the low energy working points where the emittance blow-up is worse, aiming at a fraction of the nominal vertical emittance of 1 pm for two IPs.
4. The final focus quadrupoles should reside in a zero-field region to avoid transverse beam coupling; the maximum integrated solenoid field at the final focus quadrupoles should be less than about 50 Tmm at each side of the IP.
5. The field quality of the final focus quadrupoles should have errors smaller than 1×10^{-4} for all multipoles.

Requirement 4 means that a set of screening solenoids is needed. Requirement 3 necessitates the use of a compensating solenoid placed as close as possible to the IP. This is because requirement 1 makes it impossible to have a very long screening solenoid which crosses the IP. The compensating solenoids can be fit in the region before the screening solenoids, while an area of ± 1.23 m around the IP is completely free of magnetic elements and, therefore, can accommodate the luminometer and other technical systems. Requirement 5 is very stringent due to the close proximity of the final focus quadrupoles for the two beams. At a position 2.2 m from the IP the distance (at the tips) between their magnetic centres is only 66 mm, so significant magnetic crosstalk will be present. Finally, requirement 2 is the least stringent, as it can be satisfied by tuning the overall level of compensation; no specific design provision is needed.

The magnetic design of the IR (shown in Fig. 2.20) satisfies all these requirements and is symmetrical with respect to the mid plane of the detector. The first element at 1 m from the IP is the luminosity counter, followed by the compensating solenoid (from 1.23 m to 1.95 m), followed by the screening solenoid (starting at 2 m). The detector solenoid (diameter about 3.8 m) is outside this volume. The first of the final focus quadrupoles can be seen inside the compensating solenoid, starting at a distance of 2.2 m.

This design results in an overall emittance blow-up at the Z energy of 0.4 pm for two IPs. The design fulfils requirement 1 in the sense that all magnet coils are at an angle of less than 100 mrad from the IP. Requirement 2 is met by trimming the total current of the screening and compensating solenoids until $\int B dl$ seen by electrons is arbitrarily close to zero. The current design has an integrated solenoid field inside the quadrupoles of less than 10 mTm; this can be improved further if needed.

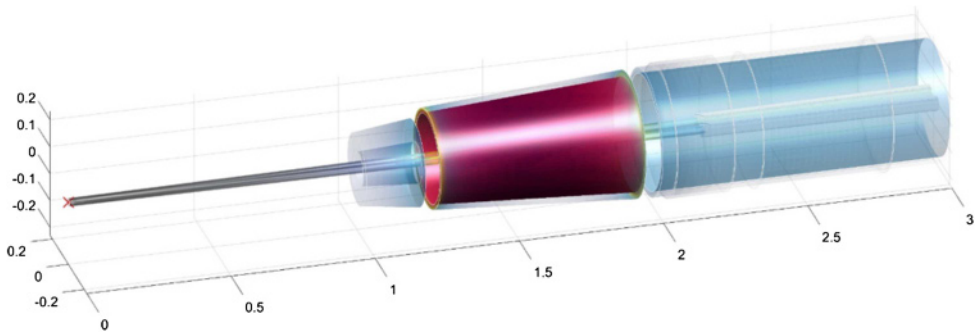


Fig. 2.20. A 3D sketch of the interaction region (IR) magnet system in the first 3 m from the interaction point (IP). Zero in the plot marks the location of the IP).

The stringent requirements of the final focus quadrupoles are satisfied by using a canted-cosine-theta design (e.g. [198]). The proposed design features iron-free coils with crosstalk and edge effect compensation, with a field quality of better than 0.1 units for all multipoles (requirement 5). Dipole and skew quadrupole correctors can be incorporated without increasing the length of the magnetic system.

A full magnetic analysis has been performed, including a misalignment analysis. The resulting field files have been processed using the full SAD optics analysis in order to have reliable emittance blow-up results. Also, a full engineering analysis (mechanical and thermal) has been performed, confirming the approach.

2.5.3 Luminometer

A precise measurement of the luminosity is delivered by the luminosity calorimeter inside the detector. The measurement is performed in an angular range between 65 and 85 mrad with an accepted cross section of 12 nb at the Z pole. This value of the cross section does not provide enough statistics for a fast luminosity measurement. Therefore, Bhabha events at lower angles have to be used. The events have to pass close to the beam through the beam pipe and will eventually be detected outside the experiment. The cross section in the μb range will provide an adequate event rate of 1 kHz at $10^{33} \text{ cm}^{-2} \text{ s}^{-1}$. Larger cross sections are provided by single bremsstrahlung events, which are in the mb range, but they suffer from higher beam background.

2.5.4 Synchrotron radiation

Two independent approaches have been used for evaluating the SR from dipoles and the final focus (FF) quadrupoles, in order to define the IR beam pipe dimensions and to place masks and shielding at the correct locations. The MDISim [199] code is used to evaluate SR from near and far dipoles, whilst a modified version of SYNC.BKG [200] (SYNC_{BKG} was originally developed by Al Clark of LBNL) is used to evaluate SR from the FF quadrupoles and design the IR with masks and shielding. In this second method, macro-particles are traced through sliced magnets, MDISim combining the standard tools MAD-X, ROOT and GEANT4. See reference [200] for a detailed description of the two methods and studies.

The upper plot of Figure 2.21 shows a 3D MDISim display of a Gaussian positron beam at 175 GeV for 5000 particles tracked from 510 m to the IP in GEANT4 with the standard electro-magnetic processes. The lower plots are the resulting distribution of the photons generated.

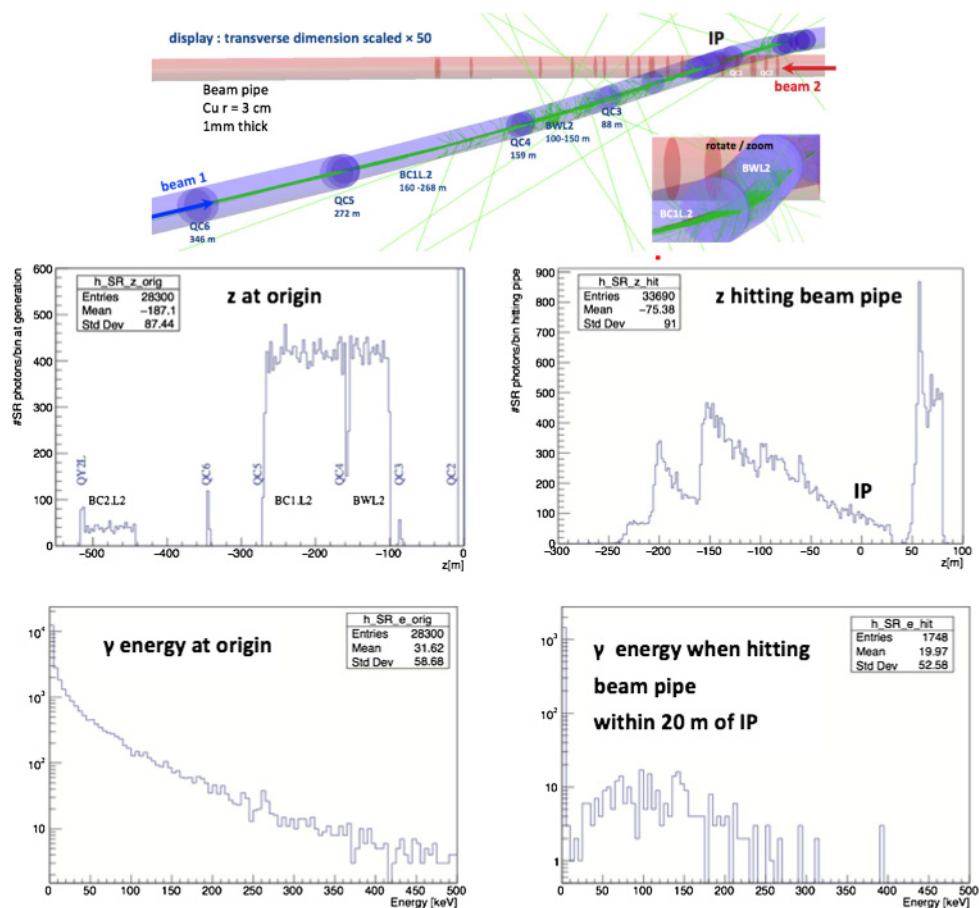


Fig. 2.21. Top: 3D representation of a positron beam track at 175 GeV beam. Bottom: simulation of the distribution of the photons generated in the interaction region for that beam.

The main sources of the SR background in the IR regions are the photons from the last bending magnets and photons emitted by higher amplitude particles in the FF quadrupoles. Several methods are employed to reduce SR backgrounds to tolerable limits. The first method, mentioned above, has been to impose a minimum distance between the dipole magnets and to limit the maximum critical energy of the SR from the dipoles for incoming beam. The SR radiation flux reaching the detectors can be further reduced by the combination of fixed and movable masks (collimators), as well as reducing X-ray reflections by optimising internal surfaces. Fixed mask tips are planned 2.1 m upstream of the IP, just in front of the first final focus defocusing quadrupole, in order to intercept the radiation fan and prevent the photons from striking the central beryllium beam pipe directly. The next level of SR background comes from photons that strike near the tip of these masks, forward scatter through the mask and then strike the central beam pipe. At the $\tau\tau$ energy, most of these scattered photons will penetrate the beryllium beam pipe and then cause background in the detector. To reduce the effect on the experiment, a thin layer of high-Z material, for example gold, will be added on the inside of the beryllium beam pipe. A study has found that at the top energy, any reasonable thickness of gold (up to $10\text{ }\mu\text{m}$) is not very effective due to the high energy of the

Table 2.7. Summary of the SR coming from the last soft bend upstream of the IP.

E_{beam} GeV	E_{critical} keV	Incident γ /crossing (500 μm from tip)	Incoming on central pipe/crossing	γ rate on central pipe (Hz)
182.5	113.4	3.32×10^9	1195	1.18×10^8
175	100	3.06×10^9	1040	1.25×10^8
125	36.4	1.05×10^9	10.3	1.01×10^7
80	9.56	6.11×10^8	0.18	7.02×10^5
45.6	1.77	9.62×10^7	1.92×10^{-4}	9.58×10^3

Notes. The second column refers to the number of photons incident at 500 μm from mask tip and with an energy $>1\text{ keV}$, the third and fourth columns give the incident number of photons in the central beam pipe per beam crossing and per second, respectively. Solenoid fields and collimators were not taken into account. Note that this table was calculated for an older version of the beam optics with a maximum beam energy of 175 GeV. For the more recent optics of Section 2.4 even at a beam energy of 182.5 GeV the critical photon energy is below 100 keV.

scattered photons from the mask tip, while at the Z energy the tip-scattered photons are so few and so soft that a gold layer is probably not needed for SR shielding. However, a layer of high conductivity metal will be necessary (especially at Z) in order to minimise beam pipe heating from image currents. Table 2.7 gives a partial summary of the SR study with details about the photon rate from the last soft bend upstream the IP for all the running beam energies of the collider. Quadrupole radiation has not been considered in this study.

2.5.5 Beamstrahlung, radiative bhabha scattering

Numerical simulations of particle losses in the IR due to beamstrahlung, radiative Bhabha and Touschek scattering, have been made for the different running conditions. Particle tracking has been performed with SAD [186] for these processes and Guinea-Pig++ [201] has been used as the radiative Bhabha scattering generator. Particles have been tracked over a sufficiently large number of turns to determine the IR loss maps. These particle loss distributions are then tracked into the sub-detectors with a full GEANT4 simulation.

For the beamstrahlung background, the beam-beam element was inserted at both IPs and tracking for 1000 turns with the full lattice was done. The beamstrahlung lifetime was estimated from the number of lost particles; this simulated beam lifetime turned out to be shorter than that obtained from the analytical formula. However, the two are consistent, given the approximations used in the simulation and in the theory. The simulated particle losses are mainly concentrated within 5 m around the IP in the vertical plane; the losses mainly happen over the first few turns.

Radiative Bhabha particles were generated in Guinea-Pig++, and then tracked in SAD, for the 45.6 GeV and 182.5 GeV lattices. At 45.6 GeV, the radiative Bhabhas are all lost in a localized region extending up to about 70 m downstream of the first IP. At 182.5 GeV, the radiative Bhabhas are lost mainly in the first half of the ring and some high-energy particles, which are also eventually lost, reach the second IP. Detailed studies have been performed to analyse the losses in the detector at 182.5 GeV and to evaluate the need for collimators to intercept this background source.

Loss maps and beam lifetime limitations due to Touschek scattering are also under investigation for all collider energies, especially for the high-intensity run at 45.6 GeV. However, the Touschek effect is not a major concern for beam-induced

background in the detectors, since its event rate is much lower than those of radiative Bhabha scattering and beamstrahlung.

2.6 Collective effects

2.6.1 Introduction

One of the major issues for the FCC-ee lepton collider is the collective effects due to electromagnetic fields generated by the interaction of the beam with the vacuum chamber, which can produce instabilities, tune shifts and spread, bunch lengthening etc., thus limiting the machine operation and performance. This chapter focusses on the impedance model and collective effects at Z running: some important sources of impedance have been included in the model to study both single bunch and multi bunch instabilities, to predict their effects on the beam dynamics and to find a possible solution for their mitigation. Another critical aspect for FCC-ee is the electron cloud which will be discussed in the last section of this chapter, together with possible strategies to suppress its effects.

2.6.2 Impedance budget

In this section, the contributions to the total impedance budget of some important vacuum chamber components are presented. The beam parameters used for these studies are summarised in Table 2.1.

2.6.3 Resistive wall impedance

Among the several sources of impedance, a critical contribution for the lepton machine is the resistive wall (RW) impedance. This is produced by the finite conductivity of the copper chamber; its value is increased by coating with films of non-evaporable getter (NEG) materials [202]. This coating is required to mitigate the electron cloud build up in the machine and to improve the vacuum pumping [203]. The essential properties of the NEG are a low photon-stimulated desorption (PSD) and a low secondary electron yield (SEY). At high current, the RW impedance results in low single-bunch intensity thresholds for both the microwave instability in the longitudinal plane and for the transverse mode coupling instability (TMCI) in the transverse plane. It has been observed [204] that the thickness of the coating plays a fundamental role in the beam dynamics while the conductivity of the material only plays a marginal role: the RW impedance decreases for a thinner coating; this results in higher single-bunch instability thresholds, thus improving the beam stability during machine operation. In this analysis, the vacuum chamber is assumed to be circular with 35 mm radius and four layers: a first 100 nm thin NEG film with resistivity $\rho_{\text{NEG}} = 10^{-6} \Omega\text{m}$, a second 2 mm thick layer of copper, then 6 mm of dielectric to account for the gap between the beam pipe and the magnet chamber and finally the magnet chamber modelled as an outer layer iron with resistivity $\rho = 10^{-7} \Omega\text{m}$ and infinite thickness. The total loss factor at nominal intensity is about 210 V/pC for a bunch length of $\sigma_z = 3.5 \text{ mm}$ without beamstrahlung.

2.6.4 RF cavities and tapers

For the Z case, the RF system consists of 56 cavities at 400 MHz with a single cell (see Fig. 2.22) which will be arranged in groups of 4 cavities connected by 14 double

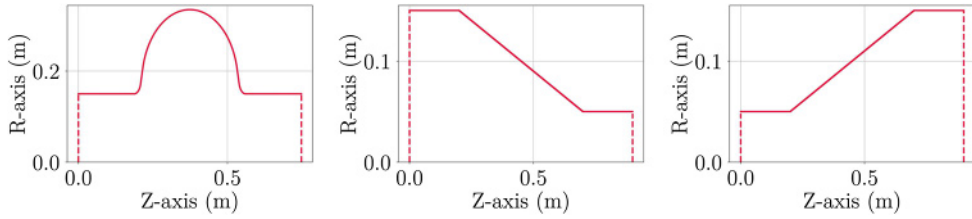


Fig. 2.22. ABCI computer models used for beam-impedance simulations of a 400 MHz single-cell cavity (left), a taper out (center) and a taper in (right).

tapers. The number and the design of these cells have been optimised for strong HOM damping and low longitudinal loss factor [205,206]. For a Gaussian bunch with a nominal bunch length of 3.5 mm, wakefield simulations using the ABCI code [207] estimated a loss factor of 0.33 V/pC for each cavity. By taking into account the 0.5 m long tapers used to connect the cavities to the beam pipe, there is an additional loss factor of 1.9 V/pC for a single double taper (in and out considered independently). In total, the loss factor for 14 4-cell cavities at 400 MHz with double tapers will be 45.1 V/pC.

2.6.5 Synchrotron radiation absorbers

Synchrotron radiation is a source of heating and photoelectrons. Sufficient RF power is needed to replace the energy lost as SR and, to control the extra heating and potential background, SR absorbers are required. Due to their large number, SR absorbers could be a very important source of impedance. In order to reduce their contribution to the machine impedance budget, it was decided to use a circular vacuum chamber with 35 mm radius with a rectangular antechamber on each side, as in the case of the SuperKEKB beam pipe [208].

The SR absorbers will be installed inside the chamber winglets every 4–6 m to intercept the radiation that would otherwise strike the beam chamber. These metallic devices are shaped like a trapezoid, with a total length of 30 cm and placed at about 42.5 mm from the beam axis within the antechamber, as shown in Figure 2.23. The combination of slots for vacuum pumps just in front of each absorber facilitates the efficient capture of the synchrotron radiation and the desorbed molecules. The pumping slots have a racetrack profile with a length of 100–120 mm and a width of 4–6 mm. A cylindrical volume and a flange will be installed to support a NEG pump behind the slots.

Numerical simulations of the beam chamber profile with one absorber insertion have been performed using CST [195]. These impedance studies do not include pumping slots and pumps. Simulations show that below 3 GHz the longitudinal impedance is purely inductive, giving a longitudinal broadband impedance $Z/n \simeq 1 \text{ m}\Omega$ for 10 000 absorbers in the ring.

2.6.6 Collimators

A total of 20 collimators (10 for each plane) for background control (see also Sect. 3.8) were included in the impedance simulations. The 3D models used for CST simulations are shown in Figure 2.24. With the minimum apertures of 5 mm and 2 mm for horizontal and vertical collimators respectively, the total loss factor is about 18.7 V/pC for the nominal bunch length of $\sigma_z = 3.5 \text{ mm}$ at Z, which is without collision.

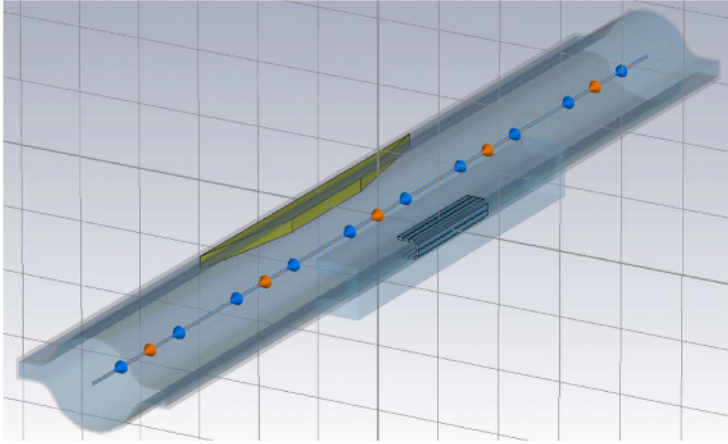


Fig. 2.23. 3D model of the FCC-ee chamber and a synchrotron radiation absorber with pumping slots used for CST simulations.

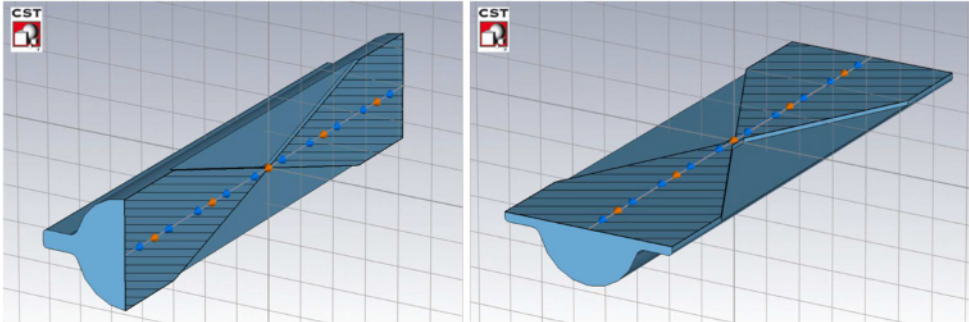


Fig. 2.24. CST perspective view of the vertical collimator (left) and the horizontal collimator (right).

2.6.7 Beam position monitors

Diagnostic elements like ~ 4000 four-button beam position monitors (BPMs), similar to LEP, KEKB and light sources, are planned to be installed in the machine. In order to avoid a special type of winglet-to-circular tapers, these elements will be installed directly on the beam pipe with a rotation angle of 45° . The geometry has been optimised from the impedance and heat transfer point of view [209]: the button has a diameter of 15 mm and a thickness of 3 mm. As an alternative a BPM design with a conical button, similar to the one used in SIRIUS [210], is also being considered in order to push the frequencies of higher order modes trapped in the BPM structure to higher values. CST simulations in the time domain have been performed and the total loss factor is about 40.1 V/pC for 4000 elements in the ring.

2.6.8 RF shielding

In addition to the previous components, 8000 bellows with RF shields will be installed before and after each BPM. Since the conventional finger-type RF shielding showed a non-negligible impedance contribution compared to the RW impedance [211], it was decided to use comb-type bellows and flanges similar to those

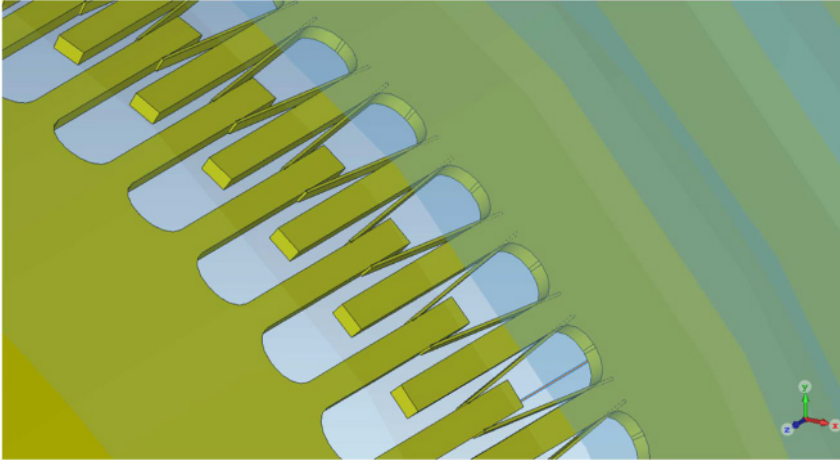


Fig. 2.25. View from inside of the RF shielding with small fingers between the teeth.

of SuperKEKB [212]. A 3D model was built using the CST code (see Fig. 2.25). In this case, the RF shielding consists of 10 mm long nested teeth, 1 mm wide, 0.5 mm radial thickness and a 2.14 mm gap between adjacent teeth, corresponding to a gap of 0.57 mm between the nested teeth. This design also includes small fingers to ensure electrical contact. The total loss factor of the bellows has been computed using CST and found to be about 49 V/pC for 8000 elements.

2.6.9 Overall impedance budget

As already mentioned, in order to evaluate the contribution of all the machine components to the longitudinal impedance budget, ABCI [207] and CST simulations in time domain were performed for a Gaussian bunch with nominal length of $\sigma_z = 3.5$ mm at Z without beamstrahlung. Figure 2.26 shows the longitudinal wake potentials of each component. The RW wake potential has been obtained analytically as the convolution between the wake function computed by Impedance-Wake2D [213] and a 3.5 mm Gaussian bunch. There is about one order of magnitude difference between the RW contribution and that of the other components, showing that the RW is the main source of impedance in the machine. Table 2.8 summarises the corresponding loss factors. The total dissipated power is about 13.7 MW at the nominal intensity, about a factor 3.6 smaller than the total SR power dissipated by the beam of about 50 MW. The loss factors have been evaluated at 3.5 mm, but the bunch length at nominal current is longer due to the bunch lengthening effect, thus giving a lower dissipated power. However, other impedance sources will add their contributions.

2.6.10 Single bunch instabilities

The following sections focus on the most important effects of the RW on the single bunch dynamics: the Microwave Instability (MI) and the Transverse Mode Coupling Instability (TMCI) in the longitudinal and transverse planes, respectively. The beam parameters used for the simulations are listed in Table 2.1. Numerical simulations have been performed by using the macroparticle tracking code PyHEADTAIL [214].

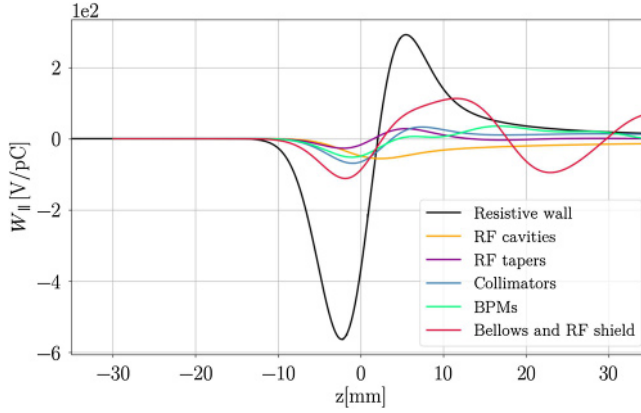


Fig. 2.26. Longitudinal wake potentials for the nominal bunch length $\sigma_z = 3.5$ mm without beamstrahlung due to main vacuum chamber components compared with the RW contribution (black line).

Table 2.8. Power loss contribution of the main FCC-ee vacuum chamber components at nominal intensity and bunch length, in the lowest energy case of 45.6 GeV.

Component	Number	k_l (V/pC)	P_l (MW)
Resistive wall	97.75 km	210	7.95
RF cavities	56	18.5	0.7
RF double tapers	14	26.6	1.0
Collimators	20	18.7	0.7
Beam position monitors	4000	40.1	1.5
Bellows	8000	49	1.8
Total		362.9	13.7

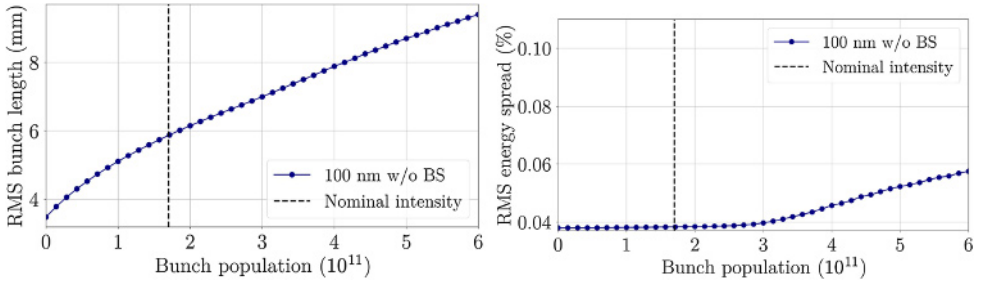


Fig. 2.27. RMS bunch length (left) and RMS energy spread (right) as a function of the bunch intensity obtained from numerical simulations, without beamstrahlung (BS), considering only the RW impedance produced by a NEG film with 100 nm thickness.

2.6.11 Microwave instability

One important effect of the longitudinal RW wakefield on the single bunch dynamics is the increase of the bunch length with the bunch intensity, as shown on the left in Figure 2.27. At nominal intensity, the bunch length obtained from numerical simulations is about 5.86 mm. This value is in good agreement with the analytical predictions by the Haissinski equation [215], as shown in Figure 2.28.

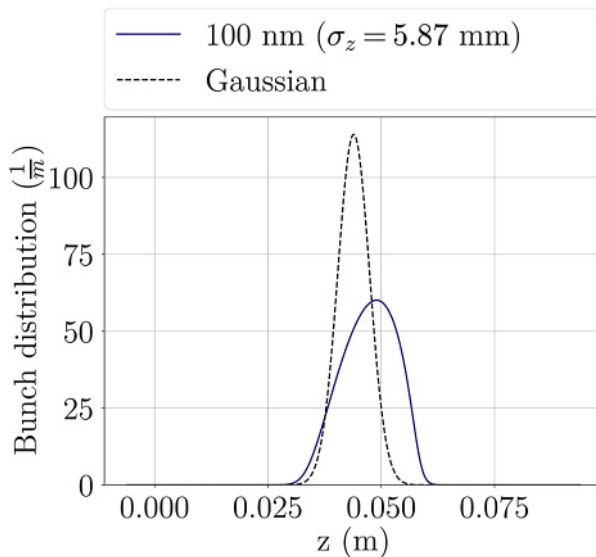


Fig. 2.28. Bunch shape distortion obtained from the Haissinski equation at nominal intensity, by considering only the RW impedance produced by a NEG film with 100 nm thickness. The dashed black line represents the Gaussian equilibrium shape.

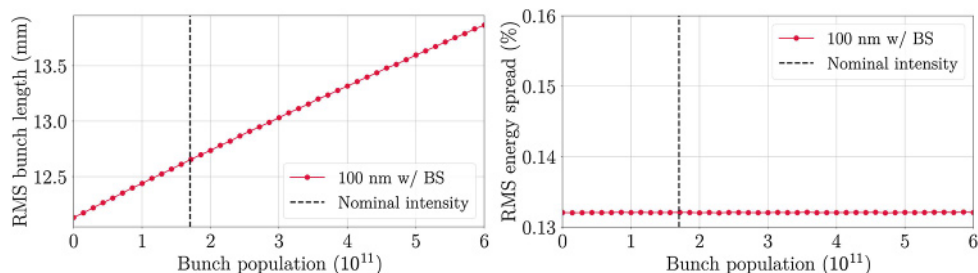


Fig. 2.29. RMS bunch length (left) and RMS energy spread (right) as a function of the bunch intensity obtained from numerical simulations, with beamstrahlung (BS), by considering only the RW impedance produced by a NEG film with 100 nm thickness. ss

Another important effect concerns the energy spread which starts to increase with the bunch intensity above the instability threshold. On the right of Figure 2.27 the energy spread obtained from simulations as a function of the bunch population is shown. In the case of a 100 nm NEG coating, the MI threshold is about a factor 2 higher than the nominal bunch intensity. It is important to note that operation with beamstrahlung results in a much longer bunch and a higher energy spread, thus helping to increase the MI threshold and to operate in stable conditions (see Fig. 2.29).

The bunch lengthening and the MI threshold have also been evaluated by including the other current machine components. The instability threshold in the longitudinal plane is about 2.5×10^{11} , a factor of 1.5 larger than the nominal bunch intensity. The threshold is much higher if the effect of beamstrahlung is included, as shown in Figure 2.30, where the energy spread remains constant at least up to 5×10^{11} . In addition, at nominal intensity, the bunch lengthening in presence of beamstrahlung amounts to only 7%, whereas without beamstrahlung it is 100%.

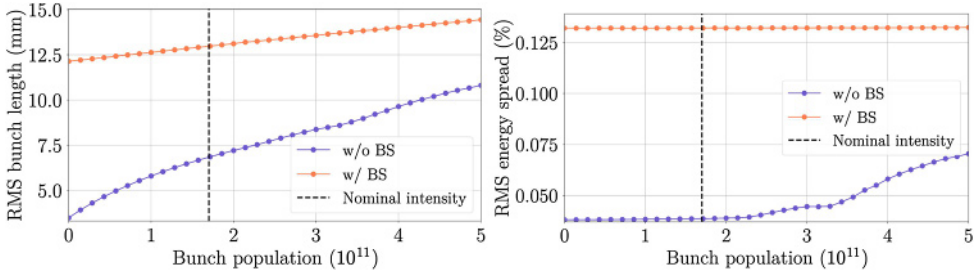


Fig. 2.30. RMS bunch length (left) and RMS energy spread (right) as a function of the bunch intensity obtained from numerical simulations, with (orange curve) and without (blue curve) beamstrahlung (BS), by considering the impedance contribution of all the machine components.

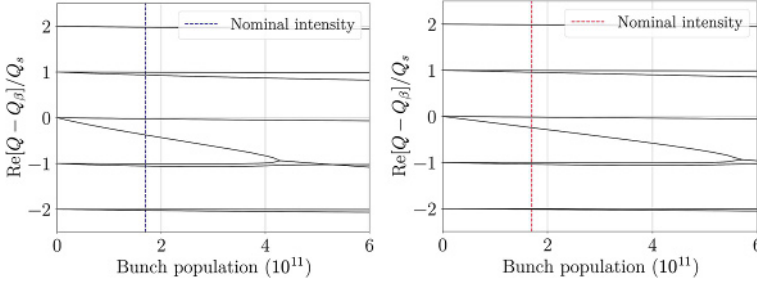


Fig. 2.31. Real part of the frequency shift of the first coherent oscillation modes as a function of the bunch population without (left) and with (right) beamstrahlung, by considering only the RW impedance produced by a NEG film with 100 nm thickness.

2.6.12 Transverse mode-coupling instability

It is known from theory [216] that the betatron frequencies of the intra-bunch modes shift when the bunch intensity increases and the instability occurs when the mode frequency lines merge. Unlike for the longitudinal case, in the transverse case above the instability threshold the bunch is lost. This makes the transverse mode-coupling instability (TMCI) particularly dangerous. Figure 2.31 shows the real part of the tune shift of the first two radial modes (with azimuthal number from -2 to 2) as a function of the bunch population, obtained with the analytical Vlasov solver DELPHI [217], by considering only the RW impedance produced by a NEG film with 100 nm thickness. This computation takes into account the bunch lengthening due to the longitudinal wake shown in Figure 2.27. As in the longitudinal case, the TMCI threshold is about a factor 2.5 higher than the nominal bunch intensity. It is increased by about a factor 3.3 in the case of operation with beamstrahlung.

In conclusion, the impedance budget satisfies the design requirements of FCC-ee.

2.6.13 Multi-bunch instabilities

Transverse resistive wall coupled-bunch instability

For the multi-bunch dynamics, the most critical situation is related to the transverse coupled-bunch instability due to the long range RW wakefield. By considering the beam motion as sum of coherent oscillation modes, the growth rate of the lowest

azimuthal mode, $m = 0$, for a Gaussian bunch is given by

$$\alpha_{\mu,\perp} = -\frac{cI}{4\pi(E_0/e)Q_\perp} \sum_{q=-\infty}^{\infty} \text{Re}[Z_\perp(\omega_q)] \quad (2.8)$$

where the form factor due to the bunch shape [218] is assumed to be equal to 1 and

$$\omega_q = \omega_0(qN_b + \mu + Q_\perp) \quad (2.9)$$

with μ an integer number from 0 to $N_b - 1$ representing a coupled-bunch mode. The instability happens when α_μ is positive, i.e. modes will be unstable for negative frequencies. By considering the most dangerous mode, which is the one with the coherent frequency ω_q closest to zero and negative, and by using a single betatron frequency line as an approximation instead of the sum over q , for the vertical plane with a fractional part of the tune of 0.22, the growth rate given by equation (2.8) is about 435 s^{-1} , corresponding to about 7 turns. There are several unstable modes that need to be damped. The rise times of these modes are in the range of a few milliseconds, corresponding to a few turns in the case of FCC-ee. Therefore, robust feedback is necessary to cope with this fast instability.

2.6.14 Bunch-by-bunch feedback

Modern high current storage rings typically operate above the threshold of dipole coupled-bunch instabilities in all planes. Active stabilisation in the form of bunch-by-bunch feedback is used to maintain the bunches at the design orbit. The conventional topology of such feedback systems uses a single pickup to measure the positions of individual bunches. A linear combination of bunch position measurements from current and previous turns is used to generate a correction kick, which is applied to the beam on the next turn through a wideband kicker structure [219].

A high current storage ring with large circumference, such as FCC-ee, presents a number of unique challenges for such feedback systems. Some of these challenges are of a purely technical nature, such as processing large numbers of bunches and generating sufficiently large kick voltages. Other challenges are more fundamental and push the physically achievable feedback damping and detection sensitivity.

When discussing the maximum achievable damping that conventional feedback topologies (single pickup, single kicker) can provide, it is convenient to consider minimum allowable growth times in the normalised form.

For the longitudinal plane, the normalisation is defined by the synchrotron oscillation period. Since the feedback system measures longitudinal position (time of arrival error) and corrects energy, it must generate a phase shift of 90° at the synchrotron frequency. To produce such a phase shift, information from a significant fraction of the synchrotron period is required. Consequently, achievable feedback damping times are of the order of the synchrotron period [220,221]. For robust operation of the feedback system, normally it is desirable to have the closed-loop damping time be roughly the same as the open-loop growth time – this provides margin for possible variations in instability growth rates and feedback performance. With that requirement, minimum growth times, controllable by the conventional longitudinal bunch-by-bunch feedback system, are of the order of two synchrotron periods. For FCC-ee at the Z pole (the most challenging case), with a synchrotron tune of 0.025, the fastest allowable growth times are around 80 turns. Such growth times correspond to an impedance limit of $26.5 \text{ M}\Omega/\text{GHz}$.

Cases where the longitudinal driving impedances exceed this limit must be addressed at the design stage. For example, one typical such source is the fundamental impedance of the RF cavities, which must be detuned by multiple revolution harmonics to compensate for heavy beam loading. To maintain longitudinal growth rates within the allowable range, feedback within the RF system is used to reduce the effective impedance at and around the synchrotron sidebands [222,223]. RF feedback can also mitigate the bunch-by-bunch phase variation caused by transient beam loading (see Sect. 3.4.5 with Fig. 3.20).

In the transverse planes, the situation is somewhat different. While the longitudinal phase advance over one turn is very small, the betatron motion produces multiple cycles of oscillation within one turn. Conventional feedback topology still needs to generate the appropriate phase shift, but the value of that phase shift not only includes the requisite 90° shift between position sensing and angular kick, but also the phase advance between the pickup and the kicker [219,224]. For moderate fractional tunes (from 0.1 to 0.4, or 0.6 to 0.9), generation of any phase shift requires 3–5 turns². For such tunes, the normalising factor is the revolution time, rather than the fractional tune. On the other hand, when the transverse tunes approach the integer or half integer, the damping available with conventional topology will drop, since phase shifting requires longer history. For moderate tunes, growth times on the order of 3–5 turns can be stabilised with the conventional feedback topology.

In order to handle faster growth rates, several options exist, which are listed below. These are currently speculative and require further study and experimental verification.

The direct energy sensing in the dispersive region (an approach used at the SLC damping rings in the late 1980s [225]), can help overcome the delay limitations in the longitudinal plane. Preliminary estimates indicate that this approach is feasible, but an experimental test in an accelerator is a must. Additional analytical studies are needed to identify the limiting factors for this method and to determine the maximum allowable instability growth rates.

Transversely, growth times down to 1.5–2 turns can be stabilised using the proposed technique of spatial sampling, where the appropriate phase advance to the kicker is synthesised from several neighbouring pickup locations instead of the past turns. Such an architecture still has a one turn delay before the kick can be applied to the bunch. An additional benefit of this method is an improvement in the signal-to-noise ratio of the feedback channel, resulting in lower residual dipole motion.

For instability growth times approaching one turn, techniques based on “out-running” the beam with the correction signal are theoretically possible. These, however, will require significant R&D for both wideband communication channels and signal processing techniques.

Another important concern for these feedback systems is the achievable transverse position detection sensitivity and residual dipole motion. As it has been demonstrated in KEKB and other colliders [226,227], in collision, residual dipole motion is converted to transverse bunch blow up, potentially leading to significant luminosity reduction. As discussed above, fast open-loop growth rates require fast closed-loop damping for robustness. In the frequency domain such fast damping corresponds to a wideband response, occupying a significant fraction of the first Nyquist zone. As a result, the closed-loop system integrates much of the thermal and quantisation noise floors at the input of the digital feedback processor. Low noise design techniques and careful attention to bandwidths of various components is required to keep residual motion in check.

² If pickup and kicker positions are spaced appropriately, feedback correction can be generated in only two turns.

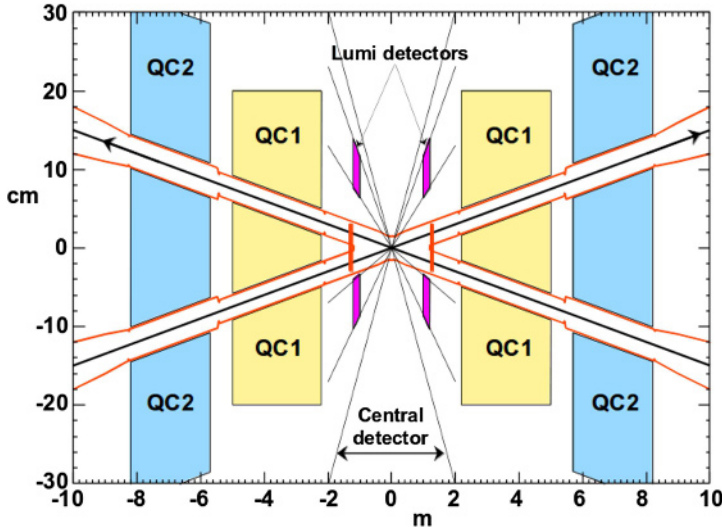


Fig. 2.32. Sketch of the interaction region. See also Figure 2.18.

Modern low-noise bunch-by-bunch feedback systems currently handle the requirements of low emittance light sources as well as SuperKEKB [228]. Since the minimum bunch spacing for the FCC-ee is an order of magnitude higher than that of the 500 MHz machines, lower analog processing bandwidths and slower sampling rates will enable a significant improvement in the achievable performance.

Another, somewhat expensive, path to reduce residual noise levels of bunch-by-bunch feedback systems is to use multiple (N) processing channels [229]. Replacing one system with several systems does not affect the maximum achievable damping (as long as all systems use the same feedback topology), but it does provide a $\sqrt{(N)}$ reduction of the residual motion.

In conclusion, transverse instability rise times down to 1.5–3 turns can be suppressed by conventional feedback topologies, as employed in many modern light sources. Longitudinally, with a synchrotron tune of 0.025 on the Z pole, the fastest allowable growth time is about 80 turns. To keep the longitudinal growth rates within the allowable range, feedback within the RF system is used to reduce the effective impedance.

2.6.15 Interaction region impedance budget

This section presents the results of studies of the impedance for the interaction region (IR) of the machine, with an evaluation of the power loss due to geometrical and resistive wall impedances and trapped modes. A sketch of the IR is shown in Figure 2.32 [230]. The distance from the interaction point to the first quadrupole QC1 is about 2.2 m.

IP resistive wall

For a circular pipe with radius b , the power loss per unit length due to resistive wall is given by

$$\frac{P_{\text{loss}}}{L} = \frac{1}{T_0} \frac{N^2 e^2 c}{4\pi^2 b \sigma_z^{\frac{3}{2}}} \sqrt{\frac{Z_0}{2\sigma_c}} \Gamma\left(\frac{3}{4}\right) n_b \quad (2.10)$$

where N is the bunch population, e the elementary charge, σ_z the bunch length, σ_c the conductivity of the material, Z_0 the vacuum impedance and n_b the number of bunches. Assuming a 15 mm radius pipe made of 1.2 mm thick beryllium at ± 80 cm and of 2 mm thick copper elsewhere, the power loss in the IR due to RW is 514 W/m.

Synchrotron radiation masks

In the IRs, SR masks are placed before and after each quadrupole, in order to protect the vacuum chamber and the detector from photons generated by the last bending magnet located 100 m from the IP. These masks are 2 cm long with a 1 cm long ramp back to the larger radius at each end and produce a variation of 2 mm in the pipe radius (from 15 mm to 13 mm in QC1 and from 20 mm to 18 mm in QC2). Geometric impedances and wake pot computed with the ABCI code indicate a power loss of about 3.8 W per bunch and $\sigma_z = 3.5$ mm with the design intensity at Z.

Trapped modes

Another important source of heating in the IR stems from high order modes (HOMs) that can remain trapped in the IR because of small variations in the beam pipe geometry which unintentionally generate cavities. In order to reduce the HOM effects, the geometry of the IR beam pipe was optimised from the impedance point of view. Various models have been considered [197] and a smooth geometry was designed, with a relatively small impedance from HOMs and only one trapped mode. Wakefield and eigenmode calculations have been carried out by using the CST and HFSS [196] codes, respectively, revealing the presence of the mode at 3.5 GHz. In order to mitigate its effects, longitudinal slots oriented perpendicularly to the HOM electric-field lines are introduced in the top and bottom walls of the beam pipe, such that the mode field can escape through them and be absorbed by a water-cooled absorber installed above and below the slots. For a bunch length of 2.5 mm and a beam current of 1.45 A, the electromagnetic power due to the trapped mode and all the other propagating modes was found to be approximately 5 kW at each end of the central pipe connection. This power will be mainly absorbed in the HOM absorbers, which require further optimisation.

2.6.16 Electron cloud

Electron-cloud (EC) effects are one of the main performance limitations for both hadron and lepton machines [231,232]. In the case of FCC-ee, the e^+ beam produces primary electrons by residual-gas ionisation and, more importantly, by photoemission due to SR. These primaries are attracted and accelerated by the e^+ beam. The resulting EC build up in the vacuum chamber can cause instabilities, emittance growth, heating of the pipe walls, beam losses, vacuum pressure increase and diagnostics degradation.

Multipacting threshold and heat load

This section presents EC studies for the lepton collider at 45.6 GeV. The EC build up has been analyzed in the drift space and in all the magnets of the

Table 2.9. Magnet parameters used for build up simulations at 45.6 GeV.

Element	Length (m)	Magnetic field
Arc dipole	23.44	0.01415 T
Arc quadrupole	3.1	± 5.65 T/m
Arc drift	–	–
QC1L1	1.2	-96.3 T/m
QC1L2	1.0	50.3 T/m
QC1L3	1.0	9.8 T/m
QC2L1	1.25	6.7 T/m
QC2L2	1.25	3.2 T/m

machine (dipoles and quadrupoles in the arcs and final focusing quadrupoles in the interaction region). The multipacting threshold has been evaluated for each component by scanning the SEY of the surface. Numerical simulations have been performed with the PyECLOUD [233,234] code to study bunch spacing effects on the build up. The bunch parameters used for simulations are those of Table 2.1.

For the components in the arcs, the vacuum chamber is modelled as a circular pipe with 35 mm radius interrupted, on either horizontal side by rectangular antechambers, inside which SR absorbers will be installed. In the IR, the beam pipe is circular with 15 mm radius for the final-focussing quadrupole QC1, and with 20 mm radius for the QC2 quadrupole. The beam optics in the arcs and around the interaction point is described in Section 2.4 and in [235]. The EC build up in each element has been simulated by assuming an initial uniform electron distribution in the vacuum chamber of 10^9 e⁻/m representing the survival of electrons between trains or between turns. The secondary emission model used in simulations is described in reference [234]. According to computations of HOM power loss and transient beam loading [236], bunch spacings of 10 ns and 17.5 ns are not acceptable for the present cavity geometry, and filling schemes with at least 100 RF buckets between the first bunches of consecutive trains are preferred. Therefore, in the following, 4 trains of 80 bunches interleaved with 25 empty buckets are considered, with bunch spacings of 2.5 ns, 5 ns and 15 ns. The nominal bunch intensity of 1.7×10^{11} e⁺/bunch has been used for all simulations. The magnetic parameters of each element are shown in Table 2.9. Table 2.10 summarises the multipacting threshold, defined as the highest SEY without multipacting, for each element and beam. These results show that the highest thresholds of EC multipacting are given by the 2.5 ns beam in the arcs and by the 15 ns beam in the IR. Figure 2.33 shows the EC induced heat load as a function of SEY for different components and bunch spacings. The heat load has been calculated as the energy of electrons impacting the pipe walls over the simulated time range rescaled to the total beam intensity. Numerical simulations have also been performed including photoemission seeding, modelled in PyECLOUD through photoelectron yield Y and photon reflectivity R . Since no experimental data exist for these parameters, in build-up simulations a typical photoelectron yield of $Y = 0.02$ and a photon reflectivity in the range $R = [30\%, 80\%]$ are assumed. Results for arc dipoles in case of 15 ns bunch spacing are presented in Figure 2.34, for the case of uniform seeding (no photoelectrons from the wall) and for different values of reflectivity and photoelectrons (obtained by assuming that 50%, 75% and 95% of photons are absorbed), showing that the heat load is not affected by photoelectrons. This means that, after an initial transient, the build up and sustenance of the EC is mainly determined by the secondary emission, while the dependence on the photoemission parameters is marginal. Similar results have been obtained for arc quadrupoles and drifts.

Table 2.10. Threshold SEY for multipacting for all the ring components.

Element	2.5 ns	5 ns	15 ns
Dipole	1.1	1.1	1.0
Quadrupole	1.2	1.0	<1.0
Drift	1.8	1.3	1.0
QC1L1	1.0	1.1	1.3
QC1L2	1.0	1.0	1.4
QC1L3	1.2	1.3	1.5
QC2L1	1.0	1.0	1.2
QC2L2	1.0	1.0	1.2

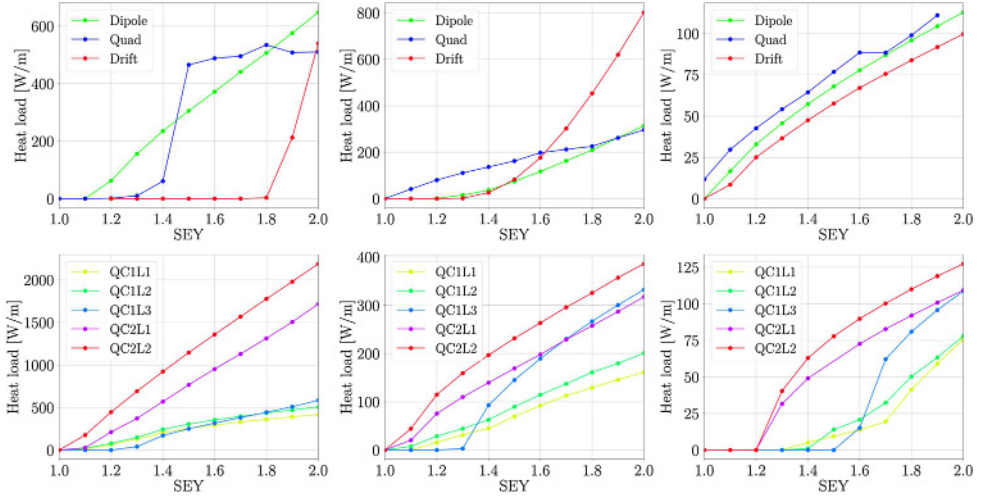
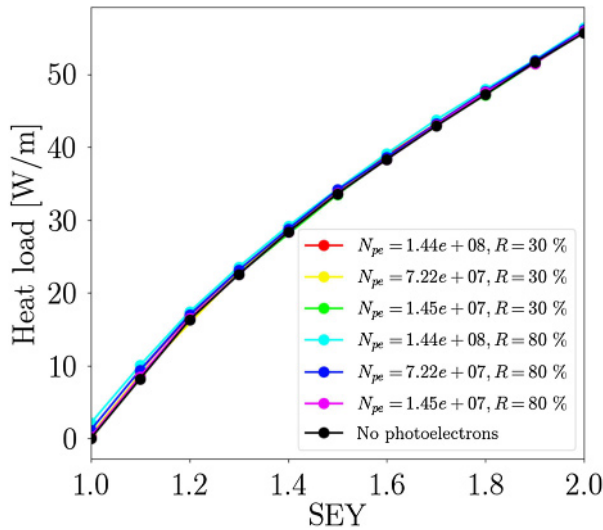
**Fig. 2.33.** Heat load as a function of SEY for arc components (top) and IR magnets (bottom) for 2.5 ns (left side), 5 ns (center) and 15 ns (right side) bunch spacings.**Fig. 2.34.** Heat load as a function of SEY for arc dipoles for the case with no photoelectrons and for various values of photoelectrons and reflectivity.

Table 2.11. Electron density threshold for the fast head-tail instability at four energies.

Energy (GeV)	45.6	80	120	175
Electron frequency $\frac{\omega_e}{2\pi}$ (GHz)	393.25	395.23	392	385.93
Electron oscillation $\frac{\omega_e \sigma_z}{c}$	28.84	24.85	25.88	22.24
Electron density threshold $\rho_{th}(10^{10}/\text{m}^3)$	2.31	11.92	12.6	30.8

Electron density threshold for the single bunch head-tail instability

Electron cloud single bunch head tail instability has been analysed and observed in several machines [237,238]. This instability depends on the electron density near the beam and the threshold is given by

$$\rho_{th} = \frac{2\gamma Q_s}{\sqrt{3}Qr_e\beta C} \tag{2.11}$$

with r_e the classical electron radius, C the machine circumference, Q_s the synchrotron tune, $\beta_{x,y} = \frac{C}{2\pi Q_{x,y}}$ the average beta of the machine and $Q = \min(\omega_e \sigma_z/c, 7)$ with ω_e the frequency of the electron oscillation near the beam centre [239]. Table 2.11 summarises the electron density thresholds at four energies, using the baseline beam parameters of Table 2.1.

In the FCC-ee, the number of photons emitted per positron per metre is equal to 0.085/m at 45.6 GeV, with a critical energy $E_c \simeq 19$ keV, and 0.329/m at 175 GeV, with $E_c \simeq 1$ MeV. Numerical simulations show that about 95% of these photons are absorbed by the SR absorbers installed in the rectangular antechambers. Therefore, by assuming a photoelectron yield of $Y = 0.02$, the number of photoelectrons per metre produced by the passage of a bunch is $10^7(Z) - 10^8$ (tt̄). Given the chamber cross section, this translates into a photoelectron density from a single bunch of about $10^9/\text{m}^3(Z) - 10^{10}/\text{m}^3$ (tt̄) which is comparable with the instability threshold. However, further investigations with numerical simulations are needed. As mentioned in the previous section, in order to mitigate the electron-cloud build up in the positron ring, the vacuum chamber will be coated with a thin film of NEG materials, which have a low SEY. Another possibility to reduce the build up in the machine is to introduce gaps in the bunch train in compliance with the RF requirements.

2.6.17 Fast beam-ion instability

Beam-induced ionisation of residual gas in the vacuum chamber generates ions, which in the electron machine can accumulate around a passing bunch train. If the density of trapped ions becomes sufficiently high, a fast beam-ion instability will be excited [240]. The FCC-ee may be vulnerable to the fast beam-ion instability, in particular for operation at the Z pole, due to the large number of bunches foreseen for operation. Ion trapping and its effect on beam stability at this mode of operation have been studied with macro-particle simulations to evaluate the constraints introduced by the mechanism [241,242].

The dynamics of the beam-ion interaction are highly sensitive to the transverse beam size and the ions are kicked with different strengths in different locations of the machine, according to the optics functions. Since it is not possible, for a machine of the size of the FCC, to comprehensively sample the machine lattice within a reasonable computation time, the machine is modelled using a smooth approximation with identical lattice functions in all segments. Because the lattice functions vary

widely between the arcs of the machine and the straight sections, the two cases are simulated independently. The arcs, which cover 86.6% of the machine, are modelled with a smooth approximation over the entire circumference with equal distances and phase advances between segments. To model the 13.4% of straight sections, each individual straight section is divided into a number of equidistant interaction points, while the arcs simply transport the beam between straight sections. To account for the different phase advances covered by the various straight sections, the phase advance between segments varies for each straight section. In both cases the lattice functions are selected to maximize ion trapping within the corresponding part of the machine.

The residual gas species H_2 , CO and CO_2 have been considered, with each species simulated independently. Due to the heavy computational burden of the simulations, trains of 50–200 bunches have been studied over 50 turns around the machine. Over this time, the expected vertical damping due to synchrotron radiation is 4%, and growths larger than this are considered unstable. As illustrated in Figures 2.35 and 2.36, although the arcs make up about 87% of the machine circumference, more stringent constraints on the vacuum are found for the straight sections. This is due to the comparatively smaller beam size in the arcs, leading to over-focussing of the ions, which are, hence, efficiently expelled from the beam core. Even for the smallest possible bunch spacing of 2.5 ns, no sign of trapping of H_2 ions can be observed in the arcs for partial pressures up to 10 nTorr, see Figure 2.35 (left). The heavier species are still weakly trapped, Figure 2.35 (centre) and (right), and induce instabilities and emittance growth, albeit with atypical behaviour for the fast beam-ion instability. In the straight sections on the other hand, H_2 ions are weakly trapped, like the heavier species in the arcs, while the heavier species are strongly trapped, displaying typical characteristics of the instability, Figure 2.36. For this bunch spacing, the partial pressure of H_2 is constrained to less than around 0.5 nTorr in the straight sections. For the heavier species, the partial pressure thresholds are much lower, around 5 pTorr. As long as the heavier species make up less than 1% of the pressure composition of the residual gas, the total pressure in the straight sections is thus constrained to around 0.5 nTorr.

The constraints in the arcs can be significantly relaxed by using a larger bunch spacing. With a spacing of 7.5 ns, the partial pressure threshold is around 1 nTorr, increased by a factor of 20 compared to 2.5 ns for CO_2 gas in the arcs, as shown in Figure 2.37. A similar effect can be expected also for CO in the arcs and H_2 in the straight sections, but the effect may not be as strong for the heavier species in the straight sections. The minimum ion mass number which is trapped by the beam is directly proportional to the bunch spacing, indicating that increasing the spacing reduces the amount of ion trapping. However, in the straight section model, both CO and CO_2 ions would still be strongly trapped for a bunch spacing of 17.5 ns, whereas 19.6 ns is the theoretical maximum spacing for the design number of bunches. To accurately determine the pressure constraints for any given bunch spacing, further studies sampling in detail the lattice functions in the straight sections should be performed.

Since the fast beam-ion instability is a coupled-bunch instability with no significant intra-bunch motion, a bunch-by-bunch feedback can typically efficiently suppress the instability, see e.g. [243]. Given that the rise times of the instability for the lowest unstable pressures are relatively long, a feedback system with a damping time of 10–100 turns should be able to increase the pressure threshold by more than a factor of 10. However, it is not clear that a feedback system would prevent the emittance growth associated with ion trapping.

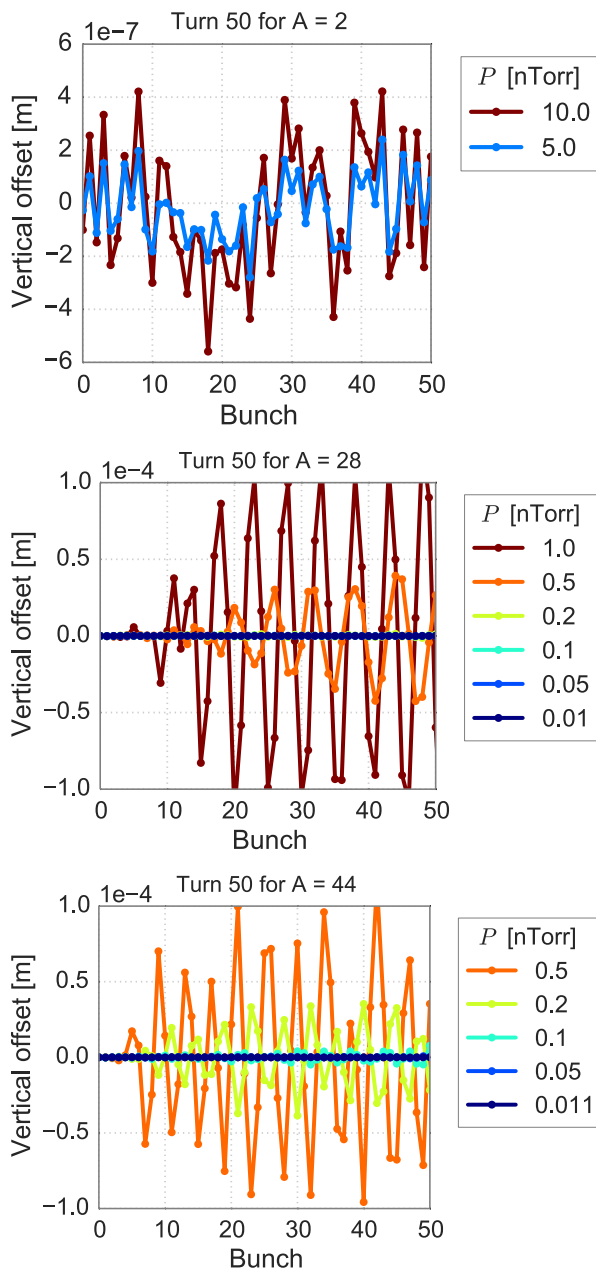


Fig. 2.35. Vertical bunch centroid offsets after 50 turns with selected pressures of H_2 , CO and CO_2 gas (from top to bottom) in the arc model with 2.5 ns bunch spacing.

2.7 Energy calibration and polarisation

Beam energy calibration by resonant depolarisation (RDP) is the basis for the precise measurements of the Z mass and width with a precision of <100 keV, and of the W mass and width with a precision of the order of 500 keV. These challenging goals can be achieved, but require a dedicated operation mode, specific hardware elements, and careful control and monitoring of the operating conditions.

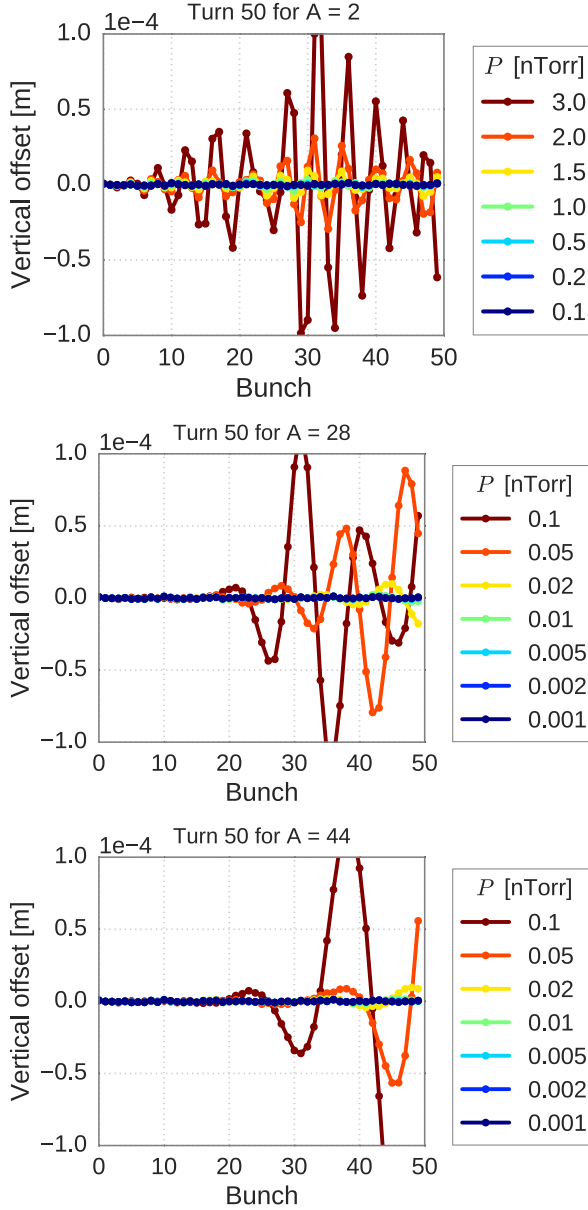


Fig. 2.36. Vertical bunch centroid offsets after 50 turns with selected pressures of H_2 , CO and CO_2 gas (from top to bottom) in the straight section model with 2.5 ns bunch spacing.

Due to the SR emission, electron (and positron) beams polarise spontaneously in storage rings, up to an equilibrium level of 92.4% in a perfectly flat machine. Simulations of the equilibrium beam polarisation were performed for realistic FCC-ee accelerator models with imperfections and optics corrections [244]. These show that, provided the corrections achieve the vertical target emittance, sufficient levels of polarisation are obtained at the Z and at the W pair threshold, as shown in Figure 2.38.

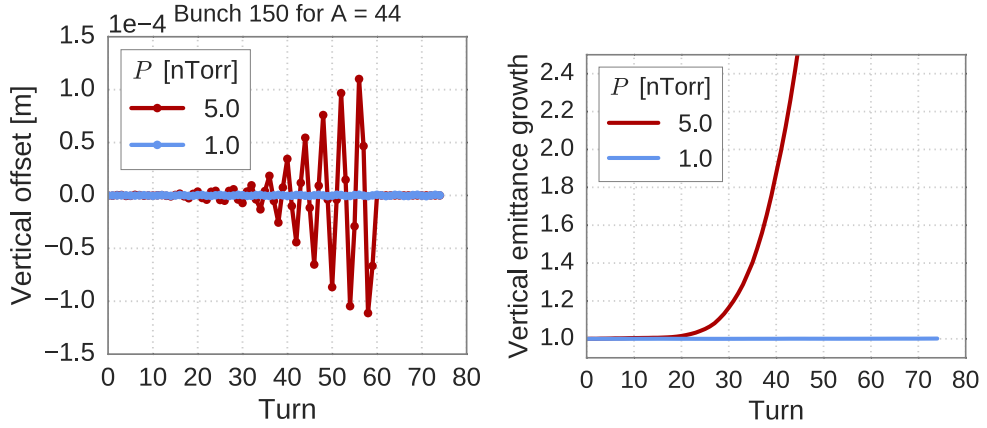


Fig. 2.37. Bunch train evolution over 75 turns for CO_2 ($A = 44$) gas in the arcs, with 7.5 ns bunch spacing: vertical centroid motion of the last bunch (left) and vertical emittance growth of most unstable bunch (right).

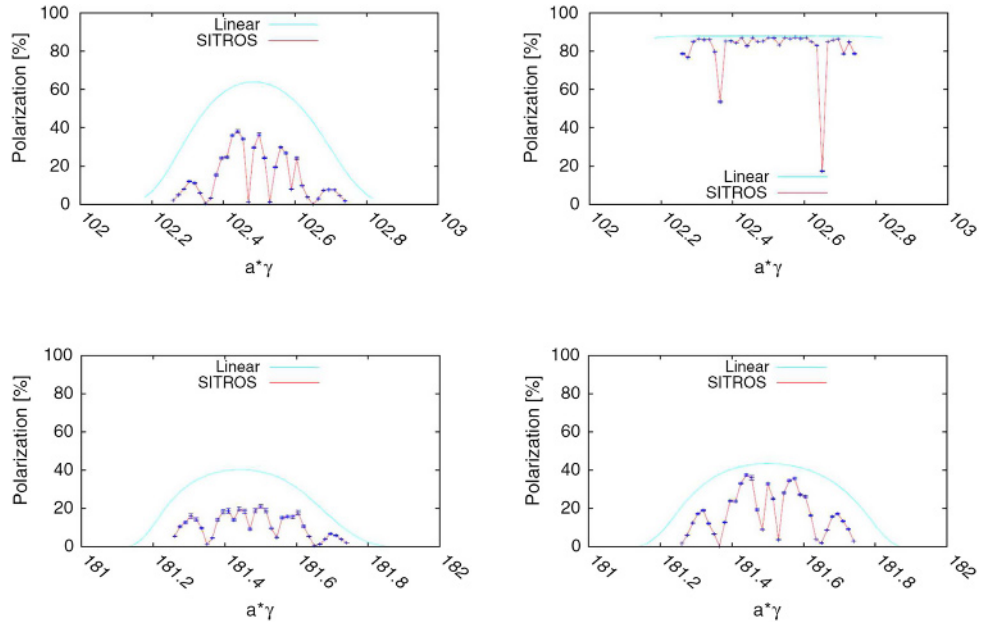


Fig. 2.38. Example of simulations of beam polarisation in FCC-ee with linear spin theory or with the tracking code SITROS [245]. Top: near the Z pole with the 60/60 FODO optics. Left: polarisation versus spin tune after orbit is corrected with 1096 correctors with $200\ \mu\text{m}$ quadrupole and BPM misalignments, plus 10% BPM calibration errors, including polarisation wigglers as described in the text. Right: adding the correction of the average spin vector through harmonic bumps. Bottom: same machine at the WW threshold, without wigglers. Left: after the orbit has been corrected with single value decomposition (SVD) in presence of BPMs errors and the spin vector further corrected by eight 3-corrector harmonic bumps, or (right) by eight dispersion-free 5-corrector harmonic bumps.

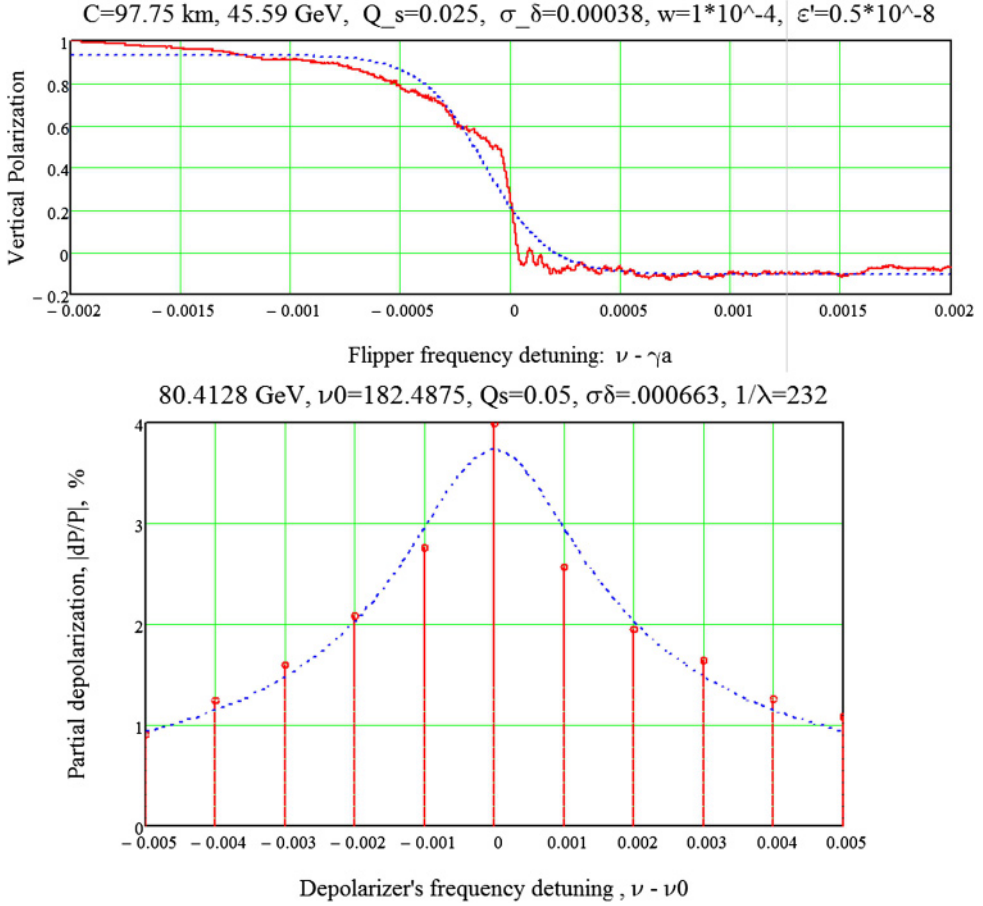


Fig. 2.39. Left: at the Z energy, simulation of a frequency sweep with the depolariser, showing a very sharp depolarisation at the exact value of the spin tune. Right: at the W pair threshold the energy spread is too large to perform a wide frequency sweep, progressing in little steps is needed. Nevertheless the spin resonance can be well located [250].

The build-up time τ_P of the beam polarisation P scales like $\tau_P \propto \rho^3/E^5$, where ρ denotes the bending radius. The polarisation time is increased by a factor ~ 43 compared to LEP, to around 250 h at the energies of the Z line shape scan, which is excessively long. The rise time may be efficiently lowered by using asymmetric wigglers but these will unavoidably increase the energy spread, which causes depolarisation. LEP observations indicated that the maximum tolerable energy spread to achieve a useful level of spontaneous polarisation was around 60 MeV [246], to be compared with the 440 MeV spacing of the integer spin tune resonances. The natural beam energy spread scales as $\sigma_E/E \propto E^2/\sqrt{\rho}$ in FCC-ee. At the Z it is 27 MeV, leaving space for lowering the rise time to ~ 12 h using wigglers. This would allow a level of 10% (5%) beam polarisation, sufficient for the energy calibration by RDP, to be obtained in 90 (45) min. A potential set of wigglers has been specified as 8 units per beam, each with three positive poles of length 0.43 m (L^+) each, with a maximum field of 0.7 T (B^+) (see Sect. 3.2.9). The ratio of total length and B-field between the strong and weak poles is $L^-/L^+ = B^+/B^- = 6$.

For the operation point at the W pair threshold, spontaneous polarisation with a rise-time of around 10 h should be observable without wigglers. This has been confirmed by spin simulations. This is an essential difference with respect to LEP, where the larger energy spread prevented the build-up of polarisation at the W pair threshold.

Resonant depolarisation is the most precise method for beam energy measurements. It relies on the relationship between the beam energy E_b in GeV, and the spin tune ν , which is the number of spin precessions of polarised electrons per turn:

$$\nu = \frac{g_e - 2}{2} \frac{E}{mc^2} = \frac{E_b}{0.44065686(1)} \quad (2.12)$$

Once the beam reaches a polarisation of a few percent, a horizontal field (kicker) oscillating at the spin precession frequency can induce resonant depolarisation (RDP), which provides an accurate measurement of the beam energy, at the level of 0.1 MeV or better. The technique was successfully applied at LEP [247–249]. A simulation of the depolarisation for FCC-ee was performed [250] showing a possible relative precision of 10^{-6} at the Z, and 5×10^{-6} at the W pair threshold.

The relationship between spin tune and beam energy (Eq. (2.12)) can be affected by the transverse component of parasitic magnetic fields, such as those occurring if the orbit is not perfectly planar. This can lead to possible biases in the beam energies and in the centre-of-mass. Many such effects have been estimated by Bogomyagkov [251]. The worst effect comes from vertical orbit distortions: at the Z, a planar defect in the collider of $300 \mu\text{m}$ will induce a possible systematic shift of around 45 keV.

The running mode is proposed as follows [252]. An improvement of the accuracy by a factor 20 over LEP can be achieved by frequent (5/h) measurements of the beam energy by RDP during luminosity data taking. To this effect, of the order of 200 non-colliding “pilot” bunches will be injected per beam, at the beginning of each fill and polarised using wigglers, before the rings are filled for luminosity running. This will allow tracking of all the effects that cause variations of the beam energy, and in particular the ground motion caused by the Earth tides, the Geneva lake level, and other geological variations. Given the very small momentum compaction factor (at the level of a few 10^{-5}), the range of energy variations, both daily and seasonally, is expected to be larger than 100 MeV. These will have to be compensated continuously by corresponding changes of the RF frequency and monitored by various means, including the horizontal offsets in the beam position monitors, and more directly by regular resonant depolarisation measurements. Since the two beams are in different magnetic channels, sizeable differences in beam energy between positrons and electrons are expected, requiring a polarimeter and a depolariser for each beam.

The depolarisation kicker(s) must be able to impose a spin rotation of up to 3×10^{-4} rad per passage of the particles. This corresponds to a maximum kick of 3×10^{-3} Tm which has to be applied during a pulse of a few nanoseconds so as to act on a single bunch without influencing the others. An electrostatic RF kicker, similar to the transverse feedback kicker [253] of the LHC, will be adequate. The exact layout of the kicker system is under study.

The proposed [179] polarimeters will be based on Compton backscattering, with a simultaneous measurement of the recoil electron (in the following the “electron” will represent particles of either sign) and of the backscattered photon. The photon measurement was done at LEP, but with modern silicon pixel technology it becomes possible to perform a complete mapping of the recoil electron in energy and angle. The device is sketched in Figure 2.40. A suitable location for the laser-beam intersection point is upstream of the last dispersion suppressor magnet on the beam located inside the ring in the insertions at Points PH and PF. The recoil electrons/positrons

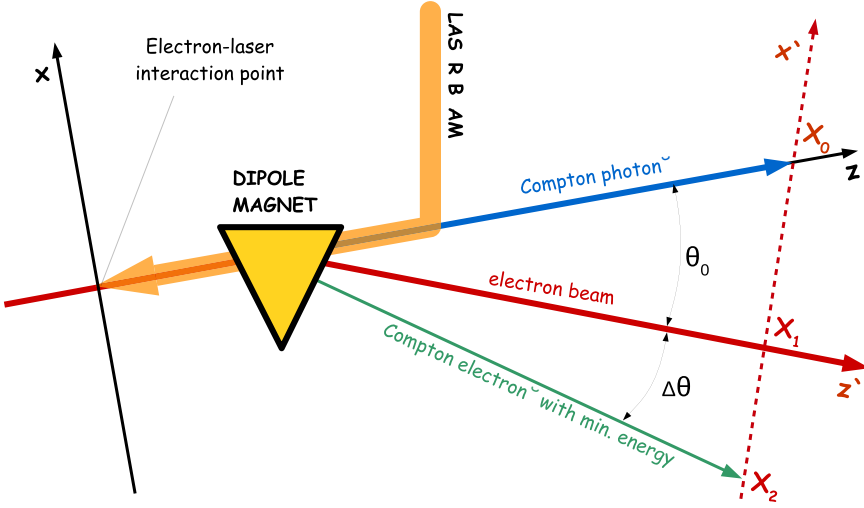


Fig. 2.40. Layout of the inverse Compton polarimeter.

are thus magnetically analysed in the magnet. The analysis of the recoil electron allows a more sensitive measurement of polarisation than the photons; furthermore the end point provides an independent and continuous beam energy monitoring at a level of 10^{-5} . This independent monitoring of the beam energy will be most useful: i) to ensure that no large variation occurs between RDP measurements; ii) it can also be used to compare the energy of the colliding and non-colliding pilot bunches; iii) it may even be possible to cross-calibrate it with the RDP to obtain a direct energy measurement of the colliding bunches.

The interpolation of the average beam energy as determined by RDP to the centre-of-mass energy requires an understanding of all sources of energy loss and energy gains: RF cavity voltages and phases, energy loss by synchrotron radiation and beamstrahlung or impedances. The effect of RF voltage and phase uncertainties is eliminated if all the RF for both beams is situated in the same straight section. In this configuration the energy gain by the RF is simply determined by the total energy loss; uncertainties due to the distribution of RF gains across the ring are eliminated. The energy offset at any of the IPs only depends on the energy loss between the RF system and the IP. The energy loss in the arcs at 45 GeV, of 9 MeV per quadrant, is expected to be known to better than 10^{-3} (9 keV) and will not introduce a significant uncertainty. This configuration has been chosen for the layout of the collider for the Z and W running.

The average energy loss by beamstrahlung is of the order of 62 keV (at the Z) but, because the pilot and colliding bunches circulate in the same magnetic structure, they will conserve the same average energy. Beamstrahlung will only affect the collision energy by a fraction of this number, if the energy loss occurs asymmetrically before or after the collision point.

The combination of opposite sign dispersion and collision offset at the IPs leads to a bias in the collision energy:

$$\Delta E_{cm} = - \langle x \rangle \frac{\sigma_E^2 \Delta D_x}{E_0 \sigma_x^2}$$

and the equivalent equation in the vertical plane. This effect must be monitored and its impact on the average centre of mass energy should be eliminated as much as possible by regular luminosity optimisation to maintain the beams head-on. The

average bias will be less than 100 keV if the average beam offset is less than 3% of the beam size [254].

Finally, the beam energy spread must be determined with a relative precision of better than 0.2%. This can be done every 5 min by the experiments themselves by looking at the acollinearity of the 10^6 muon pairs recorded at the Z pole [255]. This acollinearity also provides a measurement of the average energy difference between the two beams at the same level of precision of 50 keV every 5 min. Since all the previously systematic shifts will affect this quantity with biases at the same level as the centre-of-mass energy, this acollinearity will provide a powerful cross-check of the correct evaluation of systematics.

The targets of achieving luminosity averaged centre-of-mass uncertainties of less than 100 keV around the Z pole, and of 300 keV at the W pair threshold are well within reach.

Further studies will be required to improve the understanding of the uncertainties at the W pair threshold, and to evaluate the correlations between energy points: a large positive correlation between points would worsen the Z mass uncertainty, but reduce the uncertainties on the Z width and muon pair forward-backward asymmetry.

Longitudinal polarisation in collisions is not part of the FCC-ee baseline. It can be used for precise left-right asymmetry measurements at the Z pole and for polarisation asymmetries at the other energies. However, the high luminosity allows the same information to be gained by other means. Such an option would become interesting for polarisation levels of 30% or more. Given the topping up of the rings with unpolarised beams, this would lead to a considerable loss in luminosity.

2.8 Injection and extraction

2.8.1 Top-up injection

Beam particles in the collider rings are continuously lost due to radiative Bhabha scattering in the collisions, resulting in a rather short beam lifetime. There is a technique known as *top-up injection*, which is widely employed in lepton colliders and light sources. It keeps the beam current essentially constant by injecting electrons/positrons “on top” of a circulating beam to compensate for the beam current loss. It may be necessary to mask the data acquisition from the physics detector during the injection process [256]. However, the masking period can be short and thus the luminosity production efficiency is maximised with the constant, maximum beam currents. In addition, the stability of the machine is maximised: the constant beam current generates a constant heat load from synchrotron radiation on the accelerator components. Therefore, it is crucial to incorporate the top-up injection in the collider design.

The following conditions are taken into account in the design. Firstly, a straight section of about 1.4 km is available, which is sufficiently long. Secondly, the beam clearance, i.e. the distance between the circulating (injection) beam orbit and the septum blade must be at least 5σ in units of the circulating (injection) beam size. The injection system of SuperKEKB, for example, is designed with 3σ and 2.5σ clearances for the circulating and injection beams, respectively [257]. The rather large clearances in the FCC-ee design have been chosen to ensure a robust injection with low losses. Thirdly, it is assumed that the transverse emittance of the injection beam is equal to that of the collider ring. The injector chain can provide beams with transverse emittance smaller than or equal to that of the collider ring. The design, therefore, includes additional margins to benefit from this situation.

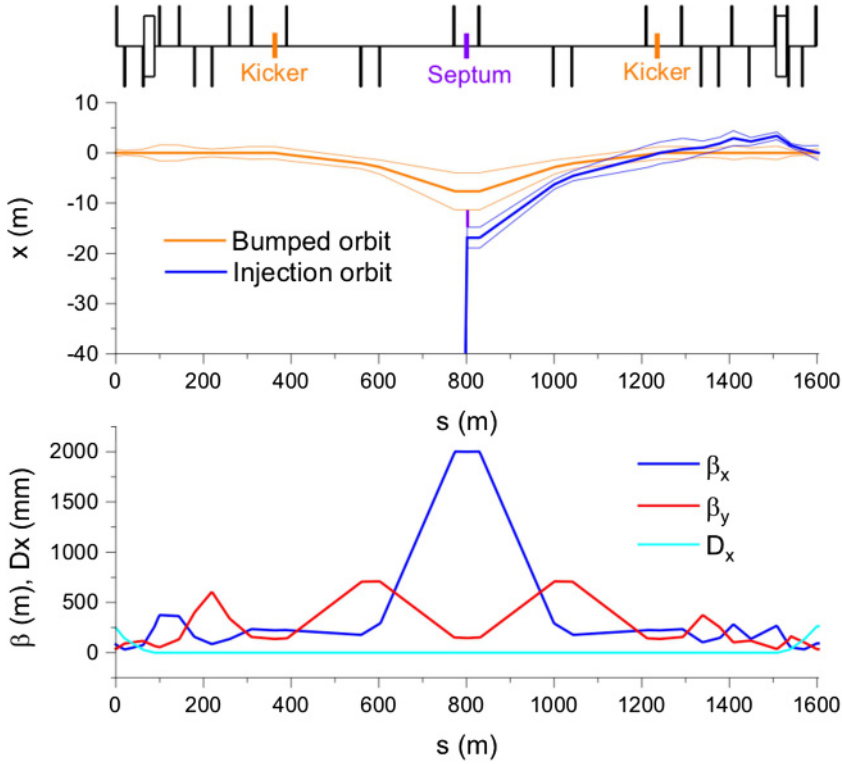


Fig. 2.41. Injection straight section layout (top), optical functions (middle) and beam orbits (bottom) together with 5σ envelopes.

The conventional injection scheme widely used in electron storage rings is applicable to FCC-ee. A septum and a dynamic orbit bump are used in this scheme. The injected beam initially separated by the septum blade merges into the circulating beam thanks to synchrotron radiation damping. In order to facilitate top-up injection, the beta function at the septum is enlarged, which has the effect of reducing the septum blade thickness in units of beam sigma. Figure 2.41 shows a possible layout of the injection straight section together with the optical functions and beam orbits. The beta function at the septum is increased to 2000 m, which sets the dynamic aperture requirement to 13.6σ and 16.0σ for the $t\bar{t}$ and Z operation modes, respectively, assuming a septum with 3.5 mm thick blade. The injection beam needs to be properly matched [258]. In the layout above the required kicker deflection angle is $20.6\mu\text{rad}$ and $11.5\mu\text{rad}$ for $t\bar{t}$ and Z, respectively, which corresponds to 0.012/0.0017 Tm. These integrated fields can easily be achieved with ferrite kickers as commonly used. A modest septum deflection angle of about 5 mrad (3.0/0.8 Tm) is sufficient to separate the injection beam line and the collider orbit.

One of the important issues in top-up injection is disturbance of the stored beam, arising from non-closure of the orbit bump. Additional kickers have to be installed and fine-tuned to accomplish a satisfactory bump closure. There will always be differences in the bunch charges of the circulating beam since the top-up injection is performed at the repetition rate of the booster. The tolerance for the charge difference is set to $\pm 5\%$ by beam-beam simulations (see Sect. 2.2). A feedback system for the filling pattern has to be implemented in the injector chain to keep the bunch charges as constant as possible.

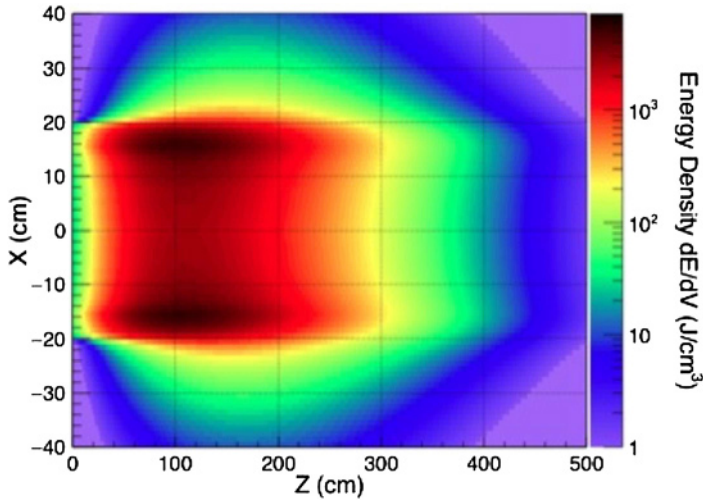


Fig. 2.42. The energy deposition on the beam dump for FCC-ee.

Finally, a few alternative injection schemes were studied, which also proved viable [176].

2.8.2 Extraction and beam dump

The extraction system is designed to remove the electron and positron beams from the main ring and transport them to the external beam dump. The system of extraction kickers and a Lambertson septum deflects the beam downwards by 12 mrad. In order not to melt the dump absorber material, the beam is spread over the front surface of the dump in a spiral pattern by means of horizontal and vertical dilution kicker magnets. The energy density deposited in the graphite in the horizontal-longitudinal (x – z) plane is shown in Figure 2.42.

2.9 Operation and performance

2.9.1 Efficiency

The FCC-ee baseline luminosity at the four different operation points is discussed in Section 2.2. Normalising the total target luminosity for each working point by the corresponding total wall-plug power (see Tab. 9.1) yields the performance characteristics presented in Figure 2.43. References [259,260] compared this normalised performance forecast for the FCC-ee with the corresponding figures for several other proposed lepton colliders. They concluded that the FCC-ee offers by far the highest performance figure-of-merit, “luminosity per electric power”, among all the possible future lepton colliders considered.

2.9.2 Physics goals

As explained in Section 1.5, the physics goals of FCC-ee require at least the following integrated luminosities, summed over two interaction points (IPs): 150 ab^{-1} at and around the Z pole (88, 91, 94 GeV centre-of-mass energy); 10 ab^{-1} at the

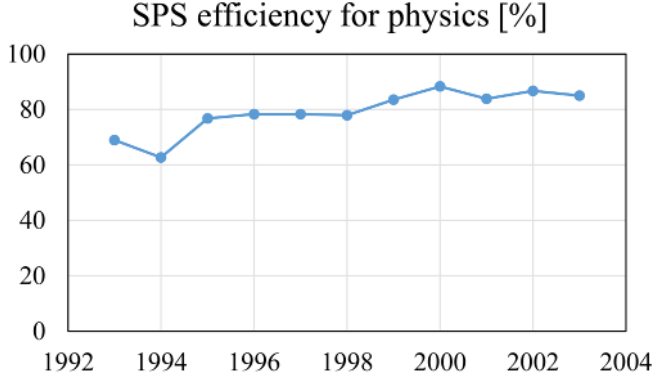


Fig. 2.43. FCC-ee total luminosity divided by total electric power as a function of c.m. energy.

WW threshold (~ 161 GeV with a $\pm \text{few}$ GeV scan); 5 ab^{-1} at the ZH maximum (~ 240 GeV); a few 100 fb^{-1} at the $t\bar{t}$ threshold, with a scan from 340 to 350 GeV; and 1.5 ab^{-1} at 365 GeV [261,262].

2.9.3 Estimated annual performance

The annual luminosity estimates for FCC-ee at each mode of operation are derived from three parameters:

- Nominal luminosity L : taken to be 10–15% lower than the luminosity simulated for the baseline beam parameters. This nominal luminosity is considered from the third year onward in phase 1 (Z pole), and from the second year in phase 2 ($t\bar{t}$ threshold). The luminosity for the first and second year of phase 1 and for the first year of phase 2 are assumed to be smaller, on average, by another factor of two, in order to account for the initial operation.
- It is assumed that 185 days per year are scheduled for physics. This number is obtained by subtracting from one year (365 days), 17 weeks of extended shutdowns (120 days), 30 days of annual commissioning, 20 days for machine development (MD), and 10 days for technical stops.
- Nominal luminosity L and time for physics T are converted into integrated luminosity L_{int} via an “efficiency factor” E , according to

$$L_{\text{int}} = ETL. \quad (2.13)$$

The efficiency factor E is an empirical factor, whose value can be extrapolated from other similar machines, or by simulations with average failure rates and average downtime. Thanks to the top-up mode of operation, it is expected that E will be, within 5%, equal to the availability of the collider complex. Therefore, assuming an availability of at least 80%, the corresponding efficiency is $E \geq 75\%$.

The 17 weeks of assumed extended shutdown is, on average, longer than the time required for the installation of new cryomodules (see Tab. 2.12), and that 20 days for machine development is larger than the corresponding number for LEP (e.g. in the year 2000 LEP had 5 days of MD [263]).

Table 2.12. Minimum lengths of FCC-ee extended shutdowns based on the number of cryomodules (CMs) to be installed and a special 12 week margin for the first three years; shutdown no. 1 refers to the first shutdown after one year running on the Z pole.

Shutdown	No. cryomodules	Length of shutdown
Shutdown 1	–	12 weeks
Shutdown 2	–	12 weeks
Shutdown 3	10 CM	12 weeks
Shutdown 4	26 CM	20 weeks
Shutdown 5	21 CM	14 weeks
Shutdown 6	42 CM	18 weeks
Shutdown 7	30 CM	15 weeks
Shutdown 8	30 CM	15 weeks
Long shutdown	104 CM	1 year
Shutdown 11	39 CM	17 weeks
Shutdown 12	–	–
Shutdown 13	–	–
Shutdown 14	–	–

2.9.4 Radiofrequency system staging

The operation starts with running at the Z energy, similar to LEP-1. This configuration requires the lowest RF voltage, implying the smallest system size installation and the associated minimum impedance. The changes in the machine configuration required between the Z, W and H running can be implemented during the regular extended shutdowns.

The length of these system reconfiguration shutdowns is likely to be dominated by the installation of new cryomodules in preparing or during transition to the next running modes. Considering a single cryomodule transport per working day, the minimum total duration is estimated as

$$n_{\text{working days}} = n_{\text{cryomodules}} + 10_{\text{installationdays}} + 10_{\text{cooldownsdays}} + 25_{\text{testandconditioning}}, \tag{2.14}$$

where the first 10 days refer to the end of the installation, the second 10 days to the cool-down, and the last 25 days to system validation and RF conditioning (5 weeks). These numbers assume that pre-installation work and pre-cabling will be done in advance, e.g. during the previous shutdowns. A minimum of 12 weeks is recommended for the first three shutdowns, even if no, or only few, cryomodules are installed. The number of cryomodules to be installed in each regular system reconfiguration shutdown is listed in Table 2.12, along with the resulting minimum lengths of the various shutdowns. From this table, the average length of the shutdown would be about 11 weeks, to be compared with an allocated number of 17 weeks.

The regular extended maintenance shutdowns offer an effective time window of about 3 or even 4 months per year for scheduled work in the tunnel. However, longer periods are needed between H and $t\bar{t}$ operation to allow for, in particular, the transverse rearrangement of all (~ 100) cryomodules, and for the installation of about 100 new RF cryomodules in the collider and of another ~ 100 cryomodules for the booster. The number of cryomodules to be installed or rearranged in this final transition significantly exceeds the amount of work done in a typical LEP shutdown. For this reason, a one year shutdown is proposed for this final reconfiguration, leading to the distinction between a phase 1 operation (Z, W and H), and a phase 2 operation ($t\bar{t}$).

The first year of the phase-2 operation is performed at a beam energy of 175 GeV, requiring somewhat fewer RF cavities than at 182.5 GeV.

Table 2.13. Peak luminosity per IP, total luminosity per year (two IPs), luminosity target, and run time for each FCC-ee working point.

Working point	Luminosity ($10^{34} \text{ cm}^{-2} \text{ s}^{-1}$)	Tot. lum./year (ab^{-1})/year	Goal (ab^{-1})	Run time (years)
Z first two years	100	24	150	4
Z other years	200	48		
W	25	6	10	1–2
H	7.0	1.7	5	3
RF reconfiguration				1
$t\bar{t}$ 350 GeV (first year)	0.8	0.20	0.2	1
$t\bar{t}$ 365 GeV	1.4	0.34	1.5	4

2.9.5 Luminosity parameters and operation plan

Table 2.13 presents the nominal luminosity, integrated luminosity per year, physics goals and the resulting running time for the different modes of operation, based on the assumptions laid out above. This yields the time line shown in Figure 3.21.

Phase 1 comprises two years of running-in and the full Z pole operation, W threshold scans, and H production modes. It can be accomplished within 8 years. After an additional year of shutdown and staging of the RF, operation phase 2, covering the $t\bar{t}$ studies, would last for another 5 years. The entire FCC-ee physics programme could be achieved within 14–15 years.

Conservatively, it is assumed that there will be another year at half the design luminosity after the one-year shutdown, for the first year of $t\bar{t}$ running. This first year of the phase-2 operation is performed at a beam energy of 175 GeV. It is noted that LEP-2 needed much less than one year to reach and exceed its design luminosity.

With 185 physics days per year, a physics efficiency of 75%, and the baseline peak luminosities (which are 10% lower than the values reached in simulations), the FCC-ee total run time amounts to 15 years.

The aforementioned assumptions are evoked to arrive at the third and fifth columns of Table 2.13. In the following, these assumptions are scrutinized by comparing with the operational performance of several similar machines.

2.9.6 Benchmarking against performance of past and present colliders

The operational conditions of several recent e^+e^- colliders offer some important lessons and provide useful performance benchmarks for the FCC-ee.

Achieved luminosity versus design luminosity

LEP was a collider similar to FCC-ee, but operating with only a few bunches and no top-up injection, at much lower luminosity. In the first year of LEP-1, with 45.6 GeV beam energy, the current per bunch exceeded the design. The design total current was attained in a single beam, but it was not achieved in 2 beams. The peak luminosity in the first year of operation was 50% of design. The vertical beam-beam tune shift (V) was less than 50% of design. The two main reasons why not all design values could be achieved in the first year were the limitation of the total beam current and the beam-beam tune shift [264]. Looking at the full 12 years of LEP operation [265], the design luminosity was surpassed in 1993, the fourth

year of operation. LEP-1 achieved 8.4 mA in both beams, higher than the 6 mA design current. It eventually achieved a luminosity of $3.4 \times 10^{31} \text{ cm}^{-2} \text{ s}^{-1}$, while the design had been $1.6 \times 10^{31} \text{ cm}^{-2} \text{ s}^{-1}$. However, this was accomplished with 8 bunches whereas the design was for 4 bunches. With the design of 4 bunches per beam LEP never reached the design beam-beam tune shift, mostly due to the lower energy (45.6 GeV) and the correspondingly slower transverse damping (confirmed by beam-beam simulations), while the design energy had been 55 GeV [266] (an energy at which LEP never operated since the Z mass was lower than expected during the design). With the faster transverse damping at higher energy for LEP-2, limitations from the beam-beam effect disappeared. LEP-2 exceeded its design luminosity at 95 GeV ($2.7 \times 10^{31} \text{ cm}^{-2} \text{ s}^{-1}$) within a few months of operation. It achieved a total beam current of 6.2 mA, and a luminosity of $1 \times 10^{32} \text{ cm}^{-2} \text{ s}^{-1}$, about 4 times higher than the design [266]. It is interesting that LEP-1 and LEP-2 changed the optics almost every year. At highest energy there was little margin in the LEP RF system. A simultaneous trip of more than two klystrons would lose the beam. The cavity gradients were also pushed to their limits. During 1998 LEP operation the most frequent cause of RF trips was “cavity maximum field” interlocks [267]. Via a number of measures the reliability of the LEP RF system was continually improved so that the impact of RF trips on collider operation became almost unnoticeable [267]. The machine availability of LEP exceeded 85%; in several years it was higher than 90% [263,268–270].

PEP-II was an asymmetric B factory, colliding a 3.1 GeV positron beam with a 9 GeV electron beam. Beam currents reached 3212 mA for the positrons and 2069 mA for the electrons. The PEP-II design luminosity was $3 \times 10^{33} \text{ cm}^{-2} \text{ s}^{-1}$, but PEP-II ultimately achieved $1.2 \times 10^{34} \text{ cm}^{-2} \text{ s}^{-1}$. In 2004 PEP-II switched to top-up injection, which significantly increased its integrated daily luminosity. The design integrated luminosity had been 130/pb/day. A much higher value of up to 911/pb per day was actually delivered. The top-up mode did not seem to affect the availability [271]. PEP-II surpassed its design luminosity after 1.5 years of operation, and ultimately reached 4 times the design value [272].

KEKB equally was an asymmetric B factory. It collided 3.5 GeV positrons with 8.0 GeV electrons. Beam currents of 1637 mA (positrons) and 1188 mA (electrons) were reached. The design luminosity was $1.0 \times 10^{34} \text{ cm}^{-2} \text{ s}^{-1}$. A peak luminosity of $2.11 \times 10^{34} \text{ cm}^{-2} \text{ s}^{-1}$ was achieved. KEBB delivered up to 1.479/fb/day. It also operated with continuous top-up injection from the year 2004 onwards. KEBB reached its design luminosity (which was 3 times higher than the design value of PEP-II) 3.5 years after the start of operation and ultimately exceeded the design luminosity by more than a factor of two [273–275].

BEPCII is a double-ring collider, which runs for high-energy physics (HEP) about 6 months per year, and, in a different configuration, as a light source (BSF), for twice 1.5 months each, before and after the HEP run, respectively. The beam energy can be varied from 1.0 to 2.3 GeV. In 2016 BEPCII achieved its design luminosity of $1.0 \times 10^{33} \text{ cm}^{-2} \text{ s}^{-1}$ at 1.89 GeV beam energy, with a current of 850 mA per beam. For the BEPC/BSF synchrotron-radiation operation, top up was successfully implemented in November 2015. By this, the availability, which on average was already well above 90%, increased even further. In 2019 top-up injection will also be implemented for the collider mode of operation.

DAΦNE is an e^+e^- double-ring collider, including injection system, which operates at the c.m. energy of the ϕ -meson resonance (1.02 GeV). DAΦNE often changes the particle detector and corresponding IR magnetic-field configuration. DAΦNE achieved 90% of its design peak luminosity of $5.3 \times 10^{32} \text{ cm}^{-2} \text{ s}^{-1}$ after about 8 years of operation, and after switching to the crab-waist collision scheme. Typical peak

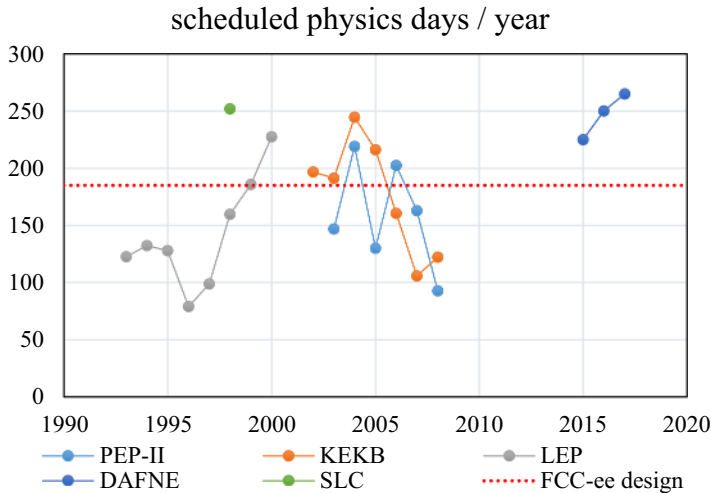


Fig. 2.44. Days per year dedicated to physics at various past and present e^+e^- colliders.

currents are 1500–1700 mA for electrons and 1200 mA for positrons, the latter limited by electron-cloud effects.

Run time

Figure 2.44 compares the annual days of physics running at the aforementioned lepton-positron colliders, for years where data were easily available. A value of 185 physics days per year appears to be a good average. It should be noted that the run lengths of the past colliders were often dictated by the available budget for operation, and not by any technical or schedule constraints. This is true, in particular, for PEP-II and KEKB. In addition, for PEP-II the 2005 run length was severely reduced by a SLAC lab-wide investigation, review, and remediation of safety concerns, and re-validation of all systems and procedures.

Every year during an extended shutdown, which was typically placed during the winter period, LEP prepared for major changes in the configuration (pretzel schemes, bunch trains, installation of SC cavities etc.). Nevertheless, LEP operated for more than 185 days in a few years.

Availability

Figure 2.45 shows the availability of the aforementioned lepton-positron colliders, for years where data were easily available.

All circular e^+e^- colliders operating over the past twenty years (LEP, KEKB, PEP-II, DAFNE, BEPCII) achieved hardware availabilities well above 80%, and some even above 90%. Since 1995 the CERN SPS including the entire PS chain delivered beams for physics with an efficiency above 80% every year.

For KEKB, a degraded availability in the year 2005 was due to technical problems at the BELLE detector, unrelated to the KEKB accelerator. In 2007, the KEKB crab cavities were being commissioned.

The LEP injector complex (PS and SPS) was operating with proton and ion beams in parallel to LEP e^+e^- operation. The SPS availability (long-term average)

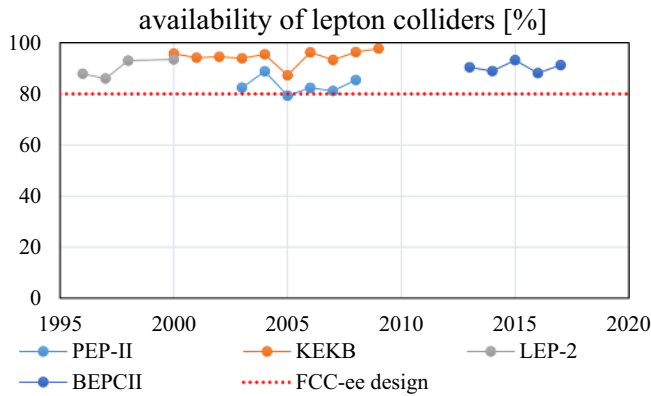


Fig. 2.45. Availability of various past and present e^+e^- colliders.

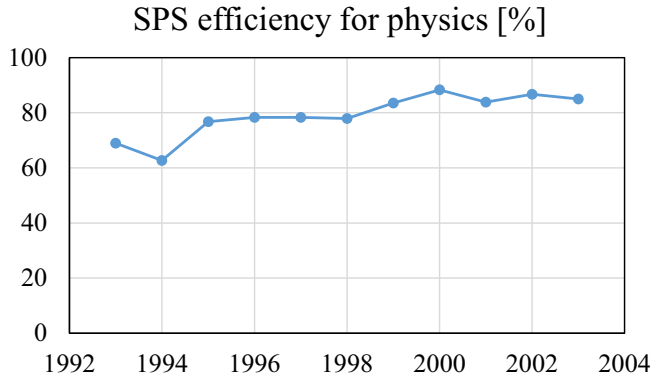


Fig. 2.46. CERN SPS availability for physics, including the pre-accelerator chain [276].

was typically 80% since the 1990s [276], as is illustrated through the “physics efficiency” in Figure 2.46; this figure includes the PS chain.

Efficiency

In the case of FCC-ee, no time is lost for acceleration and the efficiency only reflects the relative downtime due to technical problems and associated re-filling and recovery time. Therefore, the efficiency will be roughly equal to the hardware availability, taken to be at least 80%, minus ~5% reduction for beam recovery after a failure. For example, after a hardware failure in the collider rings proper, it will take less than 20 min (1.4% of a day) to refill the collider from zero to nominal beam current.

The assumed efficiency of 75% with respect to the daily peak luminosity is lower than achieved with top-up injection at KEKB and PEP-II. Figure 2.47 presents example evolutions over 24 h of beam currents and luminosity, during PEP-II operation with on-energy top-up injection in 2006 and in 2008, respectively. Beam currents and luminosity are constant, except for a few short interruptions due to hardware failures. The performance of KEKB looked quite similar, as is illustrated in Figure 2.48, with examples from 2005 and 2009.

Comparing this performance model with LEP operation, the main difference lies in the on-energy top-up injection scheme, without any luminosity decay, and in the implied absence of ramp-down and acceleration.

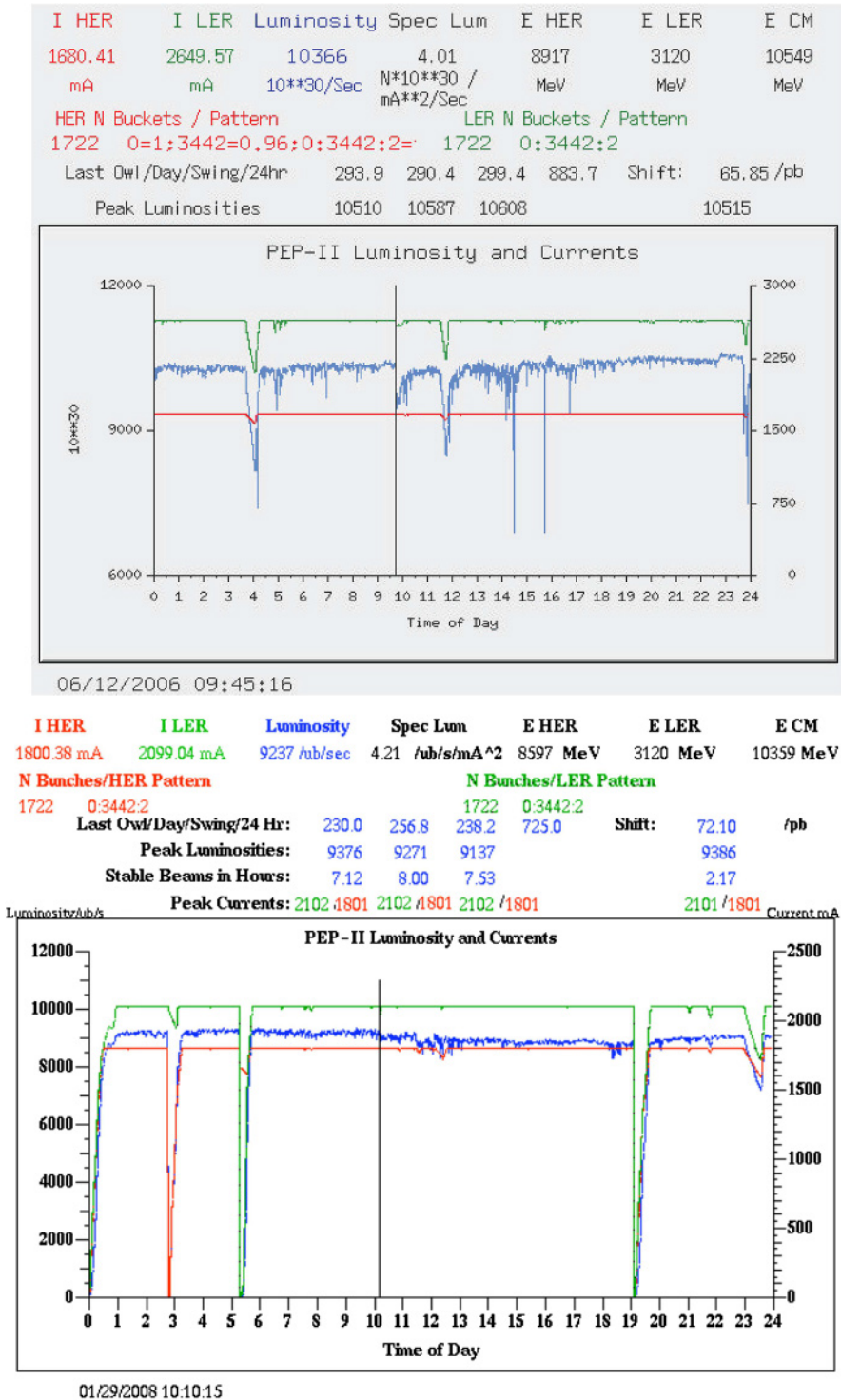


Fig. 2.47. Example evolution of PEP-II beam currents and luminosity in 2006 [277] (top) and 2008 [272] (bottom). Stored beam current of the high energy ring (red curve), the low energy ring (green curve), and luminosity (blue curve) of PEP-II over 24 h.

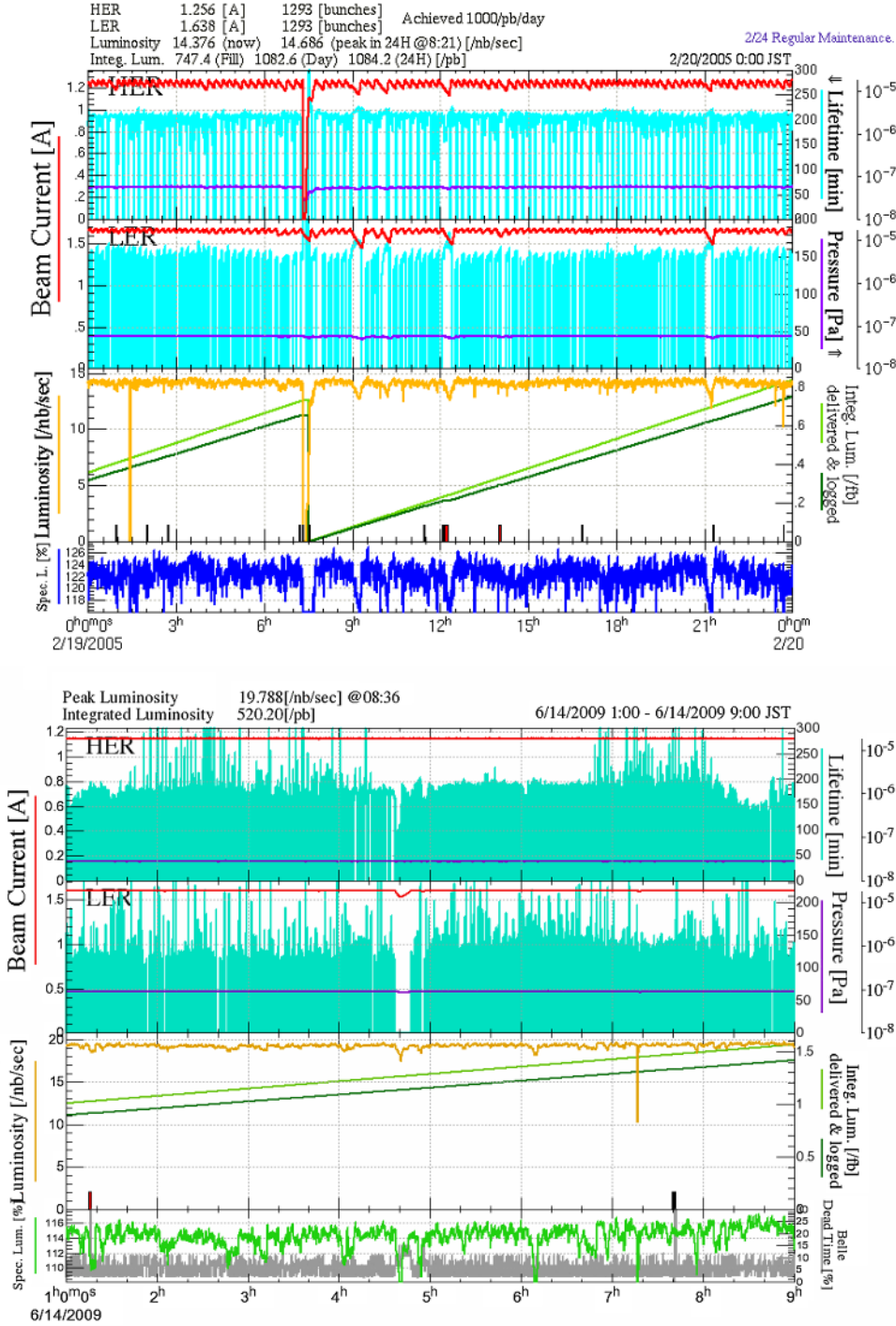


Fig. 2.48. Example evolution of KEB beam currents and luminosity in 2005 [278] (top) and in 2009 [279] (bottom). Stored beam current of the high energy ring (red line in the top figure), the low energy ring (red line in the middle figure), and luminosity (yellow line in the bottom figure) of KEB over 24 h.

In summary, the assumed annual physics run time of 185 days, a hardware availability of at least 80%, a corresponding physics efficiency of 75%, and the projected annual luminosities of FCC-ee are supported by the experience from several circular lepton colliders operated over the past 30 years. The FCC-ee design parameters leave sufficient margins to eventually exceed the design values of both peak and integrated luminosity.

2.10 Running at other energies

The FCC-ee can produce further important physics results by running at additional centre-of-mass energies. Worth mentioning are the possibility of direct H production at 125 GeV using a monochromatisation scheme and the implications of pushing the energy well beyond the $t\bar{t}$ threshold.

2.10.1 s -channel H Production

Direct s -channel H production in e^+e^- collisions, with a collision energy around 125 GeV, allows the measurement of the Higgs Yukawa coupling, provided that the centre-of-mass energy spread, σ_{ecm} , can be reduced to about 6–10 MeV to be comparable to the width of the standard model Higgs boson. The natural collision-energy spread at 125 GeV due to synchrotron radiation is about 46 MeV. Its reduction to the desired level can be accomplished by means of monochromatisation [280], which is most efficiently achieved by introducing non-zero horizontal dispersion of opposite sign at the IP for two beams in collisions without a crossing angle. This requires either a change of beam-line geometry in the interaction region or the use of crab cavities to compensate for the existing angle. However, monochromatisation is possible even in the presence of a crossing angle and without crabbing.

The decrease in σ_{ecm} is described by the monochromatisation factor A :

$$A^2 = 1 + \frac{\lambda_m^2}{1 + \phi^2(1 + \lambda_m^2)}, \quad (2.15)$$

where $\lambda_m = D_x^* \sigma_\delta / \sigma_{x\beta}$ is the ratio between synchrotron and betatron horizontal beam sizes at the IP, and ϕ is the Piwinski angle. The dependence of the Higgs event rate on luminosity and σ_{ecm} can be expressed by the function f_H :

$$\dot{N}_H \propto f_H = \frac{L}{\sqrt{\Gamma_H^2 + \sigma_{\text{ecm}}^2}}, \quad (2.16)$$

where $\sigma_{\text{ecm}} = \sqrt{2} E_0 \sigma_\delta / A$, $\sigma_\delta = 5.2 \times 10^{-4}$, $E_0 = 62.5$ GeV, $\Gamma_H \approx 4.2$ MeV.

The main parameters for the monochromatisation scheme can be obtained from the following considerations. The experiment needs an energy calibration using resonant depolarisation, which imposes a requirement on the synchrotron tune: $Q_s \geq 0.05$. To get this value, a $60^\circ/60^\circ$ lattice is required with an RF voltage $V_{\text{RF}} > 0.5$ GV. The lattice determines the natural emittance $\varepsilon_x \approx 510$ pm and the RF voltage constrains $\sigma_z \leq 2.4$ mm. The optimum $\varepsilon_y \approx 1.1$ pm can be derived from the condition $\varepsilon_y \geq 0.002 \times \varepsilon_x + 0.05$ pm, where the last term is the contribution from the detector solenoids. β_y^* should be equal or slightly less than σ_z to avoid having a strong hour-glass effect, so 2 mm was chosen. Another possibility is to increase V_{RF} , which makes the bunches shorter so that β_y^* can be reduced. On the other hand, beamstrahlung is amplified for short bunches and its negative consequences exceed the advantage of decreasing β_y^* , so this is not a good choice.

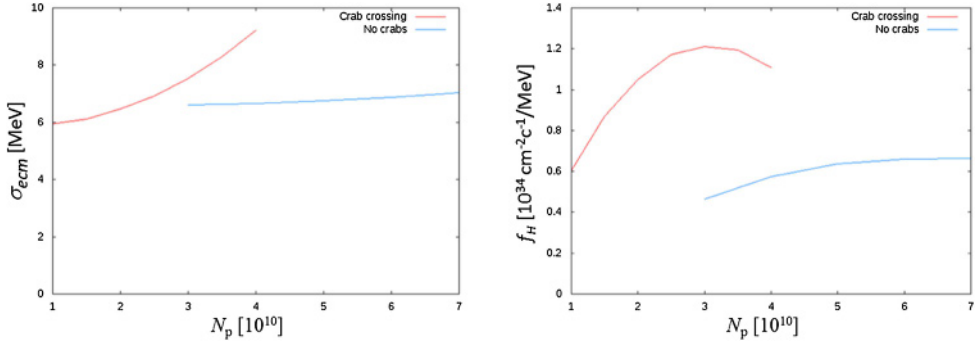


Fig. 2.49. σ_{ecm} (left) and f_H (right) as functions of the bunch population. The colors correspond to head-on collision with $D_x^* = 15$ cm (red), and collision without crabbing and $D_x^* = 50$ cm (blue).

The target value of σ_{ecm} only determines the D_x^{*2}/β_x^* ratio, but there are two reasons why it would be better to reduce them both: firstly, obtaining a large D_x^* will be difficult with the current design of the interaction region. Secondly, smaller σ_x allows the same luminosity to be achieved with less populated bunches: this is important because the bunches are rather short. Therefore, β_x^* should be about 20 cm, which is a reasonable minimum at this energy. Then the necessary D_x^* can be found from equation (2.15), so for head-on collisions (i.e. crab crossing), a value of about 15 cm is found and for a collision without any crabbing 50 cm is obtained. It is worth noting that the corresponding lattices have not yet been developed and these numbers are used simply to estimate the possible gain from monochromatisation.

The next step is to optimise the bunch population. Here it is necessary to take into account beamstrahlung, which has a very different impact in the crab waist and monochromatisation schemes. In the first case, it can lead to a significant increase in the energy spread, but does not affect the horizontal emittance. By contrast, in the second case ε_x increases due to dispersion at the IP, which has two consequences: a decrease of Λ , which affects σ_{ecm} , and an increase in ε_y (due to the betatron coupling), which affects the luminosity. Optimisation should aim at increasing f_H whilst σ_{ecm} is kept within the range of 6–10 MeV. The corresponding dependencies are shown in Figure 2.49. It can be seen that, after N_p reaches a certain threshold (which is the optimum), f_H decreases due to beamstrahlung.

In the crab waist collision without monochromatisation one can obtain $f_H \approx 0.72$ with $N_p = 3 \times 10^{10}$ and $\sigma_{\text{ecm}} = 54$ MeV. As can be seen from Figure 2.49, the Higgs event rate in the monochromatisation scheme without crab crossing will be even smaller and a higher bunch population, which can cause problems, is required to achieve maximum performance. The only advantage of this scheme is a decrease in σ_{ecm} to the desired level. In collisions with crab crossings, the production rate can be almost doubled with a moderate $N_p = 3 \times 10^{10}$, but this scheme is more complicated because it requires crab cavities; nevertheless it is considered as the main option. The corresponding luminosity per IP is about $1.3 \times 10^{35} \text{ cm}^{-2} \text{ s}^{-1}$ [281]. This translates into an integrated luminosity of almost 2 ab^{-1} per IP per year. For a c.m. energy spread commensurate with the natural width of the Higgs boson, the cross section of $e^+e^- \rightarrow H$ is about 290 ab [282]. Assuming this value, the monochromatised FCC-ee would produce approximately 500 s -channel H bosons per IP per year.

2.10.2 Higher collision energy

For $t\bar{t}$ running at a c.m. energy of 365 GeV, the RF system (common for both beams) occupies a total length of about 2 km and provides a voltage of ~ 10 GV. In principle, the FCC-ee collision energy could be pushed beyond 365 GeV by installing additional RF systems as was done in LEP-2 or by raising the RF gradient of the existing cavities, provided the other accelerator subsystems, such as the magnets and vacuum chambers, can also handle the higher energy. For example, running at a centre-of-mass energy of 475 GeV would imply a total RF voltage around 30 GV and, at constant RF power, the beam current would drop to about 2 mA at 475 GeV. Also taking into account the increase of the transverse emittance with beam energy, the luminosity per IP could be about $5 \times 10^{33} \text{ cm}^{-2} \text{ s}^{-1}$ at this collision energy.

3 Collider technical systems

3.1 Introduction

This chapter presents details of those technical systems for which substantial research and development is required. It is known that it will be possible to scale up many systems from LHC, LEP, SuperKEKB, modern light sources and linear collider studies for use in FCC-ee; these systems are not presented here. Instead, various major systems such as magnets, RF, beam transfer and vacuum are described as well as many smaller essential devices. The chapter also includes a description of the radiation environment in which they will have to perform. Details for all technical systems will be presented at a later stage in the design process, but systems which require particular attention at this conceptual design stage have been identified and are presented in the following.

3.2 Main magnet system

3.2.1 Introduction

The requirements for the FCC-ee main magnets are quite similar to those of LEP: the arcs contain many long, low-field bending magnets interleaved with short straight sections, containing quadrupoles and auxiliary magnets. As such, the resistive magnet system resembles those used at LEP and at other large lepton machines (e.g. HERA electron ring and SLC); many of its features can be retained, for example, modular cores with aluminium busbars threaded through them. However, as a major innovation, for FCC-ee it is possible to exploit a dual-aperture approach. Coupling the two collider rings through twin-aperture arc magnets does not only halve the total number of main magnets, but it also saves 50% in electric power compared with two separate sets of magnets.

Short prototypes have been built of both the main dipoles and the quadrupoles, in order to confirm the magnetic coupling. Optimisation and an analysis of various industrial manufacturing procedures will be done at a later stage.

For operation at high energy, especially at or above the $t\bar{t}$ threshold, the SR energy sawtooth is important. To compensate for its effect, the arc dipole and quadrupole fields need to be tapered, i.e. adjusted for the local beam energy. This tapering could be achieved, for example, with individual-aperture trim coils added to the main magnets. Such trim coils for the main bending magnets could also serve as horizontal orbit correctors.

Table 3.1. Parameters of the main bending magnets.

Strength, 45.6 GeV–182.5 GeV	mT	14.1–56.6
Magnetic length	m	21.94/23.94
Number of units per ring		2900
Aperture (horizontal × vertical)	mm	130 × 84
Good field region (GFR) in horizontal plane	mm	±10
Field quality in GFR (not counting quadrupole term)	10 ^{−4}	≈1
Central field	mT	57
Expected b_2 at 10 mm	10 ^{−4}	≈3
Expected higher order harmonics at 10 mm	10 ^{−4}	≲1
Maximum operating current	kA	1.9
Maximum current density	A/mm ²	0.79
Number of busbars per side		2
Resistance per unit length (twin magnet)	μΩ/m	22.7
Maximum power per unit length (twin magnet)	W/m	164
Maximum total power, 81.0 km (interconnections included)	MW	13.3
Inter-beam distance	mm	300
Iron mass per unit length	kg/m	219
Aluminium mass per unit length	kg/m	19.9

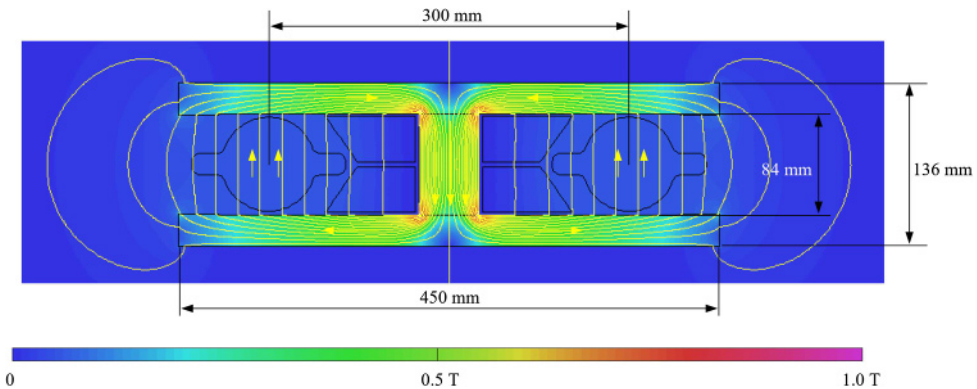


Fig. 3.1. Cross-section of the main bending magnet; the flux density corresponds to 57 mT in the gap; the outline of vacuum chambers with side winglets is also shown.

Other magnets, such as vertical orbit correctors, sextupoles, polarisation wigglers or those for the top up injector, are beyond the scope of this section. The design of a combined quadrupole-sextupole has started, along the lines of the more common combined dipole-quadrupole magnet. For the moment, this is left as an additional conceptual development, pending further discussions with beam physicists. More details about the main magnet system can be found in [283,284].

3.2.2 Main dipole magnets

Table 3.1 summarises the key parameters of the 2900 arc bending-magnet units. The main dimensions are shown in Figure 3.1. The design of the magnetic yoke is based on an I configuration, combining two back-to-back C layouts. In this way, the return conductor for one aperture provides the excitation current for the other.

As in previous large lepton machines, split aluminium busbars are used instead of coils. These busbars are generously sized (with an area of 2338 mm²) to keep the

current density low with a maximum value of less than 1 A/mm^2 , even at the highest beam energy. These busbars can be threaded through several cores and welded to each other, as in LEP. Direct cooling with water is not strictly necessary, but it might be useful to avoid adding Joule heating (up to about 200 W/m) of the tunnel air.

As magnetic lengths of up to about 24 m are needed, a modular structure for the bending magnets with $6\text{--}8 \text{ m}$ long cores is proposed. The final length will be optimised on the basis of manufacturing and handling considerations. The elastic deflection due to their weight is not critical, as it can be compensated, if necessary, by adding a pre-camber in the opposite direction during manufacture, as for the SPS dipoles [285].

Besides the I layout, the geometry of the yoke has an elongated aspect ratio of the poles: this keeps the cross-section compact and at the same time it takes the low field in the air gap and amplifies it in the iron. Therefore, a dilution in the longitudinal direction (e.g. with concrete, as in LEP [286]) is not necessary, and it would bring more complications than savings in materials.

Another key feature which makes a compact yoke possible is the small size of the good field region: in this case, the size of the vacuum chamber is not dictated by the size of the beam (which is consistent with the good field region) but by other considerations, such as impedance and absorption of synchrotron radiation. Furthermore, the quadrupole term b_2 can be disregarded in the expansion for field quality, as a systematic linear component can be compensated with the arc quadrupoles. A strong b_2 term at low dipole fields (few tens of mT) was considered an issue for LEP. This comes from two main effects: a change in relative permeability of the iron across the width of the pole at different excitation currents and the remanent field coming from the coercivity. As the FCC-ee will be operated at constant current with a top-up injector, the second effect can be disregarded: even if the machine were to operate at low energy after a high energy run, there will be time for full degaussing or preconditioning. The first effect is being evaluated with prototypes, using a noble material (ARMCO pure iron) and a less noble one (S275JR construction steel). The option preferred for the machine appears to be a low-carbon steel: it is cost effective and it still features stable permeability over time. Tight specifications on the magnetic properties, in particular the coercivity, could possibly be relaxed, as they can be compensated by shuffling the cores during installation, instead of the more classical shuffling of laminations in the yokes. This is possible due to the large number of cores in the machine. Instead of being based on punched laminations, the prototypes are based on machined iron plates, held together by precise cylinders. In the prototypes, the central cylinders give satisfactory results for mechanical assembly tolerances; magnetically they can concentrate the flux further up to 1.5 T , at the highest excitation current.

The overall dimensions of the cross section are compatible with vacuum chambers featuring side winglets (see Sect. 3.3.2), as shown in Figure 3.1. For one of the two beams, the synchrotron radiation points towards the central part of the dipole, the aluminium busbar. This is not a particular concern because this component can be made radiation hard by using a suitable material for ground insulation (e.g. an inorganic coating). Furthermore, aluminium has the advantage of becoming less activated than heavier metals.

At the highest beam energy, the total electric power needed for the bending magnets, including the connections, is $\sim 13.3 \text{ MW}$. As in LEP, the busbars of the dipoles come near to each other (to mutually compensate their magnetic effect) and are then bent away from the beams to bypass the straight sections.

Two prototypes with a magnetic length of 1 m each have been manufactured at CERN so far (see Fig. 3.2). For convenience these models had copper busbars, but

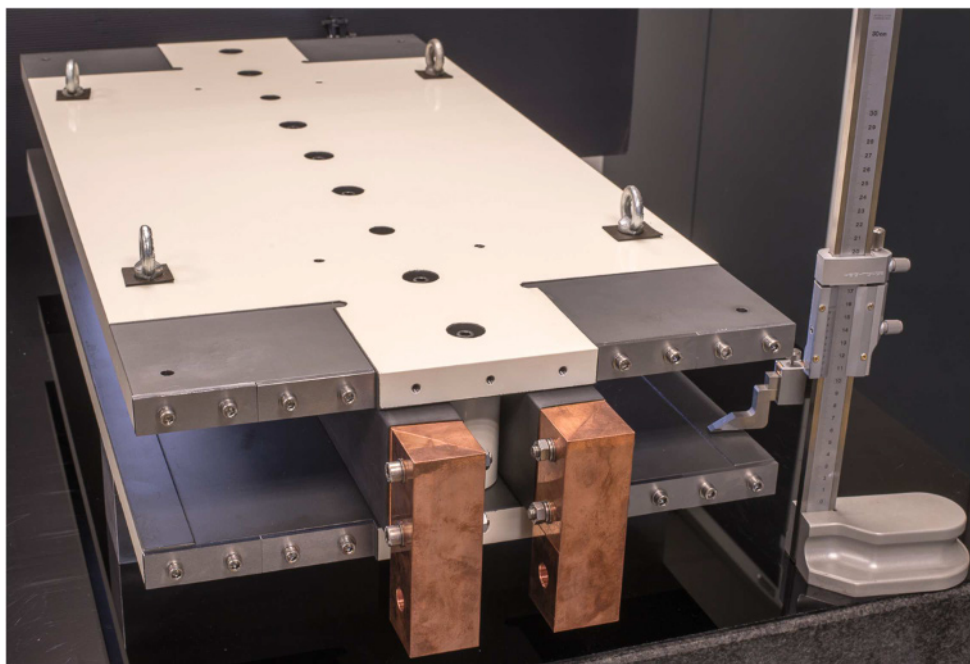


Fig. 3.2. One of the ca. 1 m long model dipole magnets manufactured at CERN.

this has no effect on the magnetic response. At the time of writing, full magnetic measurements are being made: these will be reported in [287,288]. Preliminary results from the first prototype confirm the expected magnetic coupling and show an interesting hysteresis effect on field quality (which is not a concern for this application) during ramp down.

Several lines of development for the bending magnets can be pursued after this initial conceptual phase. The first, after the magnetic measurements of the two short prototypes, is a possible further refinement of the cross-section, with the addition of $\pm 1\%$ trimming in the two apertures, to cope with the synchrotron radiation sawtooth. Then, options for materials and manufacturing techniques will be analysed from an industrial viewpoint. Topics will include cost-effective low-carbon steel, inorganic coating of aluminium busbars, machining of poles, automated assembly and dimension control of yokes and welding of busbars, etc. In parallel, the details of the interconnections between neighbouring dipole cores and around the short straight sections will need to be studied in more detail, together with the supports and the related alignment strategy, and, finally, the integration with all other components (like vacuum chambers, radiation absorbers and vacuum pumps).

3.2.3 Main quadrupole magnets

Table 3.2 lists the main parameters for the 2900 arc quadrupoles. The quadrupole dimensions are shown in the cross-section of Figure 3.3. These quadrupoles cannot be considered to be low field magnets because although the beam, which is quite small with respect to the physical aperture, sees at most 100 mT (that is, 10 T/m at 10 mm), the pole tip field reaches 0.42 T. This has an impact on the Amp-turns and the power consumption. It will be even more critical for large aperture sextupoles, where the field grows quadratically from the centre. Therefore, a twin aperture

Table 3.2. Parameters of the main quadrupole magnets.

Maximum gradient	T/m	10.0
Magnetic length	m	3.1
Number of twin units per ring		2900
Aperture diameter	mm	84
Radius for good field region	mm	10
Field quality in GFR (not counting dip. term)	10^{-4}	≈ 1
Maximum operating current	A	474
Maximum current density	A/mm ²	2.1
Number of turns		2×30
Resistance per twin magnet	m Ω	33.3
Inductance per twin magnet	mH	81
Maximum power per twin magnet	kW	7.4
Maximum power, 2900 units (with 5% cable losses)	MW	22.6
Iron mass per magnet	kg	4400
Copper mass per magnet (two coils)	kg	820

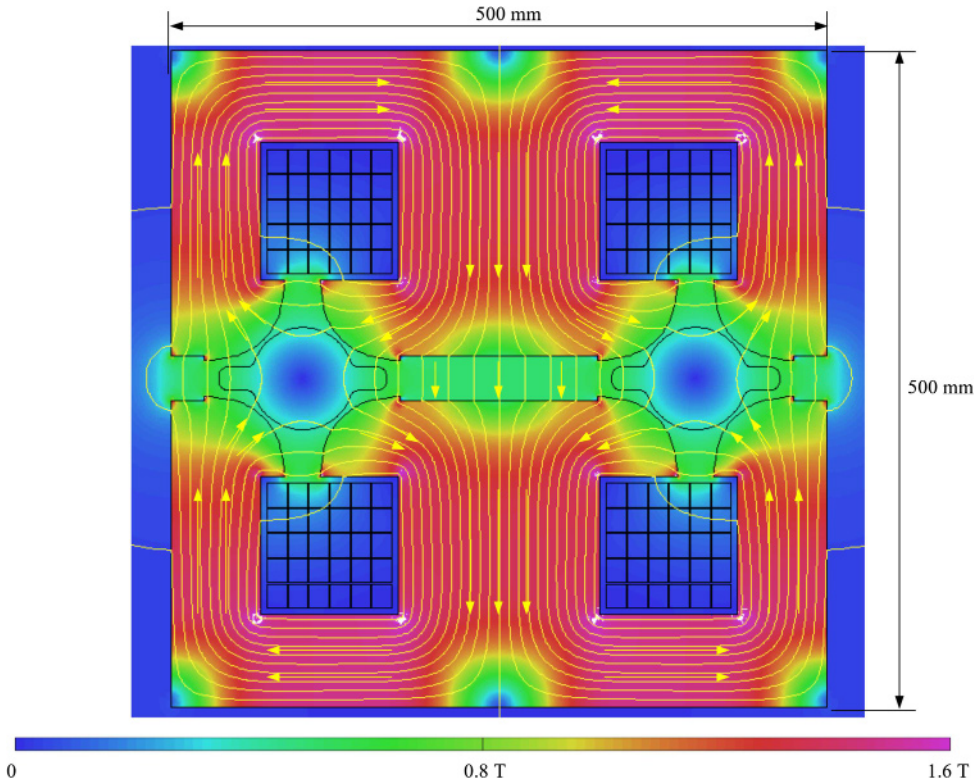


Fig. 3.3. Cross-section of the FCC-ee main quadrupole, for a 10 T/m gradient.

layout providing significant power savings is also particularly interesting for the quadrupoles, even if they are relatively short compared to the dipoles.

The magnetic coupling is achieved with a layout which resembles two figure-of-8 quadrupoles next to each other and in which the Amp-turns are concentrated in only two instead of four poles. Two simple racetrack coils excite the yoke, which is split in two halves and separated by a central non-magnetic spacer. In this way, a

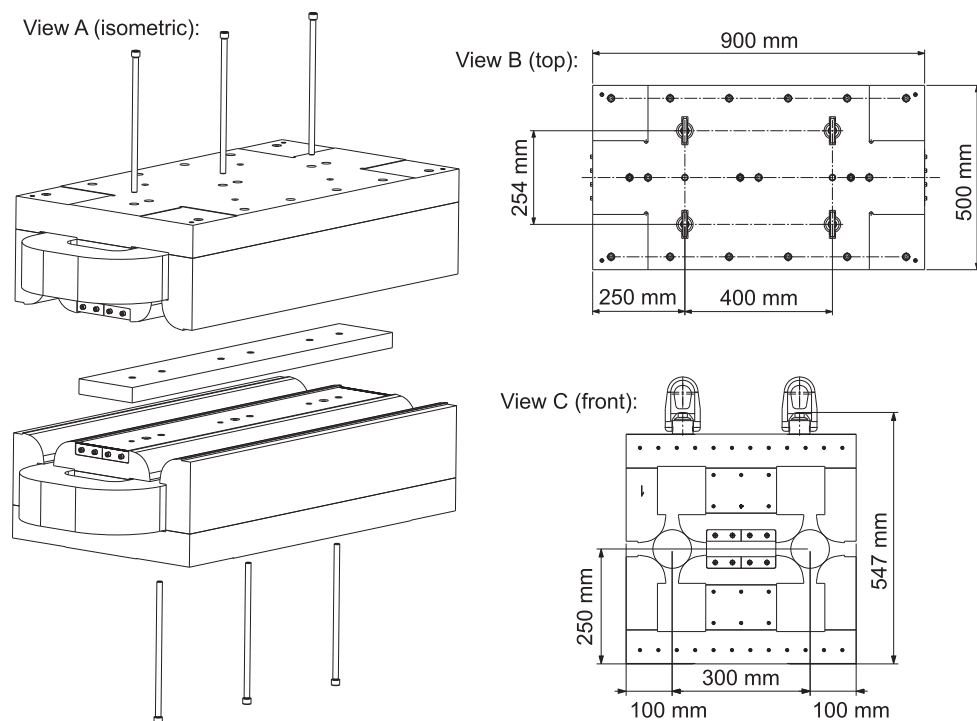


Fig. 3.4. Different views of a prototype quadrupole magnet with end pole shims to adjust the integrated field quality. The prototype has a reduced length of 900 mm. The size for the actual accelerator magnets is subject to a detailed technical design study. View A is an isometric presentation of the magnet. View B shows the magnet from the top and view C shows it from the front. The width is 500 mm and the height is 500 mm.

50% power saving with respect to single units is possible, with however, a polarity constraint: the two beams see a focusing and a defocusing field, respectively. This has been taken into consideration in the lattice design. Individual trimming at the % level, which could be provided either by additional windings on the poles or by small stand-alone correctors, can be implemented to account for beam energy sawtooth.

The starting point of the design was the inter-beam distance of 300 mm defined by the geometry of the twin aperture bending magnet. Copper is favoured over aluminium as conductor. It is operated at low current densities ($j2.5 \text{ A/mm}^2$) to help limit the power consumption, which is still larger than that of the dipoles. The electrical parameters of the magnets and power converters, such as current and resistance, will have to be optimised at the circuit level. Cooling with demineralised water is needed with several circuits per coil in parallel. The details will depend on choices at a more general level, such as the temperature increase in the water to allow for partial recuperation of heat.

From a magnetic viewpoint, the layout of Figure 3.3 breaks many of the canonical symmetries used in a classical quadrupole. As a result, the optimisation of the pole tip with 2D and 3D finite element models has been challenging, in particular the minimisation of the unwanted dipole and sextupole components. A symmetric configuration (at least at the pole tip) was adopted for the manufacture of the 1 m long prototype, which was built by milling and grinding solid iron blocks and using a stainless steel spacer for the central part. An exploded view of the prototype is shown in Figure 3.4, and a photograph in Figure 3.5. This manufacturing technique

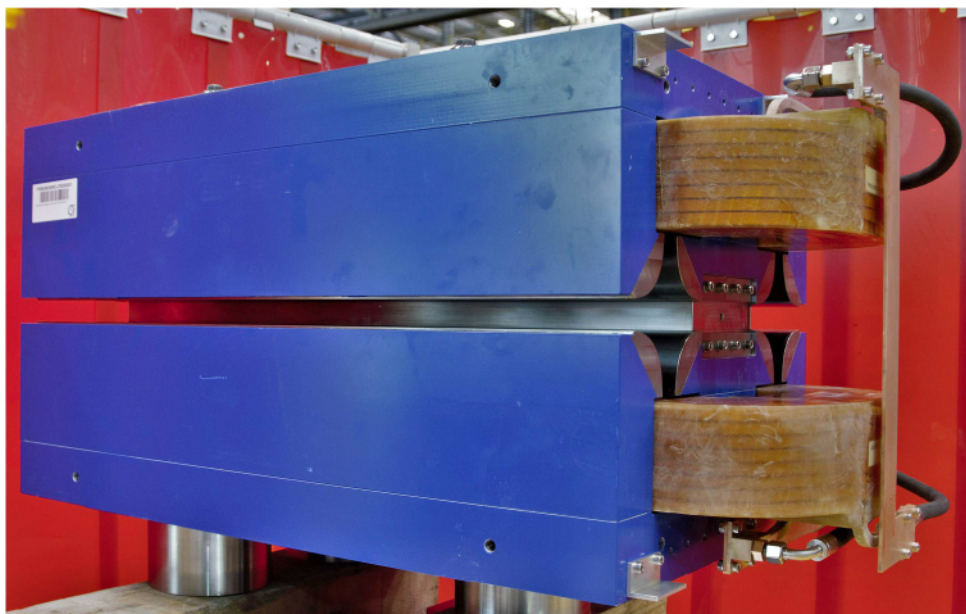


Fig. 3.5. Picture of a 1 m long quadrupole prototype magnet for the FCC-ee.

might not be the most suitable for the production of a large series, which in this case can probably be based on punched laminations, but it offers the flexibility of modifying individual details, for example on the pole tip, when iterations are needed.

The results of magnetic measurements of this first prototype will be used to refine the design, in particular at the pole tips. Individual trimming of the two apertures can be added after these refinements, possibly with embedded dual plane dipole correctors, obtained by separate windings over each pole.

3.2.4 Main sextupole magnets

Each collider ring uses 208 sextupole families for Z and W operation, and 292 sextupole families for H and $t\bar{t}$ operation. Each family consists of 4 sextupoles, with a length of 1.4 m each at Z and W, and of 8 sextupoles, 1.4 m each, at ZH and $t\bar{t}$. The maximum strength for some of the sextupoles (after dynamic aperture optimisation) is 807 Tm^{-2} at 182.5 GeV. The sextupole aperture diameter can be as low as 76 mm. The sextupole yoke is compact and compatible with an inter-beam distance of 300 mm. Table 3.3 lists the main parameters for the sextupoles. The dimensions are shown on top of the cross-section in Figure 3.6. The sextupole coil will be designed so as to limit the maximum current to 200 A or below, with probably two types of magnets, equipped with different coils depending on their actual strength. As a first estimate, the power consumption of one sextupole at 182.5 GeV beam energy (for one aperture and at maximum strength) is of the order of 15.5 kW, the average power 4.4 kW.

3.2.5 Main magnet powering

The powering of the main arc dipoles, featuring a split busbar, could be similar to the one of LEP. All magnets of a sector would be connected as a single circuit,

Table 3.3. Parameters of the main sextupole magnets.

Maximum strength, B''	T/m ²	807.0
Magnetic length	m	1.4
Number of units per ring		$208 \times 4 = 832$ (Z, W) $292 \times 8 = 2336$ (H, $t\bar{t}$)
Number of families per ring		208 (Z, W) 292 (H, $t\bar{t}$)
Aperture diameter	mm	76
Radius for good field region (GFR)	mm	10
Field quality in GFR	10^{-4}	≈ 1
Ampere turns	A	6270
Current density	A/mm ²	7.8
Maximum power per single magnet at 182.5 GeV	kW	15.5
Average power per single magnet at 182.5 GeV	kW	4.4
Total power at 182.5 GeV (4672 units)	MW	20.5

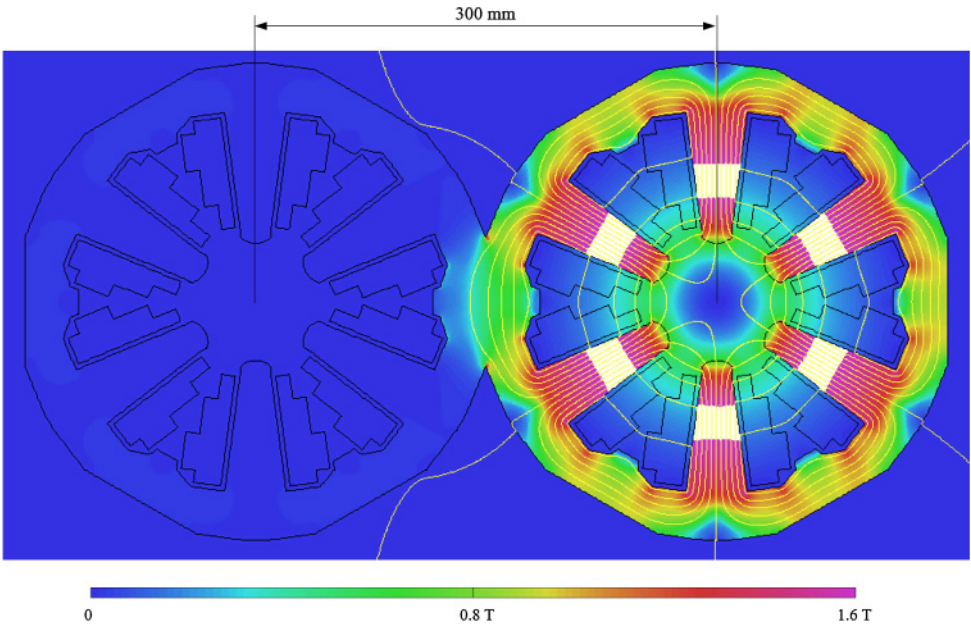


Fig. 3.6. Cross-section of the FCC-ee main sextupole magnet. The position of the sextupole for the other beam is outlined on the left.

requiring 12 one-quadrant 1.5 MW power converters, one for each of the 12 sectors. Dipole inter-magnet busbars, with a total length of up to 20 km, are needed to bypass other elements in the arcs, such as the quadrupole and sextupole magnets.

The arc-quadrupole magnets will be divided into a total of 48 circuits, namely 4 circuits on each of the 12 access points, always for the two chains of opposite polarity located towards the left and towards the right of an access point, respectively, and extending up to the centre of the adjacent arc. The longest half sector features 145 quadrupole units each for the two polarities. The 48 individual quadrupole circuits will be powered by one-quadrant 1 MW converters. These circuits can be based on air-cooled 240 mm² cable with a total length of 320 km.

A separate powering is required for each of the about 300 arc-sextupole families. Every sextupole circuit contains 4 magnets with a large variation of electric current

between circuits. The sextupoles, which are distributed all around the machine, can be powered from local alcoves, using 150 kW converters. The sextupole circuits require up to 640 km of air-cooled 120 mm² cable.

3.2.6 Interaction region and final focus quadrupoles

FCC-ee has two interaction regions, each with a detector solenoid which has a field of 2 T. The collider will run at different energies with optimised values of $\beta_{x,y}^*$ for the different operating points (see Tab. 2.1). The distance between the IP and the first quadrupole is 2.2 m and this determines the requirements for the final-focus (FF) quadrupoles.

The philosophy is to design the simplest (in terms of magnetic elements) high performance system, using state-of-the-art techniques whenever possible. The proximity of the FF magnetic elements to the interaction point (IP), where the solenoid field of the detector magnet is strong, necessitates the use of two further magnetic elements. The first is a screening solenoid, which ensures that the solenoidal field seen by the beam at the FF quadrupoles is less than 0.05 Tm. The second element is a compensation solenoid which ensures that the integrated field seen by electron and positron beams traversing the detector is zero. Both of these are essential for good performance of the accelerator (the inevitable emittance blow up caused by passing through the IP needs to be within the total emittance budget).

An iron-free design was chosen for the magnetic elements close to the IP, so the system does not suffer from non-linearities at different field strengths. Therefore the principle of superposition of the magnetic fields can always be applied, simplifying the design considerably. The iron yoke of the detector solenoid will extend to ± 4 m from the IP. The strength of the detector solenoid will be the same at all beam energies, therefore the screening and compensating solenoids will also have constant strength. The FF quadrupoles (which are split into 5 individually powered units in the vicinity of the IP) will have different strengths for each machine working point. Because the detector solenoid will always be operated at the same field, the emittance blow-up requirements are more stringent when running at the Z.

All magnetic elements will be installed within two cryostats (one per side of the IP). The beam pipe in the vicinity of the IP will be warm and liquid cooled. It will be possible to remove each cryostat and beam pipe assembly during assembly/dismantling of the detector, therefore there must be a flange at the end of the cryostat closest to the IP. NbTi has been chosen for the superconducting cable material for all of these interaction region magnets. It meets the performance requirements and the technology is well mastered at CERN. A cryostat temperature of 4.2 K would avoid operation below the helium Lambda point. It still is an open question if the advantages of cooling the FF magnets to superfluid helium temperatures (1.9 K), in particular the resulting larger quench margin, would outweigh the disadvantages, such as the higher power required to extract the same heat load.

The heat load in the vicinity of the IP and when running at the Z, which is the most challenging working point, will be around 100 W/m in normal operation. However, for full beam intensity at the Z energies with no collisions (and, therefore, no bunch lengthening due to beamstrahlung) this figure will become as high as 600 W/m.

Detector solenoid compensation scheme

As mentioned above, the compensation scheme comprises a screening solenoid and a compensating solenoid on each side of the IP. The main parameters are given in

Table 3.4. Solenoids and compensation scheme parameters, given for one side (positive z).

	Start position (m)	Length (m)	Outer diameter (mm)	Current (A – turns)
Detector solenoid	0	3.6	400	3900 A – 1000
Screening solenoid	2.0	3.6	400	3900 A – 1000
Compensation solenoid	1.23	0.77	246–398 (tapered)	10600 A – 300

Notes. The parameters for the main detector solenoid are also listed for completeness.

Table 3.5. Final focus quadrupoles parameters.

	Start position (m)	Length (m)	$B' @Z$ (T/m)	$B' @W^\pm$ (T/m)	$B' @Zh$ (T/m)	$B' @t\bar{t}$ (T/m)
QC1L1	2.2	1.2	−78.60	−96.16	−99.98	−100.00
QC1L2	3.48	1	+7.01	−40.96	−99.94	−100.00
QC1L3	4.56	1	+28.40	+22.61	+26.72	−100.00
QC2L1	5.86	1.25	+2.29	+40.09	+23.75	+58.81
QC2L2	7.19	1.25	+9.05	+3.87	+39.82	+68.18
QC1R1	−2.2	1.2	−79.66	−100.00	−99.68	−99.60
QC1R2	−3.48	1	+5.16	−37.24	−92.78	−99.85
QC1R3	−4.56	1	+36.55	+24.02	+5.87	−99.73
QC2R1	−5.86	1.25	+7.61	+45.51	+36.45	+63.03
QC2R2	−7.19	1.25	+4.09	+3.95	+44.43	+77.91

Table 3.4. For the compensation solenoid, which requires a high field, a standard LHC 13 kA Rutherford cable could be used. The screening solenoid can use eight individual LHC cable strands of 0.85 mm diameter bundled together.

3.2.7 Final-focus quadrupoles

The Canted Cosine Theta (CCT) technology without an iron yoke has been chosen for the FF quadrupoles. This technology provides excellent field quality and has many possibilities for customisation of the field which is necessary for cross talk compensation (the tips of the FF quadrupoles closest to the IP are only 66 mm from the beams). At the same time, numerically controlled machines (CNC or 3D printing machines) for the manufacture of the magnet formers, present significant cost savings compared to conventional methods.

The main parameters of the five individual elements of the FF quadrupoles, on one side of the IP (positive z) and for the electron beam only, are shown in Table 3.5. The inner diameter of the beam pipe in the vicinity of QC1 is 30 mm; around QC2 it is 40 mm. The FF quadrupoles have an inner diameter of 40 mm and an outer diameter of 68 mm (truncated to 66 mm for the first FF element, QC1L1). The beam pipe around the IP is warm; its temperature is regulated by water flow. There is enough space for the insulation vacuum and one layer of radiation screen between the beam pipe and the quadrupole (which is operated at 4.2 K). The maximum field gradient is 100 T/m. The design can easily be modified to accommodate considerably higher gradients (150 T/m) so as to provide more flexibility, if needed. Each element is positioned such that its magnetic centre sits along the ideal beam trajectory. In FCC-ee the crossing angle between electrons and positrons at the IP is 30 mrad, which means that the minimum distance between the magnetic centres of the e^+ and e^- QC1L1 magnets is 66 mm (see Fig. 3.7).

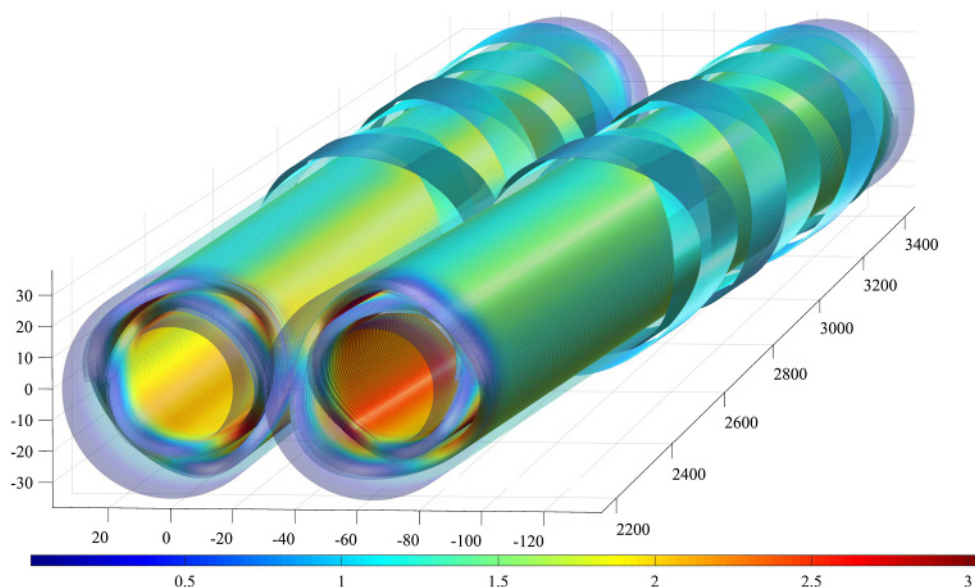


Fig. 3.7. The position of the two quadrupole magnets near the IP (QC1L1P on the left and QC1L1E on the right). The horizontal and vertical orbit correctors are shown along with the skew quadrupole corrector, fitted as extra rings on top of the QC1L1 magnets. The colours correspond to the magnitude of the magnetic field at the surface. A horizontal angle of 30 mrad separates the two beam pipes. The tips of the quadrupoles are 2.2 m from the IP. The axes are in mm and follow the positron beamline; the IP is at the origin (0,0,0).

Field quality

The field quality requirements become less stringent as one moves further away from the IP. It is planned to use the same technology for all elements. The following paragraphs concentrate on the most critical elements, QC1L1. These magnets are 1.2 m long. At the tip they are 66 mm from their counterpart for the other beam; at the far end they are 102 mm apart. The magnet has an inner aperture of 40 mm diameter and an outer diameter of 64 mm. The beam pipes for both electrons and positrons have an inner diameter of 30 mm in the vicinity of QC1L1. A traditional CCT design has excellent field quality, but there are small edge effects, which cancel out if one integrates over the whole length of the magnet. However, in a region of rapidly varying beta function and dispersion, this cancellation alone does not ensure excellent performance. Therefore, the edge effects have been corrected locally using a novel technique based on the addition of multipole components directly in the CCT-quadrupole coil geometry [289].

Furthermore, the significant amount of cross talk between the two quadrupoles which are sitting in close proximity has been corrected. The result is a quadrupole magnet with integrated multipole components of less than 10^{-5} , as can be seen in Table 3.6. It should be noted that these multipole values do not take into account the effect of imperfections like misalignments and mechanical tolerances. It is, therefore, assumed that cross talk and edge effects are perfectly compensated. The final field quality will be dominated by mechanical tolerances and misalignments.

A misalignment analysis has also been performed. Mechanical alignment of the two quadrupoles (QC1L1E and QC1L1P) should be better than $30 \mu\text{m}$ (a strict but achievable requirement for objects a few centimetres apart). The multipoles affected by a misalignment in x are B_3 (0.8 units for a misalignment in x of $100 \mu\text{m}$). For

Table 3.6. Integrated field errors in units of 10^{-4} after correction for the effect of cross talk from the adjacent quadrupole in the absence of imperfections.

n	B_n	A_n	n	B_n	A_n
2	10 000	0.01	7	0.03	<0.01
3	0.01	0.03	8	0.02	<0.01
4	-0.03	-0.01	9	<0.01	<0.01
5	-0.01	-0.01	10	<0.01	<0.01
6	-0.03	0.02			

Notes. Calculation performed at 10 mm (2/3 aperture). All multipoles can be corrected to better than 0.05.

misalignment in y , the multipoles affected are A_2 and A_3 (2.2 units and 0.7 units, respectively, for a vertical misalignment of $100\text{ }\mu\text{m}$). A beam misalignment of up to several millimetres will only have a dipole effect, with no higher order multipoles (due to the homogeneity of the field resulting from the CCT design). To a large extent, winding alignment and machining errors average out, with the final accuracy depending on the systematic machining accuracy. These errors need to be measured after a prototype magnet has been constructed. No problems are expected to arise from the machining accuracy.

Corrector magnets

The FF quadrupole design has no multipole components apart from B_2 , the main quadrupole field, so any correctors are for effects other than the imperfections of the FF quadrupoles themselves. There is room for several corrector elements (four can be easily fitted per quadrupole). An important consideration for the FF quadrupole design is that steering and skew quadrupole correctors should be installed as close to QC1L1 as possible. They will be fitted as extra rings over QC1L1, as shown in Figure 3.8. Correctors of adequate strength can be installed without affecting the packing factor. Due to the close proximity of the other beam, each corrector has to have its own compensator to ensure negligible cross talk with the other beam.

3.2.8 Final-focus sextupoles

Each final focus section accommodates two strong sextupoles, which are needed to correct the vertical chromaticity of the final quadrupole doublet, to compensate residual geometric aberrations, and to generate the crab waist. The key final focus sextupole parameters are summarized in Table 3.7. In view of the strength required at their present length, these sextupoles need to be superconducting.

3.2.9 Polarisation wigglers

Polarisation wigglers are needed in FCC-ee due to the very long natural polarisation times at the Z (more than 200 h), however, they are not needed for running at the W pair threshold (or at higher energies).

The mode of operation is as follows: polarisation wigglers will only be switched on at the beginning of every fill where only a small number of bunches would be circulating (the so-called “polarisation bunches”, which form around 2% of the total

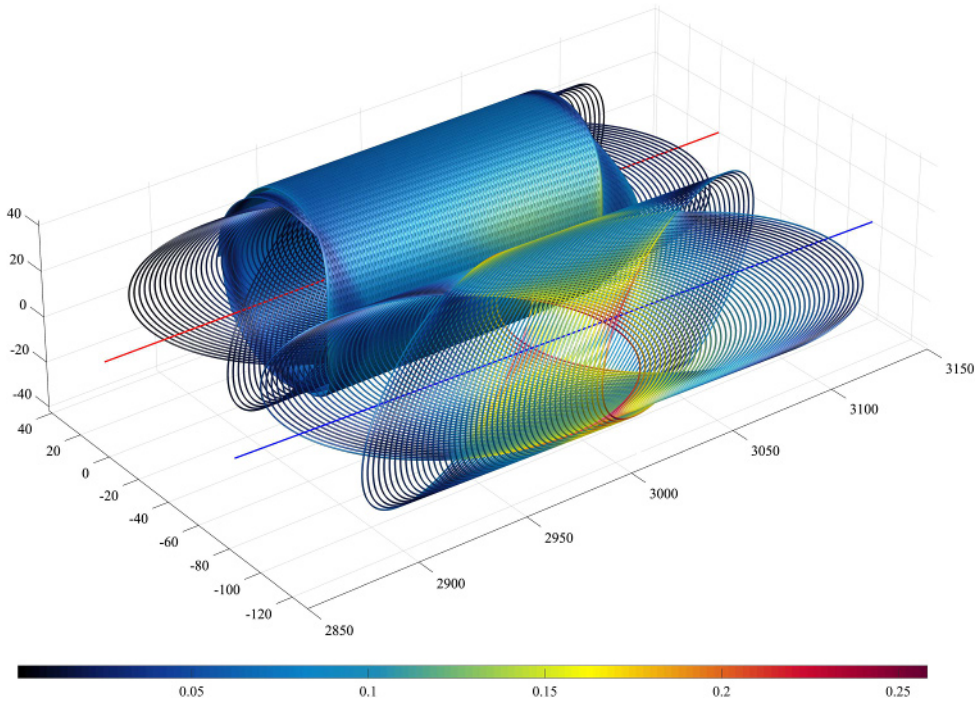


Fig. 3.8. Detail of a FCC-ee horizontal dipole corrector. The individually powered correctors for the electron and positron beams are shown, together with the positron-corrector compensation coil (fitted outside the electron corrector), which is powered in series with the positron corrector.

Table 3.7. Final-focus sextupole parameters.

Number of units per ring	—	8
Radius	mm	38
Strength B''	T/m ²	8000
Pole-tip field at 182.5 GeV	T	5.8
Length	m	0.3

number of bunches). These bunches (which will not be in collisions) will eventually be used for depolarisation measurements. With the current design adequate polarisation levels (10% transverse polarisation) will be achieved after 100 min of wiggler operation.

The number of wigglers is a compromise between the synchrotron radiation power produced by the system and the critical energy of the photons. FCC-ee will use 8 wigglers per beam, each comprising three units with three high field regions and six low field regions. The length of one wiggler unit is chosen so that the total orbit excursion in the horizontal plane is manageable (less than 3 mm for a unit length of around 3 m, see Fig. 3.9).

When operated at their nominal settings at 45 GeV they will produce a significant additional (about 40%) synchrotron radiation power per bunch. However, the total beam current in the machine would be low when the wigglers are on. The wigglers need to be located in a dispersion-free straight section; the straight sections around PH and PF are suitable. The LEP wiggler design was taken as a reference [290] and modified to meet the FCC-ee requirements. The main parameters of the polarisation

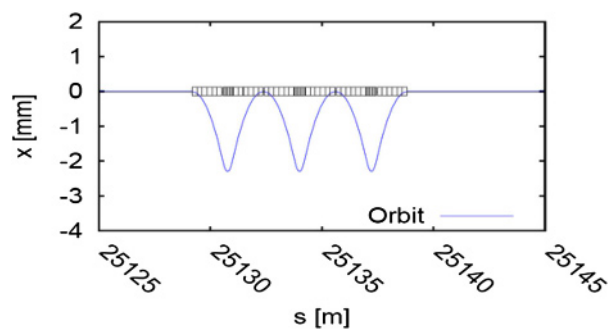


Fig. 3.9. The orbit excursion around the vicinity of one FCC-ee wiggler, comprising three magnets with asymmetric cores.

Table 3.8. Specification for the FCC-ee wiggler scheme (LEP parameters shown for comparison).

	FCC-ee	LEP
Number of units per beam	8×3	8
Full gap height (mm)	90	100
Central field B^+ (T)	0.7	1.0
Central pole length (mm)	430	760
Asymmetry ratio B^+/B^-	6	2.5
Critical energy of SR photons (keV)	900	1350

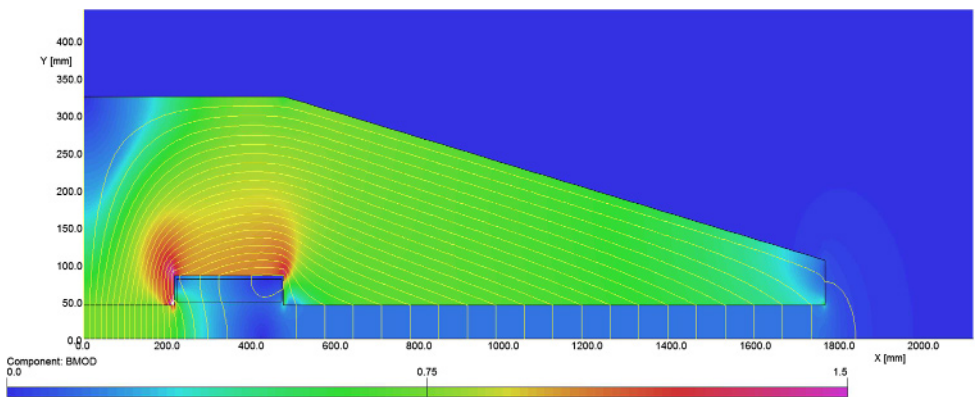


Fig. 3.10. Magnetic design of a half unit of the FCC-ee polarisation wiggler. In this representation the beam will travel in the z-direction.

wigglers for FCC-ee are given in Table 3.8. The 2D magnetic design for half of a unit is shown in Figure 3.10.

3.2.10 Magnets for the booster

A few parameters for the main magnets of the booster are given in Table 3.9. One the one hand, the powering for the dipole, quadrupole and sextupole magnets of the booster ring is due to the cycling more demanding than the powering of the collider magnets. On the other hand, it is less demanding with respect to

Table 3.9. Parameters of the booster magnets.

Magnet type	Parameter	Unit	Value
Dipole	Field at injection (20 GeV)	T	0.005
	Field at peak energy (182.5 GeV)	T	0.046
	Magnet length	m	11.1
	Number of magnets		6176
Quadrupole	Max. gradient at injection (20 GeV)	T/m	2.6
	Max. gradient at peak energy (182.5 GeV)	T/m	23.7
	Magnet length	m	1.5
	Number of magnets		3540
Sextupole	Max. strength at injection (20 GeV)	T/m ²	161
	Max. strength at peak energy (182.5 GeV)	T/m ²	1467
	Magnet length	m	0.5
	Number of magnets		1568

the average electrical power need. The booster magnets will have about half the inductance of the collider magnets. It may be possible to feed them with a similar circuit layout as for the collider (see Sect. 3.2.5), provided that the ramping voltage for the cycle is not too high.

3.3 Vacuum system and electron-cloud mitigation

3.3.1 Introduction

The FCC-ee is a challenging machine from the point of view of the design of its vacuum system, with the same total synchrotron radiation (SR) power budget of 50 MW/beam for beam energies ranging from 44 to 182.5 GeV. Naively one could think of designing it by copying the design of LEP, which was run at beam energies above 100 GeV in its final years of operation. Close scrutiny of the technical specifications of LEP and FCC-ee demonstrate, however, that such an approach is not warranted. Firstly, LEP had a single chamber, with both beams circulating inside, while FCC-ee calls for separate beams. Secondly, the FCC-ee lowest-energy versions at 44–47 GeV (Z pole), feature an extremely large, “B-factory-like”, current of almost 1400 mA. This specification, together with the operation schedule, which allocates the first 4 years to running on the Z pole with an ambitious integrated luminosity goal, calls for a radically different design of the vacuum system. Furthermore, the same vacuum system must also be compatible with the higher beam energy of up to 182.5 GeV (above the $t\bar{t}$ threshold), with its attendant very high critical energy SR spectrum (~ 1.2 MeV for arc dipoles), as well as the intermediate beam energies of 80 GeV (WW threshold) and 120 GeV (ZH production). A summary description of the proposed vacuum system, based on extensive Monte Carlo simulation ray-tracing and modelling (SYNRAD+, Molflow+) and finite-element analysis (Comsol, ANSYS), is given in the following sections.

3.3.2 Arc vacuum system

Chamber material and cross-section

The SR fan generated by the arc dipoles can be absorbed on the vacuum chamber in two ways, namely a distributed absorber (as in LEP) or a series of localised absorbers

(as in light sources). The advantage of the first option is that it is easy to extrude a vacuum chamber with an integrated cooling water channel from aluminium alloys. A similar design has also been implemented in vacuum chambers made from copper alloys, although the cooling water circuit must be welded onto the chamber, since there is no way to extrude convoluted geometries in copper. In FLUKA simulations [291] it has been demonstrated that the use of aluminium alloys is not possible at FCC-ee, because a considerable quantity of SR photons would be generated above the Compton edge energy (around 100 keV) already at beam energies around and above the W pair threshold. For aluminium chambers, therefore, SR photons of this energy cause radiation leakage from the vacuum chamber, which becomes an issue in terms of radiation protection, material activation and damage to nearby components. Copper is a better photon absorber than aluminium and has been chosen as chamber material.

The design localises the absorption of the SR fans on a finite number of water-cooled photon absorbers, as is done routinely at modern light sources. This design has a two-fold advantage, namely: (1) it concentrates the SR fan on a small surface (one absorber of ~ 150 mm length can intercept the photons which would otherwise be distributed over 4–5 m of vacuum chamber wall) and this speeds up the dynamic vacuum conditioning, which depends, to a first approximation, on the linear photon density along the beam axis; (2) localised absorbers allow the installation of local high-atomic number shielding (like Pb or W alloys), thus avoiding the need for complete cladding of the vacuum chamber system, as was done for LEP (this later proved to be a source of problems during operation, namely the depolarisation of the beams due to the thin nickel layer between the aluminium chamber and the lead cladding). The absorbers are placed strategically to intercept 100% of the primary SR fans. The total power intercepted by each absorber varies between 4 and 7 kW, depending on the location in the arc lattice. This is a typical value for SR absorbers at many of today's light sources; therefore, it is taken to be a reasonable and proven design assumption for FCC-ee.

Summarising, the aim is to design a copper alloy vacuum chamber with a suitable number of localised, short, high-Z, water-cooled photon absorbers.

An additional important technical requirement is that the vacuum chamber shape should be as close as possible to circular, since an elliptical chamber results in an unacceptable impedance [292]. Taking all these requirements into account, the proposed cross section of the vacuum chamber in the arcs is derived from the SuperKEKB collider chamber, i.e. a circular tube with two “winglets” placed symmetrically in the plane of the orbit, 20 mm wide and 11 mm tall. For FCC-ee, the round part of the chamber cross section has a diameter of 70 mm, corresponding to a specific conductance of about $421 \times \text{m/s}$ (compared to the $\sim 1001 \times \text{m/s}$ of the LEP elliptical chamber).

The winglet on the external side, where the SR fan goes, is used to lodge the localised photon absorbers, which have a tapered surface which does not protrude into the round part of the chamber where the e^-e^+ beams circulate. The absorber design is rather compact, only ~ 300 mm in length, and 11 mm tall.

Detailed finite-element calculations have shown that a 2 mm thick vacuum chamber wall is sufficient to guarantee thermo-mechanical stability, during both operation and bake-out (at $\sim 200^\circ\text{C}$).

The SuperKEKB design allows a continuous cross section, without tapered transitions, along most of the arcs. This includes all-metal gate valves (GVs) and low-impedance RF contact fingers inside the bellows. The latter are necessary for alignment and expansion of the chamber during operation and bake-out (and even to follow any slow movement of the magnets and vacuum chamber supports due, for example, to tunnel subsidence).

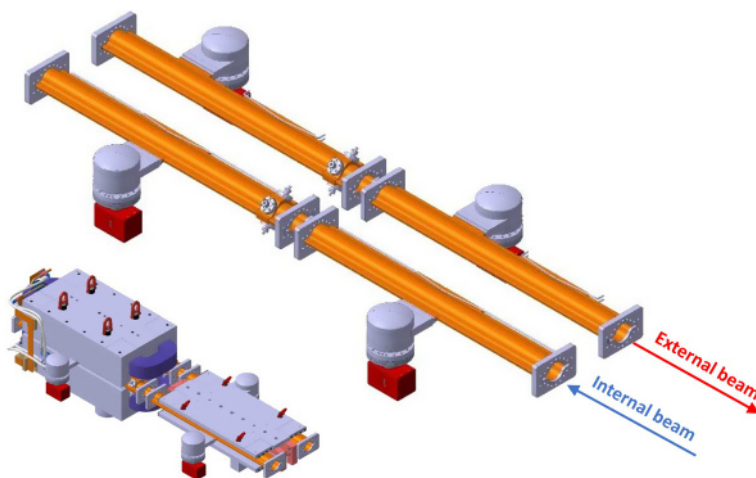


Fig. 3.11. Schematic of the FCC-ee arc vacuum system. The small picture on the bottom left shows the same vacuum system inserted into a twin quadrupole (at the back) and a twin dipole magnet (in front).

As in SuperKEKB, rectangular flanges, with a reduced vertical size, fit inside the coils of the quadrupole and inside the dipole-yoke opening, since the longitudinal space is insufficient for regular circular ConFlat flanges. The SuperKEKB team has successfully prototyped both stainless steel and “hard” copper flanges of this design, which are capable of sustaining a bake-out cycle without leaking.

The vacuum chambers are straight everywhere and even in the dipoles, straight units are placed at a small angle to each other, which is accommodated by the bellows during installation and alignment in the tunnel. The ~ 2 mm sagitta generated by the ~ 11 km bending radius can easily be accommodated inside a straight chamber of the chosen dimensions.

An important feature of the absorbers is that they localise most of the SR-induced desorption; a suitably “large” pumping speed can be installed next to each absorber. This optimises the trapping efficiency of the pumps, which in turn generates a lower average pressure along the beam. The vacuum-related beam lifetime must be longer than the luminosity lifetime (mainly limited by Bhabha scattering) which translates, for the high-current Z-pole machine, into the need for quick dynamic conditioning to achieve low SR-induced desorption yields. A localised pumping dome has, therefore, been implemented next to each photon absorber. The pumping dome is connected to the vacuum chamber via a flat rectangular connection with RF shielding slots along the chamber wall in order to minimise any trapping of high-order modes.

Two different designs are required for the vacuum chambers and the pumping domes, namely, one for the chamber placed externally with respect to the centre of the ring and one for the other placed internally. The need for two designs becomes clear from Figure 3.11, where it can be seen that the pumping dome can be placed opposite a photon absorber only for the internal beam, while for the external beam the pumping dome must be placed on the same side as the photon absorber, since the yoke of the dipole (or quadrupole) does not leave enough space for the dome. For the external beam the SR ray-tracing and FLUKA simulations indicate that it is better to place the pumping dome upstream of the corresponding photon absorber.

The vacuum sectors of LEP were about 500 m long. For FCC-ee, the sector length will ultimately be determined by balancing the practicality of long independent

vacuum sectors against the cost of the all-metal gate valves at either end of each sector. This balancing will be done in the final stage of the design.

Pumping

The first 4 years of operation with high currents at the Z-pole beam energy call for a design which guarantees fast dynamic vacuum conditioning for both rings, with the additional requirement of a sufficiently low secondary electron yield (SEY) for the positron ring, in order to minimise and possibly avoid any electron-cloud issues.

Taking the positive behaviour of the NEG-coated long straight sections of the LHC into account and the fact that many SR light sources have successfully implemented thin-film NEG-coating technology since the year 2000, a complete coating of the vacuum chambers for the FCC-ee rings is proposed. However, a “standard” 1–2 μm thick NEG layer is not compatible with the resistive-wall (RW) impedance budget of the FCC-ee [293]. An alternative, thinner NEG-coating, of the order of 120–150 nm average thickness would be compatible with the RW instability threshold [293]; this is, therefore, the proposed solution. Laboratory measurements at CERN have proven that such a thin NEG-coating can still undergo multiple activation/saturation cycles without appreciable loss of its low-SEY yield [294]. It is planned to test some tubes coated with these thin NEG films under SR irradiation at the KEK Photon Factory before the end of 2018. These tests will measure the SR-induced molecular desorption yield, which for standard thickness NEG-coatings desorb ~ 100 times fewer molecules than an uncoated system of the same geometry [295].

It has been shown that the generation of CH_4 through SR-induced desorption mechanism is much reduced by the presence of NEG coating: accordingly, a large pumping speed for such a non-getterable gas is not needed and, therefore, pumps of the NEX Torr family (SAES Getter Inc., Milan) will be installed in the pumping domes. NEX Torr pumps are based on NEG technology, using blades or discs of sintered NEG material and have an integrated ion-pump which has about 10 l/s pumping speed which should be sufficient to pump the non-getterable gases, such as CH_4 and Ar. As an alternative to the compact NEX Torr pumps, medium-sized sputter-ion pumps (e.g. 80–120 l/s) could be installed, or the two types of pumps could be alternated. The conductance of the pumping dome’s rectangular slot and RF slotted shield has been calculated to be ~ 110 l/s, so that a 120 l/s nominal pumping speed would be reduced to about 1/2 of its value, which is deemed acceptable.

Another advantage of the NEG-pumps is that they do not need any permanent local high-power cabling, since the NEG part of the pump, which produces the bulk of the pumping, can be activated with local controllers manned during the bake-out cycle. The gas capacity for CO and CO_2 of a 500–1000 l/s NEX Torr pump is very large, meaning that the pump should not need re-activation other than during the scheduled shutdown periods of the accelerator, i.e. there will be no impact on machine availability.

Given the large radius of curvature of the arc dipoles (~ 11 km), the total length of the arcs, the two-chamber design and the fact that the distance between absorbers is of the order of 5 m, the total number of pumps, if placed in front or near each absorber, would be $\sim 16\,000$. In order to optimise the cost, MC simulations were performed, which uncovered the effect of a reduced number of pumps on the average pressure, e.g. of installing one pump every 3 or 5 absorbers. The result is that the dynamic vacuum conditioning time, i.e. the integrated beam dose (Ampere-hour) before reaching a suitably low average value of the SR-induced desorption yield, is approximately doubled. This finding reveals a fundamental limit dictated by the geometry of the system, mainly the aperture of the magnets and the radius of curvature of the dipoles.

Bake-out and ancillary systems

Water vapour is always present on the surface of a chamber when it is installed in a tunnel and needs to be removed. Depending on the material, surface finish, and temperature, several monolayers of water molecules can be chemically and physically absorbed on the surface. A common procedure to remove the water vapour is to bake out the chamber, i.e. to uniformly heat it up to at least 120–130°C for times of at least one to a few days, while operating external pumps (turbomolecular pumps, typically): the higher the temperature, the shorter the duration. Since the best high-performance NEG coatings, based on ternary ZrTiV alloy, need at least 180°C in order to reach a satisfactory level of activation, a system which is capable of sustaining a bake-out cycle of several days at 200°C is proposed.

A suitable means of heating up the chamber as uniformly as possible must be envisaged: current technology provides ceramic heaters which are radiation hard and could be installed on the copper chamber at suitable locations, the high-thermal conductivity of copper will then re-distribute the heat around the profile of the chamber. An insulating bake-out jacket is required to limit the heating of any temperature-sensitive components or devices placed near or on the chamber itself. Thin multi-layer jackets corresponding to this specification exist on the market.

The RF contact fingers are based on the design employed at the SuperKEKB machine, the so-called “comb-type design” [296]. The existence of a commercial all-metal gate valve design allows the same cross section to be maintained all along the arcs, eliminating the need for tapered transitions at every flange connection. In addition, this will also reduce the geometric impedance budget. Basically, tapered transitions will only be needed in the long straight sections, which accommodate the superconducting RF cavities, and at a few other locations where special devices will be installed (e.g. injection or extraction kickers, diagnostic devices, etc.). The possibility of integrating 4-button (or 4-strip) BPM electrodes at 45° geometry has already been demonstrated at the SuperKEKB machine. The magnetic lattice team has determined that the low-emittance FCC-ee would need a BPM at each quadrupole in order to control the properties of the beam and its trajectory and therefore being able to adapt the SuperKEKB design is a very positive feature.

Chamber supports and alignment

The supports and alignment systems for the vacuum chambers have not yet been studied in detail. However, no major issues are expected, given that most of the chambers along the arcs are straight and the chamber weight low – for a 2 mm thick copper chamber it would be of the order of 6 kg/m. In fact, the heaviest component would be the 25 mm-thick SuperKEKB-type rectangular flanges, which are visible in Figure 3.11. The mechanical supports would mainly be located at the flanges and, if necessary, also at the pumping domes or photon absorbers, such that the latter can be vertically aligned with respect to the powerful SR fan. The heavy all-metal gate valves would need an independent support, possibly acting as a fixed point.

3.3.3 Interaction-region vacuum system

For most of the FCC-ee straight sections the vacuum chamber will be of the SuperKEKB type, which is similar to the arc system, except that, in the IR straight, the two beams run in separate single-yoke magnets. The SuperKEKB-type chamber profile ends immediately before the focusing doublet, where it is connected to a custom absorber, which protects, or masks, the subsequent chambers up to the IP [297].

The ray-tracing Monte-Carlo code SYNRAD+ has been applied to the entire FCC-ee interaction region [298]. A length of approximately 680 m around the IP has been modelled. The Molflow+ code was used to predict the pressure profile along the 680 m long interaction region based on the photon flux and planned pumping system [298].

Special requirements exist close to the collision point, where a 500 mm long Be pipe sits at the centre of the detector, and incident synchrotron radiation must be minimised. Without proper masking, this central beam pipe will experience a non-negligible flux of photons with energies up to several 10's of keV, which would pose a problem for the detector hardware and electronics [298]. However, a "PEP-II like" solution, with several localised short absorbers before and after the final-focusing doublet, greatly reduces the photon flux incident on the Be pipe [297]. This mitigation measure needs to be combined with a larger bore exit tube, which also helps to avoid trapped modes in the region of the Be pipe. However, the "Y" separation chamber will remain a location for one or a few unavoidable trapped HOMs. Dedicated HOM absorbers will be mounted close to the separation point behind a slotted vacuum chamber. They will be equipped with water-cooled ferrites to minimise the HOM heating in this area [299].

Space is allocated for at least one efficient NEG pump in the IP area [297], a region already densely occupied with detector components and cables (anti-solenoids, cryostats, remotely-operated flanges – possibly like SuperKEKB's, supports, and alignment systems etc.), plus the necessary water cooling circuitry.

The quadrupole magnets of the final doublet generate a rather large and extremely hard photon flux, with photons reaching the energy range of several tens of MeV (at the $t\bar{t}$ energy). These photons mostly impinge within a small spot on the exit side of the beam, about ~ 63 m downstream of the IP, beyond the outer border detector [298]. A careful shielding of this area must be envisaged.

3.3.4 Local beam-pipe shielding

The side-by-side placement of the two collider rings may have profound implications on the amount of high-energy radiation generated by one ring onto the other, through primary and secondary showers, and by either ring onto the tunnel wall and other components/devices placed inside the tunnel (also see Sect. 3.11).

To minimise the impact of this radiation, adequate shielding of the arc vacuum chamber is particularly important for the higher-energy working points (H, $t\bar{t}$), with critical photon energies extending up to 1.2 MeV for a beam energy of 182.5 GeV. In contrast, special shielding is not required for the lower energy operation modes (Z and W) due to the corresponding, much softer spectrum of synchrotron-radiation photons, which at these low energies will simply be shielded by the vacuum chamber. Therefore, in line with the operation scenario, dedicated shielding elements for the arcs, e.g. properly shaped lead blocks attached to the vacuum chamber, can be added in a staged manner, after the initial bake out and NEG activation, during the regular annual shutdowns.

For photon energies in the range 0.5–5 MeV, as expected in the later years of FCC-ee operation, Compton scattering will be the dominant process of attenuation and shielding. After a single initial Compton scattering event the memory of the initial angle of incidence is almost completely lost [301]. As a consequence, the Compton attenuation curve is rather insensitive to the initial angle of incidence.

For the FCC-ee, placing localised high- Z material shielding around the photon absorbers is an attractive option, which aims at minimising material activation

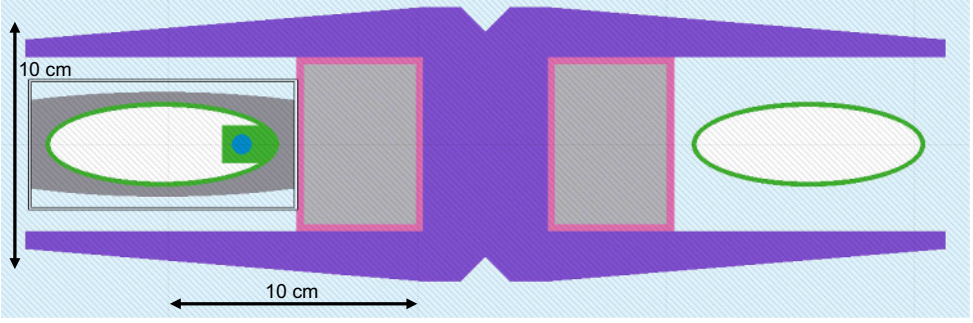


Fig. 3.12. FCC-ee arc dipole cross section, as implemented in a preliminary FLUKA model, featuring on the inner (left) side a photon absorber (in green) surrounded by lead shielding (in grey) [300].

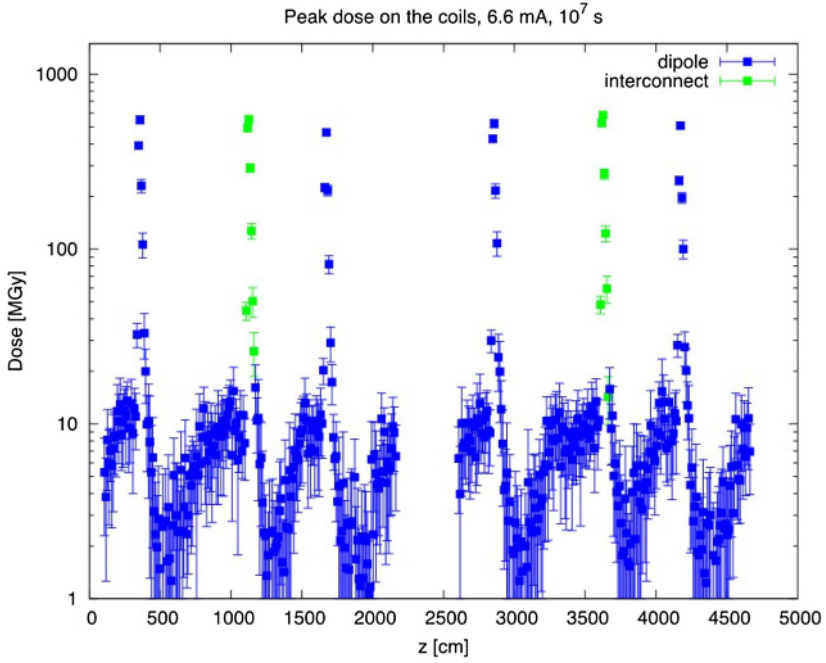


Fig. 3.13. Peak annual dose profile in the arc dipole coils along a 50 m cell, for 6.6 mA beam current over 116 days per year at 175 GeV beam energy [300]. Maxima correspond to the absorber locations, with two absorbers sitting in the interconnect rather than inside the dipole. Vertical bars give the statistical error.

and damage. Nevertheless, simulation results, for an earlier beam-pipe design as in Figure 3.12, indicate that the inner ring coils will have to withstand annual doses of several hundred MGy at the absorber positions for the final $t\bar{t}$ running mode, as shown in Figures 3.13 and 3.14.

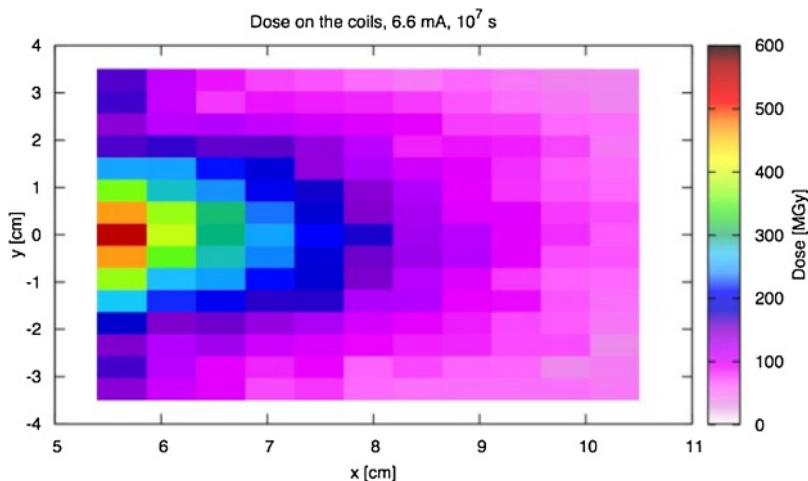


Fig. 3.14. Transverse distribution of annual dose in the arc dipole coils at the peak corresponding to the absorber location [300].

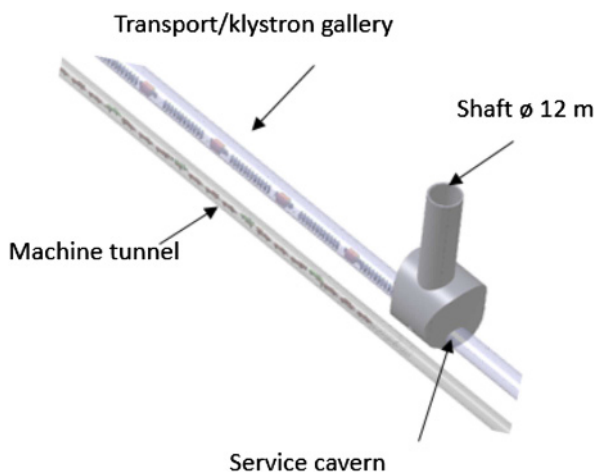


Fig. 3.15. A schematic view of the FCC-ee RF system placement at points PD and PJ. The power sources are located in a gallery, which is adjacent to the machine tunnel. The RF systems and their power sources are symmetrically distributed next to the access shafts at the points PD and PJ.

3.4 Radiofrequency system

3.4.1 Overview

Introduction

The parameter range for the e^+e^- collider is large, operating at centre-of-mass energies from 88 GeV to 365 GeV with beam currents ranging between 1.39 A and 5.4 mA, at fixed synchrotron radiation power of 50 MW per beam. These are challenging parameters for the radiofrequency (RF) system due to the voltage requirements and beam-loading conditions. The RF system is equally distributed between the two opposite straight sections at points PD and PJ as shown in Figure 3.15.

Table 3.10. Machine parameters.

Parameter	Z	WW	ZH	tt1	tt2
Beam Energy (GeV)	45.6	80	120	175	182.5
Beam current (mA)	1390	147	29	6.4	5.4
Number of bunches	16640	2000	328	59	48
Beam RF voltage (MV)	100	750	2000	9500	10 930
Run time (year)	4	2	3	1	4

System parameters

The main centre-of-mass operating points are around 91 GeV (Z pole), 160 GeV (W pair production threshold), 240 GeV (Higgs factory) and 340–365 GeV (at and above the $t\bar{t}$ threshold). Therefore, the system needs to evolve in steps. The system parameters for each step are summarised in Table 3.10 [302].

The RF voltage requirement spans from 0.1 to 11 GV. Running at the Z-pole, the collider is an Ampere-class, heavily beam loaded machine, while at the $t\bar{t}$ energy it becomes a high energy machine. A single system design to meet all four cases is not efficient [303]. For the Z-pole machine, the cavity shape must be optimised with respect to higher order modes (HOM). This favours low frequency, low shunt resistance and a low number of cells per cavity. For this energy point, a 400 MHz continuous wave (CW) RF system will be used, made up of 52 single-cell Nb/Cu cavities per beam. This frequency is also the natural choice for the FCC-hh, which can use the LHC as injector. The LHC also operates at this frequency. The chosen approach, therefore, provides the opportunity to reuse a large part of the hardware and infrastructure for a subsequent hadron collider. The 400 MHz single-cell system can be built with today’s technology. Figure 3.16 (left picture) shows a single-cell 400 MHz Nb/Cu cavity built for the LHC.

A second operating scenario is considered for the ZH and $t\bar{t}$ threshold operation points where high acceleration efficiency and multi-cell cavities are required to optimise the total size and cost of the RF system. Four-cell 400 MHz Nb/Cu cavities (Fig. 3.17) are chosen for the WW threshold and ZH modes of operation, for reasons of beam loading and practicality. This choice allows for optimum reuse of the Z pole RF power system and it minimises the installation and conditioning time.

About 2600 cells are required to produce a total RF voltage of 11 GV at the highest energy point. The small number of bunches and the low beam loading suggest the possibility of a common RF system for both beams, with a special optics described in Section 2.4.3. This common RF system can be accomplished by re-aligning the already installed cavities (which earlier, in the H production mode, are used for either one or the other beam) on a common beam axis and by installing additional cavities to achieve an additional voltage of 7 GV. For this second part, the relatively modest CW RF power per cavity at this operation point enables the deployment of 800 MHz bulk-Nb five-cell cavities. A first prototype cavity (Fig. 3.16, right picture) shows an excellent performance, with an unloaded Q value about two times the target value [304]. Although these cavities must be operated at 2 K, they provide a better acceleration efficiency and result in a significantly reduced overall footprint and, hence, in potentially significant cost savings. Higher frequencies have been excluded due to transverse impedance considerations and power coupler limitations for CW operation.

The bulk-Nb cavities will be subjected to “fast cool downs”, to take advantage of large temperature gradients to expel magnetic flux from the superconductor.



Fig. 3.16. Left: A FCC seamless single-cell 400 MHz Cu prototype cavity for Nb on Cu thin-film coating, fabricated at INFN Legnaro National Laboratory (Italy). Similar cavities will be used for operation at the Z pole. Right: A prototype FCC five-cell 802 MHz bulk-Nb cavity for $t\bar{t}$ operation, fabricated and tested at Jefferson Lab (USA) [304].

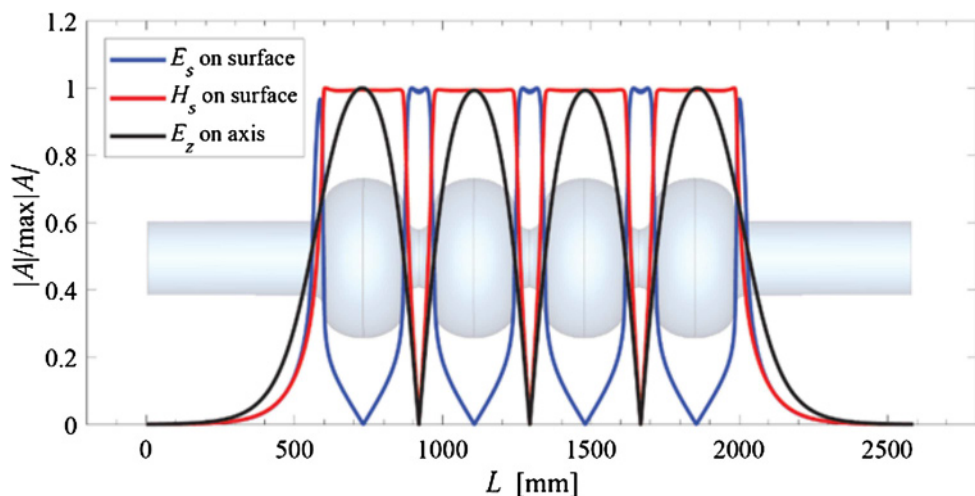


Fig. 3.17. Drawing of a four-cell Nb/Cu cavity at 400.79 MHz, proposed for the WW and ZH modes of operation, including field profiles.

This has an impact on the cryomodule design, which has to withstand the induced stress. No constraints of this type exist for the 400 MHz Nb/Cu cavities operating at 4.5 K.

RF for the booster

The RF configuration of the top-up booster ring [305] for each operating point is shown in Table 3.12. In order to optimise the cryogenic system and cryogen distribution, the same technology as for the collider will be used. Since the booster has a low duty factor, less than 10% (ratio of average to peak power), a compact RF power system can be used. The low beam loading allows for multi-cell cavities at all energies and a staged installation.

Table 3.11. Design parameters of klystrons operating at 400 and 800 MHz.

Frequency	Beam voltage	Beam current	Peak RF power	Efficiency	Power gain	Tube length
400 MHz	54 kV	9 A	357 kW	73.5%	38.5 dB	1.26 m
800 MHz	134 kV	12.6 A	1.35 MW	80.0%	38 dB	1.74 m

Table 3.12. Detailed RF configuration of each machine and booster ring.

	Z		WW		ZH		tt_1		tt_2	
	per beam	booster	per beam	booster	per beam	booster	2 beams	booster	2 beams	booster
Total RF voltage [MV]	100	140	750	750	2000	2000	9500	9500	10 930	10 930
Frequency (MHz)	400									
RF voltage [MV]	100	140	750	750	2000	2000	4000	2000	4000	2000
E_{acc} (MV/m)	5.1	8	9.6	9.6	9.8	9.8	10		10	
# cell / cav	1	4	4		4		4		4	
V_{cavity} (MV)	1.92	12	14.4	14.4	14.7	14.7	15		15	
# cavities	52	12	52	52	136	136	272	136	272	136
# CM	13	3	13	13	34	34	68	34	68	34
T operation (K)	4.5		4.5		4.5		4.5		4.5	
Dyn losses/cav (W)	14	11	210	26	202	29	210	30	210	30
Stat losses/cav (W)	8		8		8		8		8	
Q_{ext}	4.4×10^4		6.6×10^5		1.9×10^6		4×10^6		4.7×10^6	
P_{cav} (kW)	962		962		368		175		149	
Frequency (MHz)	800									
RF voltage (MV)							5500	7500	6930	8930
E_{acc} (MV/m)							19.8	20	19.8	19.8
# cell/cav							5		5	
V_{cavity} (MV)							18.6	18.75	18.6	18.6
# cavities							296	400	372	480
# CM							74	100	93	120
T operation (K)							2		2	
Dyn losses/cav (W)							66	10	66	10
Stat losses/cav (W)							8		8	
Q_{ext}							3.9×10^6		5.6×10^6	
P_{cav} (kW)							176		155	

3.4.2 Superconducting cavities

Cavity materials

A detailed analysis of performance data for different RF frequencies, temperatures and materials for the superconducting cavities [306] has led to the recommendation of Nb/Cu technology for the Z, W and ZH modes of operation.

A well-focused R&D programme on Nb thin-film coated Cu cavities could decrease the surface resistance at high RF fields by factors of two to three. As a result, the technology could be operated at 4.5 K, which makes it competitive with bulk Nb operated at 2 K. This choice also facilitates the reuse of the existing RF power system for the hadron machine, which requires a high RF acceleration efficiency with several hundred kW power input per cavity and for which a lower transverse impedance is certainly beneficial. R&D is focussing on Nb/Cu produced by high-power impulse magnetron sputtering, which will improve the micro-structure of the coating due to the larger energy made available during film growth. Any progress on substrate manufacturing and preparation will have an immediate impact on the final RF performance, as it was demonstrated by the seamless cavities produced for the HIE-ISOLDE project, where the Q slope was substantially reduced compared to their welded counterparts [307].

The A15 compounds have the potential to outperform niobium as their BCS surface resistance is much lower due to the higher critical temperatures. Nb₃Sn cavities obtained by thermal diffusion of Sn in bulk Nb have a performance at 4.5 K which is similar to state-of-the-art bulk Nb cavities at 2 K. A programme aimed at the synthesis of Nb₃Sn films on copper substrates is ongoing at CERN and has already produced high quality films on small samples [308,309].

Manufacturing

The number of cavities needed justifies investing in novel, cost-effective manufacturing technologies ensuring the best reproducibility whilst minimising the performance limitations. In addition to the traditional fabrication methods, notably spinning and deep drawing of the half-cells, electro-hydraulic forming (EHF) [310] turns out to be particularly suited for series production.

For bulk Nb and Nb-coated elliptical cavities alike, minimising the electron-beam welded joints by seamless construction helps to reduce the performance limitations arising from defects and irregularities of the welding seams and the area in their vicinity, as well as reducing possible contamination originating from them. Efforts are ongoing to push the technology beyond existing limits to produce seamless cavities within the tight tolerances required [311]. It can be expected that such Nb coated cavities will show a superior and more uniform electro-magnetic performance [307]. Surface treatments are necessary in order to eliminate the surface layer damaged during cavity fabrication and to achieve the smoothest possible substrate for Nb coatings. Efforts are ongoing to achieve full electro-polishing of seamless cavities in order to achieve these goals.

RF power couplers

In order to achieve the proposed configurations at the Z pole and at the W pair threshold, the RF coupler technology must also be pushed forward to increase their CW power transfer capability; the HOM couplers will have to deal with high beam loading and must extract kilowatts of RF power. Progress with the fundamental power couplers will be essential to limit the cost and size of the RF system. The target value for fixed couplers is 1 MW CW per power coupler at 400 MHz [312]. The design of the fixed power couplers must ensure that their coupling coefficient can easily be changed for the different machines, as imposed by the varying machine parameters and overall time line. In particular, the external Q of the coupler must be adaptable “in situ”, without venting the cavities. Fundamental power couplers for superconducting cavities are among the most important and most complex auxiliary systems. They must simultaneously deliver RF power to the beam and separate the cavity ultra-high vacuum, ultra-low temperature environment from air-filled, room temperature transmission lines, as illustrated in Figure 3.18.

3.4.3 Powering

High efficiency klystron development for FCC

The need to provide two times 50 MW of continuous RF power sets the overall scale of the system. Improving energy efficiency and reducing energy demand is crucial for such a particle collider. Therefore, highly efficient RF power sources need to be conceived [305].

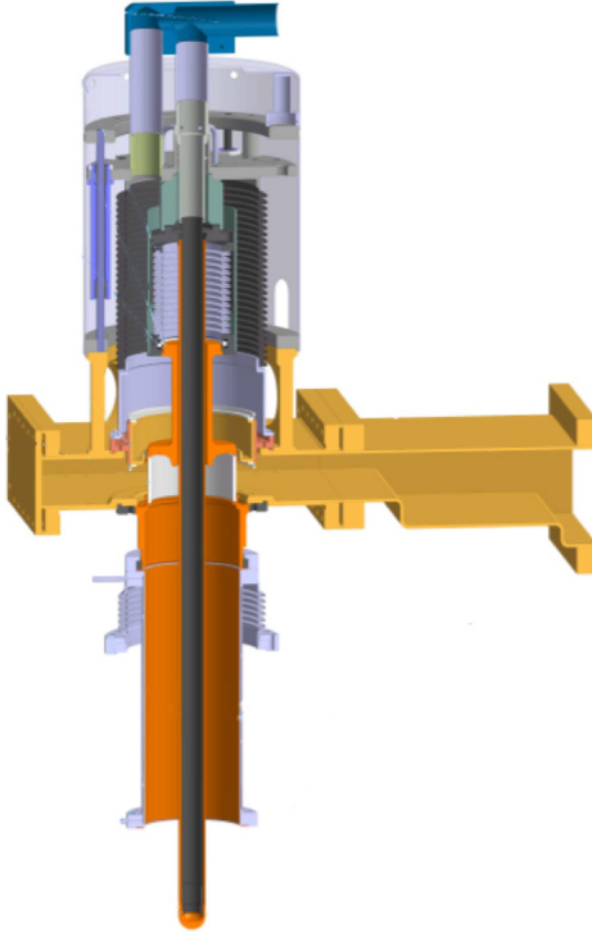


Fig. 3.18. Schematic of the LHC power coupler serving as model for a FCC-ee power coupler design.

The High Efficiency International Klystron Activity (HEIKA) [313] was initiated at CERN in 2014 to evaluate and develop new bunching technologies for high efficiency klystrons [23,314,315]. Design calculations predict efficiency increases ranging from 65% to potentially above 80%, resulting in significantly lower operation cost [316]. One critical step towards the realisation of these devices is the development and use of a software called KlyC [317] to optimise system designs with high accuracy and short iteration times.

Table 3.11 displays the main parameters obtained for a 800 MHz high efficiency klystron, optimised for the lepton collider and a scaled version at 400 MHz adapted for HL-LHC (i.e. the parameters of LHC klystron modulator were preserved). Their bunching technology is based on the core stabilisation method (CSM) described in [317]. The gain and power transfer curves of the 800 MHz tube, simulated by KlyC for different voltages, are shown in Figure 3.19. The tube has a comfortable dynamic range, preserving efficiency above 65% for the range of output power from 0.6 to 1.7 MW, and a comfortable 3 dB bandwidth of 4 MHz at 1.35 MW.

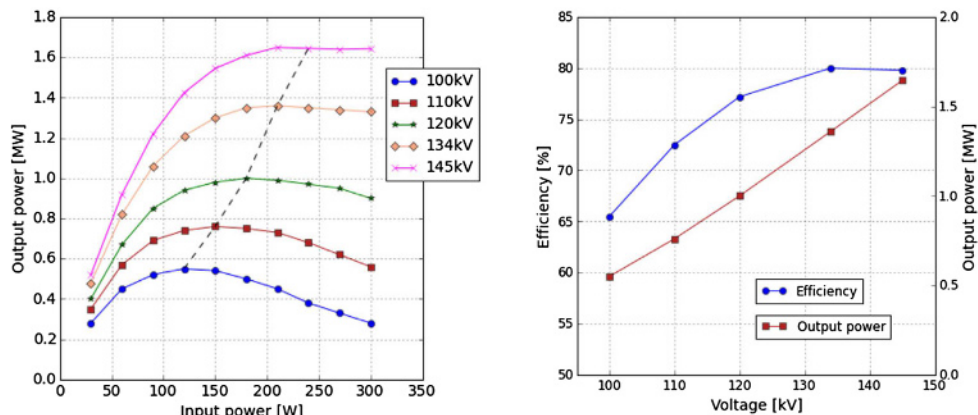


Fig. 3.19. The power gain curves simulated by KlyC for different voltages (left) and the transfer curves for saturated power (right). The dashed line in the left plot traces the saturated power.

3.4.4 Feedback

Longitudinal instabilities driven by the cavity fundamental impedance are the main concern when running at the Z-pole [318]. Their growth rate is much faster than the synchrotron radiation damping. Strong feedback around the cavities will therefore be required to maintain stability and to damp the coupled-bunch instabilities for high intensities [319]. A direct RF feedback can be supplemented by a one-turn delay feedback, giving extra impedance reduction. Bunch-by-bunch longitudinal feedback may also be required to suppress the strongest coupled-bunch modes.

3.4.5 Low-level RF

A detailed analysis of the impact of the beam interaction with the fundamental impedance of the accelerating cavities on the bunch-by-bunch parameters (bunch length, synchronous phase, etc.) for the Z machine was performed using a steady-state time-domain approach [320]. For the regular filling schemes, the main contribution to phase and amplitude modulation of the cavity voltage comes from the abort gap. The resultant peak-to-peak value of bunch-by-bunch phase modulation exceed 70 ps for abort gaps longer than $2\text{ }\mu\text{s}$. The results agree well with those of the frequency-domain method developed by Pedersen [321].

One of the ways to eliminate the shift of a collision point due to beam phase modulation is matching of abort gap transients. The direct RF feedback with the overall loop delay of 700 ns (similar to the LHC [322]) can also mitigate the transient beam loading at the cost of an additional power generator. For the example shown in Figure 3.20, about a 5% increase of the generator power (the right plot) is sufficient to reduce the bunch-by-bunch phase modulation by 20% (the left plot).

3.4.6 Staging

The RF system will be upgraded in steps, with rising maximum voltage, as shown in Table 3.10. First of all 26 400 MHz single-cell four cavity cryomodules will be installed for the Z-pole machine. Each cavity will be fed by about 1 MW CW RF

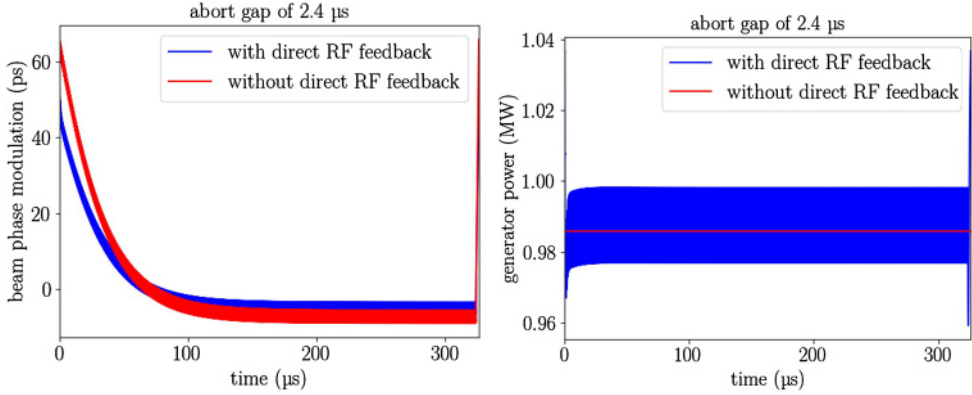


Fig. 3.20. Variation of bunch-by-bunch phase with and without the direct RF feedback (left plot) and instantaneous generator power within one turn (right plot).

power to generate the 2×50 MW beam power. Several solutions are possible to produce the required RF power, but since the space in the tunnel is restricted, the large, bulky power equipment will be installed on the surface. The underground areas will only accommodate the RF power amplifiers, the DC power distribution, the fast servos, the control and the protection systems. Given the perspective of the energy upgrades, using a combination of two or four medium-size RF power sources per cavity seems very attractive.

During a shutdown period at the end of the Z-pole campaign, these cryomodules will be replaced by 26 cryomodules, containing four 400 MHz four-cell cavities each, for the WW-threshold machine operation. The RF power sources, the control systems and the RF power distribution will remain unchanged. The step between the WW and ZH machines requires the installation of 42 additional 400 MHz four-cell four cavity cryomodules to produce the RF voltage of 2 GV/beam. The fast RF feedback requirements and the large number of bunches favour a single cavity per power source. The RF power system initially installed for the Z machine will be reconfigured to adapt to the new power requirement per cavity. Additional new RF power stations will complete the installation. The detailed powering scheme and the associated workload must be carefully studied to be in line with the available time frame. The pre-installation effort must be spread over several winter shutdowns (e.g. cabling and installation campaigns).

For the highest beam energy of 182.5 GeV the existing RF system would be rearranged. It would be shared between the two beams, to double the RF voltage available for either beam. The sharing of cavities by the two beams is possible due to the small number of bunches in this mode of operation. The 68 RF cryomodules will be moved transversely and separators will be installed at the entrance and exit of each RF straight section. The system will be completed with additional 800 MHz five-cell four-cavity cryomodules installed in series to produce the extra voltage. These 2 K cryomodules will be connected to form long cold segments in order to minimise the warm beamline sections and the relatively modest power requirement per cavity will allow for the gradual introduction of less powerful and less expensive RF power sources. A one-year shutdown will be necessary to cope with this major intervention. It will be followed by one year of an intermediate operation stage at 175 GeV. The main changes to the RF unit configuration in tandem with the required beam-energy changes are depicted in Figure 3.21. The main RF parameters for each stage are detailed in Table 3.12.

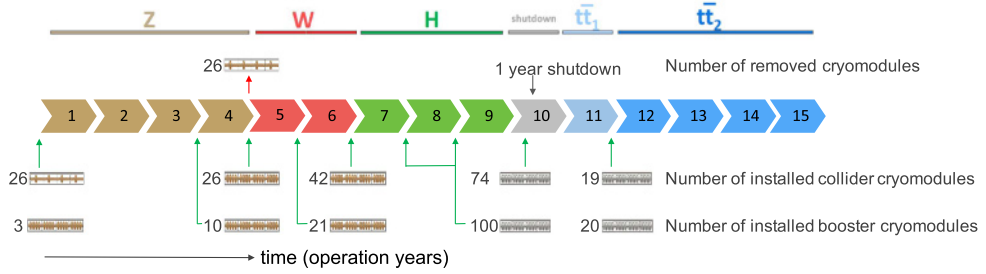


Fig. 3.21. Proposed FCC-ee staging schedule. The figures next to the RF cavity icons indicate the numbers of cryomodules to be installed (green arrows) or removed (red arrow) during the shutdowns. The coloured, numbered arrows indicate the operation years. 8 month periods are interleaved with 4 month shutdowns in one year. The different colours indicate the operation energies of the collider (Z, W, H, $t\bar{t}$).

3.4.7 Beam-cavity interaction and beam dynamics issues

In order to maximise the luminosity of the FCC-ee at the different energy steps, sufficient current must be stored in both beams. Higher-order mode (HOM) losses, optimum coupling (loaded Q values), single- and coupled-bunch instabilities, all of which might seriously affect the final performance of the machines, have been studied in detail for the different running modes [236,323]. Many of these issues appear to be more prominent in the “high-current – low-energy” operation at the Z pole and to a lesser extent at the WW threshold. The use of single-cell 400 MHz cavities at the Z, and the subsequent hybrid RF staging scheme with 400 MHz four-cell cavities for the W and ZH operation modes, complemented by 800 MHz five-cell cavities at the top threshold, relieves the requirements and allows for near-optimum RF conditions in each mode of operation [324].

The microwave instability thresholds have been computed with the BLonD code, a macro-particle tracking code developed at CERN for longitudinal beam dynamics simulations [325]. Its latest release accurately computes synchrotron radiation effects for leptons and very high energy hadrons [326]. At nominal beam current, the machine impedance leads to increased energy spread and bunch length, despite the strong synchrotron radiation damping, but does not result in unstable growth [327]. This is consistent with previous analyses [205,328] and with the results from the PyHEADTAIL code reported in Section 2.6.11.

An analytical approach was used to calculate the longitudinal coupled-bunch instability (LCBI) thresholds [329]. Although the single-cell cavity for the Z-pole machine must be further optimised, its longitudinal impedance spectrum above the cut-off frequency of the pipe sits well inside the coupled-bunch stability zone, as shown in Figure 3.22. A single HOM below the cut-off frequency should be damped, according to the calculated limit, so as to obtain a quality factor smaller than 640.

The cavity design and the beam configuration are closely intertwined. Figure 3.23 shows the calculated power loss map of a reference single cell cavity as a function of the cavity resonant frequencies for filling schemes with distances between the first two bunches of consecutive trains larger than 100 RF buckets. It can be observed, for example, that bunch spacings of 10 ns and 17.5 ns are not favourable for operation.

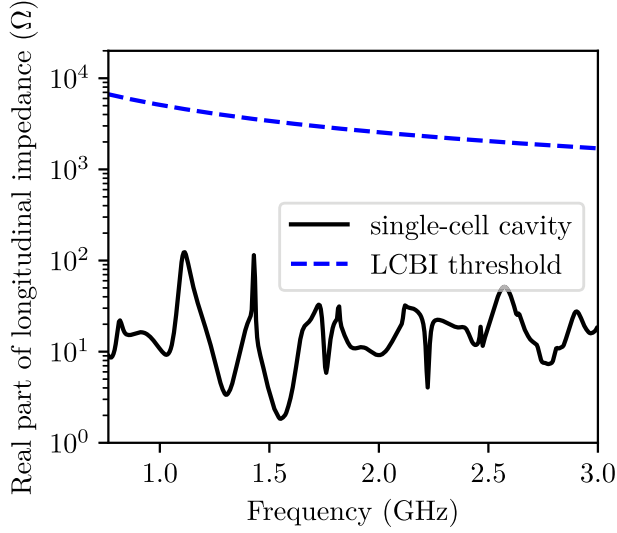


Fig. 3.22. Comparison of the Z machine longitudinal coupled-bunch instability (LCBI) threshold with the longitudinal impedance of the FCC single-cell cavity above the cut-off frequency (765 MHz). HOM damping should make sure that the impedance remains below $10\text{ k}\Omega$.

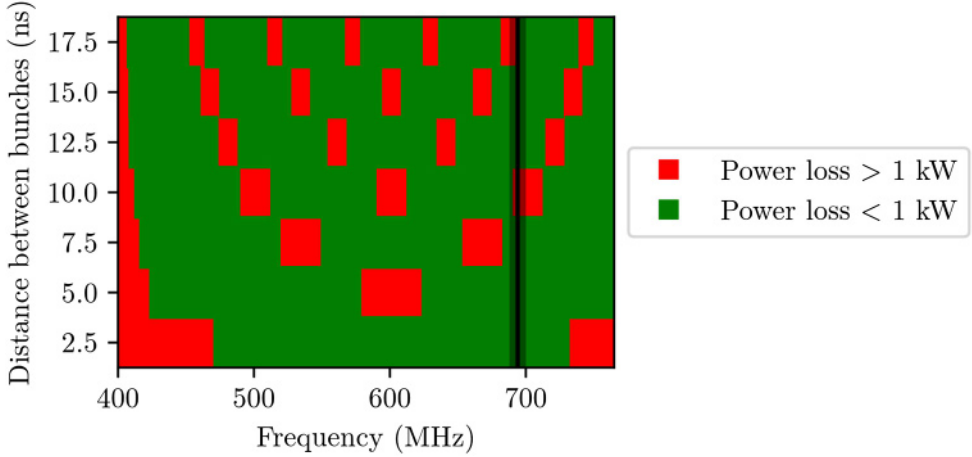


Fig. 3.23. Calculated power loss map for a single-cell cavity. Frequency ranges with acceptable power losses below 1 kW for different bunch spacing are shown in green. Regions with power losses above 1 kW are shown in red. The dark vertical line corresponds to the position of a HOM of the single-cell cavity design with the maximum frequency shift of 5 MHz . The bunch spacings of 10 ns and 17.5 ns are not acceptable for this HOM due to high power losses (see, overlap of red with black regions). The frequency range for the calculations is limited by the fundamental mode frequency (400.79 MHz) and the cut-off frequency (765 MHz).

3.5 Beam transfer systems

In this section, the conceptual design and technical systems for the FCC-ee beam transfer devices are described, including the top-up injection and the beam abort (dump) systems. Kicker and septum parameters are given, with overviews of the system concepts and references to similar systems in operation.

3.5.1 Introduction

A highly robust top-up injection scheme is imperative for FCC-ee. Various top-up methods have been investigated [330] and a number of alternative schemes developed, with requirements for kickers and septa.

The abort system must safely remove the beam from the accelerator ring and transport it to a dedicated beam dump. A technically feasible dump system concept has been developed [331]. The dilution kickers spread the beam evenly on the surface of the graphite dump block.

3.5.2 Injection system

Efficient top-up injection requires minimum perturbation to the circulating beam during injection from the kickers and septa, and large clearances at the septa ($\geq 5\sigma$ of the beam size), to ensure a robust injection with low losses.

Overview and concepts

Two designs of the injection straight have been made, for both conventional injection and multipole-kicker injection schemes, for both on-energy and off-energy injection (which would use similar kicker and septa parameters) [330]. A comparison between conventional and top-up injection is made in Table 3.13.

The conventional injection design is based on an injection septum and a closed dipole kicker bump, consisting of two kickers in the FODO structure separated by 180° phase advance. With a dynamic aperture of 15σ and clearances of 5σ for both injected and circulating beam, the injection septum needs to be a thin electrostatic type, with a width below 1 mm, since a 5 mm magnetic septum takes about 8σ of the aperture.

The multipole kicker injection design uses a strongly non-linear kicker field to minimise the perturbation to the circulating beam while deflecting the injected beam. Such a scheme has been tested and implemented at various facilities [332–335]. The multipole kicker concept allows using a 5 mm thick magnetic septum. The kicker field is zero only at the kicker axis ($x = 0$ mm), and thus the circulating beam is distorted, resulting in a temporary emittance growth. The emittance is quickly restored through synchrotron radiation damping while, for $t\bar{t}$ operation, it is evaluated to be 30–40 at the time of injection.

Dipole kicker for conventional injection bump

The integrated field of the kicker for the off-energy injection at 182.5 GeV is about 0.025 Tm. This can be achieved with a 50 cm long kicker powered at about 1000 A, with a vertical gap height of 24 mm. A 16.66Ω terminated system will need 33 kV and have a magnet filling time of below 100 ns. A faster system will need more modules and higher characteristic impedance. Tentative kicker parameters are shown in Table 3.16.

Multipole kicker

With the multipole kicker an integrated field of about 0.03 Tm is required for the injected beam [330]. The field shape, Figure 3.24, can be produced by two facing

Table 3.13. Summary of injection schemes (for 175 GeV beam).

Beam parameters	Unit	Conventional on-/off-energy	Multipole on-/off-energy
β_x at kicker and septum	m	310/310	450/380
Dx at kicker and septum	m	0/0.8	0/0.8
Type of kicker		Dipole kickers	Multipole kicker
Integrated kicker field	Tm	0.012/0.025	0.025/0.03 (Plateau)
Wire septum integrated volt.	MV	11/11	N/A
Beam disturbance		Coherent oscillation	Emittance increase
Injection beam oscillation		Betatron/Synchrotron	Betatron/Synchrotron
Required aperture	σ	15/5 (at -1.8%)	15/5 (at -2%)

Notes. The parameters of the conventional injection scheme are based on a thin electrostatic wire septum, while the multipole kicker injection can use a thicker magnetic septum.

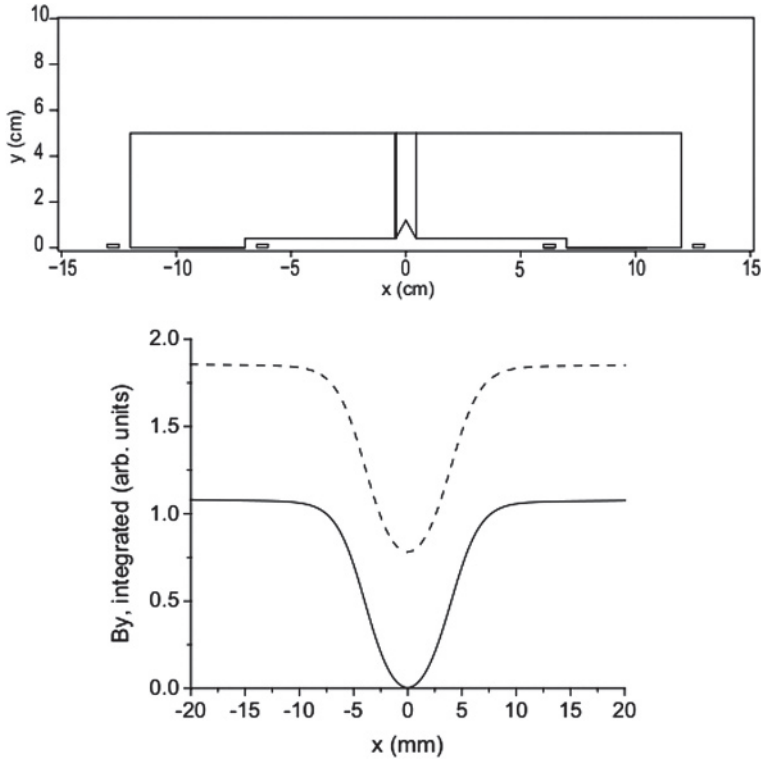


Fig. 3.24. Top: Upper half cross section of the FCC-ee multipole kicker magnet. Bottom: FCC-ee multipole kicker field profile at the injection point (solid curve with dipole compensated).

C-shaped dipole (ferrite) kickers, with a copper plate inserted in the midplane [330]. The half-kickers are powered symmetrically to avoid odd-multipoles, but this has the consequence that a residual dipole needs to be cancelled with an adjacent dipole kicker. The required field can be obtained with a single-turn coil current of about 700 A for on-energy injection (500 A for off-energy), for a 50 cm-length kicker. The kicker parameters are shown in Table 3.16.

Table 3.14. Parameters for FCC-ee top-up magnetic injection septum, for 175 GeV $t\bar{t}$ operation.

Parameter	Unit	$t\bar{t}$ value
Deflection angle (horizontal)	μrad	150
Total magnetic length	m	1.0
Modules		1
Magnetic field	T	0.1
Current	kA	3.0
Septum width (effective)	mm	5.0
Beam aperture	mm	40
Total length	m	1.5

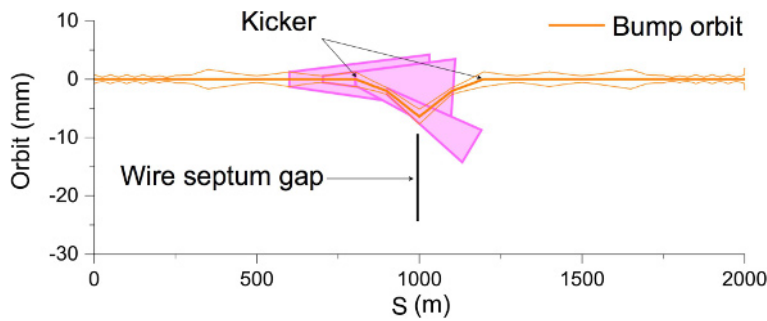


Fig. 3.25. Bump orbit and radiation fans for the FODO phase advance of 90° . Radiation from a 2σ beam and from the magnets up to 400 m upstream of the wire septum are included.

Magnetic septum

A 5 mm thick magnetic injection septum will only require a moderate field of 0.1 T and a length of less than 1 m to produce a deflection of over $150\,\mu\text{rad}$, sufficient to allow a thicker septum upstream in the injection channel. The most stringent requirements will come from the stray field penetration into the non-field region and the stability, both of which need to be below the $\pm 0.1\%$ level. Innovative approaches like an anti-septum to cancel the perturbing terms can be considered [336]. A tentative set of parameters for the septum are given in Table 3.14.

Electrostatic septum

An integrated electric field of 11 MV can be obtained with two 3 m long wire septa operated at low fields of 2 MV/m (40 kV across a 20 mm gap). The low field is chosen since high-voltage performance of the electrostatic septum (ES) in the presence of synchrotron radiation is a concern [337]. This is addressed in the design since with a 90° FODO injection insertion, the main SR fan does not impact the ES anode or cathode, as can be seen in Figure 3.25. There also may be a significant energy deposition on the wire septum from the stored beam because the wakefields can be trapped and can destroy the wires. The electrostatic septum parameters are given in Table 3.15.

Table 3.15. Parameters for FCC-ee top-up electrostatic injection septum, for 175 GeV $t\bar{t}$ operation.

Parameter	Unit	$t\bar{t}$ value
Deflection angle (horizontal)	μrad	63
Total electric length	m	6.0
Modules		2
Electric field	MV/m	2.0
Septum width (effective)	mm	0.5
Beam aperture	mm	20
Total length	m	8.0

3.5.3 Beam abort system

Overview and concept

The FCC-ee beam abort system consists of extraction kickers, septum magnets and a dilution kicker system. A set of kicker magnets is pulsed rapidly to kick the whole beam out of the machine in a single turn ($333\ \mu\text{s}$). The kicker deflects the beam horizontally into a Lambertson septum, which provides a strong vertical deflection to clear the downstream lattice quadrupole. In order not to melt the dump block absorber material, the beam is spread over the front surface of the dump by horizontal and vertical dilution kicker magnets. Geometric bending angles of 10 and 1 mrad are needed in the vertical and horizontal planes, respectively, to match the trajectory to the FCC-hh dumped beam trajectory in both planes.

Extraction kicker

For the extraction kicker the required angle is 0.5 mrad, and the overall rise time should be less than $1\ \mu\text{s}$, for a 422 ns magnet filling time. With a vertical aperture of 50 mm, the magnet current is 2 kA, with a $6.25\ \Omega$ characteristic impedance. A generator based on solid-state switches with a maximum of 25 kV is assumed. The most challenging parameter is the need for a full turn ($330\ \mu\text{s}$) flat-top. A modular system is proposed with $4 \times 1.5\ \text{m}$ long magnets for $t\bar{t}$ operation and a single such magnet for Z operation. The magnet and generator parameters are summarised in Table 3.17.

Extraction septum

The Lambertson septum deflects the beam 12 mrad downwards. The half-aperture for the circulating and extracted beams is 20 mm, with 10 mm septum width. A single magnet of 0.44 T is needed at the Z-pole, with 4 such magnets for $t\bar{t}$ operation. System parameters for $t\bar{t}$ operation are given in Table 3.19.

The septum parameters are rather comfortable compared with those of the LHC extraction system [338], where fields of 0.8 T are comfortably possible with a septum width of 6 mm.

Dilution kickers

A dilution sweep is needed to reduce the energy density and temperature on the dump block, even with the very long available drift distance. The dilution kicker

Table 3.16. Parameters for FCC-ee dipole and multipole injection kickers, for 175 GeV injected beam energy.

Parameter	Unit	Dipole kicker	Multipole kicker
Vertical gap	mm	24	24
Horizontal gap	mm	60	60
System impedance	Ω	16.66	16.66
Magnetic length	m	0.5	0.5
Magnetic field	T	0.050	0.060
Current	A	950	1150
Magnet filling time	ns	94	94
Switch voltage	kV	31.7	38.3

Notes. Two magnets at π phase advance are assumed for the dipole injection, while the single multipole injection kicker requires a compensating dipole kicker.

system has been studied assuming an Archimedean spiral [339] with equal spacing between turns (with 1 turn as the minimum). The outer sweep radius is 200 mm, and the bunch spacing depends on the inner radius, to keep the density on the dump block uniform. The kicker frequency and amplitude thus vary through the sweep (see Fig. 3.26 left), with a maximum kicker frequency of 200 kHz defined by the losses in tape-wound 50 μ m steel. A study showed that 57 turns are the optimum, with a 0.9 mm spacing between bunches and between turns. A single kicker magnet will be sufficient at tt operation energy, since the drift to the dump is very long. The kicker parameters are given in Table 3.18.

The dilution system presents the interesting technical challenge of how to modulate the frequency and amplitude on such short time scales – however, a fixed-frequency system is also possible, at the price of either increased energy deposition in the dump block or a larger sweep radius.

Beam dump block

Graphite has been chosen as the main material for the beam dump, because of its high melting temperature. A cylinder with 400 mm radius and a length of 5 m was chosen as shape of the absorber. With 57 turns of the spiral, which keeps the dilution sweep frequency below 200 kHz, the maximum energy deposition density in the graphite from the beam of electrons is found to be 130 J/cm³, equivalent to 76 J/g. The peak temperature rises in the graphite due to the impact of an electron beam is \sim 100°C (see Fig. 3.26 right).

3.5.4 Parameter tables

The parameters of the main elements of the injection and extraction systems are listed in the following tables.

3.6 Beam diagnostics requirements and concepts

The beam diagnostic requirements for FCC-ee are, to a large extent, defined using the experience gained from LEP operation (1) [340], existing electron positron colliders (2) [341] and from the low emittance ring community (3) [342]. Based on

Table 3.17. Parameters for FCC-ee beam dump extraction kicker systems, for Z and $t\bar{t}$ operation.

Parameter	Unit	Z operation	$t\bar{t}$ value
Deflection angle	mrad	0.5	0.5
Vertical gap	mm	50	50
Horizontal gap	mm	70	70
Flat-top length	μs	333	333
Flat-top ripple	$\pm\%$	5	5
System impedance	Ω	6.25	6.25
$B\rho$	Tm	151.7	583.3
Magnetic length	m	1.5	6
Modules		1	4
Magnetic field	T	0.0506	0.0486
Current	A		
dI/dT	kA/ μs	2.01	1.93
Magnet filling time	ns	422	422
Switch voltage	kV	25.1	24.2

Table 3.18. Parameters for FCC-ee beam dump dilution kicker system, for 175 GeV $t\bar{t}$ operation.

Parameter	Unit	$t\bar{t}$ value
Drift to dump	m	2400.0
Outer sweep radius	mm	200.0
Maximum deflection angle	mrad	0.083
Field	T	0.0486
Vertical gap	mm	70
Horizontal gap	mm	70
Magnet length	m	1
Number of turns		57
Sweep length	μs	333.0
Maximum frequency	kHz	193
Number of modules		1
Inductance (incl. cables + stray)	μH	3.757
Current	A	2707.8
Max dI/dT	kA/ μs	3.28
Switch voltage	kV	12.34

Table 3.19. Parameters for FCC-ee beam dump extraction septum system, for 175 GeV $t\bar{t}$ operation.

Parameter	Unit	$t\bar{t}$ value
Deflection angle (vertical)	mrad	-12
Total magnetic length	m	16.0
Modules		4
Magnetic field	T	0.44
Septum width	mm	10
Beam aperture	mm	40
Total length	m	19.0

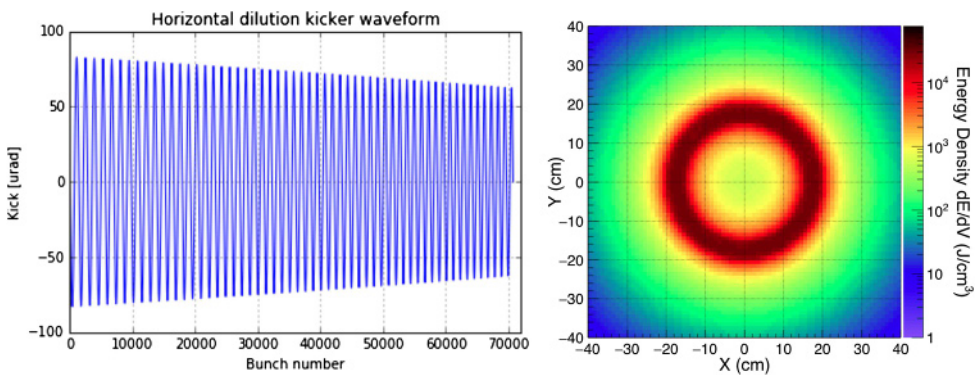


Fig. 3.26. Waveform of horizontal dilution kicker and energy deposition at 100 cm depth in graphite dump block, for a 57 turn sweep. The sweep frequency increases from 152 to 193 kHz, while the amplitude decreases from 83 to 60 μrad . The vertical kicker waveform is virtually identical with a $\pi/2$ phase shift. The spacing between bunches and between turns is 0.89 mm.

Table 3.20. Basic FCC-ee parameters of relevance for operation of beam diagnostic devices.

	Number of Bunches	Bunch Charge (e)	Beam Current (mA)	Bunch Spacing (ns)	Bunch Length (ps)	Transverse Size in Arc (μm) $\beta_x = 16\text{ m}, \beta_y = 100\text{ m}$
Min.	48	1×10^{10}	0.005	2.5	6	H: 60, V: 10
Max.	16640	2.3×10^{11}	1390	4000	40	H: 150, V: 20

the outcome of this comparison a baseline suite of beam diagnostics is proposed for FCC-ee. Any areas where further research and development is required to fulfil FCC-ee specifications are highlighted. The main beam parameters with an influence on beam instrumentation are summarised in Table 3.20.

In addition, the following machine conditions will also impact beam instrumentation:

- A large integrated radiation dose of 1–2 MGy is expected in the arcs, e.g. Figures 3.34 and 3.13, and should be taken into account when designing beam instrumentation. Shielding and radiation hardness need to be considered for any electronics located in the accelerator tunnel.
- Up to 2 MJ stored beam energy is expected in the booster ring. Injection into the main ring will, therefore, be critical and an appropriate machine protection system needs to be put in place to guarantee a safe operation of the machine.
- Transverse beam instabilities induced by electron cloud or fast ion instabilities from residual gas are a concern for FCC-ee and mitigation techniques will be put in place to minimise their impact on emittance growth. Moreover, recently a coherent $x-z$ instability due to beam–beam effects has been discovered in simulations [343,344]. This would increase the horizontal emittance by a large factor, which, via betatron coupling, would also cause vertical emittance dilution. A mitigation technique, which was studied to minimise the impact on luminosity, proposes a gradual increase of the bunch intensity while colliding. Known as “bootstrapping”, this scheme would require accurate bunch-by-bunch, turn-by-turn intensity and emittance monitoring systems. It also lowers the minimum measurable intensity for all instrumentation.

3.6.1 Beam position monitoring

The FCC-ee will be equipped with 1450 main quadrupoles per ring. Each quadrupole will have an associated beam position monitor (BPM). This yields a total of some 2000 BPMs per ring, including the long straight sections and interaction regions. Button-BPM sensors can be used in the arcs, while stripline monitors capable of distinguishing the counter-propagating beams will be required in the common beam pipe regions close to the interaction points. All electrodes will be placed at 45° in the x - y plane to avoid direct impact of synchrotron radiation, as is standard for electron synchrotrons. The geometry of the button pick-up must be optimised from the impedance and heat transfer point of view. A BPM design with a conical button, similar to the one used in SIRIUS [345], could be considered in order to push the higher order modes trapped in the BPM structure to higher frequencies. Initial simulations show that the power loss in such a BPM would be some 400 W, leading to a non-negligible total power loss of ~ 1 MW per ring [346].

To achieve the desired vertical emittances the machine must be aligned to better than $50\ \mu\text{m}$, which imposes stringent limits on BPM alignment and accuracy. The system must be capable of providing orbit measurements with sub-micron resolution and turn-by-turn data for injection oscillations, optics measurements and post mortem analysis with a resolution of a few microns. A similar performance is already achieved in 3rd generation light sources [347,348]. Their acquisition systems are based on parallel acquisition of time and frequency domain data with both RF and digital cross-bar switching [349] to minimize offsets due to slow electronic drifts and input intensity variations. The time domain signals allow bunch-by-bunch acquisition for injection oscillations and optics measurements, while the narrowband, frequency domain processing gives a high-resolution average position for the orbit measurements, which are used as input to the orbit feedback system.

The sensor and front-end electronics, comprising analogue signal shaping and digitisation circuitry would need to be located in the tunnel. A radiation-hard, bi-directional, fibre-optics link [350] could then connect each station to the processing electronics located on the surface. The challenge will lie in designing a cost effective solution, where the front-end electronics can be qualified to function in the radiation environment.

One limitation of the BPM in the common beam-pipe regions near the interaction points is the cross-talk between the two counter-propagating beams. These are also the BPMs where the requirements on precision and reproducibility are typically the most stringent. One option for FCC-ee would be to use optical BPMs relying on highly directional Čerenkov diffraction radiation [351], which becomes feasible at large distances at such high energies. It is estimated that a factor 20 improvement could be achieved using such a technique, but this still needs to be validated through further study.

3.6.2 Beam size monitoring

Beam emittance measurements, derived from the measurement of beam size must be provided on a bunch-by-bunch basis. In synchrotron rings, the measurement of small transverse beam sizes is typically performed using synchrotron radiation using x-ray imaging techniques [352–354] or visible light interferometry [355,356]. However, in the case of FCC-ee with extremely high beam energies, these techniques are no longer directly applicable as diffraction effects become dominant even in the X-ray domain. A possible solution under study is to use a two-slit X-ray interferometer to overcome this limitation [357]. Taking the source point as the last bending dipole of

the arc, a distance of ~ 100 m is necessary to separate sufficiently the photon beam from the electron or positron beam, to allow its extraction through a beryllium window. A K-edge filter can nicely select wavelengths of ~ 0.1 nm, before the X-ray photons enter the double slits of the interferometer. These can have a construction similar to a crotch absorber in synchrotron light sources. The transmitted X-rays can be separated from high energy X-rays using an elliptically deformed totally reflecting mirror to give a small, $\sim 1^\circ$ deflection. A further distance of ~ 100 m is then necessary to provide the required magnification to resolve the diffraction fringes.

The total space required for such an installation is non-negligible and needs to be considered as part of the general layout of the end-of-arc region at one location in the machine.

X-ray interferometry using near-field speckles are also being studied in this context [358]. A simpler solution may be to use Čerenkov diffraction radiation imaging systems [359], but this technique will require more R&D to prove that it can achieve the required spatial resolution.

3.6.3 Bunch length monitoring

The bunch length will be important to monitor the strength of the beamstrahlung at the interaction points and for energy calibration. As for the transverse beam size, bunch length measurements must be provided on a bunch-by-bunch basis, with the measurement of all bunches available on a time scale of minutes. The accuracy is completely dominated by the requirements of energy spread determination for energy calibration, where a resolution well below 100 fs is requested. The measurement of short bunches on ps time scales can be performed using synchrotron radiation emitted in the visible range and detected by a streak camera. Such measurements were pioneered at LEP [360] and have been further improved to provide sub-ps time resolution [361]. An alternative is the use of electro-optical crystal and short laser pulses, a technique that has been demonstrated to provide single-shot longitudinal profile measurements for ps bunches with sub-ps resolution [362]. Nevertheless, the bunch-by-bunch measurement of ps bunches with resolution well below 100 fs remains a challenge that will require further R&D.

3.6.4 Beam current and intensity measurements

Beam-current and intensity monitors must provide the total circulating current and the relative bunch-by-bunch intensities. The individual bunch currents must be transmitted to the top-up injection system to control the refill rate and stabilise the bunch intensities. These systems should also provide the overall beam lifetime and bunch-by-bunch lifetimes, that can be used to tune the machine and, for machine protection purposes, to trigger a beam abort when the total loss rate is too high.

For the bunch-by-bunch measurement, a wall current transformer coupled to fast digitisation electronics is proposed. A recent upgrade of the LHC system using such technology, combined with numerical integration, has already reached the required performance for bunches spaced by 25 ns [363]. The challenge lies in achieving the same bunch-by-bunch performance with bunch spacings which could possibly be as short as 5 ns, where improvements to both the bandwidth of the sensor and the acquisition electronics are required.

3.6.5 Beam loss monitoring

A global Beam Loss Monitoring (BLM) system will be required based on devices that are not sensitive to the SR; see e.g. [364]. The overall requirements for this system are yet to be specified. Special BLMs capable of turn-by-turn and possibly bunch-by-bunch acquisition will also be required near aperture restrictions, for example next to collimators.

3.6.6 Topics for further study

While the beam instrumentation required for FCC-ee brings new challenges, most seem feasible with modest advances to the standard technology currently employed by existing electron-positron colliders or 3rd generation synchrotron light sources. However, there are a few critical items that will require significant further R&D to reach the demanding requirements set by FCC-ee. These are listed below:

- The measurement of small beam sizes at such high energies. The feasibility of using interferometric techniques with synchrotron radiation at X-ray wavelengths to achieve the necessary resolution for FCC-ee type beams still needs to be demonstrated.
- The measurement of ps bunches with a resolution of some tens of fs. This is currently beyond the limit of streak cameras and poses issues for electro-optical sampling techniques as a relatively long bunch has to be measured with extremely fine resolution.
- Alternative non-invasive measurement techniques. Čerenkov diffraction radiation is proving to be a useful tool to measure beam properties non-invasively. The technique could be envisaged to provide a high directivity beam position monitor, non-invasive beam imaging or to monitor fast intra-bunch transverse instabilities if acquired with a streak camera. However, the application of this technique to beam diagnostics is still in its infancy and significant further R&D is required to demonstrate that it can achieve all that it promises.

3.7 Combined polarimeter and spectrometer

The resonant depolarisation technique planned for FCC-ee beam energy determination [248,365] requires polarimeters able to measure the polarisation of both electron and positron beams with a precision of $\pm 1\%$ every few seconds both for the pilot, non-colliding bunches, and for the colliding bunches themselves. This is not very different from what was obtained at LEP [247,366] using Inverse Compton scattering (ICS) of a 530 nm pulsed laser on the electron beam. In that case the backscattered photons were detected in a small, vertically segmented silicon-tungsten calorimeter, via a specially designed beam pipe, with the laser beam injected in the vacuum pipe by a system of retractable mirrors. Two similar systems will be required at FCC-ee, one for the positrons and one for the electrons (in the following “electron” will be used for either e^+ and e^-). Given the strong requirements on continuous monitoring, it is proposed to measure not only the backscattered photon beam, but simultaneously the joined angular and momentum distributions of the scattered electrons, as described by Muchnoi [367,368]. The latter provides monitoring of both transverse and longitudinal polarisation of the beam, as well as a determination of the beam energy with a relative precision of 3×10^{-4} in a one second long measurement.

The principle of the device was illustrated in Figure 2.40. The laser beam is inserted into the machine vacuum chamber and focused onto the laser-beam interaction point. This laser-beam IP is situated upstream of a dipole which separates

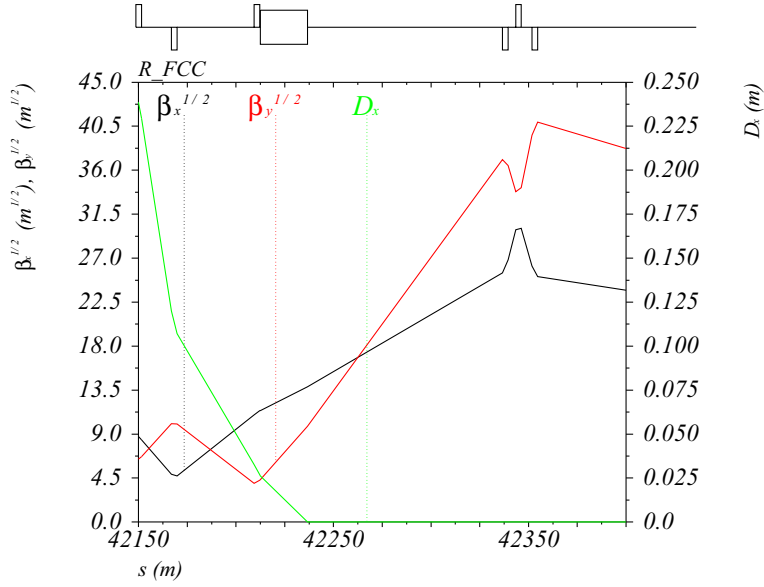


Fig. 3.27. Location of the polarimeter with respect to the FCC-ee lattice.

the scattered photons and electrons from the electron beam, and allows them to be extracted from the vacuum chamber. They will be detected in a plane situated 100 m from the dipole. It is important that there are no quadrupoles along the trajectory of the electrons over this distance. The dipole also serves as a spectrometer and should be specially measured and monitored. The scattered electrons can have energies ranging from the full beam energy down to a minimum energy E_{\min} , while the backscattered photon energies range from 0 to $\omega_{\max} = E_{\text{beam}} - E_{\min}$, with

$$E_{\min} = \frac{E_{\text{beam}}}{1 + \kappa} \quad (3.1)$$

with

$$\kappa = 4 \frac{\omega_0 E_{\text{beam}}}{(m_e c^2)^2}. \quad (3.2)$$

For a 530 nm laser (photons of energy $\omega_0 = 2.33$ eV) on a 50 GeV electron $\kappa = 1.9$. The distance between the backscattered photon spot and the end point (lowest energy) of the scattered electron swathe provides the energy measurement. The angular size of the scattered photon beam is dominated by the angular distribution in the Compton scattering, so, in spite of the much smaller electron beam emittance it will not be smaller than at LEP.

The polarimeter can be installed in the FCC-ee as shown in Figure 3.27, on the last dispersion suppressor dipole of the beam situated on the inside of the ring and entering one of the short straight sections. The electron and positron polarimeters have to be in different straight sections. Downstream of the dispersion suppressor dipole magnet, about 100 m of free beam propagation is reserved to allow clear separation of the ICS photons and electrons from the beam. The interaction of the pulsed laser beam with the electron beam occurs just between the dipole and preceding quadrupole, where there is a local minimum of the vertical β -function. Figure 3.28 shows a sketch of the polarimeter detector arrangement in the horizontal plane.

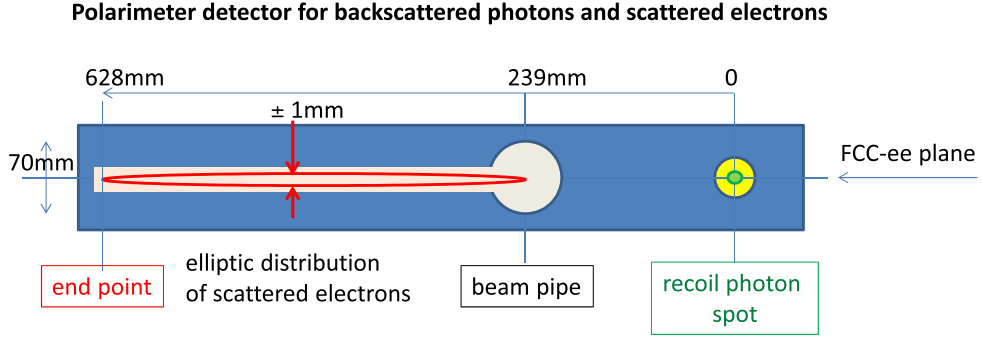


Fig. 3.28. Sketch of the detector assembly of the FCC-ee detector for backscattered photons (green) and scattered electrons (red). The detectors are assumed to be assembled into a single frame of temperature insensitive material, surrounding the beam pipe.

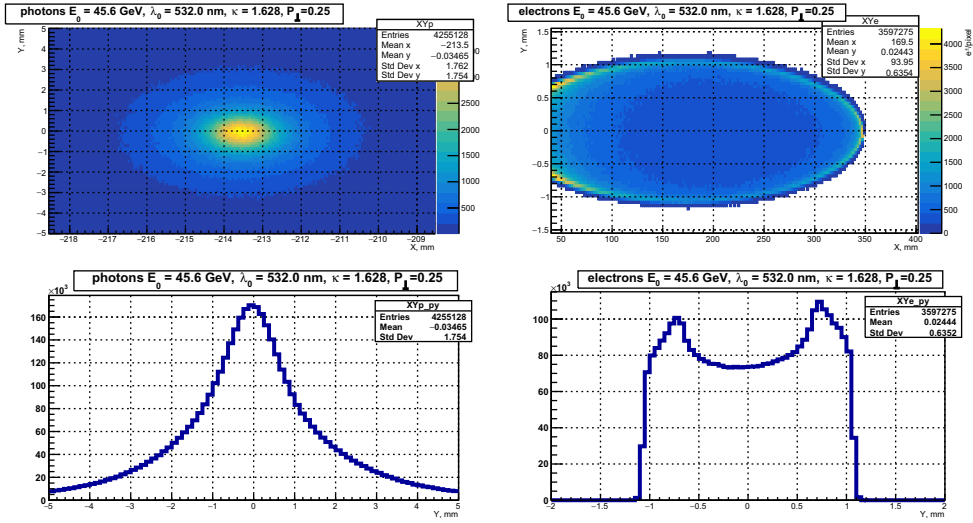


Fig. 3.29. MC results for $P_\perp = \xi_0 \zeta_\perp = 0.25$ and $\phi_\perp = \pi/2$.

A Monte-Carlo generator was written to generate the 2D (x, y) distributions of scattered photons and electrons at the detectors in the particular location and beam emittance of FCC-ee. The beam and laser energies are: $E_{\text{beam}} = 45.6$ GeV and $\omega_0 = 2.33$ eV. The spectrometer configuration is determined by the dipole bending angle $\theta_0 = 2.134$ mrad, the length of the dipole $L = 24.12$ m, the distance $L_1 = 117$ m between the laser-electron IP and the detector, and $L_2 = 100$ m is the distance between the longitudinal centre of the dipole and the detector.

The results of the simulation for an electron beam with 25% vertical spin polarisation are presented in Figures 3.29 and 3.30 for positive or negative circular polarisation of the laser. The 2D distributions for both photons and electrons are plotted. The 1D distributions in the bottom of each figure are the projections of 2D distributions to the vertical axis y . The mean y -values of these distributions are shifted up or down from zero according to the presence of beam polarisation and laser light circular polarisation and corresponding asymmetries in ICS cross section.

The difference of these distributions upon reversal of the laser polarisation is shown in Figure 3.31. Detecting the up-down asymmetry in the distribution of laser

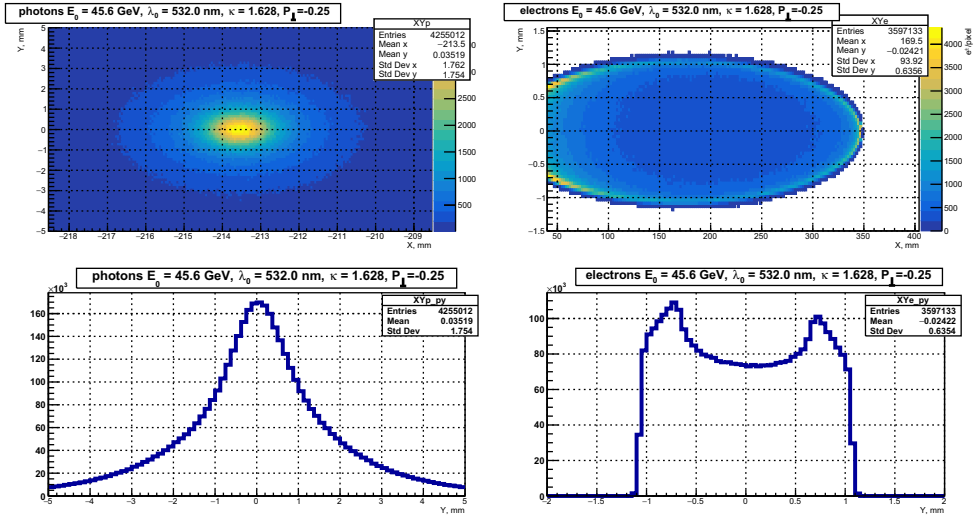


Fig. 3.30. MC results for $P_{\perp} = \xi_0 \zeta_{\perp} = -0.25$ and $\phi_{\perp} = \pi/2$.

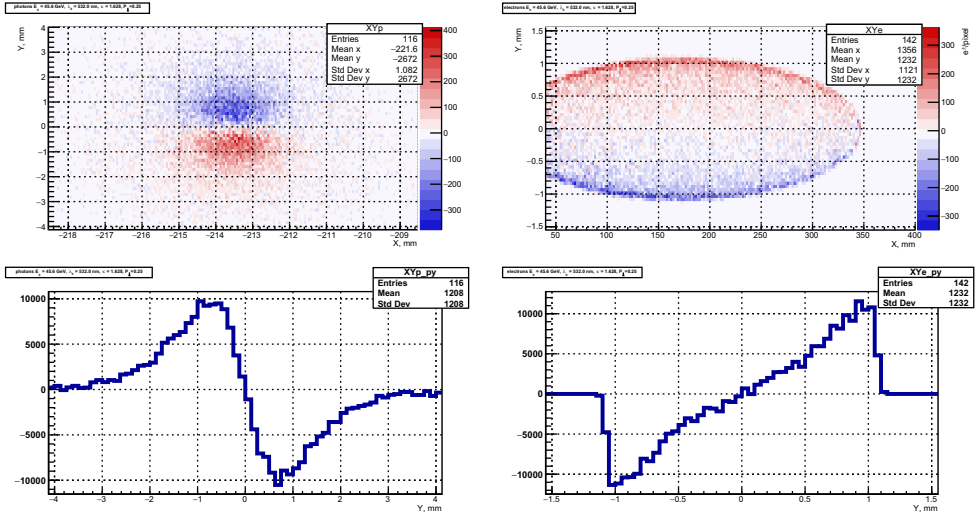


Fig. 3.31. The difference between corresponding distributions in Figures 3.29 and 3.30.

backscattered photons is a classical way to measure the transverse polarisation of the electron beam. In [369] it was proposed to use the up-down asymmetry in the distribution of scattered electrons for the transverse polarisation measurement. Measuring the distribution of scattered electrons by Silicon pixel detectors, a technology which is well developed and very radiation resistant, has been suggested. The results presented in Figure 3.32 were obtained with 2×10^7 backscattered MC events and about 1.44×10^7 of them were accepted by the scattered-electron detector. The beam polarisation degree P_{\perp} , is measured with 0.16% absolute statistical accuracy, the beam energy with a precision of 3 MeV. The knowledge of the absolute scale of the beam polarisation is unnecessary for the RDP technique.

At the FCC-ee polarised pilot bunches will be used for regular beam energy measurement by resonant depolarisation. So the laser system should provide the backscattering on a certain electron bunch, and laser operation in CW mode is thus

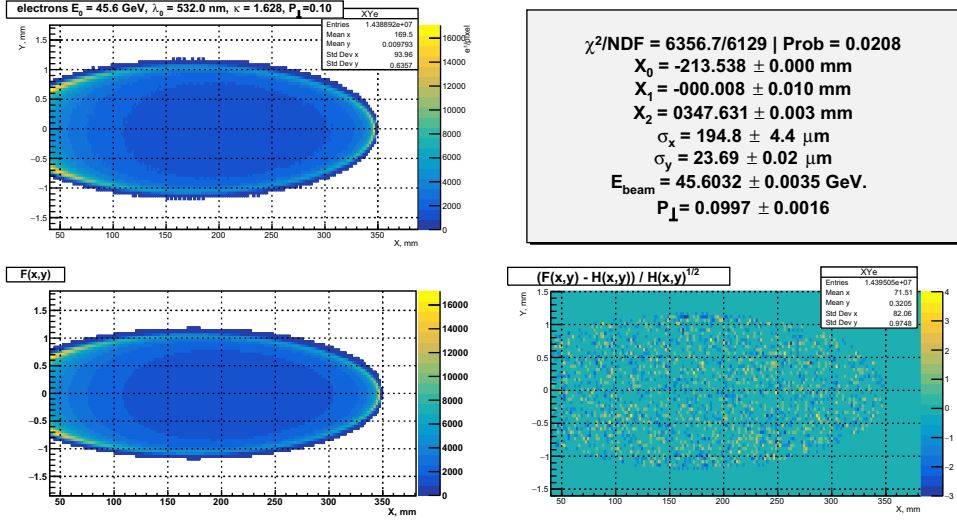


Fig. 3.32. Top-left: MC distribution of scattered electrons $H(x, y)$. Bottom-left: function $F(x, y)$ after fitting. Bottom-right: normalised difference: $(F(x, y) - H(x, y)) / \sqrt{H(x, y)}$. Top-right: the $F(x, y)$ parameters obtained by fitting (except X_0 , which is the mean x value of the scattered photons distribution).

not possible. The FCC-ee revolution frequency $\simeq 3$ kHz is comfortable for solid-state lasers operating in a Q-switched regime.

The parameters of the system are thus as follows:

- laser wavelength $\lambda_0 = 532$ nm;
- Compton cross-section correction $R_x \simeq 50\%$;
- waist size $\sigma_0 = 0.25$ mm, Rayleigh length $z_R = 148$ cm;
- far-field divergence $\theta = 0.169$ mrad;
- interaction angle $\alpha = 1.0$ mrad (horizontal crossing);
- laser pulse energy: $E_L = 1$ [mJ], pulse length: $\tau_L = 5$ [ns] (sigma);
- instantaneous laser power: $P_L = 80$ [kW], $P_L/P_c = 1.1 \times 10^{-6}$;
- ratio of laser crossing angle with beam, to laser divergence: $R_A = 5.9$, ratio of lengths of laser pulse to electron bunch length $R_L = 0.98$;
- efficiency of laser beam interaction: $\eta(R_L, R_A) \simeq 13\%$;
- scattering probability $W = P_L/P_c \cdot R_x \cdot \eta(R_L, R_A) \simeq 7 \times 10^{-8}$;
- with $N_e = 10^{10}$ e/bunch and $f = 3$ kHz rep. rate: $\dot{N}_\gamma = f \cdot N_e \cdot W \simeq 2 \times 10^6$ [s $^{-1}$];
- average laser power is $P = f \cdot E_L \simeq 3$ W.

More details can be found in [370]. The precisions given above can therefore be obtained every 20 s. The influence of the electron beam sizes on the above estimations is negligible.

To conclude, a combined polarimeter-spectrometer for FCC-ee has been proposed and the FCC-ee optics has been chosen for it; first studies of implementation and performance have been made. With commercially available lasers, the transverse beam polarisation can be measured with the required $\pm 1\%$ accuracy in one second. An independent beam energy estimate of $\Delta E/E \simeq 300$ ppm is available every second. The residual longitudinal polarisation can also be measured. The possible sources of systematic errors on the energy measurement require additional studies. Once the RDP is performed regularly, frequent cross-calibrations of the spectrometer can be made by comparison with the RDP result; this, combined with the measurements

of energy differences between e^+ and e^- at the interaction points could provide powerful cross-checks of the energy model.

A detailed design will be necessary for the beam pipe insertions, the laser room and light box, the detector including its precision mechanical support and radiation protection, and an integrated data acquisition of the detector data and beam parameters.

3.8 Halo collimators

For detector-background control and to cut off the beam halo, about 20 movable low-impedance collimators will be required (10 per plane). These will be positioned in strategic locations around the two collider rings. The collimator design can be similar to those of PEP-II [371] and SuperKEKB [372]. The corresponding impedance and a CST computer model of such a collimator are discussed in Section 2.6.6.

3.9 Machine protection

In the Z running mode a total energy of 4 MJ is stored in the FCC-ee beams. This is more than two orders of magnitude lower than the energy stored in the LHC or FCC-hh proton beams, and even lower than the energy stored in a linear-collider bunch train, e.g. at ILC or CLIC. While a linear collider dumps such a beam up to hundred times per second, beam dumps at the FCC-ee will be a rare exception. An appropriate machine protection system, with an early detection of beam instabilities or relevant technical failure modes, will trigger a beam abort, and safely extract the FCC-ee beams to their corresponding beam dumps, before any damage to machine components can occur.

Unavoidable collision-related beam losses will continually impact machine components, however. For a beam lifetime of 20 min, in all operation modes the total beam loss power is less than 20 kW. If these losses are limited to a few locations, the latter require appropriate shielding and cooling measures.

The energy stored in the magnets is tremendously reduced compared with the energy stored in the high-field superconducting magnets of the LHC or FCC-hh.

3.9.1 Architecture and powering of magnet circuits

With normal-conducting main magnets in the baseline design, the architecture of the magnet circuits is largely simplified with respect to the hadron machine [373]. The main limitations will be related to the overall power consumption and energy efficiency during the operational cycle, which should be considered at the design phase of the magnets and power converters.

3.9.2 Magnet protection and energy extraction

Protecting a normal-conducting magnet will focus on mitigating the possibility of overheating of the magnets and the associated powering components. This can be achieved by designing the magnet with sufficient margins, including cooling, and by an active protection system, which has interlocks for thermal overheating and loss of cooling. The main dipole chain, the arc quadrupole circuits, the sextupole families and critical IR magnets may require active interlocks. A suitable level of reliability and availability needs to be defined.

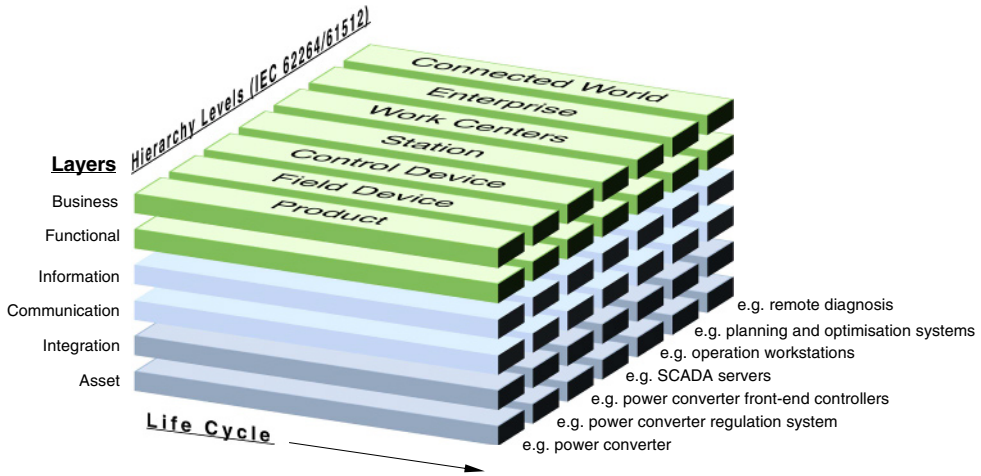


Fig. 3.33. Reference Industry 4.0 architecture model.

3.9.3 Beam protection concepts

A balance between availability and reliability can be obtained for the major systems involved in machine protection by introducing a voting logic on redundant interlock channels. A voting logic – of at least three redundant connections – will, in addition, facilitate the testing of the beam interlock system from the user side up to the beam dumping system.

Detailed studies of fast failures arising from the short decay time constants of the normal conducting magnets circuits need to be performed, in particular for magnets in regions with high beta functions.

While the stored beam energies will result in much reduced risks of damaging accelerator equipment by local beam losses compared with hadron machines, the activation of the machine remains a point of concern. This is true, in particular, for the injection and extraction regions, which typically are regions of higher accumulated losses, and also for the vicinity of the positron production target in the injector complex. A beam interlock system for a loss-free beam transfer will be implemented for electron injection into, and extraction from, the collider.

3.10 Controls requirements and concepts

With the ever larger particle accelerator facilities that have been constructed over the last two decades [374–377] and the entry of versatile particle accelerators in industry and healthcare, the development of control systems for particle accelerators has become a well understood task. The work of companies worldwide towards an Industry 4.0 architecture [378] extends the traditional architecture with enterprise resource planning and intelligent device tiers in the hierarchy and includes life cycle and functional layers (see Fig. 3.33).

With a steady increase of computing and communication technology capacities, a move to wireless communication including safety-related data exchange and ever more flexible embedded computing systems and re-programmable hardware, functionality is shifting from the upper tiers of the system architecture to the lower ones. Front-end systems that are cooperating more autonomously can overcome the constraints that result from centralised control over long distances. Scalable synchronisation and the reliable coordination of actions on a time scale of ns to support

Table 3.21. Number of front-end control units in different systems.

Category	System	Number of front-end control units
Particle accelerator	CERN PS booster	81
Particle accelerator	CERN PS	115
Particle accelerator	XFEL	ca. 200
Particle accelerator	CERN SPS	257
Particle accelerator	CERN LHC	525
Aerospace	International space station	660
Particle accelerator	Future circular collider	ca. 1500
Fusion research	ITER	ca. 5000 expected

acquired data correlation are soon to be widely available [379–383]. Femtosecond timing distribution over kilometer distances, as currently used in free electron lasers [384,385], demonstrates that the performance of timing systems can already meet FCC collider (hh, ee, and HE) demands. An ever better understanding of how to adapt off-the-shelf designs to radiation environments leads to more affordable intelligent controls in equipment that has to be close to the accelerator [386]. Industry is asking for greater use of commercial-off-the-shelf (COTS) components in mission-critical applications [387–391] and the factory of the future [392] has comparable requirements and these facts will drive the development of commercially available technologies within a few years [393].

Although the system sizes are gradually increasing (see Tab. 3.21), the main challenges for a control system infrastructure are shifting from technical to organisational domains. The potential loss of expertise from previous projects needs to be mitigated by establishing a system-engineering process [394,395] with adequate documentation support to capture operation requirements, architecture and design components as well as end-to-end test scenarios, well before a new facility is constructed.

Developers of industrial embedded systems have understood that traditional programming is a time consuming, costly and error-prone activity [396]. Particle accelerators are no exception and therefore new development paradigms are needed to come to a sustainable long-term operation concept, reducing loss of knowledge, easing the management of software and its evolution and facilitating working with external partners in a cost effective way. Medical particle accelerator facilities have been successfully applying this approach for several years [397–402]. The need for continuous operation of CERN’s particle accelerator complex calls for a gradual modernisation that has to be mastered from a managerial perspective. Such a scheme indicates a gradual evolution towards a new generation of accelerator control systems. It allows suitable concepts to be assessed early using the existing accelerators as test beds for new concepts.

Although fault-tolerant designs can help to meet the reliability requirements of these geographically extended machines, automated and remote maintenance/repair will play a role in ensuring the overall availability of a particle accelerator. As embedded systems become more powerful and flexible they also become more vulnerable to intentional and unintentional misuse. Cyber-security became an important concern during the development of the control systems for the LHC [403]. For a future facility, this topic needs to be included from the beginning in the systems engineering process in close cooperation with the planning for the IT infrastructure. A well coordinated, complex-wide information and communication technology management environment covering requirements, planning, procurement, maintenance and upgrades will help accelerator groups to focus on the provision of the core

control functionality. This approach will ease the transition towards the concept of “Controls as a Service” which can evolve and scale with the underlying technology platforms, focusing on technology independence as much as reasonably possible.

As is the case in other domains [404], support for closed-loop settings optimisation and including an accelerator physics point of view towards controls will help to improve the efficiency of the accelerator complex [405]. This will become possible with the higher computing power and data exchange capacities, more flexible analysis using “Big Data” approaches, the introduction of machine learning, model driven approaches and an end-to-end cost/benefit sensitivity analysis.

3.11 Radiation environment

3.11.1 Reference radiation levels

Radiation levels in the collider scale with energy and, as LHC has shown, degradation of components exposed to radiation can become an operation-limiting factor. Two complementary approaches are needed: the reduction of the dose to equipment by shielding (e.g. local shielding around the photon stops, as discussed in Sect. 3.3.4) and developing fault tolerant or radiation resistant electronics and equipment. A structured approach for radiation hardness assurance (RHA) will ensure that the electronics and materials developed perform to their design specifications after exposure to the radiation in the collider environment.

Radiation to electronics (R2E) is an issue in the design of any high energy and high intensity machine [406]. Radiation effects in electronic devices can be divided into two main categories: cumulative effects and stochastic effects (Single Event Effects – SEE). Cumulative effects are proportional to the total ionising dose (TID) – the damage induced by ionising radiation, and the 1 MeV neutron-equivalent fluence which concerns displacement damage. On the other hand, SEE, which are proportional to the high energy hadron fluence (HEH, i.e. hadrons with energies >20 MeV), are due to the direct or indirect ionisation by a single particle which is able to deposit sufficient energy to disturb the operation of the device. SEE can only be defined by their probability to occur and the effect strongly depends on the device, the intensity and the kind of radiation field. The FCC-ee staging schedule which has several operational phases at energies of 45.6, 80, 120, and 170–175 GeV, before the highest energy of 182.5 GeV is reached, gives confidence for the selection process of radiation-hard equipment. In addition, using shielded alcoves to house electronics will reduce the radiation levels, thus increasing the equipment lifetimes and reducing the probability of stochastic effects.

Monte Carlo (MC) simulation is an indispensable tool to evaluate the impact of radiation on the machine equipment, but it relies on both a refined implementation of physics models of the particle interaction with matter and an accurate 3D-description of the region of interest. In this context, FLUKA [407,408] which is widely employed at CERN, is a well benchmarked, multi-purpose and fully integrated particle physics MC code for calculations of particle transport and interactions with matter. FLUKA is employed in the majority of CERN technical and engineering applications such as machine protection, energy deposition calculations, damage to accelerator elements and shielding design. For a high intensity and energy machine like FCC-ee, typical sources of radiation are luminosity debris, direct losses on collimators and dumps and, particularly for the ee collider, synchrotron radiation.

A FLUKA model of half an arc cell has been created [409]. The geometry consists of a 25 m long half FODO cell, with five absorbers 24 cm long each. While the geometry parameters are still being optimised, no major impact on the efficiency

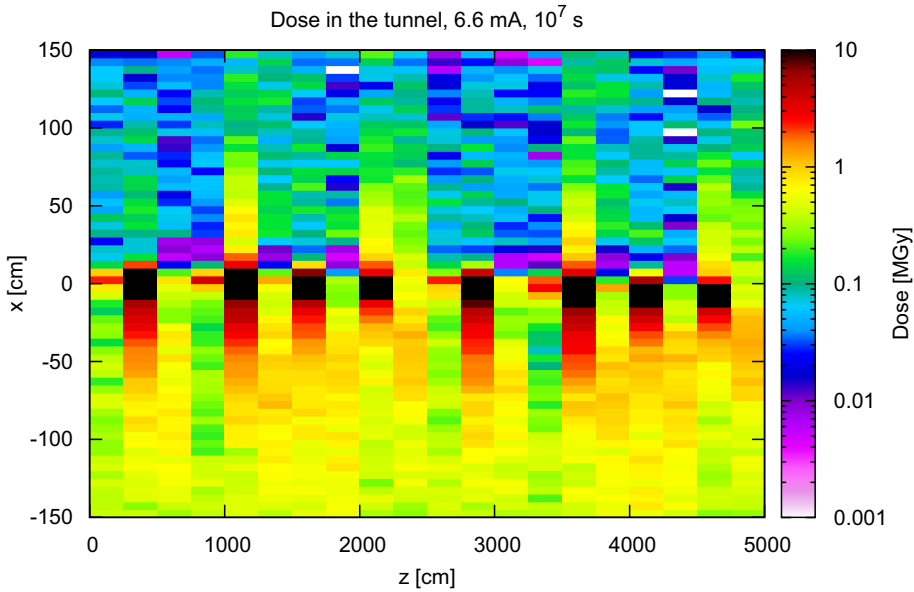


Fig. 3.34. Dose distribution in an FCC-ee arc half-cell. Results were normalised for 10^7 s of data taking and a beam current of 6.6 mA.

of the local shielding, the residual radiation to equipment or the critical radiation levels for the electronics is expected.

FLUKA was set up to sample, from the 175 GeV electron beam, an SR spectrum taking into account the photon angular distribution and polarisation. Photonuclear production was enabled and variance reduction techniques were applied to obtain a statistically meaningful result. Figure 3.34 shows the dose distribution in the beam plane. Similar distributions are found for the HEH and 1 MeV neutron equivalent fluence.

The pattern in Figure 3.34 shows hot spots along the beam pipe corresponding to the interconnects where the synchrotron radiation absorbers are placed. The results show that equipment installed in certain locations in the tunnel will be affected by the TID effects which will limit the equipment lifetime, in addition to experiencing SEE failures. In particular, the TID values of the order of 100 kGy–1 MGy are an enormous challenge for the electronics in the vicinity of the FCC-ee machine, and they will limit the use of COTS components, which typically have limits in the 50 Gy–1 kGy range. For this reason, the quantity of active electronics needs to be minimised and based on components which are “radiation-hardened by design”, as is the case for high-criticality space missions, high-energy physics experiments or ITER. The impact of the radiation-hardened design on the cost, availability and lead time of the components is significant.

3.11.2 Radiation hardness

As is the case for the present LHC machine, the power converters, beam position and loss monitors (BPM and BLM) and quench protection system (QPS) have to be close to the accelerator itself. Such equipment is mainly based on COTS components and therefore the equipment needs to be qualified for use in the radiation environment [410].

The FCC RHA strategy is based on a *full-availability* approach based on: (i) a remote control approach, moving the processing tasks from the equipment under control and (ii) failure self-diagnosis, online hot swapping and remote handling. System designs, therefore, are based on a modular approach, which will allow switching to a redundant sub-system without any impact on operation. This will be particularly beneficial for transient errors, which can typically be corrected with a reset. The approach will also relax the constraints on the error qualification limits, which will be obtained through accelerator radiation testing.

In the case of events which cause permanent effects such as hard SEEs (occurring stochastically) or cumulative damage, online hot-swapping will need to be complemented by the substitution of the faulty board. This procedure will need to be carefully optimised, especially for cumulative damage, where similar sub-systems exposed to similar radiation levels are expected to fail at around the same time. Therefore, remote handling and the possibility to replace faulty units with spares which have been stored in radiation-safe areas, is one way to mitigate the risk.

The proposed scheme will bring benefits from the use of a selected set of semiconductor components that can be used in different sub-systems. The related procurement and qualification processes can be optimised and the impact of variability in sensitivity across batches and deliveries can be reduced. In specific cases, the use of radiation-hardened solutions at component level (e.g. FPGA) can be considered in combination with the use of COTS devices.

3.11.3 Radiation-hard technology trends

In parallel with the rapid advance of electronics development and market trends, intensive work on radiation hardening is ongoing for electronics, components, materials and detectors with the main focus on HL-LHC. Continuous technology scouting and early technology analysis throughout the FCC design phase will be an important activity.

Communication links

A reliable, high performance communication link is a fundamental component of a new collider. It helps to move processing and control logic away from the radiation areas. Possibilities include fibre optic links and wireless technologies. A first study has been carried out on an Ethernet-based solution.

The basic building blocks of such a system can be seen in Figure 3.35. In this case, three components need to be radiation tolerant: the Ethernet physical layer component (PHY), a transceiver that bridges the digital world (including processors), field-programmable gate arrays (FPGAs), and application-specific integrated circuits (ASICs), which bridge to the analogue world. The Media Access Control (MAC) is usually integrated in a processor, FPGA or ASIC and controls the data-link-layer portion of the OSI model. Finally, an FPGA, a processor or an ASIC is needed to implement the application protocol. This solution will allow rates of several tens of Mbps with a low packet loss/failure factor to be reached.

Preliminary studies to evaluate the feasibility of using such a system to reliably transmit data over long distances in a radiation environment have been conducted [411]. This solution would use either hard or soft processors which are part of a microcontroller or FPGAs so that the system is able to conduct additional operations. The processor-based solution is not only chosen to simplify the implementation of transmission protocols, but also to process the input/output data. In

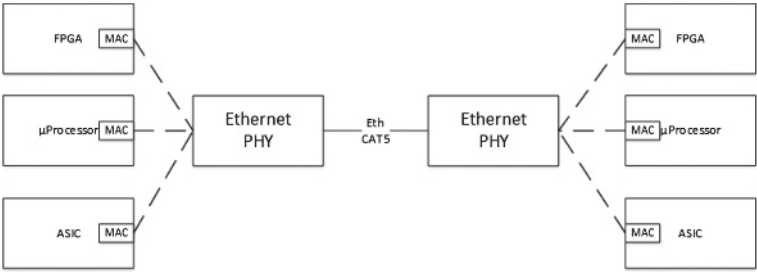


Fig. 3.35. Ethernet subsystem.

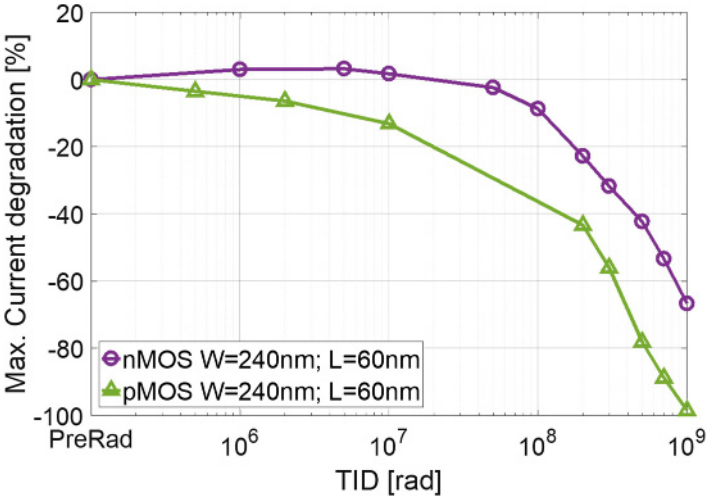


Fig. 3.36. Percent degradation of the current capability for small-size nMOS and pMOS transistors in the 65 nm technology node up to 10 MGy.

order to achieve higher radiation tolerance in terms of single event upset, the best choice would be the use of a radiation tolerant flash-based FPGA with a radiation mitigated soft-core processor implementing the application protocol.

CMOS technologies

Most of the on-detector ASICs being developed for HL-LHC make use of CMOS technologies in the 130 and 65 nm nodes. The study of radiation tolerance of these technologies has revealed that parasitic oxides used in the manufacturing processes are responsible for a significant degradation which limits their application. This is even the case in the pixel detector of the HL-LHC [412–414], where the current plan is to replace the inner detector layers after 5 years of operation. As an example, Figure 3.36 shows the dramatic degradation in the current capability of small size 65 nm transistors. This study is now extended to 40 and 28 nm technologies, where preliminary results show different phenomena and demonstrate slightly more promising radiation tolerance.

CMOS technologies have been shifted from planar to bulk FinFETs starting from a nominal gate length of about 22 nm and have now reached the 7 nm pattern size. The literature consistently [415] shows that TID tolerance has decreased with this miniaturisation due to radiation-induced leakage currents in the neck region of these

devices, a characteristic that cannot be addressed by any design technique. This evidence shows that the construction of reliable electronics systems for FCC detectors cannot simply rely on the improved radiation performance which accompanies miniaturisation, a concept exploited largely for LHC and HL-LHC. The situation calls for an R&D programme on technologies and front-end systems, possibly nurturing new concepts such as disposable detectors.

4 Civil engineering

4.1 Requirements and design considerations

The civil engineering design and planning is a key factor in establishing the feasibility of the FCC-ee. The machine tunnel will be one of the longest tunnels in the world; only water supply tunnels with smaller diameters are longer. It will be similar in scope to the recently completed Gotthard Base Tunnel (total of 151.84 km including two 57 km long tunnel tubes) in Switzerland.

Following analysis of various options, the tunnel layout is now quasi-circular. The current baseline layout has a circumference of 97.75 km. In addition to that, approximately 8 km of bypass tunnels, 18 shafts, 12 large caverns and 12 new surface sites are foreseen.

The emphasis for the study of the underground structures has been on locating the machine within the natural boundaries defined by the geological formations of the Geneva basin, with as short as possible connections to the existing CERN accelerator complex. For the access points and their associated surface structures, the focus has been on identifying possible locations which are feasible from socio-urbanistic and environmental perspectives. The construction methods, and hence the technical feasibility of construction has been studied and deemed achievable.

The underground structures for LEP were designed for a lifespan of 50 years. They were completed in 1989 and will thus reach the end of their specified lifetime around 2040. Refurbishment, continuous monitoring and maintenance are therefore necessary to extend their lifetime for use with a future particle collider. Such activities have already started to meet the requirements of the HL-LHC project.

4.2 Layout and placement

4.2.1 Layout

The principal structure for the FCC-ee collider is a quasi-circular 97.75 km long tunnel with 5.5 m internal diameter, comprising straight sections and arcs. In addition, large caverns are required at points PA and PG to house the experiments. These caverns have a maximum clear span of 35 m, which is at the limit of what is possible today, given the ground conditions. At each of the 12 access points around the ring, a service cavern with a span of 25 m is required. These caverns are connected to the surface via shafts with diameters ranging from 10 m to 18 m. Auxiliary structures are required in the form of connection and bypass tunnels and of alcoves, to house electrical equipment. Figure 4.1 shows a 3D, not-to-scale schematic of the underground structures. The chosen layout satisfies the requirements of the FCC-ee and the FCC-hh machine.

The excavation of the underground structures will produce approximately 9 million cubic metres of spoil. With the current placement, this will primarily be made up of sedimentary deposits, a mixture of marls and sandstone. A small fraction of the tunnel (approximately 5%) will be excavated in limestone.

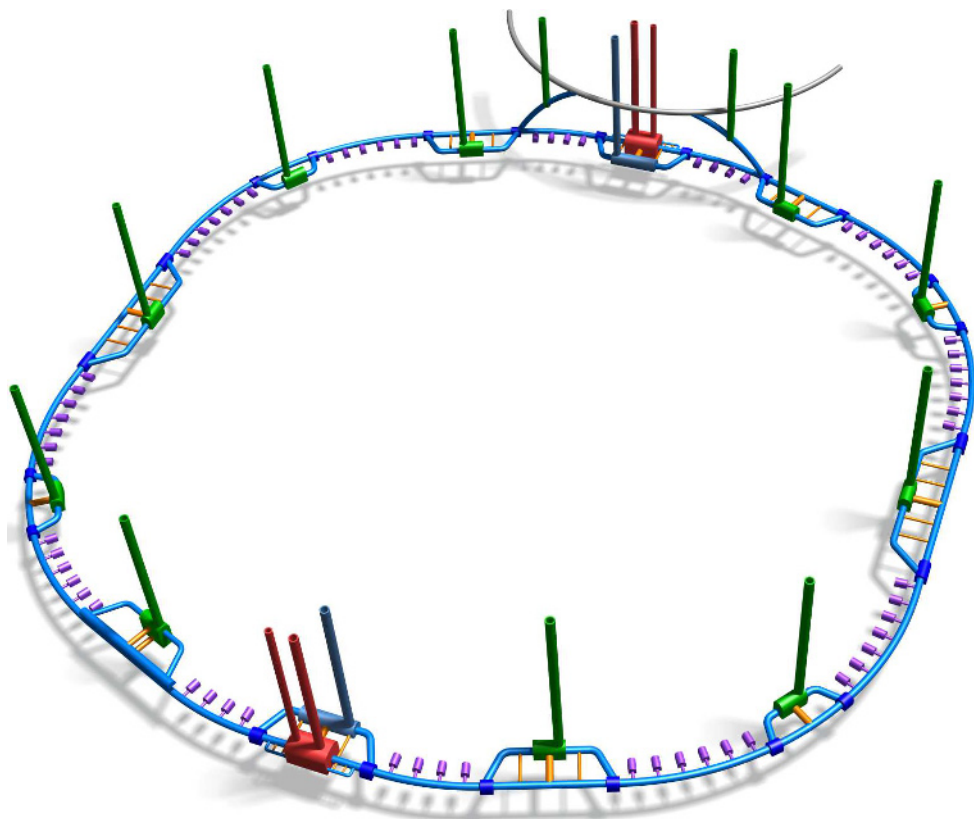


Fig. 4.1. 3D, not-to-scale schematic of the underground structures. The main collider tunnel and the service tunnels are indicated in blue colour. Connection caverns between main and service tunnels are indicated in dark blue colour. The two red caverns indicate the experiment caverns. They are reached by two, red marked, shafts: a large one for the detector elements and a smaller one for the service. Secondary caverns and shafts for detector-related equipment and services are shown in blue color next to the experiments. Technical equipment caverns and the shafts to access them are indicated in green colour. Yellow tubes indicate the connections between the machine tunnel and certain equipment galleries, for instance to connect the power sources to the radiofrequency cryomodules. Equipment alcoves along the entire machine tunnel are indicated in violet colour. The upper part of the image shows an exemplary connection to the injector accelerator.

4.2.2 Placement

Experience from the LEP and LHC construction has shown that the sedimentary rock in the Geneva Basin, known as molasse, provides good conditions for tunnelling. In contrast, during the excavation of the LEP tunnel, water ingress from the limestone formations in the Jura mountains caused significant problems. For this reason, one of the primary aims when positioning the FCC tunnel was to maximise the fraction of the tunnel in the molasse and minimise that in the limestone. Another prominent concern was to orientate the tunnel in a way that limited the depth around its perimeter, thereby minimising the depth of the shafts, reducing the overburden pressure on the underground structures, and reducing the length of service infrastructure (cables, ducts, pipes). These concerns, along with the need to connect to the existing accelerator chain, led to the definition of the study boundary,

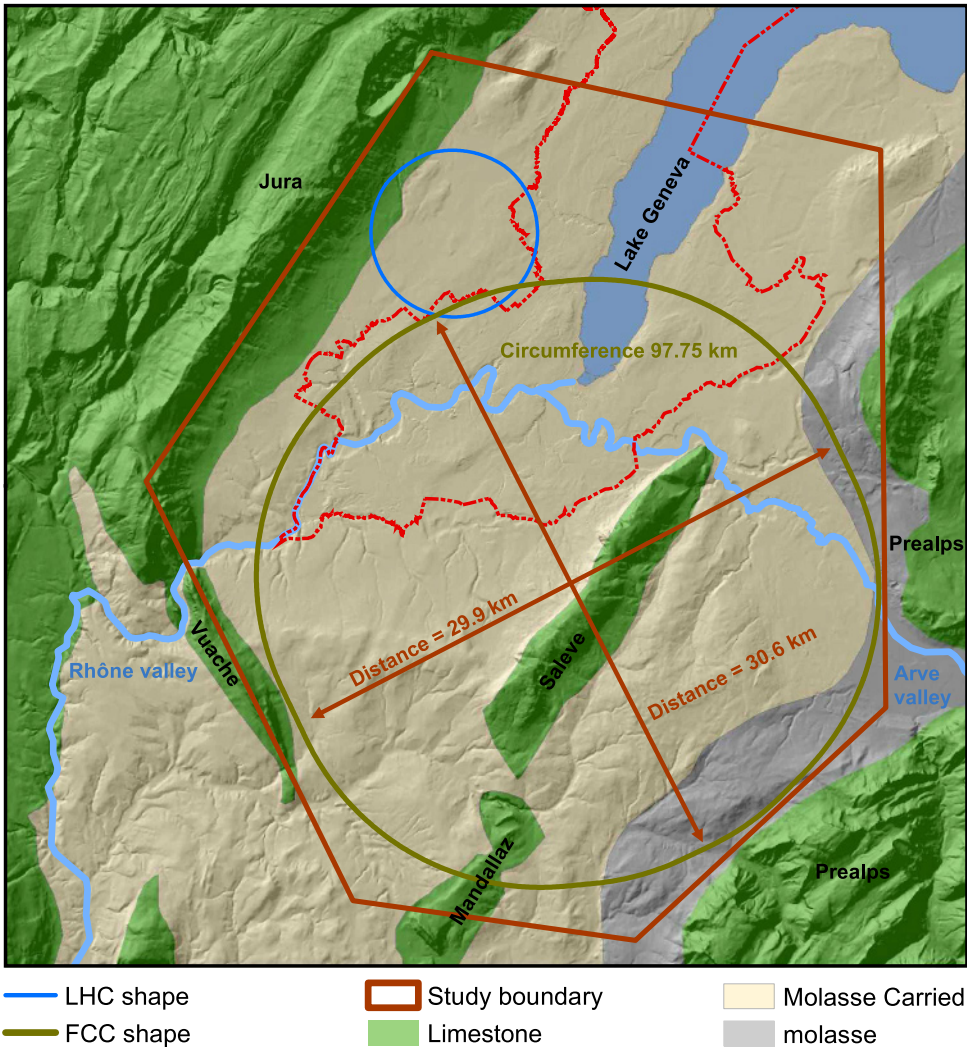


Fig. 4.2. Study boundary (red polygon), showing the main topographical and geological structures and the layout of the current FCC tunnel baseline with a perimeter of 97.75 km. This version with an approximate inner diameter of 30 km serves as the baseline for the planned layout and placement optimisation.

within the Jura range to the north-west, the Vuache mountain to the south-west and the Pre-Alps to the south-east and east. An additional boundary is placed to the north due to the increasing depth of Lake Geneva in that direction. Figure 4.2 shows the boundary of the study in red.

In order to evaluate different layouts and positions within the boundary area, a software tool incorporating a 3D geological model was developed. This tunnel optimisation tool (TOT) is based on an open source driven Geographical Information system (GIS), which enables multiple sets of data to be arranged spatially, together with a topographical map. The ensemble can then be manipulated, managed and analysed as one. This means that the TOT user is able to input any size, shape and position of the tunnel and quickly see how this interacts with the geology, the terrain, the environment and the surface structures in the study area.

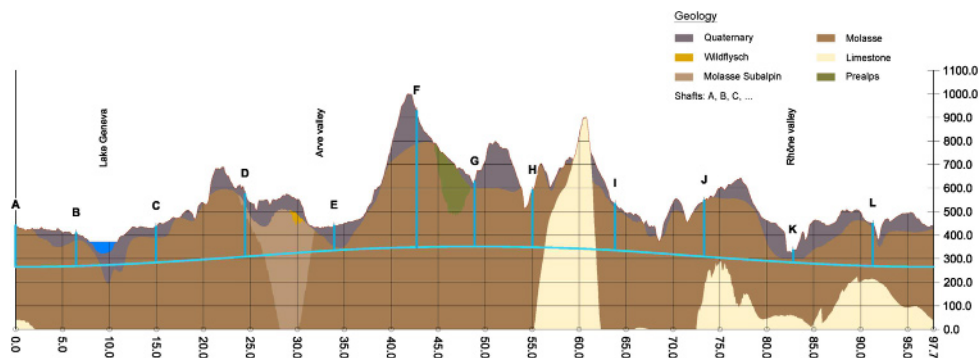


Fig. 4.3. Geological profile along the collider circumference. The horizontal axis labels the kilometers along the entire collider circumference starting with km 0 at point A. The so called “alignment elevation” is shown in meters above seal level (mASL) on the vertical axis. Different brown shades indicate different soil types such as molasse (dark brown) and limestone (light beige). The collider ring and the access shafts are indicated in light blue. Access points are labelled with letters in alphabetical order (A to L). Point A is close to the CERN Meyrin site. The collider tunnel is visualised along a sinuidal shape, since the tunnel in a single plane is tilted. The lake Geneva zone is shown in blue at about kilometer 10.

The geological data for the tool were collected from various sources [416], but not limited to: previous underground projects at CERN, the French Bureau de Recherches Géologiques et Minières (BRGM), and existing geological maps and boreholes for geothermal and petroleum exploration. The data were processed to produce rock-head maps that form the basis of TOT. All of the geological data for the study have come from previous projects and existing data. No specific ground investigations have yet been conducted for FCC-ee.

The machine studies demonstrated that it was necessary to have a circumference of ~ 100 km in order to meet the physics goals. The alignment of the tunnel has been optimised based on criteria such as geology along the tunnel, overburden, shaft depth and surface locations. A good solution has been found in which the tunnel is located primarily in the molasse (90%). It avoids the limestone of the Jura mountains and the Prealps but passes through the Mandallaz limestone formation, which is unavoidable. The tunnel passes through the moraines under Lake Geneva at a depth where they are believed to be well consolidated. Whilst there will be some additional challenges during excavation, the long-term stability of the tunnel is not a major concern. The topographical and geological profile of the tunnel in the chosen position is shown in Figure 4.3.

The tunnel position places the shafts in suitable positions with acceptable depths of less than 300 m, apart from the shaft at PF which requires special attention as it is 558 m deep. It is being considered to replace this shaft with an inclined access tunnel.

4.2.3 Necessary site investigations

Based on the available geological data for the region, the civil engineering project is deemed feasible. However, in order to confirm this and to provide a comprehensive technical basis for further detailed design iterations, to establish a comprehensive project risk management and to improve the accuracy of the construction cost estimates, dedicated ground and site investigations are required during the early stage of a preparatory phase. These investigations will rely on non-invasive techniques

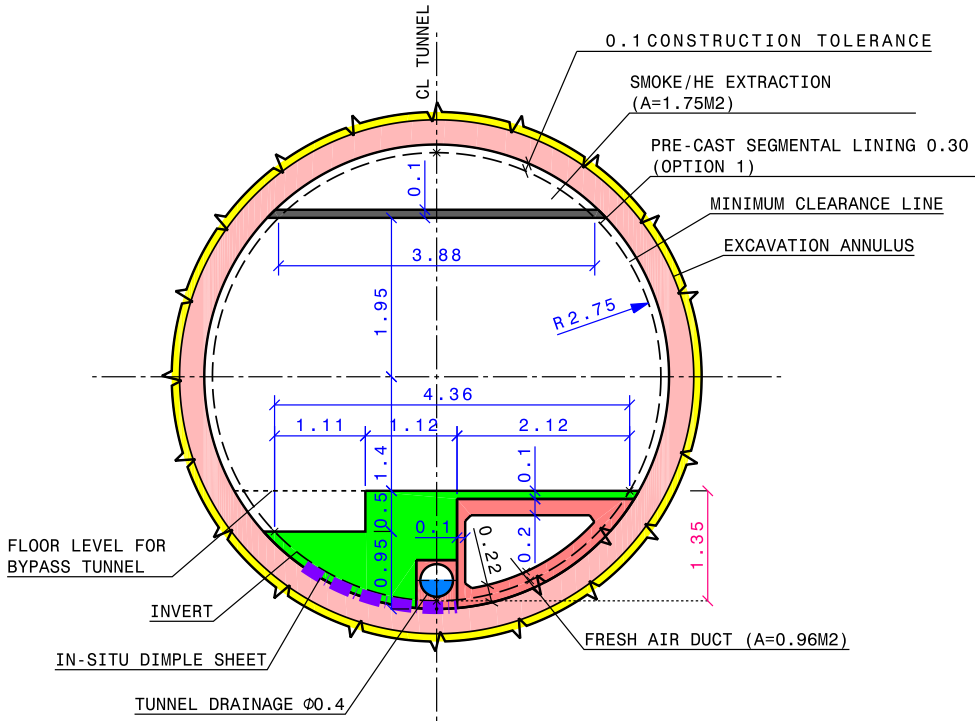


Fig. 4.4. Machine tunnel cross-section in “good” molasse.

such as walkover surveys and geophysical analysis, and will also use invasive techniques, such as the analysis of samples from boreholes that need to be constructed at regular distances. A combination of in-situ tests, such as the standard penetration test (SPT) and the permeability test, in combination with laboratory testing of samples, will give a comprehensive understanding of the geological situation.

The initial site investigations must focus on the highest risk areas: the crossing of Lake Geneva, the Rhône and the Arve valleys. In addition, the access point location candidates should be investigated in order to optimise the placements. This can be conducted via geophysical investigations and could lead to a recommendation to adjust the alignment in order to optimise the construction cost and reduce residual project-related risks.

4.3 Underground structures

4.3.1 Tunnels

A 5.5m internal diameter tunnel is required to house all the necessary equipment for the machine, while providing sufficient space for transport. Figure 4.4 shows the cross-section of the empty tunnel with the air supply and smoke extraction ducts, which have been integrated into the civil engineering design (these are discussed in Sect. 5.3). The air-supply duct in the floor is a pre-cast structure. The rest of the floor will be cast in concrete around it.

The tunnel will be constructed with a slope of 0.2% in a single plane, in part to optimise for the geology intersected by the tunnel and the shaft depths and in part to use a gravity drainage system.

Table 4.1. Proposed TBM excavation and lining parameters.

Parameter	TBM tunnel in “good” rock	TBM tunnel in “poor” rock	TBM tunnel in moraines
Minimum internal diameter (m)	5.5	5.5	5.5
Characteristic compressive concrete strength for pre-cast concrete, f_{ck} (MPa)	50	50	50
Pre-cast concrete thickness (m)	0.30	0.30	0.45
Reinforcement density for pre-cast concrete	Steel fibre (50%) and bars at 80 kg/m ³	Steel fibre (50%) and bars at 80 kg/m ³	150 kg/m ³
Gasketed segments	Yes	Yes	Yes
Cast in-situ concrete thickness (m)	None	0.25	0.25
Characteristic compressive concrete strength for in-situ concrete, f_{ck} (MPa)	–	40	40
Reinforcement for in-situ concrete	–	Local reinforcement cages	Local reinforcement cages
Total radial construction tolerance (m)	0.10	0.10	0.10
Excavation diameter (m)	6.3	6.8	7.1

It is anticipated that the majority of the machine tunnel will be constructed using tunnel boring machines (TBM). The sector passing through the Mandallaz limestone will be mined. For the TBM excavations, different lining designs have been developed corresponding to “good” or “poor” conditions of the rock. For TBM excavation in a sector with “good” conditions, a single-pass pre-cast lining is adopted. This is the fastest and cheapest construction method but is reserved for sectors that are completely located in molasse with a good rock coverage and hence a low risk of water inflow. For sectors in “poor” conditions to be excavated with a TBM, an optional second in-situ cast lining can be incorporated. This reduces the risk of water inflow in sectors which are located in the molasse, but where the depth of rock to the water bearing layers is minimal. Construction under the lake presents another situation which is similar to “poor” conditions but with a thicker initial pre-cast lining. Table 4.1 shows the excavation and lining parameters for each of the TBM lining cases.

Widening of the machine tunnel is required on each side of the experiment caverns at points PA and PG. These enlargements extend for 1.1 km on either side of the caverns. For construction purposes, the enlargements will be created in a “stepped” design as shown in Figure 4.5. This allows the formwork to be reused for optimal lengths whilst at the same time not constructing an excessive volume. The widest part of the enlargement will have a span of ~ 18 m. These enlargements can either be constructed by allowing the TBM to pass through to the experiment cavern and then excavating the additional volume with a roadheader, or stopping the TBM before the start of the enlargement and then excavating the entire remaining volume with a roadheader. The costs and construction rates for these two methods are comparable. The method chosen will be based on compatibility with the construction schedule as a whole.

The tunnel under Lake Geneva will be excavated in water bearing moraines in sector PB-PC (see Fig. 4.3). In order to achieve this, it is necessary to employ a slurry shield TBM. During excavation with this type of machine, the excavated material

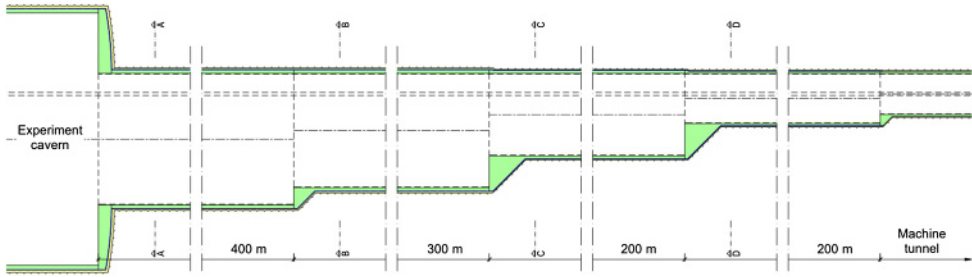


Fig. 4.5. Tunnel enlargement counterclockwise and clockwise of the experiment points PA and PG.

behind the cutter face is pressurised to support the tunnel face. Consequently, the excavation can be achieved safely and efficiently in wet and unstable conditions. It is anticipated that the layer of moraines to be excavated is impermeable enough that the tunnel would not be affected by the fluctuating depth of the lake and hence would not impact on accelerator operation, however, this risk must be evaluated once additional ground investigations have been conducted.

In addition to the machine tunnel, auxiliary tunnels are required for bypasses, connections, beam dumps and transfer lines. These have requirements similar to the machine tunnel and, depending on their diameter and position in relation to the TBM launch points, will be constructed using a TBM or roadheaders.

4.3.2 Shafts

Eighteen large-diameter shafts are included in the design:

- one 12 m diameter shaft at each of the 12 surface sites for access and service requirements;
- one 15 m diameter and one 10 m diameter shaft at each of two experiment points PA and PG;
- two shafts located near the existing CERN accelerators to facilitate the removal of spoil during construction of the beam transfer tunnels from the LHC or SPS.

At least one of the access and service shafts will have a wider diameter to lower large accelerator or infrastructure elements.

The shaft depths range from 52 m to 274 m (without point PF). As mentioned, the shaft at PF is considered to be replaced with an inclined access tunnel, with a length of 2750 m and a gradient of 15%. This is deemed a better solution than a 578 m vertical shaft for which a lift system would not be easy. A better location for the access portal can be found and an inclined access tunnel would be slightly faster and cheaper to build. The feasibility to route all services through it needs to be verified.

Internal structures in the form of staircases and lift shafts are required within the service shafts. Figure 4.6 shows the layout of these items; the lift shafts and staircases are pre-fabricated concrete structures. The initial excavation for each shaft will be through the moraines. This will be achieved either by using a diaphragm wall or a vertical shaft sinking machine (VSM). The remainder of each shaft will be constructed using traditional excavation techniques with shotcrete followed by an in-situ cast lining.

Table 4.2. Example of the main surface structures at a typical experiment site.

Structure name	Structure type	Dimensions ($W \times H \times L$)
Shaft head/detector building	Steel-frame	$25 \times 25 \times 100$ m
Reception/office building		$10 \times 11 \times 30$ m
Gas building	Concrete	$15 \times 4 \times 40$ m
Data centre		$20 \times 10 \times 40$ m
Workshop		$30 \times 12 \times 15$ m
Cryogenic plant building	Steel-frame (noise insulated)	$15 \times 12 \times 40$ m
Ventilation building	Steel-frame	$25 \times 14 \times 40$ m
Electrical building	Steel-frame	$20 \times 6 \times 80$ m
Power converter building	Steel-frame	$25 \times 14 \times 40$ m
Access control building		$10 \times 4 \times 10$ m

4.3.6 Junction caverns

There are three types of junction caverns which are required for structural purposes when tunnels of similar size connect, for example a bypass tunnel connecting to the machine tunnel. There are 26 locations which require a junction cavern, ranging in length from 30 m to 400 m and with a cross-section of approximately $16 \text{ m} \times 8 \text{ m}$ ($W \times H$). The longest junction caverns also serve as reception points or crossing points for the TBMs. A 400 m long junction cavern is required for each of the beam dumps to accommodate the dump beamline up to the point where it is possible to have a separate tunnel for it.

4.4 Surface sites

4.4.1 Experiment surface sites

The conceptual designs for surface sites range from classical sites similar to the LHC to semi-underground installations. Specific designs will reflect the particular machine and environmental requirements. It is anticipated that each site will be approximately 6 to 9 hectares in size, housing buildings and spaces for infrastructure needs (e.g. electrical distribution, cooling and ventilation, cryogenics). A large shaft head building will be foreseen at the experiment sites, which will act as detector assembly hall during installation. The surface sites will also serve as temporary spoil storage during construction and storage and assembly space during installation. Every effort will be made during the design process to minimise the visual, environmental and acoustic impact of these sites, which could mean building parts of the site below ground.

Using TOT, it has been possible to quickly identify candidate surface sites, considering the proximity to existing infrastructures, protected areas and transport links. With the current machine placement, site PA is located near the CERN Meyrin campus. Points PL, PA, PB and PC are located in Switzerland, the others are located in France. Table 4.2 gives an impression of the typical structures for surface sites and their dimensions. Most of the buildings will use standard industrial construction techniques, unless additional considerations dictate other designs.

4.4.2 Technical surface sites

The 10 access points without experiments will require surface sites for the technical facilities. The requirements are similar to those for the experimental surface sites,

while experiment-related buildings will be omitted and the shaft head building will be smaller.

4.4.3 Access roads

It is preferable for the surface sites to be largely accessible via existing roads. It is however anticipated that additional roads and even tunnels or bridges may be necessary for the more remote sites. Large accelerator and detector components will need to be transported along these roads, as well as the vehicles and machinery for construction, hence the roads must be able to withstand heavy loads. For the purpose of the siting study it has been assumed a new 5 km long road is required for each surface site.

5 Technical infrastructure

5.1 Requirements and design considerations

The technical infrastructure for FCC-ee comprises a large and diverse set of services to enable and support the operation of the lepton collider, full-energy booster and experiments. These include the supply of electrical energy and cryogens, the air and water cooling systems, facilities to transport people and material, the geodetic network, survey and alignment, control of accelerator equipment, data acquisition, computing and networking, as well as access control and other safety related functions.

As is customary for other facilities at CERN, the FCC-ee will make as much use of the existing chain of pre-accelerators as possible, but it will require a specific linac, new damping rings and transfer lines. As a new large-scale accelerator facility, the FCC will require new infrastructure systems. Some of them, like computer networks, will integrate with the existing infrastructure; others, like the supply of electrical energy, will extend existing facilities.

Building a large research infrastructure which crosses borders in a densely populated area like the Geneva basin requires that a wide range of conditions and regulations are respected to ensure its environmental and socio-cultural compatibility. The whole FCC-ee, including its technical infrastructure, must be designed and built for safe, high-performance operation, with high reliability and availability in mind. The equipment must generally be energy- and cost-effective. Future-oriented, yet technically solid approaches must be chosen to ensure enduring high performance and affordable operation.

5.2 Piped utilities

5.2.1 Introduction

The piping systems for the FCC mainly concern the various water systems for the machine and its infrastructure. Accelerator and detector equipment such as electronic racks, cryogenics plants, conventional magnets etc. will all require industrial and demineralised water. Chilled water will be needed for the air handling units of the ventilation systems. Raw water will be used in primary cooling circuits and for fire fighting purposes. Supply of drinking water will be needed for sanitary purposes as well as for the make-up of raw water cooling circuits. There will also be a drainage

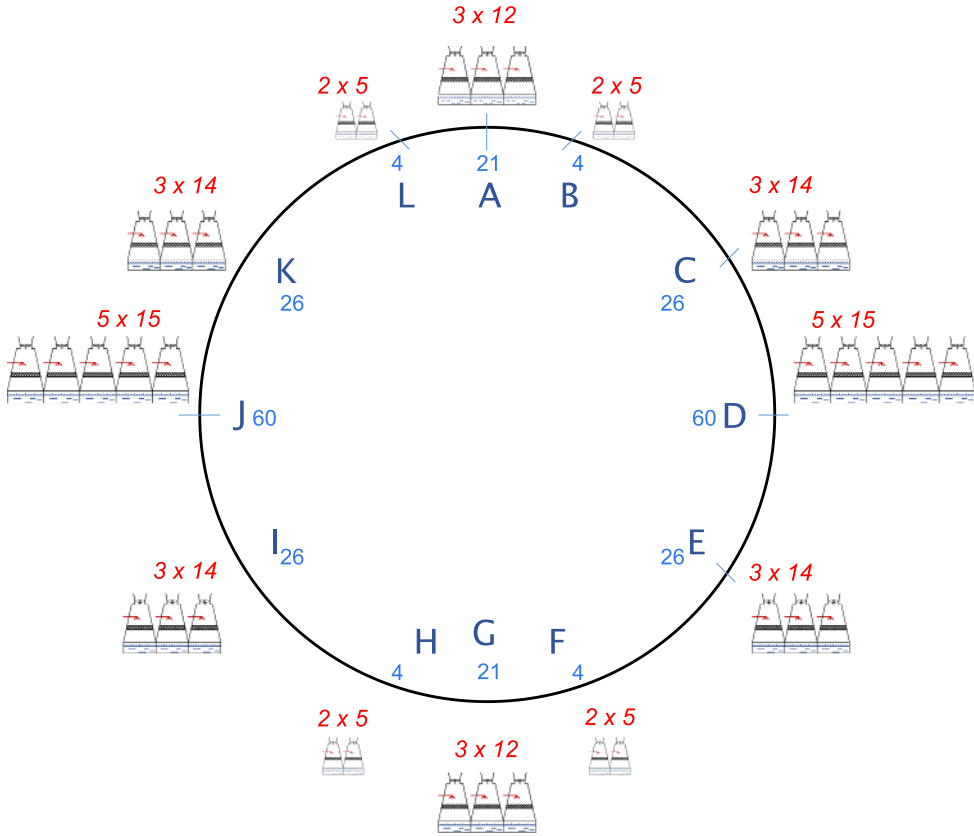


Fig. 5.1. Schematic view of the primary water cooling system installed around the accelerator ring (black circular line). The numbers in blue indicate the primary cooling power needed per access point in MW. The red numbers denote the cooling cells per access point including backup units \times the cooling capacity per cell in MW).

network for the waste water which comprises the rejected and drained water from the surface facilities and the underground areas. The other main piped utility is for compressed air which will be used both underground and on the surface.

5.2.2 Water cooling

Using raw water, the cooling plants will remove most of the heat generated by the accelerator equipment, the detectors and in the technical areas. It is planned to install one plant in each of the 12 surface sites. The primary circuit of the water cooling plant will use raw industrial water and will be cooled by means of open wet cooling towers. Some equipment, in particular cryogenics systems, will be cooled directly by the primary circuit. The secondary circuit will be connected to the primary system through a heat exchanger. In most cases the secondary circuit will use demineralised water in a closed loop. Figure 5.1 gives a schematic view of the primary water cooling system and its requirements.

Distribution circuits will be grouped according to the typology of the equipment to be cooled and to the equipment pressure ratings. Since the underground areas will be up to 400 m below ground level (point PF), it will be necessary to install an underground cooling station in the service cavern at each point. Here a heat exchanger will separate the circuit coming from the surface (with a static pressure

of up to 40 bar) from the underground distribution circuit. Wherever possible this separation will correspond to the separation between the primary and secondary circuit, but it will also be applied for other circuits such as those of the underground cryogenic equipment. The decoupling of the surface from the underground circuit will allow safer operation of the underground circuit as well as a cost reduction resulting from the ability to use pipes with a lower nominal pressure rating. For operability and maintenance purposes, both surface and underground cooling stations will be accessible during accelerator running.

The cooling area of all service caverns hosts secondary circuit stations to cool adjacent sectors or special equipment such as power converters. Points PA, PB, PG and PL also host the secondary circuit station to cool the equipment in the experiment areas. In points PD and PJ a similar area will be dedicated to the cooling of RF equipment. The secondary circuit in each sector will also cool the air handling units in the alcoves.

Primary circuits will use raw industrial water with a make-up of drinking water, to compensate for evaporation, losses and blow-down. Continuous water treatment against legionellae, scaling and proliferation of algae will also be included. The make-up is assumed to be provided by the local water supplier from the network serving each point.

Secondary circuits will use demineralised water with a maximum conductivity of $0.5 \mu\text{S}/\text{cm}$ in a closed loop. A set of demineralisation cartridges will be installed in each circuit to control the conductivity. The demineralised water will be produced in a central station. However, given the long distances, it will not be possible to have automatic refill pipework from this station to all the circuits in the various points via the tunnel without degrading the quality of the water. If there is a leak, the refill will be made by transporting the required volume of water in tanks from the production station to the point concerned.

To ensure continuous operation if one plant stops, the level of redundancy of the primary and secondary circuits is set at $N + 1$ for pumps, chillers and cooling towers. No redundancy is needed for plate heat exchangers, power or control cubicles. The safe power supply is at present only planned for systems related to safety. No equipment needs continuous cooling to prevent damage. Some cooling towers with a lower capacity will be installed to backup the main towers in order to allow essential cryogenic equipment to be kept at low temperature during mandatory stops for maintenance and cleaning.

Each cooling tower will contain a plant to concentrate the chemicals in the rejected water and to recycle most of it. This will allow the amount of make-up water, compared to today, to be reduced by about 50% and the rejected volume by more than 70%.

5.2.3 Operational parameters

The design parameters for the cooling plants are:

- primary circuit: 40°C at the inlet of the cooling towers and 25°C at their outlet;
- secondary circuit: 42°C at the inlet of the heat exchanger and 27°C at its outlet.

The temperature difference between inlet and outlet is 15 K with a tolerance of about 0.5 K. Tables 5.1 and 5.2 list the total power and the nominal diameter for the circuits in the underground area and at the surface of each point, respectively.

The diameter of pipework in the tunnel is optimised with respect to the pressure loss of the circuit due to its length. This permits to reduce the pressure rating for the pipeline or to avoid installing booster pumps at regular intervals in the sectors.

Table 5.1. Cooling power and pipe diameter for circuits in the FCC-ee underground areas.

Point		Cryo- genics	Expe- riment	Power con- verters	RF	Tunnel left	Tunnel right	Total under- ground
PA	P (MW)		0.5	0.25		7.5	7.5	15.8
	ND (mm)		100	80		500	500	400
PC, PK	P (MW)			0.4		9.9	11.1	21.4
	ND (mm)			80		500	600	450
PD, PJ	P (MW)	1.8			22.5			23.0
	ND (mm)	150			500			450
PE, PI	P (MW)			0.4		11.1	10.3	21.8
	ND (mm)			80		600	600	450
PG	P (MW)		0.5	0.2		7.1	7.1	14.9
	ND (mm)		100	80		500	500	350

Notes. “Tunnel left” designates the counter-clockwise adjacent machine tunnel sector; “Tunnel right” the clockwise adjacent machine tunnel sector.

Table 5.2. Cooling power and pipe diameter for circuits at FCC-ee surface sites.

Point		Cryo- genics	Expe- riment	Gen. services	Chilled water	Total under- ground	Total point
PA	P (MW)		0.5	2.0	2.4	15.8	20.6
	ND (mm)		100	200	200	400	600
PB, PL	P (MW)			2.0	2.0		4.0
	ND (mm)			200	200		350
PC, PK	P (MW)			2.0	2.5	21.4	25.8
	ND (mm)			200	250	450	650
PD, PJ	P (MW)	27		2.0	7.7	23.0	59.7
	ND (mm)	500		200	400	450	800
PE, PI	P (MW)			2.0	2.5	21.8	26.2
	ND (mm)			200	250	450	650
PF, PH	P (MW)			2.0	2.0		4.0
	ND (mm)			200	200		200
PG	P (MW)		0.5	2.0	4.6	14.9	22.0
	ND (mm)		100	200	300	350	600

Notes. “Total underground” is identical to the last column of Table 5.1.

5.2.4 Chilled water

The cooling for ventilation plants (dehumidification or air cooling) will require to install chilled water production stations at each surface point and some distribution circuits for the air handling units on the surface and in the underground areas. At present, no chilled water is needed in the accelerator arcs.

The chilled water will be produced at a temperature of 6°C and return at 12°C. The chillers will be water cooled and connected to the cooling towers at each point.

The redundancy level for the cooling circuits ensures continuous operation in the case of a breakdown of a single element (chiller or distribution pump). In case of a general power failure, a buffer tank in each production circuit will ensure sufficient autonomy of part of the plant for a limited period of time. The distribution pumps will therefore be connected to the secure electrical network.

Table 5.3. Main characteristics of chilled water circuits.

Point	Cooling power (kW)	Flow rate (m ³ /h)	Number of chillers	Cooling power/chiller (kW)
PA	1780	255	3	900
PB, PL	1500	215	3	800
PC, PK	1850	115	3	900
PD, PJ	5440	781	4	2000
PE, PI	1860	267	3	1000
PF, PH	1490	214	3	800
PG	3460	497	4	1200

Table 5.3 presents the total power and the main characteristics of the chilled water circuits at each point.

5.2.5 Drinking water

Drinking water will be used by personnel and as make-up water for cooling towers. It is planned that this will be provided by the local water network at each point. If the relevant water network does not have enough capacity to provide the required flow for the cooling tower make-up, this water will be provided from the closest point with sufficient capacity via a pipeline in the tunnel. In such cases, the same pipe will also be used for fire fighting purposes in the sector concerned.

5.2.6 Fire fighting network

It is planned to install a water network for fire fighting purposes in the underground areas and tunnel. This will comprise a pipe connected to fire hoses with Storz connections at regular intervals. In the case of major damage to this pipe, valves installed along the sector will allow isolation of the damaged part whilst maintaining the rest of the circuit operational for the fire brigade. It is planned to keep this pipe dry to avoid stagnation and corrosion during normal operation, In case of a fire, water will be supplied from the surface by opening isolation valves. Each sector can be supplied by the adjacent points, thereby guaranteeing a redundant supply.

Surface premises will be protected by a hydrant network and by dedicated water hoses inside the buildings where necessary.

It is planned that the fire fighting water will be delivered by the local public water network at each point. If this network is not able to deliver the required water flow, volume or redundancy level, the water can be supplied from the adjacent point via a pipe in the tunnel.

5.2.7 Reject water

Two separate pump systems to lift clear water and sewage will be installed underground at each point. They will be connected to the local drainage network of the point. All underground equipment (tunnel and caverns) must be redundant in order to avoid affecting operation in case of breakdown. Alarms for “high level” and “level too high” will be implemented in all basins.

The main parameters (e.g. temperature, pH) of the rejected water will be monitored before release. If the rejected water does not comply with the quality level

required, or it presents a risk of environmental pollution, compensatory measures, such as retention basins at each point, will be implemented.

5.2.8 Compressed air

The compressed air for all equipment and actuators will be provided by compressed air stations located on the surface at each point. These will supply both surface and underground premises. It is planned to have a level of redundancy of $N + 1$ to ensure the reliability and maintainability of the plant.

5.3 Heating, ventilation, air conditioning

5.3.1 Overall design concept

The installations have to provide a supply of fresh air for personnel working within the facilities as well as heating for the working environment. At the same time, the ambient temperature has to be suitable for the installed accelerator equipment. It is important that the air supplied has been dehumidified in order to prevent condensation on equipment and structures. In addition to being able to purge the air in the tunnel before access is allowed, the extraction systems have to be capable of removing smoke and gases. The extracted volumes have to be filtered before release.

5.3.2 Interior conditions

The interior conditions to be provided by the ventilation system are the following:

- FCC-ee tunnels (with maximum heat load): max. 32°C;
- experiment caverns: 18/32°C – from floor to ceiling;
- surface buildings with controlled temperature: 18°C during winter, 25°C during summer.

The values for surface buildings are mean values at heights where people and equipment are expected.

The relative humidity does not need to be regulated except for some specific areas which might require it (Faraday cage, clean rooms or other laboratories). If needed, such systems will be designed at a later stage. The dew point will be kept below 12°C to avoid condensation.

The outdoor conditions for the Geneva region which were used to specify the air handling equipment are 32°C for dry bulb temperature and 40% for relative humidity during summer and –12°C and 90% during winter.

As a general principle, a free cooling and air recycling approach will be adopted in order to reduce the electrical consumption (the term “free cooling” refers to the use of outside air at ambient temperature to cool equipment or areas, instead of using artificial air cooling).

5.3.3 Ventilation of underground areas

The underground areas are generally ventilated by air handling units located on the surface, which are therefore accessible at all times. It is planned to have redundant

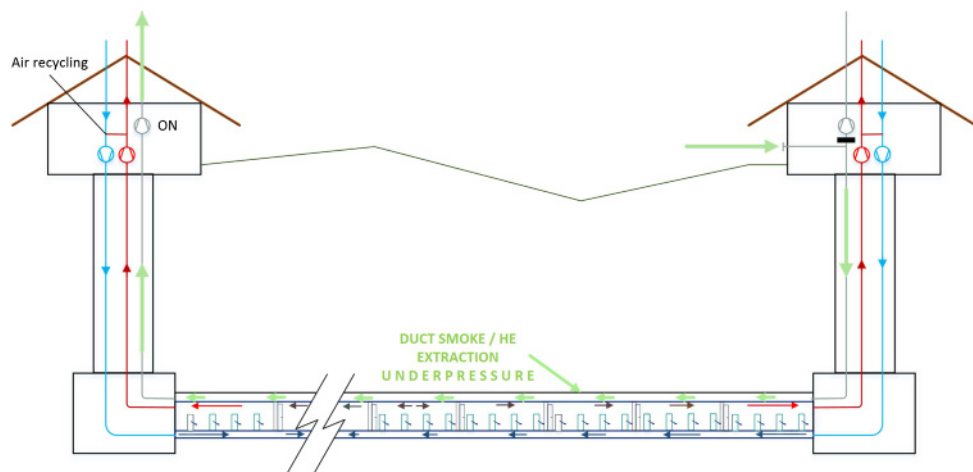


Fig. 5.2. Schematic view of the main ventilation elements of a machine sector.

units (level $N + 1$) everywhere in order to avoid affecting accelerator operation if there is a breakdown.

One of the two air extraction units will not be equipped with filters since it will be used to extract smoke, which could clog them. All systems related to safety will be powered by the secure electrical network.

5.3.4 Machine tunnel

The tunnel will be compartmentalised every 440 m by fixed fireproof panels and mobile doors, to control the propagation of smoke in case of fire or of helium gas in case of an accidental leak on an RF module or the cryogenic distribution line (points PD and PJ). In addition, a semi-transverse ventilation scheme has been adopted. The air is supplied via a specific duct throughout the sector and extracted either through the tunnel itself, or by an emergency extraction duct. Air is supplied to each sector from both end points to ensure an air supply even if there is a duct failure; the same configuration has been adopted for the extraction. In the case of the failure of one unit, the other will accelerate to ventilate both adjacent sectors. A schematic view of the main ventilation elements of a sector of the machine is given in Figure 5.2.

The air supply duct runs in the concrete floor slab and supplies air to the tunnel about every 100 m via diffusers at floor level. For emergency extraction, a closed circular segment in the upper part of the tunnel is used. It is formed by a 70 mm thick steel structure with passive fire protection on both sides, connected to the lining using post-drilled anchors (Fig. 4.4). Inlet diffusers and extraction grills are offset with respect to each other in order to ensure better distribution of the air in the tunnel and to avoid shortcuts between supply and extraction. Fire resistant dampers will be installed at every connection with diffusers and grills for the extraction. In the case of a fire or helium release, they will allow better management of the ventilation in the concerned tunnel compartment.

During normal operation, all emergency extraction dampers are closed and the doors are open in the whole sector (Fig. 5.3). The emergency duct will be under-pressured by extracting air from one extremity of the sector. When smoke or helium is detected, only the dampers of the extraction duct in the compartment affected and the adjacent ones will open; the doors of these compartments will be closed (Fig. 5.4).

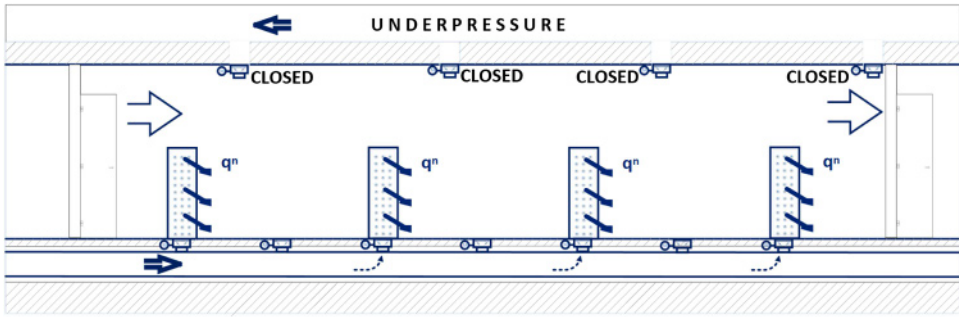


Fig. 5.3. Operation of the ventilation elements in one compartment of the machine tunnel during normal operation.

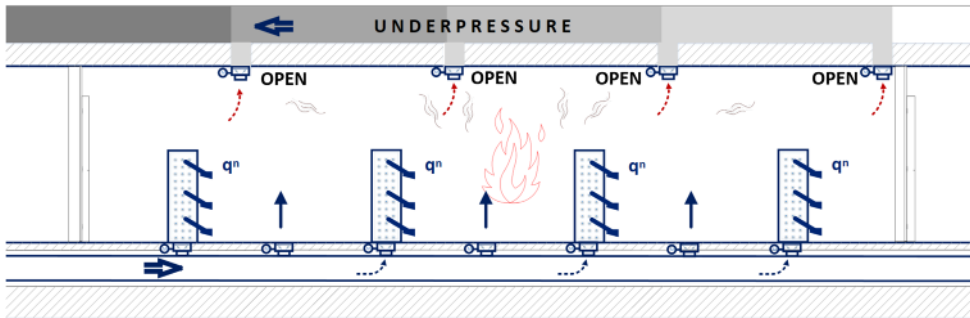


Fig. 5.4. Operation of the ventilation elements in one compartment of the machine tunnel in an emergency situation (in this case a fire).

Additional air supply to the affected and adjacent compartments will be achieved by opening other dampers in the supply duct. For the remaining compartments, the air supply will still be maintained. The extraction will be done via different air handling units on the surface.

5.3.5 Experiment caverns

For the ventilation of the experiment caverns, the air is blown in through diffusers at floor level (or the different floor levels) and extracted through one or more ducts located on the ceiling. Dedicated gas extraction systems will be installed where needed.

5.3.6 Other areas

Local air handling units will be added in areas housing equipment with particularly high heat dissipation. These units will be fitted with coils cooled by chilled water produced on the surface.

5.3.7 Operating modes

It is planned to have different modes for the ventilation systems depending on the machine operating conditions; these are presented in Table 5.4. All motors for ventilators will be equipped with variable speed drives in order to adjust the flow rates, to

Table 5.4. Operating modes and conditions for ventilation systems.

Mode	Conditions
Run	No access, accelerators running and equipment powered, full air recycling
Shutdown	Open access, accelerator stopped, maintenance interventions, fresh air/partial recycling
Purge	Where needed, before allowing access to personnel, accelerator stopped, fresh air

Table 5.5. Working parameters for the ventilation of a long machine tunnel sector.

Air flow from each side in run and shutdown modes (m ³ /h)	25 000
Air flow from each side in purge mode (m ³ /h)	50 000
Number of diffusors and extraction grills per compartment	4
Air flow per diffuser (m ³ /h)	520
Supply duct nominal diameter (mm)	1200

Table 5.6. Working parameters of air handling units for underground areas.

Underground structure	Nominal flow rate (m ³ /h)	Nominal duct diameter (mm)	Air recycling
Shaft and safe area pressurisation	45 000	1200	No
Ventilation of service caverns in experiment points (PA, PG)	45 000	1200	Possible
Ventilation of service caverns in technical points (PB-PF, PH-PL)	15 000	1000	No
Ventilation of RF areas (PD, PJ)	6000	700	Possible

Table 5.7. Main heat dissipation at the surface (in [kW]).

Point	Cryogenics	Experiment	General services
PA, PG		50	500
PB, PC, PE, PF, PH, PI, PK, PL			500
PD, PJ	1100		500
Total	2200	100	6000

adapt the working conditions to the operational needs and to achieve the requested dynamic confinement between adjacent areas, where requested.

5.3.8 Working parameters

Table 5.5 shows the main ventilation parameters of a long FCC-ee tunnel sector, e.g. sector PH-PI. The parameters of the ventilation plants for the underground points are presented in Table 5.6.

The filtering level of the exhaust air before release to the atmosphere will be defined mainly according to the radiation protection constraints.

The dissipated heat that needs to be removed by the ventilation systems for various types of equipment on the surface is shown in Table 5.7. Table 5.8 specifies the underground thermal loads.

Table 5.8. Main heat dissipation underground (in [kW]; “Adjacent machine tunnel” designates the adjacent clockwise sector).

Point	Cryo- genics	Expe- riment	Power con- verters	RF	Adjacent Sector	Underground Cooling Station Area
PA		50	7		375	200
PB			7		493	
PC			14		557	200
PD	120		14	2050	557	
PE			14		515	200
PF			7		356	
PG		50	7		356	200
PH			7		515	
PI			14		557	200
PJ	120		14	2050	557	
PK			14		493	200
PL			7		375	
Total	240	100	126	4100	5706	1200

5.3.9 Ventilation of surface buildings

Each surface building will be ventilated by a dedicated air handling unit. Where the building size requires it, it is planned to have several units in the same building, each of them taking care of a part of the building.

At present, it is not considered necessary to have redundant units in these buildings. Should this be needed, redundancy can easily be implemented. All surface buildings will be equipped with a mechanical system on the roof to extract smoke, designed and certified for operation at 400°C for a minimum period of 2 h.

5.3.10 Safety

In general, smoke extraction is planned for all facilities with a risk due to fire loads or where it is necessary to ensure the safety of personnel. If there is a fire, in addition to the automatic actions, the fire brigade will be able to switch off or reconfigure manually the ventilation system.

All air supply handling units are equipped with smoke detection sensors downstream of the ventilator in order to avoid injection of smoke into underground areas.

The concrete module for the lift and staircase in the shafts is kept over-pressure with respect to the surrounding underground areas and will therefore be used as a safe area in emergencies.

In compliance with safety norms, to prevent the passage of activated air from areas with higher levels of activation to areas with lower levels, a pressure cascade will be established. Therefore it is planned that the machine tunnel will be at a lower pressure with respect to the experiment caverns and adjacent areas. Volumes with higher activation risk are separated from less activated areas by airlocks kept pressurised by dedicated fans installed in the less activated areas.

Exhaust air ducts will have branches to connect air monitoring equipment for radiation protection monitoring of the air before its release into the atmosphere.

5.4 Electricity distribution

5.4.1 Conceptual layout

The concept for the design of the FCC-ee electrical network is driven by three factors:

- the estimated electrical power requirements (Tab. 9.1 in Sect. 9.2);
- the location and type of equipment to be supplied, and
- the expected level of electrical network availability and operability.

The electrical network is composed of a transmission and a distribution level. The transmission level transmits the power from three sources to three FCC-ee points and between the 12 FCC-ee points. This level operates at voltages of 400 kV and 135 kV. The distribution level distributes the power from the transmission level to the end users at medium and low voltage levels comprised between 36 kV and 400 V. The present baseline uses conventional AC schemes. Emerging new technologies based on DC schemes, which could improve the power quality and power consumption efficiency, are presented in Section 12.5.

5.4.2 Source of electrical energy

For the most demanding FCC-ee configuration, $t\bar{t}$, the estimated 359 MW electrical power requirement is supplied from the European grid. The current configuration of the European grid provides three 400 kV sources in France in the area of the collider facilities (Fig. 5.5). The three sources are self-redundant and, according to French network provider RTE (Réseau Transport Électricité), each of them is capable of providing 200 MW on top of their current load by the year 2035 (the present maximum daily load by CERN on source I is 191 MW).

5.4.3 Transmission network topology

The transmission network includes:

- The 400 kV transmission lines connecting the three 400 kV sources on the European grid to three incoming substations;
- Three 400/135 kV transformer substations;
- The 135 kV transmission line ring composed of 12 segments connecting each of the 12 surface points to its two neighbouring points;
- A 135/36 kV transformer substation at each point.

Figure 5.6 shows a schematic view of the transmission network. Analysing the power requirements for each point for the four machine configurations (Z, W, H, $t\bar{t}$) with nominal beam operation, one finds that the highest power is demanded at points PD and PJ, where the RF systems are located, each of which requires 93–111 MW. The remaining 10 points require less power – between 8 and 28 MW each. Two 400 kV sources supply PD and PJ directly, the third source supplies PA.

Through the transmission line ring, each of the three incoming substations supplies four neighbouring points. This transmission network layout provides full redundancy, enhanced availability and operability in case of a fault on one of the transmission line segments. A redundant scheme of 400/135 kV voltage step-down transformers supplies the transmission line segments connecting two adjacent points. In PB, PC, PD, PF, PG, PH, PI, PK and PL a substation will receive the incoming 135 kV transmission line segments. In all points 135/36 kV step-down transformers supply the distribution networks level. Figure 5.7 shows a simplified scheme of a 400 kV incoming substation and the connection to the two adjacent points with the corresponding step-down transformers.

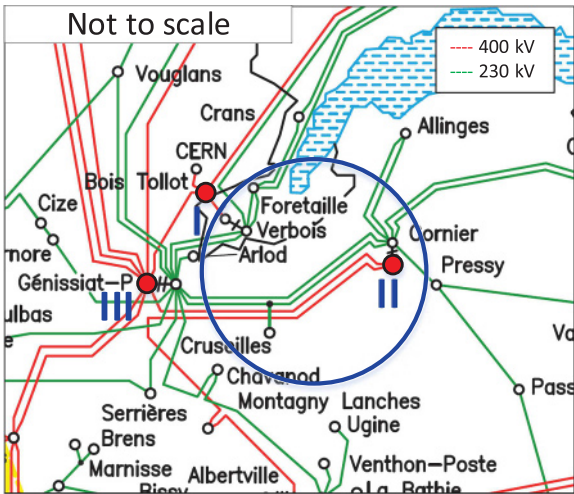


Fig. 5.5. Schematic representation of the 400 kV and 230 kV lines in the region. Red dots denote the three possible 400 kV sources.

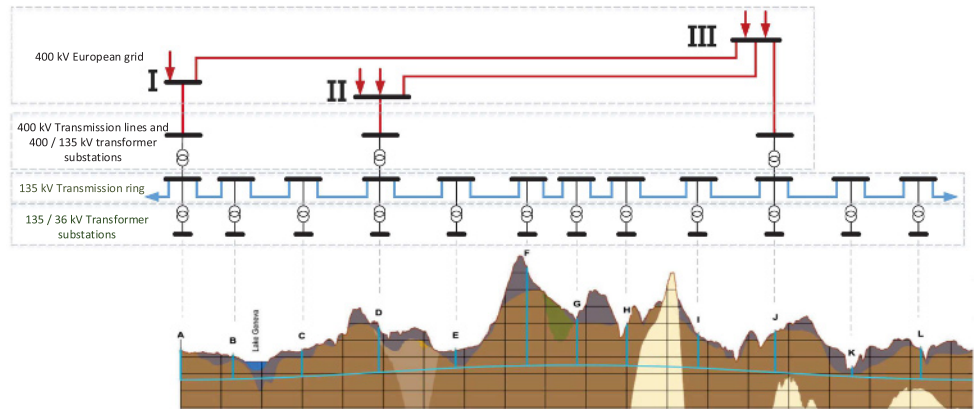


Fig. 5.6. Schematic representation of the transmission network.

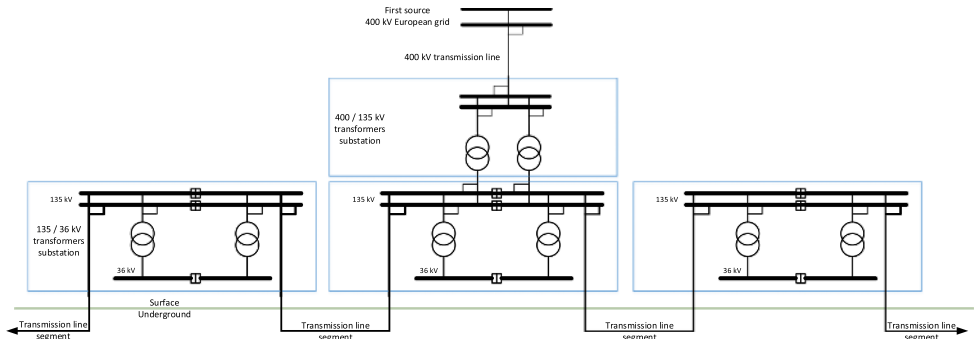


Fig. 5.7. Simplified scheme of a 400 kV incoming substation and the connection to the two 135 kV substations at the adjacent points.

5.4.4 Distribution network topology

The distribution networks connect the transmission network to the surface and underground equipment and systems. During nominal operation, the transmission network supplies the distribution network. Alternative sources of supply are needed to meet the required level of network availability and to cope with a degraded scenario such as a disruption of the general or local power supply. Therefore, the distribution network includes a second supply, rated between 2 and 10 MVA, fed from a regional grid node (due to the limited power request one can connect directly to the medium voltage level (20 kV in France and 18 kV in Switzerland)), a third source of supply rated 1–5 MVA from local, diesel-powered generator power stations and a fourth source which provides uninterruptible power. Figure 5.8 shows the single line diagram of the distribution network of one point including the alternative power sources.

The distribution network is composed of a primary indoor substation comprising five bus bars located on the surface. The incoming feeders are the two redundant 135/36 kV transformers supplied from the transmission network, the second supply from a regional source and the third supply from the local diesel power station. The outgoing feeders supply secondary substations. These are located either on the surface or underground, near the load. The operating voltages of the distribution network are typically 36 kV for the power distribution over distances greater than 750 m. Voltage step-down transformers feed end users from the secondary substations over a maximum cable length of 750 m. End users are supplied from the secondary substations at voltage levels between 400 V for wall plug equipment and 3.3 kV for high power motors for cooling, ventilation and cryogenic systems.

5.4.5 Power quality and transient voltage dip mitigation

The main issues concerning power quality are voltage stabilisation, harmonic filtering and reactive power compensation as well as the mitigation of transient voltage dips. Transient voltage dips as shown in Figure 5.9, which are typically caused by lightning strikes on the 400 kV network overhead lines, often cause undesired stops of CERN's accelerators. Due to its geographic extent, the FCC-ee infrastructure will be exposed to a higher number of transient network disturbances than the current CERN accelerators. The powering system design must include mitigation measures against these. Extrapolation from LHC operation forecasts a total of 100–200 transient voltage dips per year.

The following mitigation measures are being studied:

- Dynamic Voltage Restorer (DVR) technology: the voltage will be restored by dynamic series injection of the phase voltage between the distribution network and the loads. An integrated energy storage system provides the required energy to restore the load voltage during transient voltage dips (Fig. 5.10a).
- High-Voltage DC (HVDC) back-to-back link: HVDC is a well-established technology for long distance transmission of large powers and for decoupling different high voltage networks. Combined with energy storage, an HVDC system provides performance similar to a very large uninterruptible power supply (UPS). Such a system would prevent transient voltage dips in the 400 kV transmission network from entering the collider network. In addition it would allow the reactive power to be controlled (see Fig. 5.10b).
- Static Synchronous Compensator (STATCOM): this technology is already used for reactive and active power compensation. STATCOM would fully restore the load voltage during transient voltage dips by dynamic shunt (parallel) injection, combined with an integrated energy storage system (Fig. 5.10c).

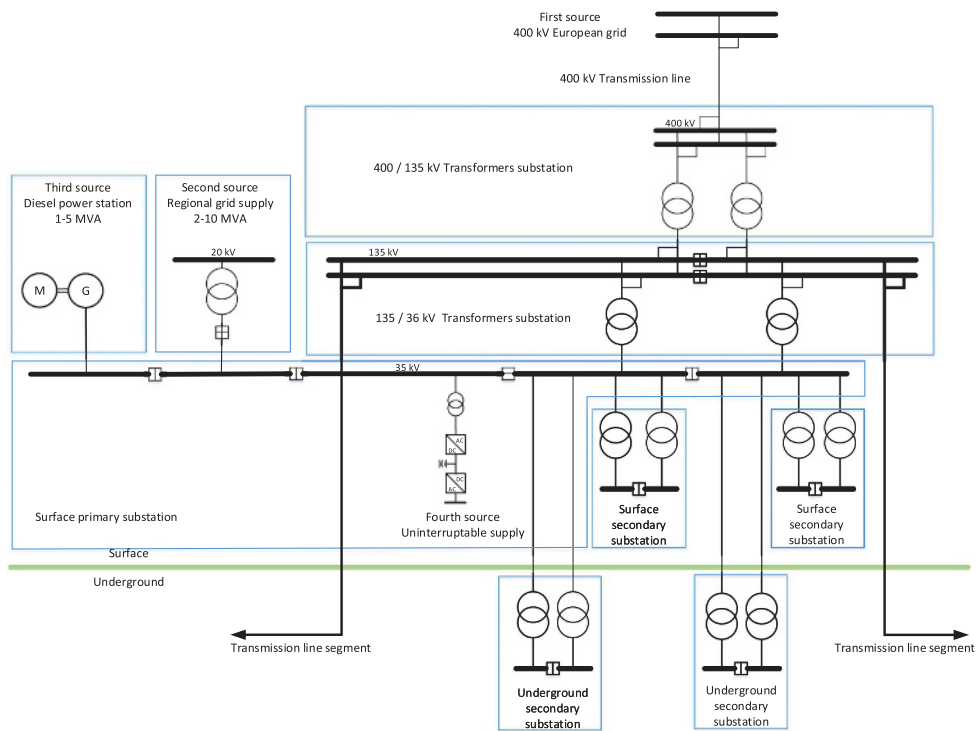


Fig. 5.8. Diagram of the baseline distribution network of one FCC point including the alternative power sources.

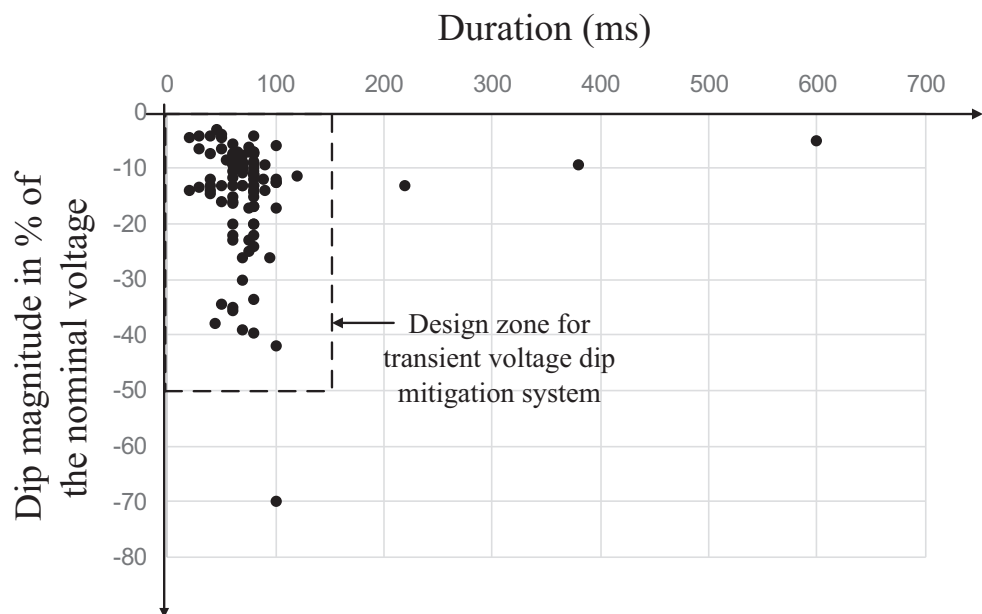


Fig. 5.9. Typical distribution of transient voltage dips recorded within the existing CERN network (collected between 2011 and 2017); the design zone covers most of the transient voltage dips, which are within 0–150 ms and 0–50% magnitude.

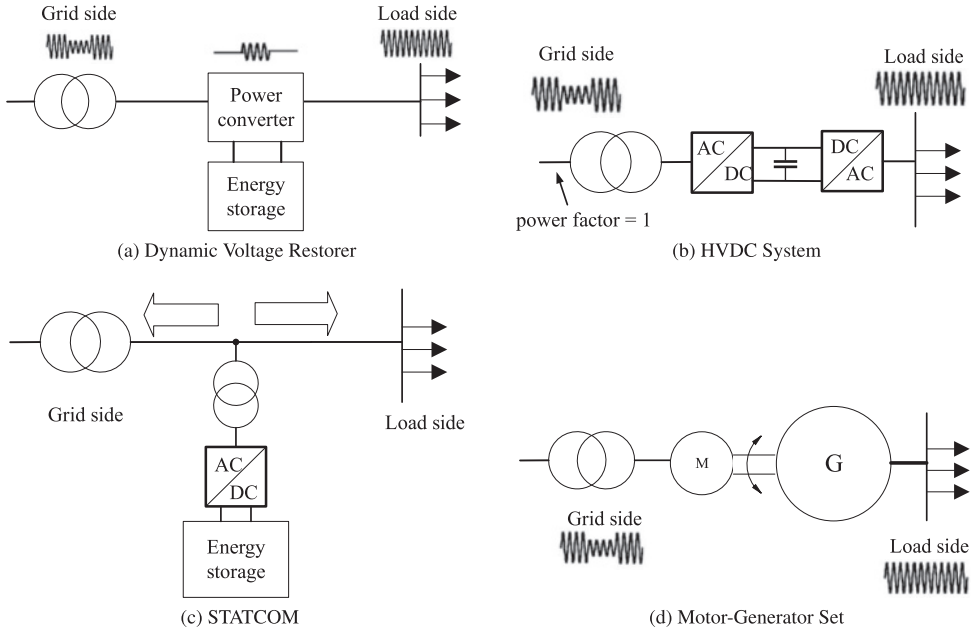


Fig. 5.10. Simplified layout of various methods for transient voltage dip mitigation.

- Motor-Generator Set: such a system would decouple the network from the load. During transient voltage dips, the load voltage is restored by using the energy stored in a rotating mass (Fig. 5.10d).
- Medium-Voltage DC (MVDC) distribution network: the principle of this approach is the distribution of power using DC. In combination with energy storage, this technology mitigates transient voltage dips, eliminates the reactive power, reduces the distribution losses and, compared to AC distribution, permits a larger spacing between electrical substations in the tunnel. This promising technology is still in its early stage of development and would require considerable R&D efforts before its use (see Sect. 12.5).

5.5 Emergency power

The emergency power concept is based on the requirement to keep essential parts of the accelerator infrastructure operational if the normal power source fails. Particular emphasis is put on loads related to personnel and machine safety during degraded situations. The various load classes and types can be characterised as shown in Table 5.10. The main ranking parameters are the acceptable duration of the power interruption and whether the load is part of a personnel or accelerator safety system.

Machine loads are energised from the transmission network through the distribution network and do not have a second source of supply. The general services loads typically accept power cuts of several minutes to hours. They can switch to an alternate source or wait until the main source is restored. Secured loads include personnel and machine safety equipment or systems that can only accept short power cuts up to a duration of 30 s. They require three staged supplies. In a degraded situation, the first backup is implemented by a generator power station, which typically starts up within 10 seconds. If the power station is unavailable, the second backup is implemented by supplying power from the regional grid.

Table 5.9. Power quality and transient voltage dip mitigation.

	DVR	Back-to-back	DC grid	STATCOM	Motor-generator set
Transient voltage dips	Covered	Covered	Covered	Covered	Covered
Compensation of reactive power on the load side	Not covered, although the resulting voltage deviations on the load side can be compensated	Covered	Covered	Covered	Covered
Compensation of active power on the load side	Not covered	Covered	Covered	Covered	Covered
AC Harmonic filtering capability	Yes (although additional HF filter required)	No (additional harmonic filtering required)	No (not necessary)	Yes	No (additional harmonic filtering required)
Steady-state power losses	Very Low	High	Medium	Very Low	Medium
Technology readiness level	Available in industry	Available in industry	Design and standardisation phase	Available in industry	Available in industry
Protection aspects	Bypass is needed	Bypass is needed	Under development	Bypass is needed	Very high protection

Table 5.10. Load classes and main characteristics.

Load class	Load type (non-exhaustive list)	Power unavailability duration in case of degraded scenario
Machine	Power converters, radio frequency, cooling pumps, fan motors	Until return of main supply
General Services	Lighting, pumps, vacuum, wall plugs	Until return of main or secondary supply
Secured	Personnel safety: lighting, pumps, wall plugs, elevators	10–30 s
Uninterruptable	Personnel safety: evacuation and anti-panic lighting, fire-fighting system, oxygen deficiency, evacuation Machine safety: sensitive processing and monitoring, beam loss, beam monitoring, machine protection	Interruptions not allowed, continuous service mandatory

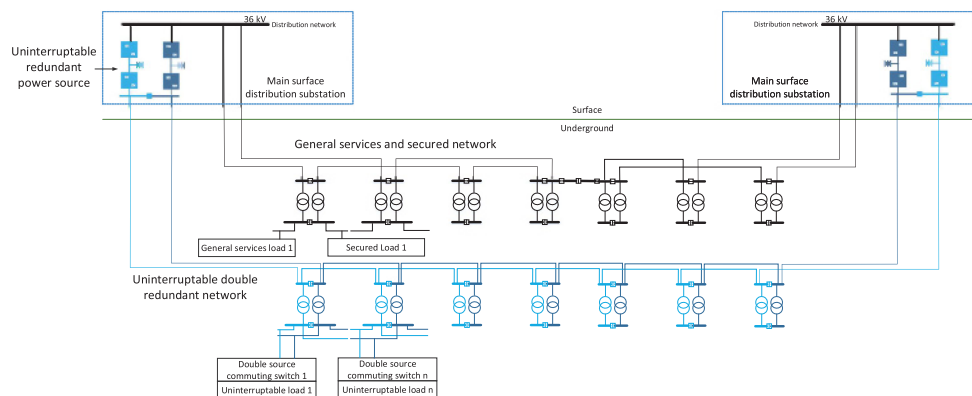


Fig. 5.11. Functional scheme of the general services load network and the doubly redundant uninterruptible load network.

High availability loads require true uninterruptible power supply. The network scheme is composed of two redundant uninterruptible power supply (UPS) systems that are supplied from the distribution network in the two adjacent points. Downstream of the redundant UPS systems, a doubly redundant network delivers two independent sources, each coming from an adjacent point to the end-user plug. Each piece of end-user equipment has two entries and will manage the double source of supply. To meet safety and access requirements, UPS and batteries are located outside the tunnel and above ground. Figure 5.11 shows the functional scheme of the general services loads network and the doubly redundant uninterruptible load network.

5.6 Cryogenic system

5.6.1 Overview

The FCC-ee is designed for four physics working points with various electron-positron beam parameters. The beams will be accelerated by 400 and 800 MHz superconducting radio-frequency (SRF) cavities operating at 4.5 and 2 K, respectively. The staging of the four machines requires a gradual increase of the number of SRF modules (Fig. 4.6) and consequently a staging of the cryogenics system.

5.6.2 Functions and constraints

The 400 MHz SRF cavities will be housed in cryomodules (CM) where they will be immersed in a saturated helium bath at a temperature of 4.5 K at 1.3 bar. The 800 MHz cavities will equally be housed in CMs but be immersed in a saturated superfluid-helium bath at 2 K at 30 mbar. For operation at the first three working points (Z, W, H) the FCC-ee will be exclusively equipped with 400 MHz CMs and only require refrigeration at 4.5 K. For the fourth working point ($t\bar{t}$) the installed 400 MHz CMs will remain in place and be complemented by 800 MHz CMs, then requiring refrigeration at 4.5 and 2 K. The SRF cavities for the booster ring will be similarly staged.

The cryogenic system must cope with load variations and the large dynamic range imposed by operation of the accelerator. Even if the mass of the cavities is not an

issue, the cryogenic system must be able to cool down and fill the CM baths, whilst avoiding thermal gradients greater than 50 K in the cryogenic structures (CMs, cryogenic distribution line). The same thermal gradient limit also applies to the forced emptying and warm-up of the machine prior to shutdown periods.

At point PJ the requisite cooling power will be produced for the Z and WW working points, by a single 4.5 K refrigeration plant. For the H working point a second 4.5 K refrigeration plant will be installed at point PD. Finally, two 2 K refrigeration plants will be installed at PD and PJ for $t\bar{t}$ operation.

Each of the long straight sections in PD and PJ will contain three distinct stretches of SRF equipment, one for the electron ring, one for the positron ring and one for the booster ring. During operation at the $t\bar{t}$ working point, both electrons and positrons will pass through the same SRF sections of the collider.

For reasons of simplicity, reliability and maintenance, the number of active cryogenic components around the SRF sections will be minimised. The CMs will be equipped with cold-warm transitions. To simplify their design, the cryogenic headers distributing the cooling power as well as all remaining active cryogenic components in the tunnel will be contained in a compound cryogenic distribution line, which will run alongside the SRF sections over distances of up to 1.1 km and feed each CM via a jumper connection. The tunnel is inclined at 0.2% with respect to the horizontal which could generate instabilities in two-phase, liquid-vapour, flow. All fluids should be transported over large distances in mono-phase state to avoid these harmful instabilities, i.e. in the superheated vapour or supercritical regions of the phase diagram. Local two-phase circulation of saturated liquid, in a controlled direction can be tolerated over limited distances.

As much of the cryogenics equipment as possible will be installed above ground, to avoid increasing the space needed underground. Only certain components, which must be close to the SRF, will be installed underground. To limit the effect of gravity (hydrostatic head and relative enthalpy variation) in areas up to 266 m deep, the cold part of the helium cycle below 40 K, including cold compressors, must be located underground. For reasons of safety, the use of nitrogen in the tunnel is forbidden. Discharge of helium is restricted to small quantities. The cryogenic system is designed for fully automatic operation outside of shutdown periods, when maintenance is being performed.

5.6.3 Layout and architecture

Figure 5.12 shows the cryogenic layout of the four machines, with two cryogenic “Islands” at points PD and PJ where all refrigeration and ancillary equipment will be concentrated. Equipment at ground level includes the electrical substations, warm compressor stations, cryogen storage (helium and liquid nitrogen), cooling towers and upper cold-boxes. The lower cold-boxes, interconnecting lines and interconnection boxes will be located underground. The Z-machine requires limited refrigeration capacity; its refrigerator cold-box can be fully integrated in the service cavern. Figure 5.13 shows the general architecture of the cryogenic system. At each cryogenic island, an interconnection box couples the refrigeration equipment to the cryogenic distribution line. Where possible these will also facilitate redundancy amongst the refrigeration plants.

The 800 MHz CMs require very-low-pressure pumping and must be located close to their 2 K refrigeration unit. Consequently, the 400 MHz cryomodules will be located at the far end of the straight sections, thus requiring 1.4 km of cryogenic transfer line per straight section.

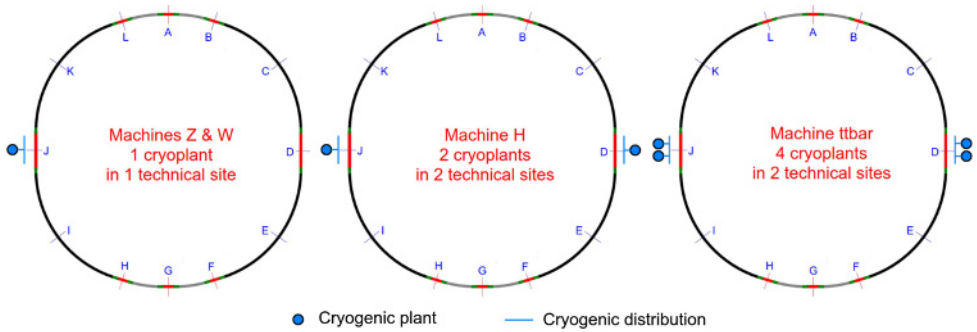


Fig. 5.12. General cryogenic layout.

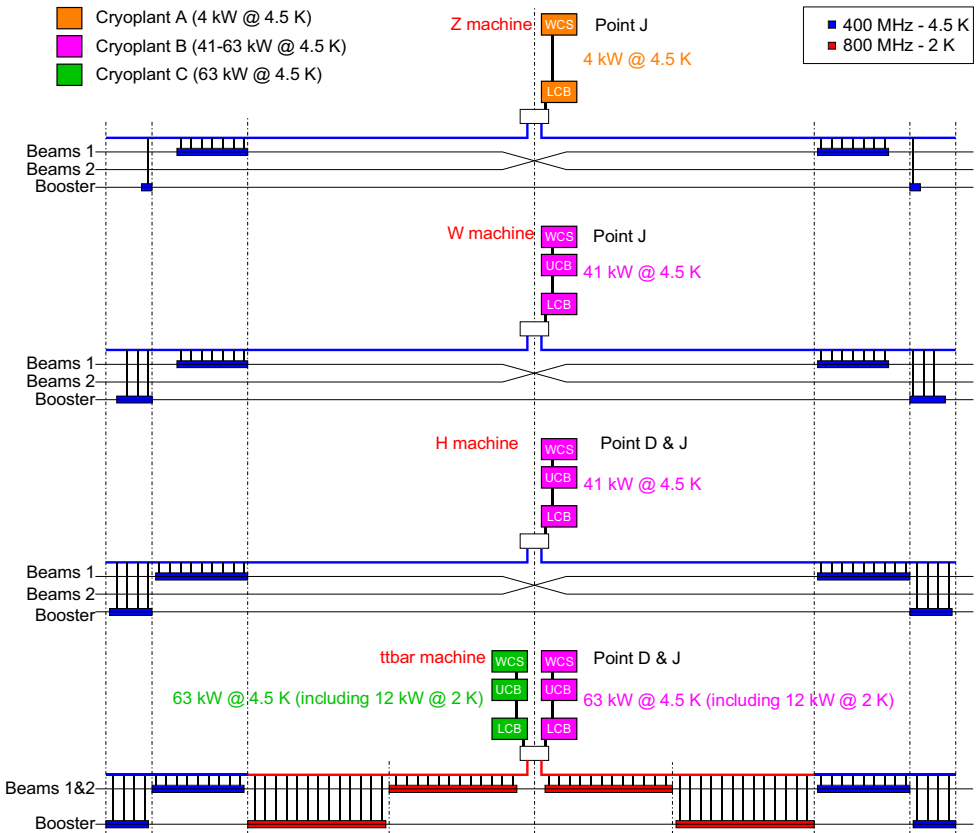


Fig. 5.13. Cryogenic plant architecture.

5.6.4 Temperature levels

In view of the high thermodynamic cost of refrigeration at 2 K and 4.5 K, the thermal design of cryogenic components aims at intercepting the largest fraction of heat loads at higher temperature, hence the use of multiple, staged temperature levels. These are:

- 50 K–75 K for thermal shield as the first major heat intercept, sheltering the cavity cold mass from the bulk of heat inleaks from the environment;

Table 5.11. Steady-state heat loads in FCC-ee (nominal conditions).

	Machine									
	Z		WW		ZH		$t\bar{t}1$ ($t\bar{t}2$)			
	Per beam	Boost.	Per beam	Boost.	Per beam	Boost.	2 beams	Boost.	2 beams	Boost.
Frequency	400 MHz								800 MHz	
Temperature	4.5 K								2 K	
# cells / cavity	1	4	4		4		4		5	
# cavities	52	12	52	52	136	136	272	136	296 (372)	400 (480)
# cryomodules	13	3	13	13	34	34	68	34	74 (93)	100 (120)
Dynamic losses / cav [W]	14	11	210	26	202	29	210	30	66	10
Static losses / cav [W]	8		8		8		8		8	

- 4.5 K normal saturated helium for cooling 400 MHz superconducting cavities;
- 2 K saturated superfluid helium for cooling the 800 MHz superconducting cavities.

The CM and cryogenic distribution line combine several low temperature insulation and heat interception techniques which will have to be implemented on an industrial scale. These techniques include low-conduction support system made of non-metallic fibreglass/epoxy composite, low impedance thermal contacts under vacuum for heat intercepts and multi-layer reflective insulation for wrapping the cold surface.

For FCC-ee, the beam-induced heat load is dominated by RF losses dissipated in the cavity baths at 4.5 K and 2 K. These depend strongly on the bunch intensity and the number of bunches in the circulating beams.

5.6.5 Heat loads

Inward static heat leaks (inleaks) depend on the CM design and originate from the ambient temperature environment. The thermal calculations for the CMs and the distribution system are based on the thermal performance data from similar cryo-assemblies.

Table 5.11 gives the steady-state heat loads for nominal conditions for the four machines.

5.6.6 Cooling scheme and cryogenic distribution

The cryogenic flow scheme is shown in Figure 5.14 for the CMs at 4.5 K and 2 K. The 4.5 K cavity cold masses are immersed in saturated helium baths, which are supplied by line C through expansion valve V1. The saturation pressure is maintained by line D, which recovers the evaporated vapour. The 2 K cavity cold masses are immersed in saturated helium baths, which are supplied by line A through expansion valve V2. The low saturation pressure is maintained by pumping the vapour through line B. Each CM has a dedicated thermal shield and heat intercept circuit cooled in parallel between line E and F. The flow rate is controlled by valve V3. Table 5.12 gives the size of the main cryogenic distribution system components.

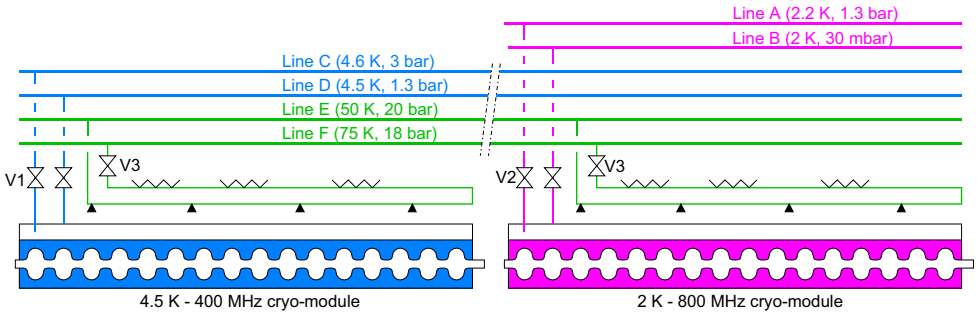


Fig. 5.14. Cryogenic flow scheme of FCC-ee CMs (here the cryogenic plant is located to the right of the 800 MHz section).

Table 5.12. Dimensions of the main cryogenic distribution line components.

Component	Diameter (mm)
Line A	50
Line B	300
Line C	100
Line D	200
Line E	80
Line F	80
Vacuum jacket 400 MHz cryomodules	550*
Vacuum jacket 800 MHz cryomodules	750*

Notes. *+100 mm for bellows and flanges.

Table 5.13. Nominal cooling capacity per cryogenic plant.

Working point	50–75 K (kW)	4.5 K (kW)	2 K (kW)	Cryoplant size (kWeq @ 4.5 K)	No. of cryoplants (–)
Z	5.5	3.7		4	1
WW	6.4	32		33	1
ZH	7.1	41		41	2
tt1	6.6	21	10	55	4
tt2	7.6	21	12	63	4

Notes. Including an operational margin factor of 1.3.

5.6.7 Cryogenic plants

Table 5.13 gives the nominal cooling capacity per cryogenic plant required at the various temperature levels for the four working points, including an operational margin factor of 1.3.

The cooling of the superconducting 800 MHz CMs requires a refrigeration capacity of 12 kW at 2 K per cryogenic plant, larger than the capacity of state-of-the-art plants. Specific research and development will be required to design larger cold compressors and/or to operate cold compressor trains in parallel. In order to optimise the staging (Fig. 5.15), it is proposed to use a small cryogenic plant (cryoplant A) for the Z-machine, then to replace this by a new plant (cryoplant B) for running at the WW threshold. This could be upgraded for the H machine. Finally, two new cryogenic plants (cryoplant C) could be added for tt. The electrical power to the

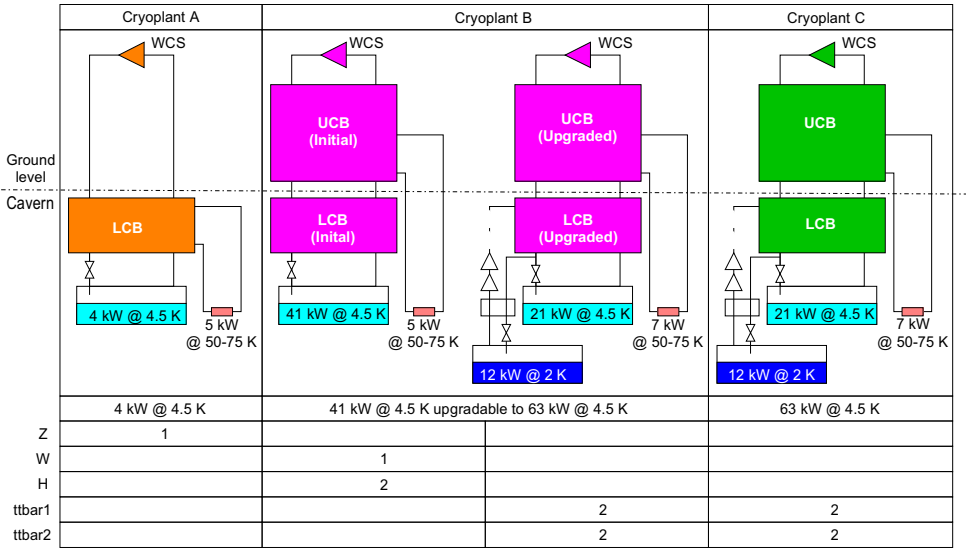


Fig. 5.15. Cryogenic plant staging for FCC-ee.

Table 5.14. Electrical power required by the cryogenic plants.

Working point	Installed power (MW)			Nominal power (MW)		
	Per plant	Per site	Total	Per plant	Per site	Total
Z	0.9	0.9	0.9	0.8	0.8	0.8
WW	9.5	9.5	9.5	7.1	7.1	7.1
ZH	9.5	9.5	19	8.3	8.3	17
tt1	14	29	58	12	23	46
tt2	14	29	58	13	25	50

cryogenic plants, based on a Carnot efficiency of 28.8% (LHC cryogenic plant value), is given in Table 5.14. In nominal operation, the electrical consumption varies from 1 MW (for the Z machine) to 50 MW (for tt2).

5.6.8 Cryogen inventory and storage

The cryogenics system will require helium and nitrogen. Nitrogen will only be needed for the regeneration of absorbers and dryer beds; consequently, one standard 50 m³ LN₂ reservoir is planned for each point PD and PJ. The helium inventory is mainly driven by the CM cold mass baths (40 kg of He per CM) and the cryogenic distribution system. Table 5.15 gives the inventory of helium and its storage for the FCC-ee machines. The Z and WW machines are dominated by the helium distribution inventory. The tt machine requires up to 26 t of helium which can be stored in 250 m³ medium-pressure (MP, 20 bar) storage tanks.

5.7 Equipment transport and handling

5.7.1 Underground vehicles

The vehicles which will be used in the tunnels will comply with the relevant European Directives (Machinery Directive 2006/42/EC, RoHS Directive 2011/65/EU)

Table 5.15. Inventory of helium and its storage for the FCC-ee machines.

Machine	Z	WW	ZH	tt1	tt2
Cryomodules (t)	1.2	1.6	4.1	11.0	12.6
Distribution (t)	3.9	3.9	7.9	8.9	8.9
Cryoplant (t)	1	1	2	4	4
Total (t)	6	7	14	26	26
Number of 250 m ³ MP storage tanks	8	8	18	30	32

as well as CERN safety codes and EN standards. All equipment will have integrated recovery mechanisms and procedures (on-board or separate).

The transport system comprises tractors and trailers which are combined to form convoys tailored to match the dimension and weight of the payload and installation situation. A tractor can tow one or more trailers. The vehicles will be equipped with an automatic guidance system and powered by batteries. The speed and the number of vehicles will be adjusted to meet the installation schedule. All required equipment can be supplied by industry using currently available technologies.

Tractor characteristics

Each tractor will be equipped with two trailer hitches (one each at the front and rear) to connect the tractor to the trailers. The tractor will be equipped with electric motor drives and therefore run emission-free in the tunnel. An intelligent navigation and control system will drive the tractor autonomously in the tunnels. The general characteristics of the tractors are summarised in Table 5.16.

Trailer characteristics

The trailer (Fig. 5.16) uses an electronic steering system, a drawbar and a vibration-damped support for the load. The special wheels are mounted on pendulum axles (swing axle). The general characteristics of the trailers are summarised in Table 5.17.

Magnet transport

A single-trailer option is preferred for this purpose since it possesses the most favourable properties for the application. It includes the loading and unloading mechanism to install the magnet directly in its final position. The power for the hydraulic lifting and transfer mechanism can either be supplied from the tractor battery or from a local power supply.

5.7.2 Overhead cranes

The electrical overhead travelling (EOT) cranes for the FCC will comply with relevant European Directives (2006/42/EC, 2014/30/EU and 2014/35/EU) as well as CERN safety codes and EN standards.

They are classified as light/medium duty cranes depending on their frequency of use and load spectra. Their FEM (European Federation of Material Handling) classification is A4/M4.

Table 5.16. General characteristics of the transport tractors.

General characteristics	Type/value	Complementary information
Type	Battery powered	1 or 2 tractors per convoy Front and rear (optional)
Power	Electric	Equipped with batteries
Operator position (for non-standard operations)	Seated	In longitudinal position
Use	Underground	
Rated capacity (nominal)	60 t	
Maximum Slope	2.5%	
Steering	Automatic	Optical guidance device
Wheels/tyres	Heavy duty traction wheels	
Travel speed: Loaded Unloaded	Up to 10 km/h Up to 20 km/h	Nominal speed on flat surface
Slope travelling capacity (loaded)	Min. 2.5% gradient	For min. 1 km distance
Motors/battery	Type/value	Complementary information
Motors	Electric	All
Battery type	Gel or lead acid	
Autonomy (at nominal load – 60 t)	Min. 25 km	On flat surface

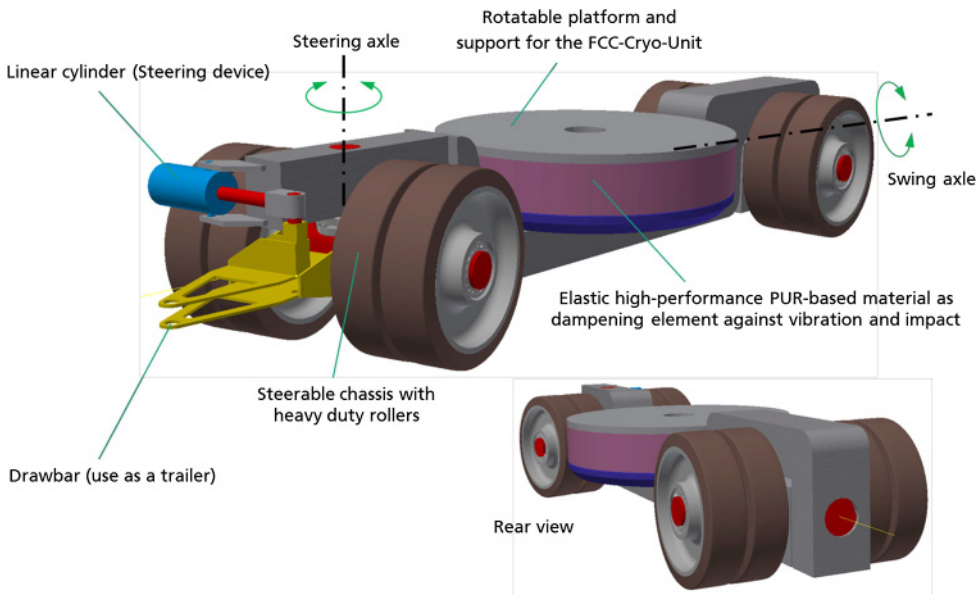


Fig. 5.16. A conceptual view of a trailer.

Table 5.17. General characteristics of the transport trailers.

General characteristics	Type/Value	Complementary information
Type	Separate trailers	1, 2 or 3 trailers per convoy
Power	Electric/battery	For steering device
Suspension	Damping element	Elastic high-performance PUR-based material
Steering	Steerable chassis	Automatic guidance device
Use	Underground	
Rated capacity (nominal)	30 t	
Maximum Slope	2.5%	Brakes
Wheels/tyres	Heavy duty rollers	
Travel speed: LoadedUnloaded	Up to 10 km/h Up to 20 km/h	Nominal speed on flat surface

The hoist design ensures that hook lifting and lowering can be performed without horizontal drift. An emergency brake is installed to avoid dropping the load should any elements of the hoisting drive chain fail. To obtain smooth acceleration, electric motors are driven by inverters. The crane is therefore suited to handle fragile objects. The maximum speeds are chosen in the following ranges:

- Lifting speed: 8–10 m/min;
- Cross-travel speed: 12–15 m/min;
- Long-travel speed: 15–20 m/min.

Laser sensors and a programmable logic controller (PLC) control the hook position in order to ensure precise positioning and to define multiple areas where the hook must not access.

A shaft crane is an overhead crane installed in a surface building, whose hook can reach an underground cavern and the shaft leading to it. Shaft cranes also comply with the following requirements:

- FEM classification of the hoisting gearbox is M6;
- The hoist is fitted with redundant electric motors;
- The hoist runs at twice the nominal speed if no load is attached to the hook;
- A weighing system takes into account the effect of the cable’s own weight.

The installation of a crane takes between 3 weeks and 3 months depending on the capacity and lifting height.

5.7.3 Lifts

The lifts for the FCC will comply with the relevant European Directives (2006/42/EC and 2014/33/EU) as well as CERN safety codes and EN standards.

The lifts can use standard technologies like those used in high-rise buildings where they already cover heights of up to 450 m. The FCC-ee has 12 access shafts which will be equipped with two lifts each.

The lifts are the only authorised means for personnel access to and from the underground areas, therefore the lift shaft concrete modules will be over-pressured. The lifts will be powered from the secure power network in order to remain fully operational should the standard electrical network fail. For the same reason, the lift shaft modules were designed with 2 lifts in order to create redundancy (safety) and

to ease operational (access) and maintenance (availability) aspects. A view of an access shaft, showing the two lift locations, is given in Figure 4.6.

The lift capacity and speed will determine how many people can simultaneously work in the underground areas. A time of about 4 min has been defined as duration of each lift cycle, including people entering the lift, the time for the lift to travel from underground to the surface, and people exiting the lift (for shaft depths of 300 m and a lift speed of 4 m/s).

Since both lifts can operate simultaneously and independently, up to 300 people can be evacuated from the underground areas at a single access point within 30 min. This reduces to 150 people if only one lift is operational.

Studies showed that around 80% of the LHC non-machine components were transported with lifts. Lifts with 3 t capacity have the best cost/capacity ratio; these were thus chosen as baseline solution.

The installation of a lift takes between 3 and 6 months depending on the shaft depth. The main characteristics of a lift are:

- Speed : 4 m/s
- Capacity : 3000 kg/38 persons
- Shaft height : (up to) 400 m
- Car (length \times width \times height) : 2700 mm \times 1900 mm \times 2700 mm
- Door (width \times height) : 1900 mm \times 2700 mm
- Shaft width : 2750 mm
- Shaft length : 3750 mm
- Headroom : 7700 mm
- Pit depth : 5900 mm

5.8 Personnel transport

For collective or individual transport of personnel (e.g. to and from installation, maintenance and repair locations), including the transport of tools and spare parts, trailer-towing vehicles can be used. The characteristics and performance requirements correspond to those of the rescue vehicles (see below). The overall width of any vehicle has to be compatible with the aperture of the fire-compartment door.

Since the maximum distance from an access point to an intervention location does normally not exceed 5 km, alternative means of individual transport such as electric bicycles can be used. The bicycles must carry spare batteries and an on-board charger.

5.8.1 Transport for emergency services

Transport of emergency teams and their equipment for fire fighting and rescue is a safety-related function. Today, solutions exist for both safety related and normal personnel transport that comply with the relevant regulations and standards. While current CERN vehicles respect European Directives, international standards and CERN safety codes, they will not meet FCC requirements because of the greater distances. Furthermore, the need to transport sufficient quantities of breathing apparatus has to be considered.

The concept of trailer-towing tractors satisfies all requirements. One trailer could be equipped with a compressed air foam (CAF) fire fighting system and extinguishers, while a second trailer could carry injured people. The convoy comprises three fire fighters (two on the tractor, one standing on the trailer). The battery powered vehicles will be equipped with an on-board charger. The general specifications for the tractors and trailers are given in Tables 5.18 and 5.19.

Table 5.18. Tractor specifications.

General conditions	
Type	Tow tractor without cabin
Driver position	Standing straight (front) and seated (back)
Passenger position	1–2 seated passengers (backward)
Propulsion	Electric/AC drive technology
Gears	1 forward/1 backward
Performance	
Speed	Variable up to 25 km/h
Minimum speed	4 km/h (fully loaded on a 12% slope)
Ascending capacity	Minimum 12% slope (“loaded” for a min. distance of 1 km)
	Minimum 20% slope (“unloaded” for a min. distance of 50 km)
Mileage minimum	50 km at 25 km/h (“loaded” on flat floor)
Turning radius	1800 mm maximum
Payload/towed load	300 kg/1 000 kg
Basic dimensions	
Overall width	750 mm maximum
Overall length	2100 mm maximum
Overall height	940 mm maximum
Clearance between the chassis and the floor	100 mm minimum
Tare weight (including battery)	800 kg maximum

5.9 Geodesy, survey and alignment

5.9.1 Introduction

As was already the case for the Large Electron Position (LEP) collider in the 1980s, the FCC-ee will be the most demanding project in terms of positioning accuracy over a circle with nearly 100 km circumference. Present technical possibilities have to be compared to future physics requirements, to define which developments need to be undertaken.

5.9.2 Alignment tolerances

The alignment precision requirements will drive any survey study. The absolute accuracy in the vertical direction is the deviation from the theoretical plane of the collider, whilst in the transverse plane it is the variation of its radius with respect to the theoretical value. The differential variations between several consecutive magnets represent the relative accuracy. This latter type of error has a more direct effect on the closed orbit of the particles. A value of several mm has been assumed as the requirement for the absolute accuracy (this was achieved for LEP and LHC). A relative misalignment of 0.1 mm (1σ) between consecutive quadrupoles and 0.1 mrad (1σ) for the roll angle are indications from beam physics simulations. This error budget has to be split between mechanical errors, due mainly to the assembly process, and alignment errors, including misalignments due to ground motion or mechanical constraints.

Table 5.19. Emergency trailer specifications.

General conditions	
Assisting fire fighter	1 standing on a platform facing the victim
Passenger	1 lying on the back on a stretcher
Performance	
Minimum turning radius	1100 mm
Ascending capacity	12% slope
Full load tractive force with acceleration from 0 to 15 km/h in 10 s	850 N
Storage	Permanently stored with full load
Material transport	
Total maximum capacity	450 kg
Persons transport	
Weight victim on stretcher	100 kg
Weight fire fighter	100 kg
Total maximum capacity	450 kg
Basic dimensions	
Overall width	750 mm
Overall length	2300 mm maximum
Overall height	940 mm maximum
Clearance between the chassis and the floor	60 mm minimum
Useful length	2200 mm
Useful width	740 mm
Trailer floor height	340 mm
Void weight	150 kg

5.9.3 Geodesy

As the area covered by the FCC is ten times larger than that of the LHC, an extension of the mean sea level equipotential surface of gravity (also called the geoid) has to be studied. The very tight relative accuracy will necessitate to determine a geoid at the level of a few hundredths of a mm, which has already been demonstrated in the framework of the CLIC studies [417]. To achieve the absolute accuracy of the surface geodetic network, Global Navigation Satellite Systems (GNSS) will be used, possibly complemented by electro-optical distance measurements. The transfer of the geodetic network points from the surface to the tunnel, through shafts with a depth of up to nearly 300 m, will require new developments. The underground network will necessitate gyro-theodolite traverses, as well as accurate distance and angle measurements and possibly offsets with respect to a stretched wire.

5.9.4 Metrological aspects

Metrological checks and alignments have to be integrated at different times in the manufacturing and assembly processes. This includes the fiducialisation, which determines the survey reference points with respect to the reference axes of a component. The techniques proposed are similar to those proposed for CLIC, i.e. laser trackers and photogrammetry. Co-ordinated measuring machines (CMM) and new techniques such as frequency scanning interferometry (FSI) may be used when justified by the accuracy required. If the FCC-ee dipoles are split into three longitudinal

segments for transport, their assembly and fiducialisation will be done in the tunnel; this process will have to be studied. The positioning of the alignment targets (fiducials) has to take into account the survey needs and the experimental cavern or accelerator tunnel constraints. The equipment supports have to comply with the alignment specifications and constraints.

5.9.5 Alignment of accelerator components

The alignment of accelerator components will be done in two steps:

- The first “absolute” alignment from the underground network will be performed using a standard digital level and total station measurements.
- The “relative” alignment or smoothing. Given the length of the FCC-ee cell and the accuracy required, the standard techniques of levelling and offset measurements with respect to a stretched wire cannot be used. The alignment tolerances of the FCC-ee accelerator elements, can, currently, only be met by a monitoring and alignment system such as that proposed for the CLIC. The alignment tolerance on the dipoles are significantly lower than those of the quadrupoles, however, it is assumed that all beamline elements will be measured and aligned with the CLIC system. If the dipoles are split into three segments, this may well be justified by the relative alignment tolerances of the three segments, and this will be re-assessed once the situation is clarified.

The CLIC alignment system in the tunnel depends on three reference networks: a geodetic reference network (GRN) of reference points on which survey instruments and targets can be placed; a metrological reference network (MRN) composed of overlapping stretched wires, wire positioning sensors (WPS) and a hydrostatic levelling system (HLS); together with a support pre-alignment network (SPN) incorporating WPS on the beamline elements and assemblies, measuring the wires of the MRN. The geodetic reference network is used for marking out, together with the pre-alignment of the MRN sensor supports. The MRN provides a global reference for the accelerator alignment, and the SPN determines the beamline element and assembly positions and orientations with respect to the MRN.

Low cost sensors are being developed as part of the CLIC and HL-LHC projects. The development of similar sensors, with a lower measurement precision, could reduce costs even further. The CLIC tele-operated positioning system [417] has a range of ± 3 mm. If the expected movements of the newly built tunnel are significant, an increase in this range is feasible.

These permanent monitoring and alignment systems have the big advantage of minimising the intervention times for the alignment of an accelerator. However, given the lower alignment tolerances of the FCC-ee, the research and development of different monitoring and alignment system concepts should be considered. Such systems could aim to reduce the number of permanent sensors and instruments, and costs, by incorporating mobile platforms such as a “Survey Train”.

A monorail is not included in the FCC tunnel, and drones, now frequently used for monitoring, will not be allowed. A ground transport robotic system such as those already used at CERN for inspection and manipulation is a possibility, or, for example, a measurement platform transported by a cable car type system might be an alternative providing quicker intervention times. Such developments are the more important if one considers the limited access to the FCC-ee machine once the booster ring will be installed.

Another area where new developments are required are for the remote maintenance of these systems. This would involve exchanging sensors without removing

their reference systems (e.g. wires and water pipes), and also minimising the impact of exchanging a beamline element. Two possibilities are: to consider the sensors as an integral part of the beamline elements; or to move the reference systems away from the beamline and use non-contact measurement to permanent targets.

5.9.6 Interaction regions and collimator areas

The alignment accuracy for the interaction regions is assumed to be the same as for the LHC, i.e. 0.1 mm for the triplets located on the same side of the IP, 0.2 mm from left side of the IP to the right side and 0.5–1.2 mm from the triplets to the detector (all values given at 1σ) [418]. To achieve these specifications, survey galleries will be needed to host part of a permanent monitoring system based on the latest sensor technology available.

The final focussing magnets are located very close to the IP, crossing from the end caps into the central barrel, and will be very challenging to align. A similar configuration was initially proposed in the CLIC design, and no satisfactory solution was found for their support, position monitoring and alignment. Their alignment tolerance is not yet clearly defined, and limited space is available. Further research and development will have to be done on this aspect.

Due to the high level of radiation in the collimator areas, the challenge will be to find a solution to either allow the exchange of collimators without dismantling the survey system or to dismantle and re-install the survey system remotely.

5.9.7 Experiments

The alignment accuracy for assembly of the experiment is assumed to be similar to those of Atlas and CMS i.e. 0.5 mm. The positioning of the experiment with respect to the beam line is done using a geodetic network for the experiment derived from the underground network. It is composed of points distributed across the whole cavern volume on the walls and floor. It is used at all stages of the assembly and positioning of the detectors. It is measured once the cavern has been delivered and is still empty, using mainly distances, angles and levelling measurements. The use of 3D laser tracker technology is appropriate for this type of 3D network. From this network, only the outer skin of the experiment is visible and therefore the position of the inner detectors will be reconstructed from the position of the external fiducials and the fiducialisation and assembly measurements.

5.10 Communications, computing and data services

During the LHC operation era computing for particle accelerators and the experiments has evolved into a service for a world-wide user community. Adopting products and best practices that emerge from an ever-growing Information and Communication Technologies (ICT) industry has proven to be a cost and performance effective path to serve the community. Large-scale science projects used to be a driver of IT infrastructure developments [419–424]. A future particle collider research facility can again be a case and a driving force for advanced ICT developments in areas that go beyond the hardware and software domains, which dominated the particle accelerator projects of the 1980s and 90s.

A set of general services comprising wired and wireless networks, desktop, mobile and centralised computing for all users, various storage system tiers, software and

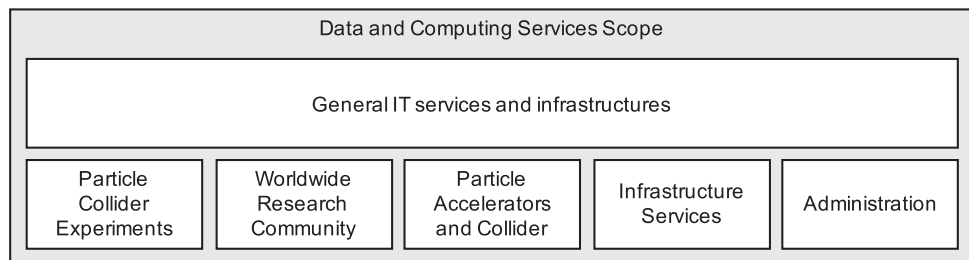


Fig. 5.17. Scope of the IT services found in a high-energy physics research facility.

data provisioning, authentication and authorisation, assistance and consultancy, training and much more, form the backbone of services for individual business units (see Fig. 5.17). Depending on the activity type, different levels of quality of service apply. The particle collider experiments require an elastic data communication and processing infrastructure for data acquisition and high-level event filtering. The data need to be made accessible for a world-wide research community together with data organisation, archiving, retrieval and the management of a dynamically evolving federation of participating organisations. The provision of openly accessible information and the engagement of the public through services to develop citizen-science projects are additional functions for this domain. Computing for the particle accelerator, on the other hand, involves various different networks for data, voice and video communication as well as infrastructures comprising embedded and real-time computing facilities.

Service units of the facility such as the fire brigade and medical services, security and site protection, environmental monitoring, safety-related systems and industrial installations require dedicated IT services. In particular, remote monitoring and intervention has become an important means to reduce service level agreement costs for industrial plants over the last ten years. Finally, administration units ranging from human resources and finance to different types of workflow systems need to be appropriately served whilst taking into account the length of the construction and operation phases which will last for decades. For all domains, resilience, data protection, cyber-security, technology evolution and migration and long-term data accessibility are topics that call for a dedicated organisation to ensure proper coverage with an appropriate mix of in-house personnel, external suppliers and industry/academia partnerships.

The significant geographical extent of the services and long-term sustainability of a new large-scale particle-collider research facility require a shift of activities, traditionally covered by individual detector and accelerator engineering groups, to a business oriented scientific IT unit. This approach allows tenders, contracts and operation to be optimised at an organisation-wide scale as well as influencing the value of member state contributions favourably for the member countries, the organisation and the world-wide community. In particular, this approach for the construction and operation of data centres can be beneficial for experiment users, accelerator engineers and users with generic needs.

Computing and interconnect technologies are evolving rapidly and generation changes need to be expected. At the same time the optimum cost effectiveness is continuously swinging between buying and leasing. This ever changing IT environment can best be accommodated by a continuous cost/benefit analysis considering all users in the organisation, carried out by a team which is working closely with industry on one side and with the users on the other.

Embedded and real-time computing including programmable logic controllers are also a concern for a technology infrastructure that is characterised by its longevity and thus dominated by operating costs. Given the significant increase in the number of devices for a future collider, further standardisation, coordinated testing and certification and procurement and maintenance/repair services, available to all users of the organisation, will help to improve the cost effectiveness. A large-scale particle accelerator building on decades of engineers experience presents an ideal case for an openly available architecture and platform for supervisory control to integrate the diverse subsystems. A system that can evolve with emerging “Internet of Things” (IoT) products and yet unanticipated device technologies can create impact far beyond the particle accelerator community.

Cyber-security plays an increasingly important role in IT systems and embedded computing is no exception to this. The use of processors, operating systems and embedded Web servers in the majority of programmable laboratory equipment such as simple digital I/O devices, measurement instruments, oscilloscopes and autonomous robots already require a well organised infrastructure. This is supported by a process that leads to a secure environment on one side and which has the least possible impact on usability on the other side. For example, it should allow the possibility of developing and deploying across network boundaries, create islands and sandboxes to limit potential harm, have transparent virus and malware checking and isolation, have system updates that have little or no impact on work efficiency, provide coordinated rollback and much more. This evolution is expected to continue and the IoT approach will also require an organisation wide vertical integration of services across the horizontal user domains [378].

Cooperation on IT standards, technology developments and organisation with other research facilities which have similar requirements (e.g. DESY, ESRF, ESS, Fermilab) needs to be strengthened. Synergies with other scientific domains (e.g. astronomy and radioastronomy facilities, material sciences with light sources and FELs, astrophysics installations such as neutrino and gravitational wave observatories, particle accelerators for medical applications and nuclear fusion experiments) can be developed to lead to more effective operation of world-wide IT services for research. Activities spawned by DESY on front-end computing hardware [425] and CERN’s openlab [426] are good examples for such initiatives.

The geographical extent of a 100 km long particle collider across the Canton of Geneva and far into the Haute Savoie region suggests the development of cooperation with the host state communication network providers and with telecom operators. Improving the high-tech communication, computing and data service infrastructure in the region is high on the agenda of the host state authorities with an ambition to become a “European Silicon Valley” [427]. It creates further potential for the strengthening of CERN as a focal point of high-technology in a region in which the population approaches 2 million (departments Ain and Haute Savoie, canton Geneva) and which also has a high annual growth rate [428].

Possible services do not only include fibre optics and data centres that can be shared with academic partners but can also include mobile communication and the cooperation with emergency and rescue services in a cross-border context. CERN’s activities concerning the establishment of the TETRA radio communication system in the region are a first step in this direction [429]. CERN’s particular status as carrier-neutral Internet eXchange Point (CIXP) [430] will gain importance in a technology ecosystem that becomes ever more dominated by profit making organisations which are building and operating global communication infrastructures. These collaborations may help to ensure that non-profit making organisations continue to operate independently and become less dependent on infrastructure operator priorities, which may favour financially stronger commercial clients.

Beyond the regional scale, the LHC programme has shown the value of a world-wide computing and communication infrastructure to make the research data available to scientists in all participating countries [431]. The success of a future particle collider programme will rely even more on international participation. Many potential participating countries are not part of CERN's global vision today and some are still technologically underserved. The SESAME light-source under the auspices of UNESCO is a great example of such an initiatives [432]. The capacity to plan, develop and implement a world-wide inclusion policy goes beyond the scope of the high energy physics community and is therefore also a good opportunity to establish a common strategy with other scientific disciplines. A timely development of such an initiative will help raising the interest and acceptance level of large-scale investments in an infrastructure focusing on fundamental scientific research.

Considering the fast evolution of information technologies in all domains [433], the long term cost impact of in-house technology developments and their potentially limited large scale impact, it is prudent to base architectures for the particle accelerator and the experiment data processing environments on industrial hardware, software and service infrastructures. The particular needs of an FCC-scale facility may, however, also represent attractive test-beds for emerging technologies. Co-innovation projects with industrial partners during the early construction phase, permitting pre-commercial procurement initiatives that can lead to high-performance infrastructure services at a competitive cost are one way to optimise this situation [434].

A preliminary cost-benefit-analysis of the LHC/HL-LHC programme [435] revealed that more than the impact value generated by training corresponds to more than one third of the infrastructure's cost (sum of capital and operation expenditures). The ICT sector represents an ideal case for training at large with ever growing societal and industrial demands. Early stage researchers and engineers are much appreciated participants in CERN's technology programmes, which give them opportunities to acquire skills that are also high on the wish list of industry. It would be possible to extend these training programmes to participating industrial partners, generating value for industry directly. The CERN openlab public-private partnership already demonstrates the validity of this approach. Further industrial cooperation can focus on field testing of pre-commercial products and services, common optimisation, development of standards and best-practices and co-innovation with the research infrastructures as a demonstration case. These activities would be carried out in low risk environment for industrial partners of any size. The scaling up of the open, industrial SCADA platform PVSS around the year 2000 is one example of the success of this approach [436]. Eventually, the company was integrated in the SIEMENS group and the software has been re-branded as WinCC OA to become the SIEMENS flagship SCADA system on the global scale.

Finally, long-term data availability [437] has become an important aspect of ensuring the lasting impact of the facility [438]. The accessibility of several decades worth of raw LHC data, all metadata and previous analysis results has turned out to be a major topic for the ICT community. With a future particle collider, the time span will extend to the end of the 21st century, calling for evolving data storage and management systems that serve the worldwide particle physics community for more than 100 years. Considering the continuous evolution of data formats, the ever-changing particle detectors and a highly dynamic user community, data quality management is a primary topic. The value of a particle collider research facility depends directly on its quality and long term world-wide accessibility for as large a community of scientists as possible.

5.11 Safety and access management systems

A safety management system (SMS) for a future large-scale particle collider will be based on an industry best-practice system which integrates, in a uniform and regulatory-compliant way, everything which contributes to safe operation. This system also includes the procedures associated with the different operating conditions encountered during the lifetime of the collider. A high-level computer-based safety management system integrates underlying safety related functions, including fire detection, oxygen deficiency detection, smoke and helium extraction systems, fire extinction systems, access and authorisation management, door supervision and control, video surveillance, radiation monitoring, conventional environmental monitoring, evacuation signalling, supervision and control of lifts, communication with people in underground zones, emergency lighting and acoustics and communication with emergency services (fire fighting, rescue, healthcare providers, public and private security forces). The sub-systems function autonomously.

There are two complementary systems for personnel protection in the underground areas: the access safety system and the access control system. During machine operation, the access safety system protects personnel from the hazards arising from the operation of the accelerator and from the beams. It acts through interlocks on important safety elements of the accelerator. By interlocking these elements it is possible to establish the right accelerator and equipment conditions in order to allow authorised personnel to access the underground installations or to allow the restart of the accelerator equipment when access is finished. When the accelerator is not operating with beam and is in access mode, the access control system allows the positive identification of any person requesting access and ensures that all pre-requisites and authorisations for that person are valid. For operational and/or safety reasons, the access control system also limits the number of people present simultaneously in the underground areas.

An automatic fire detection system consisting of detectors and air sampling networks to detect the presence of smoke is connected to control and monitoring equipment located in one of the surface buildings at each point. If fire or smoke is detected, the system launches automatic safety functions and alerts the fire and rescue service. Fire detection is installed in all underground areas and will allow accurate location of a fire. An automatic oxygen deficiency detection system warns users of the danger and alerts the fire and rescue service. Underground areas will also be equipped with communication channels to allow a user to contact the fire and rescue service directly.

The SMS launches safety functions if there is a fire or oxygen deficiency is detected. These functions include compartmentalisation, evacuation and smoke extraction. The CERN fire brigade has the possibility to trigger these functions remotely and to broadcast safety instructions in the various areas of the facility.

The emergency evacuation system is a part of the automatic protection system. It broadcasts audible evacuation signals triggered either automatically by a safety system, such as fire or oxygen deficiency detection, or manually by pushing one of the emergency evacuation buttons installed within the area in question.

The SMS provides prioritised and homogeneous visualisation of the status of all safety relevant parameters, allows the supervisory control of all sub-systems and handles the sub-system interconnections. The SMS communicates with the sub-systems through fail-safe protocols, over a dedicated communication infrastructure. It guarantees that critical alarms are automatically transmitted to the competent services (e.g. fire brigade, radiation protection team) and that all incidents are recorded and suitably documented for potential internal and external examination (auditing). Furthermore, the SMS ensures that any condition which is incompatible with safe beam operation (e.g. intrusion) is detected and the beam is aborted.

Table 5.20. Examples for typical safety management system solutions for large-scale applications.

Supplier	Product
Advancis Software & Services	PSIM
ATS Elektronik	AES5000, DLS4000
Bosch Security Systems	Building Integration System
CENARIO solutions	CENARIO
digivod	CRISP PSIM
ETM/SIEMENS	WinCC OA
Genetec	Security Center
GEOBYTE	Metropol BOS
Honeywell	Enterprise Buildings Integrator, WINMAG plus
KÖTTER Security	LENEL OnGuard
PKE	AVASYS
Scanvest	ScanVis.Pro
Securiton	Universal Management System SecuriLink UMS, IPS
SIEMENS	GMA-Manager, Siveillance Vantage
Tyco Integrated Fire & Security CKS Systeme	CELIOS, C-cure 9000
WAGNER Group	VisuLAN X3

Such supervisory systems are in daily operation in most large-scale plants (e.g. particle-accelerator-based ion therapy facilities, oil and gas rigs, manufacturing and processing plants). Examples for typical Safety Management System solutions are listed in Table 5.20.

The future system must be compliant with international norms, be open and extensible and be configurable to the specific application (e.g. GIS and CAD integration, user interface designer). Processing speed is generally not critical, but the system must work extremely reliably, be highly scalable and be open to the integration of a continuously growing set of diverse subsystems from different suppliers. Implementation details (e.g. positioning of a central supervision point, the number and position of decentralised facilities to interact with the system, hard- and software choices, rights management, means to identify people requesting access, or locating people in the machine) will be subject to a requirements specification phase, once the detailed design of the infrastructure and its individual technical systems are well known.

6 Injector complex

6.1 Injector overview

The injector complex of the FCC-ee comprises an e^+e^- linac (for energies up to 6 GeV), a pre-booster synchrotron ring (PBR), accelerating from 6 to 20 GeV, and a full energy booster synchrotron ring (BR), integrated in the collider tunnel. A schematic layout of the injector complex can be seen in Figure 6.1.

Table 6.1 contains a list of parameters for the injection schemes for the different collider energies and filling modes (top-up or initial filling). The baseline parameters are established assuming an SLC/SuperKEKB-like linac [439,440] (C-band 5.7 GHz RF system) with 1 or 2 bunches per pulse and a repetition rate of 100 or 200 Hz. The full filling for Z running is the most demanding with respect to the number

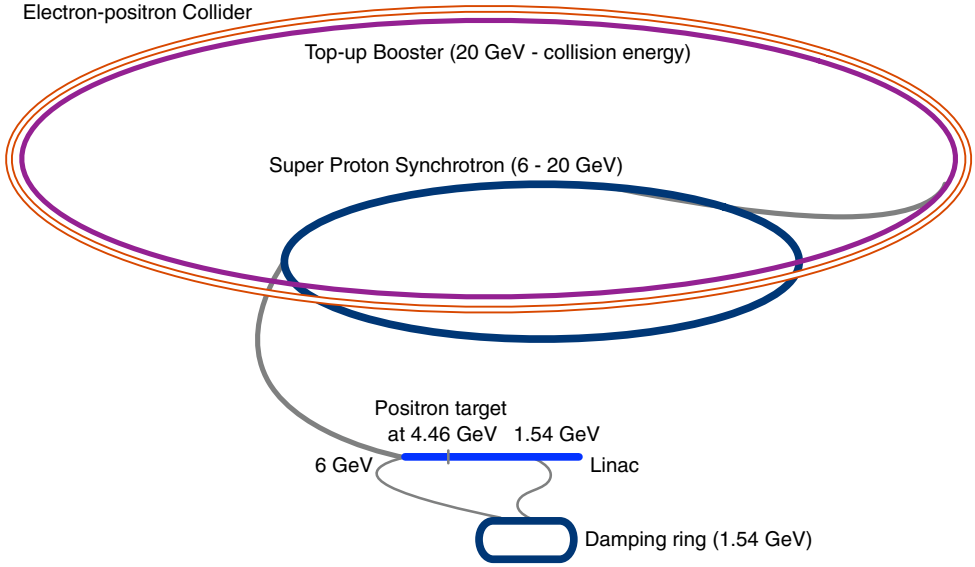


Fig. 6.1. Schematic layout of the FCC-ee injector complex, with the SPS serving as PBR.

Table 6.1. FCC-ee injector parameters.

Parameter (unit)	Z		W		H		tt	
Beam energy (GeV)	45.6		80		120		182.5	
Type of filling	Initial	Top-up	Initial	Top-up	Initial	Top-up	Initial	Top-up
Linac bunches/pulse	2				1			
Linac repetition rate (Hz)	200		100					
Linac RF frequency (GHz)	2.8							
Bunch population (10^{10})	2.13	1.06	1.88	0.56	1.88	0.56	1.38	0.83
No. of linac injections	1040		1000		328		48	
PBR minimum bunch spacing (ns)	10		10		70		477.5	
No. of PBR cycles	8		1					
No. of PBR bunches	2080		2000		328		48	
PBR cycle time (s)	6.3		11.1		3.7		0.9	
PBR duty factor	0.84		0.56		0.30		0.08	
No. of BR/collider bunches	16640		2000		328		48	
No. of BR cycles	10	1	10	1	10	1	20	1
Filling time (both species) (s)	1034.8	103.5	266	26.6	137.6	13.8	223.2	11.2

of bunches, bunch intensity and therefore injector flux. It requires a linac bunch intensity of 2.13×10^{10} particles for both species. The electron linac used for positron production should provide around a factor of two higher bunch charge, i.e. 4.2×10^{10} electrons, allowing for a 50% conversion efficiency. The bunch intensity requirements include a comfortable 80% transfer efficiency throughout the injection complex (from the source to the collider).

A schematic of the injection process through the different accelerators is shown in Figure 6.2. Using a bunch-to-bucket transfer, bunches from multiple linac pulses will be injected into the PBR, which is equipped with a 400 MHz RF system. Between 48 and 832 injections will fill the PBR depending on the collider running mode (Z, W, H or tt).

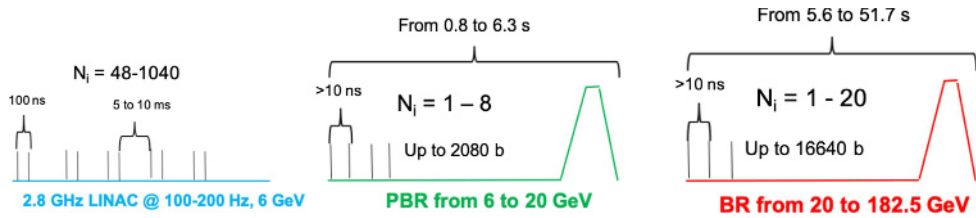


Fig. 6.2. Schematic representation of the FCC-ee injector scheme showing the bunch structures and the magnetic cycles in the PBR and BR (green and red respectively).

In the current baseline, the SPS is considered as the PBR, using a scheme similar to the one used for injection into LEP [441]. The PBR cycle length is dominated by the injection plateau and includes a fast ramp of 0.2 s up to 20 GeV and a minimum fast extraction flat top of 0.1 s. The total number of bunches required (48 to 16 640 bunches) is transferred to the main booster in at most 10 PBR cycles. If the SPS serves as PBR, the fraction of overall machine time that needs to be dedicated to filling the booster (the duty factor quoted in Tab. 6.1) varies between 8% for the $t\bar{t}$ mode and 84% on the Z pole. Accelerating a larger number of bunches per linac pulse or injecting more bunches per PBR cycle would provide additional time for other parallel SPS beam users. Alternative injector options studied, which would not impact SPS fixed-target operation, include a more compact “green field” PBR or an extension of the linac to reach an energy of 20 GeV for direct injection into the main booster.

The bunch trains from the PBR can be directly injected into the bunch structure required by the collider, within the 400 MHz RF. The bunches are then accelerated with a maximum ramp time of 2 s, and a maximum total cycle length of up to 51.7 s, dominated again by the long injection flat bottom, corresponding to the Z running. Due to the short beam lifetimes of 40–70 min, which depend on the parameter sets and running energies, continuous top-up injection from the BR is required. For the initial filling, the bunches are accumulated in the collider in less than 20 min. At other times, the beam is used to top up the current, to maintain the collider beam lifetime limits within the $\pm 3\%$ current drop ($\pm 5\%$ for the Z). The filling of the two particle species in the machine is interleaved and is able to accommodate the current bootstrapping [442].

6.2 Electron gun

The custom built RF gun has a normalised transverse emittance of $\leq 10 \mu\text{m}$, and provides 6.5 nC of charge at 11 MeV. The charge is intentionally high to allow for a high charge injection for the initial fill of the collider at startup. Briefly, the RF gun (see Fig. 6.3) is based on a parallel coupled accelerating structure [443, 444] and has permanent magnets in the irises to reduce the beam size and limit emittance dilution. It is planned to use material based on IrCe alloy [445, 446] as the photocathode because this provides acceptable lifetime with high charge extraction at high repetition rate. The design was made with the aid of the ASTRA code [447] and some parameters are presented in Table 6.2.

6.3 Linac

The normal conducting linac will be fed by two electron sources, one will be the RF gun for the low emittance e^- beam, and the second is the thermionic gun to provide

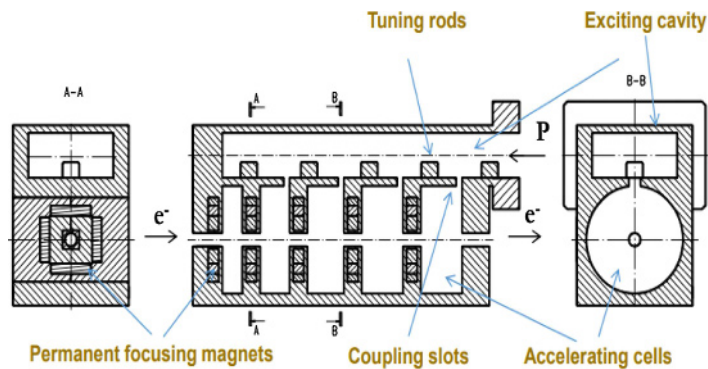


Fig. 6.3. A schematic drawing of the RF gun.

Table 6.2. Design parameters of the RF gun.

Parameter	Value
Initial geometrical emittance	0.6 μm
Injection kinetic energy	11 MeV
Total charge	6.5 nC
Cathode spot size	5 mm
Initial distribution	Radially uniform
Laser pulse duration	8 ps
Laser injection phase	variable
Magnetic field on the cathode	0 T
Peak accelerating field	100 MV/m
Focussing solenoid field	0.5 T

Table 6.3. Linac S-band accelerating structures.

Parameter (unit)	Value
Frequency (MHz)	2855.98
Length (m)	2.97
Cavity mode	$2\pi/3$
Aperture diameter (mm)	20
Unloaded cavity gradient (MV/m)	25

higher charge needed for creating enough positrons from a hybrid target [448,449]. The linac consists of S-Band structures accelerating the beam up to 6 GeV, with the parameters presented in Table 6.3.

The wakefields [450] have been included in linac simulations, together with the misalignments and offsets which are presented in Table 6.4. The preservation of emittance and charge is ensured by an automatic orbit steering code. With ideally deployed BPMs, the impact of misalignments cancels out perfectly. The performance of the linac has been studied in simulations with different bunch charges and for various random error seeds [451].

The low energy part of the linac starts with the beam from the RF gun at 11 MeV. With the optics shown in Figure 6.4 and the singlet, doublet, and triplet magnets not set to high fields, kicks from the misaligned quadrupoles are minimised. These settings produce the results presented in Table 6.5.

Table 6.4. RMS linac misalignments and offsets; Gaussian distributions are assumed.

Parameter	Simulated error
Injection offsets (h/v)	0.1 mm
Injection momentum offset (h/v)	0.1 mrad
Quadrupole misalignment (h/v)	0.1 mm
Cavity misalignment (h/v)	0.1 mm
BPM's misalignment w.r.t. cavity (h/v)	30 μ m

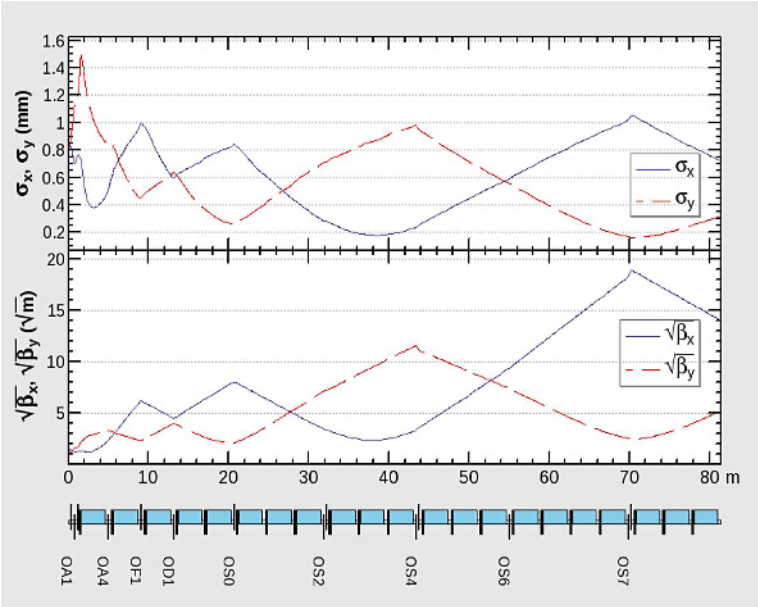


Fig. 6.4. Optics of the 1.54 GeV linac.

Table 6.5. Some parameters of the linac up to 1.54 GeV.

Parameter	Value
Length	79.1 m
Number of cavities, quadrupoles	21, 14
Injected emittance (h/v)	0.35/0.5 μ m
Average extracted emit. (h/v)	6.4/5.0 nm
Transmission for 3.2 nC	100%

At 1.54 GeV, the linac has a bending magnet to send the e^- beam towards the damping ring (DR) for cooling before delivering it to the collider. Electrons will be stored for 25ms in the DR, which is capable of curing emittance dilution due to misalignments and space charge, even by up to two orders of magnitude with respect to the output emittance. After cooling, the beam is transferred back to the linac via turnaround loops and bunch compressor. Thus, the emittance of the beam delivered to the 1.54 GeV linac is determined by the DR cooling. Due to the rather relaxed emittance requirements at the entrance of the booster, the damping ring may not be necessary for the e^- beam (Fig. 6.5).

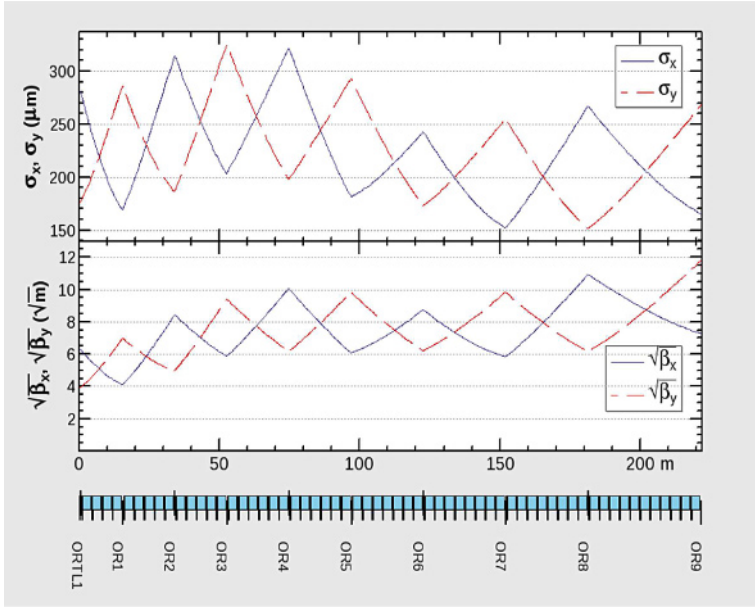


Fig. 6.5. Optics of 1.54–6 GeV linac.

Table 6.6. Some parameters of the 1.54–6 GeV linac.

Parameter	Value
Length	221.9 m
Injection-extraction energy	1.54 GeV–6 GeV
Injected emittance (h/v)	1.9/0.4 nm
Average extracted emit. (h/v)	1.1/0.4 nm
Transmission for 3.2 nC	100%

Some parameters of the 1.5–6 GeV part of the linac are presented in Table 6.6. In the 6 GeV linac option, the beam will be injected into a pre-booster damping ring. The emittance and charge requirements for all of the four FCC-ee working points can be safely met with a near-perfect transmission and a factor of ten safety margin in transverse emittance at 6 GeV. More specifically, the transverse emittance of the beam injected in the PBR can be as big as 10/100 nm (h/v), which leaves a very large margin for the extracted emittance from the linac.

6.4 Linac at 20 GeV

For the option of direct injection into the top-up booster, it is proposed to use C-band high gradient accelerating structures to accelerate the beams from 6 to 20 GeV. The specifications of the accelerating structures are presented in Table 6.7.

The 20 GeV linac presented in Figure 6.6 is not just an extended version of the S-band linac, but it is re-optimised in order to increase the transmission. The drift spaces, with length L , between the cavities and steering magnets are lengthened in order to reduce the impact of BPM offsets which are proportional to σ_{BPM}/L . Furthermore, the increase in the spacing lowers the steering magnets' fields and in turn decreases the dispersion created by the steering. Consequently, the emittance dilution is decreased, however, it almost meets the requirement of the booster which

Table 6.7. C-band linac structures for acceleration from 6 to 20 GeV.

Parameter (unit)	Value
Frequency (MHz)	5711.96
Length (m)	1.80
Cavity mode	$2\pi/3$
Aperture diameter (mm)	14
Unloaded cavity gradient (MV/m)	50

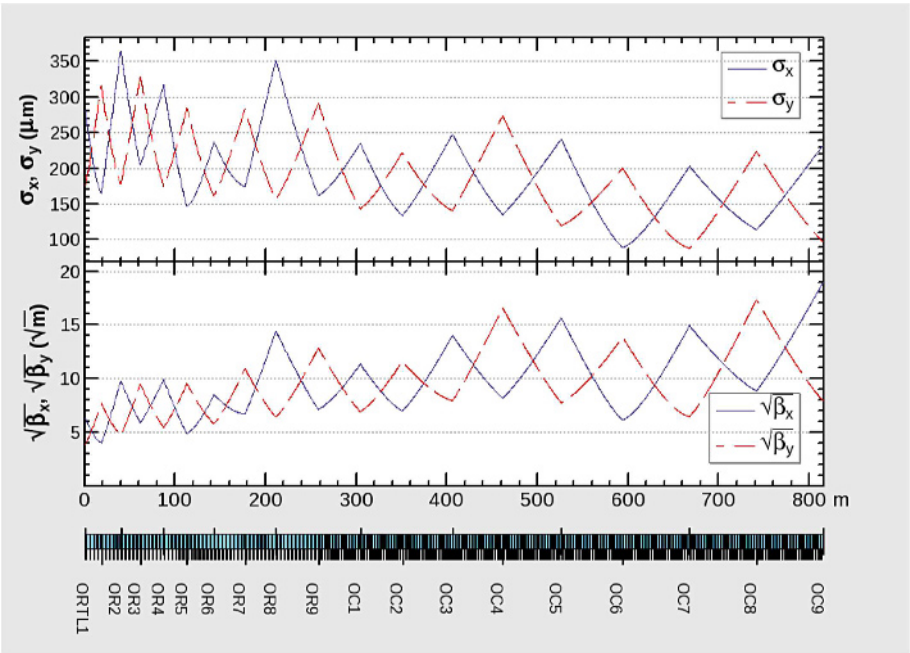


Fig. 6.6. Optics of the 1.5–20 GeV part of the linac. Note that the C-band structures start after QR9.

is 3.4/0.3 (h/v) for 15σ acceptance. Some parameters of the 1.5–20 GeV part of the linac are presented in Table 6.8.

Additionally, the orbit steering for the 20 GeV linac may be improved through dispersion-free steering and Balakin-Novokhatsky-Smirnov (BNS) damping [452], to reduce the emittance blow up and hence the transmission loss. It should be noted that an 8% transmission loss is already envisaged and acceptable.

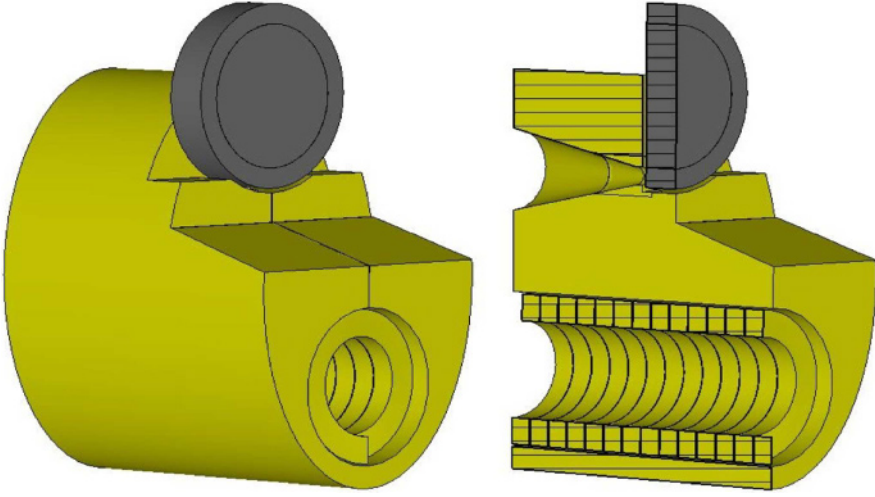
6.5 Positron source and capture system

For positron production, the same 6 GeV electron linac is used with a higher bunch intensity of 4.2×10^{10} particles at an energy of 4.46 GeV. Taking into account the production efficiency and transfer losses, this allows almost a 50% margin with respect to the collider requirements. The positron beam emittances are reduced in the the DR at an energy of 1.54 GeV and the beam is then transferred back to the linac for further acceleration and injection into the PBR.

There are two commonly used production schemes: the conventional one employs a target made from a material with high atomic number and high melting point. The positrons are created from the impinging electrons through bremsstrahlung and pair conversion. This type of source has been employed in several modern lepton

Table 6.8. Some of the parameters of the 1.54–20 GeV part of the linac.

Parameter	Value
Length	858 m
Injection-extraction energy	1.54 GeV–20 GeV
Injected emittance (h/v)	1.9/0.4 nm
Average extracted emit. (h/v)	4.0/0.3 nm
Transmission for 3.2 nC	92%

**Fig. 6.7.** Model of the flux concentrator at the FCC-ee e^+ target; parameters are listed in Table 6.9.

colliders [181,439]. The main limitation of this scheme is the high heat load in the target and the peak energy deposition density (PEDD). This limitation can be overcome in the second option which uses a hybrid target in a two-stage process. An intense photon beam is emitted by GeV electrons channeled along a crystal axis. The charged particles are swept off after the crystal target and thereby the deposited power and PEDD are significantly reduced [453–455]. A further improvement involves the use of a granular target which provides better heat dissipation [448]. Several experiments had been conducted to study the hybrid e^+ source [454,456]. After the target, an adiabatic matching device (AMD) with a flux concentrator is used to match the positron beam (with very large transverse divergence and energy spread) to the acceptance of the pre-injector linac. Figure 6.7 shows a proposed flux concentrator. Table 6.9 lists its key parameters.

The performance of several existing positron sources is compared to a preliminary design of a conventional source (the first option described above) in Table 6.10. The production schemes presented employed electron beams with various energies, bunch charges and finally positron yields (number of positrons per electron impinging onto the target). In comparison, the FCC-ee parameters are very similar to those of the existing sources and designs, therefore the FCC requirements can be achieved even with a conventional positron source [449].

Table 6.9. FCC-ee flux concentrator parameters.

Parameter (unit)	Value
Target diameter (mm)	90
Target thickness (mm)	15.8
Gap between target and FC (mm)	2
Grooving gap between target side face and FC body (mm)	2
Elliptical cylinder size (mm)	120 × 180
Total length (mm)	140
Conical part length (mm)	70
Min cone diameter (mm)	8
Maximum cone diameter (mm)	44
Cone angle (deg.)	25
Cylindrical hole diameter (mm)	70
Coil turns (–)	13
Current profile pulse length (μs)	25
Peak field (T)	7
Peak transverse field (mT)	135–157
Gap between coil turns (mm)	0.4
Gap between coil and FC body (mm)	1
Turns size	9.6 × 14 mm

Table 6.10. Performance of other positron sources compared to a conventional source for FCC-ee.

Accelerator	SLC	LEP (LIL)	SuperKEB	FCC-ee (conv.)
Incident e [–] energy (GeV)	33	0.2	3.3	4.46
e [–] /bunch (10 ¹⁰)	3–5	0.5–30	6.25	4.2
Bunch/pulse	1	1	2	2
Rep. rate (Hz)	120	100	50	200
Incident beam power (kW)	20	1	3.3	15
Beam size @ target (mm)	0.6–0.8	<2	>0.7	0.5
Target thickness (X ₀)	6	2	4	4.5
Target size (mm)	70	5	14	>30
Deposited power (kW)	4.4	0.1	0.6	2.7
Capture system	AMD	λ/4 transformer	AMD	AMD
Magnetic field (T)	6.8 → 0.5	1 → 0.3	4.5 → 0.4	7.5 → 0.5
e ⁺ yield	1.6	0.003	0.5	0.7

6.6 Damping ring

The damping ring design has been presented in [457] and some of its features are described in the following paragraphs. The repetition rate of 200 Hz allows hosting of 5 trains, each with 2 bunches per RF pulse. After taking into account the longitudinal wakefields in the linac, the bunch to bunch spacing was chosen as 60 ns [458]. Two bunches per RF pulse in the linac will become a train in the DR. Altogether 5 trains with a 100 ns spacing (for the kicker rise/fall time) and a bunch-to-bunch spacing of 60 ns in the linac have resulted in the requirement that the damping ring should have a circumference of at least 240 m (i.e. ~800 ns).

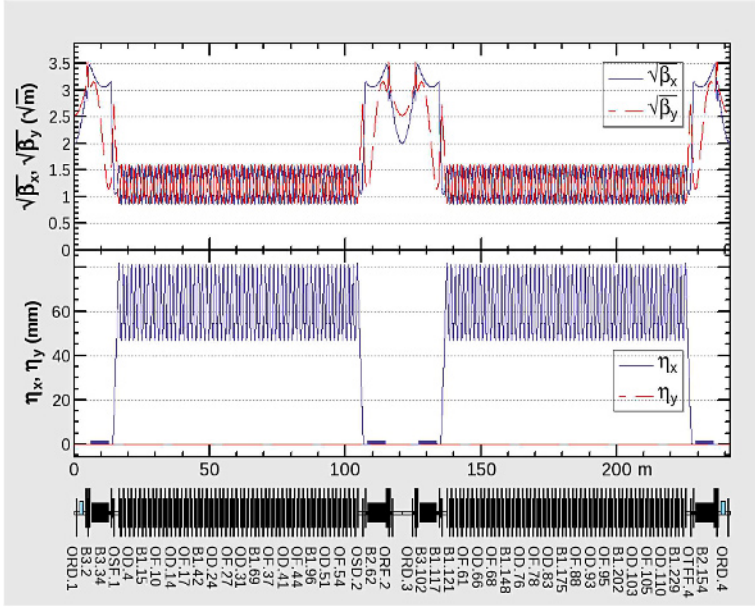


Fig. 6.8. Damping ring optics.

Table 6.11. 1.54 GeV damping ring design parameters.

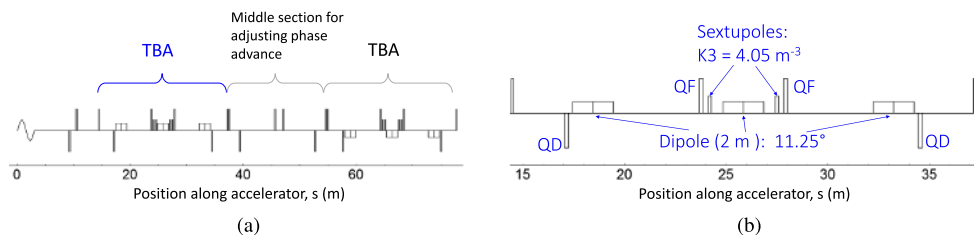
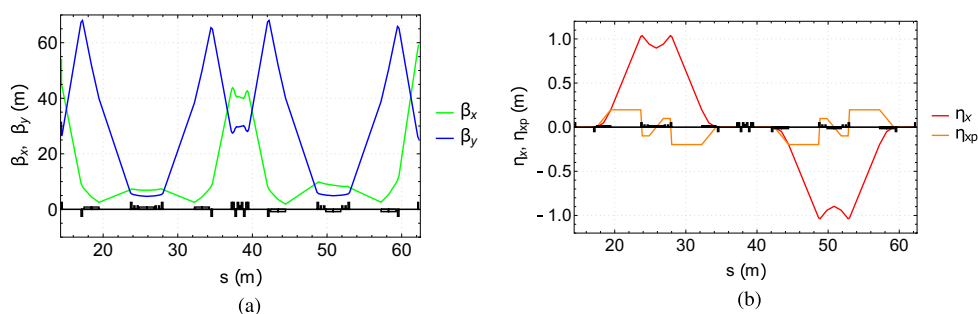
Parameter	Value
Circumference	241.8 m
No. trains, bunches/train	5, 2
Train, and bunch spacings	100 ns, 61 ns
No. of cells in arc, cell length	57, 1.54 m
FODO cell phase advance (h/v)	69.5/66.1 deg
Betatron tune (h/v)	24.19/23.58
Natural emittance (h/v)	1.16/- nm
Damping time (h/v)	10.6/11.0 ms
Bending radius, wiggler field	15.5 m, 1.8 T
Energy loss per turn	0.22 MeV
RF voltage, frequency	4 MV, 400 MHz

The DR optics and parameters are presented in Figure 6.8 and Table 6.11, respectively. The DR consists of 2 straight sections housing four 6.64 m long wigglers. One of the straight sections also contains a 7.4 m drift space reserved for injection/extraction and the opposite section hosts two LHC-type 400 MHz, 1.5 m long (3.5 m with cryostat) superconducting cavities. Injection of the e^+ beam from the linac [459] into the DR for a store time of 45 ms has been simulated. This storage is derived from the interleaved injection/extraction of the 5 trains.

The $\pm 7.8\%$ energy acceptance of the DR may be reduced to $\pm 3.5\%$ by lowering the voltage in order to increase the bunch length so that emittance dilution due to coherent synchrotron radiation (CSR) is avoided. For this reason, the incoming e^+ beam may be collimated at the end of the linac at $\pm 3.5\%$ or an energy compressor could be installed.

Table 6.12. Damping ring performance without errors.

Parameter	Value
Transv., long. acceptance	22.4 μm , 14.7 mm
Energy spread	7.09×10^{-4}
Bucket height	8.0 %
Energy acceptance	± 7.8 %
Injected emittance (h/v/l)	1.29/1.22/75.5 μm
Extracted emittance (h/v/l)	1.81/0.37 nm/1.52 μm

**Fig. 6.9.** (a) Magnet layout of the dogleg bunch compressor. The TBAs are identical except that they bend in opposite directions. (b) Detailed layout of one TBA.**Fig. 6.10.** (a) Beta functions through the dogleg bunch compressor, where β_x is indicated by the green line, and β_y by the blue line. (b) Horizontal dispersion function, η_x , shown by the red line, and the horizontal angular dispersion function, η_{xp} shown by the orange line.

6.7 Bunch compressors

Before injection into the linac, the bunch length of the positron beam needs to be compressed from approximately 5–0.5 mm. It is proposed to have a dogleg bunch compressor comprising two triple bend achromats (TBA) to achieve this compression. A schematic drawing of the bunch compressor layout is shown in Figure 6.9. Each dipole has a bending angle of 11.25°, and a quadrupole and sextupole are placed in mirror symmetry between the dipoles. A section for adjusting the phase advance is installed between the two TBAs. The quadrupole magnets are used to control the dispersion function, ensuring it goes to zero at the end of each achromat. The longitudinal dispersion properties of the bunch compressor are: $R_{56} = 0.40$ m, $T_{566} = 11.09$ mm, and $U_{5666} = 15.89$ mm.

An energy chirp is put in the beam by an S-band RF cavity upstream of the bunch compressor. The RF cavities have the following properties: $f_{\text{RF}} = 2.86$ GHz, $\phi_{\text{RF}} = 180^\circ$, and an accelerating gradient of 22.3 MV/m, to establish an energy chirp of $h_1 = \frac{1}{E_0} \frac{dE}{ds} = -2.75 \text{ m}^{-1}$.

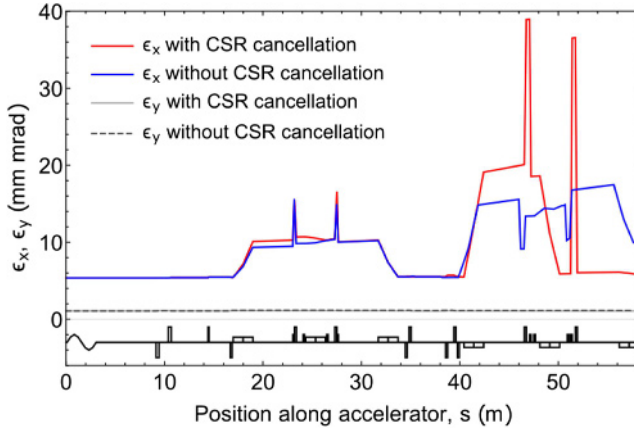


Fig. 6.11. Emittance along the bunch compressor, before CSR cancellation techniques are applied (red) and after (blue).

The design presented here does not require a harmonic cavity. Instead a form of optical linearisation is used to minimise the non-linear terms encountered in bunch compression [460,461]. Sextupole magnets are placed at a position where the dispersion is near maximum and are optimised to correct the transverse chromaticity, rather than being optimised to cancel the second-order terms of the transport equations. Fortunately, despite being optimised for chromaticity, the resulting T_{566} is close to the optimum for reducing the effect of the non-linear compression terms, negating the need for a harmonic cavity [462].

In spite of the relatively long bunch length ($\sigma_{z,f} = 0.5$ mm), coherent synchrotron radiation (CSR) has the potential to degrade the beam quality. This is because the reasonably large value of R_{56} that is required necessitates a large degree of bending in a dogleg bunch compressor. Fortunately, CSR cancellation techniques [463–467] can be used to mitigate the emittance growth to an acceptable level.

Careful control of β_x , and α_x in each dipole, as well as the phase advance between each dipole, cancels out the CSR kicks (Δx_k and $\Delta x'_k$) almost completely. To compensate for the CSR kicks, an additional quadrupole magnet is needed in the section between the TBAs. A comparison of the emittance growth obtained with and without this CSR kick mitigation is shown in Figure 6.11. Initially (i.e. before the CSR kick cancellation method applied), the horizontal emittance growth was 68.3%. After the inclusion of the additional quadrupole and after the phase advance and Twiss parameters of the second TBA are manipulated, the emittance growth is reduced to 9.5% (this includes CSR in the drifts).

6.8 Pre-booster

Two options are being considered for the pre-booster synchrotron: using the existing SPS (baseline) or a new ring.

Using the SPS as pre-booster for the FCC-ee imposes various constraints, as only certain modifications can be made to the existing machine. There were similar constraints when the SPS was used as an injector for the LEP collider [265]. The SPS is filled with FODO cells and the emittance can be minimised by tuning them to a horizontal phase advance of around 135° . This phase advance provides an equilibrium transverse emittance of below 30 nm at 20 GeV. In addition, it ensures dispersion suppression, as the total arc phase advance is a multiple of 2π [468].

Table 6.13. SPS Parameters with/without wiggler magnets.

	6 GeV (injection)		20 GeV (extraction)	
	Without wiggler	With wiggler	Without wiggler	With wiggler
ϵ_x (nm)	2.43	0.13	27	10
τ (s)	1.7	0.1	0.04	0.02
U_0 (MeV)	0.15	2.7	19	47

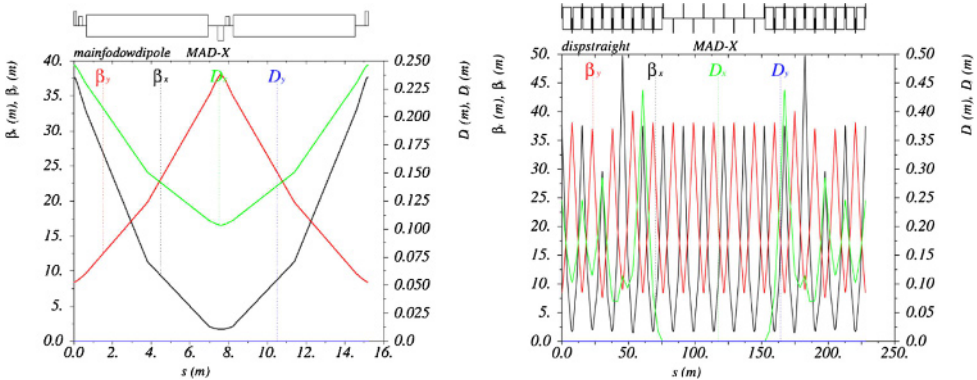


Fig. 6.12. Beta functions and dispersion of the main cell (left) and straight section(right).

The damping time is quite long, around 1.7 s for the SPS at 6 GeV. This would lengthen the SPS injection plateau and consequently the whole injector cycle. Wiggler magnets with a field of 5 T and a total length of 4.5 m can shorten the damping times by roughly an order of magnitude. Some parameters of the SPS with and without wiggler magnets are shown in Table 6.13. In particular, the horizontal equilibrium emittance is reduced to 0.13 and 10 nm.rad at injection and extraction, respectively, whereas the corresponding energy loss per turn is greatly increased to 2.7 and 47 MeV.

An alternative study of a green-field pre-booster ring has also been made. The booster requirements for dynamic aperture constrain the extracted emittance of the PBR to around 3 nm.

The linear lattice of the PBR is based on analytic calculations and simulations. A FODO type cell has been chosen and the ring has a racetrack shape consisting of 2 arcs and 2 straight sections. The total circumference is 2280 m. Each arc has 60 FODO cells with sextupole magnets in each main cell, whereas each straight section has two matching cells. The horizontal (black) and vertical beta (red) functions and horizontal dispersion (green) of a cell and one straight section are presented in Figure 6.12. The phase advance per cell was chosen following a study to reduce chromaticities and anharmonicities and thereby maximise dynamic aperture.

A cell comprises two 6.3 m long dipoles located between 30 cm long quadrupoles. The dipoles have a field of 70 Gauss at injection. The chromaticity is controlled by two families of 20 cm long sextupoles. The damping time reduction to 0.1 s can also be achieved by using 2 T wiggler magnets.

6.9 Booster

The high target luminosities of $10^{34} - 10^{36} \text{ cm}^{-2} \text{ s}^{-1}$ lead to short beam lifetimes in the collider, due to beamstrahlung and radiative Bhabha scattering. To sustain this

Table 6.14. Horizontal equilibrium emittances of the booster compared to the collider for all four beam energies.

Beam energy (GeV)	Booster emittance (nm.rad)	Collider emittance (nm.rad)
45.6	0.24	0.24
80.0	0.73	0.84
120.0	0.55	0.63
182.5	1.30	1.48

Notes. The 60° optics is used for 45.6 and 80 GeV; the 90° optics for 120 and 182.5 GeV.

short beam lifetime, a full-energy booster, installed in the collider tunnel, enables continuous top-up injection.

The injection energy for the booster is determined by the field quality and reproducibility of the magnetic field in the dipole magnets of the arc sections. The current design features an energy of 20 GeV, corresponding to a magnetic field of $B = 6$ mT.

The layout of the booster follows the footprint of the FCC-hh collider, whereas the lepton collider rings will have a transverse offset of about 1 m to the outside. The interaction points will even have an offset of about 10 m as a result of the optimisation for the crossing angle and synchrotron radiation mitigation around the experiments. Therefore the booster can simply bypass the detectors on the inside of the cavern. As for the collider, the RF sections are located in points PD and PJ.

In order not to spoil the luminosity and to reduce background from lost particles, the equilibrium emittance of the beam extracted from the booster must be similar to that in the collider rings. The length of the basic FODO cell was chosen to be 53 m in the short arc and about 54 m in the long arcs. The different lengths are necessary to fit the FCC-hh layout. In the collider, the lattice is optimised for two optics: an optics with 60° phase advance per cell is used for operation at the Z pole and the W pair production threshold (45.6 and 80 GeV) and a 90° phase advance per cell will be used for ZH production and the $t\bar{t}$ production threshold (120 and 182.5 GeV). The resulting horizontal equilibrium emittances for these lattices are summarised in Table 6.14.

The radius of curvature in the arc sections is $R = 13.15$ km. At the beginning and end of each arc, a distance of 566 m is reserved for the hadron collider dispersion suppressors. Therefore, this region has a different radius of curvature of $R = 15.06$ km. 10 FODO cells of 56.6 m long and with less bending strength are installed in the booster to follow the tunnel geometry. A quadrupole based dispersion suppressor in the last five cells is used to match the optics to the straight section FODO cells. In the straight sections around points PA, PB PF, PG, PH and PL the cell length is 50 m and in the extended straight sections around points PD and PJ the cell length has been increased to 100 m in order to maximise the space available for RF installation. The transition of the optics from the arcs to these long FODO cells is shown in Figure 6.13. Unlike for the lepton collider, no “tapering” (scaling of the magnet strengths to the local beam energy) is foreseen.

Table 6.15 compiles parameters characterizing the cycling and energy ramp of the booster for the various modes of collider operation. The maximum rate of dipole field change, which is the same for all working points, stays below 0.03 T/s.

The beam parameters at injection energy need particular examination. The damping time becomes longer than 10 s due to the weak radiation damping. This is not compatible with the booster cycle and the top-up requirements. Also the horizontal equilibrium emittance shrinks to 12 pm leading to emittance blow-up due to intra-beam-scattering. Therefore, 16 \sim 9 m long wigglers are installed in the

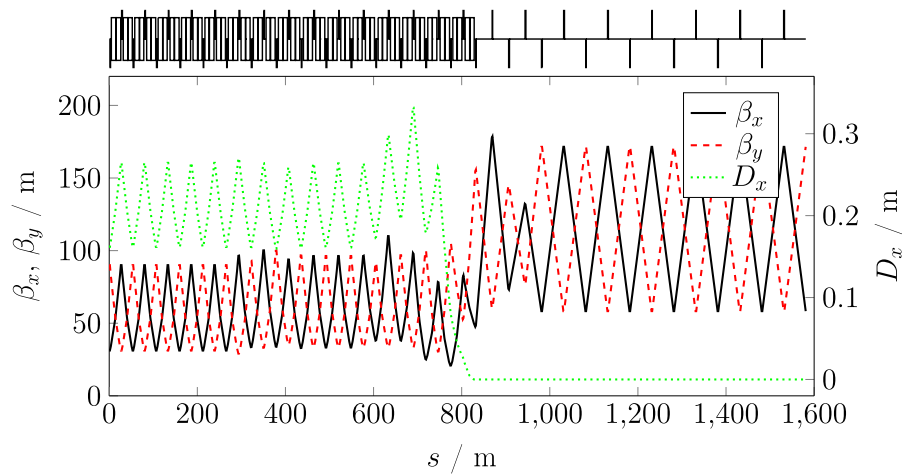


Fig. 6.13. Beta functions and horizontal dispersion function of the transition from the arc lattice into a straight section with an RF installation. The first five cells are regular arc FODO cells with a length of 54 m. The following section of 566 m consists of ten FODO cells with a different bending angle to fit the geometry of the dispersion suppressor of the hadron collider. They also serve as quadrupole based dispersion suppressor and matching section to the optics of the 100 m long straight FODO cells.

Table 6.15. Booster cycle parameters.

Parameter	Unit	Z	W	H	$t\bar{t}_1$	$t\bar{t}_2$
Dipole field at injection	G			63.5		
Dipole field at extraction	G	144.8	254.1	381.1	555.6	579.7
Flat bottom duration	s	51.1	11.8	5.0	1.6	1.6
Cycle duration	s	51.7	13.3	7.5	5.5	5.7
Ramp rate up	G/s			254		

straight sections around the points PA and PG. These normal-conducting wigglers are designed such that a damping time of 0.1 s is reached and the emittance is increased to 240 pm for the 60° optics and 180 pm for the 90° optics. However, the additional energy loss in the wigglers needs to be compensated by the RF system and the voltage therefore needs to be at least 140 MV. The wigglers will be switched off adiabatically to reduce the energy loss during the energy ramp. As a consequence, no extra RF voltage is required for the higher beam energies and the RF voltage is the same as that in the collider.

Tracking studies based on the survival of the particles after 1000 turns have shown that a non-interleaved sextupole scheme (as in the collider) provides the largest dynamic aperture. The tracking studies were performed with the MADX-PTC [469] code which includes radiation damping and quantum excitation. Also Gaussian distributed quadrupole misalignments with $\sigma = 150 \mu\text{m}$ were introduced.

6.10 Transfer lines

The beam transfer between the different systems utilises a few hundred metres of conventional transfer lines. The specific optics design and matching between the different lattices has to be studied in the future, but no particular show-stopper has

been identified. In addition, and depending on the use of the the SPS as a PBR, the possible usage of existing transfer line tunnels and equipment as used for LEP injection will be further explored and detailed.

7 Experiment environment and detector designs

Two complementary detector designs, the “CLIC-Like Detector” (CLD) and the “International Detector for Electron-positron Accelerators” (IDEA), are being studied for the FCC-ee. Before outlining these two concepts in Sections 7.3 and 7.4, respectively, aspects common to the two detectors are presented, namely a description of the experimental environment including an estimate of beam-induced background levels in Section 7.1, and the measurement of luminosity in Section 7.2. The detector magnet systems, the constraints on the readout, and the infrastructure requirements are discussed in Sections 7.5–7.7, respectively.

7.1 Experiment environment

The colliding electron and positron beams of the FCC-ee cross with an angle of 30 mrad at two interaction points (IP). A detector is placed at each IP, with a solenoid that delivers a magnetic field parallel to the bisector of the two beam axes, called the z axis. The two beam directions define the (x, z) horizontal plane (Fig. 7.1). Each beam therefore traverses the axial magnetic field from the detector solenoid at an angle of 15 mrad, which imposes an upper limit of 2 T on the field strength. In order to preserve the beam emittance, and thus a high luminosity, it is necessary to place a set of two compensating solenoids around the beam line just in front of the final focussing quadrupoles (Sect. 2.5.2). The compensating solenoids intrude into the detector to a distance $z \simeq \pm 1.20$ m from the IP. All machine elements, including the compensating solenoids, are kept inside a cone with an opening angle of 100 mrad around the z axis. The cylindrical central part of the beam pipe, which fully covers the angular range down to 150 mrad in front of the tracking detectors, has an inner radius of 15 mm and a total thickness of 1.7 mm, and is made up of two beryllium layers of 0.6 mm each, separated by a 0.5 mm leak-less water cooling layer [470]. At normal incidence, this material corresponds to 0.47% of a radiation length (X_0).

The time between two bunch crossings (BX) varies from a minimum of 20 ns at the Z pole to a maximum of 7 μ s at the highest energy, $\sqrt{s} = 365$ GeV. The unprecedented luminosity – 10^5 times that delivered by LEP at the Z pole – calls for a thorough assessment of various beam-induced backgrounds (synchrotron radiation, photon-photon collisions, beam-gas interactions) and their impact on the detector performance.

7.1.1 Synchrotron radiation

Synchrotron radiation [283] sets constraints on the asymmetric design of the interaction region (Sect. 2.5.4). As shown in Figure 2.18, an appropriate set of tungsten masks needs to be added in front of the final focus quadrupoles to protect the interaction region from direct hits of SR photons from the last bending magnet. The number of SR photons that scatter from the masks to the detector volume increases strongly with beam energy (Tab. 2.7). Bringing this background to a tolerable level at the highest energy therefore ensures that it becomes negligible at lower energies.

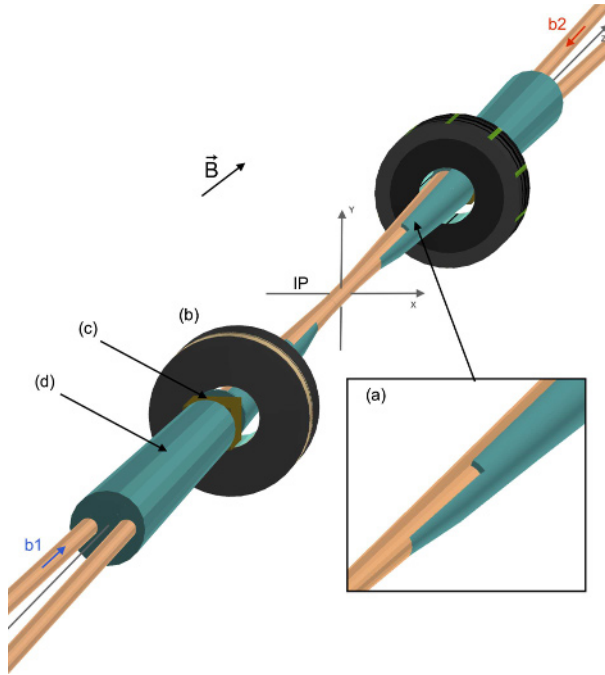


Fig. 7.1. Sketch of the implementation of the interaction region in GEANT4. The tungsten shielding of the beam pipe appears in turquoise blue. The shielding from 330 mm (a) to the rear of the luminometer at 1191.4 mm (b) is 0.1 mm thick and covers only a 68° azimuthal wedge on the positive- x side of the beam pipe. Further back at the rear of the HOM absorber (c), a full 15 mm thick tungsten cone (d) covers both beam pipes to protect the tracking detectors from synchrotron radiation.

These masks (in orange in Fig. 2.18) are placed inside the beam pipe, at the exit of the final focus quadrupoles (QC1), about 2.1 m from the IP. To further limit the fraction of the SR fan that scatters off the masks and showers into the detector area, an ingenious shielding scheme has been developed to minimise the impact on the detector performance. Tungsten shields (in turquoise blue) are positioned outside the beam pipe. A requirement for the position of the shield comes from the need to leave the acceptance window in front of the luminometers (in magenta) unshielded, from 50 to 100 mrad around the outgoing beams. This constraint results in an asymmetric azimuthal coverage of the shielding material around the beam pipe in the luminometer acceptance window, $330 < |z| < 1191.4$ mm, which leaves the vertex detector partially unshielded against SR. Figure 7.1 shows the implementation of the shield in the GEANT4 detector model used for background simulation studies. The thickness of the shield up to the rear end of the luminometer, $|z| < 1191.4$ mm, is limited to 0.1 mm, whereas it becomes 15 mm with full coverage of the two beam pipes from the rear end of the luminometer up to QC1.

Photons from the last bend that hit the masks may partially forward-scatter into the detector area. The forward-scattered photons were simulated with SYNC_BKG, a software developed at LBNL and it was found that the distribution of their energies, with peaks at 70 keV and 250 keV, does not exceed 1 MeV. The photon interactions were modelled in a full GEANT4 [471] simulation that includes the interaction region with or without beam-pipe shielding, the luminometer (Sect. 7.2), and the CLD detector model (Sect. 7.3). While no hits are produced in the whole tracker

Table 7.1. Total numbers of e^\pm created per BX by incoherent pair production, their total energy, and the rates of these particles that would reach the CLD vertex detector within a magnetic field of 2 T. Numbers are obtained from GuineaPig, prior to any detector simulation.

\sqrt{s} (GeV)	91.2	365
Total particles	800	6200
Total E (GeV)	500	9250
Particles with $p_T \geq 5$ MeV and $\theta \geq 8^\circ$	6	290

volume at lower energies, a few hits (164 per BX) are observed at $\sqrt{s} = 240$ GeV, and most (6.6×10^4 per BX) at $\sqrt{s} = 365$ GeV. These numbers reduce to 2.5 or 700 hits per BX at 240 and 365 GeV, respectively, with the proposed shield in place. Therefore, thanks to this shielding, the effect of the SR on the detector is not expected to be an issue. More details are given in Section 7.3.2.

7.1.2 Pair-production background

With the extreme FCC-ee luminosities, the production of low-energy e^+e^- pairs from photon-photon collisions becomes a significant source of background, in particular in detector elements close to the beam pipe. At the FCC-ee, the dominant production mode is incoherent pair creation (IPC), whereby the e^+e^- pairs are produced in interactions involving virtual or real photons from beamstrahlung. The GuineaPig++ [201] event generator was used to study this background at $\sqrt{s} = 91.2$ and 365 GeV. Table 7.1 summarises the e^\pm production rates at both centre-of-mass energies, together with their total energy. The table also shows the rates of particles that eventually enter the CLD vertex detector acceptance. While a large number of particles is created, only those that are emitted with a significant angle, θ , with respect to the z -axis and momentum transverse to that axis (p_T), enter the detector volume. The others remain trapped around the axial magnetic field lines from the detector solenoid.

The kinematics of the e^\pm produced with $E > 5$ MeV is illustrated in Figure 7.2. The peak of particle flux seen at $\theta \sim 15$ mrad corresponds to particles emitted close to the direction of the outgoing beams. The dense region at higher θ corresponds to e^- (e^+) particles that are emitted in the direction of the outgoing e^+ (e^-) beam and that are deflected towards larger polar angles by the electromagnetic field of the bunch. With a magnetic field of 2 T, only the particles produced with $p_T > 5$ MeV would reach the first layer of the CLD vertex detector, within its angular acceptance $\theta > 8^\circ$. The numbers given in Table 7.1 indicate that this background is rather moderate. More details are given in Section 7.3.2.

Photon-photon collisions can also give rise to hadrons, possibly resulting in jets in the detector acceptance. These interactions were simulated with a combination of GuineaPig and Pythia6 [472]. Less than 10^{-3} (10^{-2}) events are produced per BX at $\sqrt{s} = 91.2$ (365) GeV with an invariant mass of the $\gamma\gamma$ system in excess of 2 GeV. This background was therefore found to be negligible.

7.2 Luminometer

For cross-section measurements, an accurate knowledge of the integrated luminosity is required. The potential precision of the Z line shape determination (Sect. 1.2)

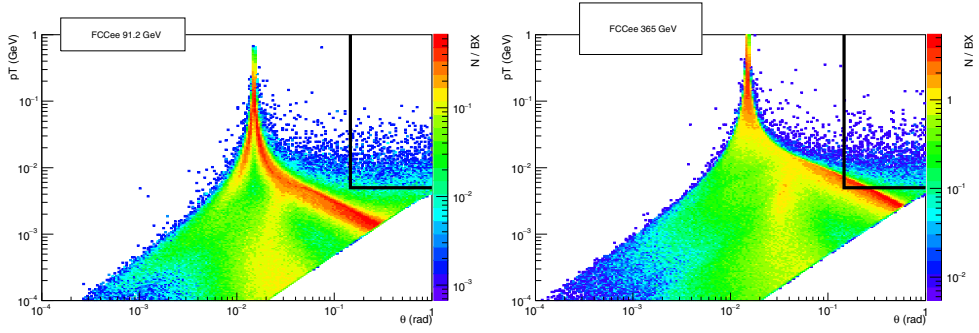


Fig. 7.2. Rates of e^\pm from IPC in the (p_T, θ) plane, in the detector frame, for $\sqrt{s} = 91.2$ GeV (left) and 365 GeV (right). The black line in the upper-right corner delineates the CLD vertex detector acceptance within a field of 2 T.

sets the goal for the *absolute* luminosity measurement to a precision of 10^{-4} . The *relative* luminosity between energy scan points must also be controlled to better than 5×10^{-5} . The requirement for the absolute measurement is more challenging, since many sources of systematic uncertainty for the absolute luminosity measurement, including errors in the geometrical definition of the detector acceptance, cancel for the relative measurement.

Due to its large cross section, of the same order as the Z production cross section at the Z pole, the reference process for the luminosity measurement is small angle Bhabha scattering $e^+e^- \rightarrow e^+e^-$. This process may also be complemented by the large-angle $e^+e^- \rightarrow \gamma\gamma$ production. In spite of a cross section several orders of magnitude smaller, this process statistically suffices to reach and exceed an absolute precision of 10^{-4} at the Z pole in the FCC-ee luminosity conditions, and enjoys entirely different sources of systematic uncertainties. More studies are needed to prove the reliability of this alternative measurement. This section therefore describes only the detector and the methodology for luminosity measurement with small angle Bhabha scattering.

7.2.1 Design

Based on the experience from LEP [473,474] and on linear collider studies [16,475], the luminometer consists of a pair of small angle calorimeters made of silicon-tungsten layers. The calorimeters are centred around – and tilted to be perpendicular to – the outgoing beams to measure the scattering angle of the elastically scattered electrons and positrons precisely. The space available for the luminometers is severely constrained. The compensating solenoids, extending to $z \simeq \pm 1.2$ m, push the luminometers far into the detector volume. At their inner radius, the luminometers have to stay clear of the incoming beam pipe. At their outer radius, they must not interfere with the forward coverage of the tracking detectors and must, therefore, stay fully inside a cone of 150 mrad around the main detector axis of symmetry.

The proposed luminometer design is shown in Figure 7.3. The mechanical inner (outer) radius is 54 (145) mm. The sensitive region, instrumented with silicon sensors, extends from 55 to 115 mm. The calorimeters consist of 25 layers, with each layer comprising a 3.5 mm tungsten plate, equivalent to $1 X_0$, and a silicon sensor plane inserted in the 1 mm gap. In the transverse plane, the silicon sensors are finely partitioned into pads. The proposed number of divisions is 32 both radially

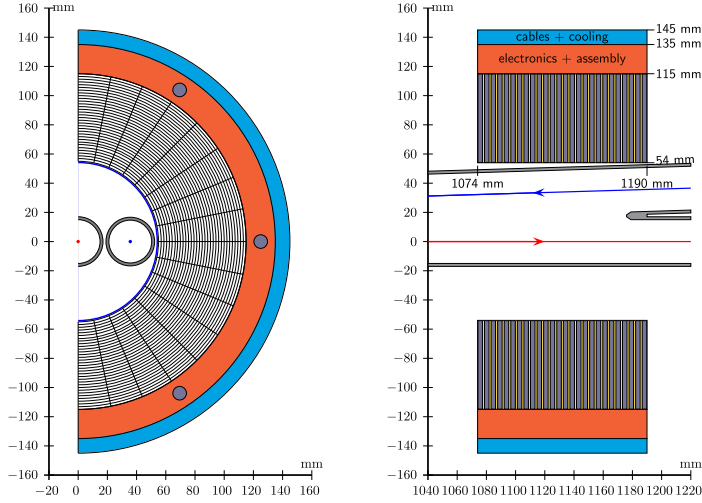


Fig. 7.3. The luminosity calorimeter centred around the outgoing beam line: front view (left), top view (right).

and azimuthally for 1024 readout channels per layer, or 25 600 channels in total for each calorimeter. The calorimeter sandwich extends along the outgoing beam axis between 1074 and 1190 mm from the interaction point. The inactive region with radii between 115 and 145 mm is used for services, which include the assembly of the tungsten-silicon sandwich, front-end electronics, cables, cooling, and mechanical alignment equipment.

Each calorimeter is divided vertically into two half barrels clamped together around the beam pipe. The calorimeters have a weight of about 65 kg each. Due to the compactness of the devices it is possible to produce each silicon half-layer from a single silicon tile, which minimises potential inactive regions between sensors and facilitates precise geometrical control of the acceptance. Meticulous care is required for the design of the vertical assembly of the two half-barrels, both in order to avoid a non-instrumented region and to precisely control the geometry. In order to decouple the luminometers mechanically from the magnetic elements of the collider, it is being considered to fix the beam pipe to the luminometers, and the luminometers to a support tube connected to the end-cap calorimeter system. This arrangement would in addition allow the two luminometers and the beam pipe to be extracted altogether from the detector when an intervention is required. Detailed engineering studies are needed for the actual design of this crowded machine-detector interface region.

The silicon sensor pads are connected to the compact front-end electronics positioned at radii immediately outside the sensors. To limit the high detector occupancy to manageable levels, it is desirable to read out the detector for each bunch crossing, which calls for the development of readout electronics with a shaping time below 20 ns. A power budget of 5 mW per readout channel is estimated, for a total of 130 W per calorimeter, which has to be removed by cooling. In order to maintain the geometrical stability required (Sect. 7.2.2), the temperature of the luminometers must be kept stable and uniform to within ± 1 K or better. Evaporative CO₂ cooling is an interesting option to be pursued. With its low viscosity and high latent heat, less flow is needed for CO₂ than for other coolants and small diameter tubing (few mm) is therefore feasible.

7.2.2 Acceptance and luminosity measurement

The Si–W sandwich has an effective Molière radius of about 15 mm. For a robust energy measurement, the fiducial acceptance limits are kept about one Molière radius away from the borders of the instrumented area, effectively limiting the acceptance to the 62–88 mrad range. To ensure that the luminosity measurement depends only to second order on possible misalignments and movements of the beam spot relative to the luminometer system, the method of asymmetric acceptance [476] will be employed. Bhabha events are selected if the e^\pm is inside a narrow acceptance in one calorimeter, and the e^\mp is inside a wide acceptance in the other. A 2 mrad difference between the wide and narrow acceptances is deemed adequate to accommodate possible misalignments. The narrow acceptance thus covers the angular range 64–86 mrad, corresponding to a Bhabha cross section of 14 nb at the Z pole (to be compared to 40 nb for Z production), equivalent to 6.4×10^{-4} events per bunch crossing.

The forward-peaked $1/\theta^3$ spectrum of the Bhabha scattering process causes the luminosity measurement to be particularly sensitive to the determination of this angular range. The Bhabha acceptance A , and therefore the luminosity, is indeed affected by any change ΔR_{in} (ΔR_{out}) of the inner (outer) edge radial coordinate as follows: $\Delta A/A \approx -(\Delta R_{\text{in}}/1.6 \mu\text{m}) \times 10^{-4}$ and $\Delta A/A \approx +(\Delta R_{\text{out}}/3.8 \mu\text{m}) \times 10^{-4}$. Similarly, A is affected by any change ΔZ of the half-distance between the effective planes of the radial measurements in the two calorimeters: $\Delta A/A \approx +(\Delta Z/55 \mu\text{m}) \times 10^{-4}$. With the 30 mrad beam crossing angle, the two calorimeters are centred on different axes, and Z should then be interpreted as $Z = \frac{1}{2}(Z_1 + Z_2)$, where Z_1 and Z_2 are the two distances, measured along the two outgoing beam directions, from the (nominal) IP to the luminometers.

With the method of asymmetric acceptance, only a weak, second-order, dependence of the acceptance on the IP position remains. The size of this effect was investigated through a high-statistics study of a Bhabha event sample generated with the event generator BHLUMI [477]. The study, based on a parameterised detector response, confirmed the second order dependence as long as shifts of the IP are small enough to be covered by the difference between the wide and narrow acceptance definitions: in this case, up to shifts of about $\delta r = 0.5$ mm transversely and $\delta z = 20$ mm longitudinally. Inside this range, the changes of the acceptance observed could be parameterised as $\Delta A/A \approx +(\delta r/0.6 \text{ mm})^2 \times 10^{-4}$ and $\Delta A/A \approx -(\delta z/6 \text{ mm})^2 \times 10^{-4}$. It should be noted that such shifts of the IP position give rise to asymmetries in the Bhabha counting rate either azimuthally (radial shift) or between the two calorimeters (longitudinal shifts) and can thus be monitored and corrected for directly from the data. No such possibility of correction from the data exists for the detector construction tolerances, ΔR and ΔZ , discussed in the previous paragraph, which therefore need to be controlled via precise metrology (ΔR) and alignment (ΔZ) devices. As a reference, the OPAL experiment [473] at LEP achieved control of a similar calorimeter inner radius to a precision of $4.4 \mu\text{m}$ through precise metrology. Several uncertainty contributions would vanish if each half-barrel silicon sensor were made of a single silicon tile. The dominant remaining contribution stems from the stability of the half-barrel separation, which was $1.9 \mu\text{m}$ in the case of OPAL.

In summary, to reach a precision of 10^{-4} on the absolute luminosity measurement, the radial dimensions of the luminometers have to be controlled to the one micron level, whereas the distance between the two luminometers has to be controlled to about $100 \mu\text{m}$. The requirements on the alignment of the luminometer system with respect to the interaction point position are considerably more relaxed: accuracies of order 0.1 mm and 1 mm are called for in the radial and longitudinal directions, respectively.

7.2.3 Electromagnetic focussing of bhabha electrons

The final state e^\pm from Bhabha scattering are focussed [478] by the strong electromagnetic field of the opposing bunch in the same way as the beam particles. The effect and its mitigation are being studied with events generated by BHWIDE [479] and injected into GuineaPig++ [201], which then tracks the final state particles to the outside from a randomly chosen scattering point within the collision diamond.

Early results indicate an average focussing of the final state e^\pm in the luminometer region of about $40\text{ }\mu\text{m}$ corresponding to a relative decrease in acceptance of about 20×10^{-4} . The focussing is most pronounced in the positive x direction, i.e. for the tracks closest to the outgoing beam direction. This azimuthal asymmetry is found to be strongly correlated to the magnitude of the focussing effect. Studies are being performed to show that the direct measurement of this asymmetry can be used to correct the induced bias on the luminosity. The correction can be determined every few minutes with the required statistical accuracy, but is needed much less frequently, typically once per fill.

7.2.4 Machine and beam-induced backgrounds in the luminometer

A full simulation of the impact of IPC on the luminometers was performed for $\sqrt{s} = 91.2\text{ GeV}$, where the requirements for the precision of the luminosity measurement are the strongest. The total energy deposited by IPC pairs in each calorimeter is only 350 MeV per bunch crossing. The calorimeter cells that see the largest energy deposits are at the lowest radii and at the rear of the calorimeter, thus outside the fiducial volume relevant for the luminosity measurement. Consequently, the IPC background is not expected to compromise the precision of the luminosity measurement. In any case, it was verified that this background could be eliminated by placing a thin layer of tungsten shielding at the inner radius of the luminometers.

The total energy released per BX by synchrotron radiation in each luminosity calorimeter at $\sqrt{s} = 365\text{ GeV}$ (where the effect of SR is largest) was found to be reduced from 340 MeV without shielding to only 7 MeV with the proposed beam-pipe shield, without any significant effect on the performance of the luminometer.

At LEP, the primary source of background for the luminosity measurement was from off momentum particles generated by beam scattering with the residual gas in the beam pipe, in the straight sections before the experiments, and deflected by the quadrupoles into the luminometers [473]. Early studies [480] of beam-gas interactions at FCC-ee were performed, for $\sqrt{s} = 91.2\text{ GeV}$, with a vacuum of 10^{-9} mbar of N_2 at 300 K . The studies demonstrate an induced rate of particles leaving the beam pipe of 140 kHz per metre per beam in the region close to the IP. It was found that only a small fraction of these particles are deflected sufficiently by the quadrupoles to point towards the opposite side luminosity calorimeter, and that most of those that do point there will be effectively stopped by the tungsten shielding around the beam pipe. The remaining small number of particles that enter the luminometer have low energy, typically less than half the beam energy. The coincidence rate between the two calorimeters caused by beam-gas interaction was found to be more than two orders of magnitude below the Bhabha rate. This observation puts the FCC-ee in a favourable situation with respect to LEP, where the two rates were comparable at this point. Energy and angular requirements, which were able to considerably reduce the LEP coincidence rate, bring this background down to a negligible level at the FCC-ee.

Table 7.2. Comparison of key parameters of CLD and CLIC detector models.

Concept	CLICdet	CLD
Vertex inner radius (mm)	31	17
Tracker half length (m)	2.2	
Tracker outer radius (m)	1.5	2.1
ECAL absorber	W	
ECAL X_0	22	
HCAL absorber	Fe	
HCAL λ_I	7.5	5.5
Solenoid field (T)	4	2
Overall height (m)	12.9	12.0
Overall length (m)	11.4	10.6

7.3 The CLD detector design

The CLD detector has been adapted to the FCC-ee specificities from the most recent CLIC detector model [481], which features a silicon pixel vertex detector and a silicon tracker, followed by highly granular calorimeters (a silicon-tungsten ECAL and a scintillator-steel HCAL). A superconducting solenoid provides a 2 T magnetic field, and a steel yoke interleaved with resistive plate muon chambers (RPC) closes the field.

To compensate for the lower field strength, the tracker radius was enlarged from 1.5 to 2.1 m. The HCAL depth was reduced from 7.5 to 5.5 nuclear interaction lengths (λ_I) to profit from the lower centre-of-mass energy. Another difference with respect to CLIC stems from the continuous operation of the circular collider, which hinders the use of power pulsing for the electronics. The impact on cooling and material depends on technology choices and therefore detailed engineering studies on cooling systems are needed. Based on the developments for the ALICE inner tracking system upgrade (ITS) [482], the amount of material per layer for the vertex detector has been increased by a factor 1.5 with respect to the CLIC vertex detector.

A comparison of the main parameters in the CLD concept and the CLIC detector model is presented in Table 7.2. The CLD concept is illustrated in Figure 7.4. Figure 7.5 sketches a CLD installation in the experimental cavern; it also indicates the shifted location and larger size of a later FCC-hh detector.

7.3.1 CLD tracking system

The CLD vertex detector (VXD) consists of a cylindrical barrel closed off in the forward directions by disks. The layout is based on double layers, made of two sensitive layers fixed on a common support structure, which includes cooling circuits. The barrel consists of three double layers ($0.63 X_0$ each) and the forward region is covered by three sets of double disks ($0.70 X_0$ each).

The CLD concept features an all-silicon tracker. Engineering and maintenance considerations led to a design with a main support tube for the inner tracker region including the vertex detector. The inner tracker (IT) consists of three barrel layers and seven forward disks. The outer tracker (OT) completes the system with an additional three barrel layers and four disks. The overall geometrical parameters of the tracker are given in Table 7.2.

Preliminary engineering studies have been performed for the CLIC detector to define the support structures, cooling systems, etc. needed for the tracker barrel

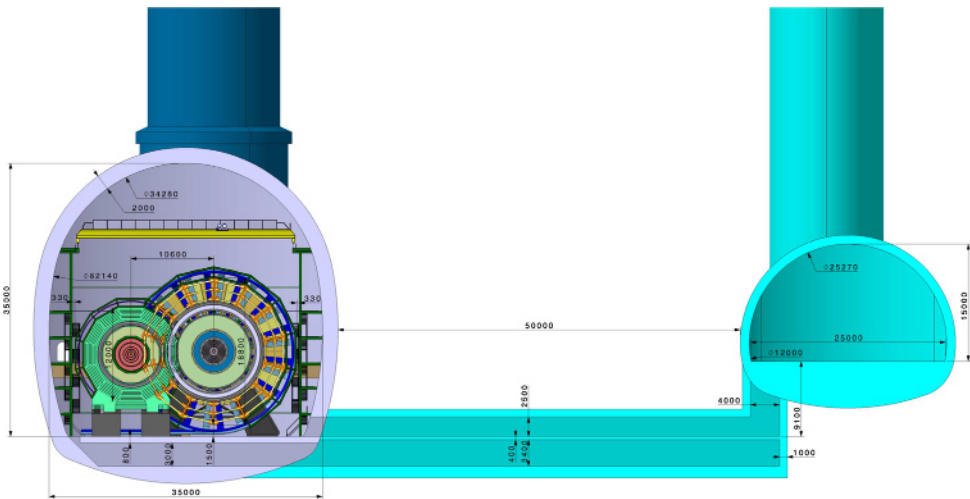
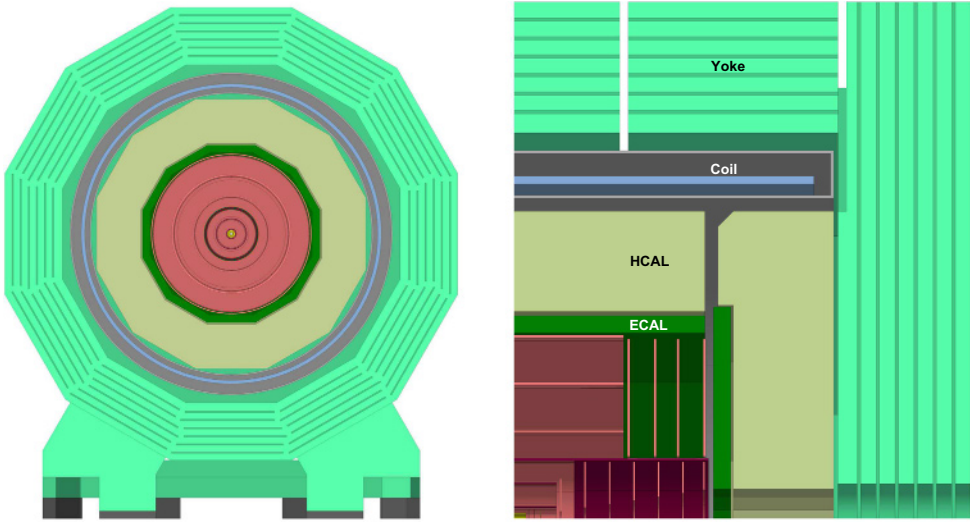


Fig. 7.5. Sketch of FCC-ee detector CLD inside the experiment cavern (left side of cavern, in green, yellow and red), along with a subsequent, larger FCC-hh detector (right side of cavern, in blue, yellow and orange).

layers and disks. For the outer tracker barrel support, these studies were completed by building and testing a prototype. The same concepts and material thicknesses are currently used for CLD. The additional material needed for the 200 μm thick layer of silicon including the extra support structures, cables and cooling infrastructure has been estimated. The total material amounts to about 11%(20%) X_0 in the barrel (forward) region.

Full simulation studies have been carried out in order to assess the performance of the CLD tracker. The single-point resolutions for each sub-detector element were assumed to be $3 \times 3 \mu\text{m}^2$ for the vertex detector, $5 \times 5 \mu\text{m}^2$ for the inner-most disk of the inner tracker, and $7 \times 90 \mu\text{m}^2$ for the other layers of the inner tracker and

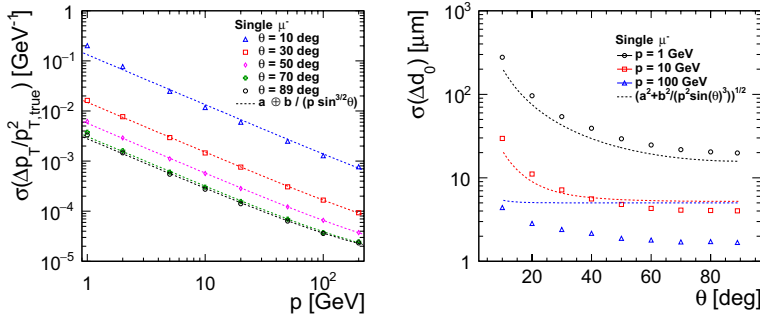


Fig. 7.6. Transverse momentum resolution for single muons as a function of momentum at fixed polar angle $\theta = 10, 30, 50, 70$ and 89° (left); Impact parameter resolution for single muons as a function of polar angle, at fixed momentum $p = 1, 10$, and 100 GeV (right). The dashed lines show the resolution goals.

those of the outer tracker. The momentum resolution obtained for muons is shown in Figure 7.6. For high momentum muons in the central region, a resolution of $\Delta(1/p_T) < 5 \times 10^{-5} \text{ GeV}^{-1}$ is achieved. The study showed a tracking efficiency of 100% for single muons with a transverse momentum above 1 GeV. The efficiency also remains high for softer muons, falling off gradually to reach about 96% for $p_T = 0.1$ GeV.

The tracking efficiency for particles in high-occupancy environments was studied with light-quark pair events at $\sqrt{s} = 91.2$ and 365 GeV. A tracking efficiency of almost 100% was found whenever $p_T > 1$ GeV.

7.3.2 Backgrounds in the CLD tracking system

The effect of IPC and SR backgrounds on the CLD tracker performance has been studied through a full GEANT4 simulation of the interaction region and the CLD detector. The simulation used DD4hep [483], and the ddsim software framework developed by the CLIC-dp collaboration. Hits with an energy deposit above a threshold of a few keV in the silicon sensors are assumed to be recorded. When occupancies are determined, the numbers of such hits are multiplied by an average cluster size, chosen to be 5 (2.5) for the pixel (strip) sensors, and by a safety factor of three. A pitch of $25 \times 25 \mu\text{m}^2$ was taken for the pixels of the vertex detector and of $1 \times 0.05 \text{ mm}^2$ for the strips of the inner and outer tracker.

The IPC background on average causes about 50 (1100) hits per BX in the VXD, at $\sqrt{s} = 91.2$ (365) GeV. The occupancy is highest in the innermost barrel layer of the VXD, on average reaching 7×10^{-6} (1.5×10^{-4}) per BX. The peak occupancy reaches 1×10^{-5} (4×10^{-4}) at the edges of the VXD barrel ladders, and about half of these values for low radii of VXD end-caps. As an illustration, Figure 7.7 shows the hit density in the VXD at $\sqrt{s} = 365$ GeV.

The highest hit density in the tracker is observed at the inner radii of the first disk. The induced occupancy is 2×10^{-5} (1×10^{-4}) per BX. When operating at the Z pole, the readout electronics is likely to integrate the deposited charge over several BXs. Even with a “slow” readout electronics integrating over $1 \mu\text{s}$ (50 BXs), the maximum occupancy observed would remain below 10^{-3} . In summary, detector occupancies induced by IPC backgrounds are not expected to affect the tracking performance.

As discussed in Section 7.1, synchrotron radiation in the detector volume is negligible at all energies except the top energy. At this energy, the resulting large

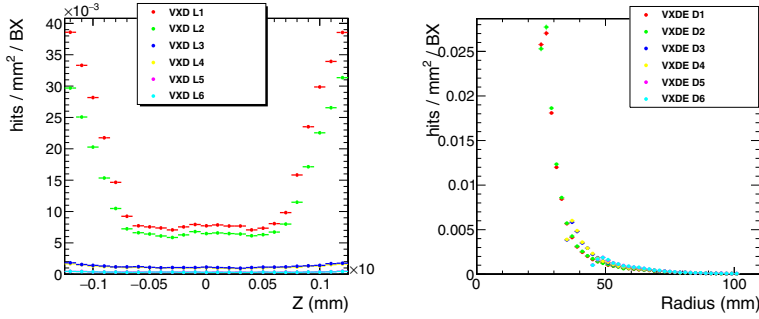


Fig. 7.7. Hit density per BX in the CLD VXD induced by the IPC background at $\sqrt{s} = 365$ GeV; barrel layers (left), endcap disks (right).

number of hits ($\sim 60\,000$ per BX) in the inner and outer tracking detectors without shielding is very effectively reduced to a negligible level by the tungsten shielding of the beam pipe. The shielding does not fully protect the vertex detector, however, where a total of about 350 hits per BX would be created, mostly in the first and second double layers. The maximum occupancy is of order of 10^{-4} , and is not expected to affect the tracking performance.

7.3.3 CLD calorimetry

Studies in the context of linear colliders have concluded that high-granularity calorimetry associated with a silicon tracker may be an option to reach a jet energy resolution of $\sim 4\%$ with particle-flow reconstruction. In contrast to a purely calorimetric measurement, particle-flow reconstruction enables the identification and the reconstruction of all visible particles in an event [484,485]. An overview of the CLD particle-flow reconstruction and the associated Pandora PFA software can be found in [486]. Experimental tests are described in [487].

An ECAL segmentation of $5 \times 5 \text{ mm}^2$ is deemed adequate to resolve energy deposits from nearby particles in jets. The technology chosen as baseline option is a silicon-tungsten sandwich structure. In order to limit the leakage beyond the ECAL, a total depth of $22 X_0$ was chosen. A longitudinal segmentation with 40 identical Si-W layers was found to give the best photon energy resolution. A full simulation study with the Pandora PFA reconstruction has been performed for single photons with energies between 10 and 100 GeV. The resulting photon energy resolution is shown in Figure 7.8.

The hadron calorimeter is made of steel absorber plates, each 19 mm thick, interleaved with scintillator tiles. The polystyrene scintillator, in a steel cassette, is 3 mm thick with a tile size of $30 \times 30 \text{ mm}^2$. Analogue readout of the tiles with SiPMs (silicon photomultipliers) is envisioned. The HCAL consists of 44 layers and is $5.5\lambda_I$ deep, which brings the combined thickness of ECAL and HCAL to $6.5\lambda_I$. A study of the CLD performance with the Pandora PFA reconstruction was carried out with light-quark pair events at $\sqrt{s} = 91.2$ and 365 GeV. Figure 7.8 shows the jet energy resolution obtained as a function of polar angle.

7.3.4 CLD Muon system

The CLD muon system comprises six detection layers with an additional seventh layer in the barrel immediately following the coil. The latter may serve as a tail

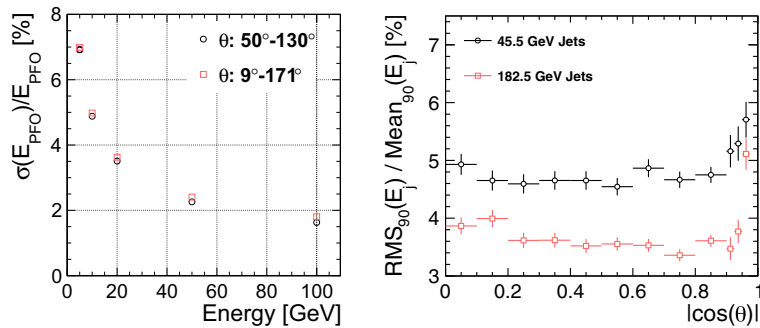


Fig. 7.8. CLD calorimeter performance. Photon energy resolution as a function of energy (left), comparing the barrel region with the full detector acceptance. Jet energy resolution for light quark jets as a function of polar angle (right).

Table 7.3. Key parameters of the IDEA detector.

Vertex technology	Silicon
Vertex inner/outer radius	1.7 cm/34 cm
Tracker technology	Drift chamber + silicon wrapper
Tracker half length/outer radius	2.0 m/2.0 m
Solenoid bore radius/half length	2.1 m/3.0 m
Preshower/calorimeter absorber	Lead/lead
Preshower inner/outer radius	2.4 m/2.5 m
DR calorimeter inner/outer radius	2.5 m/4.5 m
Overall height/length	11 m/13 m

catcher for energetic hadron showers. The detection layers are proposed to be built as RPCs with cells of $30 \times 30 \text{ mm}^2$. (Alternatively, crossed scintillator bars could be envisioned.) The yoke layers and thus the muon detectors are staggered to avoid non-instrumented gaps.

7.4 IDEA detector concept

The IDEA detector concept, developed specifically for FCC-ee, is based on established technologies resulting from years of R&D. Additional work is, however, needed to finalise and optimise the design. The structure of the IDEA detector is outlined in Figure 7.9, and its key parameters are listed in Table 7.3. The detector comprises a silicon pixel vertex detector, a large-volume extremely-light short-drift wire chamber surrounded by a layer of silicon micro-strip detectors, a thin, low-mass superconducting solenoid coil, a pre-shower detector, a dual-readout calorimeter, and muon chambers within the magnet return yoke.

7.4.1 IDEA vertex detector

The innermost detector, surrounding the beam pipe, is a silicon pixel detector. Recent test-beam results on the detectors planned for the ALICE ITS upgrade, based on the ALPIDE readout chip [488], indicate an excellent ($\sim 5 \mu\text{m}$) resolution, high efficiency at low power, and low dark-noise rate [489]. These very light detectors, 0.3 (1.0)% X_0 per innermost (outermost) layer, are the basis for the IDEA vertex detector.

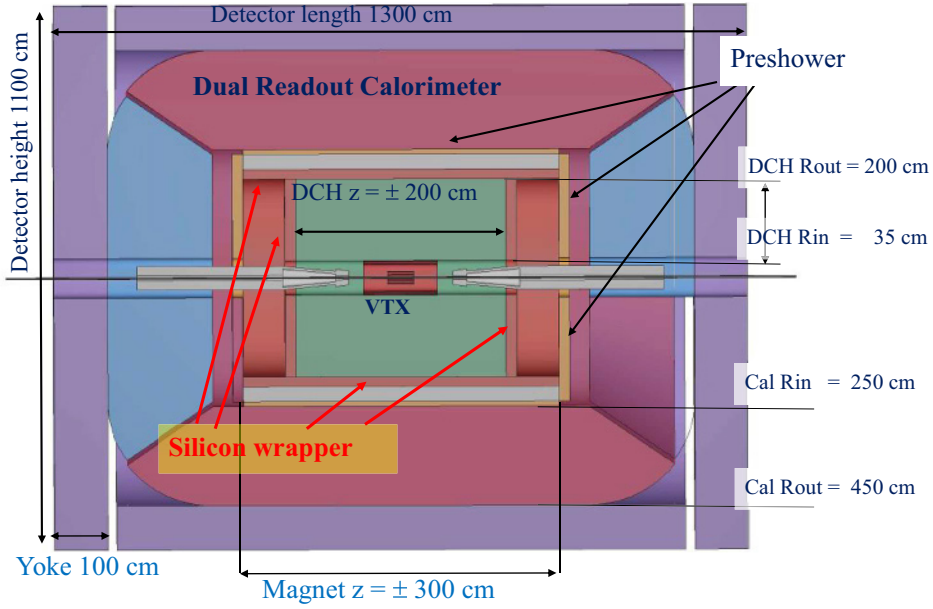


Fig. 7.9. Schematic layout of the IDEA detector.

7.4.2 IDEA drift chamber

The drift chamber (DCH) is designed to provide good tracking, high-precision momentum measurement and excellent particle identification by cluster counting. The main peculiarity of this chamber is its high transparency, in terms of radiation lengths, obtained as a result of the novel approach adopted for the wiring and assembly procedures [490]. The total amount of material in the radial direction towards the barrel calorimeter is of the order of $1.6\% X_0$, whereas, in the forward direction, it is about $5.0\% X_0$, 75% of which are in the end plates instrumented with the front-end electronics. The original ancestor of the DCH design is the drift chamber of the KLOE experiment [491], which was more recently developed as the MEG2 [492] drift chamber.

The DCH is a unique-volume, high-granularity, all-stereo, low-mass, cylindrical, short-drift, wire chamber, co-axial with the 2 T solenoid field. It extends from an inner radius $R_{\text{in}} = 0.35 \text{ m}$ to an outer radius $R_{\text{out}} = 2 \text{ m}$, for a length $L = 4 \text{ m}$ and consists of 112 co-axial layers, at alternating-sign stereo angles, arranged in 24 identical azimuthal sectors. The approximately-square cell size varies between 12.0 and 14.5 mm for a total of 56 448 drift cells. The challenges potentially arising from a large number of wires are addressed by the peculiar design of the wiring, which was successfully employed for the recent construction of the MEG2 drift chamber [493]. The chamber is operated with a very light gas mixture, 90% He – 10% $i\text{C}_4\text{H}_{10}$ (isobutane), corresponding to a maximum drift of $\sim 400 \text{ ns}$. The number of ionisation clusters generated by a minimum ionising particle (m.i.p.) is about 12.5 cm^{-1} , allowing cluster counting/timing techniques to be employed to improve both spatial resolution ($\sigma_x < 100 \mu\text{m}$) and particle identification ($\sigma(dN_{\text{cl}}/dx)/(dN_{\text{cl}}/dx) \approx 2\%$). The angular coverage extends down to $\sim 13^\circ$, and could be further extended with additional silicon disks between the DCH and the calorimeter end caps.

A drift distance resolution of $100 \mu\text{m}$ has been obtained in a MEG2 drift chamber prototype [494] (7 mm cell size), with very similar electrostatic configuration and gas mixture. A better resolution is expected for the DCH, as a result of the

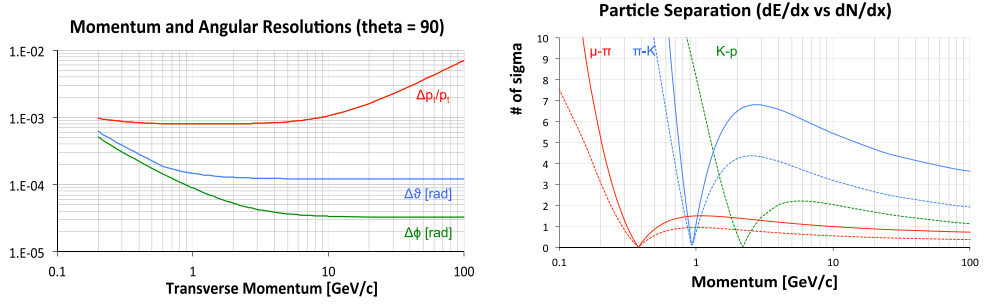


Fig. 7.10. IDEA drift chamber performance. Left: momentum and angular resolutions for $\theta = 90^\circ$ as a function of momentum. Right: particle type separation in units of standard deviations as a function of momentum, with cluster counting (solid curves) and with dE/dx (dashed curves).

longer drift distances and the employment of cluster timing techniques. Analytical calculations for the expected momentum, transverse momentum and angular resolutions, conservatively assuming a $100\ \mu\text{m}$ point resolution, are plotted in the left panel of Figure 7.10.

The expected particle identification performance is presented in the right panel of Figure 7.10. Results are based on cluster counting, where it is assumed that the relative resolution on the measurement of the number of primary ionisation clusters (N_{cl}) equals $1/\sqrt{N_{cl}}$. For the whole range of momenta, particle separation with cluster counting outperforms the dE/dx technique by more than a factor of two. The expected pion/kaon separation is better than three standard deviations for all momenta except in a narrow range from 850 MeV to slightly above 1 GeV.

A layer of silicon micro-strip detectors surrounds the outside of the drift chamber providing an additional accurate space point as well as precisely defining the tracker acceptance.

7.4.3 IDEA tracking system performance

Simulations were performed to obtain a first estimate of the performance of the IDEA tracking system. In this study, a seven-layer cylindrical vertex detector, and a two-layer silicon wrapper, both with a $r\phi$ pitch of $20\ \mu\text{m}$, were placed inside and around the cylindrical drift chamber, respectively. Details of ionisation clustering for cluster counting/timing analysis were not simulated, such that the spatial resolution is conservatively limited to $100\ \mu\text{m}$. The results of this study, consolidated by those derived from a fast simulation, point to a transverse momentum resolution of $\sigma(1/p_T) \simeq a \oplus b/p_T$, with $a \simeq 3 \times 10^{-5}\ \text{GeV}^{-1}$ and $b \simeq 0.6 \times 10^{-3}$. The lightness of the drift chamber is reflected in the small multiple scattering b term. Correspondingly, an impact parameter resolution of $\sigma_{d_0} = a \oplus b/p \sin^{3/2} \theta$, with $a = 3\ \mu\text{m}$ and $b = 15\ \mu\text{m GeV}$, is found. Lastly, angular resolutions of better than 0.1 mrad in both azimuthal and polar angle are demonstrated for tracks with momenta exceeding 10 GeV.

7.4.4 Backgrounds in the IDEA tracking system

A GEANT4 simulation of the central parts of the IDEA detector has been implemented in the common software framework developed for the FCC experiments [495].

Table 7.4. Average occupancy of the drift chamber due to beam-induced backgrounds, when timing information is used for photon signal suppression as described in the text.

Background	Average occupancy	
	$\sqrt{s} = 91.2 \text{ GeV}$	$\sqrt{s} = 365 \text{ GeV}$
e^+e^- pair background	1.1%	2.9%
$\gamma\gamma \rightarrow$ hadrons	0.001%	0.035%
Synchrotron radiation	–	0.2%

A study of the IPC background, expected to be the dominant beam-induced background in the IDEA drift chamber, was performed. Only very few of the primary e^\pm particles have a transverse momentum large enough to reach the inner radius of the drift chamber (35 cm). The majority of the hits observed in the drift chamber are thus from secondary particles (mainly photons of energy below 1 MeV) produced by scattering off the material at lower radii. The average occupancy of the drift chamber due to this background was found to be about 0.3% (3%) per bunch crossing at 91.2 (365) GeV, with a smooth decrease by a about a factor two from low to large radii. At the Z pole, a naive and very conservative integration over 20 bunch crossings – corresponding to the 400 ns maximum drift time – yields a maximum occupancy of about 10% in the inner-most drift cells. Based on experience from the MEG2 drift chamber, this occupancy, which allows over 100 hits to be recorded per track on average in the DCH, is deemed manageable.

The level of occupancy is actually expected to be much smaller than this conservative estimate with the use of the drift chamber timing measurement. As opposed to charged particles that leave a string of ionisation in the drift cells they traverse, photons are characterised by a localised energy deposition. Signals from photons can therefore be effectively suppressed at the data acquisition level by requiring that at least three ionisation clusters appear within a time window of 50 ns. In addition, a charge string with a hole longer than 100 ns can be interpreted as two separate signals, so as to avoid the integration of any remaining photon-induced background over 20 bunch crossings, but rather integrate over a time corresponding to only four bunch crossings. With this effective suppression of photon-induced signals, the background from IPC is expected to remain low and is unlikely to cause adverse issues for the track reconstruction. According to these considerations, the average occupancy from IPC, SR, and $\gamma\gamma \rightarrow$ hadrons is summarised in Table 7.4.

7.4.5 IDEA preshower detector

A preshower detector is located between the magnet and the calorimeter in the barrel region and between the drift chamber and the end-cap calorimeter in the forward region. In the barrel region, the magnet coil (Sect. 7.5) works as an absorber of about $1X_0$ and is followed by one layer of Micro Pattern Gas Detector (MPGD) chambers; a second layer of chambers follows after another $1X_0$ of lead. A similar construction occurs in the forward region, however, here with both absorber layers made from lead.

The MPGD chamber layers provide an accurate determination of the impact point of both charged particles and photons, and therefore define the tracker acceptance volume with precision. They also further improve the tracking resolution. In addition, a large fraction of the π^0 s can be tagged by having both photons from their decay identified by the preshower. The optimisation of the preshower system and the evaluation of its performance is in progress.

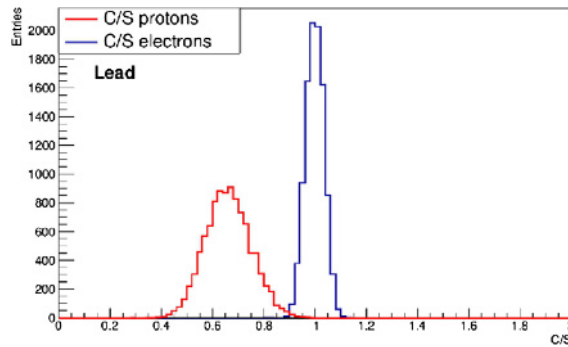


Fig. 7.11. Particle identification performance of the dual-readout calorimeter: C/S ratio for 80 GeV isolated electrons and protons.

7.4.6 IDEA dual-readout calorimeter

A lead-fibre dual-readout calorimeter [496] surrounds the second preshower layer. This calorimeter concept has been extensively studied and demonstrated over ten years of R&D by the DREAM/RD52 collaboration [497,498]. The calorimeter is 2 m deep, which corresponds to approximately $7 \lambda_I$. Two possible layouts have been implemented in the simulation for a realistic 4π detector. Both cover the full volume down to 100 mrad of the z axis, with no inactive region. In the first configuration, the calorimeter is made of truncated rectangular-base pyramidal towers with 92 different sizes. In the second, it is built with rectangular prisms coupled to pyramidal towers. The total number of fibres is of the order of 10^8 in both cases.

The dual-readout calorimeter is sensitive to the independent signals from scintillation light (S) and Čerenkov light (C) production, resulting in an excellent energy resolution for both electromagnetic and hadron showers. By combining the two signals, the resolution estimated from GEANT4 simulations is found to be close to $10\%/\sqrt{E}$ for isolated electrons and $30\%/\sqrt{E}$ for isolated pions with negligible constant terms.

The dual-readout calorimeter provides very good intrinsic discrimination between muons, electrons/photons and hadrons for isolated particles [499]. Figure 7.11 demonstrates a nearly perfect separation in the C/S ratio for 80 GeV electrons and protons: for an electron efficiency of 98%, a simulated rejection factor of up to 600 can be reached for isolated protons. The rejection factor in jets remains to be evaluated experimentally. In addition to the C/S ratio, a few other variables, like the lateral shower profile, the starting time of the signal, and the charge-to-amplitude ratio, can be used to enhance the intrinsic calorimeter particle separation performance.

In addition to the intrinsic particle identification capabilities, the fine transverse granularity allows close showers to be separated and provides good matching to tracks in the inner, preshower signals, and also to muon tracks, making this calorimeter a good candidate for efficient particle-flow reconstruction. The need for disentangling signals produced by overlapping electromagnetic and hadron showers is likely to require longitudinal segmentation as well. Several ways to implement this segmentation were envisioned and are being studied, e.g. the classical division of the calorimeter in several compartments, an arrangement with fibres starting at different depths, the extended use of the timing information, etc. The specific advantages and drawbacks of each approach need to be studied through both simulations and beam tests.

7.4.7 IDEA muon system

The muon system consists of layers of chambers embedded in the magnet return yoke. The area to be covered is substantial, which calls for a cost-effective chamber technology. Recent developments in the industrialisation of μ -Rwell-based large area chambers [500], proposed for the CMS detector phase-II upgrade, are promising.

7.5 Detector magnet systems

The 2 T solenoids for the two detector concepts are quite different in design. The proposed magnet for CLD is a conventional solenoid surrounding the calorimeters (Fig. 7.4), in order to minimise the material along the particle trajectories. For IDEA, a much smaller, ultra-thin, and transparent solenoid, positioned in front of the dual-readout calorimeter (Fig. 7.9), is proposed in order to minimise its cost. A significant R&D effort is required to engineer this solution. In addition, simulation studies still need to be performed to validate the physics performance, especially in view of particle-flow reconstruction. Both the CLD and IDEA baseline designs include an iron return yoke which, in both cases, houses the muon system and protects the beams from emittance blow-up that would otherwise result from stray field over very large distance along the beam line.

7.5.1 The CLD detector magnet

The CLD detector magnet is based on the proven concept of the CMS solenoid [501]. Several design aspects were investigated, including magnetic field distribution, conductor optimisation, mechanical support and quench behaviour. The simulated magnetic field map is shown in Figure 7.12 (left), and the main magnet parameters are listed in Table 7.5. Two scenarios with different operational currents, 20 and 30 kA, are considered. The first corresponds to the currents used in ATLAS and CMS and the second to what is proposed for the FCC-hh detector magnets.

The cryostat, which mechanically supports the calorimeters and the tracker, is equipped with rails inside the bore for the sliding of the HCAL, and with four feet, under the lower half shells close to the end flanges. Local end-flange reinforcements are required to transfer the HCAL weight to the floor. To prevent buckling, local outer shell reinforcements are included, in such a way that the cryostat wall thickness is kept to a minimum. The cryostat has to withstand the HCAL weight (1.6 kt), the external pressure (0.101 MPa), the self weight (80 t if aluminium is used, 130 t for steel), the cold-mass weight, and the thermal shrinkage of the suspension rods (1765 kN). A safety margin of a factor of three has been included for the weight of the cold mass.

7.5.2 The IDEA Detector Magnet

The IDEA detector magnet is an ambitious, ultra-thin and light, thus “radiation-transparent”, superconducting solenoid equipped with a thin iron return yoke. The main feature is that the solenoid is positioned between the tracker volume and the calorimeter system, a solution currently employed in ATLAS [502]. From a detector performance perspective, the material thickness for the complete magnet, including the cold mass and the cryostat, must be kept as small as possible, both in radiation and geometrical lengths, typically well below $1 X_0$ and 20 cm. By positioning the coil

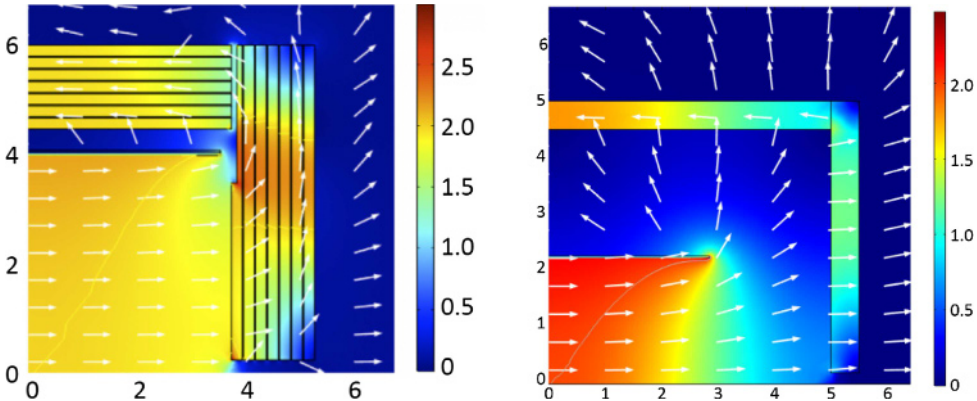


Fig. 7.12. Magnetic field maps in the top right quadrant of CLD (left) and IDEA (right). The colours represent the field intensity. Arrows are not to scale and only show the field direction.

Table 7.5. Key parameters of magnet systems of CLD and IDEA detector concepts.

Concept	CLD	IDEA
Cryostat length (m)	7.4	6.0
Cryostat inner radius (m)	3.7	2.1
Cryostat outer radius (m)	4.4	2.4
Cryostat total mass (t)	71/144 (Al/steel)	7.4
Al thermal shield thickness (mm)	5.0	3.0
Cold mass inner radius (m)	4.02	2.235
Cold mass thickness (mm)	90	30
Return yoke inner radius, barrel/endcap (m)	4.48/0.28	4.50/0.20
Return yoke outer radius (m)	6.00	5.00
Return yoke length (m)	7.4	10.0
Return yoke total mass (kt)	5.2	1.8
Magnetic field at IP, total/from field/from yoke (T)	2.0/1.45/0.55	2.0/1.9/0.1
Operating current (kA)	20 or 30	20
Stored energy field/magnetisation (MJ)	470/130	160/4

inside the calorimeter, the stored energy is reduced by a factor four and the cost can be halved [503]. Figure 7.12 (right) shows the magnetic field map; key parameters are listed in Table 7.5.

The amount of material in a magnet can be split between that used for the cold mass and that used for the cryostat. Material for the cold mass can be considerably reduced if a high yield-strength superconductor is available to allow it to be a self-supporting cold mass. This concept has been demonstrated for smaller magnets but remains a challenge for the solenoid dimensions proposed here [504]. To avoid a high hot-spot temperature after quench causing an unacceptably long recovery time, a high fraction of stored energy has to be extracted, rather than being dumped into the cold mass. Besides a thin cold mass, the cryostat walls should also be as thin as technically possible. Several detector magnets with minimal material amounts have been built in the past. The cryostat walls were made using unconventional techniques that require further investigation. Cryostat walls can be made of high-strength aluminium alloys, but carbon fibre composite is an alternative option [504].

Instead of solid plates, a structured material like an advanced sandwich, corrugated plates or honeycombs, may lead to a reduction of mass. More R&D is required to confirm the technology. Extremely low thermal conductivity insulation material can also be used instead of the standard technique for a classical vacuum vessel, multi-layer insulation and radiation shield. The new material can also provide structural support and transfer forces. The vacuum vessel walls can then be reduced to thin foils as they do not have to withstand vacuum pressure [503]. More ambitious designs are also being developed elsewhere [505].

The current baseline design is an ultra-optimised conventional material based cryostat that can provide a thickness of $0.74 X_0$ (and 30 cm) at normal incidence, of which $0.46 X_0$ is for the cold mass and $0.28 X_0$ for the cryostat. The self-supporting conductor features a nickel-doped aluminium stabiliser co-extruded with a NbTi/Cu Rutherford cable, like in the ATLAS solenoid, further reinforced with a high-yield strength aluminium alloy. A honeycomb structure for the outer cryostat wall can further reduce the cryostat thickness to about $0.04 X_0$.

7.6 Constraints on readout systems

The rate of events to be read out and recorded by the FCC-ee detector data acquisition systems is largest at the Z pole, and is dominated by Z production (~ 100 kHz), low-angle Bhabha's (~ 50 kHz), and $\gamma\gamma \rightarrow$ hadrons events (~ 30 kHz). While Bhabha events can be recorded in a dedicated stream, in which only the data from the luminometers are read out, the entire detector must be read out with a trigger rate in excess of 100 kHz.

With 20 tracks on average in each hadronic Z decay, about 800 readout channels are expected to be hit in the vertex detector of CLD, each of which uses 13 bits to be encoded, corresponding to 1 kB per event. For an integration time of the VXD readout electronics of $1 \mu\text{s}$ (covering 50 bunch crossings at the Z pole), however, the 750 hits induced by the IPC background for each bunch crossing largely dominate the VXD data volume, with 50 kB per physics event. With a trigger rate of 100 kHz, the data that have to be read out amount to a bandwidth of 6 GB/s. The data volume for the IDEA vertex detector is not expected to be significantly different. The CLD tracker contributes similarly to the data volume: with 22 bits per read-out channel, the size of a hadronic Z decay amounts to about 1.4 kB, and the IPC background adds about 2 kB per BX. For a read-out time window of $1 \mu\text{s}$, a bandwidth of 10 GB/s is needed to read out the tracker data.

With a drift chamber, all digitised hits generated on the occurrence of a trigger are usually transferred to data storage. The IDEA drift chamber transfers 2 B/ns from both ends of all wires hit, over a maximum drift time of 400 ns. With 20 tracks/event and 130 cells hit for each track, the size of a hadronic Z decay in the DCH is therefore about 4 MB, corresponding to a bandwidth of 400 GB/s at the Z pole. The contribution from $\gamma\gamma \rightarrow$ hadrons amounts to 60 GB/s. As reported in Section 7.4.4, the IPC background causes the read-out of additional 1500 wires on average for every trigger (including a safety factor of 3), which translates into a bandwidth of 250 GB/s. A similar bandwidth is taken by the noise induced by the low single electron detection threshold necessary for an efficient cluster counting. Altogether, the various contributions sum up to a data rate of about 1 TB/s.

Reading out these data and sending them into an “event builder” would not be a challenge, but the data storage requires a large reduction. Such a reduction can be achieved by transferring the minimum information needed by the cluster timing/counting, for each hit drift cell i.e. the amplitude and the arrival time of

each peak associated with each individual ionisation electron – each encoded in 1 B – instead of the full signal spectrum. The data generated by the drift chamber, subsequently digitised by an ADC, can be analysed in real time by a fast readout algorithm implemented in an FPGA [506]. This algorithm identifies the peaks corresponding to the different ionisation electrons in the digitised signal, stores the amplitude and the time for each peak in an internal memory, filters out spurious and isolated hits and sends these reduced data to the acquisition system on the occurrence of a trigger. Each cell hit integrates the signal of up to 30 ionisation electrons, which can thus be encoded within 60 B per wire end instead of the aforementioned 800 B. Because the noise and background hits are filtered out by the FPGA algorithm, the data rate induced by Z hadronic decays is reduced to 25 GB/s, for a total bandwidth of about 30 GB/s.

The data volume delivered by the dual-readout calorimeter of the IDEA detector has also been estimated at the Z pole. On average, the calorimetric showers from hadronic Z decays are expected to hit 8×10^5 fibres with an assumed density of 50 fibres per cm^2 . Single readout channels collect the signal from nine fibres and encode it in four words of 2 B, yielding a size of 0.7 kB per event and a bandwidth of 70 GB/s. The data volume corresponding to the CLD calorimeter is under investigation.

In total, the data to be sent to the IDEA acquisition system for each trigger is of the order of 100 GB/s, i.e. more than one order of magnitude lower than the amount of data that will be readout by ATLAS and CMS at the HL-LHC. On the other hand, the throughput to disk should be reduced by a factor of 5 to 10 in order to be comparable with the anticipated storage and processing capacities of ATLAS and CMS. Software algorithms, running in a computer farm, would have to be designed to achieve such a data reduction.

A traditional hardware trigger system to select signal events of interest for physics analyses should not be too difficult to design in the clean FCC-ee environment. The expected accuracy of the physics measurements would require, however, the efficiency of this trigger system to be known with a precision of 10^{-5} at the Z pole, which may be an insurmountable challenge. The feasibility of a “trigger-less” scheme as in LHCb, in which software algorithms perform the event selection using the full detector readout, is under investigation.

7.7 Infrastructure requirements

At the present conceptual design stage of the CLD and IDEA detectors, the infrastructure needs of these experiments have not yet been assessed in detail. However, some preliminary requirements can be listed, based on the experience from CMS and on a first assessment made for the CLIC detectors [507,508].

One may assume that sufficient capacity will be available for the equipment handling for installation and maintenance of the detectors due to the requirements of the much larger and heavier FCC-hh detectors. Similarly, the heating, ventilation and air-conditioning (HVAC) of the detector caverns is assumed to be covered by the requirements from FCC-hh.

The detector-specific power requirements have been documented in detail for the CMS experiment [508]. The total power needed for this experiment is about 3.5 MW. Since CLD and IDEA are of a similar size and complexity, the same total power needs can be assumed for each of these detectors. This estimate is very likely an upper limit, as the superconducting magnet systems in the FCC-ee detectors are operated at only 2 T, compared to 4 T at CMS and CLIC. The cryogenics and powering of the CMS magnet requires 0.9 MW of power.

8 Safety

8.1 Safety policy and regulatory framework

The concept study aims at demonstrating that hazard and risk control for a future collider is possible with best practices and industrial standards, which are complemented, where necessary, with techniques specific for a particle accelerator facility. The approach is introduced below by first presenting CERN's legal context and then the hazard and risk management in place for the existing accelerator complex. The subsequent sections show how occupational health and safety topics are addressed, which are specific for a particle collider, and how the risks associated with ionising radiation are managed. For the conceptual design, a two-stage process has been chosen: first, a hazard register lists the safety hazards that will be present at the facility and identifies those, for which standard best practices can be applied to control the associated risks. Second, a detailed analysis will be carried out, for the remaining safety risks, to assess the risk levels and to identify mitigation measures.

8.1.1 Legal context of CERN

CERN's status as international organisation requires that it defines a safety policy in a pro-active and consensus-based process with the host states (see Art. II 2 de l'accord de statut de 1973 entre le CERN et la France [509]). This approach is applicable for non-standard installations like the accelerators, the experiments and the technical infrastructure needed to operate these facilities. Where standard infrastructure dominates (e.g. offices, car parks and workshops), CERN ensures uniformity in the safety conditions across its sites, taking into account the laws and regulations of the host states and EU regulations and directives. Where uniformity cannot be achieved or where compliance is not required to ensure the proper functioning of the organisation, a dedicated risk management process is applied, including the planning, implementation and verification of risk mitigation measures.

8.1.2 Hazard register and safety performance based design

A systematic collection of safety hazards associated with the construction and operation of the accelerator complex is the starting point of the safety assessment. Hazard registers are an established technique in industry. To compile the register, a process-centred approach has been used [510]. In a first step, a systematic description of the processes during the life cycle of the accelerator facility has been established, based on the Project Breakdown Structure (PBS). Each process is characterised by *activities*, *equipment* and *substances* used or released. Hazards may emerge from these activities, equipments and substances at different locations.

As an example, the process of providing electrical power to accelerator magnets is active during commissioning and operation of the accelerator. It relies on transformers and power converters (equipment) at the surface and in underground locations. This equipment is at the origin of electrical hazards, noise and potential environmental pollution in case of dispersion of insulating fluids.

It is assumed that the relevant risks associated with the hazards will be mitigated by standard best practices, implementing compliance with laws and regulations of the host states, EC regulations and directives, international regulations, standards and directives and recommendations from technical or prevention organisations.

Where standard best practices cannot be applied or would affect the proper operation of the organisation, a performance-based design approach is used [511].

Table 8.1. Safety objectives in the design-oriented study.

Life Safety	Environmental Protection	Property Protection	Continuity of Operation
Safety of authorised occupants	Limited release of pollutants to air	Continuity of essential services	Limited downtime
Safe evacuation or staging of injured occupants	Limited release of pollutants to water	Incident must not cause further incidents	
Safe intervention of rescue teams		Limited property loss	

It is proposed to use a standard method like “Failure Mode, Effects and Criticality Analysis” (FMECA) [512] to identify those risks which remain unacceptable. From this starting point, the performance based approach is used. In this process, essential safety objectives, such as preservation of human lives or prevention of environmental damage, are defined. The safety performance of design choices is evaluated for different incident scenarios. If the objectives are met, the design can be retained as mitigation measure.

8.2 Occupational health and safety

The study has initiated a methodological approach in tackling occupational health and safety aspects. The hazard registry classifies relevant sources of risks to permit identifying those, which can be addressed by standard approaches and those, for which project-specific assessments need to be performed, followed by a definition of mitigation measures against residual risks. This preliminary activity has permitted to identify that two main hazards are present in underground areas: fire and oxygen deficiency (ODH). The latter one is a residual risk that emerges after applying “safety-by-design” to cryogenic hazards, such as the avoidance of cold surfaces and functional measures such as combined vacuum and superinsulation blankets. This report, focusing on the feasibility and concept elements of a future particle accelerator research infrastructure does not permit to present the technical risk management files in a comprehensive manner. It focuses therefore only on the presentation of the approach for the two main hazards (fire and oxygen deficiency). The results of the studies [513,514] are summarised in the following sections. The agreed safety objectives for these two hazards are listed in Table 8.1.

To create safe zones along the entire perimeter of the particle collider, smoke and fire resistant compartment walls are recommended to be installed every eight accelerator lattice cells (450 m). Under normal conditions, their doors are open. Each compartment receives fresh air from the underfloor air duct; the used air is evacuated along the tunnel. Smoke and ODH detectors trigger the closure of the doors. An extraction duct traverses all compartments and can extract smoke or helium. The fresh air admission and extraction for each compartment can be controlled individually.

8.2.1 Fire hazard

The most critical phases for a fire hazard are (1) the operation with beam, (2) a long shutdown and (3) a technical stop. During operation, all electrical systems are

Table 8.2. Fire scenarios in the design-oriented safety study.

Scenario	Description	Ignition source
Fire 1	Cable tray fire	Electrical fire
Fire 2	Cable drum fire	Hot work
Fire 3	Transport vehicle fire	Battery malfunction

powered and potential ignition sources. During other periods, personnel is present who may inadvertently cause a fire, e.g. during welding. Table 8.2 shows the three fire scenarios studied.

The fire compartment size is sufficiently small to ensure fire fighter safety during an intervention, in conjunction with secure communications and structural stability of the tunnel. The size has been chosen as a trade-off between keeping evacuation times low, to provide sufficient margins for the intervention teams, to limit the damage of the equipment and to keep cost at reasonable levels. Smoke would still spread in at least one neighbouring compartment and might affect the equipment there. Worst-case scenarios for incidents with equipment loss point to a downtime of about one year. This compartment size has also been adopted by another, recently commissioned accelerator project, the European XFEL. It is based on a safety concept that has been developed by an independent underground engineering society, which has been accepted by the relevant authorities [515] as part of the authorisation to construct the facility. The FCC study gained valuable insight from this project in the framework of a multi-year collaboration with the project designers.

Life safety, safety of occupants and rescue teams were quantified by Fractional Effective Dose (FED), a measure of the harm from toxic fire products as a function of temperature conditions, and visibility through the developing smoke. These parameters were estimated with the industry-standard Computational Fluid Dynamics (CFD) program for fire and smoke propagation, Fire Dynamics Simulator 6.5 [516] from the National Institute of Science and Technology. The studies revealed that uninjured occupants can evacuate the concerned compartment in all scenarios. A smoke and fire detection system with a response time of under two minutes is needed. That shall be combined with an autonomous fire extinguishing system with an intervention time of less than 15 min, to ensure also the safety of injured persons with restricted mobility. Standby rescue teams in the vicinity of the access sites, which can be established with the assistance of host state emergency services, also in remote locations, are a viable approach to establish a working intervention programme. Fire fighting and rescue equipment will be kept available underground in ready-to-use state. The latter approach will already be put in place for the HL-LHC upgrade project.

Protection of the environment calls for a careful selection of fire-fighting agents (e.g. water, foam) which will be done at a later, detailed design stage. The system configuration shall help keeping the release of smoke, chemical and radioactive contaminants to quantities as low as reasonably possible.

Main conclusions. The proposed safety concept fulfils the

- life safety objective for physically fit occupants and the safety of rescue forces in all scenarios,
- life safety objective for injured occupants with an early fire detection and early intervention system,
- continuity of operation goal by limiting the high impact downtimes to the unlikely worst case scenarios and
- environmental impact management goal with standard, best-practice measures.

Table 8.3. Basic parameters for the LHC type RF cryomodules.

Cryomodule	Set pressure (barg)	Vol LHe (l)	Relief temperature	Accidental orifice (mm)	Relief mass flow (kg/s)
LHC-type	0.8	320	5.1	50	2.9

8.2.2 Oxygen deficiency

For the FCC-ee machine the use of liquid helium is limited to the superconducting RF sections in the tunnel. The accidental scenario chosen to assess the oxygen deficiency hazard in these areas was an external impact leading to partial or complete rupture of the beam pipe. At this stage, air at 300 K flows into the cryomodule through the orifice, condensing onto the inner cold surface of the beam pipe. This is also known as a loss of insulation vacuum where the transfer of heat vaporises the liquid helium and leads to an increase of pressure in the helium volume. For the superconducting RF cavities the surface area in contact with the beam vacuum is substantially higher compared to e.g. the superconducting magnets in the LHC arcs with their multilayer insulation (MLI). Due to the ultra-high beam vacuum specifications, MLI cannot be installed inside the beam pipe, hence, the accidental venting of air yields the maximum heat flux into the helium (38 kW/m²).

Since the design of the FCC-ee RF cryomodules is not yet finalised, modules similar to those of the LHC with the parameters listed in Table 8.3 are considered.

Despite having a larger relief mass flow, the helium inventory is considerably lower compared to that of superconducting magnets, hence helium would be accidentally spilled into the tunnel for a minimum amount of time (about 30s considering a volumetric flow at 5.1 K). Due to the outflow of cold gas and the buoyancy effects, a so-called “turbulent zone” around the release point will be created, with an approximately homogeneous helium-air mixture at breathing level [517]. After the helium mass is released into the sector, the gas stratifies at the ceiling level, restoring the oxygen level below the helium layer. Standard organisational measures shall be put in place to ensure no occupant is in the “turbulent zone” during the release. The extent of the turbulent zone will be assessed when a more detailed description of the FCC-ee cryomodules is available. It is assumed that there will be vacuum barriers between each cryomodule.

Once the helium is stratified at the ceiling, the amount of gaseous helium (~250 m³) corresponds to a layer of about 35 cm.

8.3 Radiation protection

For the mitigation of risks associated with ionising radiation, the standard prescriptive methods of the existing CERN radiation protection rules and procedures have been used. Risks resulting from ionising radiation are analysed from a very early design phase onwards, to develop mitigation approaches along the entire design process. Design constraints will ensure that the doses received by personnel working on the sites as well as the public will remain below regulatory limits [518,519] under all operation conditions. A reliable radiation monitoring system coupled with an effective early warning and emergency stop system will therefore be an essential part of the system implementing risk control measures.

The FCC-ee will be comparable in terms of radiological hazards to LEP. LEP and LHC are reliable sources of experience to take into account when planning

the radiation protection measures during the design phase. The main differences for FCC-ee are the higher beam energy and the much higher beam currents. The four FCC-ee configurations have to be studied separately. The low energy versions, comparable to LEP, will operate at much higher beam current. The high energy versions will have similar beam currents as LEP, but the higher energy synchrotron radiation will have a greater radiological impact.

Radiation protection is concerned with two aspects: protection of personnel operating and maintaining the installations and the potential radiological environmental impact. The second topic is addressed in Section 10.2.1. To enable the assessment of the potential radiological risks to the personnel working on the sites, the radiological hazards are classified by their sources: (1) particle beam operation, (2) activated solids, liquids and gases.

8.3.1 Particle beam operation

Radiation hazards from high energy particle beams arise from their interaction with matter and other particles. Shielding protects personnel by absorbing the primary radiation and the subsequently generated stray radiation. An access control system prevents people from accessing hazardous areas. An interlock system prevents beam operation in case of an unauthorised access. An emergency stop system ensures that the operation with beam is terminated quickly and in a controlled way if needed. Areas accessible during beam operation will be designated as non-radiation areas to avoid the need for specific restrictions for radiation protection reasons.

Depending on the position in the accelerator, several metres of rock or concrete will sufficiently shield from the radiation resulting from a total beam loss. Chicanes will effectively reduce radiation streaming through feed-throughs and passages. Access to the accelerator tunnel and the experimental caverns will not be permitted during operation.

The shafts above the experiments connect directly to the surface. With the shielding effect of the detectors around the interaction points, more than 100 m distance to the surface and a concrete shielding cap on top of the shaft, the radiation levels on the surface will be low enough to prevent any relevant direct exposure to stray radiation or sky-shine effects on the surface sites or beyond.

8.3.2 Activation of solids

Activation of solids represents a potential hazard to persons through exposure to gamma radiation during interventions inside the accelerator tunnel such as in-situ maintenance or handling of radioactive parts. The radiation levels differ considerably amongst the various sectors of the accelerator and depend on the type of beam operation and on the time that has passed since the machine was stopped [520].

A specific source of activation in high energy lepton synchrotrons is the synchrotron radiation that they generate. At the FCC-ee beam energies of up to 182.5 GeV, the photon critical energy reaches 1.25 MeV. The high energy fraction of the synchrotron photons can induce activation through (γ, n) reactions where the neutrons also contribute to the subsequent activation. Simulations of an initial vacuum chamber layout indicate that residual dose rate levels of a few tens of $\mu\text{Sv/h}$ along the beamline can be present after the beam is stopped. This would rapidly decay to less than one $\mu\text{Sv/h}$ within a few days.

The first means to mitigate risks from this hazard will be to optimise installation, maintenance and repair processes: automated and remotely controlled interventions

are one way to reduce the exposure of personnel. Bypass tunnels for high radiation areas will also help to keep exposure low.

Activated materials are routinely removed from the accelerator tunnel and experimental caverns for maintenance or disposal. Dedicated and specially equipped areas for handling and storage of this equipment [520] will be foreseen. Corrosion and machining of activated materials can produce dispersed activated solids in the accelerator and workshop areas. Experience from high energy accelerators at CERN shows that this does not lead to relevant radiation risks; therefore, standard procedures apply.

8.3.3 Activated or contaminated liquids

Infiltration water and leakage water from closed water circuits will be collected by the tunnel drainage system. The water will be pumped to the surface sites for collection and further treatment before being cleared and released. Continuous monitoring and confinement will ensure that no activated and/or contaminated water will be released.

The demineralised water filtering units collect and concentrate radioactive particles and will be treated through standard procedures. Ventilation cooling units for the tunnel and experimental areas can, under certain operational conditions, concentrate airborne radioactivity in their condensates, mainly in the form of tritiated water. This liquid waste water will be collected and treated according to standard procedures.

8.3.4 Activated or radioactive gases and radioactive aerosols

Air in the accelerator and experimental areas will become radioactive during beam operation. Ventilation systems will be fault-tolerant and either be partially or fully recycling, depending on the assessments to be done at a later design stage for a specific particle collider scenario. Areas will be ventilated with fresh air before allowing access to avoid undue exposure of personnel. Areas with different activation potentials will be separated, such that only those areas are vented where access is required, thus avoiding unnecessary releases of radioactive air. Experience shows that outgassing from activated concrete or radon decay products will only be present in small concentrations in the tunnel air because they are continuously removed by the ventilation system. Dust activation and airborne corrosion products are no relevant sources of exposure to intervening personnel, since aerosols are continuously removed by the air treatment systems.

9 Energy efficiency

9.1 Requirements and design considerations

Energy efficiency is a topic which is high on the societal agenda in general and must consequently also be a core value of any future research facility, especially energy-intensive facilities like particle accelerators. It concerns the availability and cost of electricity, the reduction of climate-relevant emissions, and other side-effects linked to energy production, transmission and conversion. Operating the FCC in an energy efficient way will enhance its public acceptance. Moreover, the FCC is an opportunity to drive the evolution of energy efficient technologies leading to

socio-economic benefits. A sign of the importance of the topic is the “Energy for Sustainable Science” workshop series [521] established several years ago. Concerted efforts are being made in the framework of the EuCard2 Project [522] (Work Package 3 – Energy efficiency of particle accelerators [523]) and the ARIES Project [524] in the EC Horizon 2020 Research and Innovation Programme. An overview of activities in view of greater energy efficiency of particle accelerators can be found in [525].

Applying fine-grained monitoring of energy use will help to raise energy-awareness, control the peak power and energy losses and allow better predictions of energy use to be made. All equipment or facilities not currently in use will be switched off or ramped down. Surface buildings will be constructed to follow high environmental standards, bearing in mind that by far the dominant share of the energy consumption comes from the operation of the accelerator. As far as possible, electrical energy will be purchased from renewable sources. Generally, it should be noted that reconciling the demand for highest performance of the facility over extended running periods with sustainability and reasonable/acceptable energy use is not a simple task. Experts specialising in matters of energy efficiency or energy saving will be consulted to devise a comprehensive and coherent concept from the outset.

The FCC-ee collider rings will be operated in a different way than the FCC-ee injector complex. The collider runs at constant energy level and, therefore, it does not create a cyclic peak power demand from the power grid like the hadron collider ring. The injection complex, however, has a cyclic power demand. Therefore, a combination of different ways of supplying power is considered:

- **Supply of peak power from external network:** the peak power is provided by the external network. This is the simplest solution; it might, however, require partial reinforcements of the external network, which is operated by Réseau de transport d’électricité (RTE).
- **Use of energy storage systems:** this concept uses a combination of switch-mode power converters (Fig. 9.1) and local energy storage systems to power magnet circuits. Peak demands during the ramp-up are fully or partially provided by the storage system. During the ramp-down the energy is recovered and fed back into the storage system. This principle is already being used to power the PS magnets (POPS system) and will also be used to power the PS Booster (PSB) at CERN after its upgrade to 2 GeV (POPS-B). The energy storage system for the injector can be based on a set of different energy buffering technologies such as high voltage DC capacitors and batteries. This concept eliminates the positive power peak during ramp-up and the negative during ramp-down, thus resulting in a flat power profile seen by the grid. As a consequence, the external power transmission and the machine internal distribution networks can have lower component ratings for substations, cables and transformers, and will also cause less distribution losses.

9.2 Power requirements

The FCC-ee will be operated according to the model discussed in Section 2.8.1. The electrical power consumption depends on the centre-of-mass energy. It therefore varies throughout the entire operation period of the project. An estimation of the upper limit of the power drawn by the various systems [526] during regular luminosity production compared to the LEP collider is summarised in Table 9.1. Although the FCC-ee is four times larger than LEP, the design concept leads to an overall electrical energy consumption of only about 2.5 times the one of LEP. With

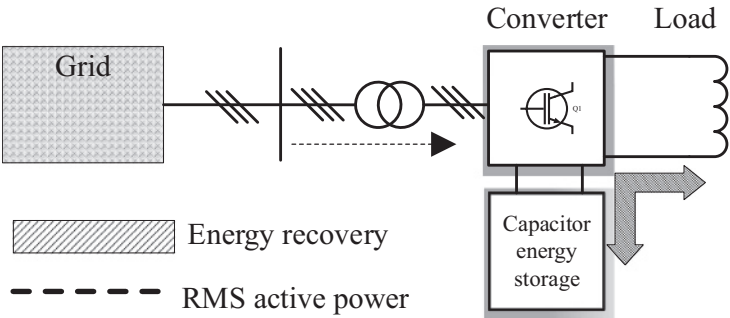


Fig. 9.1. Simplified schematic of the principle of combining switch-mode converters with energy storage.

Table 9.1. Power requirements of accelerator subsystems and comparison with the LEP collider.

Subsystem	Electrical needs (approx. MW)					
	LEP2	Z	WW	ZH	tt	tt optimised
Collider cryogenics	18	1	9	14	46	ca. 35 (−25%)
Booster RF and cryogenics	n/a	3	4	6	8	ca. 6 (−25%)
Radiofrequency	42	163	163	145	145	145
Magnets	16	4	12	26	60	59
Cooling and ventilation	16	30	31	33	37	37
General services	9	36	36	36	36	36
Two experiments	9	8	8	8	8	8
Two data centres	?	4	4	4	4	4
Injector complex	10	10	10	10	10	10
Total	120	259	277	282	354	340

Notes. Indicated power consumption values are upper level estimates with further improvement potential for the non accelerator systems.

additional technology advancements and optimisations during operation, the overall energy consumption is expected to remain close to 300 MW even at highest collision energies (see 9.3).

The energy consumption levels indicated are first reached by basing the collider design on novel energy-efficient twin-aperture main dipoles and quadrupoles (see Sect. 3.2), saving about 50 MW of power for $t\bar{t}$ operation (LEP had only a single aperture). The value includes the electricity needed for the magnets of the booster ring. The value indicated for the RF system results from deploying novel power sources with at least 15% higher efficiency than conventional klystrons (Sect. 3.4.3), reducing the electrical power requirement by about 30 MW. The new bunching technologies for high-efficiency klystrons also relax the water cooling requirements. The value for the cryogenic system is based on state-of-the-art Q_0 values for Nb/Cu cavities at 400 MHz and bulk Nb cavities at 800 MHz, with the accelerating gradients indicated in Section 3.4.2. Both the Q_0 value and the accelerating gradient are much higher than at the time of LEP, translating into significant savings of power and cost. While the static losses in an optimised cryomodule are also expected to be up to 40% lower than at LEP and LHC, recent findings on alternative cavity materials promise further substantial progress in cutting the dynamic losses by another 60% for the $t\bar{t}$ machine [527]. This potential additional saving is reflected in the “ $t\bar{t}$ optimised” parameters of Table 9.1.

The total power consumption can be kept below 300 MW for the majority of the operation period, while running with only 400 MHz cavities. For $t\bar{t}$ operation with 800 MHz cavities, additional refrigeration power is required for their 1.8 K working point. Applying technology-driven optimisation, it appears feasible to reduce the total power demand to a level close to 300 MW also for the working point with the highest centre-of-mass energy. This type of optimisation study will be carried out during the detailed technical design phase.

To derive the power to be supplied by the grid, losses of the order of 5–7% in the electrical distribution chain (e.g. magnetisation losses in transformers) must be added to the values of Table 9.1.

Using similar data for other significant phases along the operation cycle (injection) and incorporating the projected yearly programme (185 days of luminosity production at peak energy, 30 days of beam commissioning, 20 days of machine development, and 10 days of technical stops) one obtains at this point of the conceptual study an energy consumption during a typical year of operation of ~ 1.9 TWh. For comparison, CERN's energy consumption in 2016 was close to 1.2 TWh.

9.3 Energy management and saving

One of the principal challenges of the 21st century will be to develop solutions for the sustainable use of energy. In this context, one of the key design aspects of FCC-ee must be a strict focus on energy efficiency, energy storage and energy recovery. This project can and must be used as a technology driver, pushing towards more efficient ways to use electrical and thermal energy.

It is worth highlighting that the efficiency of the FCC-ee in terms of luminosity per input energy is far higher than that of any other proposed e^+e^- particle collider [528]. In other words, the FCC-ee collider concept itself is the best showcase of putting forward a sustainable research infrastructure that features energy efficiency at its very core, the design and operation concept of the particle accelerator. While energy efficiency at system design level is the strongest lever, subsystem efficiency further contributes to keeping the resource consumption within limits.

The foundation for sustainable energy management is real-time energy monitoring, for example using smart meters. This opens the possibility to precisely predict and optimise the overall powering profile, with the objective to reduce the peak power as well as the electrical losses. For the reduction of the peak power demand, cyclic loads of the injector chain need also to be taken into consideration.

By systematically applying the concept of energy storage for the powering of the magnet circuits, the FCC will be able to recover a significant part of the energy stored in the magnets. When combining energy storage with complementary measures such as optimisation of the power cycles, the costs for the electrical infrastructure as well as for electrical losses can be greatly reduced.

Electricity transmission over long distances and voltage step-down or step-up lead to power losses. The overall losses of a conventional transmission and distribution network range between 5% and 7%. Power line losses are resistive losses due to the Joule effect. Transformers contribute with load losses which will vary according to the load on the transformer and no-load losses which are caused by the magnetising current needed to energise the transformers and which are steady losses. The proposed baseline transmission and distribution scheme also considers providing the required level of availability, maintainability and operability from the early concept phase onwards. As an example, where needed, two 135/3 kV transformers are operated on access points in parallel, each at a nominal load level of 50%. Such a configuration responds to the above mentioned, non-functional requirements, but

it is not optimised for energy efficiency. Alternative schemes aiming at improving the overall efficiency of the transmission and distribution network while maintaining the required level of availability, maintainability and operability therefore need to be studied. Industrial partners will lead the development, potentially demonstrating the technology in a pilot scheme at CERN's LHC so that a system at acceptable cost and with the necessary reliability level can be obtained from market suppliers when needed.

The RF system energy efficiency can be improved by optimising the electrical to RF power conversion efficiency and the cryogenic refrigeration system energy consumption. With new bunching technologies for high efficiency klystrons, efficiencies are expected to rise from 65% to above 80%. These improvements reduce the water cooling requirements by the same amount. The cryogenic losses can be reduced by improving the static and dynamic losses of the cavity cryomodule. The static losses in an optimised cryomodule are expected to be up to 40% lower than in the LHC. Recent findings on alternative cavity materials promise real progress in cutting the dynamic losses [527].

The design of each individual element of the power system must contribute to loss reduction and energy saving and will therefore be scrutinised in terms of energy efficiency during the detailed technical design phase.

9.4 Waste heat recovery

Currently, a project is being implemented to connect the cooling system of LHC at Point 8 to a "thermal energy exchange" loop which will supply a new industrial zone near Ferney-Voltaire (France) with warm and cold water circuits for both heating and refrigeration purposes (see Fig. 9.2) [529]. This is a hybrid system, consisting of waste-heat recovered from cryogenic machinery that is stored by heating the ground and which is made available via geothermal probes. Similarly, plans have been developed to feed waste heat from LHC Point 1 into CERN's distributed heating system. Installations of this type can also be envisaged for the infrastructure sites. However, the waste heat can also be supplied directly or through storage in dedicated buffers rather than in the ground. Although a significant potential for waste heat recovery from FCC exists, the needs and opportunities and the infrastructure conditions need to be evaluated for the specific collider and for each specific technical system (e.g. whether a distributed heating system exists already, or whether it could be implemented for a new industrial or housing area close to a surface site). Points PA, PB and PC are currently located in areas with a high population density, whereas most of the other points are located in rather rural areas. Potential applications of such recuperated heat are being envisaged. The definitive energy recovery potential depends on the developments planned in the vicinity of the surface sites and must be studied in collaboration with the host states.

The amount of recoverable energy increases with the proximity to the consumer and also with the temperature of the medium, typically water which is at 10–15°C above ambient temperature. How much this can be increased, by e.g. operating specific equipment at higher temperatures, will be studied. The most promising candidates for waste heat recovery are the cryogenic plants, which are the top electrical energy consumers, and the conventional cooling systems. The host states have requested that an effort is made to reduce the water consumption with respect to today's operating installations.

It should be noted that the host state representatives expect that project owners develop a plan in cooperation with industrial and public partners to ensure that ongoing efforts on a transition towards a sustainable and circular society are given

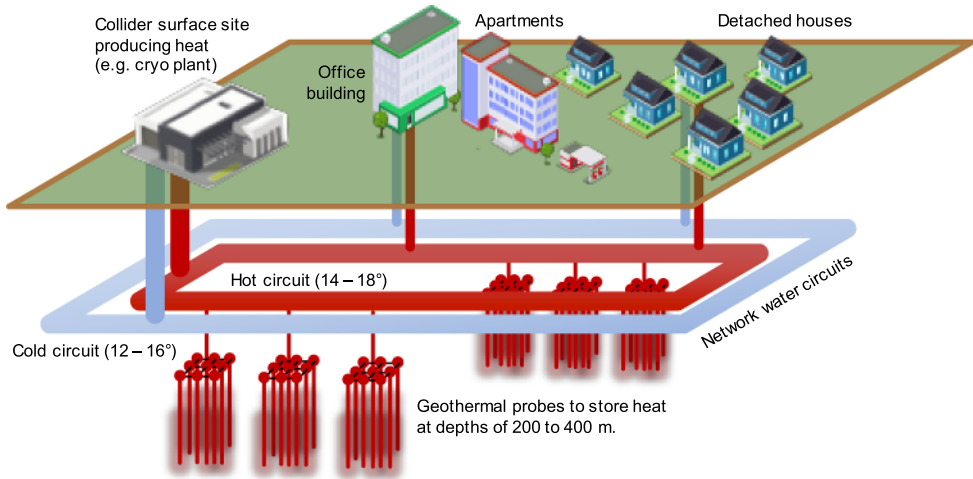


Fig. 9.2. Concept of a heat recovery facility based on a thermal network. The concept is similar to a project, which is currently under construction in the vicinity of CERN. In that project, waste heat is supplied from LHC point 8 to consumers in an industrial zone in Ferney-Voltaire, France. The distance between the LHC surface point and the industrial zone is 2 km.

priority. This is comparable to approaches which are currently being developed in the frame of smart-city projects.

Another potential area of interest is the return to the supplier of cooling water after use for subsequent heating purposes. GeniLac³, a 280 MCHF investment project close to the United Nations district (Geneva, Switzerland) with a total cooling capacity of 280 MW, can be further investigated with a view to optimising the overall energy balance. This concept is relevant for point PB in particular. The cooling water could also be transported to remote points through the tunnel, thus opening the possibility of extending the concept to points PC and PD. The access sites in France are mainly in rural areas, therefore a dedicated study needs to be carried out to assess the potential for this technology. This study should take the distances from potential consumers and the evolution of urban areas up to the middle of the century into consideration. Potential consumers include, first of all, public institutions such as healthcare providers, schools, public buildings and industrial zones. Next, innovation potential such as indoor farming, health care centres and support for private district heating can be considered.

A third concept involves a step increase of the water temperature in the outer circuits such that the heat supplied becomes an interesting resource for industries such as chemical and food processing. Systems for vapour generation stepping up from 25°C quickly become economically feasible [530], but a client needs to be close to the heat production source and willing to engage in a project that does not require the research infrastructure to function as a reliable energy supplier.

Eventually, direct power generation from waste heat can also be envisaged. Today, the effectiveness of such systems is still low, in the few percent range, but industrial interest [531] in increasing the efficiency of industrial plants is driving R&D activities, for instance via ORC [532] devices. For a large-scale research facility with a system that generates of the order of 100 MW of heat, even modest gains

³ <https://www.genie.ch/project/h/genilac-une-innovation-energetique-majeure-et-durable-pour-geneve.html>.

from converting heat into electrical or mechanical energy can be beneficial, particularly considering technological advances on a time scale of twenty years.

10 Environment

10.1 Requirements and approach considerations

10.1.1 Legal context

For the correct operation of CERN's facilities, its status as an international organisation requires that it establishes the requirements and constraints concerning the management of its environmental impact in a pro-active and consensus-based process with the host state on whose territory the installation lies (see Art. II 2 of "L'accord de statut de 1972 entre le CERN et la France" [533]). Where there is standard infrastructure on the surface sites (e.g. office buildings, car parks, ordinary workshops), CERN implements the national laws and regulations that apply at the location where the facility is located (see also "Art. II Convention entre la France et la Suisse de 1965" [534]). A specific process is necessary for the non-standard installations like the accelerators, the experiments and the technical infrastructure needed to operate these facilities. Different rules apply to a project with underground infrastructure which crosses the international border and which has surface sites in both Switzerland and France:

Underground infrastructure. In Switzerland, underground volumes below a depth that is considered *useful* for the land owner is not subject to the acquisition of rights-of-way and the law applying to private property. A communication from the Département Fédéral des Affaires Étrangères (DFAE) on 16 July 1982, informs CERN that it is exempt from right-of-way acquisition regulations for the LEP/LHC underground structures. In France, land ownership extends to the centre of the earth. Therefore either a process to acquire the underground volumes or to acquire the rights-of-way needs to take place. For both host states, CERN remains liable for any potential impact on the population and the environment resulting from the construction and operation of underground and surface installations.

Surface sites. The land plots for surface sites need to be acquired or leased in both host countries. According to a preliminary study carried out with an environmental impact assessment contractor [535], in Switzerland, an environmental impact assessment needs to be performed when new car parks with more than 500 places are constructed or if per year more than 10 000 t of excavation material are processed on Swiss territory with the purpose to reuse that material [536]. The "Ordonnance relative à l'étude de l'impact sur l'environnement (OEIE, Oct. 1988 and 2016)" and the manual "L'étude de l'impact sur l'environnement (EIE) (2009)" [537] define the scope and contents of the assessment. In France, a recent law revision⁴ introduced a new environmental impact management process [538]. This new process explicitly requires a public consultation process on the scope, objectives, socio-economic potential and the impact on the development of the territory that needs to take place well before a specific technical design is developed and before a decision to construct is taken⁵. The host countries require an early and continuous involvement

⁴ <https://www.ecologie-solidaire.gouv.fr/levaluation-environnementale>.

⁵ See also Art. L121-15-1 of law 2018-148 of 2 March 2018.

of the population in the project development and construction preparation phases that goes beyond information exchange. It calls for an active participation, giving people the possibility to contribute in well-defined and limited ways in shaping the project and in particular in developing the potential for added value. Consequently, France and Switzerland require that the initial assessment process is carried out from the early design phase onwards, followed by regular reviews of the effectiveness of the mitigation measures and assessment of residual or new impacts which become apparent during the construction and operation phases.

Both host states have regulations and laws concerning the continuous assessment and limitation of environmental impact for a variety of different topics. While the processes comprise very similar topics, the organisation of the information and the reporting templates are different for the two host states. In Switzerland the impact study may be limited to certain topics depending on the project needs, whereas in France all topics need to be discussed. In Switzerland the reporting is topically structured and in France the reporting is chronological across the entire project life cycle.

Since the project is international, the Espoo agreement applies [539]. CERN has to ensure that both host states are informed about the effects of any new infrastructure project in their country and the effects on the neighbouring countries. This includes for instance the use of energy, consumption of water, traffic and the management of waste across the borders.

10.1.2 Environmental compatibility management concept

The international nature of the project and the similarity of the surface points suggest a uniform and streamlined framework to carry out an environmental impact assessment across both host states. This approach splits the project into locations (e.g. underground structure, individual surface points, associated infrastructures), topics relevant for the impact assessment (e.g. water, air, noise) and the life cycle phases of the project (e.g. construction, operation, maintenance and retirement). Different requirements and constraints apply to the various locations and phases. For some it may be necessary to meet the standard national guidelines of the relevant host state or, for some particular installations, the guidelines need to be agreed between CERN and the host state on a case-by-case basis.

It is planned to have a central, uniform platform to manage the analysis, the assessment of proposed mitigation measures, the follow up of the effectiveness of mitigation measures and the analysis of the residual impact. This platform will permit the extraction of information according to the specific needs of the individual host states. Specialised companies and software solutions exist and should be used whenever possible (e.g. Envigo by eon+, see Fig. 10.1). A market survey and competitive selection process should be performed in cooperation with the host state partners in order to ensure that a suitable set of experts and tools are selected for this process. It is considered good practice in Switzerland that the owner of a large-scale project delivers a “Notice d’Impact sur l’Environnement (NIE)”, which is more comprehensive than the minimum required environmental impact assessment. The uniform framework mentioned here permits this approach.

The need to perform the environmental impact assessment and management process before a decision to construct is made, calls for the preparation of the assessment framework with the help of experienced consultants and the host state authorities in the years 2019–2021. Given some basic infrastructure, consultants and authority partners who know the project vision and goals can work with the scientific and engineering team until the design has reached maturity by 2023. By this time, CERN

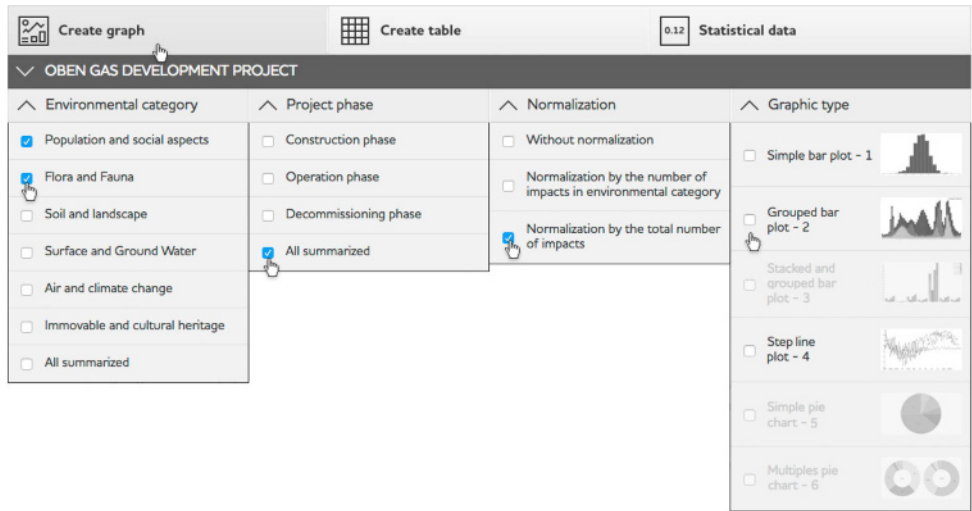


Fig. 10.1. Example of a continuous environmental impact assessment system supported by an information system.

must have reached consensus with the authorities and the population that permits the formal initiation of a public consultation process as required in both host states. The process is considered lengthy in both countries and is expected to require a few iterations. The goal is to obtain clearance to submit a request for construction permits by 2026, i.e. before an international consortium (e.g. the CERN member states or an international consortium bound by a memorandum, a letter of intent or a similar type of collaboration agreement) takes a formal decision to build the facility.

10.2 Environmental impact

10.2.1 Radiological impact

Depending on the operating phase, the beam energy of FCC-ee is between 0.45 and 1.75 times that of LEP, but the luminosities are significantly higher. Compared to the hadron machine, the stored beam energy will be many orders of magnitudes lower. The significant difference of the processes lead to much lower activation of material [540,541]. In general, the potential radiological impact of the lepton collider is about two orders of magnitude lower than the hadron collider.

The potential sources for environmental radiological impact are identical to those for the hadron collider: (1) dose from stray radiation emitted during beam operation, (2) dose from radiation emitted by radioactive materials and waste, (3) operation of sources and X ray emitting devices and (4) the dose from release of activated water and air. Safeguards will be included in the design of the accelerator infrastructure to control the impact on the environment. Dedicated monitoring systems and procedures will ensure continuous parameter recording and auditing throughout the entire operational phase of the facility and will facilitate the control of the impact.

FCC-hh and FCC-ee share the same infrastructure, in particular that for the treatment of air and water, the main exposure pathways. Measures foreseen to control and limit the environmental radiological impact of the FCC-hh will therefore also be adequate for the FCC-ee. During the detailed design phase, emphasis can include adequate, but not over-engineered, measures for this particular machine.

The impact of ionising radiation on trained personnel during operation and maintenance phases as well as the management of radioactive waste are described in Sections 8.3 and 10.3.1 respectively.

10.2.2 Conventional impact

A preliminary review of underground and surface sites has been performed with expert organisations in France and Switzerland [535,542]. The studies established a working framework for the subsequent optimisation of the placement of the particle collider which is compatible with the existing requirements and constraints of both host states. The first investigation revealed that a placement of the collider, which is compatible with the legal and regulatory boundary conditions in both countries can be developed. No conflicts with geothermal boreholes, seismic activities, underground technical features such as pipelines, critical power and communication lines could be found so far. Also, no relevant conflicts with underground water layers or hydrocarbons could be identified and puncture of protected water reservoirs can be avoided with an optimised layout and placement. However, the current, first preliminary placement does not meet all requirements and constraints at the same time (technical requirements, lepton and hadron collider optimised layout, environmental exclusion zones, socio-urbanistic constraints). Therefore, further iterations need to be done on the layout and placement optimisation in order to come to an overall coherent proposal that meets all the criteria. In addition, dedicated underground investigations need to be carried out soon in order to validate the preliminary findings with more accurate data and first surface site field studies need to be carried out in order to validate those locations, which need to be considered for an optimised layout and placement. The entire Geneva basin features water-saturated ground, but the water remains locally confined. Consequently, it is unlikely that water, which is for human consumption and which reaches the surface or rivers would be activated by ionising radiation.

Compatibility with protection of flora and fauna as well as agricultural activities has been considered from the beginning by taking into account a number of national and European conservation laws and guidelines. In this context, preliminary surface site candidates have been identified. Potential sites for a next iteration of the surface sites to be considered for a layout and placement iteration for a specific particle collider scenario have been identified.

Some surface sites require further optimisation in the design phase in order to simplify potential landscaping or indemnity processes and to ease accessibility by road. Swiss law requires the reservation of a certain surface area for agricultural activities in order to remain self-sufficient in case of crisis [543]. This constraint imposes the launch of a declassification and ground/right-of way acquisition process in the subsequent design phase. Dedicated working groups are currently being established with representatives of the Swiss confederation and the relevant offices of the Canton and State of Geneva in order to facilitate this multi-year process. The legal framework in both countries require further detailed information in order to jointly develop an optimised placement. These data can only be obtained by dedicated ground investigations and need to occur before the relevant environmental impact analysis can take place. Confirmation that inadvertent activation of water due to infiltration can be avoided may need to be verified by targeted surveys in a limited number of locations. The environmental impact during the construction phase, which extends over many years, needs to be studied. The reuse of the excavated material (in order of priority: on-site use, processing and reuse, landscaping, storage), construction site traffic, noise and dust are all elements which also need to be considered.

Official bodies of both host countries (Secrétariat Générale de la Région Auvergne-Rhône-Alpes and Département de l'aménagement, du logement et de l'énergie de la République et canton de Genève) have informed the study management that for emerging urban areas and where there is a region with high-value natural assets, early participation of the authorities and representatives of the population in the further development of the project plans is required. Surface sites need to blend into the landscape. Synergies with local and regional activities that profit from the infrastructure in the host countries need to be developed. Examples include cooling via the GeniLac [544] water project, waste-heat recovery for residential districts and healthcare providers, possibilities for temporary energy storage and release in cooperation with neighbouring industries. For the construction phase, particular attention needs to be given to noise, dust and traffic. For the operation phase, topics include the consumption of water, electricity, the emission of noise and the increased need to provide all kinds of infrastructure for an ever growing community of scientists, engineers and visitors.

The immediate subsequent design phase of the project will focus on the further optimisation of the collider and surface site placement, based on the findings already obtained in cooperation with the host state authorities and their nominated technical advisory bodies for the concept phase. This work will, in compliance with the regulations of both host countries, involve representatives of the local population in order to ensure a seamless evolution of the project design towards a later construction decision.

10.3 Waste management

10.3.1 Radioactive waste management

CERN has a radioactive waste management system which has been implemented in agreement with its host states [520]. The production, temporary storage, processing and elimination of radioactive waste is performed according to the processes defined in the radioactive waste management system. During the technical design phase of the collider, the production of waste and its provisional classification will be addressed and quantified and the temporary storage and treatment facilities required will be evaluated in detail. The choice of materials to be used in terms of their isotope production and known elimination pathways will be optimised during the design phase.

The FCC-ee will produce similar types of radioactive waste as LEP and LHC. Given the similarity in materials used, the radionuclide inventory is not expected to change significantly. Due to the larger machine, the volume of waste will increase accordingly. The fact that the lepton collider will have only two major experiments at PA and PG, unlike the four experiments at a hadron collider like LHC, does not have a significant impact on the amount of waste produced during its operation. For the highest energies of 175 GeV and above, the high energy synchrotron radiation will lead to activation of the beam pipe. Given the beam energy, beam current and luminosity during the different operation phases, one can assume that the LHC will provide an envelope case for waste production.

The construction and operation of a high intensity lepton collider in a new tunnel will use the SPS as a pre-booster and a new accelerator in the FCC tunnel as a top-up machine. During the operation phase of the accelerator complex, radioactive waste will be produced from the collider and the injector chain, mostly during the long shutdown periods. Based on the experience with LHC [545], a conservative estimate of the production of radioactive waste during operation is given in Table 10.1.

Table 10.1. Estimates of radioactive waste for the high-intensity lepton collider.

	TFA Waste	FMA Waste
Construction phase	no additional radioactive waste	
Operation phase		
Injectors	<250 m ³ /year	<10 m ³ /year
Collider (including top-up ring)	<1450 m ³ /year	<70 m ³ /year

Table 10.2. Examples for conventional waste.

Class	Description	Subsequent reuse
Inert waste	Excavation materials	Use on construction site, processing for create raw materials for industry and construction and isolation materials, landscaping, environmental protection measures, addition to construction material, final disposal (e.g. quarries)
Inert waste	Construction materials	Recycling, final disposal (e.g. quarries)
Inert waste	Polluted excavation materials (e.g. from drill & blast)	Final disposal in dedicated sites
Wood (treated)	Cable drums, palletes, construction wood, packaging materials	Taken back by supplier
Wood (untreated)	Cable drums, palletes, construction wood, packaging materials	Recycling, incineration
Plastics	Packaging materials	Taken back by supplier, recycling
Metals (low quality)	Construction	Recycling
Metals (high quality)	Wires, cables, machinery, sheets	Taken back by supplier for re-integration into production cycle
Electronics	Cards, computers, outdated devices	Recycling
Insulation materials	Construction, machine construction	Taken back by supplier, reuse
Paint, solvents, glue	Construction, maintenance	Residuals from construction taken back by suppliers, recycling after stabilisation
Chemicals	De-mineralised water production, cooling tower cleaning and anti-legionella treatment	Favour bio-degradable products and processes involving less or no chemicals
Paper and cardboard, textile, filters, glass	Packaging	Recycling
Plaster, coating, gypsum, tiles	Residual construction materials	Taken back by contractors
Oil	Hydraulics, cooling, insulation, lubrication	Taken back by contractors with obligation to decontaminate and recycle

10.3.2 Conventional waste management

A large-scale research facility produces conventional waste during the construction and operation phases. Typical classes of waste produced during construction are shown in Table 10.2.

While plans for the management of waste during both phases need to be established, the regulatory frameworks of both host countries require the development of waste prevention plans for the construction phase as part of a preparatory phase. In France, the “Plan régional de prévention et de gestion des déchets” [546] requires the project owner to include approaches that work towards a circular economy, taking into account the possibilities offered by the regional infrastructures. Waste reduction targets are documented in the “Loi relative à la transition énergétique et à la croissance verte” [547]. In Switzerland, the “Ordonnance relative à l’étude d’impact sur l’environnement (OEIE)” [536] specifies the activities related to the planning of how conventional waste is managed. In the canton of Geneva, the “Plan directeur cantonal 2030” documents the specific waste reduction targets [548].

The management of waste follows three priorities: (1) keeping the amount of conventional waste as low as reasonably possible, (2) develop a plan to reuse the waste locally and regionally and (3) keep the impacts of residual waste transport low.

Today, excavation material is still considered waste by law, but the legislation is evolving in many European countries. Millions of cubic metres of excavation material can be a valuable primary resource. Large-scale processes to transform and make the materials available on the market remain to be developed. The FCC study has launched a research activity with the French tunnel design center (CETU), the Geneva based “Service de géologie, sols et déchets” (GESDEC) and Montanuniversität Leoben (Austria) on this subject. The study will serve as an input to the environmental impact assessment. Furthermore, detailed plans for the construction phase, including the identification of waste, its collection, treatment, reuse and disposal in compliance with the individual national laws have to be developed as part of the environmental impact assessment process. This plan should include measures that can be included in procurement procedures and in the agreements concerning in-kind contributions from collaboration members. The procedures should address the sharing of the responsibility between project owner and suppliers for dealing with conventional waste.

11 Education, economy and society

11.1 Implementation with the host states

11.1.1 Overview

Assuming 2039 for the start of physics operation, a decision point for a construction project in 2026 and start of construction around the end of 2028, a number of administrative processes need to be set up with the two host states and to be carried out during a preparatory phase. Therefore, work with the host state authorities has been launched in order to develop a workable schedule for the available time window. The results of this work so far show that an eight-year preparatory process is required, in cooperation with both host states and involving a diverse set of administrative processes with public engagement. A large portion of this schedule has to be completed before a decision for construction is taken. Only the activities concerning the preparation of the construction sites can be postponed until after a decision to build.

The preparatory phase schedule, which has been developed jointly by CERN, government representatives of France and Switzerland is shown in Figure 11.1. The plan represents a minimum-duration process, owned and steered by the project owner. This is an international consortium, represented by CERN, including its

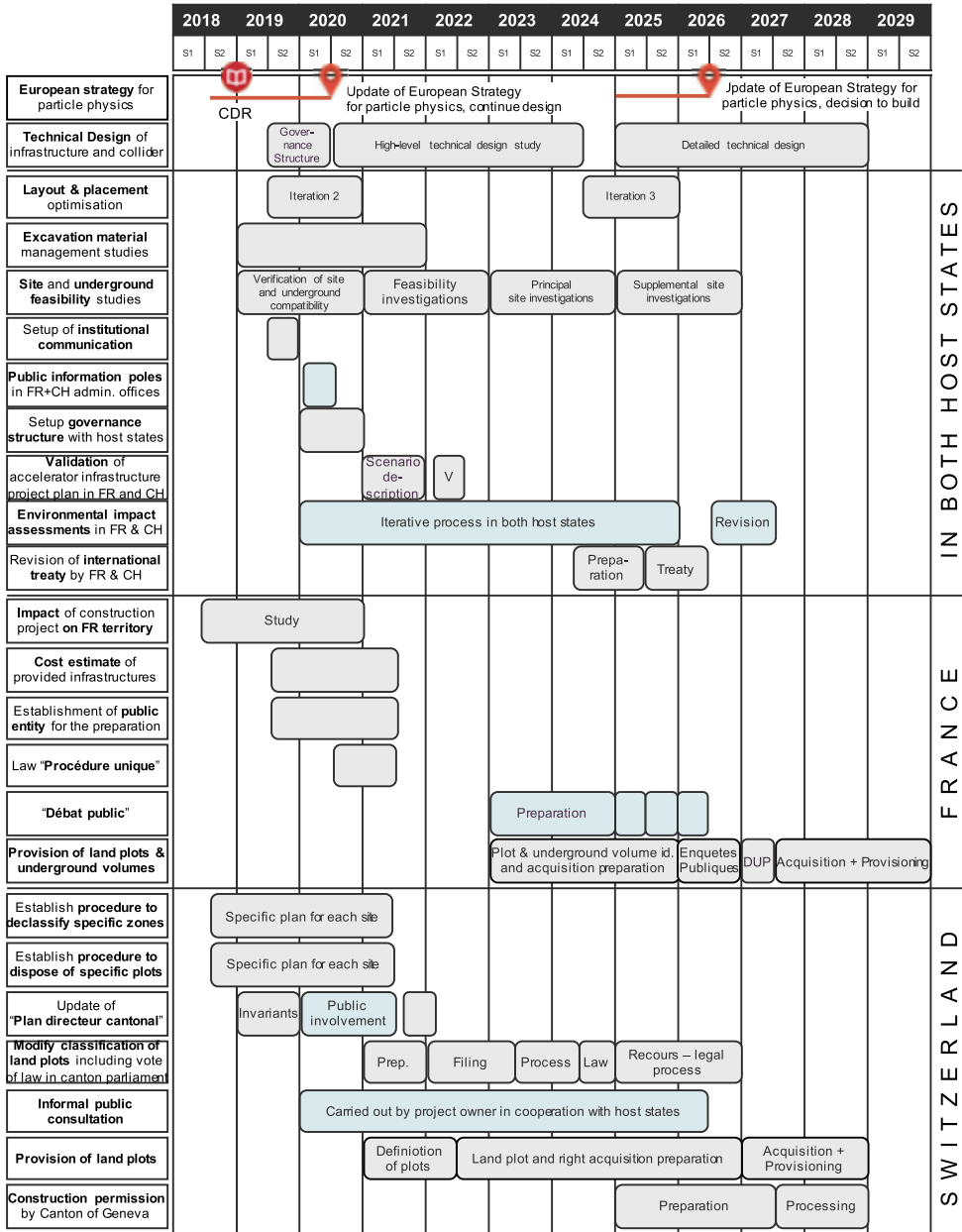


Fig. 11.1. Schema for the administrative processes required in both host states including those needed during a preparatory phase, before a decision to construct is taken.

member states and, potentially, additional project partners from non-member states. Additional time may be needed to accommodate further design iterations, in order to integrate feedback and additional requirements by authorities and to adapt to potentially evolving regulations in the host states.

The host state authorities recommend working with locally experienced contractors for tasks that relate to the development of an implementation scenario in the region, to benefit from their knowledge concerning territorial specificities and to set

up a working environment that permits putting workforce and contracts quickly in place and to be able to adjust to the evolving requirements in a timely manner. Both host states have demonstrated their will to accompany CERN throughout the preparatory phase in order to ensure a coherent development of the project, thus increasing the likelihood of success when a decision to move forward with construction is taken by the research community. Although the legal frameworks and government structures in the two host states differ and different types of actors need to be involved on each side of the border, the goals and scope of the individual processes are similar. Some specific elements have to be planned and carried out in an international framework, e.g. the environmental impact assessments according to the Espoo “Convention on Environmental Impact Assessment in a Transboundary Context” [539] and the establishment of an international agreement between France and Switzerland for the purpose of preparing, implementing and operating an extension of CERN’s current particle accelerator infrastructure on the two territories.

11.1.2 France

The Auvergne-Rhône-Alpes regional government is headed by a *prefect* who is supported by an office (Secrétariat Général de la Région Auvergne-Rhône-Alpes, SGAR) located in Lyon. Within this administration, the prefect is the representative of the French Republic. The SGAR and the prefect’s office work together on all development activities in the area. In 2016 the SGAR launched an analysis so that the prefect, and in turn the French national administration, could be informed about a significant extension of CERN’s infrastructure and to estimate the associated administrative and financial impacts for France. This activity led to the establishment of a series of regular meetings with CERN for the development of the preparatory phase. France promotes a “participative democracy” [549–551], calling for a process to find a consensus through open discussions amongst all stakeholders in the project from the conceptual stage onwards. The process starts with the development of the basic concept, a feasibility study concerning the infrastructural challenges, a proposal for the governance and funding and a socio-economic cost-benefit analysis. The infrastructural changes concern a wide range of topics: the use of excavation material, a concept for managing conventional waste during all project phases, an energy management plan that can be integrated with the territorial energy balance plan, plans for the consumption of resources such as water, proposals for synergies with the host state to contribute to the territorial development, the development of traffic and mobility concepts and further topics. CEREMA⁶, a public entity associated with the ministry of ecological transition and solidarity and the ministry of territorial cohesion, has produced a report for the SGAR and the prefect on the impact of an FCC for the host state concerning administrative processes and the associated financial engagements [552].

Initially, a specific project scenario needs to be produced since government offices cannot work on concrete preparatory tasks based on generic processes, but need to base their actions on so called *project invariants* that need to be considered in the update of regional development plans. This scenario description will cover a wide range of subjects including for instance, the purpose of the research facility, an initial proposal for the placement of the underground and surface sites, known technical infrastructure requirements including the resources and services (e.g. electricity, water, communication, transport, emergency and security services), the high-level construction and operation project plans, a catalogue of initial risks and benefits,

⁶ <http://www.cerema.fr>.

a list of known uncertainties, a construction and operation cost estimate, a cost-benefit analysis, a first realisation plan, a governance and management structure and a preliminary analysis of the administrative impact on the host states. Once the scenario is validated by the office of the President of the Republic, which is where the regional and national stakeholders come together, the preparation of the legally required process for the public to participate in the project (“débat public”) [553] can begin. The goal of this process is to develop an acceptance and appreciation of the project amongst the population, which forms the basis for a governmental clearance for the project owner to continue with the preparation. A commission defines which topics are relevant for the population and where there can be reasonable involvement in this process. The formal procedure lasts six months, but it requires about two years of preparation and is concluded with a one-year phase for its implementation.

After this internal preparatory phase, the project owner in close cooperation with the public debate commission, prepares information material (documents, databases, Web contents, booklets, videos, travelling information stands, town meetings), organises the nation-wide process, employs consultants and companies experienced with this process, sets up the required technical infrastructure and finally, defines a schedule that will allow all relevant public representatives to be involved. This takes about one year. According to the law revised in 2017 [554], the three-year period also involves the publication of summaries of the environmental impact assessment. At the end of the formal “débat public” phase, a follow-up consultation process, which continues until the end of the construction phase, must be put in place. Its findings need to be integrated in an iteration of the technical design and the project documents.

Once the national committee of the public enquiry (CNDP) [553] agrees that the documentation is mature, the formal open discussion can be launched. This milestone is associated with a certain risk. If the process is insufficiently mature, an extension of the preparatory period will be required. During this consultation phase, the plan for the project is presented and discussed with representatives of the population at local, regional and national levels during formal, recorded and audited sessions [555]. The project owner is asked to collect all questions and provide answers in a secure and auditable way. The findings lead to another iteration of the required project documentation (e.g. environmental impact assessment, plan for the management of excavation material and waste, energy management plan, traffic and mobility concept, land and rights-of-way acquisition plan, final land plot valuation). After the successful completion of this phase, the acquisition of rights-of-way of underground volumes and surface plots can start.

A public enquiry (“Enquête publique”) concludes the process by confirming the agreed infrastructure design which emerged from the public debate phase. If the tribunal has no objections, the French government will issue the approval of the infrastructure project’s utility for the nation (“Déclaration d’utilité publique”) [556] and the project owner can proceed with the preparation of a construction project. The acquisition of the rights-of-way and land plots can take place concurrently with the civil engineering calls for tender.

The entire process relies on the parliamentary submission and acceptance of a law that needs to be prepared for defining a *unique process for the environmental authorisation* [557] of a new research infrastructure project. Such a law includes a list of national laws and regulations that apply to the specific project, adjustments of existing laws, indications of which laws do not apply and specific regulations concerning particularly relevant topics such as the management of excavation material. This instrument, which appeared in 2016, specifically targets the timely preparation of large-scale projects of public interest such as the Grand-Paris [558] project.

11.1.3 Switzerland

Switzerland is a republic, federating significantly autonomous “Cantons”; this system of semi-direct democracy which has been in place since 1848, is unique. The country has a long standing tradition of involving the population at all levels (municipal, cantonal and federal) and at all phases of infrastructure projects. The procedures differ substantially in the different Cantons. Therefore, a workable process has been developed with the assistance of the Canton and State of Geneva, the Swiss permanent mission for international organisations in Geneva, the representatives of the Swiss Confederation and a consultant for public construction project administrative procedures.

Although CERN’s primary communication partner for administrative matters in Switzerland is the permanent mission and the ministry of foreign affairs (DFAE), the common work so far revealed that for the preparatory phase of a large scale particle collider project located in the Canton of Geneva the majority of processes will be carried out together with the State Office of Geneva. The federal government will be involved in the entire process with respect to the approval of applicable federal laws, regulations and financial contributions. In 2017, the “Structure de Concertation Permanente” (SCP) was established for this purpose. It includes Swiss government representatives at federal and cantonal levels, experts from different administrative domains on an “as-needed” basis and representatives of CERN for various development areas, including future projects.

The schedule, which has been developed in the frame of the SCP takes note of the status of CERN as an international organisation developing research instruments on a global scale, which are technically and organisationally unique. Several years before initiating the cantonal formal processes to obtain permission to construct, the acquisition of rights of way on land plots and the declassification of those agricultural zones needed for construction have to be launched and successfully completed. The authorities assume that CERN also carries out a set of informal processes which include a public consultation process, which is similar to the French “débat public”, with a preparatory period to create public information booths, information materials and events, public hearings, the establishment of an office to collect questions and to develop responses. In addition, the engagement of a diverse set of stakeholder groups at municipal, cantonal and federal levels is required, with an initial institutional communication strategy and plan which will be developed in close cooperation with the cantonal and federal authorities.

In order to be able to meet the envisaged overall schedule, which aims to start construction towards the end of 2028, two major preparatory actions have been identified by the representatives of the Swiss Federation and the Canton of Geneva that need to be initiated as soon as possible: a working group needs to develop a procedure in cooperation with the representatives of the Swiss Federation and the Canton of Geneva that permits CERN to request the Canton of Geneva to process the re-classification of agriculturally reserved, green-belt zones, called “Surface d’assolement” (SDA) [559,560]. The working group needs to tackle the process based on concrete, yet preliminary and non-binding assumptions of surface sites in order to develop concrete plans for the de-classification process, which will include mitigation and compensation measures. This process goes along with the development of a re-classification plan for a concrete set of potential plots of land that need to be acquired or rented long-term, for the construction project at a later stage. At the same time, another working group needs to develop the procedures to obtain the rights of way or the acquisition of those specific plots of land on behalf of CERN. The procedures are expected to differ for the different specific plots and involve the development of negotiation and acquisition strategies and the drawing up of plans to

provide the sites to the international organisation. Some areas may be provided only for limited periods of time, for instance during the construction and commissioning periods. Expropriation of land in the interest of the public is generally avoided in Switzerland and therefore negotiation with the owners of potential surface sites must be started early in the preparatory phase, to allow sufficient time to adjust the placement if needed. This work goes along with an evaluation of the market value of the land plots, notification of the cantonal authorities of the intent to use the plots for an infrastructure project and pre-agreements with land owners for obtaining the rights of way. These processes have to be managed by CERN or a mandated project consultant and rely on the active participation of a number of federal and cantonal offices.

Although an environmental impact assessment is formally only required for the creation of parking spaces for more than 500 cars and for the processing of excavation materials of more than 10 000 t per year on a site [536], it is seen as good practice and in agreement with the Espoo Convention that the project owner pro-actively carries out this process. A specific framework needs to be developed to be able to perform one single integrated environmental impact assessment of the project across the two host states with the possibility to provide information in a way that is accepted by the relevant administration offices in the two nations.

Referenda and federal approval processes may be applicable. They need to be identified during the preparatory phase as soon as specific topics are identified by the authorities that may require public approval. In such cases, dates need to be agreed with the federal and cantonal authorities to limit public initiatives to a certain period so that appropriate reaction to enquiries from citizens and interest groups can be made without jeopardizing the overall project schedule.

In order to get started with a number of different federal and cantonal offices efficiently, CERN is asked to initially put emphasis on the establishment of an institutional communication plan and its implementation. This will inform all officials who have to support the work of CERN about the project scope, goals, scale and schedule. Regular informal meetings with the regional population, their representatives and various interest groups are welcomed from the initial design phase, since transparency is considered the most efficient aspect of activities for the preparation of a potential project.

Authorisation for construction can be requested after successful completion of the necessary steps and before a decision to build takes place. The French authorities ask for a Cost-Benefit-Analysis (CBA). The Swiss authorities encourage the idea of aiming at creating added value from training, tourist development, creation of a technology pole and synergies concerning transport and energy recovery in the Geneva region.

11.2 Socio-economic opportunities

11.2.1 Introduction and motivation

Cost-Benefit-Analysis (CBA) [561] for conventional infrastructures such as roads, power plants, energy distribution networks and public transport systems is a useful tool to identify, quantify and communicate the potential value, in addition to the gain of scientific knowledge, that a new research facility can bring to society.

A preliminary, quantitative study of the LHC/HL-LHC project using this method has been carried out [435]. This work serves as a foundation for a dedicated Cost-Benefit-Analysis of one particular future collider scenario that needs to be carried out at an early stage of the preparatory phase. The study has been performed by three

independent organisations: University of Milan, University Roma Tre and the Centre for Industrial Studies (CSIL), Italy. The result reveals that the estimated Net Present Value (NPV) for the entire, combined LHC/HL-LHC programme over a period of 45 years (from 1993 to 2038) is positive, taking into account an annual social discounting rate of 3%. The likelihood of generating benefits of up to 5 billion CHF over the life of the programme is 80% [435]. This shows that a research facility like the FCC can generate added value for both industry and society. Despite the significant investment for constructing a new particle-collider infrastructure (CAPEX), the overall costs are dominated by operational expenditure (OPEX).

CBA has become a requirement for the preparatory phase of research facilities. The upcoming ESFRI roadmap includes a specific request [562] for it and the EC staff working document on sustainability of research facilities asks for it. In 2018 an EC supported H2020 project, RI Impact Pathways [563], was launched with CERN's participation to develop guidelines that help homogenising benefit and impact assessment for research facilities in the European Research Era (ERA). Here, the results from the study on the combined LHC/HL-LHC programme are presented. The results of the investigations so far triggered a set of complementary surveys and studies by the university of Milan in cooperation with CSIL in order to establish a set of solid input parameters and assumptions for a CBA of a post-LHC particle collider scenario.

So far, the studies of the LHC/HL-LHC programme revealed six economically relevant benefits: (1) the value of scientific publications, (2) technological spillover, (3) training and education, (4) cultural effects, (5) services for industries and consumers and (6) the value of knowledge as a public good. There are two direct socio-economic benefits that stem from the dissemination of scientific information [564–566] (publications, reports, conference presentations): first, the direct value of scientific products is conservatively estimated to be equivalent to their production costs [567,568]. Second, the value of publications produced by an additional tier of scientists which cite the scientific products directly emerging from the research infrastructure is equivalent to the cost of their production. For the LHC/HL-LHC project, this added value is around 2% of the total benefits [565]. This report focusses on the findings concerning training, impact on industry and cultural effects in the following sections.

11.2.2 The value of training

The value of education and training is the single largest socio-economic benefit of a large-scale, hi-tech research facility. The impact is high, if the project is carried out in an open, international environment with strong cooperation between educational institutes, research centres and industrial partners (the “knowledge triangle”) [569]. A conservative estimate of the net present value added to the lifetime salary of early stage researchers (master's degree, doctoral degree and post-doctoral researcher) after leaving the LHC/HL-LHC project has been estimated. The lifetime salary premium for people who perform research and development in the scope of the LHC/HL-LHC project at CERN ranges between 5% and 13% in excess of the salary premium of the acquired academic degree. This translates into an absolute lifetime salary premium of about 90 000 euro to 230 000 euro per person with an average added value of ca. 160 000 euro for a doctorate degree obtained during a research period at CERN (2018 currency value) [570,571]. Based on CERN's current training programme capacity, during a 15 year construction phase and an initial operational phase of 20 years, 40 000 individuals would generate more than 6 billion euros for the economies of the participating nations. The training value potential depends significantly on the possibility to acquire intersectoral and transferable skills [572]

and the number of supervisors that are available to ensure the quality of the training provided.

These results triggered a process with the two host states [573] to find how the value of training can be further increased. Proposals include extending the training to non-academic teaching levels (apprentices, technical schools), continuous professional training (partnerships with companies in the frame of maintenance and upgrades as well as the increasing exploitation of under-used equipment), partnerships with public services (healthcare providers, public security and emergency services) and the continued enlargement of the training opportunities for non-technical domains (e.g. management, finance, economy, law, business administration). Also, joint academic education through partnerships with universities and industry should be further strengthened. The EASITrain H2020 Marie Skłodowska Curie Action Innovative Training Network project [574], launched by 11 institutes collaborating in the FCC study and 13 industry partners is a first step in this direction. It includes as goal the development of a European joint doctorate in applied superconductivity.

11.2.3 Opportunities for industries and technological spillover

The industrial activities that emerge from physics research projects are important for the European economy [575]. The “utility factor” is a key figure on which all estimates of industrial impacts are based. It indicates that every Swiss franc spent on co-development and customisation projects with industrial partners generates, on average, three Swiss francs worth of follow-up sales revenues for the industrial partner [576]. The LHC/HL-LHC CBA study provides quantitative evidence that companies participating in the project and exhibiting medium to high levels of innovation also benefit from a measurable increase of their earnings before interest and taxes (EBITDA) [577,578]. The relevance of this effect has been tested using the accounting figures of 669 companies involved in CERN procurements worth more than 10 000 CHF and a control group [579]. The majority of companies report that the main benefit stems from the learning experience in such a project.

The LHC/HL-LHC CBA also reveals that there is added economic value due to improved products, services and operation models including information and communication technologies (ICT) of ~ 10 billion CHF: more than 40% of the total cost (capital and operation expenditures). Further intensification of industrial involvement in core R&D activities in the framework of a well-planned industrialisation strategy can increase this share, so that a payback of 50% of the total costs can become realistic. The most prominent example for such research-induced industrialisation is the development of Nb-Ti superconducting wires for the Tevatron collider which triggered the mass production of medical magnetic resonance imaging (MRI) devices [580]. Another noteworthy example is the development of large-scale cryogenic refrigeration plants – the architecture and machinery developed for helium liquefaction for use in particle accelerators has been the industry standard for almost 40 years [581].

For a future particle collider, the benefits emerging from procurement and co-innovation depend on (a) the investment volume, (b) the potential for innovation related to the individual subsystems and (c) on the value of the utility factor. It is not yet possible to reliably quantify the overall impact for industry. A dedicated study for a specific accelerator scenario needs to be carried out, once the detailed technical design starts. Technologies that lead to innovation on a broader scale (see Fig. 11.2) for the different particle collider scenarios include superconducting radiofrequency systems for a lepton collider (estimated benefit for industries about 150 MCHF), superconducting wires for a hadron collider (estimated benefit for industries around

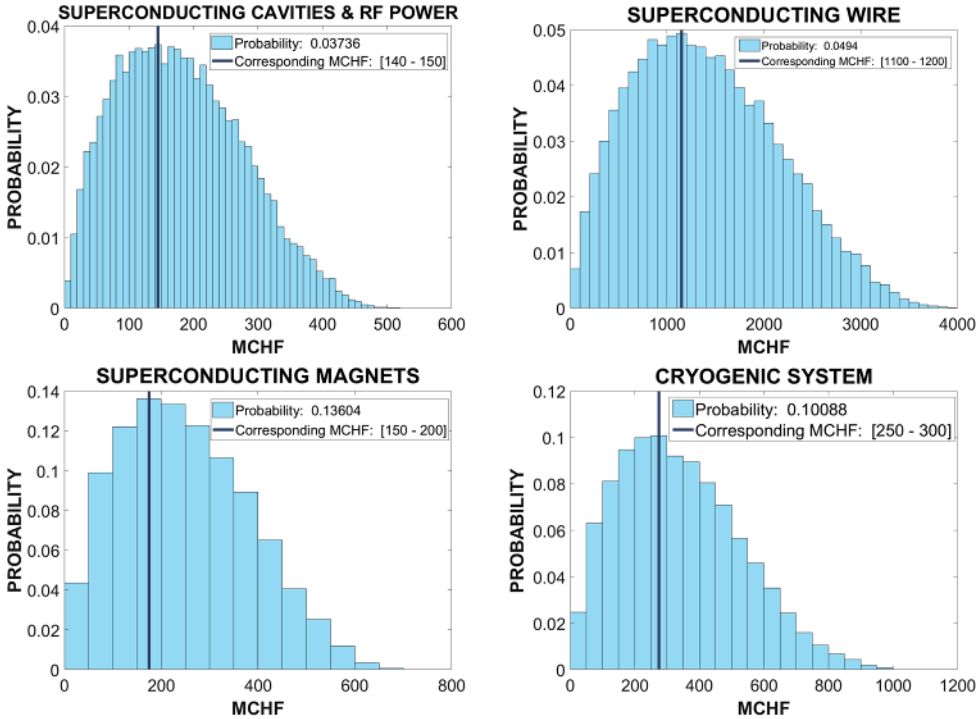


Fig. 11.2. Initial estimates for industrial spillovers of individual technology projects carried out as co-developments with industrial partners for different particle collider scenarios (selected FCC-ee and FCC-hh related technologies). The left upper figure indicates the industrial impact potentials stemming from the construction of superconducting RF and associated powering systems, the right upper figure highlights the potentials that superconducting wire manufacturing can create. The lower left image depicts the potentials stemming from the superconducting magnet project and the lower right image highlights the potentials that a new cryogenic refrigeration system can generate. The x-axis indicates estimates for expected benefits and the y-axis denotes the probabilities of the expected benefits as resulting from 25000 Monte Carlo simulation rounds. The vertical line denotes the overall average expected benefit. Estimates include social discounting and are reported in 2018 currency values.

1200 MCHF depending on the revenue margin that the supplier is able to generate for non-research customers), construction and testing of superconducting magnets for a hadron collider (estimated benefit for industries from 150 to 200 MCHF, depending on the potentials of the different technologies along the magnet manufacturing value chain) and large-scale cryogenic refrigeration infrastructure for a hadron collider (estimated benefit for industries from 250 to 300 MCHF).

An earlier study [582] has shown that hi-tech companies can transfer the knowledge and experience acquired during work with CERN to new products and services easier than companies who offer off-the-shelf products and services. Therefore, it is crucial to make an effort to cooperate with industry on increasing the potentials for other fields, such as civil engineering. As Figure 11.3 shows, the potential industrial spillover for a 100 km civil engineering project with tunnel and caverns is quite different, if the project is carried out purely as contractor work or if co-innovation is introduced for advanced excavation material analysis, separation, processing and use.

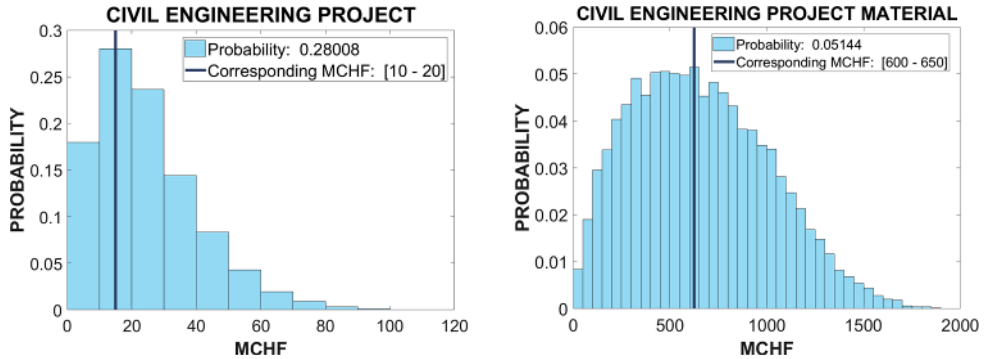


Fig. 11.3. Initial estimates for industrial spillover of the civil engineering project, which is common to both 100 km particle collider scenarios (FCC-ee and FCC-hh related technologies). The left analysis reports on the industrial spillover opportunities for a classic civil engineering project and the right analysis reports the spillover potentials if innovations such as the use of the excavation materials are introduced during the project phase. The x-axis indicates estimates for expected benefits and the y-axis denotes the probabilities of the expected benefits resulting from 25 000 Monte Carlo simulation rounds. The vertical line indicates the overall average expected benefit. Estimates include social discounting and are reported in 2018 currency values.

Treating the excavation material as a primary resource rather than waste that needs to be disposed of can lead to significant additional economic benefits of the order of several hundred million CHF⁷. Today, excavation material is still considered waste, but the necessity to revise CERN’s existing international agreement with France and Switzerland and the drafting of the law in France that is needed for the preparatory phase, renders this opportunity a realistic scenario. The Grand-Paris [583] and the Lyon-Turin railway projects [584] serve as pre-cursors of this approach.

The introduction of Information and Communication Technologies (ICT) [585] are also important levers. One topic is the development of open source software and open ICT specifications that can be used in other scientific domains or for business. The HTML and HTTP specifications that form the basis of the World Wide Web are prime examples [586]. However, since its value for society cannot be reliably quantified, this invention was not considered in the LHC/HL-LHC CBA study. Selected cases for which the impact is currently being estimated include: software tools used in other physics research (ROOT⁸), software used for medical imaging (GEANT4⁹), collaborative tools (Indico¹⁰), library software (INVENIO¹¹), scalable storage systems (EOS, cernbox [587]), scalable modelling and simulation tools needed to devise reliable and energy efficient industrial systems (ELMAS [588, 589]¹²), measurement and control systems (for instance add-on components and extensions for SIEMENS WinCC OA and National Instruments Labview).

⁷ 8.5 million tons of molasse at a value of ca. 35 CHF/t and 260 000 tons of limestone at ca. 85 CHF/t.

⁸ <https://root.cern.ch>.

⁹ <https://geant4.web.cern.ch/applications>.

¹⁰ <https://getindico.io>.

¹¹ <https://invenio-software.org>.

¹² <http://www.ramentor.com/products/elmas/>.

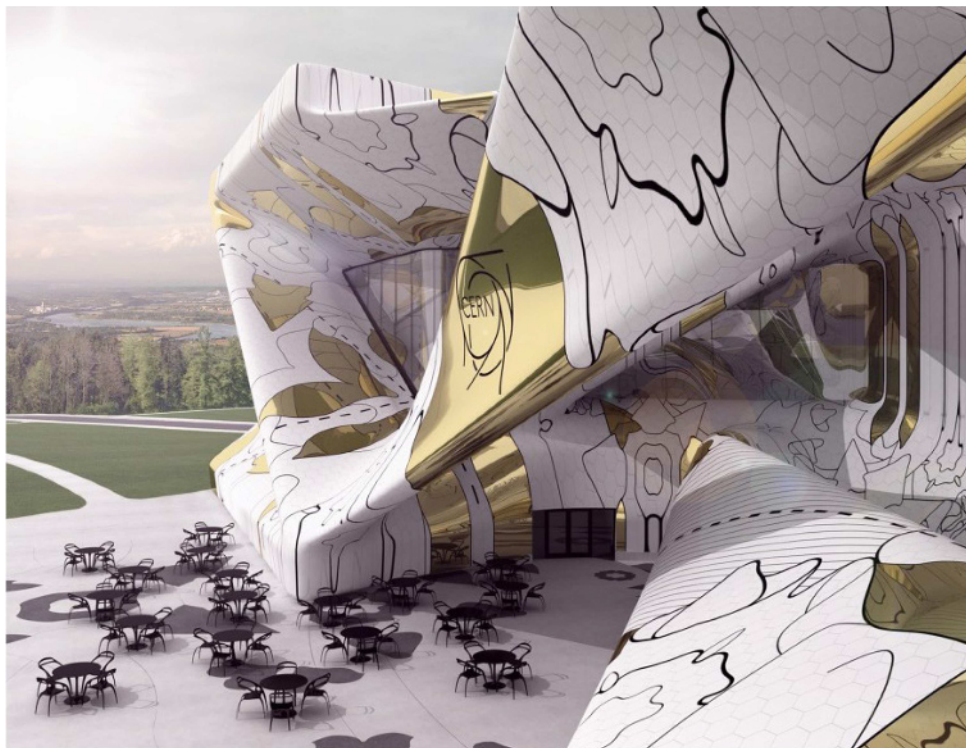


Fig. 11.4. One of many concepts for a visitor centre at a new surface site that FCC collaboration member institute, the University of Michigan, is probing in order to identify paths for working with novel materials, to conceive energy efficient and environmentally friendly buildings, which blend into the region and which can be implemented in cost effective ways.

11.2.4 Cultural effects

The creation of cultural activities generates economic value and helps to involve the public in research. With 130,000 visitors¹³ per year [565], CERN is Geneva's leading tourist attraction. The travel-cost method [590–592] estimates the value of this activity to be ~120 million CHF per year [593]. Designing future surface sites with this in mind and gradually transferring the responsibility for public involvement to a dedicated operation and marketing organisation leads to a sustainable concept, which can increase this figure. A preliminary investigation of such a concept by one of the FCC collaboration members led already to the award of a prestigious architecture prize [594] (see also Fig. 11.4). First estimates for the net benefits from 180 000 visitors (to a dedicated visitor centre at the main site) and 280 000 visitors (with an additional visitor centre on French territory) per year suggest additional annual societal benefits of 25–80 million CH [595]. This initial estimate includes annually assumed costs of 1 million CHF for the operation of these services. NASA's approach for a self-sustaining and independently operated visitor centre, which has been operating since 1967, is evidence for the success of this model [596].

Web and social media have become key communication platforms and their importance is expected to grow quickly with the introduction of new features and full coverage, high-speed mobile networks. The value of the contents directly produced by

¹³ See also at <https://visit.cern/tours/guided-tours-individuals>.

CERN and the LHC experiment collaborations, measured by the time people spend on average consuming the contents, is estimated to be in the order 120 million CHF per year [595], with videos being the largest contributor in the order of 90 million CHF per year. Channels combining different types of media have the highest impact (text interleaved with short videos, interactive info-graphics, apps, functions that encourage the reader to provide interactive feedback and to participate in collective tasks to shape opinion and to create new contents). The documented impact suggests that investing further in the provision of complementary, media-rich contents permits multiplying today's measured impacts many times. If technology evolutions such as augmented reality, tailored contents for different audiences, multi-language support and high-resolution virtual reality are adopted quickly, the research facility can significantly leverage the cultural effects.

In all cases, the research infrastructure operator should ensure that the content is made available by independent Web and social media content producers via well-working communication networks to achieve high technical quality and user satisfaction. Other powerful cultural products are computer programs ("apps") which engage their users in the research. Higgs Hunters [597] is a good example of such a citizen science project – it attracted 32 000 volunteers in a single year. The strong use of this technology by other research communities [598] motivates the development of further cases in the particle accelerator and high-energy physics domains. Computational physics applications as needed for the lepton collider FCC-ee and data analysis challenges as created by the hadron collider are ideal topics to create citizen science and public engagement programmes that also help disseminating the concepts of modern physics ("the Standard Model of Particle Physics"), which have so far not reached a wide audience.

Exhibitions such as *Extreme* [599] in Italy and *Begin* [600] in Austria, combined with interactive sessions and public events are an effective way to introduce the public to the research carried out in their countries in their own language. Their value, measured by the number of visitors and the time visitors dedicate, has been estimated to be in the order of 4.4 million CHF per year. The most successful item is the travelling LHC interactive tunnel, which alone creates about 1.1 million CHF of societal benefit per year, because it engages a large number of people for substantial amounts of time. When designed and created in cooperation with experienced museums and science exhibition centres in the member states and when accompanied by Web and social media contents that help to amplify the impact, the concept is a powerful vehicle to create a lasting awareness and promote the vision of a future particle collider facility.

The value of numerous books, TV shows, films and music produced by people not directly participating in the research programme undoubtedly has a further economic impact. It is a challenge to provide evidence for a causal relationship between a particular communication product and the research facility's activity. Therefore it is difficult to quantify the impact and the study is ongoing, focussing on video productions, TV and journal coverage and books.

CERN builds an image amongst the population of all member states through its communication activities. Because it exists and deals with questions that touch everybody, CERN has a value for everybody. This value has been estimated with "Willingness To Pay" (WTP) [561] surveys in CERN's member states specifically targeting the topic of a future particle collider. An initial LHC/HL-LHC CBA study suggested a total discounted value of 3.1 billion CHF for the total project period from 1993 to 2038. It is based on the assumption that the average annual voluntary contribution per year and person is 1.5 euro. For the LHC/HL-LHC programme this very conservative, lower-bound discounted estimate represents about $\sim 12\%$ of the total forecast impact [435]. However, a recent survey among French taxpayers [601],

Table 11.1. Opportunities to generate societal impact with a large-scale particle collider infrastructure.

Domain	Actions
Training	Common intersectorial education programmes with universities world-wide, extension of trainee programmes with industry, extension of adult training in the scope of development and service contracts, strengthening of the involvement of non-STEM domains in the training programmes. Reliable reporting of the research infrastructure induced salary premium will require periodic surveys via the CERN Alumni network, HR offices of collaborating universities and research centres as well as cooperation with national and international statistics institutes and selected industrial partners.
Industry	Technological competence leveraging projects to increase the probability of creating products and services from leading-edge technologies developed in the framework of the new particle accelerator, strengthening of the participation in the development of standards and specifications, develop technological spillovers for conventional project domains such as civil engineering, increase the focus on the development of information technologies, open specifications and open source software with use cases outside the particle accelerator and high-energy physics domain, closer work with national ministries of economy and industry interest groups to create denser networks with industrial partners.
Cultural goods	The channels with the highest impact potentials feature multi-media and on-line contents. It makes sense to further strengthen the presence in this domain, to complement it with media-rich contents (videos, interactive applications, augmented reality, citizen engagement). Creation and operation of high-quality and high-capacity visitor centres by an independent profit-making organisation that continuously involves the scientists, citizen science projects in collaboration with academic partners worldwide, promoting exhibitions developed by professional organisations in the member states, particular projects in other areas of the world (Africa, Asia, South America).

that has been performed to establish solid assumptions for a CBA of a post-LHC particle collider infrastructure, suggests a much higher WTP of around 4.7 CHF per taxpayer and year. In comparison, French taxpayers contribute to space research through funding of CNES with 35 euro per year [602]. A number of eligible contributors in CERN member states of the order of 350 million people, needs to be considered for future WTP estimates.

11.2.5 Impact potential

An initial set of recommendations to increase the impact of a post-LHC particle collider beyond the science community was developed in the frame of the CBA work carried out during the FCC study. It involved the University of Milano, the Centre for Industrial Studies and the University Roma Tre in Italy, a field study carried out by the company “iddest”, which specialises in public consultation processes [603] and finally the common working groups with French [573] and Swiss [604] host state representatives. Some impact pathways are outlined in Table 11.1.

All consultants for relations with the public recommended the creation of a *future collider ambassador programme*. A dedicated communication plan, regular

training and support material for target groups at different levels (institutional, local, regional, national, international) should make project members at all levels and from all sectors effective advocates of a future project. In the member states, this source of information will be the first and most effective communication channel to promote future research, to explain its benefits and challenges and to explain its purpose in simple terms. It is important that this programme also addresses common concerns. It should include a balanced set of ambassadors with different professional, cultural and personal backgrounds. The narratives should focus on what stimulates people's imagination like the origin of the universe, the nature of the matter which we are made of and where we come from.

12 Strategic research and development

12.1 Introduction

The information presented in this volume presents a feasible concept for a future circular collider. The level of detail corresponds to the conceptual development stage requirements as defined in the European Strategy for Research Infrastructures (ESFRI) methodology roadmap [605,606]. At this level, a number of concepts are presented that can be screened by experts in the domain, funding agencies and other stakeholders. It forms the basis for an implementation project of one of the scenarios and prepares the ground for developing a funding concept. The subsequent preparatory phase will focus on the development of the implementation plans, relying on credible designs that need to be based on a set of technologies that enable the research infrastructure to be built.

At this stage, any project of such scale, ambition and with a long-term vision spanning many decades, comprises a number of uncertainties with different probabilities and potential impact. [Appendix B](#) compiles the most relevant uncertainties for the specific collider scenario presented in this volume. Before a decision to build is taken, the most relevant technical uncertainties require investments in research and development to bring the technologies to readiness levels that permit the construction and subsequent operation with acceptable project risks. Therefore, the immediate next step, the design phase, will include the development of a technically achievable and coherent blueprint, which successfully responds to the requirements and concepts presented at this first stage.

The R&D topics presented in this section are considered “strategic”, since they represent those key elements, which are considered necessary prerequisites to come to a technical design that can actually be implemented within acceptable time and cost envelopes. The topics are not ranked in any way and many more research topics need to be addressed before arriving at a particle collider technical design, which can meet the physics goals and which can be operated in a sustainable fashion throughout the planned operational period. However, additional topics which are not considered decisive in terms of technical feasibility or operational sustainability are not presented in this volume. This allows the scenario to be screened whilst remaining focused on the physics opportunities, the long-term importance for the worldwide particle and high energy physics community and on the most essential technical feasibility questions. It is assumed that also the existing diverse and vibrant set of R&D activities in the field of particle accelerator technology will continue and will lead to a converging programme for a future particle collider, nourished by cross-fertilisation of different particle acceleration technologies, design studies and the continuous optimisation of facilities in operation. Some of the enabling technologies are equally important for all three particle collider scenarios (FCC-hh, FCC-ee and HE-LHC). The following subsections present R&D plans for the following topics:

- Efficient radiofrequency power sources and high-power solid state amplifiers;
- A15 materials and coating for high-efficiency radiofrequency cavities and manufacturing processes;
- Decentralised, high-capacity energy storage and network topology;
- Efficient and cost-effective DC power distribution;
- Efficient treatment and use of excavation material.

12.2 High efficiency radiofrequency power sources

Motivation

Energy efficiency and controlled electrical energy consumption are key factors for the sustainable operation of both the lepton and hadron colliders. In particular the electron-positron collider, which requires 100 MW of RF power, is limited by the efficiency of the power sources that convert the electrical energy into radiofrequency energy.

Objectives

The goal is to raise the current power conversion efficiency from 65% to above 80%. For this purpose, the findings of initial investigations of the High Efficiency International Klystron Activity (HEIKA) need to be developed to a significantly higher level. The initiative is based on the development of new bunching technologies for klystrons and the objective is to design and build a demonstration device, almost at commercial product level, which can subsequently be adopted by industrial partners.

Description of the work

The work includes the following steps:

1. Simulate the designs of the radiofrequency section of the klystron.
2. Develop an optimised design, based on the simulation results.
3. Investigate the impact of the solenoidal magnetic field and the klystron gun.
4. Produce a detailed mechanical design of the klystron.
5. Construct and test the concept using a demonstration klystron.
6. Validate the approach under realistic conditions in the LHC.

All activities also require the development of tools, ancillary equipment, the development and construction of the necessary test environments and the possibility to eventually integrate the device in the LHC collider.

Cooperation with universities and research institutes

In 2014, a consortium of academic and industrial partners was formed to set the foundation for a high-efficiency klystron R&D initiative. The group includes SLAC (USA), the European Spallation Source (Sweden), CEA (France), IPN Orsay (France), Lancaster University (UK) and MUFA (Russia). The academic contributions focus on simulations, designs, testing and feedback of the results into the design as well as on the construction and operation of the demonstration test bench.

Cooperation with industrial partners

The commitment of industrial partners in this R&D activity is strong, ranging from Thales (France), Toshiba (Japan), L3 (USA) and ScandiNova (Sweden) to VRDB (Russia). Industrial participation is expected in all aspects related to the design, construction, testing and product development of a novel klystron.

Impact potential

The practical implications of an innovative, high-efficiency klystron are significant for research infrastructures and industrial applications beyond the FCC. Frontier science instruments such as spallation sources and free electron lasers would profit as much as industrial and medical particle accelerators. All installations deploying klystrons ranging from 400 MHz to 12 GHz would directly benefit from such a device. In industry, wherever high-power microwaves are needed, such a device is applicable. Examples include, but are not limited to radar, pulsed-power forming, industrial heating and drying, welding, high-power laser applications, food processing with pulsed electrical fields, flue gas treatment, oil recovery, isotope production, broadcasting, satellite communications and, of course, high-power medical accelerators.

Milestones and deliverables

The milestones and deliverables are presented in Table 12.1.

Table 12.1. Milestones and deliverables for high efficiency RF power sources.

Title and description	Year
Simulation of the klystron RF section completed	2019
Solenoidal magnetic field aspects studied	2019
Klystron gun design revised	2020
Klystron design developed	2020
Mechanical device design developed	2021
Demonstrator built	2022
Test bench operational	2022
Klystron validated in LHC	2023

12.3 High efficiency superconducting radiofrequency cavities

Motivation

Energy efficiency and controlled electrical energy consumption are key factors for the sustainable operation of both the lepton and hadron colliders. In particular, the electron-positron collider requires a significant number of superconducting radiofrequency (SRF) cavities with high acceleration gradients. For the past five decades, bulk niobium has been the material of choice for SRF cavities. In recent years, RF cavity performance has approached the theoretical limit for this superconductor and the large scale production cost is another limiting factor. Therefore, the recently renewed R&D efforts need to be reinforced to deliver an alternative. The primary driver of this R&D initiative is to find a competitive alternative to bulk niobium that can deliver high acceleration gradients, a high quality factor up to high acceleration gradients and at low cost.

Objectives

Nb thin-film on Cu substrate and Nb₃Sn alloy have the potential to outperform bulk Nb technology and the objective is to develop these for cavity production. For this purpose, accelerator-quality 400 MHz and 800 MHz cavities, based on superconducting thin-films on copper have to be designed, built and optimised under realistic operating conditions. The main operating target is to significantly lower the cryogenics power consumption at RF fields comparable to those used in the LHC and to achieve break-even performances with respect to 800 MHz with bulk Nb technology.

Description of the work

The main target of research is to find a way to mitigate the Q-slope of superconducting thin films up to 10–15 MV/m and then to develop a method to produce thin-film coated cavities that have a performance/cost ratio that outperforms bulk Nb technology.

This work covers several domains including materials research, cavity design and manufacturing technologies. The baseline is to determine the RF performance limits at moderate to high fields at frequencies in the 400–800 MHz range for classical and novel superconducting materials. This involves an in-depth study of the underlying Bardeen-Cooper-Schrieffer theory for those materials and extrinsic sources of RF losses (e.g. surface preparation, thermal treatments, flux expulsion, thermal currents). The investigation will lead to a systematic determination of those material parameters which have an impact on the surface resistance (e.g. microstructure, chemistry, I, λ , ξ , HC1) and the establishment of models of how they relate to RF performance.

Eventually, technologies based on the verified models need to be demonstrated at an industrial scale for the production of the copper cavities and the application of the thin films such that the target cost/performance ratio can be achieved.

Cooperation with universities and research institutes

During the FCC study phase, an academic consortium started the investigation of superconducting thin-film technology with the aim of developing a viable cost-effective alternative to bulk Nb RF cavities. The EASITrain H2020 project, which runs until autumn 2021 federates Helmholtz Zentrum Berline (Germany), Universität Siegen (Germany), INFN Legnaro National Laboratory (LNL, Italy) and Technische Universität Wien (Austria) for superconducting thin-film production and specification. The University of Geneva (Switzerland) is also a partner in this type of investigation. For the study of advanced copper-based cavities, INFN LNL, Jefferson Laboratory (JLAB, USA) and Science & Technology Facilities Council governed institutes (STFC, UK) are cooperating with CERN. I-CUBE Research (France) is in cooperation with the sister-company BMax and CERN pursuing in depth studies of a novel approach to validate a high-speed forming process for the production of RF cavities. The active H2020 project and the established research collaboration with the above-mentioned partners forms the core of a multi-year programme to develop a new, cost-effective particle acceleration technology.

Cooperation with industrial partners

The participation of industry is key in developing a technology that can eventually be supplied at a competitive price on an industrial scale. Company BMax (France),

which is working on high-speed forming, CemeCon (Germany) and Research Instruments (Germany) are already active partners in the EASITrain H2020 project. The R&D activity will attract further industrial partners for the development of a high-tech coating process that has potential application areas stretching far beyond SRF. In particular, a scenario to use ultra-high quality factor RF cavities and superconducting thin-film circuits for qubit control and readout can be an enabling technology for quantum computers is an impact potential which raises strong interest in the international engineering research and information technology sectors.

Impact potential

A validated alternative to bulk Nb-based superconducting RF cavities would help to promote high-performance particle accelerators faster and in more countries. In addition to fundamental physics research, particle accelerators for applied sciences and industrial purposes rely on this technology. Free-electron lasers like the recently commissioned European XFEL at DESY are a good example for such machines. This research project can make a lasting impact in industry for each domain where expensive materials and engineered surfaces are required.

Milestones and deliverables

The milestones and deliverables are presented in Table 12.2.

Table 12.2. Milestones and deliverables for high efficiency RF cavities.

Title and description	Year
Evaluation of Nb-on-Cu samples (QPR tests)	2019
Evaluation of A15-on-Cu samples (QRP tests)	2020
Evaluation of 1.3 GHz Nb-on-Cu cavities produced using seamless substrates	2020
RF tests of A15 on-Cu cavities performed	2021
Demonstration of 1.3 GHz Nb-on-Cu cavities with new coating methods that preserve performance and quality	2022
RF tests of 800 MHz Nb-on-Cu cavity performed	2023
Demonstration of 400 MHz Nb-on-Cu cavities with new coating methods that preserve performance and quality	2024
Process for superconducting thin-film coating documented	2025

12.4 Energy storage and release R&D

Motivation

The development of novel energy storage systems has seen impressive progress over recent years, mainly driven by the automotive sector and the increasing use of renewable energies. Batteries appear today to be the most promising solution to store the energy recovered from superconducting magnets at the end of a cycle, to support the powering of the accelerator during the subsequent ramp phase. This approach could significantly reduce the requirements for peak power and would keep the overall energy consumption and cost of the electrical infrastructure within the limits that have been established based on average power consumption estimates. Batteries are the focus of the R&D programme due to the continuing developments

towards ever higher energy storage densities. Today, the most suitable battery technology for this application includes lithium batteries, in particular lithium titanium oxide (LTO). On a longer time scale, other technologies will also be considered. The targeted R&D initiative would feature an ongoing assessment of technology options in cooperation with academic and industrial partners. For a machine that needs a significant amount of battery storage at high-capacities, considering environmental friendly production and recycling is one other important non-functional requirement that will need to be included in the R&D programme.

Objectives

This R&D initiative aims to develop a suitable battery-based energy storage and release system to recover the energy stored in superconducting magnets, to temporarily buffer the energy and to provide the energy to magnet power converters to support the accelerating phase of the cycle. Such a system would require batteries capable of at least 20 000 charge-discharge cycles suitable for the power profile of the magnet cycles. Due to the underground space limitations, energy density and volume reduction are additional requirements to be considered. The system must comply with the safety requirements for underground installation and operation. Maintenance, reliability and total-cost-of-ownership (TCO) need to be part of the investigation from the beginning.

Description of the work

The first stage of this programme consists of drawing up a battery-supported powering system concept for a particular particle collider. This scheme will be used to develop requirement specifications for a battery-supported energy storage and release system that can be used with a superconducting magnet/power converter circuit. An essential part of this work is the definition of the interface and the interplay between the battery storage system and the power converter, which is part of the magnet circuit. The second stage focuses on the technical design studies for the energy storage systems, including the co-development activities with industrial partners for all major system components. A third stage would focus on a demonstration of a battery-based energy storage system at an existing particle accelerator, such as the HL-LHC.

Collaboration with universities and research institutes

The cooperation with universities and research institutes focuses on the requirements finding process and on the development of a concept for energy recovery, buffering and release in the particle accelerator domain. The work on developing a concept for a future circular collider will also be carried out as a cooperative effort with universities and research centres. The construction of the HL-LHC upgrade, in particular an energy recovery system for the inner triplet magnets, opens an ideal opportunity and time window for this activity.

Collaboration with industrial partners

The cooperation with industrial partners focuses on the design, development, testing and co-innovation of major system components to build an energy recovery system

for a particle accelerator. The following equipment components would be candidates for such an activity: battery cells and modules that can meet the operation and deployment conditions and the reliability requirements, battery management and protection systems. Energy friendly production and recycling is another factor that is becoming ever more relevant. Finally, cooperation on assessing the total cost of ownership, that permits a cost-benefit analysis to be carried out, will be included in the work with industry.

Milestones and deliverables

The milestones and deliverables are presented in Table 12.3.

Table 12.3. Milestones and deliverables for an energy buffering and recovery project.

Title and description	Year
Definition of a demonstration case for an existing particle accelerator	2019
Documentation of requirements and constraints for an energy recovery system	2020
Creation of a consortium for the research project	2021
System concept specification and architecture definition	2022
Key component definition and start of research work with industry	2023
Development of test bed complete	2024
Testing of key components performed	2026
Demonstrator operational	2028

12.5 Efficient power distribution infrastructure

Motivation

Power quality is a primary concern for all three colliders studied (FCC-hh, FCC-ee and HE-LHC). Achieving adequate availability to ensure good use of the new infrastructure, to avoid costly downtimes and to achieve energy efficient operation by reducing the need for recovery and restore actions is closely linked to those parameters that determine power quality: transient voltage dip mitigation, reactive power control, harmonic filtering and voltage stability. Switching from an alternating current (AC) distribution network to a direct current (DC) power distribution in combination with local energy buffering addresses several of the key impact factors. Frequent transient power dips can be tolerated, active and reactive power can be compensated on the load side, AC harmonic filtering is not needed, distribution losses are significantly reduced and larger spacing between electrical infrastructures compared to AC distribution is permitted which leads to reduced infrastructure component investments.

Today, this technology is still in its infancy, mainly lacking adequate standardisation of operating parameters and the availability of a set of equipment from different vendors due to its lack of widespread adoption. Viable designs of electrical components for DC current and voltage switching, short-circuit current switching, fault detection and protection system selectivity remain to be developed and still represent technical challenges.

Objectives

The objective is to raise the readiness level of medium-voltage DC distribution network technology by demonstrating its merits at CERN in close cooperation with

an industry-driven demonstrator project. This case serves as a platform for a consortium of industry partners to develop standards for this grid technology and to trigger the development of market-ready equipment. Technical challenges that still remain to be addressed mainly concern electrical components for current and voltage switching and protection elements such as short-circuit current switching, the detection of faults and an appropriate approach to implement selective protection for the network (e.g. a fast fault-detection and protection communication system to separate only the faulty element, maintaining overall high system reliability). This project aims at facilitating the acceptance of the technology among potential end-users in the commodity market. Eventually, if this technology becomes wide-spread, it will be available to large-scale research infrastructure customers at the time when a future particle accelerator is to be installed.

Description of the work

The first phase to be carried out during a particle collider preparatory phase aims to establish a stable consortium of companies who are active in standardisation bodies and who actively study the market opportunities of commodity sectors, companies who have an interest in the development of key components and integrating them in a demonstrator at one of CERN's accelerators. Universities and research centres that develop solutions for the technical challenges and who have the necessary experience should also be part of this consortium. The first phase of the work consists in analysing a specific use case to provide power for one of CERN's accelerators, the capture of the requirements and a detailed technical gap analysis in cooperation with academic and industrial partners. In a second phase, consortium members draw up an architecture and propose a design for a demonstrator that includes the development of novel components to address the most critical technical challenges. In a third phase, prototypes of the technical components are developed by different contributors, fostering the co-development of academia and industry. Finally, a demonstrator setup is installed at CERN that can also serve as a showcase for industries to raise the acceptance of the technology at large scale. This work programme needs to be accompanied with the conceptual and technical design work of a DC network for a specific particle collider scenario.

Collaboration with universities and research institutes

MVDC distribution systems are an active area of academic research that spans various sectors including electrical engineering, electronics, information and computing technologies, reliability engineering, functional safety, economics and business analysis. Consequently, this is an ideal application to bring academic partners with complementary competencies from different geographical regions together at CERN in a concrete technological research project with tangible impact potential at academic levels, with high-educational value and with opportunities to work in a close-to-market environment. Specifically, EPFL (Lausanne, Switzerland), a technical university, has an active programme on the development of MVDC power distribution networks with support from the Swiss Federal Office of Energy (SFOE).

Collaboration with industrial partners

With the increasing availability of modern power electronics technologies such as switch-mode converters with higher power ratings, DC networks are being increasingly considered for high voltage transmission lines (HVDC). DC networks start

to be deployed for specific applications such as the supply of power for trains in underground metropolitan transport facilities.

In addition to point-to-point and residential collection grids, MVDC is an interesting solution for industrial applications due to its efficient operation, the small footprint and the low installation and operating costs. Companies like Hyundai, ABB, Siemens and Rolls-Royce are investigating the suitability of this technology for off-shore and maritime vessel applications as well as for heavy industries (e.g. aluminium manufacturing) and DC microgrids like those found in shopping centres, office blocks and in particular ever power hungry data centres, smart residential areas and also rural electrification. Since the technology is also ideal for integrating environmentally friendly power sources such as photovoltaic panels (PV) and to a lesser extent fuel cells, companies, that are active in the power generation market, are also starting to have an interest in this technology. The “EMerge Alliance” (www.emergealliance.org) built around this elusive technology is a mirror of who-is-who in the electrical industry. Also the world’s most important standardisation organisations IEEE and ISO are involved in the ongoing activities. Hence, this is an ideal opportunity for an international community with a vision for a large-scale research infrastructure to provide a test bed for academia and industry world-wide with the potential of large benefits for society and at the same time preparing the path for large-scale science infrastructures to be operated in a sustainable fashion.

Initially, the focus can be on designing and standardising components, such as DC current breakers, rectifiers, rectifier-transformer solutions and protection systems. The co-developments should leverage existing application development efforts, such as DC railway systems.

Milestones and deliverables

The milestones and deliverables are presented in Table 12.4.

Table 12.4. Milestones and deliverables for a MVDC demonstrator project.

Title and description	Year
Definition of demonstration case for an existing particle accelerator	2019
Creation of a consortium for a showcase project	2020
Definition of requirements and corresponding sub-projects complete	2021
Test bed design and key challenges documented	2022
Component prototyping complete	2024
Development of key components for test bed complete	2026
Testing of key components performed	2026
Design iteration of test bed complete	2027
Demonstrator operational	2028

12.6 Efficient use of excavation materials

Motivation

A 100 km long underground infrastructure for a circular collider will generate around 10 million m³ of excavation material. Both the French and Swiss host state authorities require a plan for the treatment and management of this material. The recent evolution of Europe’s society towards a circular economy calls for novel approaches, viewing the excavated material as a resource, rather than waste for which final

repository scenarios need to be developed. A consensus exists among leading civil engineering experts in France, Switzerland and Austria that the development of novel approaches for the processing of excavation material not only leads to an increased acceptance of new large-scale projects, but also has a potential significant beneficial economic impact which scales with the size of the endeavour.

Objectives

The objectives of the programme are threefold:

1. The legal frameworks in France and Switzerland have to be explored, since the majority of countries currently treat excavation material as waste, preventing further processing or supply of the material to third parties for commercial use. The first objective is therefore to identify the legal instruments that can be engaged to permit using excavation materials and to identify the administrative processes to obtain such permission.
2. A transnational plan for the processing and use of the excavation material needs to be developed.
3. An innovative processing technology, that can lead to an end-user product as an alternative to existing treatment and final storage, needs to be developed for the molasse material.

Description of the work

The project consists of the following steps:

- An in-depth study of the regulations and guidelines applicable in France and Switzerland will lead to an understanding of the current situation. It will, on one hand, permit the identification of those areas where the use of excavation materials is possible within the legal framework and, on the other hand, will provide input for the process of changing the legal framework either in the host states or at European level. Such efforts have already been initiated by leading organisations, which are also partners of CERN in these matters.
- Sampling and analysis of the material expected to be excavated during the tunnelling project. The civil engineering activities, which started in July 2018 in the frame of the HL-LHC project present an ideal opportunity to obtain a representative set of samples that covers many of the different molasse-type soils expected from the FCC tunnelling. Further analysis will require exploratory drillings down to about 300 m at selected sites. The analysis includes mineralogical, geotechnical, geophysical and petrophysical parameters and will lead to a first qualitative indication of uses for the materials.
- Development of a novel treatment and an innovative product for pre-processed molasse material that can form a case for the use of excavation material on a large scale.
- Development of a trans-national plan for the pre-processing, dispatching and use of the excavation material. The study needs to include the socio-economic optimisation including cost of pre-processing, logistics and transport, usability for industries, project risks and the development of scenarios for the deposition of non-usable materials.
- Development of input for the legal “procedure unique” for the project in France and the “plan sectoriel” in Switzerland which create the legal boundary conditions under which the use of the material can take place.

Cooperation with universities and research institutes

Academic institutes, which are active in the advancement of montanistic research, material sciences, novel construction materials and economic studies are highly motivated to collaborate in this R&D programme. In particular the European Union incentives to speed up the transformation towards a circular economy are encouraging the commitment of resources to this highly-attractive topic which has potential impacts beyond the research and accelerator community. The Montanuniversität Leoben (Austria), the Centre d'Etudes des Tunnels (France) and the Ecole Normale Supérieure de Lyon (France) are committed to form a core of the research activities mentioned. Further universities in Switzerland such as the University of Geneva, the Vienna University of Economy (Austria), the Politecnico Milano (Italy), who are already engaged in similar projects (e.g. Lyon-Turin) are potential additional partners. Eventually, detailed technical developments such as the fast identification of soil characteristics during the excavation process, permitting efficient material separation and pre-processing, are key topics for mechatronic and mechanical engineering schools and dedicated research institutes.

Cooperation with industrial partners

The development of advanced technologies and a new legal framework for use of excavation material creates a highly attractive case for industrial cooperation partnerships. Civil engineering companies such as Porr Group (Austria), Tunnelling machinery developers such as Herrenknecht (Germany) and material system analysis integrators such as Microtec (Italy) are interested in participating in such an activity.

Impact potential

The economic potential for this engineering domain are high. A new tunnel infrastructure designed and built in the frame of a scientific project by an international organisation features legal, contractual and organisational frameworks which differ from ordinary public infrastructure projects such as railway or road tunnels. This makes the project attractive for industrial partners as a showcase for advanced technologies and as a training environment for professionals in different fields for many years, far beyond the scope of the current project. Identifying if molasse material can be processed in such a way that it can be used for an innovative product would permit an entirely new market to be developed. In any case, the development of advanced mechanisms to pre-process and separate the material on-line during the excavation process will generate benefits beyond a pure margin-oriented business. The accompanying development of a legal framework in at least two European countries (France and Switzerland) is an ideal starting point for a Europe-wide development to make civil engineering enterprises more competitive through an alternative approach. European industry has been searching for a long time for such a demonstration project and is eagerly awaiting a tangible possibility to develop the administrative framework that permits tapping into this, so far, largely undervalued raw-material.

Milestones and deliverables

The milestones and deliverables are presented in Table [12.5](#).

Table 12.5. Milestones and deliverables concerning excavation materials.

Title and description	Year
Applicable legal and administrative frameworks documented	2018
Initial set of soil samples analysed	2019
Study of potential economic impact available	2020
First proposal for material processing available	2021
National plan for management of excavation material in France established	2021
Input for law of unique project procedure in France available	2021
National plan for management of excavation material in France established	2022
Soil samples from exploratory drilling analysed	2023
Excavation material processing demonstrated	2024
European guidelines for use of excavation material published	2024
Input for contractual documents for underground works available	2025
Excavation-material based product showcased	2026
Machinery for material pre-processing commercially available	2027

We would like to thank the **International Advisory Committee members**:

R. Assmann, DESY, Germany
C. Biscari, CELLS-ALBA, Spain

M. Diemoz, INFN, Italy
G. Dissertori (Chair), ETH Zürich,
Switzerland

V. Egorychev, ITEP, Russia
W. Fischer, BNL, USA
G. Herten, University Freiburg, Germany
P. Lebrun, JUAS, France
J. Minervini, MIT, USA

A. Mosnier, CEA, France
A. Parker, University of Cambridge,
UK

C. Quigg, Fermilab, USA
M. Ross, SLAC, USA

M. Seidel, PSI, Switzerland
V. Shiltsev, Fermilab, USA
T. Watson, ITER, IEIO
A. Yamamoto, KEK, Japan

and the **International Steering Committee members**:

S. Asai, University of Tokyo, Japan
F. Bordry, CERN, IEIO

P. Campana (ECFA & Chair from 2016), INFN,
Italy

P. Chomaz, CEA, France
E. Colby, DOE, USA
G. Dissertori, ETH Zürich, Switzerland

E. Elsen, CERN, IEIO
M. Krammer (Chair 2014-2016),
HEPHY/CERN, Vienna, Austria
A. Lankford, UCI, USA

S. Peggs, DOE/BNL, USA
L. Rivkin, PSI, Switzerland
J. Womersley, ESS, Sweden

for the continued and careful reviewing that helped to successfully complete this report.

The editors wish to thank all the scientific, engineering and technical personnel, the students and early stage researchers and all members of personnel involved in the investigations, designs and prototyping for their invaluable contributions that made this work possible.

We also want to express our thanks to the administration officers who prepared the ground and created a framework in which this work could be carried out efficiently. The FCC study management team thanks in particular John Poole for his enthusiastic dedication during the editing phase, contributing significantly to deliver a coherent, consistent and readable set of report volumes. Finally, we wish to thank the CERN management for their strong

support and encouragement.



The research, which led to this publication has received funding from the European Union's Horizon 2020 research and innovation programme under the grant numbers 654305 (EuroCirCol), 764879 (EASITrain), 730871 (ARIES), 777563 (RI-Paths) and from FP7 under grant number 312453 (EuCARD-2). The information herein only reflects the views of its authors. The European Commission is not responsible for any use that may be made of the information. **Trademark notice:** All trademarks appearing in this report are acknowledged as such.

Open Access This is an open access article distributed under the terms of the Creative Commons Attribution License (<http://creativecommons.org/licenses/by/4.0/>), which permits unrestricted use, distribution, and reproduction in any medium, provided the original work is properly cited.

Appendix A: Theoretical physics computations

Motivation

One of the highlights of the FCC-ee physics programme is a comprehensive campaign of measurements of Standard Model (SM) precision observables, spanning the Z pole, the WW threshold, the maximum of the Higgs boson production, the $t\bar{t}$ threshold, and above. Through this campaign, the FCC-ee will provide a set of ground-breaking measurements of a large number of new-physics sensitive observables, with improvement by one to two orders of magnitude in precision with respect to the present status. The FCC-ee will also improve the precision on input parameters, m_Z , m_{top} and $\alpha_S(m_Z^2)$. This particle collider offers the possibility to measure directly and for the first time $\alpha_{\text{QED}}(m_Z^2)$, which will considerably reduce the parametric uncertainties in the SM predictions.

The unprecedented experimental precision accessible for measurements of electroweak observables and the Higgs boson opens a window to shed light on new phenomena at higher energies or smaller couplings. It is therefore a powerful discovery tool.

The possibility to fully exploit the particle collider's capabilities depends, however, much on the capability to perform theoretical computations that provide precise and accurate predictions of Standard Model phenomena at levels where quantum field theory can be checked at the next order(s) of perturbation theory.

Today, predictions with the required precision and accuracy levels are unavailable.

Objectives

To be able to fully leverage the potentials of an intensity frontier lepton collider, a leap-jump in the precision and accuracy of theoretical computations that precisely and accurately predict Standard Model phenomena needs to be induced. This involves the development of new event generation techniques, in particular involving a campaign to advance the theoretical physics calculation methods as an input to conceive highly efficient software tools that are capable of performing the computations. Furthermore, tools need to be developed to compare the experimental

results and the theoretical predictions to a level of precision that is better than the anticipated experimental uncertainties. This activity will include a gap analysis to identify, which additional calculations and experimental inputs are required to be able to achieve the set physics goals with the particle collider. Such an activity is expected to strengthen the cooperation between theoretical and experimental physicists, leading to a more coherent world-wide community by developing common goals and a sense of shared responsibility. One output of that process is the common definition of observables and ratios between observables for which theoretical uncertainties are low.

Description of the work

The work on the development of novel methods and tools and a commonly agreed set of observables involves technical tasks that are combined with ingenious approaches to calculate multi-loop integrals for EW three-loop, mixed EQ/QCD and leading EW four-loop topologies. Additional effort will be dedicated to the following items:

1. Evaluation of higher-order QED and QCD corrections to cross sections and angular distributions, needed to convert experimentally measured cross sections back to “pseudo”-observables: couplings, masses, partial widths, asymmetries, etc. This activity remains closely linked to the experimental measurements so that the relation between measurements and the forecast quantities does not lead to a change of the possible physics programme. For this, the development of novel event generators is essential;
2. Calculations of the pseudo-observables of the Standard Model with a precision and accuracy required to be able to take full advantage of the experimental precision delivered by the particle collider;
3. Identification of limiting factors, in particular those related to the definition of parameters (e.g. the treatment of quark masses, and more generally of QCD objects);
4. Investigation of the sensitivity of the proposed and new experimental observables to new physics for the relevant scenarios. This essential work needs to be carried out at a very early project phase, because it can affect both the detector design and the operation plan for the collider.

Collaboration with universities and research institutes

This work, which will be the result of a world-wide collaborative effort of theoretical and experimental physicists and contributors from related relevant disciplines, is best carried out in the framework of an academic environment. An initial workshop “*Precision EW and QCD calculations for the FCC studies: methods and tools*” was held at CERN in January 2018 to start a process to prepare this kind of long-term research. The conclusions were documented: “We anticipate that at the beginning of the FCC-ee campaign of precision measurements, the theory will be precise enough not to limit their physics interpretation. This statement is however, conditional on having sufficiently strong support by the physics community and the funding agencies, including strong training programmes”. An initial estimate of the effort required points to about 500 person years, corresponding to about 25 full-time-equivalent experts throughout the design, construction and operation phases of the FCC-ee programme.

Appendix B: Uncertainties

This chapter summarises those uncertainties, which have the highest potential of leading to adverse impacts on the project. They are grouped by technological and implementation-related elements, depending on their origin. The preliminary information provided in this volume is a non-exhaustive, simplified assembly of risks, risk origins, impacts and mitigation measures. It merely serves to give a glimpse of the comprehensive risk management process, which has been set up and which is currently ongoing in the Future Circular Collider study. A risk assessment database is maintained by the study group in order to establish an early warning and mitigation process that is expected to grow into a comprehensive project risk management scheme during the project preparatory phase.

B.1 Accelerator and technologies

Table B.1. Technological uncertainties with decisive impact potential on the project.

Uncertainty	Impacts	Mitigation measures
Limited availability of high-power RF power amplifier (klystron) manufacturers.	Cost increase and delay of construction and operation; reduced performance, reliability and availability.	Dedicated R&D programme with industrial partners on highly efficient klystrons to ensure continued availability of such devices. To avoid vendor locking situation, ensure in-house expertise on the technology and open standards and designs.
Cost of high accelerating gradient superconducting radiofrequency system based on bulk material is too high.	Increase of project costs.	Cure the Q slope of superconducting thin-film coated cavities and bring a viable production process to a technology readiness level that permits using this lower-cost technology instead of bulk material-based cavities.
Inefficient cavity series manufacturing and limited availability of companies with comparable manufacturing capacities and adequate quality management.	Project cost increase or reduced performance and reliability of the machine; possible need to extend the operation schedule.	Invest in R&D to conceive manufacturing methods that are cost-effective and which lead to high quality results, in particular ones that aim at streamlined production, testing and installation. Optimise the system internal interfaces with respect to number and simplicity as well as the external system interfaces, including test points for total quality management. Launch studies to improve the assembly efficiency, considering interfaces, simplification and speed-up of individual production and processing steps. Invest in automation of production, assembly, testing and the integration into a total quality management system considering a production process that involves multiple suppliers.

Table B.1. (continued.)

Uncertainty	Impacts	Mitigation measures
Electrical peak power consumption need is too high.	Cost of classical electrical infrastructure equipment and installation becomes prohibitive.	Invest in bringing more efficient cryogenic refrigeration with less electrical energy requirements for the same cooling performance to higher technology readiness level in cooperation with industrial partners through a dedicated R&D activity. Invest in R&D to develop a system that can recover energy from the accelerator subsystems, buffer that energy temporarily and use it during the subsequent cycle to reduce the peak power needs during the ramp phase. Invest in R&D on more efficient electricity conversion and distribution systems which exhibit lower equipment costs and reduced losses.
High contraction of conventional cryogenic distribution system during cooldown and significant losses during operation.	Complicated design of a conventional cryogenic distribution system results in significant cost increase, lower reliability and thus unsustainable operation costs. In addition, high loss rates and excessive maintenance and repair cause potentially unacceptable downtimes and are operation cost drivers.	Bring a cryogenic distribution system based on a low-thermal expansion material to industrial production grade through a focused R&D activity and a co-innovation approach with industrial partners. This activity, which will also reduce the number of equipment components and lead to a simpler design will also help controlling the total cost of ownership through reduced losses and reduced maintenance and repair needs.
High electrical energy consumption resulting from sustained supply of 100 MW radiofrequency power.	Higher than foreseen operation expenditures.	Invest in improving the efficiency of electrical to radiofrequency power conversion through a targeted R&D project. Improve the efficiency of electrical power distribution and lower the equipment cost by bringing non-conventional DC power distribution to the commodity market through a co-innovation project with industrial partners. Develop a highly reliable and long-lasting electrical energy buffering and recovery system that can recuperate the energy in the pulsed booster and use it during the subsequent cycle together with industrial partners.

Table B.1. (continued.)

Uncertainty	Impacts	Mitigation measures
Depending on the particle collider scenario and the foreseen physics research programme, current particle detection technologies do not meet the performance, reliability and cost needs.	Underuse of the potentials of the particle-collider leading to not meeting the physics programme goals or not meeting the goals within the foreseen schedule and cost envelope. Excessive costs of experiment detectors. Low maintenance intervals and long repair times as well as equipment replacement costs that lead to unsustainable operation of the research infrastructure. Loss of interest of the worldwide science community due to limited physics research reach, loss of a science vision within a graspable time frame and non-beyond-state-of-the-art scientific research methods and tools.	Definition of a world-wide coordinated, strategic R&D initiative focusing on detector technologies that with the selection of a preferred particle collider scenario becomes more specific as technical designs advance, research communities become organised and the specification of experimental physics investigations are developed in greater detail.

B.2 Implementation

Table B.2. Project implementation related uncertainties with decisive impact potential.

Uncertainty	Impacts	Mitigation measures
Limited availability of capacities for excavation materials in the host states, relevant for all particle collider scenarios, including the HE-LHC due to the need of new underground facilities.	Significant delay of construction phase start or increase of construction costs due to unplanned waste disposal needs. Non-acceptance of project plan by host-state representatives with or without public opposition.	Early start to develop a territorial waste management plan that considers the current legal situation in the host states and the transnational context of the project, contributing through the involvement of relevant experts at international level to the evolution of the current initiatives on moving towards a circular economy at European scale. Through the work at a stage in which a detailed project design remains yet to be developed, invest in R&D, e.g. through EC funded projects on circular economy and infrastructure construction efficiency, to identify novel separation and processing techniques, identify existing and so far not considered use cases and bring them to credible technology readiness levels. Develop a territorial concept for the logistics of tracing and transporting the excavation materials with the support of ICT systems, involving the host states, potentially relevant industries and consumers throughout the entire process.
Cost of the underground infrastructure.	Cost uncertainty leads to unaffordable project.	Invest in novel tunnel construction technologies to lower the cost risk probability. Develop a competitive tendering approach early on in the preparatory phase to avoid supplier-locked situation. Perform detailed surveys and ground investigations early on, before a detailed design is developed in order to come to a cost/risk optimised particle collider layout and placement scenario.
The regional and national administrative frameworks in France and the culture of direct democracy in Switzerland require the acceptance of an infrastructure development project plan by the public before a detailed technical design is presented to the authorities and before a decision to construct is taken.	Delays of acceptance or unforeseen requirements to substantially adjust the project scope can result in a significant stretch of the project preparation and construction phases. This can lead to a delay of the start of collider operation beyond the 2050 time horizon and to substantial re-scoping needs of the project. Consequently the world-wide research community may loose interest in the project, which in turn can have an adverse impact on the project implementation.	The study team has already in the early phases established working structures with both host states. In the frame of these structures, viable realisation strategies and schedules have been commonly developed. The approach foresees an early start of concrete preparatory work topics with both host state authorities, with their notified bodies and with additional external, experienced consultants in order to develop an optimised infrastructure project scenario as a cooperative effort between project owner, government named bodies and the public during the time period 2019–2025. If adequately set-up and staffed, this preparatory phase activity for an infrastructure aims at a civil engineering project start before the end of 2028. It foresees work with competent partners who have gained experienced in comparable large-scale infrastructure projects at

Table B.2. (continued.)

Uncertainty	Impacts	Mitigation measures
		international level and work with stakeholder representatives of the population in both countries to be able to understand and consequently meet the expected acceptance levels. The process aims at winning the host state representatives as advocates of the project through timely involvement as partners.
Timely availability of the rights of way on required land plots and underground volumes in France and in Switzerland.	Delay of the project preparatory and construction phases. Excessively growing project costs due to real-estate speculations. This can lead to a delay of the start of collider operation beyond the 2050 time horizon and to substantial re-scoping needs of the project and unacceptable project goal compromises. Consequently, the world-wide research community may loose interest on the project, which in turn can adversely impact the project realisation.	Early optimisation of the layout and placement of the collider and surface sites as a cooperative effort between project owner and named governance bodies, involving public stakeholder representatives. Apply the strategy of “avoid – reduce – compensate” to prevent the need for excessive socio-environmental impact mitigation as far as reasonably possible. Inclusion of a project scenario in the territorial development plans of both countries from 2020 onwards to anticipate the needs and to avoid conflicts of use with other development projects.
Uncontrolled resource usage during the operation phase (examples include, but are not limited to, water for conventional cooling, in particular if intake and reject occur in different countries, electricity consumption, generation of waste-heat, cryogenes, potentially harmful chemicals, introduction of sealed surfaces on the land – asphalt, concrete etc.)	Project-specific regulatory requirements imposed already at early stages during the preparatory phase (e.g. in the frame of developing the law for the unique project procedure in France) can lead to unsustainable operation costs. Alternatively, project acceptance of public stakeholder representatives may be delayed, leading to a longer than acceptable project preparation, construction and commissioning period, potentially also requiring technical adaptations at a stage, where the design intervention can be costly.	Timely work with the host-state representatives on establishing a communication culture between administration offices, external experts and project engineers has started during the conceptual design phase. Subsequent early common work in the form of a partnership can on one hand help developing a technical project with reduced resource needs and on the other hand trigger targeted investigations to identify alternative approaches to cope with the resource needs. Consequently, a number of design studies dealing with resource-related questions during the preparatory phase, including experience from the LHC and HL-LHC projects is indicated. Examples include applications for making the waste-heat available, studying alternative cooling and ventilation technologies, studying surface site designs that correspond to the ecological needs and that can fit with the cost envelopes, identify approaches to limit losses and to recover energy.

Table B.2. (continued.)

Uncertainty	Impacts	Mitigation measures
Sustainable site security and effective emergency intervention during operation.	Site surveillance, security enforcement, emergency intervention and rescue under the exclusive management responsibility of the project owner can lead to unsustainable operation. Intervention times which are too long and inadequate coverage can result in the need to reduce operational goals or failure to meet the operational targets may result in acceptable costs.	Early identification of the needs as a collaborative effort between the project owner, drawing on experience of the LHC project, and relevant host-state representatives will permit defining integrated concepts, making the best use of existing public security, emergency and intervention services combined with joint a continuous training programme. This approach also has the advantage of leading to increased acceptance of the project by key members of society and to create a reliable set of project advocates among the non-scientific community.
Sustainable site security and effective emergency intervention during operation.	Site surveillance, security enforcement, emergency intervention and rescue under the exclusive management responsibility of the project owner can lead to unsustainable operation. Intervention times which are too long and inadequate coverage can result in the need to reduce operational goals or failure to meet the operational targets may result in acceptable costs.	Early identification of the needs as a collaborative effort between the project owner, drawing on experience of the LHC project, and relevant host-state representatives will permit defining integrated concepts, making the best use of existing public security, emergency and intervention services combined with joint a continuous training programme. This approach also has the advantage of leading to increased acceptance of the project by key members of society and to create a reliable set of project advocates among the non-scientific community.
Low cost-effectiveness and quality of materials and services supplied due to excessive constraints on public tendering processes. This includes the limitations of a well-defined cost/performance based procurement scheme for the project, ineffective international networks with industries and potential suppliers of all sizes, too much generic focus on either in-house or out-sourced services, insufficient personnel (in-house or contracted) resources for procurement, contract follow up and inadequate business processes as well as a lack of legal advisers with extensive industrial experience during peak periods.	High effort required for administrative procedures resulting in lengthy and costly procurement processes which have an impact on the duration of the project preparation and construction phases. These can lead to the selection of under-performing suppliers which in the long run leads to potentially unacceptable high total costs of ownership (re-construction of subsystems, high repair or maintenance costs, high operating costs).	Timely preparation of an adequate procurement and academia/industry co-development framework. Timely investment in preparing the basis of a well staffed project procurement system, taking into account the changing needs during various phases of the project (preparation, CE construction, machine construction, commissioning). Timely development of an appropriate concept for in-kind participation of member- and non-member states with a corresponding project governing and management structure that includes effective levers to proceed with the implementation of the project (early stall warning, re-prioritisation, re-scheduling, re-assignment).

Table B.2. (continued.)

Uncertainty	Impacts	Mitigation measures
Availability of stable and effective governing and management structures driving forward the technical design of a collider, the associated experiment detectors, the host state activities and the financing strategy.	The lack of a vision of the priorities, which is propagated in the framework of a governing and management structure with adequate resource assignment, leads to a stall in the progress of the technical design and the development of mitigation measures for the uncertainties. This fails to strengthen the momentum, which is a pre-requisite of a project of such scale, of an ever growing international community. Consequently, investments made so far and being made for limited activities cannot have lasting impacts. Consequently the research community may choose to re-orient towards alternative projects.	With the next update of the European strategy for particle physics, an adequate governing and management structure for the preparatory project phase needs to be established for the accelerator and infrastructure project and for a particle detector design project. This should be well anchored in CERN's structure and mission programme, which has the financial and personnel resources to carry out the planned tasks before a decision to build is taken. Consequently, the successful preparation of a new research infrastructure for high-energy particle physics relies on the unambiguous recommendation emerging from the next strategy update, permitting the available resources to be focused on the tasks which need to be accomplished with highest priority.

Appendix C: Communities

The impact on the community can be presented in terms of an “onion” type model, starting with the innermost layer comprising the core scientific communities, which need, conceive and use such a facility. Further communities in the European Research Area and beyond, which will benefit throughout the entire lifecycle, starting with the early design phase, include: other sciences, engineering communities, higher education, industrial partners, researchers from non-technical domains, and ultimately all members of society.

Particle physics

The FCC-ee has broad physics discovery potential with an opportunity to attract a world-wide community of more than 20 000 physicists (see arXiv:1707.03711). It addresses the communities involved with the high energy and precision frontier, electroweak, Higgs and heavy flavour physics as well as the neutrino physics and Dark Matter communities, presently working on the LHC, flavour factories, neutrino and Dark Matter experiments. The theory community is needed to produce Standard Model calculations to match the exquisite precision of FCC-ee measurements. The model builders will be guided by unprecedented precision on masses and coupling constants and the possibility of studying domains of rare processes.

Experimental physics

The detector builders will encounter a vast field of opportunities concerning high precision – low material vertex tracking, large volume tracking and high precision

calorimetry with unprecedented micrometric definitions of fiducial volumes, particle identification techniques and ultra-thin detector magnets. Very large tracking volumes might be considered for detection of long-lived new particles.

Accelerator physics

The FCC-ee accelerator with top-up injection and unprecedented beam power will attract the world-wide community from electron storage rings, synchrotron light sources and high luminosity factories. Fully automated operating procedures, integrating luminosity optimisation, clean backgrounds and the energy calibration by resonant depolarisation constitute a wealth of interesting topics that call for the integration of diverse domains of competence.

Other physics communities

The research at the FCC-ee will have implications for astrophysics and cosmology, offering an unprecedented opportunity to federate these scientific fields.

Technology, engineering, computing

The project will drive the development of higher efficiency radio-frequency power generation. The development of cost-effective high-performance thin-film coated, superconducting cavities by material scientists also requires expertise from manufacturing experts. Specific engineering areas include precision mechanics, surface treatment, superconductivity, novel materials, electronic and reliability engineering to improve the particle accelerator efficiency. The development of energy efficient cryogenics engages the cold-temperature engineering sciences together with mechanical engineering.

Electrical engineering communities will be involved in bringing medium voltage DC technology to the market, to conceive lower-loss electricity distribution systems which are more reliable and develop environmentally friendly and sustainable energy recovery and buffering systems. Designers will be needed to develop waste-heat recovery and reuse systems.

To design and construct the underground infrastructure in a cost-effective way, the civil engineering community needs to make advances in tunnelling technologies and to develop ways for the recovery and reuse of excavation materials. This work will be carried out as a joint endeavour with material scientists, geologists and chemists. Information and communication technology communities will be involved everywhere. Their activities include simulation algorithms and software infrastructure; parallel and high-performance computing; distributed computing; real-time and embedded systems; mechatronics to conceive new standards and technologies for low-maintenance and easy-to-repair systems in the areas of protection, access, remote handling and autonomous interventions; data acquisition, data visualisation, modelling and operation optimisation; the introduction of artificial intelligence in machine and detector operation; radiation and fault tolerant systems; environmental information systems; data mining technologies; wireless communications including safety-related functions; data and document management facilities; world-wide computing infrastructures; long-term data stewardship; open access data models and infrastructures and much more.

Higher education

The design and construction of the accelerator and the detectors will offer many opportunities for science teachers and students at master, doctorate and post-doc levels. Eventually the findings from all the scientific activities will enrich the academic curricula: state-of-science today will become state-of-the art tomorrow. This project will enlarge the impact potential of higher education on highly qualified personnel and apprentices.

Industry

A project of such scale must be designed, constructed, operated and maintained with strong involvement of industrial partners from all of the participating nations. Where reasonably possible, a gradual shift towards co-development will lead to a research infrastructure which on one hand is sustainable in the long-term and which has greater impact for industry on the other. A specific initiative during the detailed design phase will focus on identifying the fields of cooperation, also elucidating where companies can best profit from enhanced learning to increase their competitiveness and improve the quality of their product and internal processes.

One particular area of interest is to develop ways to increase the technology level in the field of civil engineering: novel methods for on-line excavation material analysis and separation, pathways for reuse of the materials by other industries such as chemical and construction are important levers to increase the economic utility in this domain.

Non-technical sciences

This project will engage a variety of scientific communities, beyond the physics, technology and engineering domains. Examples include, but are not limited to, research in logistics and systems engineering around the world-wide production chain for the accelerator and detectors (logistics, operations, sales, HR, procurement, accounting, management and organisation, business administration). Architecture and arts will be involved in surface site development. Media and visual arts as well as museums and marketing experts are needed to efficiently engage the public and to communicate with institutional stakeholders.

Radiation protection, technical risk management and waste management experts will facilitate the control of hazards and risks in all areas throughout the entire life cycle. Environmental and urban sciences will help avoiding, reducing and mitigating impacts.

Economics, innovation management and political sciences form another group of non-technical sciences, which have already shown during the FCC study phase that they are essential for the successful preparation of the project.

Members of the global society

The continued deep exploration of our universe tackles fundamental questions that intrigue everyone: What is the origin of the universe? What is the nature of the matter that we are all made of? Where do we come from? Why is there something and not nothing?

This project addresses these questions directly and creates opportunities to engage everyone who is interested. During the preparatory phase, an effort will

be made to intensify such involvement through community science and a modern communication plan.

The conceptual study phase has revealed that the greatest challenge is, however, to create interest among people who are unaware. FCC-ee is an opportunity not to be lost for the particle physics and accelerator communities to raise awareness on a global scale and to strengthen the support for continued investment in this research by policy makers, funding agencies and ultimately, by every member of society.

Appendix D: Timeline

The overall project duration is 18 years, composed of two major parts: the preparation phase spanning 8 years and the construction phase spanning 10 years. The preparation phase includes:

- all administrative procedures with the host states, ultimately leading to the construction permits and delivery of the surface and underground rights of way;
- the consultation process with authorities and public stake holders;
- the development of project financing, organisation and governing structures;
- the site investigations, civil engineering design, tendering for consultant and construction contracts.

The construction phase includes:

- all underground and surface structures;
- technical infrastructure;
- accelerators and detectors, including hardware and beam commissioning.

The implementation timeline for FCC-ee is shown in Figure D.1. The underground and surface civil engineering construction can be completed in less than 7 years. The first sectors would be ready for technical infrastructure installation about 4.5 years after the start of construction.

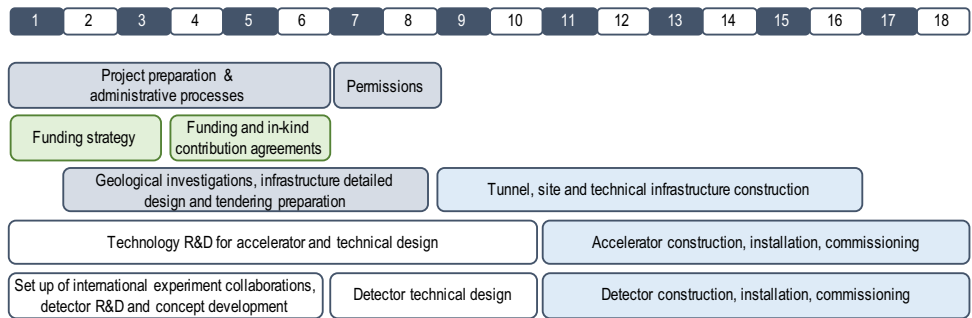


Fig. D.1. Overview of the FCC-ee implementation timeline starting in 2020. Non technical tasks marked in grey and green are compulsory for any new particle collider project and precede the actual construction. Numbers in the top row indicate the year. Physics operation would start in 2039 according to this schedule.

Appendix E: Costs

E.1 Construction costs

A cost study was performed for the FCC-ee based on the conceptual design. The cost estimates for the accelerators (collider and injector complex) and the technical infrastructure are based on machine and system inventories. The cost estimate for civil engineering is based on an analysis of construction methods for underground and surface structures, the associated material quantities and unit prices, derived from several recent large-scale tunnel and civil engineering projects in Central Europe. The resulting precision of the overall cost estimate is at $\pm 30\%$ level.

The capital cost for construction of the project is summarised in Table E.1. Cost items are indicated in millions of Swiss francs (MCHF) at 2018 values. This cost includes all equipment for operation at the Z, W and H working points. Operation of the FCC collider at the $t\bar{t}$ working point will require later installation of additional RF cavities and associated cryogenic cooling infrastructure with a corresponding total cost of 1100 MCHF.

Table E.1. Summary of capital cost for the implementation of the FCC-ee project for the Z, W and H working points.

Domain	Cost [MCHF]
Collider and injector complex	3100
Technical infrastructure	2000
Civil engineering	5400
Total cost	10 500

The total construction cost amounts to 10 500 MCHF (for Z, W and H working points) as shown in Figure E.1, with civil engineering accounting for 51% or 5400 MCHF of this. The capital cost for the technical infrastructure is 2000 MCHF corresponding to 19% of the total construction cost and the remaining 30% or 3100 MCHF corresponds to the accelerator construction. Both, civil engineering and general technical infrastructures can be fully reused for a subsequent hadron collider FCC-hh.

The capital expenditure can also be related to the physics goals: Taking the H mode running as an example, with 5 ab^{-1} accumulated over 3 years, the total investment cost corresponds to 10 kCHF per Higgs boson produced; for the Z running with 150 ab^{-1} accumulated over 4 years, the total capital investment cost corresponds to 10 kCHF per 5×10^6 Z bosons – the number of Z bosons collected by each experiment during the entire LEP programme.

E.2 Operation costs

Operating costs are a major factor for any research facility and design efforts need to be made from the early conceptual stage to enable sustainable operation. The history of large-scale technical infrastructures reveals a trend of steadily decreasing normalised operating costs: while at the peak of LEP operation CERN had 3300 staff members, in the LHC era the laboratory's staff complement has shrunk to 2300 employees, even though the LHC together with its injectors is a much more complex machine. This decreasing number of personnel is a manifestation of progress in technology, operation and maintenance concepts.

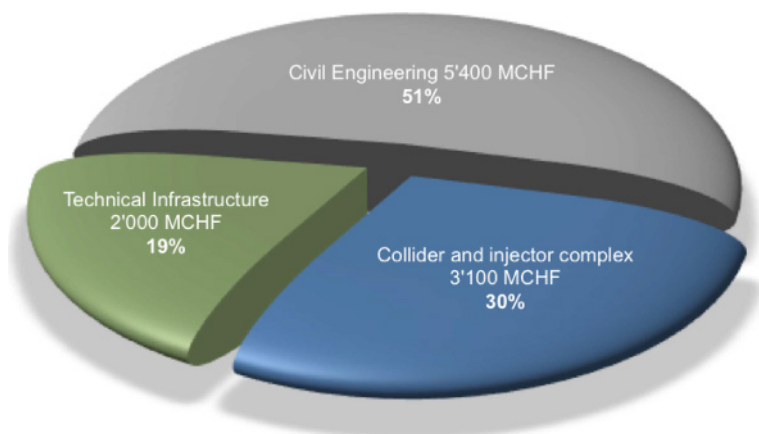


Fig. E.1. FCC-ee capital cost per project domain.

This optimisation trend is expected to continue for the FCC-ee with major improvements in the areas of automation of operation, monitoring, inspection and repair activities. Even though the FCC-ee is nearly four times larger than LEP and has two separate vacuum systems, the total number of different elements in the machine is increasing by less than a factor 2. Consequently, the number of component series does not scale with the size of the machine and the associated operation and maintenance costs will not do so either. An increase in the absolute number of components goes along with a growth in the maintenance, repair and restore effort required. However, this fact does not necessarily imply higher complexity, i.e. dynamic system behaviour leading to significantly higher operation and mitigation costs should not be a consequence. The training and experience requirements for maintenance personnel are further optimised by the use of industry-based standardised, modular designs for accelerator components. The detailed technical design phase will, however, focus on ensuring that the operation of such a machine is sustainable in the long term.

Sustainable maintenance. The machine design will place emphasis on conceiving the individual systems and subsystems such that they can be monitored, maintained and repaired by service suppliers as much as reasonably possible. Experience with this approach for particle accelerators and imaging devices for healthcare applications has been gained over more than 15 years. Examples include the remote maintenance of power converters and the servicing of superconducting devices including cryogenic refrigeration infrastructure. The effects of this approach are (1) the possibility to re-negotiate operation and maintenance contracts during the operation phase and, thus, to profit from an ever improving understanding of the infrastructure's operational behaviour, (2) the possibility to engage financial resources only when needed and with the possibility to reduce them when no longer needed, (3) the creation of "local economic benefits" in each of the contributing nations and regions resulting from the financial revenue over sustained periods for companies and a long-term education effect for highly qualified personnel.

Modular design. Investing early-on in modular designs of basic components and equipment to be installed will enable streamlined operation, service and repair. The successfully demonstrated concept of a vertically integrated "column" that will be

replicated many times is the underlying principle of this approach, leading to a scalable system. Thorough analysis with potential industrial partners and the consequent application of best practices will be one of the requirements in the preparatory work plan. One key topic in this approach is the reduction of, and facility-wide agreement on, standard interfaces at all levels (e.g. mechanical, electrical, fluids and their parameters, communication and software). A dedicated activity for interface management is the key to cost-effective production and testing, installation and long-term sustainable operation.

In-kind, collaborative operation. The LHC experiments have already indicated the way in which long-term operability of an experiment can be achieved through a committed involvement of the international collaborating institutes. Intensifying and extending this concept to the entire accelerator and experiment infrastructure is an essential lever to fully engage the entire community in this project. Particle accelerator experts and equipment specialists exist in numerous academic institutes around the globe. Operating a world-class particle collider creates a unique learning experience for scientists and engineers at all levels. It is also an essential way to reduce the operating budget through the assignment of in-kind contributions to operation, maintenance and repair. Information and communication technologies in twenty years from now will permit the distributed monitoring and root-cause analysis of numerous systems. Through unified supervisory control infrastructures, it should be straightforward to operate the technical infrastructure of all experiments with a single set of trained personnel and to share the task across the globe. The CMS “remote operations center” pioneered by FNAL in the US is a first step in this direction.

The electric power consumption is one of the operating costs, but the analysis of the conceptual design indicates that it is not the cost-driver. In order to arrive at a long-term, sustainable highest-luminosity particle collider, the FCC-ee conceptual design already integrates a number of energy reduction measures:

- Use of power-saving two-in-one magnet designs for arc dipoles and quadrupoles.
- A booster-ring for continuous top-up, more than doubling the availability of the collider rings for luminosity production, thus leading to a sustainable physics programme, which can be completed within 15 years.
- Use of superconducting radiofrequency cavities based on thin-film coating technology at 4.5 K with a higher energy efficiency than bulk superconducting materials at 2 K.
- Development of high-efficiency klystrons to increase the effectiveness of electrical to RF power conversion.
- Using medium-voltage DC electricity distribution to optimise the size of the powering infrastructure, enabling the introduction of renewable energy and storage systems and suppressing the need for a power quality system.
- Waste heat recovery and reuse inside the facility, and for storage and provision to district services (heating and air conditioning).

The total electrical energy consumption over the 14 years of the research programme, including the highest energy stage, is estimated to be around 27 TWh, corresponding to an average electricity consumption of 1.9 TWh/year over the entire operation programme, to be compared with the 1.2 TWh/year consumed by CERN today and the expected 1.4 TWh/year for HL-LHC. For LEP2 the energy consumption ranged between 0.9 and 1.1 TWh/year. Based on the 2014/15 CERN electricity prices, the electricity cost for FCC-ee collider operation would be about 85 Meuro per year.

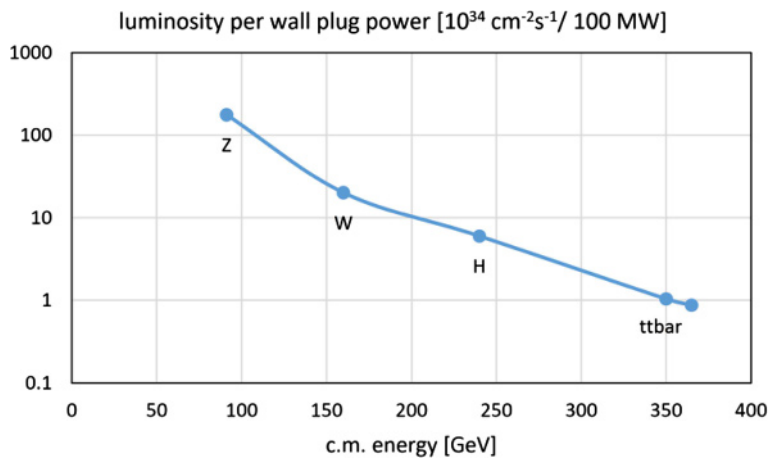


Fig. E.2. FCC-ee total luminosity divided by total electric power as a function of c.m. energy.

For a total luminosity production of 5 ab^{-1} in the 3 years of the HZ running mode, about 1.1 GWh or ca. 50 keuro for electricity would need to be invested for producing 1 fb^{-1} of integrated luminosity. This translates into an electricity cost of about 260 euro per Higgs boson. Figure E.2 illustrates the efficiency of the FCC-ee with regard to electrical power consumption.

Glossary

- Ω** The ohm is the SI derived unit of electrical resistance.
- 4DCHM** 4-dimensional composite Higgs model.
- A** The ampere (symbol: A) is the base unit of electric current in the International System of Units (SI).
- A15** A15 is the Strukturbericht notation for the crystal structure of Cr_3Si , originally reported for β -tungsten. This structure is shared by a family of intermetallic compounds with the formula A_3B , where A is a transition metal. Several of these compounds, with $\text{A} = \text{Nb}$ or V , are superconducting with a critical temperature T_c of around 20 K and an upper critical magnetic field H_{c2} exceeding 20 T. The most commonly applied example is Nb_3Sn .
- ab** An attobarn corresponds to an area equal to 10^{-46} m^2 .
- ABCI** The azimuthal beam cavity interaction is software which solves the Maxwell equations directly in the time domain when a bunched beam goes through an axi-symmetric structure on or off axis. An arbitrary charge distribution can be defined by the user.
- AC** Alternating current.
- a-C** Amorphous carbon.
- ADC** Analogue-to-digital converter.
- ADT** The ADT is a transverse damping system deployed in the LHC to reduce the oscillations of the injected proton beam, to reduce emittance blow-up due to ground motion and magnetic noise or ripple and to stabilise the beam against the resistive wall instability and other possible instabilities caused by narrow band parasitic transverse impedances in the ring.

Alcove An alcove is a recessed area open from a larger room but enclosed by walls, pillars, or other architectural elements.

AMD Adiabatic matching device.

APC Artificial pinning centre: a particle, defect or other feature intentionally introduced to act as a site for flux pinning.

Ar Argon is a chemical element with symbol Ar and atomic number 18.

Arc A circular collider is composed of curved cells called arcs that are separated by straight sections (see LSS). An arc half-cell forms the periodic part of the arc lattice (see lattice).

ARIES A H2020 EC funded research and development project in the area of particle accelerator technologies.

ARMCO American Rolling Mill Company pure iron became synonymous with the purest steel mill produced iron with a purity of more than 99.85% Fe.

ASIC An application-specific integrated circuit is an integrated circuit (IC) customised for a particular use, rather than intended for general-purpose use.

ATLAS A toroidal LHC apparatus is one of the seven particle detector experiments constructed at the LHC.

B The byte is a unit of digital information that most commonly consists of eight bits, representing a binary number.

b The bit, a binary digit, is a basic unit of information used in computing and digital communications. A binary digit can have only one of two values, and may be physically represented with a two-state device.

B_i The dispersion function of a beam line is determined by the strength and placement of dipole magnets. As a consequence, dipole field errors also contribute to the dispersion function. Multipole components corresponding to a magnetic flux distribution, which can be added up are denoted by B_i and A_i . B_1 corresponds to a normal dipole component, B_2 to a normal quadrupole component, B_3 to a normal sextupole component, A_1 to a skew dipole, A_2 to a skew quadrupole and A_3 to a skew septupole.

barn A barn (symbol: b) is a unit of area equal to 10^{-28} m^2 . It is best understood as a measure of the probability of interaction between small particles. A barn is approximately the cross-sectional area of a uranium nucleus.

BCS Theory named after John Bardeen, Leon Cooper, and John Robert Schrieffer. It is the first microscopic theory of superconductivity since Heike Kamerlingh Onnes's 1911 discovery. The theory describes superconductivity as a microscopic effect caused by a condensation of Cooper pairs into a boson-like state.

Be Beryllium is a rare chemical element with symbol Be and atomic number 4.

Beam pipe Volumes of different shape (e.g. cylindrical, conical, flanges and bellows) and material (e.g. metallic, ceramic) used to transport the beam. The ultrahigh-vacuum within it reduces beam-gas interactions to a level at which the beam lifetime is acceptable.

Beamline A series of functional elements, such as magnets and vacuum pipe, which carry the beam from one portion of the accelerator to another.

Beamscreen Perforated tube inserted into the cold bore of the superconducting magnets in order to protect the cold bore from synchrotron radiation and ion bombardment.

Beta function An optical function proportional to the square of the local transverse beam size. The beta function describes how the beam width changes around the accelerator. There are separate β -functions for the x and y planes.

B-factory A B-factory, or sometimes a beauty factory, is a particle collider experiment designed to produce and detect a large number of B mesons so that their properties and behaviour can be measured with small statistical uncertainty. Tauons and D mesons are also copiously produced at B-factories.

BFPP Bound-free pair production is one of the new types of processes that occur in relativistic collisions of atoms and ions. It is the production of an electron-positron pair with the electron not produced as a free state but as a bound state of one of the ions.

Bhabha scattering The electron-positron scattering process: $e^+e^- \rightarrow e^+e^-$. There are two leading-order Feynman diagrams contributing to this interaction: an annihilation process and a scattering process.

BHWISE A Monte Carlo event generator software simulating Bhabha-scattering, developed for linear collider detector luminosity studies.

BIM Building information modeling is a process involving the generation and management of digital representations of physical and functional characteristics of places.

BLM Beam loss monitor.

BPM Beam position monitor.

Bq The becquerel is the SI derived unit of radioactivity. One becquerel is defined as the activity of a quantity of radioactive material in which one nucleus decays per second. The becquerel is therefore equivalent to an inverse second, s^{-1} .

BR In particle physics and nuclear physics, the branching ratio for a decay is the fraction of particles which decay by an individual decay mode with respect to the total number of particles which decay.

BR (machine) The booster ring is an accelerator in the collider tunnel, which provides the particle collider continuously with particles at collision energy.

BRGM Bureau de Recherches Géologiques et Minières, France.

BS Beamstrahlung.

BSCCO Bismuth strontium calcium copper oxide (pronounced “bisko”), is a family of high-temperature superconductors. Specific types of BSCCO are usually referred to using the sequence of the numbers of the metallic ions. Thus Bi-2201 is the $n = 1$ compound ($\text{Bi}_2\text{Sr}_2\text{CuO}_{6+x}$), Bi-2212 is the $n = 2$ compound ($\text{Bi}_2\text{Sr}_2\text{CaCu}_2\text{O}_{8+x}$), and Bi-2223 is the $n = 3$ compound ($\text{Bi}_2\text{Sr}_2\text{Ca}_2\text{Cu}_3\text{O}_{10+x}$).

BSM Beyond Standard Model.

Bunch A group of particles captured inside a longitudinal phase space bucket.

BX Bunch crossing.

C The coulomb (symbol: C) is the SI (international system of units) unit of electric charge. It is the charge (symbol: Q or q) transported by a constant current of one ampere in one second.

C band The C band is a designation by the IEEE (institute of electrical and electronics engineers) for a part of the microwave band of the electromagnetic spectrum covering frequencies from 4 to 8 gigahertz.

C++ An object-oriented programming language.

CAD Computer-aided design is the use of computer systems to aid in the creation, modification, analysis, or optimisation of a design.

CAF A compressed air foam system is used in firefighting to deliver fire retardant foam for the purpose of extinguishing a fire or protecting unburned areas.

CAPEX Capital expenditures are the funds used to acquire or upgrade fixed assets, such as expenditures towards property, plant, or equipment.

Carnot Efficiency Carnot efficiency describes the maximum thermal efficiency that a heat engine can achieve as permitted by the second law of thermodynamics.

- CBA** Cost-benefit analysis is a systematic process for estimating and comparing benefits and costs of a project. The purpose of CBA is to facilitate a more efficient allocation of resources, demonstrating the convenience for society of a particular intervention rather than possible alternatives.
- CC60** The CC60 facility at CERN uses a ^{60}Co source for the qualification of components against TID effects.
- CCT** A canted-cosine-theta magnet is an accelerator magnet that superposes fields of nested and tilted solenoids that are oppositely canted.
- CDR** A conceptual design report completes the first stage of the ESFRI roadmap methodology, permitting concept screening, consortium formation, access policy and funding concept preparation, scientific and project leadership definition.
- CEA** The French alternative energies and atomic energy commission (Commissariat à l'Énergie Atomique et aux Énergies).
- CepC** The circular electron positron collider is an electron-positron collider proposed by the Chinese high energy physics community, acting as a Higgs-factory in a new tunnel 80–100 km in length.
- CEREMA** The French “Centre d'Etude et d'Expertise sur les Risques, l'Environnement, la Mobilité et l'Aménagement” is a public administration organisation, governed by the “ministre chargé de l'écologie, du développement durable et de l'énergie” and the “ministre du transport, de l'égalité des territoires et de la ruralité”. The organisation works with the territorial state services during all development projects, notably with respect to implement sustainable development goals (urbanism, environment, infrastructures and transport, risk management).
- CERN** European Organisation for Nuclear Research.
- CETU** The “centre d'études des tunnels” is a technical service of the French “ministère de l'Écologie, du Développement et de la Mer”, a notified body for the safety of tunnels in France.
- CFC** Carbon fibre composite.
- CFD** Computational fluid dynamics uses numerical analysis to solve and analyse problems that involve fluid flows.
- CH₄** Methane is a chemical compound.
- CHARM** CERN high energy accelerator mixed field facility, located in the CERN east area, supplies a wide spectrum of radiation types and energies.
- CHF** ISO code of the Swiss franc currency.
- Chilled Water** Chilled water is a commodity used to cool a building's air and equipment. It's temperature is between 4°C and 7°C.
- CIR** Circuit.
- CIXP** CERN internet exchange point.
- CL** Confidence level.
- CLD** The CLic detector is a conceptual design for an experiment detector at CLic, which also serves as a design model for an experiment detector at the FCC-ee.
- CLIC** The compact linear collider (CLIC) is a concept for a future linear electron-positron collider in a new tunnel, ranging from 11 to 50 km, depending on the collision energy.
- CLIC-dp** The CLIC detector and physics study is an international collaboration currently composed of 30 institutions.
- CLIQ** The coupling-loss-induced quench method is a superconducting magnet protection approach.
- CM** Cold mass.
- CMM** Coordinated measuring machines.
- CMOS** Complementary metal oxide semiconductor is a technology for constructing integrated circuits patented in 1963 by Frank Wanlass while working for Fairchild Semiconductor.

- CMS** The compact muon solenoid is one of the seven particle detector experiments constructed at the LHC.
- CNDP** The French “Commission nationale du débat public” was created in 1995 and is since 2002 an independent administration authority. The organisation ensures that the public participates in the process of construction projects of national interest.
- CNES** The National Centre for Space Studies is the French government’s space agency.
- CNRS** The French national center for scientific research (Centre National de la Recherche Scientifique).
- COL** Collimation.
- Collimator** A device that removes beam particles at large amplitudes. They are used to keep beam-losses low and to protect critical elements of the accelerator.
- Collision** A close encounter of particles during which dynamic quantities such as energy, momentum, and charge may be exchanged.
- Comsol** A cross-platform, finite element analysis, solver and multiphysics simulation software developed by private company COMSOL Inc. (Sweden). It allows conventional physics-based user interfaces and coupled systems of partial differential equations.
- Cooper pair** Two electrons that appear to “team up” in accordance with theory, BCS or other, despite the fact that they both have a negative charge and normally repel each other. Below the superconducting transition temperature, paired electrons form a condensate, a macroscopically occupied single quantum state, which flows without resistance. However, since only a small fraction of the electrons are paired, the bulk does not qualify as being a “Bose-Einstein condensate”.
- COTS** Commercial-off-the-shelf.
- CP** Charge conjugation parity symmetry is the product of two symmetries: C for charge conjugation, which transforms a particle into its antiparticle, and P for parity, which creates the mirror image of a physical system. The strong interaction and electromagnetic interaction seem to be invariant under the combined CP transformation operation, but this symmetry is slightly violated during certain types of weak decay. Historically, CP-symmetry was proposed to restore order after the discovery of parity violation in the 1950s.
- Cr₂O₃** Chromium(III) oxide is an inorganic compound. It is one of the principal oxides of chromium and is used as a pigment. In nature, it occurs as the rare mineral eskolaite.
- Critical temperature** Temperature T_c below which characteristics of superconductivity appear. The value varies from material to material and depends on the magnetic field.
- Cryo magnet** Complete magnet system integrated in a cryostat, including main magnet coils, collars and cryostat, correction magnets and powering circuits.
- Cryogenic system** A system that operates below a temperature set by convention at 150 K (−123.15°C).
- CST** Computer simulation technology is a computational tool from Dassault Systems for 3D electromagnetic design and analysis.
- Cu** Copper is a chemical element with symbol Cu and atomic number 29.
- CW** A continuous wave is an electromagnetic wave of constant amplitude and frequency, almost always a sine wave, that for mathematical analysis is considered to be of infinite duration.
- Cybersecurity** Cybersecurity is the protection of computer systems from theft or damage to their hardware, software or electronic data, as well as from disruption or misdirection of the services they provide.

DA Dynamic Aperture.

DAΦNE The double annular Φ factory for nice experiments is an electron-positron collider at the INFN Frascati National Laboratory in Frascati, Italy. It has been colliding electrons and positrons at a centre of mass energy of 1.02 GeV to create φ mesons Since 1999.

DAQ Data acquisition.

Dark matter Invisible matter that makes up 26% of the universe and which can only be detected from its gravitational effects. Only 4% of the matter in the Universe are visible. The remaining 70% are accounted to dark energy.

dB The decibel (symbol: dB) is a unit of measurement used to express the ratio of one value of a physical property to another on a logarithmic scale. When expressing power quantities, the number of decibels is ten times the logarithm to base 10 of the ratio of two power quantities. That is, a change in power by a factor of 10 corresponds to a 10 dB change in level.

DC Direct current.

DCAL Digital hadron calorimeter.

DCCT A direct current-current transformer is a current-to-voltage transducer, employed when measurement of very high current is required.

DCH Drift Chamber.

DD4hep A detector description toolkit for high energy physics.

DELPHES Delphes is a C++ framework, performing a fast multipurpose detector response simulation. The simulation includes a tracking system, embedded into a magnetic field, calorimeters and a muon system.

DELPHI The detector with lepton, photon and hadron identification was one of the four main detectors of the large electron-positron collider (LEP) at CERN.

DESY The German electron synchrotron (Deutsches Elektronen-Synchrotron).

DFAE The Département Fédéral des Affaires Étrangères is the Swiss foreign ministry.

Dipole A magnet with two poles, like the north and south poles of a horseshoe magnet. Dipoles are used in particle accelerators to keep particles moving in a circular orbit.

DIS Dispersion suppressor.

DM Dark matter.

DN Diametre nominal, the European equivalent of NPS (nominal pipe size) defines a set of nominal pipe sizes in standard ISO 6708. The dimensionless number after the letters DN indicate the physical size in millimetres of the bore.

DOE The United States Department of Energy.

DPA Displacement per atom.

DR A damping ring reduces the emittances produced by the particle source to the small values required for the collider. Emittance reduction is achieved via the process of radiation damping, i.e. the combination of synchrotron radiation in bending fields with energy gain in RF cavities.

DRAM Dynamic random-access memory.

DVR Dynamic voltage restorer.

Dynamic aperture Maximum transverse oscillation amplitude that guarantees stable particle motion over a given number of turns. If the motion amplitude of a particle exceeds this threshold, the betatron oscillation of the particle will not have any bounds, and the motion will become unstable, leading to loss of the particle. It is expressed in multiples of the beam size together with the associated number of turns. Unlike the physical aperture, dynamic aperture separating stable and unstable trajectories is not a hard boundary.

Dynistor A dynistor is an unidirectional thyristor breakover diode. It can be used as switches in micro- and nanosecond power pulse generators.

EASITrain A H2020 EC funded Marie Skłodowska Curie innovative training network project to advance superconducting wire and thin film technologies as well as cryogenic refrigeration systems for particle accelerators.

EBITDA A company's earnings before interest, taxes, depreciation, and amortisation is an accounting measure calculated using a company's net earnings, before interest expenses, taxes, depreciation, and amortisation are subtracted, as a proxy for a company's current operating profitability (i.e. how much profit it makes with its present assets and its operations on the products it produces and sells, as well as providing a proxy for cash flow).

EC Electron cloud.

ECal Electromagnetic calorimeter (also ECAL).

ECFA European Committee for Future Accelerators.

Eddy current Eddy currents are loops of electrical current induced within conductors by a changing magnetic field in the conductor due to Faraday's law of induction. Eddy currents flow in closed loops within conductors, in planes perpendicular to the magnetic field.

EDLC Electrical double-layer capacitors.

EES Energy extraction system.

EFT An effective field theory is a type of approximation, or effective theory, for an underlying physical theory, such as a quantum field theory or a statistical mechanics model.

EHF Electrohydraulic forming is a type of metal forming in which an electric arc discharge in liquid is used to convert electrical energy to mechanical energy and change the shape of the workpiece.

EIA Environmental impact assessment.

EIE Étude de l'impact sur l'environnement is the Swiss name for the environmental impact assessment in the scope of the OEIE.

EIR Experimental insertion region.

Electron cloud A cloud of electrons generated inside an accelerator beam pipe due to gas ionisation, photoemission from synchrotron radiation, or "beam-induced multipacting" via electron acceleration in the field of the beam and secondary emission. Electron clouds may cause single- and multi-bunch beam instabilities as well as additional heat load on the beamscreen inside the cold magnets.

electronvolt In physics, the electronvolt (symbol eV, also written electron-volt and electron volt) is a unit of energy equal to approximately 1.6×10^{-19} joules (symbol J) in SI units. By definition, it is the amount of energy gained (or lost) by the charge of a single electron moving across an electric potential difference of one volt. The electronvolt is not an SI unit, and its definition is empirical. By mass-energy equivalence, the electronvolt is also a unit of mass, expressed in units of eV/c^2 , where c is the speed of light in vacuum.

Electroweak symmetry breaking Although electromagnetism and the weak force have the same strength at high energies, electromagnetism is much stronger than the weak force in our everyday experience. The mechanism by which, at low energies, a single unified electroweak force appears as two separate forces is called electroweak symmetry breaking.

EM Electro magnetic.

EMB Electromagnetic barrel calorimeter.

EMEC Endcap electromagnetic calorimeter.

EMF Forward electromagnetic calorimeter.

- Emittance** The area in phase space occupied by a particle beam. The units are mm-milliradians for transverse emittance and eV-s for longitudinal emittance.
- EN** European norms are documents that have been ratified by one of the three ESOs (European Standardisation Organisations), CEN, CENELEC or ETSI; recognised as competent in the area of voluntary technical standardisation as for the EU Regulation 1025/2012.
- EOT** The most common type of overhead crane, found in many factories. These cranes are electrically operated by a control or remote control pendant, or from an operator cabin attached to the crane.
- EPFL** The École polytechnique fédérale de Lausanne is one of the two Swiss Federal Institutes of Technology.
- EPPSU** European Particle Physics Strategy Update. See also <https://europeanstrategy.cern>.
- ERL** Energy recovery Linac.
- ERMC** Enhanced racetrack model coil.
- ES** Electro static.
- ESD** Electron-stimulated desorption.
- ESFRI** European strategy forum for research infrastructures.
- Espoo Convention** The Espoo Convention sets out the obligations of parties to assess the environmental impact of certain activities at an early stage of planning. It also lays down the general obligation of states to notify and consult each other on all major projects under consideration that are likely to have a significant adverse environmental impact across boundaries.
- ESPP** European Strategy for Particle Physics. See also <https://europeanstrategy.cern>.
- ESRF** The European Synchrotron Radiation Facility is a joint research facility situated in Grenoble, France, and supported by 22 countries (13 member countries: France, Germany, Italy, UK, Spain, Switzerland, Belgium, The Netherlands, Denmark, Finland, Norway, Sweden, Russia and 9 associate countries: Austria, Portugal, Israel, Poland, Czech Republic, Hungary, Slovakia, India and South Africa).
- ESS** Energy storage system.
- ETHZ** The Eidgenössische Technische Hochschule Zürich is one of the two Swiss Federal Institutes of Technology.
- EU** European Union.
- EuCARD2** A FP7 EC funded research and development project in the area of particle accelerator technologies.
- EuroCirCol** A H2020 EC funded research and development project to develop the foundations of a future circular hadron collider.
- EW** Electroweak.
- EWPO** Electroweak precision observables.
- EWPT** Electroweak phase transition.
- EWSB** Electroweak symmetry breaking.
- EXP** Experiment.
- Experiment insertion region** Place in the particle collider hosting the interaction region in which the two beams are brought to collision and the surrounding particle physics experiments.
- EXT** Extraction.
- fb** A femtobarn corresponds to an area equal to 10^{-43} m^2 .
- FCC** Future circular collider is a feasibility study aiming at the development of conceptual designs for future particle colliders with energies and intensities at the

frontier, based on a technically feasible and affordable circular layout permitting staged implementation.

FCC-ee Future circular intensity-frontier electron-positron collider with multiple centre-of-mass collision energies ranging from the Z peak to $t\bar{t}$ collision energies at luminosities up to almost $5 \times 10^{36} \text{ cm}^{-2} \text{ s}^{-1}$ in a new circular tunnel of about 100 km length.

FCC-eh Future circular energy-frontier electron-hadron collider interaction point scenario. The scenario foresees an energy recovery linac (ERL) to generate electron beams and to collide them with high-energetic proton or ion beams of a hadron collider in a new circular tunnel of about 100 km length.

FCC-hh Future circular energy-frontier hadron-hadron collider reaching up to 100 TeV centre-of-mass collision energies at luminosities of $5\text{--}10 \times 10^{34} \text{ cm}^{-2} \text{ s}^{-1}$ in a new circular tunnel of about 100 km length. Operation with protons and ions is envisaged.

FDS Fire dynamics simulator is a software developed and maintained by the U.S. Department of Commerce National Institute of Standards and Technology for the simulation of smoke and heat transport from fires.

FED Fractional effective dose.

FEM European federation of material handling.

FF Final focus.

FIB An FIB setup is a scientific instrument that resembles a scanning electron microscope (SEM). However, while the SEM uses a focused beam of electrons to image the sample in the chamber, a FIB setup uses a focused beam of ions instead.

FinFET A type of non-planar or “3D” field effect transistor used in the design of modern processors. The transistor architecture uses raised channels called “fins”, from source to drain.

FLUKA A particle physics Monte Carlo simulation package for high energy experimental physics and engineering, shielding, detector and telescope design, cosmic ray studies, dosimetry, medical physics and radio-biology.

Flux pinning In practical applications, a type II superconductor in a magnetic field is usually in the mixed state, in which the superconducting material is penetrated by magnetic flux. When carrying a current, a force (the Lorentz force) acts on these flux lines. If this was not opposed, the resulting movement of flux would result in energy dissipation, rendering the material useless for current-carrying applications. Flux pinning is the phenomenon by which defects in a superconducting material immobilise flux lines, producing a pinning force to oppose the Lorentz force. The volumetric flux pinning force effectively defines the J_c of a type II superconductor. The type of defects providing effective flux pinning depend on the material (e.g. grain boundaries in Nb_3Sn).

FMA Radioactive waste of “faible et moyenne activité” (low and intermediate activity), the classification depends on the level of activity and on the radionuclides.

FMECA The failure mode, effects, and criticality analysis is a bottom-up, inductive analytical method which may be performed at either the functional or piece/part level. It is used to chart the probability of failure modes against the severity of their consequences. The result highlights failure modes with relatively high probability and severity of consequences, allowing remedial effort to be directed where it will produce the greatest value.

FNAL Fermi National Accelerator Laboratory.

FODO The focusing and defocusing cell is a widespread lattice concept for designing a particle accelerator based on a magnet structure consisting alternately of focusing and defocusing quadrupole lenses.

FPC Fixed power coupler.

FPGA A field-programmable gate array is an integrated circuit designed to be configured by a customer or a designer after manufacturing.

Free (air) cooling Free cooling is an economical method of using low external air temperatures to assist in chilling water, which can then be used for industrial processes, or air conditioning systems.

FSI Frequency scanning interferometry.

GB A gigabyte is by definition of the IEC, 10^9 B.

Gd Gadolinium is a chemical element with symbol Gd and atomic number 64.

Gd₂O₃ Gadolinium(III) oxide is an inorganic compound. It is one of the most commonly available forms of the rare-earth element gadolinium, derivatives of which are potential contrast agents for magnetic resonance imaging.

GEANT4 GEANT4 is a platform for the simulation of the passage of particles through matter using Monte Carlo methods. It is the successor of the GEANT series of software toolkits developed by CERN.

GeniLac A project planned in Geneva to use the water of lake Geneva for cooling and heating of public buildings and international organisations.

GESDEC The “service de géologie, sols et déchets” is the office of the canton and state of Geneva in charge of questions related to excavation materials, ground acquisition and classification, protection of underground volumes and underground water.

GeV 10^9 electronvolt.

Gfitter A generic fitter software for for the statistical analysis of parameter estimation problems in high-energy physics.

GHz 10^9 Hz.

Gif++ The gamma irradiation facility is located in the CERN north area. It combines a ¹³⁷Cs source with a high-energy particle beam from the SPS H4 beam line.

GIM In quantum field theory, the GIM mechanism (or Glashow-Iliopoulos-Maiani mechanism) is the mechanism through which flavour-changing neutral currents (FCNCs) are suppressed in loop diagrams. It also explains why weak interactions that change strangeness by 2 are suppressed, while those that change strangeness by 1 are allowed, but only in charged current interactions.

GIS Geographical information system.

GNSS The global navigation satellite system is the standard generic term for satellite navigation systems that provide autonomous geo-spatial positioning with global coverage. This term includes e.g. the GPS, GLONASS, Galileo, Beidou and other regional systems.

GRI A global research infrastructure is mandated by the G8+5 and addresses worldwide science and technology challenges, following the “GSO Framework for Global Research Infrastructures”. The GSO maintains a list of potential GRIs.

GRN Geodetic reference network.

GSO Group of senior officials mandated by G8+5 to develop GRI concepts.

GTO A gate turn-off thyristor (GTO) is a special type of thyristor, which is a high-power semiconductor device. It acts as a bistable switch, conducting when the gate receives a current trigger, and continuing to conduct until the voltage across the device is reversed biased, or until the voltage is removed. GTOs, as opposed to normal thyristors, are fully controllable switches which can be turned on and off by their third lead, the gate lead.

Guinea-Pig++ An electron-positron beam-beam simulation software developed at CERN.

GV 10^9 volt.

GV (vacuum) Gate valve.

- Gy** The gray (symbol: Gy) is a derived unit of ionising radiation dose in the International System of Units (SI). It is defined as the absorption of one joule of radiation energy per kilogram of matter.
- H** The Higgs boson (symbol: H) is an elementary particle in the Standard Model of particle physics, produced by the quantum excitation of the Higgs field. The particle has a spin of 0.
- H2020** Horizon 2020 is an EU Research and Innovation funding programme over 7 years (2014–2020). It is the financial instrument implementing the “Innovation Union”, a Europe 2020 flagship initiative aimed at securing Europe’s global competitiveness.
- H_c** The critical magnetic field of a superconductor. For current-carrying and magnet applications of a type II superconductor, in practice the upper critical field H_{c2} must be considered instead.
- H_{c2}** The upper critical magnetic field of a type II superconductor, above which the material enters the normal state and does not show superconducting behaviour.
- ha** The hectare is an SI accepted metric system unit of area equal to a square with 100 m sides, or 1 ha = 10 000 m².
- Hadron** A subatomic particle that contains quarks, antiquarks, and gluons, and so experiences the strong force. The proton is the most common hadron.
- HB** Barrel hadron calorimeter.
- HCAL** Hadron calorimeter.
- HCal** Hadron calorimeter.
- HEB** High energy booster.
- HEC** Endcap hadron calorimeter.
- HEH** High energy hadron fluence, i.e. hadrons with energies greater than 20 MeV.
- HEIKA** The high efficiency international Klystron activity was initiated at CERN in 2014 to evaluate and develop new bunching technologies for high-efficiency Klystrons.
- HEL** Hollow electron lens.
- HE-LHC** High-energy large hadron collider. A new particle collider with about twice the LHC collision energy in the existing LHC tunnel, using technologies conceived for the FCC-hh.
- HERA** The hadron-elektron-ringanlage (English: hadron-electron ring accelerator) was a particle accelerator at DESY in Hamburg. It began operating in 1992. At HERA, electrons or positrons were collided with protons at a center of mass energy of 318 GeV. It was the only lepton-proton collider in the world while operating. HERA was closed down on 30 June 2007.
- HF** Hadron forward calorimeter.
- HFSS** A 3D electromagnetic simulation software for designing and simulating high-frequency electronic products from ANSYS.
- HIE-ISOLDE** The high-intensity and energy upgrade of ISOLDE project incorporates a new linear accelerator (linac) into CERN’s ISOLDE facility (isotope mass separator on-line device).
- Higgs boson** An elementary particle linked with a mechanism to model, how particles acquire mass.
- HiRadMat** The high-radiation to materials facility at CERN provides high-intensity pulsed beams to an irradiation area where material samples as well as accelerator component assemblies can be tested.
- HL-LHC** High Luminosity upgrade of the LHC to a levelled constant luminosity of $5 \times 10^{34} \text{ cm}^2 \text{ s}^{-1}$. A dedicated FP7 design study (HiLumi LHC DS) precedes the implementation of the upgrade.
- HLS** Hydrostatic levelling system.

HLT High level trigger.

HOM Higher order modes are undesired Eigenmodes parasitically excited in a resonant (accelerating) radiofrequency cavity.

HTML Hypertext markup language.

HTS High temperature superconductors have critical temperatures above 77 K.

HTTP Hypertext transfer protocol.

HV High voltage.

HVDC High voltage direct current power distribution.

HX Heat exchanger.

Hz The hertz (symbol: Hz) is the derived unit of frequency in the International System of Units (SI) and is defined as one cycle per second.

IBS Iron-based superconductors (IBS) are iron-containing chemical compounds whose superconducting properties were discovered in 2006.

IC Integrated circuit.

ICS Inverse compton scattering.

ICT Information and communications technology.

IDEA The international detector for electron accelerator is a conceptual design for an experiment detector at the FCC-ee.

IEEE The Institute of Electrical and Electronics Engineers is the world's largest association of technical professionals. Its objectives are the educational and technical advancement of electrical and electronic engineering, telecommunications, computer engineering and allied disciplines.

ILC The international linear collider (ILC) is a proposed linear electron-positron particle collider aiming at collision energies of 500 GeV and an upgrade to 1000 GeV (1 TeV).

Impedance A quantity that quantifies the self-interaction of a charged particle beam, mediated by the beam environment, such as the vacuum chamber, RF cavities, and other elements encountered along the accelerator or storage ring.

INFN Istituto Nazionale di Fisica Nucleare.

INJ Injection.

Innovation New ideas that respond to societal or economic needs and generate new products, services, business and organisational models that are successfully introduced into an existing market and are able to create new markets and that contribute value to society.

Invar Invar, also known generically as FeNi36 (64FeNi in the US), is a nickel-iron alloy notable for its uniquely low coefficient of thermal expansion (CTE). The name Invar comes from the word invariable, referring to its relative lack of expansion or contraction with temperature changes. It was invented in 1896 by Swiss physicist Charles Édouard Guillaume. He received the Nobel Prize in Physics in 1920 for this discovery, which enabled improvements in scientific instruments.

Ion An atom or molecule that is not electrically neutral but that carries a positive or negative charge (electrons removed or added).

IP Interaction point.

IPC Incoherent pair creation.

IR Interaction region.

IrCe Iridium-cerium is an alloy used as a photocathode.

ISD Ion-stimulated desorption.

ISO The International Organisation for Standardisation is an international standard-setting body composed of representatives from various national standards organisations.

IT Information technology.

ITER ITER is an international nuclear fusion research and engineering project. It is an experimental Tokamak fusion reactor that is being built next to the Cadarache facility in Saint-Paul-lès-Durance, in Provence, southern France.

ITS Inner tracking system.

J The joule (symbol: J) is a derived unit of energy in the International System of Units. It is equal to the energy transferred to or work done on an object when a force of one newton acts on that object in the direction of its motion through a distance of one metre. It is also the energy dissipated as heat when an electric current of one ampere passes through a resistance of one ohm for one second.

J_c The scientific notation representing the “critical current density” or maximum current that a superconductor can carry. As the current flowing through a superconductor increases, the T_c will usually decrease.

JLab Thomas Jefferson National Accelerator Facility (TJNAF), commonly called Jefferson Lab or JLab.

K See Kelvin.

Karst Karst is a topography formed from the dissolution of soluble rocks such as limestone, dolomite, and gypsum. It is characterized by underground drainage systems with sinkholes and caves.

kB A kilobyte refers traditionally to 1024 bytes. In december 1998, the IEC defined $2^{10} = 1024$ bytes as 1 kibiye (KiB).

KEKB KEBK is a particle accelerator used in the Belle experiment to study CP violation. KEBK is located at the KEK (High Energy Accelerator Research Organisation) in Tsukuba, Ibaraki Prefecture, Japan.

Kelvin Unit of measurement for temperature (K) using as null point the absolute zero, the temperature at which all thermal motion ceases. $0\text{ K} = -273.15^\circ\text{C}$.

keV 10^3 electronvolt.

kg The kilogram or kilogramme (symbol: kg) is the base unit of mass in the International System of Units (SI), and is defined as being equal to the mass of the International Prototype of the Kilogram (IPK, also known as “Le Grand K” or “Big K”), a cylinder of platinum-iridium alloy stored by the International Bureau of Weights and Measures at Saint-Cloud, France.

KLOE A particle physics experiment at the INFN Frascati National Laboratory, Italy

KlyC Software developed at CERN for the optimisation and design of high efficiency Klystrons based on new bunching mechanisms.

Klystron A specialised linear-beam vacuum tube, which is used as an amplifier for high radio frequencies.

Kr Krypton is a chemical element with symbol Kr and atomic number 36.

kW 10^3 Watt.

l The litre (SI spelling) or liter (American spelling) (symbol l in this document) is an SI accepted metric system unit of volume equal to 1000 cubic centimetres or 1/1000 cubic metre.

L* The distance from the IP to the start of the magnetic field of the first magnet closest to the IP. The physical equipment is larger and is closer to the IP.

LAL Laboratoire de l’Accélérateur Linéaire (LAL) of CNRS in Orsay in France.

LAr Liquid argon.

LASE Laser-ablated surface engineering.

Lattice In accelerator physics, a magnetic lattice is a composition of electromagnets at given longitudinal positions around the vacuum tube of a particle accelerator, and thus along the path of the enclosed charged particle beam. Many lattices are composed of identical substructures or cells, which denote a special magnet arrangement that may reoccur at several positions along the path.

LCB Lower cold box.

LCBI Longitudinal coupled bunch instability.

LCCS Local Chromatic Correction System.

LEP The large electron-positron collider, which was operated at CERN until 2000.

LEP3 A concept for an electron-positron collider in the existing LHC tunnel with a centre-of-mass of 240 GeV and a peak luminosity of $1 \times 10^{34} \text{ cm}^{-2} \text{ s}^{-1}$ at each of two experiments.

Lepton A class of elementary particles that do not experience the strong force. The electron is the most common lepton.

LF Low field.

LFV Lepton flavour violation.

LGAD Low gain avalanche detectors.

LHC The large hadron collider is a circular particle collider for protons and heavy ions with a design centre-of-mass energy of 14 TeV for proton-proton collisions at a peak luminosity of $1 \times 10^{34} \text{ cm}^2 \text{ s}^{-1}$ at CERN in Geneva, Switzerland.

LHCb The large hadron collider beauty experiment is one of the seven particle detector experiments constructed at the LHC.

LHeC A study to extend the current LHC collider with an energy recovery linac (ERL) to generate electron beams and to collide them with high-energetic proton or ion beams of the LHC.

LIL LEP injector linac.

Limestone Limestone is a sedimentary rock, composed mainly of skeletal fragments of marine organisms such as coral, forams and molluscs. Its major materials are the minerals calcite and aragonite, which are different crystal forms of calcium carbonate (CaCO_3).

Linac A linear accelerator for charged particles in which a number of successive radiofrequency cavities that are powered and phased such that the particles passing through them receive successive increments of energy.

Linac4 The linear accelerator 4 at CERN accelerates negative hydrogen ions (H^- , consisting of a hydrogen atom with an additional electron) to 160 MeV to prepare them to enter the PSB (proton synchrotron booster), which is part of the LHC injection chain.

LIU LHC injector upgrade.

LLRF Low Level RF.

LN_2 Liquid nitrogen is nitrogen in a liquid state at an extremely low temperature.

LSP Lightest supersymmetric particle.

LSS Long straight section: quasi-straight segments of a circular collider, which are available for beam interactions or utility insertions (e.g. injection, extraction, collimation, RF).

LTO Lithium titanium oxide.

LTS Low temperature superconductors have critical temperatures below 77 K.

Luminometer A calorimeter inside the detector to precisely measure the luminosity.

Luminosity Luminosity is the rate of collision events normalised to the cross section. It is expressed as inverse square centimetre and inverse second ($\text{cm}^{-2} \text{ s}^{-1}$) or barn ($1 \text{ barn} = 10^{-24} \text{ cm}^2$).

LV Low voltage.

MAC The medium access control sublayer and the logical link control (LLC) sublayer together make up the data link layer (DLL). Within that data link layer, the LLC provides flow control and multiplexing for the logical link (i.e. EtherType, 802.1Q VLAN tag), while the MAC provides flow control and multiplexing for the transmission medium. MAC is responsible for the transmission of data packets to and from the network-interface card, and to and from another remotely shared channel.

MAD-X MAD-X is a project and computational physics software to aid particle accelerator design and simulation.

MADX-PTC MAD X polymorphic tracking code.

MAPS Monolithic active pixel sensor. A silicon detector technology for high-energy physics particle detectors.

MB A megabyte are by definition of the IEC, 1 000 000 bytes (10^6 B).

MC Main corrector magnet.

MCHF 10^6 CHF.

MD (magnet) Main dipole.

MDI The machine detector interface refers to the topics and regions where the beamlines of the accelerator overlap with the physics experiment's detector. Key elements include mechanical support of final beamline elements, luminosity monitoring, feedback, background suppression and radiation shielding.

MDISim A tool set developed in the frame of the FCC study for Machine Detector Interface SIMulations using and combining the standard tools MAD-X, ROOT and GEANT4.

MDT Monitored drift tube.

MEG A particle physics experiment at the Paul Scherrer Institute, Switzerland.

MeV 10^6 electronvolt.

MgB₂ Magnesium diboride is the inorganic compound. It is a dark gray, water-insoluble solid. The compound becomes superconducting at 39 K.

MGy 10^6 gray.

MHz 10^6 Hz

MI Microwave instability.

MIIT Millions of amp squared seconds. A performance indicator of a superconducting cable that determines two primary factors of the adequate quench protection system: how quickly the current in the magnet must be reduced once a quench is detected and how quickly a quench must be detected, once the initiating spot quenches.

MJ 10^6 J.

MLI Multi layer insulation.

mm 10^{-3} m

MO Main octupole corrector magnet.

Molasse Variable sedimentary deposits comprising sandstones, shales and conglomerates that form as terrestrial or shallow marine deposits in front of rising mountain chains. It is the typical soil type found in the Franco-Geneva basin.

MolFlow+ Software developed at CERN to calculate the pressure in an arbitrarily complex geometry when ultra-high vacuum condition is met.

MOSFET Metal-oxide-semiconductor field-effect transistor.

MoU Memorandum of understanding.

MP Medium pressure, around 20 bar.

MPGD Micro pattern gas detector.

MQ Main quadrupole.

MQDA Main quadrupole dispersion suppressor magnet.

MQS Main quadrupole skew magnet.

MQT Main quadrupole tuning magnet.

MQTL Main quadrupole trim magnet.

MRI Magnetic resonance imaging.

MRN Metrological reference network.

MS Main sextupole.

MTE Multi turn extraction.

MTTF Mean time to failure.

MTTR Mean time to repair.

MVDC Medium voltage direct current power distribution.

MW 10^6 Watt

N The newton (symbol: N) is the SI unit of force. A newton is how much force is required to make a mass of one kilogram accelerate at a rate of one metre per second squared.

NASA National Aeronautics and Space Administration.

Nb Niobium, formerly known as columbium, is a chemical element with symbol Nb (formerly Cb) and atomic number 41. It is a soft, grey, crystalline, ductile transition metal, often found in the minerals pyrochlore and columbite, hence the former name “columbium”. Niobium is used in various superconducting materials.

Nb₃Sn An intermetallic compound of niobium (Nb) and tin (Sn) with the A15 structure, and a type II LTS with $T_c = 18.3$ K and $H_{c2} = 25$ T.

NbTi Niobium-titanium is an alloy of niobium (Nb) and titanium (Ti) and a type II LTS with $T_c = 9.5$ K. Nb–Ti wires, containing Nb–Ti filaments in an aluminium or copper matrix, are produced industrially and are used in the majority of superconducting magnets.

NEG Non-evaporable getter materials are mostly porous alloys or powder mixtures of Al, Zr, Ti, V and iron (Fe). They help to establish and maintain vacuums by soaking up or bonding to gas molecules that remain within a partial vacuum.

Nelium A light gas mixture made of neon and helium.

NEXTorr A patented flanged vacuum pumping solution, combining NEG and ion pumping technologies by the saes group, Milan, Italy.

NIE The notice d’impact sur l’environnement is an assembly of the results of environmental impact assessments for large projects in Switzerland.

NMR Nuclear magnetic resonance.

NN Neural network.

NPV Net Present Value is a measurement of profit calculated by subtracting the present values (PV) of cash outflows (including initial cost) from the present values of cash inflows over a period of time. It is determined by calculating the costs (negative cash flows) and benefits (positive cash flows) for each period of an investment. After the cash flow for each period is calculated, the PV of each one is obtained by discounting its future value at a periodic rate of return.

NTU The number of transfer units is defined as a ratio of the overall thermal conductance to the smaller heat capacity rate. It may also be interpreted as the relative magnitude of the heat transfer rate compared to the rate of enthalpy change of the smaller heat capacity rate fluid.

NuPECC Nuclear physics European Collaboration Committee.

\mathcal{O} Big O notation is a mathematical notation that describes the limiting behavior of a function when the argument tends towards a particular value or infinity.

OBS Organisation breakdown structure.

ODH Oxygen deficiency hazard.

OEIE The ordonnance relative à l’étude de l’impact sur l’environnement is the Swiss environmental impact assessment regulation.

- OFHC** Oxygen-free copper (OFC) or oxygen-free high thermal conductivity (OFHC) copper is a group of wrought high conductivity copper alloys that have been electrolytically refined to reduce the level of oxygen to 0.001% or below.
- OPEX** An operating expense, operating expenditure, operational expense, operational expenditure or opex is an ongoing cost for running a product, business, or system.
- Optics** An optical configuration refers to a powering scheme of the magnets. There can be several different optics for a single lattice configuration. Different optics exist for instance, for injection and for luminosity operation corresponding to different β^* values in the experiment insertions.
- ORC** The organic rankine cycle is named for its use of an organic, high molecular mass fluid with a liquid-vapor phase change, or boiling point, occurring at a lower temperature than the water-steam phase change. The fluid allows Rankine cycle heat recovery from lower temperature sources. The low-temperature heat is converted into useful work, that can itself be converted into electricity.
- OSI** The open systems interconnection model is a conceptual model that characterises and standardises the communication functions of a telecommunication or computing system without regard to its underlying internal structure and technology.
- OSI Model** The open systems interconnection model is a conceptual and logical layout that defines network communication used by systems open to interconnection and communication with other systems.
- Overburden** Material (rock, soil) that lies above an underground structure, e.g. a tunnel or cavern.
- Pa** The pascal is the SI derived unit of pressure. A common multiple unit of the pascal is the hectopascal (1 hPa = 100 Pa) which is equal to one millibar.
- Pandora PFA** The pandora particle flow algorithm is an event reconstruction software developed for future linear collider studies ILC and CLIC.
- Pb** Lead is a chemical element with symbol Pb (from the Latin plumbum) and atomic number 82.
- PBR** The pre booster ring is an injector to the booster top-up ring (BR), which continuously provides the particle collider with particles at collision energy.
- PBS** Product breakdown structure.
- PCB** Printed circuit board.
- PCO** Power CONverter.
- PDF** The parton name was proposed by Richard Feynman in 1969 as a generic description for any particle constituent within the proton, neutron and other hadrons. These particles are referred today as quarks and gluons. A parton distribution function is defined as the probability density for finding a particle with a certain longitudinal momentum fraction at a certain resolution scale.
- PEDD** Peak energy deposition density.
- PEP-II** The PEP-II facility consists of two independent storage rings, one located atop the other in the at the Stanford Linear Accelerator Center (SLAC). The high-energy ring, which stores a 9 GeV electron beam, was an upgrade of the existing Positron-Electron Project (PEP) collider; it reused all of the PEP magnets and incorporated a state-of-the-art copper vacuum chamber and a new radio-frequency system capable of supporting a stored beam of high current. The low-energy ring, which stores 3.1 GeV positrons, was newly constructed. Injection is achieved by extracting electrons and positrons at collision energies from the SLC and transporting them each in a dedicated bypass line. The low-emittance Stanford Linear Collider (SLC) beams are used for the injection process. The collider was completed in July 1998.

PERLE Powerful energy recovery Linac for experiments, an envisaged test facility for an energy recovery linac (ERL) at Laboratoire de l'Accélérateur Linéaire (LAL) of CNRS in Orsay in France.

PFL Pulse forming line.

PFN Pulse forming network.

pH A logarithmic scale used to specify the acidity or basicity of an aqueous solution. It is approximately the negative of the base 10 logarithm of the molar concentration, measured in units of moles per liter, of hydrogen ions.

Phase Space A six-dimensional space consisting of a particle's position (x, y, z) and divergence (x', y', z'). Phase space is represented in two dimensions by plotting position on the horizontal axis and the corresponding divergence on the vertical axis.

PHY In the seven-layer OSI model of computer networking, the physical layer or layer 1 is the first and lowest layer. This layer may be implemented by a dedicated PHY chip. The physical layer consists of the electronic circuit transmission technologies of a network.

Pile-up The situation where a particle detector is affected by several events at the same time.

PIT The powder-in-tube process is often used for making electrical conductors from brittle superconducting materials such as niobium-tin or magnesium diboride and ceramic cuprate superconductors such as BSCCO.

PLC Programmable logic controller.

PMNS The Pontecorvo-Maki-Nakagawa-Sakata matrix, Maki-Nakagawa-Sakata matrix (MNS matrix), lepton mixing matrix, or neutrino mixing matrix is a unitary mixing matrix which contains information on the mismatch of quantum states of neutrinos when they propagate freely and when they take part in the weak interactions. It is a model of neutrino oscillation. This matrix was introduced in 1962 by Ziro Maki, Masami Nakagawa and Shoichi Sakata, to explain the neutrino oscillations predicted by Bruno Pontecorvo.

PMT Photomultiplier tube.

pNGB Pseudo Nambu-Goldstone boson.

PoT Protons on target.

PPLP Parabolic parabolic linear parabolic.

ppm Parts per million (10^{-6}).

PS The proton synchrotron is a particle accelerator at CERN. It was CERN's first synchrotron, beginning operation in 1959. It has since served as a pre-accelerator for the ISR (intersecting storage rings) and the SPS (super proton synchrotron), and is currently part of the LHC (large hadron collider) accelerator complex. In addition to protons, PS has accelerated alpha particles, oxygen and sulphur nuclei, electrons, positrons and antiprotons.

PSB The proton synchrotron booster at CERN is an accelerator made up of four superimposed synchrotron rings that receive beams of protons from the linear accelerator Linac 2 or 4 at 50 MeV and accelerate them to 1.4 GeV for injection into the PS (proton synchrotron).

PSD Photon stimulation desorption is a phenomenon whereby a substance is released from or through a surface.

PSO In computational science, particle swarm optimisation is a computational method that optimises a problem by iteratively trying to improve a candidate solution with regard to a given measure of quality. It solves a problem by having a population of candidate solutions, here dubbed particles, and moving these particles around in the search-space according to simple mathematical formulae over the particle's position and velocity. Each particle's movement is influenced by its local best known position, but is also guided toward the best known positions

in the search-space, which are updated as better positions are found by other particles. This is expected to move the swarm toward the best solutions.

PU Pile-up.

PV Photovoltaics.

PVSS Prozessvisualisierungs- und steuerungssoftware. A SCADA product from SIEMENS company ETM professional control now called WinCC OA.

Px One of the 12 FCC access points. x can be one of A, B, C, D, E, F, G, H, I, J, K, L, e.g. PA is the access point A close to the CERN Meyrin site.

PyHEADTAIL A macroparticle tracking software designed specifically to simulate collective effects in circular accelerators.

Pythia A Monte Carlo event generator software.

Q The quality factor or Q factor is a dimensionless parameter that describes how underdamped an oscillator or resonator is, and characterises a resonator's bandwidth relative to its centre frequency. Higher Q indicates a lower rate of energy loss relative to the stored energy of the resonator. For an RF cavity it characterises RF losses in the cavity: an RF cavity having a higher Q factor is a more efficient user of RF power.

QC1 First final focus quadrupole next to the IP.

QC2 Second final focus quadrupole, behind QC1.

QCD In theoretical physics, quantum chromodynamics is the theory of the strong interaction between quarks and gluons, the fundamental particles that make up composite hadrons such as the proton, neutron and pion.

QD Defocusing quadrupole.

QED In particle physics, quantum electrodynamics is the relativistic quantum field theory of electrodynamics.

QF Focusing quadrupole.

QFT Quantum field theory.

QGP Quark gluon plasma.

QPS Quench protection system.

QPU Quench processing unit.

QRL Cryogenic distribution line.

QS Quench instrumentation units in the tunnel.

Quench The change of state in a material from superconducting to resistive. If uncontrolled, this process damages equipment due to thermal stress induced by the extremely high-currents passing through the material.

R&D Research and development refers to activities to develop new services and products, or to improve existing services and products. Research and development constitutes the first stage of development of a potential new service or the production process.

R2E Radiation to electronics.

rad The radian (SI symbol rad) is the SI unit for measuring angles. The length of an arc of a unit circle is numerically equal to the measurement in radians of the angle that it subtends; 360° correspond to 2π rad.

RAMS Reliability, availability, maintainability and safety. Four non-functional key characteristics that determine the performance and total cost of technical systems.

RD52 A research and development project at CERN, carried out by an international collaboration, to develop a detector technology for a future electron-positron particle collider using the simultaneous measurement of scintillation light and Čerenkov light generated in the shower development process.

RDC Radiation dependent capacitor.

RDP Resonant depolarisation.

RDR Radiation dependent resistor.

ReBCO Rare-earth barium copper oxide is a family of chemical compounds known for exhibiting high temperature superconductivity.

RF Radiofrequency.

RF cavity An electromagnetically resonant cavity used to convey energy (accelerate) to charged particles as they pass through by virtue of the electric field gradient across the cavity gap(s). Radio Frequency is a rate of oscillation in the range of around 3 kHz–300 GHz.

RH Relative humidity is the ratio of the partial pressure of water vapor to the equilibrium vapor pressure of water at a given temperature. Relative humidity depends on temperature and the pressure of the system of interest. The same amount of water vapor results in higher relative humidity in cool air than warm air.

RHA Radiation hardness assurance.

RI A research infrastructure is a facility, a set of resources and services that are used by research communities to conduct research and foster innovation in their fields. This includes major scientific equipment or sets of instruments, knowledge-based resources such as collections, archives and scientific data, e-infrastructures, such as data and computing systems and communication networks and any other tools that are essential to achieve excellence in research and innovation.

RMC Racetrack model coil.

RMM Racetrack model magnet.

RMS The root mean square is square root of the arithmetic mean of the squares of a set of numbers.

Roadheader Excavation equipment consisting of a boom mounted cutting head with a hydraulic mechanism.

Rockbreaker A hydraulically powered tool used to break up rock during the excavation process.

RoHS The restriction of hazardous substances directive 2002/95/EC, (RoHS 1), short for directive on the restriction of the use of certain hazardous substances in electrical and electronic equipment, was adopted in February 2003 by the European Union.

ROOT ROOT is a modular scientific software toolkit. It provides functionalities needed to deal with big data processing, statistical analysis, visualisation and storage.

ROXIE Software developed at CERN for the electromagnetic simulation and optimisation of accelerator magnets.

RPC Resistive plate chamber.

RRP The restacked-rod restack process is a manufacturing process for Nb₃Sn wires developed by the OST company (Oxford instruments technologies), which has been subsequently acquired by BEST Inc. (Bruker Energy and Supercon. Technologies).

RRR The residual resistivity ratio is defined as the ratio of the electrical resistivity of a material at room temperature and at a chosen cryogenic temperature. For superconducting materials, a cryogenic temperature above T_c must be chosen. RRR serves as a measure of the purity and overall quality of a sample: as electrical resistivity usually increases as defect prevalence increases, a large RRR is associated with a pure sample.

RTE Réseau de Transport d'Électricité is the French electricity transmission system operator. It is responsible for the operation, maintenance and development of the French high-voltage transmission system.

- RW** The resistive wall impedance is one of the main sources for beam instabilities in synchrotrons and storage rings.
- S** The siemens (symbol: S) is the derived unit of electric conductance, electric susceptance and electric admittance in the International System of Units (SI). Conductance, susceptance, and admittance are the reciprocals of resistance, reactance, and impedance respectively; hence one siemens is redundantly equal to the reciprocal of one ohm, and is also referred to as the mho.
- \sqrt{s} The total centre of mass energy of the colliding particles.
- S band** The S band is a designation by the IEEE (institute of electrical and electronics engineers) for a part of the microwave band of the electromagnetic spectrum covering frequencies from 2 to 4 gigahertz.
- S275JR** A structural steel grade according to EN 10025: part 2: 2004.
- SAD** Strategic accelerator design is a software tool for particle accelerator design developed at KEK since 1986.
- SC coating** A very thin layer of superconducting material on normal-conducting material (e.g. copper). Used for various purposes such as quench avoidance of a neighbouring superconductor, reduction of production costs due to use of cheaper support material and impedance reduction.
- SCADA** Supervisory control and data acquisition.
- SCP** The “Structure de Concertation Permanente” federates representatives of CERN, the Swiss federal and cantonal governments as well as the Swiss permanent mission at the international organisations in order to work in common on adequate administrative frameworks for CERN’s operation and future developments on Swiss territory.
- scSPS** The superconducting SPS is a superconducting synchrotron, replacing the current SPS accelerator at CERN.
- SDA** The “surfaces d’assolement” are land plots in Switzerland, which are reserved for potential agricultural purposes in the event of crisis. They are not constructible.
- SEE** Single event effect is a general class of radiation effects in electronic devices. There are two types of effects: those which cause permanent damage to the equipment’s functionality and those, which cause a transient fault.
- SEM** A scanning electron microscope (SEM) is a type of electron microscope that produces images of a sample by scanning the surface with a focused beam of electrons.
- SESAME** The synchrotron-light for experimental science and applications in the middle east is a third-generation synchrotron light source. SESAME is located in Allan, Jordan (30 km from Amman and 30 km from the King Hussein/Allenby Bridge crossing of the Jordan River).
- SEU** A single event upset is a change of state caused by one single ionising particle (ions, electrons, photons) striking a sensitive node in a micro-electronic device, such as in a microprocessor, semiconductor memory, or power transistor. It is not considered to permanently damage the equipment’s functionality. It is an example of a general class of radiation effects in electronic devices called single event effects (SEE).
- SEY** Secondary electron yield.
- SFOE** The Swiss Federal Office of Energy.
- SFOPT** Strongly first order phase transition.
- SGAR** The Secretariat Général de la région Auvergne-Rhône-Alpes assists the prefect of the region in the implementation of the government’s policies in the region.
- Shotcrete** A sprayed concrete lining that is projected at high velocity via a hose onto a surface.

- SI** The international system of units (SI, abbreviated from the French système international (d'unités)) is the modern form of the metric system, and is the most widely used system of measurement. It comprises a coherent system of units of measurement built on seven base units that are ampere, kelvin, second, metre, kilogram, candela, mole, and a set of twenty prefixes to the unit names and unit symbols that may be used when specifying multiples and fractions of the units. The system also specifies names for 22 derived units, such as lumen and watt, for other common physical quantities.
- SiC** Silicon carbide (SiC) devices belong to the so-called wide band gap semiconductor group. They offer a number of attractive characteristics for high voltage power semiconductors when compared to commonly used silicon (Si). In particular, the much higher breakdown field strength and thermal conductivity of SiC allow devices to be created which by far outperform the corresponding Si ones. This way previously unattainable efficiency levels can be achieved.
- SiD** The silicon detector is a conceptual design for an experiment detector at the ILC.
- SiPM** Silicon photomultiplier.
- SIRIUS** Sirius is a synchrotron light source facility based on a 4th generation low emittance storage ring that is under construction in Campinas, Brazil.
- SITROS** A tracking program developed at DESY in 1983 for the simulation of polarising and depolarising effects in electron-positron storage rings.
- Sixtrack** A single particle 6D symplectic tracking code optimised for long term tracking in high energy particle accelerators.
- SLC** Stanford Linear Collider.
- Slurry shield TBM** A TBM fitted with a full face cutterhead which provides face support by pressurizing boring fluid inside the cutterhead chamber. These machines are most suited for tunnels through unstable material subjected to high groundwater pressure or water inflow that must be stopped by supporting the face with a boring fluid subjected to pressure.
- SM** Standard Model.
- SMC** Short model coil.
- sMDT** Small diameter muon drift tube.
- SME** Small and medium-sized enterprises.
- SMEFT** The Standard Model effective field theory is a model independent framework for parameterising deviations from the Standard Model in the absence of light states.
- SMS** A safety management system integrates autonomously working safety-related subsystems for higher-level operation, such as intrusion alarms, entrance and access control systems, fire and smoke detection, communication with public emergency services, public address and evacuation systems and many more.
- SPN** Support pre-alignment network.
- SPS** The super proton synchrotron is a particle accelerator at CERN. It is housed in a circular tunnel, 6.9 km in circumference and delivers beams to fixed target experiments and the LHC.
- SPT** The standard penetration test is an in-situ dynamic penetration test designed to provide information on the geotechnical engineering properties of soil. The test procedure is described in ISO 22476-3, ASTM D1586 and Australian Standards AS 1289.6.3.1.
- SR** Synchrotron radiation.
- SRF** Superconducting radiofrequency.
- SSM** Sequential Standard Model.
- SSS** Short straight section.

Standard Model The Standard Model explains how the basic building blocks of matter interact, governed by four fundamental forces.

STATCOM Static synchronous compensator.

STFC Science and Technology Facilities Council in the UK.

Storz Storz is a type of hose coupling invented by Carl August Guido Storz in 1882 and patented in Switzerland in 1890, and patented in the U.S. in 1893 that connects using interlocking hooks and flanges. It is widely used on fire hoses in firefighting applications.

Strand A superconducting strand is a composite wire containing several thousand superconducting filaments (e.g. Nb_3Sn) dispersed in a matrix with suitably small electrical resistivity properties (e.g. copper).

Strong force One of four known fundamental forces (the others are the weak force, electromagnetism and gravity). The strong force is felt only by quarks and gluons, and is responsible for binding quarks together to make hadrons. For example, two up quarks and a down quark are bound together to make a proton. The strong interaction is also responsible for holding protons and neutrons together in atomic nuclei.

Superconducting cable Superconducting cables are formed from several superconducting strands in parallel, geometrically arranged in the cabling process to achieve well-controlled cable geometry and dimensions, while limiting the strand deformation in the process. Cabling several strands in parallel results in an increase of the current carrying capability and a decrease of the inductance of the magnet, easing protection.

Superconductivity A property of some materials, usually at very low temperatures that allows them to carry electricity without resistance.

Superferroc magnet An iron-dominated magnet based on a magnetic steel structure with a minimal amount of superconductor. The structure is the same as a normal conducting magnet, but the coil is built from superconducting material. The yoke is cooled to cryogenic temperature.

SuperKEKB SuperKEKB is a particle accelerator located at KEK (High Energy Accelerator Research Organisation) in Tsukuba, Ibaraki Prefecture, Japan. SuperKEKB will collide electrons at 7 GeV with positrons at 4 GeV. The accelerator is an upgrade of KEKB, providing approximately 40 times higher luminosity, due mostly to superconducting quadrupole focusing magnets.

SUSY Supersymmetry.

Synchrotron A circular machine that accelerates subatomic particles by the repeated action of electric forces generated by RF fields at each revolution. The particles are maintained on constant circular orbits by synchronously increasing the magnetic fields.

Synchrotron Radiation Electromagnetic radiation generated by acceleration of relativistic charged particles in a magnetic or electric field. Synchrotron radiation is the major mechanism of energy loss in synchrotron accelerators and contributes to electron-cloud build-up.

SynRad+ A modified MolFlow+ software developed at CERN to trace photons in order to calculate flux and power distribution caused by synchrotron radiation on a surface.

t The “metric ton” is a unit of measure. It corresponds to 1000 kg in this document.

T_c The critical temperature of a superconducting material, above which material enters the normal state and does not show superconducting behaviour.

Tantalum Tantalum is a chemical element with symbol Ta and atomic number 73. It is a rare, hard, blue-gray, lustrous transition metal that is highly corrosion-resistant. It is part of the refractory metals group, which are widely used as minor

components in alloys. The chemical inertness of tantalum makes it a valuable substance for laboratory equipment and a substitute for platinum.

TBA Triple bend achromat.

TBM A tunnel boring machine is a machine used to excavate tunnels with a circular cross section through a variety of soil and rock strata. They can bore through anything from hard rock to sand. Tunnel diameters can range from one metre to more than 17 m to date.

TCLA Active tungsten absorber.

TCLD Dispersion suppression collimator.

TCO Total cost of ownership.

TCP Primary collimator.

TCSG Secondary collimator.

Technology Spillover Technology spillover refers to the unintentional technological benefits to firms coming from the research and development efforts of other organisations without the costs being shared.

TEM Transmission electron microscopy (TEM) is a microscopy technique in which a beam of electrons is transmitted through a specimen to form an image.

Tesla Unit of magnetic field strength. 1 T is the field intensity generating one newton (N) of force per ampere (A) of current per metre of conductor.

TETRA Terrestrial trunked radio, a European standard for a trunked radio system, is a professional mobile radio and two-way transceiver specification.

TeV Tera electron Volts (10^{12} eV). Unit of energy. 1 eV is the energy given to an electron by accelerating it through 1 Volt of electric potential difference.

Tevatron A 2 TeV proton on anti-proton collider that was operated at Fermilab in Batavia, Illinois (USA) until 2011. The top quark was discovered using this collider.

TFA Radioactive waste of “très faible activité” (very low level activity), the classification depends on the level of activity and on the radionuclides.

Thyratron A type of gas-filled tube used as a high-power electrical switch and controlled rectifier. Thyratrons can handle much greater currents than similar hard-vacuum tubes. Electron multiplication occurs when the gas becomes ionised, producing a phenomenon known as Townsend discharge.

TID Total ionising dose.

TileCal TileCal is a hadronic calorimeter covering the most central region of the ATLAS experiment at the LHC.

TLEP A concept for a circular electron-positron collider in a new 80–100 km long tunnel acting as a Tera-Z factory

TM Transverse magnetic modes have no magnetic field in the direction of propagation.

TM₂₁₀ In rectangular waveguides, rectangular mode numbers are designated by two suffix numbers attached to the mode type, such as TM_{mn} , where m is the number of half-wave patterns across the width of the waveguide and n is the number of half-wave patterns across the height of the waveguide. In circular waveguides, circular modes exist and here m is the number of full-wave patterns along the circumference and n is the number of half-wave patterns along the diameter.

TMCI Transverse model coupling instability.

TOT The tunnel optimisation tool is software that has been developed under a cooperation contract for CERN by the company ARUP (UK).

TRL Technology readiness levels (TRLs) are indicators of the maturity level of particular technologies. This measurement system provides a common understanding of technology status and addresses the entire innovation chain. There are nine technology readiness levels; TRL 1 being the lowest and TRL 9 the highest.

TTB Turbo Brayton box.

Tungsten Tungsten, or wolfram is a chemical element with symbol W and atomic number 74.

UFO Unidentified falling object.

UNESCO The United Nations Educational, Scientific and Cultural Organization is a specialised agency of the United Nations based in Paris.

UPS Uninterruptible power supply.

V The volt (symbol: V) is the derived unit for electric potential, electric potential difference (voltage), and electromotive force.

VA A volt-ampere is the unit used for the apparent power in an electrical circuit, equal to the product of root-mean-square (RMS) voltage and RMS current. In direct current (DC) circuits, this product is equal to the real power (active power) in watts. Volt-amperes are useful only in the context of alternating current (AC) circuits.

Vacuum Pressures much below atmospheric pressure.

Variant A variant of a product has a specific set of characteristics that distinguish it from other products in the same product line. All variants are derived from a common base and share common design features. The development of different variants is managed by distinct processes and different variants co-exist at the same time.

VBF Vector boson fusion.

Version A version of a product represents that same product at a different time. It may or may not have undergone some change (revision).

VFET Vacuum field-effect transistor.

VLP Very low pressure.

VSM An established compact shaft sinking technology for all ground conditions for soft and stable soils, originally developed by Herrenknecht AG.

VXD CLD vertex detector.

W (particle) The W and Z bosons are together known as the weak or more generally as the intermediate vector bosons. They mediate the weak interaction. The W bosons have either a positive or negative electric charge of 1 elementary charge and are each other's antiparticles. The particles have a spin of 1.

W (Watt) The watt (symbol W) is a unit of power. In the international system of units (SI) it is defined as a derived unit of 1 joule per second, and is used to quantify the rate of energy transfer.

WBS Work breakdown structure.

WCS Warm compressor station.

Weak force A force carried by heavy particles known as the W and Z bosons. The most common manifestation of this force is beta decay, in which a neutron in a nucleus is transformed into a proton, by emitting an electron and a neutrino. Weak neutral current is a very weak interaction mediated by the Z boson that is independent of the electric charge of a particle. Particles can exchange energy through this mechanism, but other characteristics of the particles remain unchanged.

Willingness To Pay An indicator of how much a person values a product or device, measured by the maximum amount she or he would pay to acquire one.

WIMP Weakly interacting massive particles are hypothetical particles that are thought to constitute dark matter.

WinCC OA WinCC Open Architecture is a SCADA system for visualising and operating processes, production flows, machines and plants in all lines of business. It was formerly called PVSS.

WLS Wave length shifting.

WPS Wire positioning sensors.

Xe Xenon is a chemical element with symbol Xe and atomic number 54.

XFEL A free-electron laser generating high-intensity electromagnetic radiation by accelerating electrons to relativistic speeds and directing them through special magnetic structures.

XRD X-ray powder diffraction (XRD) is a rapid analytical technique primarily used for phase identification of a crystalline material and can provide information on unit cell dimensions. The analysed material is finely ground, homogenised, and average bulk composition is determined.

YBCO Yttrium barium copper oxide is a family of crystalline chemical compounds, displaying high-temperature superconductivity. YBCO is often categorised as a rare-earth barium copper oxide (REBCO).

Z The W and Z bosons are together known as the weak or more generally as the intermediate vector bosons. They mediate the weak interaction. The Z boson is electrically neutral and is its own antiparticle. The particles has a spin of 1.

ZrTiV A zirconium-titanium-vanadium alloy that is used as a coating for a large surface getter pump.

References

1. CERN Council, *European strategy session of Council*, CERN-Council-S/106 (May 30, 2013)
2. *Future Circular Collider Study Kickoff Meeting* (University of Geneva, February 12–15, 2014), <http://indico.cern.ch/e/fcc-kickoff>
3. E. Todesco, F. Zimmermann (eds.), *Proceedings of EuCARD-AccNet-EuroLumi workshop: The High-Energy Large Hadron Collider – HE-LHC10*, Malta, CERN-2011-003 (October 14–16, 2010), [arXiv:1111.7188](https://arxiv.org/abs/1111.7188) [physics.acc-ph]
4. J. Osborne, C. Waaijer, *Pre-feasibility assessment for an 80 km tunnel project at CERN*, contribution to the update of the European Strategy for Particle Physics **165** (July 27, 2012), <http://indico.cern.ch/event/175067/call-for-abstracts/165/file/1.pdf>
5. *Joint Snowmass-EuCARD/AccNet-HiLumi meeting “Frontier Capabilities for Hadron Colliders 2013” a.k.a. EuCARD VHE-LHC Day*, CERN (February 21–22, 2013), <http://indico.cern.ch/event/223094>
6. A. Blondel, F. Zimmermann, *A High Luminosity e^+e^- collider in the LHC tunnel to study the Higgs boson* (2011), [arXiv:1112.2518](https://arxiv.org/abs/1112.2518) [hep-ex]
7. EuCARD LEP3 workshop (June 18, 2012); 2nd EuCARD LEP3 workshop (October 23, 2012); 3rd EuCARD TLEP3 workshop (January 10, 2013); 4th EuCARD TLEP workshop (April 4–5, 2013)
8. The TLEP Design Study Working Group, *JHEP* **1**, 164 (2014)
9. D. Schulte, *ICFA Beam Dyn. Newslett.* **72**, 99 (2017)
10. B. Richter, *Nucl. Instr. Methods* **136**, 47 (1976)
11. P. Raimondi, D. Shatilov, M. Zobov, *Beam-Beam Issues for Colliding Schemes with Large Piwinski Angle and Crabbed Waist* (2007), [arXiv:physics/0702033](https://arxiv.org/abs/physics/0702033) [physics.acc-ph]
12. P. Raimondi, D. Shatilov, M. Zobov, *Conf. Proc. C070625*, 1469 (2007)
13. T. Behnke, J.E. Brau, B. Foster, J. Fuster, M. Harrison, J. McEwan Paterson, M. Peskin, M. Stanitzki, N. Walker, H. Yamamoto, *The International Linear Collider Technical Design Report – Volume 1: Executive Summary* (2013), [arXiv:1306.6327](https://arxiv.org/abs/1306.6327) [physics.acc-ph]

14. Linear Collider Board, *Conclusions on the 250 GeV ILC as a Higgs Factory proposed by the Japanese HEP community*, Presentation (November, 2017) <http://icfa.fnal.gov/wp-content/uploads/LCB-Short-Conclusion-Nov2017.pdf>
15. K. Fujii, C. Grojean, M.E. Peskin, T. Barklow, Y. Gao, S. Kanemura, H. Kim, J. List, M. Nojiri, M. Perelstein, R. Poeschl, J. Reuter, F. Simon, T. Tanabe, J.D. Wells, J. Yu, M. Berggren, M. Habermehl, S. Jung, R. Karl, T. Ogawa, J. Tian, J. Brau, H. Murayama, *Physics Case for the 250 GeV Stage of the International Linear Collider* (2017), [arXiv:1710.07621](https://arxiv.org/abs/1710.07621) [hep-ex]
16. M. Aicheler, P. Burrows, M. Draper, T. Garvey, P. Lebrun, K. Peach, N. Phinney, H. Schmickler, D. Schulte, N. Toge, *A Multi-TeV Linear Collider Based on CLIC Technology*, CERN Yellow Reports: Monographs (CERN, Geneva, Switzerland, 2012) <https://cds.cern.ch/record/1500095>
17. CLICdp, CLIC Collaboration, M.J. Boland et al., *Updated baseline for a staged Compact Linear Collider*, DOI: [10.5170/CERN-2016-004](https://doi.org/10.5170/CERN-2016-004)
18. CEPC-SPPC Study Group, *CEPC-SPPC Preliminary Conceptual Design Report. 1. Physics and Detector* (2015), IHEP-CEPC-DR-2015-01, IHEP-TH-2015-01, IHEP-EP-201501
19. CEPC-SPPC Study Group, *CEPC-SPPC Preliminary Conceptual Design Report. 2. Accelerator* (2015), IHEP-CEPC-DR-2015-01, IHEP-AC-2015-01
20. CEPC Study Group, *CEPC Conceptual Design Report* (IHEP, CAS, 2018), [arXiv:1809.00285](https://arxiv.org/abs/1809.00285) [physics.acc-ph], IHEP-CEPC-DR-2018-01, IHEP-AC-2018-01
21. A. Blondel, M. Koratzinos, R.W. Assmann, A. Butterworth, P. Janot, J.M. Jimenez, C. Grojean, A. Milanese, M. Modena, J.A. Osborne, F. Zimmermann, H. Piekarczyk, K. Oide, K. Yokoya, J. Ellis, M. Klute, M. Zanetti, M. Velasco, V. Telnov, L. Rivkin, Y. Cai, *LEP3: A High Luminosity e^+e^- Collider to Study the Higgs Boson* (2012), [arXiv:1208.0504](https://arxiv.org/abs/1208.0504) [physics.acc-ph]
22. A. Apollonio et al., FCC-ee operation model, availability, and performance, in *Proceedings of ICFA Advanced Beam Dynamics Workshop eeFACT2018* (Hong Kong, 2008)
23. C. Marrelli, I. Syratcev, A. Yu, IEEE Trans. Electron. Devices **62**, 3406 (2015)
24. A. Milanese, Phys. Rev. Accel. Beams **19**, 112401 (2016)
25. *The European Strategy for Particle Physics Update*, CERN-Council-S-0106 (CERN Document Server, 2013), <https://cds.cern.ch/record/1567258>
26. A. Blondel, F. Zimmermann, *A High Luminosity e^+e^- Collider in the LHC tunnel to study the Higgs Boson* (2011), [arXiv:1112.2518](https://arxiv.org/abs/1112.2518) [hep-ex]
27. The LEP Electroweak Working Group and the SLD Electroweak Group and the SLD Heavy Flavour Group and the ALEPH, DELPHI, L3, OPAL and SLD Collaborations, Phys. Rept. **427**, 257 (2006)
28. The LEP Electroweak Working Group and the ALEPH, DELPHI, L3, OPAL Collaborations, Phys. Rept. **532**, 119 (2013)
29. M.J.G. Veltman, Nucl. Phys. B **123**, 89 (1977)
30. CDF, D0 Collaboration, The Tevatron Electroweak Working Group, *2012 Update of the Combination of CDF and D0 Results for the Mass of the W Boson, 2012 Update of the Combination of CDF and D0 Results for the Mass of the W Boson* (2012), [arXiv:1204.0042](https://arxiv.org/abs/1204.0042) [hep-ex]
31. CDF Collaboration, F. Abe et al., Phys. Rev. Lett. **74**, 2626 (1995)
32. D0 Collaboration, S. Abachi et al., Phys. Rev. Lett. **74**, 2632 (1995)
33. The Particle Data Group, M. Tanabashi et al., Phys. Rev. D **98**, 030001 (2018)
34. The Gitter Group, M. Baak, J. Cúth, J. Haller, A. Hoecker, R. Kogler, K. Mönig, M. Schott, J. Stelzer, Eur. Phys. J. **74**, 3046 (2014)
35. J. Haller, A. Hoecker, R. Kogler, K. Mönig, T. Peiffer, J. Stelzer, Eur. Phys. J. C **78**, 675 (2018)
36. F. Jegerlehner, Nuovo Cim. **C034S1**, 31 (2011)
37. P. Janot, JHEP **2**, 53 (2016) [Erratum: JHEP **11**, 164 (2017)]

38. P. Janot, *Presentation given at The First FCC-ee Beam Polarization and Energy Calibration Workshop* (Indico presentation, October, 2017), <https://indico.cern.ch/event/669194/contributions/2764992/attachments/1547206/2429244/EnergySpread.pdf>
39. D. d’Enterria, M. Srebre, Phys. Lett. B **763**, 465 (2016)
40. M. Béguin, *Poster presented at the 2018 FCC Week annual conference in Amsterdam*, Presentation at FCC Week Annual Meeting (April, 2018), https://indico.cern.ch/event/656491/contributions/2960955/attachments/1628478/2594424/poster_Beguिन_FCCweek2018.pdf
41. C. Jarlskog, Phys. Lett. B **241**, 579 (1990)
42. L.G. Trentadue, G. Barbiellini, X. Berdugo, G. Bonvicini, P. Colas, L. Mirabito, C. Dionisi, D.A. Karlen, F.L. Linde, C. Luci, C. Maña, C. Matteuzzi, O. Nicrosini, R. Ragazzon, A.D. Schaile, F. Scuri, *Neutrino Counting* (1989), <http://cds.cern.ch/search?sysno=000112318CER>, CERN-TH-5528-89
43. OPAL Collaboration, G. Abbiendi et al., Eur. Phys. J. C **18**, 253 (2000)
44. ALEPH Collaboration, A. Heister et al., Eur. Phys. J. C **28**, 1 (2003)
45. L3 Collaboration, P. Achard et al., Phys. Lett. B **587**, 16 (2004)
46. DELPHI Collaboration, J. Abdallah et al., Eur. Phys. J. C **38**, 395 (2005)
47. P. Janot, JHEP **4**, 182 (2015)
48. P. Azzi, C. Bernet, C. Botta, G. Gomez-Ceballos, P. Janot, M. Klute, P. Lenzi, L. Malgeri, M. Zanetti, *Prospective Studies for LEP3 with the CMS Detector* (2012), [arXiv:1208.1662](https://arxiv.org/abs/1208.1662) [hep-ex]
49. M. Cepeda et al., *Higgs Physics at the HL-LHC and HE-LHC* CERN-LPCC-2018-04 (CERN, Geneva, 2018), <https://cds.cern.ch/record/2650162>
50. M.E. Peskin, *Comparison of LHC and ILC Capabilities for Higgs Boson Coupling Measurements* (2012), [arXiv:1207.2516](https://arxiv.org/abs/1207.2516) [hep-ph]
51. A. Hoecker, *Presentation given at the CERN Faculty Meeting “Measurement of Higgs Properties at Present and Future Facilities”* (Indico presentation, June, 2018), <https://indico.cern.ch/event/716380/contributions/2944841/attachments/1660046/2660284/epfaculty-hoecker-1jun2018.pdf>
52. T. Barklow, K. Fujii, S. Jung, R. Karl, J. List, T. Ogawa, M.E. Peskin, J. Tian, Phys. Rev. D **97**, 053003 (2018)
53. H. Abramowicz et al., *Higgs physics at the CLIC electron-positron linear collider*, Eur. Phys. J. C **77**, 475 (2017)
54. CEPC Study Group, *CEPC Conceptual Design Report Volume 2 Physics & Detector* (2018), [arXiv:1811.10545](https://arxiv.org/abs/1811.10545) [hep-ex]
55. ATLAS Collaboration, M. Aaboud et al., Phys. Lett. B **784**, 173 (2018)
56. CMS Collaboration, A.M. Sirunyan et al., Phys. Rev. Lett. **120**, 231801 (2018)
57. P. Roloff, *Presentation given at the CERN Faculty Meeting “Measurement of Higgs Properties at Present and Future Facilities”* (June, 2018), Indico website: https://indico.cern.ch/event/716380/contributions/2944866/attachments/1660285/2659566/faculty_meeting_01_06_2018_roloff.pdf
58. M.L. Mangano, *Presentation given at the CERN Faculty Meeting “Measurement of Higgs Properties at Present and Future Facilities”* (June, 2018), Indico website: <https://indico.cern.ch/event/716380/contributions/2944842/attachments/1660297/2659606/Mangano-EPH.pdf>
59. K. Fujii, C. Grojean, M.E. Peskin, T. Barklow, Y. Gao, S. Kanemura, H. Kim, J. List, M. Nojiri, M. Perelstein, R. Poeschl, J. Reuter, F. Simon, T. Tanabe, J. Yu, J.D. Wells, H. Murayama, H. Yamamoto, *Physics Case for the International Linear Collider* (2015), [arXiv:1506.05992](https://arxiv.org/abs/1506.05992) [hep-ex]
60. M. McCullough, Phys. Rev. D **90**, 015001 (2014) [Erratum: Phys. Rev. D **92**, 039903 (2015)]
61. S. Di Vita, G. Durieux, C. Grojean, J. Gu, Z. Liu, G. Panico, M. Riembau, JHEP **2**, 178 (2018)
62. F. Maltoni, D. Pagani, X. Zhao, JHEP **10**, 87 (2018)
63. S. Jadach, R.A. Kycia, Phys. Lett. B **755**, 58 (2016)

64. A. Faus-Golfe, M.A. Valdivia Garcia, F. Zimmermann, *Towards a Monochromatization Scheme for Direct Higgs Production at FCC-ee* (May, 2016), <https://cds.cern.ch/record/2159683>, CERN-ACC-2016-0077
65. D. d'Enterria, PoS ICHEP2016 **282**, 434 (2017)
66. J. Brod, U. Haisch, J. Zupan, JHEP **11**, 180 (2013)
67. ATLAS Collaboration, G. Aad et al., Eur. Phys. J. C **75**, 476 (2015) [Erratum: Eur. Phys. J.C **76**, 152 (2016)]
68. CMS Collaboration, V. Khachatryan et al., Phys. Rev. D **92**, 012004 (2015)
69. A. Drozd, J. Ellis, J. Quevillon, T. You, *The Universal One-Loop Effective Action*, JHEP **3**, 180 (2016)
70. J. Fuentes-Martin, J. Portoles, P. Ruiz-Femenia, JHEP **9**, 156 (2016)
71. A. Pich, I. Rosell, J. Santos, J.J. Sanz-Cillero, JHEP **4**, 012 (2017)
72. J. de Blas, J.C. Criado, M. Perez-Victoria, J. Santiago, JHEP **10**, 109 (2018)
73. B. Grzadkowski, M. Iskrzynski, M. Misiak, J. Rosiek, JHEP **10**, 85 (2010)
74. A. Freitas, Prog. Part. Nucl. Phys. **90**, 201 (2016)
75. J. de Blas, M. Ciuchini, E. Franco, S. Mishima, M. Pierini, L. Reina, L. Silvestrini, JHEP **12**, 135 (2016)
76. J. de Blas, M. Ciuchini, E. Franco, S. Mishima, M. Pierini, L. Reina, L. Silvestrini, PoS ICHEP2016, 690 (2017)
77. J. de Blas, M. Ciuchini, E. Franco, S. Mishima, M. Pierini, L. Reina, L. Silvestrini, *The global electroweak and higgs fits in the LHC era in 5th Large Hadron Collider Physics Conference (LHCP 2017) Shanghai, China, 15–20 May 2017* (2017) [arXiv:1710.05402](https://arxiv.org/abs/1710.05402) [hep-ph]
78. I. Esteban, M.C. Gonzalez-Garcia, M. Maltoni, I. Martinez-Soler, T. Schwetz, JHEP **1**, 87 (2017)
79. R.N. Mohapatra, Phys. Rev. Lett. **56**, 561 (1986)
80. R.N. Mohapatra, J.W.F. Valle, Phys. Rev. D **34**, 1642 (1986)
81. J. Bernabeu, A. Santamaria, J. Vidal, A. Mendez, J.W.F. Valle, Phys. Lett. B **187**, 303 (1987)
82. G.C. Branco, W. Grimus, L. Lavoura, Nucl. Phys. B **312**, 492 (1989)
83. M. Malinsky, J.C. Romao, J.W.F. Valle, Phys. Rev. Lett. **95**, 161801 (2005)
84. M.B. Gavela, T. Hambye, D. Hernandez, P. Hernandez, JHEP **9**, 38 (2009)
85. S. Iso, N. Okada, Y. Orikasa, Phys. Lett. B **676**, 81 (2009)
86. S. Iso, Y. Orikasa, PTEP **2013**, 023B08 (2013)
87. V.V. Khoze, G. Ro, JHEP **10**, 75 (2013)
88. V.V. Khoze, A.D. Plascencia, JHEP **11**, 25 (2016)
89. T. Asaka, S. Blanchet, M. Shaposhnikov, Phys. Lett. B **631**, 151 (2005)
90. T. Asaka, M. Shaposhnikov, Phys. Lett. B **620**, 17 (2005)
91. L. Canetti, M. Shaposhnikov, JCAP **1009**, 001 (2010)
92. L. Canetti, M. Drewes, M. Shaposhnikov, Phys. Rev. Lett. **110**, 061801 (2013)
93. M. Drewes, B. Garbrecht, JHEP **3**, 96 (2013)
94. L. Canetti, M. Drewes, T. Frossard, M. Shaposhnikov, Phys. Rev. D **87**, 093006 (2013)
95. L. Canetti, M. Drewes, B. Garbrecht, Phys. Rev. D **90**, 125005 (2014)
96. P. Hernández, M. Kekic, J. López-Pavón, J. Racker, N. Rius, JHEP **10**, 67 (2015)
97. G. Arcadi, A. Abada, V. Domcke, M. Lucente, JCAP **1511**, 41 (2015)
98. P. Hernández, M. Kekic, J. López-Pavón, J. Racker, N. Rius, JHEP **8**, 157 (2016)
99. M. Drewes, S. Eijima, Phys. Lett. B **763**, 72 (2016)
100. M. Drewes, B. Garbrecht, D. Gueter, J. Klaric, JHEP **12**, 150 (2016)
101. T. Asaka, S. Eijima, H. Ishida, Phys. Lett. B **762**, 371 (2016)
102. M. Drewes, B. Garbrecht, D. Gueter, J. Klaric, JHEP **8**, 18 (2017)
103. T. Asaka, S. Eijima, H. Ishida, K. Minogawa, T. Yoshii, Phys. Rev. D **96**, 083010 (2017)
104. G. Arcadi, A. Abada, V. Domcke, M. Lucente, JCAP **1712**, 24 (2017)
105. L. Wolfenstein, D. Wyler, Nucl. Phys. B **218**, 205 (1983)
106. M.C. Gonzalez-Garcia, J.W.F. Valle, Phys. Lett. B **216**, 360 (1989)
107. E.K. Akhmedov, M. Lindner, E. Schnapka, J.W.F. Valle, Phys. Rev. D **53**, 2752 (1996)

108. E.K. Akhmedov, M. Lindner, E. Schnapka, J.W.F. Valle, Phys. Lett. B **368**, 270 (1996)
109. S.M. Barr, Phys. Rev. Lett. **92**, 101601 (2004)
110. A. Pilaftsis, Z. Phys. C **55**, 275 (1992)
111. A. Abada, C. Biggio, F. Bonnet, M.B. Gavela, T. Hambye, JHEP **12**, 61 (2007)
112. D. Aristizabal Sierra, A. Degee, J.F. Kamenik, JHEP **7**, 135 (2012)
113. C.S. Fong, M.C. Gonzalez-Garcia, E. Nardi, E. Peinado, JHEP **8**, 104 (2013)
114. V. Cirigliano, B. Grinstein, G. Isidori, M.B. Wise, Nucl. Phys. B **728**, 121 (2005)
115. Y. Cai, T. Han, T. Li, R. Ruiz, Front. Phys. **6**, 40 (2018)
116. S. Antusch, C. Biggio, E. Fernández-Martínez, M. Belen Gavela, J. López-Pavón, JHEP **10**, 84 (2006)
117. S. Antusch, O. Fischer, JHEP **10**, 94 (2014)
118. C.P. Burgess, S. Godfrey, H. König, D. London, I. Maksymyk, Phys. Rev. D **49**, 6115 (1994)
119. F. del Aguila, J. de Blas, M. Perez-Victoria, Phys. Rev. D **78**, 013010 (2008)
120. E. Akhmedov, A. Kartavtsev, M. Lindner, L. Michaels, J. Smirnov, JHEP **5**, 81 (2013)
121. L. Basso, O. Fischer, J.J. van der Bij, EPL **105**, 11001 (2014)
122. E. Fernández-Martínez, J. Hernandez-Garcia, J. Lopez-Pavon, JHEP **8**, 33 (2016)
123. M. Blennow, P. Coloma, E. Fernandez-Martinez, J. Hernandez-Garcia, J. Lopez-Pavon, JHEP **4**, 153 (2017)
124. S. Antusch, E. Cazzato, O. Fischer, Int. J. Mod. Phys. A **32**, 1750078 (2017)
125. DELPHI Collaboration, P. Abreu et al., Z. Phys. C **74**, 57 (1997) [Erratum: Z. Phys. C **75**, 580 (1997)]
126. A. Blondel, E. Graverini, N. Serra, M. Shaposhnikov, Nucl. Part. Phys. Proc. **273–275**, 1883 (2016)
127. S. Antusch, E. Cazzato, O. Fischer, JHEP **12**, 007 (2016)
128. S.B. Nielsen, Prospects of Sterile Neutrino search at FCC-ee, Master thesis, University of Copenhagen and 25th Nordic Particle Physics Meeting (Spåtind 2018), 2017, <https://indico.cern.ch/event/666278/>
129. S. Antusch, E. Cazzato, M. Drewes, O. Fischer, B. Garbrecht, D. Gueter, J. Klaric, JHEP **9**, 124 (2018)
130. Z. Chacko, H.-S. Goh, R. Harnik, Phys. Rev. Lett. **96**, 231802 (2006)
131. Z. Liu, L.-T. Wang, H. Zhang, Chin. Phys. C **41**, 063102 (2017)
132. J. Liu, L.-T. Wang, X.-P. Wang, W. Xue, Phys. Rev. D **97**, 095044 (2018)
133. R. Contino, Y. Nomura, A. Pomarol, Nucl. Phys. B **671**, 148 (2003)
134. G. Panico, A. Wulzer, Lect. Notes Phys. **913**, 1 (2016)
135. G.F. Giudice, C. Grojean, A. Pomarol, R. Rattazzi, JHEP **6**, 45 (2007)
136. R. Contino, C. Grojean, D. Pappadopulo, R. Rattazzi, A. Thamm, JHEP **2**, 6 (2014)
137. A. Thamm, R. Torre, A. Wulzer, JHEP **7**, 100 (2015)
138. S. De Curtis, M. Redi, A. Tesi, JHEP **4**, 42 (2012)
139. E. Accomando, D. Barducci, S. De Curtis, J. Fiaschi, S. Moretti, C.H. Shepherd-Themistocleous, JHEP **7**, 68 (2016)
140. D. Barducci, S. De Curtis, S. Moretti, G.M. Pruna, JHEP **8**, 127 (2015)
141. S.L. Glashow, J. Iliopoulos, L. Maiani, Phys. Rev. D **2**, 1285 (1970)
142. G. Mann, T. Riemann, Ann. Phys. **40**, 334 (1984)
143. A. Abada, V. De Romeri, S. Monteil, J. Orloff, A.M. Teixeira, JHEP **4**, 51 (2015)
144. COMET Collaboration, Y. Kuno, PTEP **2013**, 022C01 (2013)
145. L3 Collaboration, O. Adriani et al., Phys. Lett. B **316**, 427 (1993)
146. OPAL Collaboration, R. Akers et al., Z. Phys. C **67**, 555 (1995)
147. DELPHI Collaboration, P. Abreu et al., Z. Phys. C **73**, 243 (1997)
148. ATLAS Collaboration, G. Aad et al., Phys. Rev. D **90**, 072010 (2014)
149. M. Dam, Tau physics at the FCC, in *15th Workshop on Tau Physics* (2018), <https://indico.cern.ch/event/632562/>
150. W. Altmannshofe, D.M. Straub, Eur. Phys. J. C **73**, 2646 (2013)
151. A. Buras, M.V. Carlucci, F. De Fazio, J. Girrbach, JHEP **2**, 23 (2013)
152. R. Gauld, F. Goertz, U. Haisch, JHEP **1**, 69 (2014)
153. S. Descotes-Genon, L. Hofer, J. Matias, J. Virto, JHEP **6**, 92 (2016)

154. LHCb Collaboration, R. Aaij et al., Phys. Rev. Lett. **113**, 151601 (2014)
155. LHCb Collaboration, R. Aaij et al., JHEP **2**, 104 (2016)
156. Belle Collaboration, A. Abdesselam et al., Angular analysis of $B^0 \rightarrow K^*(892)^0 \ell^+ \ell^-$, in *LHC Ski 2016* (2016) [arXiv:1604.04042](https://arxiv.org/abs/1604.04042) [hep-ex], <https://inspirehep.net/record/1446979/files/arXiv:1604.04042.pdf>
157. J.F. Kamenik, S. Monteil, A. Semkiv, L.V. Silva, Eur. Phys. J. C **77**, 701 (2017)
158. A. Blondel, P. Janot, *Future Strategies for the Discovery and the Precise Measurement of the Higgs Self Coupling* (2018), [arXiv:1809.10041](https://arxiv.org/abs/1809.10041) [hep-ph]
159. A. Blondel, *FCC-ee Requirements on Beam Polarization and Energy Calibration, Presentation given at 2017 FCC week in Berlin* (Indico presentation, May, 2017), <https://indico.cern.ch/event/556692/contributions/2510756/attachments/1467287/2268828/Blondel-E-Pol-Requirements-Berlin.pdf>
160. A. Blondel, J. Gluza, S. Jadach, P. Janot, T. Riemann, A. Akhundov, A. Arbuzov, R. Boels, S. Bondarenko, S. Borowka, C.M. Carloni Calame, I. Dubovyk, Y. Dydyshka, W. Flieger, A. Freitas, K. Grzanka, T. Hahn, T. Huber, L. Kalinovskaya, R. Lee, P. Marquard, G. Montagna, O. Nicrosini, C. G. Papadopoulos, F. Piccinini, R. Pittau, W. Placzek, M. Prausa, S. Riemann, G. Rodrigo, R. Sadykov, M. Skrzypek, D. Stockinger, J. Usovitsch, B.F.L. Ward, S. Weinzierl, G. Yang, S.A. Yost, Standard model theory for the FCC-ee: the Tera-Z, in *Mini Workshop on Precision EW and QCD Calculations for the FCC Studies : Methods and Techniques CERN, Geneva, Switzerland, January 12–13, 2018* (2018), [arXiv:1809.01830](https://arxiv.org/abs/1809.01830) [hep-ph]
161. J. Gluza, *EW Precision Calculation Mini-workshop at CERN, Report in Preparation and Talk Given at the Second FCC Physics Workshop* (Indico presentation, 2018), <https://indico.cern.ch/event/669224/>; <https://indico.cern.ch/event/618254/>
162. K. Oide, M. Aiba, S. Aumon, M. Benedikt, A. Blondel, A. Bogomyagkov, M. Boscolo, H. Burkhardt, Y. Cai, A. Doblhammer, B. Haerer, Phys. Rev. Accel. Beams **19**, 111005 (2016)
163. P. Raimondi, *Status on SuperB effort*, presentation at the 2nd Workshop on Super B-Factory (2006)
164. A. Bogomyagkov, E. Levichev, D. Shatilov, Phys. Rev. ST Accel. Beams **17**, 041004 (2014)
165. J. Augustin et al. eConf C781015, 009 (October, 1978)
166. P. Raimondi, *Scaling of high-energy e^+e^- ring colliders*, KEK Accelerator Seminar, 15 March 2012 (2012)
167. P. Raimondi, FCC-ee/CepC beam-beam simulations with Beamstrahlung, in *Proceedings of the IPAC'14, Dresden, Germany* (2014)
168. V. Telnov, Phys. Rev. Lett. **110**, 114801 (2013)
169. P. Raimondi, M. Zobov, *Tune shift in beam-beam collisions with a crossing angle* (April, 2003), LNF-G-58
170. K. Ohmi, N. Kuroo, K. Oide, D. Zhou, F. Zimmermann, Phys. Rev. Lett. **119**, 134801 (2017)
171. N. Kuroo, K. Ohmi, K. Oide, D. Zhou, F. Zimmermann, Phys. Rev. Accel. Beams **21**, 031002 (2018)
172. D. Shatilov, ICFA Beam Dyn. Newslett. **72**, 30 (2017)
173. Particle Data Group, *High-Energy Collider Parameters: e^+e^- Colliders* (January, 2016), website: <http://pdg.lbl.gov/2017/reviews/rpp2017-rev-hep-collider-params.pdf>
174. G. von Holtey, A.H. Ball, E. Brambilla, H. Burkhardt, P. Estabrooks, F.J. Harris, G. Lutters, J. Rothberg, P. Roudeau, P. Siegrist, J. Wear, Nucl. Instrum. Meth. A **403**, 205 (1998)
175. M. Sands, Conf. Proc. **C6906161**, 257 (1969)
176. M. Aiba et al., B. Goddard, K. Oide, Y. Papaphilippou, Á. Saá Hernández, D. Shwartz, S. White, F. Zimmermann, Nucl. Instrum. Meth. A **880**, 98 (2018)

177. K. Oide, E. Levichev, F. Zimmermann, K. Ohmi, A. Milanese, M. Koratzinos, M. Boscolo, H. Burkhardt, A. Blondel, M. Benedikt, B. Holzer, Progress in the design of beam optics for FCC-ee collider ring, in *Proceedings of the IPAC'17, Copenhagen, Denmark* (May 15–19, 2017)
178. K. Oide, ICFA Beam Dyn. Newslett. **72**, 19 (2017)
179. N. Muchnoi, Compton polarimeter, in *FCC-ee Polarization Workshop, CERN, Geneva, Switzerland* (October 17–28, 2017)
180. K.L. Brown, R. Servranckx, IEEE Trans. Nucl. Sci. **26**, 3598 (1979)
181. H. Koiso et al., Lattice of the KEKB colliding rings, Prog. Theor. Exp. Phys. **2013**, (2013) no.3, 03A009
182. K. Oide, KEKB B-factory, the luminosity frontier, Prog. Theor. Phys. **122**, 69 (2009)
183. Y. Ohnishi, T. Abe, T. Adachi, K. Akai, Y. Arimoto, K. Ebihara, K. Egawa, J. Flanagan, H. Fukuma, Y. Funakoshi, K. Furukawa, PTEP **2013**, 03A011 (2013)
184. K. Oide, Int. J. Mod. Phys. Proc. Suppl. **2**, 861 (1993)
185. P. Azzi, *FCC-ee Progress on physics and experiment studies*, FCC Week, Rome, Italy (April 11–15, 2016)
186. SAD, Website and software repository, <http://acc-physics.kek.jp/SAD/index.html>; <https://github.com/KatsOide/SAD>
187. E. Forest, J. Milutinović, Nucl. Instrum. Meth. A **269**, 474 (1988)
188. T. Tydecks, S. Aumon, B. Härer, K. Oide, T. Charles, B. Holzer, J. Wenninger, Y. Papaphilippou, FCC-ee Dynamic Aperture Studies and Frequency Map Analysis, *Proceedings of the IPAC'18, Vancouver, BC, Canada* (April 29–May 4, 2018)
189. R.W. Aßmann, P. Raimondi, G. Roy, J. Wenninger, Phys. Rev. ST Accel. Beam **3**, 121001 (2000)
190. A. Franchi, L. Farvacque, J. Chavanne, F. Ewald, B. Nash, K. Scheidt, R. Tomás, Phys. Rev. ST Accel. Beam **14**, 034002 (2015)
191. J. Feikes, P. Goslawski, J. Li, M. Ries, *Particle swarm optimization algorithm applied in online commissioning at the MLS and BESSY II*, in *Proceedings of the 8th IPAC'17, Copenhagen, Denmark* (May 14–19, 2017), p. THPAB008
192. R. Eberhart, J. Kennedy, A new optimizer using particle swarm theory, in *MHS'95. Proceedings of the Sixth International Symposium on Micro Machine and Human Science* (October, 1995), pp. 39–43
193. W. Cheng, Y. Li, R. Rainer, L.H. Yu, Phys. Rev. Accel. Beams **21**, 054601 (2018)
194. GEANT4, website: <http://geant4.web.cern.ch>
195. Dassault Systems, Computer Simulation Technology, website: <https://www.cst.com>
196. HFSS, website: <http://www.ansys.com/Products/Electronics/ANSYS-HFSS>
197. A. Novokhatski, M. Sullivan, E. Belli, M.G. Costa, R. Kersevan, Phys. Rev. Accel. Beams **20**, 111005 (2017)
198. S. Caspi, F. Borgnolutti, L. Brouwer, D. Cheng, D.R. Dietderich, H. Felice, A. Godeke, R. Hafalia, M. Martchevskii, S. Prestemon, E. Rochepault, C. Swenson, X. Wang, IEEE Trans. Appl. Supercond. **24** (2014), DOI: [10.1109/TASC.2013.2284722](https://doi.org/10.1109/TASC.2013.2284722)
199. M. Boscolo, H. Burkhardt, Tracking Simulation for Beam Loss Studies with Application to FCC, in *Proceedings of the IPAC'15* (2015)
200. M. Boscolo, H. Burkhardt, M. Sullivan, Phys. Rev. Accel. Beams **20**, 011008 (2017)
201. GUINEA-PIG, Wiki page, <https://twiki.cern.ch/twiki/bin/view/ABPComputing/Guinea-Pig>
202. Non evaporable getter coatings, website: <https://kt.cern/technologies/non-evaporable-getter-neg-thin-film-coatings>
203. A. Rossi, *SEY and Electron Cloud Build-up with NEG Materials* (CERN, Geneva, Switzerland, 2005)
204. E. Belli, *Impedance Model and Collective Effects for FCC-ee* (FCC Week, Berlin, Germany, May 29–June 2, 2017)
205. A. Butterworth, *Cavity Design and Beam-cavity Interaction* (FCC Week, Berlin, Germany, May 30, 2017), <https://indico.cern.ch/event/556692/contributions/2484361/>

206. S. Zadeh, Cavity Design approaches and HOM damping for FCC-ee, in *Proceedings of the FCC Week, Berlin, Germany*, <https://indico.cern.ch/event/556692/contributions/2484333/>
207. ABCI, website: <http://abci.kek.jp/>
208. H. Hisamatsu, K.I. Kanazawa, K. Shibata, T. Ishibashi, H. Hisamatsu, M. Shirai, S. Terui, J. Vac. Sci. Technol. A **30**, 031602 (2012)
209. F. Marcellini, M. Serio, A. Stella, M. Zobov, Nucl. Instrum. Methods Phys. Res. Sect. A **402**, 27 (1998)
210. A. Rodrigues, C. Rodrigues, F. Arroyo, S. Marques, R. Farias, F. Rodrigues, J. Citadini, O. Bagnato, R. Seraphim, L. Liu, J. Franco, Sirius status report, in *Proceedings of the IPAC'16* (2016), WEPOW001
211. E. Belli, M. Migliorati, B. Spataro, S. Persichelli, A. Novokhatski, G. Castorina, M. Zobov, Coupling impedances and collective effects for FCC-ee, in *Proceedings of the 8th IPAC'17, Copenhagen, Denmark* (May 14–19, 2017)
212. K. Shibata, M. Shirai, Y. Suetsugu, Phys. Rev. ST Accel. Beams **6**, 103201 (2003)
213. N. Mounet, *ImpedanceWake2D*, Wiki page (2011), <https://twiki.cern.ch/twiki/bin/view/ABPComputing/ImpedanceWake2D>
214. *PyHEADTAIL*, Software repository, <https://github.com/PyCOMPLETE/PyHEADTAIL>
215. J. Haissinski, II Nuovo Cimento B **18**, 72 (1973)
216. A.W. Chao, *Physics of Collective Beam Instabilities in High Energy Accelerators* (Wiley, 1993)
217. *DELPHI*, Wiki page, <https://twiki.cern.ch/twiki/bin/view/ABPComputing/DELPHI>
218. E. Belli, M. Migliorati, S. Persichelli, M. Zobov, *Single beam collective effects in FCC-ee due to beam coupling impedance* (2016), [arXiv:1609.03495](https://arxiv.org/abs/1609.03495) [physics.acc-ph]
219. M. Lonza, Multi-bunch feedback systems, in *Proceedings of CAS CERN Accelerator School on Beam Diagnostics* (2009), pp. 467–511
220. D. Teytelman et al., Development and testing of a low group-delay woofer channel for PEP-II, in *Proceedings of the EPAC'04* (2004), pp. 2822–2824
221. D. Teytelman et al., Operating performance of the low group delay woofer channel in PEP-II, in *Proceedings of the PAC'05* (2005), pp. 1069–1071
222. D. Boussard, IEEE Trans. Nucl. Sci. **30**, 2239 (1983)
223. K. Akai, E. Ezura, T. Takashima, S. Yoshimoto, Experiment of the RF Feedback using a Parallel Comb Filter, in *Proceedings of the PAC'95* (1995), pp. 2675–2677
224. D. Teytelman, Overview of system specifications for bunch by bunch feedback system, in *Proceedings of the PAC'11* (2011), pp. 1475–1479
225. P. Corredoura, J. Pellegrin, H.D. Schwarz, J.C. Sheppard, An active feedback system to control synchrotron oscillations in the SLC damping ring, in *Proceedings of the PAC'89* (IEEE, 1989), pp. 1879–1881
226. K. Ohmi, M. Tobiya, Study of beam size blowup due to transverse bunch feedback noise on e+e- collider, in *Proceedings of the DIPAC'11* (2011), pp. 212–214
227. K. Ohmi et al., The beam-beam limit and feedback noise, in *Proceedings of the EPAC'06* (2011), pp. 619–621
228. W. Cheng et al., Developments of bunch by bunch feedback system at NSLS-II storage ring, in *Proceedings of the IPAC'18* (2011) WEPAF011
229. A. Drago, DAFNE horizontal feedback upgrade, in *Proceedings of the PAC'09* (2009), pp. 4123–4125
230. *MDI: Synchrotron Radiation Protection*, Indico presentation, <https://indico.cern.ch/event/556692/contributions/2590394/>
231. G. Rumolo et al., *Electron cloud in the CERN accelerator complex*, CERN-ACC-2016-0099 (2016)
232. H. Fukuma, ICFA Beam Dyn. Newslett. **48**, 112 (2009)
233. G. Iadarola et al. website: <https://github.com/PyCOMPLETE/PyECLOUD>
234. G. Iadarola, *Electron cloud studies for CERN particle accelerators and simulation code development*, CERN Report CERN-THESIS-2014-047 (2014)

235. K. Oide, *Status of Optics*, FCC Week 2017 – 31 May 2017, Berlin, Germany (2017), <https://indico.cern.ch/event/556692/contributions/2590161/>
236. I. Karpov, R. Calaga, E. Shaposhnikova, *Phys. Rev. Accel. Beams* **21**, 071001 (2018)
237. G. Rumolo, F. Zimmermann, Theory and simulation of the electron cloud instability, in *Proceedings of the LHC Workshop Chamonix XI* (2001)
238. K. Ohmi, F. Zimmermann, *PRL* **85**, 3821 (2000)
239. K. Ohmi, E. Perevedentsev, F. Zimmermann, *Study of the fast head-tail instability caused by the electron cloud*, CERN-SL-2001-011 AP (2001)
240. T.O. Raubenheimer, F. Zimmermann, *Phys. Rev. E* **52**, 5487 (1995)
241. L. Mether, A. Oeftiger, G. Rumolo, Modeling of fast beam-ion instabilities, in *Proceedings of the ICF mini-Workshop on impedances and beam instabilities in particle accelerators, Benevento, Italy* (2017), pp. 63–68, <https://cds.cern.ch/record/2642470>
242. L. Mether, A. Oeftiger, *Acceptable vacuum pressures for FCC-ee at 45.6 GeV*, FCC-ACC-RPT-0025 (EDMS 1895017) (2017)
243. A. Chatterjee, K. Blaser, W. Hartung, D. Rubin, S.T. Wang, *Phys. Rev. ST Accel. Beams* **18**, 064402 (2015)
244. E. Gianfelice-Wendt, *Phys. Rev. Accel. Beams* **19**, 101005 (2016)
245. J. Kewisch, *Simulation of Electron Spin Depolarization with the Computer Code SITROS DESY-83-032* (DESY, Hamburg, Germany, May, 1983), <http://inspirehep.net/record/190447>
246. R.W. Aßmann, J. Badier, A. Blondel, M. Böge, M. Crozon, B. Dehning, H. Grote, J.P. Koutchouk, M. Placidi, R. Schmidt, F. Sonnemann, F. Tecker, J. Wenninger, *AIP Conf. Proc.* **570**, 169 (2001)
247. J. Badier, J.P. Koutchouk, M. Placidi, R. Schmidt, M. Crozon, J. Badier, A. Blondel, B. Dehning, *Phys. Lett. B* **270**, 97 (1991)
248. L. Arnaudon, L. Knudsen, J.P. Koutchouk, R. Olsen, M. Placidi, R. Schmidt, M. Crozon, A. Blondel, R. ASSmann, B. Dehning, *Phys. Lett. B* **284**, 431 (1992)
249. R.W. Aßmann, LEP Energy Working Group, *Eur. Phys. J. C* **6**, 187 (1999)
250. I. Koop, Session on FCC-ee Beam Polarization and Energy Calibration (FCC Week, Amsterdam, The Netherlands, April, 2018)
251. A. Bogomyagkov, Session on FCC-ee Beam Polarization and Energy Calibration (FCC Week, Amsterdam, The Netherlands, April, 2018)
252. A. Blondel, E. Gianfelice-Wendt, M. Koratzinos, F. Zimmermann, FCC-ee: energy calibration, in *Proceedings of the 6th IPAC'15, Richmond, Virginia, USA* (May 3–8, 2015), p. TUPTY063, [arXiv:1506.00933](https://arxiv.org/abs/1506.00933) [physics.acc-ph], <https://inspirehep.net/record/1374263/files/arXiv:1506.00933.pdf>
253. W. Höfle, G. Kotzian, T. Levens, D. Valuch, LHC transverse feedback in *Proceedings of the 5th Evian Workshop on LHC Beam Operation: Evian-les-Bains, France, June 02–04, 2014* (CERN, Geneva, Switzerland, 2014), pp. 105–110 http://inspirehep.net/record/1639517/files/1638883_105-110.pdf
254. T. Tydecks, Mini-Workshop on FCC-ee Beam Polarization and Energy Calibration, CERN (October 18–27, 2017), <https://indico.cern.ch/event/669194/>
255. P. Janot, *Mini-Workshop on FCC-ee Beam Polarization and Energy Calibration, CERN* (October 18–27, 2017), <https://indico.cern.ch/event/669194/>
256. J.T. Seeman, Top up injection at PEP-II and applications to a circular e+e- Higgs factory, in *Proceedings of the 55th ICF Advanced Beam Dynamics Workshop on High Luminosity Circular e+e- Colliders 2013 Higgs Factory* (2014), pp. 205–209
257. T. Mori et al., Design study of beam injection for SuperKEKB main ring, *Proceedings of the IPAC'12* (2012), pp. 2035–2037
258. R.P. Fliller III, Optimum twiss parameters for top off injection in a synchrotron light source, in *Proceedings of the IPAC'10* (2010), pp. 1814–1816
259. J.P. Delahaye, *Muon Collider Compared with Others*, ARIES Muon Collider Workshop, Padua, 2–3 July 2018 (2018), <https://indico.cern.ch/event/719240/>
260. M. Zanetti, F. Zimmermann, Report from ARIES Muon collider workshop in Padua, *Proceedings of the eeFACT2018, Hong Kong* (September 24–27, 2018)
261. M. Bicer, *JHEP* **2014**, 164 (2014)

262. P. Janot, *Perspectives for Future Circular Colliders (1/3)* (CERN Academic Training, Geneva, Switzerland, October 11, 2017)
263. B. Desforges, A. Lasseur, *2000 SPS & LEP Machine Statistics*, CERN SL-Note-00-060 OP (2000)
264. S. Myers, *First Year of LEP Operation*, John Adams Lecture 26 November 1990, Yellow Report CERN 91-08 (1991)
265. P. Collier, *Synchrotron phase space injection into LEP*, in *Proceedings of the PAC'95* (1995), pp. 551–553
266. R.W. Aßmann, M. Lamont, S. Myers, Nucl. Phys. B – Proc. Suppl. **109**, 17 (2002)
267. A. Butterworth, RF Reliability and Operation, in *Proceedings of the 9th LEP-SPS Performance Workshop, Chamonix, France, CERN-OPEN-99-100* (January 25–29, 1999), pp. 189–192
268. M. Colin, G. Cultrut, B. Desforges, *1996 SPS & LEP Machine Statistics*, CERN SL-Note 97-01 OP (1997)
269. M. Colin, G. Cultrut, B. Desforges, *1997 SPS & LEP Machine Statistics*, CERN SL-Note 97-79 OP (1997)
270. M. Colin, G. Cultrut, B. Desforges, D. Picard, *1998 SPS & LEP Machine Statistics*, CERN SL-Note 98-68 OP (1998)
271. C. Allen, W. Colocho, R. Erickson, M. Stanek, IEEE Trans. Nucl. Sci. **52** (2005)
272. J. Seeman, Last year of PEP-II B-factory operation, in *Proceedings of the EPAC'08, Genoa, Italy* (2008)
273. S. Fuke, Y. Funakoshi, T. Kawasumi, KEKB operation statistics, in *Proceedings of the 3rd Annual Meeting of Particle Accelerator Society of Japan and the 31th Linear Accelerator Meeting in Japan, Sendai, Japan* (August 2–4, 2006)
274. H. Asai, M. Tanaka, Y. Funakoshi, Operation statistics of KEKB in FY2009, in *Proceedings of the 7th annual meeting of Particle Accelerator Society of Japan* (2010), p. 1231.
275. H. Asai, M. Tanaka, Y. Funakoshi, KEKB Accelerator — Commissioning of KEKB, Prog. Theor. Exp. Phys. 03A010 (2013)
276. E. Durieu-Thiry (ed.), *Operation Statistics of the CERN Accelerators Complex for 2003*, CERN AB-Note-2004-027-OP (2004)
277. J. Seeman et al., A Luminosity of $10^{34} \text{ cm}^{-2} \text{ s}^{-1}$ in the PEP-II B-factory in *Proceedings of the EPAC'06, Edinburgh, Scotland* (2006), p. 643
278. J. Seeman, KEKB and PEP-II Operational Status, in *Proceedings of the PAC'05, Knoxville, USA* (2005)
279. M. Akemoto et al., Prog. Theor. Exp. Phys. **2013**, 03A002 (2013)
280. A. Renieri, *Possibility of Achieving Very High Energy Resolution in e^+e^- -Storage Rings*, Frascati Preprint **INF/75/6 (R)** (1975)
281. M.A.V. Garcia, F. Zimmermann, Optimized monochromatization for direct higgs production in future circular e^+e^- Colliders, in *Proceedings of the 8th IPAC'17, Copenhagen, Denmark* (May 14–19, 2017), pp. 2950–2953
282. S. Jadach, R.A. Kycia, Lineshape of the Higgs boson in future lepton colliders, Phys. Lett. B **755**, 58 (2016)
283. M. Boscolo, H. Burkhardt, M. Sullivan, Phys. Rev. Accel. Beams **20** 011008 (2017)
284. M. Bohdanowicz, A. Milanese, IEEE Trans. Appl. Supercond. **28**, 1 (2018)
285. *SPS dipole magnets*, March, 1974, <https://cds.cern.ch/record/1528674>, Technology Note issued for the CERN Technological Exhibition (April 1974).
286. M. Giesch, J.P. Gourber, The bending magnet system of LEP, in *11th International Conference on Magnet Technology, Tsukuba, Japan* (1989)
287. C. Petrone, *Magnetic measurement of the quadrupole magnet PXMQNDI8WC-CR000001 – main twin for FCC-ee*, Technical Note **2018_10** (October, 2018), <https://edms.cern.ch/document/1995897/1>
288. C. Petrone, *Magnetic measurement results of the dipole magnet PXMBHAACAC – main twin for FCC-ee*, Technical Note **2018_19** (November, 2018), <https://edms.cern.ch/document/2050314/1>

289. E.R. Bielert, G. Kirby, M. Koratzinos, J.V. Nugteren, *IEEE Trans. Appl. Supercon.* **28**, 1 (2018)
290. J.M. Jowett, T.M. Taylor, *IEEE Trans. Nucl. Sci.* **30**, 2581 (1983)
291. F. Cerutti, *Presentation at FCC Week 2015* (Washington, DC, USA, 2015)
292. E. Belli, M. Migliorati, S. Persichelli, M. Zobov, *Single beam collective effects in FCC-ee due to beam coupling* (2016) , [arXiv:1609.03495](https://arxiv.org/abs/1609.03495) [physics.acc-ph]
293. E. Belli, M. Migliorati, M. Zobov, *Phys. Rev. Accel. Beams* **21**, 041001 (2018)
294. T. Sinkovits et al., Minimum effective thickness for activation and low total electron yield of TiZrV non-evaporable getter coatings, *Presentation at FCC Week 2018*, Amsterdam (2018)
295. P. Chiggiato, R. Kersevan, *Vacuum* **60**, 67 (2001)
296. Y. Suetsugu, M. Shirai, K. Shibata, *Phys. Rev. ST Accel. Beams* **6**, 103201 (2003)
297. M. Sullivan, *IR Layout with SR Masks and Shielding*, FCC-ee MDI Workshop, CERN, 31 January 2018, CERN, Geneva, Switzerland (2018)
298. M.G. Costa, R. Kersevan, *IR Vacuum Concept*, FCC-ee MDI Workshop, CERN, 2 February 2018, CERN, Geneva, Switzerland (2018)
299. A. Novokhatski, M. Sullivan, E. Belli, M. Gil Costa, R. Kersevan, *Phys. Rev. Accel. Beams* **20**, 111005 (2017)
300. R. Kersevan, *FCC-ee Vacuum Effects and Simulations*, Presentation at FCC Week 2016, Rome (2016)
301. R.D. Evans, *Compton Effect, Handbuch der Physik XXXIV* (Springer-Verlag, Berlin, 1958)
302. A. Blondel et al., *FCC-ee Parameter Update*, private communication (2017)
303. R. Calaga, S.G. Zadeh, U. van Rienen, *Preliminary Cavity design for FCC-ee fcc-acc-rpt-0005* (Rostock University, 2016), EDMS NO. 1612380
304. P. Charitos, F. Marhauser, *Accel. News* **25** (2018)
305. A.K. Ciftci, O. Etisken, Y. Papaphilippou, *J. Phys.: Conf. Ser.* **874** (2017)
306. S. Aull, O. Brunner, A. Butterworth, N. Schwerg, *Material Options for the Superconducting RF System of the Future Circular Collider*, FCC-DRAFT-TECH-2017-002 (2017), <https://cds.cern.ch/record/2289506>
307. W.V. Delsolaro, *Thin film research: CERN experience and possible future applications* (TESLA Technology Collaboration (TTC) Meeting, Milano, Italy 2018)
308. D.L. Hall, S. Posen, *Supercond. Sci. Technol.* **30**, 033004 (2017)
309. K. Ilyina-Brunner, Magnetron sputtering of Nb₃Sn thin films on copper for SRF application, in *Fourth Annual Meeting of the Future Circular Collider study, Amsterdam, The Netherlands* (2018)
310. C.A. Clemente, Surface quality and improvements on the SRF cavity manufacturing by electrohydraulic forming, in *Fourth Annual Meeting of the Future Circular Collider study, Amsterdam, The Netherlands* (2018)
311. E. Palmieri, C. Pira, Coating studies on 6 GHz seamless cavities in *Fourth Annual Meeting of the Future Circular Collider study, Amsterdam, The Netherlands* (2018)
312. E. Montesinos, *FPC challenges and perspectives for FCC*, Third Annual Meeting of the Future Circular Collider Study (Berlin, Germany, CERN, 2017), https://indico.cern.ch/event/556692/contributions/2484366/attachments/1466409/2269379/20170530_FCC_week_FPC.pdf
313. I. Syrathev, *Introduction to HEIKA. Tentative structure and objectives CLIC Workshop 2015* (CERN, Geneva, Switzerland, CERN, 2015), <https://indico.cern.ch/event/336335/contributions/789041/>
314. I.A. Guzilov, BAC method of increasing the efficiency in Klystrons in *IEEE Vacuum Electron Sources Conference 2014, St. Petersburg, Russia* (2014)
315. G. Burt et al., Particle-in-cell simulation of a core stabilization method klystron, in *IEEE International Vacuum Electronics Conference, IVEC 2017, London, UK* (2017)
316. I. Syrathev, *High efficiency klystron technology*, Third Annual Meeting of the Future Circular Collider Study (Berlin, Germany, CERN, 2017), <https://indico.cern.ch/event/556692/timetable/#20170530.detailed>

317. J. Cai, I. Syratchev, *KlyC: Large Signal Simulation Code for Klystrons*, submitted to IEEE TED, January 2016 (2017)
318. J. Fox, T. Mastorides, C. Rivetta, D. Van Winkle, D. Teytelman, *Phys. Rev. ST Accel. Beams* **13**, 052802 (2010)
319. P. Baudrenghien, *LLRF Lessons Learned LHC and PEP-II Relevance to FCC hh/ee*, Second Annual Meeting of the Future Circular Collider study (Rome, Italy, 2016)
320. P. Baudrenghien, I. Karpov, Beam loading and longitudinal stability evaluation for the FCC-ee Rings, in *Proceedings of the HB'18, Daejeon, Korea, Jun. 2018*, paper WEP2PO003, to be published (2018)
321. F. Pedersen, *IEEE Trans. Nucl. Sci.* **22**, 1906 (June, 1985)
322. P. Baudrenghien, T. Mastoridis, *Phys. Rev. Accel. Beams* **20**, 1 (January, 2017)
323. S.G. Zadeh, *Cavity Design approaches and HOM damping for FCC-ee*, Third Annual Meeting of the Future Circular Collider study (Berlin, Germany, 2017)
324. R. Calaga, F. Gerigk, S.G. Zadeh, U. van Rienen, FCC-ee hybrid rf scheme, in *Proceedings of the IPAC'18, Vancouver, BC, Canada* (2018), <http://jacow.org/ipac2018/papers/MOPMF028.pdf>, <http://ipac2018.vrws.de/papers/mopmf036.pdf>
325. *The BLonD code*, website: <http://blond.web.cern.ch>
326. J.F.E. Müller, *Modification of the simulation code BLonD for lepton rings fcc-draft-tech-2017-001* (CERN, 2017), <https://cds.cern.ch/record/2284587>
327. J.F.E. Müller, *FCC-ee broadband impedance and longitudinal single bunch stability fcc-draft-acc-2017-035* (CERN, 2017), <http://cds.cern.ch/record/2289514>
328. R. Calaga, *Beam dynamics issues for FCC-ee*, First FCC-ee RF mini review (2016)
329. M. Migliorati, *Single-beam collective effects in FCC-ee*, Second Annual Meeting of the Future Circular Collider study (Rome, Italy, 2016)
330. M. Aiba, B. Goddard, K. Oide, Y. Papaphilippou, Á. Saá Hernández, D. Shwartz, S. White, F. Zimmermann, *Nucl. Instr. Meth. A* **880**, 98 (2018)
331. A. Apyan et al., Extraction Line and Beam Dump for the FCC-ee, Presented at *ICFA workshop eeFACT 2016*, Cockcroft Institute at Daresbury Laboratory, UK (2016)
332. R. Takai et al., Beam profile measurement during top-up injection with a pulsed sextupole magnet, in *Proceedings of the European Workshop on Beam Diagnostics and Instrum. for Part. Accel. 2011* (2011), pp. 305–307
333. T. Atkinson et al., Development of a non-linear kicker system to facilitate a new injection scheme for the BESSY II storage ring, in *Proceedings of the IPAC'11* (2011), pp. 3394–3396
334. L.O. Dalin, S.C. Leeman, Progress on pulsed multipole injection for the MAX IV storage rings, in *Proceedings of the PAC'13* (2013), pp. 1052–1054
335. C. Pappas et al., *Development of nonlinear injection kicker magnet for ALS accelerator*, in *Proceedings of the IPAC'15* (2015), pp. 1837–1839
336. M. Aiba, C.H. Gough, Top-up injection with anti-septum in *Proceedings of the IPAC'17, Copenhagen, Denmark JACoW, Geneva, Switzerland* (May 14–19, 2017), pp. 774–776, <http://jacow.org/ipac2017/papers/mopik104.pdf>
337. N. Garrel, B. Goddard, W. Kalbreier, R. Keizer, Performance limitations in high voltage devices in the LEP Electron Positron Collider and its SPS Injector, in *2nd International Conference on Space Charge in Solid Dielectrics (CSC'2) Juan-les-Pins, Antibes, France* (April 2–7, 1995)
338. S. Bidon et al., Steel septum magnets for the LHC beam injection and extraction in *European Physical Society Accelerator Group, Proceedings of the EPAC'02, Paris, France* (June 3–7, 2002), pp. 2514–2516, <https://jacow.org/e08/papers/MOPLE083.pdf>
339. Archimedes of Syracuse, *On Spirals*, 225 BC
340. C. Bovet, LEP Beam Instrumentation, in *Proceedings of the Workshop on Advanced Beam Instrumentation, KEK, Tsukuba, Japan, CERN SL/91-17* (1991)
341. M. Arinaga et al., Beam Instrumentation for the SuperKEKB rings, *Proceedings of the IBIC'12, Tsukuba, Japan* (2012), p. 67
342. M. Arinaga et al., WP7: Rings with Ultra-Low Emittance (RULE), <https://aries.web.cern.ch/content/wp7>

343. K. Ohmi, N. Kuroo, K. Oide, D. Zhou, F. Zimmermann, *Phys. Rev. Lett.* **119**, 134801 (2017)
344. N. Kuroo, K. Ohmi, K. Oide, D. Zhou, F. Zimmermann, *Phys. Rev. Accel. Beams* **21**, 031002 (2018)
345. S.R. Marques, Beam diagnostics systems for Sirius light source, in *Proceedings of the IBIC'17, Grand Rapids, MI, USA* (2017), p. 89
346. E. Belli, Single bunch instabilities in FCC-ee, in *Proceedings of the IPAC'18, THPAK052, Vancouver, BC, Canada* (2018)
347. Website: <https://www.i-tech.si/accelerators-instrumentation/libera-brilliance-plus/benefits>
348. W. Koprek et al., Development of a new BPM electronics for the Swiss light source, in *Proceedings of the IBIC'12, Tsukuba, Japan* (2012), p. 399
349. U. Mavric, Innovative RF design unites benefits of multiplexed and multi-channel system, in *11th Beam Instrumentation Workshop, 2004, Knoxville, USA* (2004)
350. M. Barros Marin, A. Boccardi, C. Donat Godichal, J.L. Gonzalez, T. Lefevre, T. Levens, B. Szuk, *J. Instrum.* **11**, C02062 (2016)
351. T. Lefevre et al., Cherenkov diffraction radiation from long dielectric material: an intense source of photons in the NIR-THz range, in *Proceedings of the IPAC'17, Copenhagen, Denmark* (JACoW, Geneva, Switzerland, May 14–19, 2017), pp. 400–403, <http://jacow.org/ipac2017/papers/mopab118.pdf>
352. D. Cocq, A. Manarin, E. Rossa, J. Spanggaard, *Nucl. Instr. Meth. Phys. Res. A* **380**, 366 (1996)
353. C. Thomas, G. Rehm, I. Martin, R. Bartolini, *Phys. Rev. Accel. Beams* **13**, 022805 (2010)
354. M. Masaki, S., Takano, M. Takao, Y., Shimosaki, *Phys. Rev. Accel. Beams* **18**, 042802 (2015)
355. T. Mitsuhashi, T. Naito, *Phys. Rev. Accel. Beams* **9**, 122802 (2006)
356. W.J. Corbett et al., Transverse beam profiling and vertical emittance control with a double-slit stellar interferometer in *Proceedings of the IBIC'16, Barcelona, Spain, September 13–18, 2016* (JACoW, Geneva, Switzerland, February, 2017), pp. 237–240, <http://jacow.org/ibic2016/papers/mopg70.pdf>
357. T.M. Mitsuhashi, K. Oide, F. Zimmermann, Conceptual design for SR monitor in the FCC beam emittance (Size) diagnostic, in *Proceedings of the IPAC'16, Busan, Korea, May 8–13, 2016* (JACoW, Geneva, Switzerland, June, 2016), pp. 133–136, <http://jacow.org/ipac2016/papers/mopmb022.pdf>
358. M. Siano, B. Paroli, M.A.C. Potenza, U. Iriso, A.A. Nosych, L. Torino, S. Mazzoni, G. Trad, A.N. Goldblatt, *Phys. Rev. Accel. Beams* **20**, 110702 (2017)
359. R. Kieffer et al., submitted to *Phys. Rev. Lett.* (2018)
360. E. Rossa, N. Adams, F. Tomasini, J.M. Roth, Double sweep streak camera for LEP, in *Proceedings of the EPAC'90, Nice, France* (1990), pp. 783–785
361. C.P. Welsch, H.H. Braun, E. Bravin, R. Corsini, S. Döbert, T. Lefèvre, F. Tecker, P. Urschütz, B. Buonomo, O. Coiro, A. Ghigo, *J. Instrum.* **1**, P09002 (2006)
362. R. Pan, S.P. Jamison, T. Lefevre, W.A. Gillespie, *Nucl. Instrum. Methods Phys. Res. A* **821**, 8 (2016)
363. M. Gasior, M. Krupa, The wall current transformer – a new sensor for precise bunch-by-bunch intensity measurements in the LHC, in *Proceedings of the IBIC'16, Barcelona, Spain* (2016), p. 568
364. K. Wittenburg, *The PIN-diode beam loss monitor system at HERA, 9th Beam Instrumentation Workshop, Boston, USA, AIP Conference Proceedings* (2000), Vol. 546, pp. 3–8
365. Y.M. Shatunov, A.N. Skrinskii, *Sov. Phys. Usp.* **32**, 548 (1989)
366. M. Placidi, R. Rossmanith, e^+e^- polarimetry at LEP, *Nucl. Instrum. Meth. A* **274**, 79 (1989)
367. N. Muchnoi, H.J. Schreiber, M. Viti, *Nucl. Instrum. Methods Phys. Res. Sect. A* **607**, 340 (2009)

368. N.Y. Muchnoi, Measurement of beam polarisation and beam energy in one device, in *58th ICFA Advanced Beam Dynamics Workshop on High Luminosity Circular e^+e^- Colliders* (2016), <https://indico.cern.ch/event/588898/contributions/2374651/attachments/1373491/2084417/Nickolai-WET1H4-1.pdf>
369. G. Alexander, I.B. Mordechai, A transverse polarimeter for a linear collider of 250 GeV beam energy, in *Helmholtz Alliance Linear Collider Forum Proceedings of the Workshops Hamburg, Munich, Hamburg 2010–2012, Germany* (DESY, DESY, Hamburg, 2013), pp. 577–590
370. N. Muchnoi, *Session on FCC-ee beam polarization and energy calibration* (FCC Week, Amsterdam, The Netherlands, April, 2018)
371. S. DeBarger et al., *The PEP-II movable collimators*, SLAC-PUB-11752 (2001)
372. T. Ishibashi et al., Low impedance movable collimators for SuperKEKB, in *Proceedings of the IPAC'17, Copenhagen, Denmark* (May 14–19, 2017)
373. Conceptual design report for FCC-hh, *CLIQ – A New Quench Protection Technology for Superconducting Magnets* (CERN, Switzerland, 2018)
374. Q. Bai, B. Jin, D. Wang, Y. Wang, X. Liu, J. Instrum. **13**, T04004 (2018)
375. T. Wilksen et al., The control system for the linear accelerator at the European XFEL: status and first experiences, in *Proceedings of the 16th ICALEPCS'17, Barcelona, Spain, October 8–13, 2017* (2018), p. MOAPL01, <http://inspirehep.net/record/1656098/files/moapl01.pdf>
376. R. Ganter et al., *SwissFEL Conceptual Design Report* PSI Bericht 10–14, Paul Scherrer Institut (July, 2010), https://www.psi.ch/swissfel/SwissFELCDREN/SwissFEL_CDR_web_small.pdf
377. R. Huhmann et al., The FAIR control system – system architecture and first implementations, in *Proceedings of the ICALEPCS'13, San Francisco, CA, USA* (2013), p. MOPPC097, <http://accelconf.web.cern.ch/AccelConf/ICALEPCS2013/papers/moppc097.pdf>
378. M. Hankel, B. Rexroth, *The Reference Architectural Model Industrie 4.0 (RAMI 4.0)* Whitepaper Version 1.0, ZVEI: Die Elektroindustrie (April, 2015), https://www.zvei.org/fileadmin/user_upload/Themen/Industrie_4.0/Das_Referenzarchitekturmodell_RAMI_4.0_und_die_Industrie_4.0-Komponente/pdf/ZVEI-Industrie-40-RAMI-40-English.pdf
379. E.P. Boven, White rabbit in radio astronomy, in *Proceedings of the ICALEPCS'17, Barcelona, Spain* (2017), p. TUCPL03, <http://accelconf.web.cern.ch/AccelConf/icalepcs2017/>
380. N. Moreira, J. Lázaro, U. Bidarte, J. Jimenez, A. Astarloa, IEEE Trans. Smart Grid **8**, 1932 (2017)
381. R. Excel, G. Gaderer, P. Loschmidt, Comput. Netw. Commun. **2012**, 1 (2012)
382. As-2d2 Deterministic Ethernet and Unified Networking, *Time-Triggered Ethernet Standard AS 6802*, SAE International (September 11, 2016), <https://doi.org/10.4271/AS6802>
383. J. Allnut et al., *Timing Challenges in the Smart Grid* (Natl. Inst. Stand. Technol. Spec. Publ. 1500-08, U.S. Department of Commerce, January, 2017), <https://doi.org/10.6028/NIST.SP.1500-08>
384. C. Sydlo et al., Femtosecond Timing Distribution at the European XFEL, in *Proceedings of the FEL'15, Daejeon, Korea* (2015), p. WEP047, <http://accelconf.web.cern.ch/AccelConf/FEL2015/papers/wep047.pdf>
385. A. Aghababian et al., The Large Scale European XFEL Control System: Overview and Status of the Commissioning, in *Proceedings of the ICALEPCS'15, Melbourne, Australia* (2015), p. MOA3O02, http://tesla.desy.de/doocs/doocs_papers/ICALEPCS2015/moa3o02.pdf
386. A. Dinius, Q. King, B. Todd, S. Uznanski, J. Instrum. **7**, C11012 (2012)
387. F. Abdi et al., Application and System-Level Software Fault Tolerance through Full System Restarts, in *ACM/IEEE 8th International Conference on Cyber-Physical Systems (ICCPs)*, Pittsburgh, PA, USA (April 18–21, 2017), pp. 6505–6519, <https://ieeexplore.ieee.org/document/7945009/>

388. W. Benjamin et al., An open architecture for embedded systems: Hardware Open Systems Technologies, in *IEEE SoutheastCon, Charlotte, NC, USA* (March 30–April 2, 2017), pp. 6505–6519, <https://doi.org/10.1109/SECON.2017.7925388>
389. P. Bieth, V. Brindejone, *COTS-AEH – Use of complex COTS in airborne electronic hardware – failure mode and mitigation*, Research Project EASA.2012.C15 Report EASA.2012/04 (European Aviation Safety Agency, 2013), <https://www.easa.europa.eu/sites/default/files/dfu/Final%20Report%20EASA%202012-04.pdf>
390. National Instruments, *Considerations When Navigating Build or Buy Decisions for Industrial Embedded Control Projects*, White Paper 54072 (National Instruments, August 30, 2017), <http://www.ni.com/white-paper/54072/en/>
391. L. Yubin, L. Yucheng, 2010 Int. Forum Inf. Technol. Appl., **2**, 184 (2010)
392. B. Chen, J. Wan, L. Shu, P. Li, M. Mukherjee, B. Yin, *IEEE Access*, **6**, 6505 (2017)
393. I. Dai, P. Oleniuk, B. Todd, A. Voto, *J. Instrum.* **11**, C01047 (2016)
394. IEEE, *Systems and Software Engineering – System Lifecycle Processes*, Standard ISO 15288:2008 (IEEE/ISO/IEC, 2008) https://en.wikipedia.org/wiki/ISO/IEC_15288
395. K. Forsberg, H. Mooz, System engineering for faster, cheaper, better, in *INCOSE International Symposium Systems Engineering Past, Present and Future I, Brighton, England* (June 6–11, 1999), Vol. 9, pp. 924–932
396. European Commission, *Horizon 2020 Work Programme 2016–2017. 5.i. Information and Communication Technologies*, European Commission Decision C (European Commission, April 24, 2017), p. 2468, http://ec.europa.eu/research/participants/data/ref/h2020/wp/2016_2017/main/h2020-wp1617-leit-ict_en.pdf
397. J. Gutleber, A. Brett, R. Moser, M. Marchhart, C. To rcato de Matos, J. Dedic, The MedAustron accelerator control system, in *Proceedings of the ICALEPCS’11, Grenoble, France* (October 10–14, 2011), pp. 9–12, <https://accelconf.web.cern.ch/accelconf/icalepcs2011/papers/mobaust03.pdf>
398. J. Gutleber, R. Moser, The MedAustron accelerator control system: design installation and commissioning, in *14th International Conference on Accelerator and Large Experimental Physics Control Systems, San Francisco, CA, USA* (March 6–11, 2013), p. TUCOAAB04, <https://cds.cern.ch/record/1697002>
399. Cosylab, *Accelerator Control System for PT* (2018), <https://www.cosylab.com/accelerator-control-system-for-pt/>
400. D. Ondreka, U. Weinrich, The Heidelberg Ion Therapy (HIT) accelerator coming into operation, in *European Physical Society Accelerator Group, Proceedings of EPAC 2008, Genoa, Italy* (June 23–27, 2008), pp. 979–981, <https://accelconf.web.cern.ch/accelconf/e08/papers/tuocg01.pdf>
401. S. Rossi, *Eur. Phys. J. Plus* **126**, 78 (2011)
402. S. Giordanengo, M.A. Garella, F. Marchetto, F. Bourhaleb, M. Ciocca, A. Mirandola, V. Monaco, M.A. Hosseini, C. Peroni, R. Sacchi, R. Cirio, M. Donetti, *Med. Phys.* **42**, 263 (2016)
403. P. Bryant, L. Evans, *J. Instrum.* **3**, 98 (2008)
404. B. Kihei, Automotive Doppler sensing: The Doppler profile with machine learning in vehicle-to-vehicle networks for road safety, in *18th IEEE International Workshop on Signal Processing Advances in Wireless Communications, Sapporo, Japan* (July 3–6, 2017)
405. ICFA, *Beam Dynamics Mini-Workshop: Machine Learning Applications for Particle Accelerators. SLAC National Accelerator Laboratory, Menlo Park, CA, USA* (Indico presentation, 27 February–2 March, 2018), <https://indico.fnal.gov/event/16327/other-view?view=standard>
406. R.G. Alia, M. Brugger, S. Danzeca, F. Cerutti, J.P. de Carvalho Saraiva, R. Denz, A. Ferrari, L.L. Foro, P. Peronnard, K. Røed, R. Secondo, J. Steckert, Y. Thurel, I. Toccafondo, S. Uznanski, *Semicond. Sci. Technol.* **32** (2017)
407. T.T. Böhlen, F. Cerutti, M.P.W. Chin, A. Fassò, A. Ferrari, P.G. Ortega, A. Mairani, P.R. Sala, G. Smirnov, V. Vlachoudis, *Nucl. Data Sheets* **120**, 211 (2014)

408. A. Fassò, A. Ferrari, J. Ranft, P.R. Sala, *FLUKA: A Multi-particle Transport Code*, Report CERN-2005-10 (CERN, Geneva, Switzerland, 2005), Also available as INFN/TC_05/11 and SLAC-R-773
409. R. Kersevan, *FCC-ee Vacuum Effects and Simulations*, Presentation at FCC Week 2016 (Rome, Italy, 2016), <https://indico.cern.ch/event/438866/contributions/1085121/>
410. A. Apollonio et al., Roadmap towards high accelerator availability for the CERN HL-LHC Era, in *Proceedings of the 6th IPAC'15, Richmond, Virginia, USA* (May 3–8, 2015), TUPTY053
411. G. Tsiliannis, S. Danzeca, R. García Alía, A. Infantino, A. Lesea, M. Brugger, A. Masi, S. Gilardoni, F. Saigné, IEEE Trans. Nucl. Sci. **65**, 1 (2018)
412. S. Bonaldo, G. Borghello, E. Lerario, D.M. Fleetwood, R.D. Schrimpf, H. Gong, E.X. Zhang, P. Wang, S. Michelis, S. Gerardin, A. Paccagnella, IEEE Trans. Nucl. Sci. **65**, 164 (January 2018),
413. S. Bonaldo et al., Dose rate sensitivity of 65 nm MOSFETs exposed to ultra-high doses, in *2017 17th European Conference on Radiation and Its Effects on Components and Systems* (RADECS, October 2017)
414. D. Cornale et al., *Radiation-Induced Short Channel (RISCE) and Narrow Channel (RINCE) Effects in 65 and 130 nm MOSFETs*, IEEE Transactions on Nuclear Science **62.6** (Dec. 2015), pp. 2933–2940
415. M.L. Alles et al., IEEE Trans. Nucl. Sci. **64**, 285 (2017)
416. Geoconsult and Gibb and SGI Ingenieure, *LHC Civil Engineering Consultancy Services, Package 2 – Geotechnical Interpretative Report*, CERN (1996)
417. T. Touzé, *Feasibility of the CLIC Metrological Reference Network* (CERN, Geneva, Switzerland, 2010), http://iwaa2010.desy.de/e107506/e107507/e113375/e119274/IWAA2010_TT_CLIC.pdf
418. H. Mainaud-Durand, *Alignment Requirements for the LHC Low-beta Triplets* (CERN, Geneva, Switzerland, 2006), <https://edms.cern.ch/ui/file/344496/1.2/LHC-G-ES-0016-10-20.pdf>
419. D. Clark, IEEE Comput. Sci. Eng. **5**, 84 (1998)
420. I. Bird, L. Robertson, J. Shiers, Deploying the LHC computing grid – the LCG service challenges, in *2005 IEEE International Symposium on Mass Storage Systems and Technology* (June, 2005), pp. 160–165, <https://doi.org/10.1109/LGDI.2005.1612486>
421. J.C. Webber, The ALMA Telescope, in *2013 IEEE MTT-S International Microwave Symposium Digest (MTT)* (June, 2013), pp. 1–3, <https://doi.org/10.1109/MWSYM.2013.6697433>
422. D. Ding, D. Wu, F. Yu, An overview on cloud computing platform spark for Human Genome mining, in *2016 IEEE International Conference on Mechatronics and Automation* (August, 2016), pp. 2605–2610, <https://doi.org/10.1109/ICMA.2016.7558977>
423. G. Antchev et al., IEEE Trans. Nucl. Sci. **47**, 293 (2000)
424. K. Anikeev et al., Comput. Phys. Commun. **140**, 110 (2001)
425. DESY, *MicroTCA Technology Lab* (2018), website: <https://techlab.desy.de>
426. CERN, *openlab* (2018), website: <https://openlab.cern>
427. Conseil régional Auvergne-Rhône-Alpes, *Numérique. Feuille de route stratégique de la Région Auvergne-Rhône-Alpes 2017–2021* (2018), Website of the ARA region <https://www.auvergnerhonealpes.fr/95-infrastructures-economie-usages-numeriques.htm>
428. Grand Genève Agglomération Franco-Valdo-Genevoise, *Charte d'engagement du projet de territoire Grand Genève 2016–2030* (December, 2016), website: http://www.grand-geneve.org/sites/default/files/fichiers/projet-agglomeration3/charte_2016-projet-territoire.pdf
429. Sepura, *Case study: advancing safety and communications at CERN* (January, 2014), website: <https://www.seapura.com/media/166841/cern-case-study.pdf>
430. Euro-IX, *Information on carrier neutrality* (2018), website: <https://www.euro-ix.net/en/forixps/set-ixp/ixp-models/neutrality>

431. CERN, *Documents and maps of the Worldwide LHC Computing Grid (WLCG)* (2018), website: <http://wlcg.web.cern.ch/documents-reference>
432. H. Schopper, *Rivista del Nuovo Cimento* **40**, 199 (2017)
433. B. Panzer-Steindel, *IT Technology and Markets, Status and Evolution* (Indico presentation, March 26, 2018), https://indico.cern.ch/event/658060/contributions/2889027/attachments/1622791/2583013/tech_market_BPS_Mar2018_v9pptx.pdf
434. A.D. Meglio, M. Girone, A. Purcell, F. Rademakers, *CERN Openlab White Paper on Future ICT Challenges in Scientific Research* (January, 2018), <http://cds.cern.ch/record/2301895>
435. A. Bastianin, M. Florio, *Social Cost Benefit Analysis of HL-LHC*, CERN-ACC-2018-0014 (CERN, Geneva, Switzerland, May, 2018), <https://cds.cern.ch/record/2319300>
436. S. Schmeling, *IEEE Trans. Nucl. Sci.* **53**, 970 (2006)
437. D. Collaboration, *Data Preservation in High Energy Physics (DPHEP)* (2018), website: <https://hep-project-dpheap-portal.web.cern.ch>
438. F. Berghaus et al., *CERN Services for Long Term Data Preservation*, CERN-IT-Note-2016-004 (CERN, Geneva, Switzerland, July, 2016), <https://cds.cern.ch/record/2195937>
439. *SLAC linear collider conceptual design report* (SLAC, Palo-Alto, CA, USA, 1980), <http://inspirehep.net/record/154130/files/slac-r-229.pdf>, SLAC-229.
440. T. Miura et al., Upgrade Status of Injector LINAC for SuperKEKB, in *Proceedings of the IPAC'14, Dresden, Germany* (2014), pp. 59–61
441. The LEP injector study group, *The LEP injector chain*, CERN-SPS/63-26 (CERN, Geneva, Switzerland, 1980), <http://inspirehep.net/record/154130/files/slac-r-229.pdf>
442. S. Ogur et al., Bunch Schedules for the FCC-ee Pre-injector, in *Proceedings of the IPAC'18, Vancouver, Canada* (2011), pp. 2857–2861
443. A.V. Andrianov et al., *J. Instrum.* **11**, P06007 (2016)
444. A.V. Chernousov et al., *Accelerating structure with parallel connection*, Report
445. G.I. Kuznetsov, *J. Phys.: Conf. Ser.* **2**, 35 (2004)
446. D. Satoh et al., *Energy Procedia* **13**, 326 (2017)
447. K. Floettmann, *ASTRA, A Space Charge Tracking Algorithm* Private website: <http://www.desy.de/~mpyflo/>
448. I. Chaikovska et al., Experimental Activities on High Intensity Positron Sources Using Channelling, in *Proceedings of the IPAC'17, Copenhagen, Denmark* (2017), pp. 2910–2913
449. I. Chaikovska et al., *Positron source* (Indico presentation, 2017), https://indico.cern.ch/event/556692/contributions/2590440/attachments/1468997/2272259/e_FCCweek2017_IC.pdf
450. K. Yokoya, *Short-Range Wake Formulas for Infinite Periodic Pill-Box* (1998)
451. S. Ogur et al., Towards a Preliminary FCC-ee Injector Design, in *Proceedings of the eeFACT'16, Daresbury, UK* (2016), pp. 90–93
452. T. Raubenheimer, *Nucl. Instr. Meth. A* **306**, 61 (1991)
453. R. Chehab et al., Study of a positron source generated by photons from ultrarelativistic channelled particles, in *Proceedings of the IPAC'89* (1989), pp. 283–285
454. R. Chehab, R. Cizeron, C. Sylvia, V. Baier, K. Beloborodov, A. Bukin, S. Burdin, T. Dimova, A. Drozdetsky, V. Druzhinin, M. Dubrovin, Experimental study of a crystal positron source, *Phys. Lett. B* **525**, 41 (2002)
455. X. Artrue, R. Chehab, M. Chevallier, V.M. Strakhovenko, A. Variola, A. Vivoli, *Nucl. Instrum. Methods B* **266**, 3886 (2008)
456. Y. Uesugi, T. Akagi, R. Chehab, O. Dadoun, K. Furukawa, T. Kamitani, S. Kawada, T. Omori, T. Takahashi, K. Umemori, J. Urakawa, *Nucl. Instrum. Methods B* **319**, 17 (2014)
457. S. Ogur, A. Barnyakov, K. Furukawa, N. Iida, A. Levichev, F. Miyahara, D. Nikiforov, K. Oide, Y. Papaphilippou, F. Zimmermann, *J. Phys.: Conf. Ser.* **874**, 012003 (2017)

458. F.J. Decker et al., *Long-Range Wakefields and Split-Tune Lattice at the SLC*, SLAC-PUB-7259 (1996)
459. N. Iida et al., *Beam dynamics in positron injector systems for the next generation b-factories*, in *Proceedings of the IPAC'11, San Sebastian, Spain* (2011), pp. 2857–2861
460. S. Thorin et al., Bunch compression by linearising achromats for the MAX IV injector, in *Proceedings of the FEL'10, Malmö, Sweden* (2010), pp. 471–474
461. Y. Sun, P. Emma, T. Raubenheimer, J. Wu, *Phys. Rev. ST Accel. Beams* **17**, 110703 (2014)
462. T.K. Charles et al., Bunch compression and turnaround loops in the FCC-ee injector complex, in *Proceedings of the IPAC'18, Vancouver, Canada* (2018)
463. D. Douglas, *Suppression and Enhancement of CSR-Driven Emittance Degradation in the IR-FEL Driver*, Technical Report JLAB-TN-98-012 (1998)
464. S. Di Mitri, M. Cornacchia, S. Spampinati, *Phys. Rev. Lett.* **110**, 014801 (2013)
465. M. Cornacchia, S. Di Mitri, *Phys. Rep.* **539**, 1 (2014)
466. R. Hajima, *Jpn. J. Appl. Phys.* **42**, L974 (2003)
467. Y. Jiao, X. Cui, X. Huang, G. Xu, *Phys. Rev. ST Accel. Beams* **17**, 060701 (2014)
468. Y. Papaphilippou, L. Evans, R. Corsini, The SPS as an ultra-low emittance damping ring test facility for CLIC, in *Proceedings of the IPAC'13, Shanghai, China* (2013), pp. 1661–1663
469. CERN-BE/ABP Accelerator Beam Physics Group, *MAD-Methodical Accelerator Design*, Project website
470. BaBar Collaboration, B. Aubert et al., *Nucl. Instrum. Meth. A* **729**, 615 (2013)
471. S. Agostinelli et al., *Nucl. Instrum. Methods Phys. Res. Sect. A* **506**, 250 (2003)
472. S. Mrenna, T. Sjöstrand, P.Z. Skands, *JHEP* **5**, 26 (2006)
473. OPAL Collaboration, G. Abbiendi et al., *Eur. Phys. J. C* **14**, 373 (2000)
474. D. Bédérède et al., *Nucl. Inst. Meth. A* **365**, 117 (1995)
475. T. Behnke, J.E. Brau, P.N. Burrows, J. Fuster, M. Peskin, M. Stanitzki, Y. Sugimoto, S. Yamada, H. Yamamoto, *The International Linear Collider Technical Design Report – Volume 4: Detectors* (2013), [arXiv:1306.6329](https://arxiv.org/abs/1306.6329) [physics.ins-det]
476. J.F. Crawford, E.B. Hughes, L.H. O'Neill, R.E. Rand, *Nucl. Instrum. Methods* **127**, 173 (1975)
477. S. Jadach, W. Placzek, E. Richter-Wąs, B.F.L. Ward, Z. Wąs, *Comput. Phys. Comm.* **102**, 229 (1997)
478. P. Bambade, K. Mönig, C. Rimbault, D. Schulte, *J. Instrum.* **2**, P09001 (2007)
479. S. Jadach, W. Placzek, B.F.L. Ward, *Phys. Lett. B* **390**, 298 (1997)
480. O. Blanco et al., *Study of Inelastic Beam-Gas for FCC-ee* (Indico presentation, March, 2018), <https://indico.cern.ch/event/709474/>
481. N. Alipour Tehrani et al., *CLICdet: The post-CDR CLIC detector model* (March, 2017), <https://cds.cern.ch/record/2254048>, CLICdp-Note-2017-001
482. ALICE Collaboration, *J. Phys. G* **41**, 087002 (2014), ALICE-TDR-017
483. M. Frank, F. Gaede, C. Grefe, P. Mato, *J. Phys.: Conf. Ser.* **513**, 022010 (2014)
484. ALEPH Collaboration, D. Buskulic et al., *Nucl. Instrum. Meth. A* **360**, 481 (1995)
485. CMS Collaboration, A.M. Sirunyan et al., *JINST* **12**, P10003 (2017)
486. J.S. Marshall, M. Thomson, *Eur. Phys. J. C* **75**, 439 (2015)
487. F. Sefkow, A. White, K. Kawagoe, R. Pöschl, J. Repond, Experimental Tests of Particle Flow Calorimetry, *Rev. Mod. Phys.* **88**, 015003 (2016)
488. ALICE Collaboration, M. Mager, *Nucl. Instrum. Meth. A* **824**, 434 (2016)
489. ALICE Collaboration, G. Aglieri Rinella, *Nucl. Instrum. Meth. A* **845**, 583 (2017)
490. G. Chiarello, C. Chiri, A. Corvaglia, F. Grancagnolo, A. Miccoli, M. Panareo, A. Pepino, C. Pinto, P. Primiceri, M. Spedicato, G.F. Tassielli, *Nucl. Instrum. Methods Phys. Res. A* **824**, 512 (2016)
491. M. Adinolfi et al., *Nucl. Instrum. Meth. A* **488**, 51 (2002)
492. A.M. Baldini et al., *MEG Upgrade Proposal* (2013), [arXiv:1301.7225](https://arxiv.org/abs/1301.7225) [physics.ins-det], <http://adsabs.harvard.edu/abs/2013arXiv1301.7225B>

493. G. Chiarello, A.M. Baldini, G. Cavoto, F. Cei, M. Chiappini, A. Corvaglia, M. Francesconi, L. Galli, F. Grancagnolo, M. Grassi, M. Hildebrandt, A. Miccoli, D. Nicol , A. Papa, M. Panareo, C. Pinto, F. Raffaelli, F. Renga, G. Signorelli, G.F. Tassielli, C. Voena, *The construction technique of the new MEG II tracker, Poster presented at the 14th Pisa meeting on advanced detectors, La Biodola, Italy*, Poster presentation (May, 2018), <https://agenda.infn.it/getFile.py/access?contribId=410&sessionId=17&resId=0&materialId=poster&confId=13450>
494. A.M. Baldini, E. Baracchini, G. Cavoto, M. Cascella, F. Cei, M. Chiappini, G. Chiarello, C. Chiri, S. Dussoni, L. Galli, F. Grancagnolo, M. Grassi, V. Martinelli, D. Nicol , M. Panareo, A. Pepino, G. Piredda, F. Renga, E. Ripiccini, G. Signorelli, G.F. Tassielli, F. Tenchini, M. Venturini, C. Voena, *J. Instrum.* **11**, P07011 (2016)
495. The FCC Design Study Software Group, C. Bernet, B. Hegner, C. Helsens, et al., *FCCSW, the common software framework for FCC experiments*, website: <http://fccsw.web.cern.ch/fccsw/index.html>
496. DREAM Collaboration, R. Wigmans, *Nucl. Instrum. Meth. A* **617**, 129 (2010)
497. N. Akchurin, F. Bedeschi, A. Cardini, M. Cascella, F. Cei, D. De Pedis, R. Ferrari, S. Fracchia, S. Franchino, M. Fraternali, G. Gaudio, P. Genova, J. Hauptman, L. La Rotonda, S. Lee, M. Livan, E. Meoni, A. Moggi, D. Pinci, A. Policicchio, J.G. Saraiva, F. Scuri, A. Sill, T. Venturelli, R. Wigmans, *Nucl. Instrum. Meth. A* **735**, 130 (2014)
498. RD52 (DREAM) Collaboration, R. Wigmans, *Nucl. Instrum. Meth. A* **824**, 721 (2016)
499. N. Akchurin, F. Bedeschi, A. Cardini, M. Cascella, D. De Pedis, R. Ferrari, S. Fracchia, S. Franchino, M. Fraternali, G. Gaudio, P. Genova, J. Hauptman, L. La Rotonda, S. Lee, M. Livan, E. Meoni, D. Pinci, A. Policicchio, J.G. Saraiva, F. Scuri, A. Sill, T. Venturelli, R. Wigmans, *Nucl. Instrum. Methods Phys. Res. Sect. A* **735**, 120 (2014)
500. G. Bencivenni, L. Benussi, L. Borgonovi, R. de Oliveira, P. De Simone, G. Felici, M. Gatta, P. Giacomelli, G. Morello, A. Ochi, M. Poli Lener, A. Ranieri, M. Ressegotti, E. Tskhadadze, I. Vai, V. Valentino, *J. Instrum.* **12**, C06027 (2017)
501. G. Acquistapace, J. Andre, M.H. Bovard, A. Calvo, D. Campi, B. Cure, D. Delikaris, A. Desirelli, P. Fabbicatore, S. Farinon, F. Feyzi, J.C. Gelebart, H. Gerwig, J.P. Girod, J.P. Grillet, L. Greenler, G.M. Gregerson, Alain Herve, I.L. Horvath, V. Kaftanov, A. Le Coroller, C. Lesmond, B. Levesy, J.C. Lottin, J.P. Lottin, R. Loveless, C. Lyraud, W.P. Mason, J.M. Maugain, R. Musenich, G. Passardi, C. Pes, P. Petiot, R. Pintus, J. Pippin, O. Pogorelko, C. Priano, J.M. Rey, F. Rondeaux, J.Y. Rousse, R. Smith, T. de Visser, L. Veillet, B. Wands, G. Waurick, *CMS, the Magnet Project: Technical Design Report CERN-LHCC-97-10*, CMS (1997)
502. The ATLAS Collaboration, *J. Inst.* **3**, S08003 (2008)
503. H.H.J. Ten Kate, *Presentation given at the 2018 FCC collaboration meeting in Amsterdam*, FCC Week presentation (April, 2018), https://indico.cern.ch/event/656491/contributions/2939122/attachments/1629705/2597192/20180409-TenKate_-_FCCee_IDEA_thin_2T_Solenoid.pdf
504. H. Pais da Silva, *Priv. commun.* (June, 2018)
505. A. Bragin, *Presentation given at the 2018 super tau-charm factory workshop, "Thin solenoid for the CTF detector placed in front of the identification system"*, (Indico presentation, May, 2018), <https://indico.inp.nsk.su/event/13/other-view?view=standard>
506. G. Chiarello et al., *The Use of FPGA in Drift Chambers for High Energy Physics Experiments in Field – Programmable Gate Array* (InTech, May, 2017) DOI: [10.5772/66853](https://doi.org/10.5772/66853)
507. L. Linssen, A. Miyamoto, M. Stanitzki, H. Weerts, *Physics and Detectors at CLIC: CLIC Conceptual Design Report* (Geneva, Switzerland, 2012), [arXiv:1202.5940](https://arxiv.org/abs/1202.5940) [physics.ins-det], <https://cds.cern.ch/record/1425915>, CERN-2012-003, ANL-HEP-TR-12-01, DESY-12-008, KEK-Report-2011-7
508. CERN Linear Collider Detector collaboration, D. Dannheim, A. Gaddi, *CLIC Detector Power Requirements* (December, 2013), <https://cds.cern.ch/record/1602917>, LCD-Note-2013-011

509. Gouvernement de la République française and CERN, *Accord entre le Gouvernement de la République française et l'Organisation Européenne pour la Recherche Nucléaire relatif au statut juridique de ladite Organisation en France* CERN institutional documents (CERN, Geneva, Switzerland, August, 1973), <https://cds.cern.ch/record/436804/files/CM-B00042459.pdf>
510. U. Forsblom-Pärli, S. Aschwanden, R. Burri, L. Escher, R. Hauser, W. Scheidegger, *Connaissez-vous le potentiel des phénomènes dangereux dans votre entreprise?* instruction, système selon commission fédérale de coordination pour la sécurité au travail, SUVA – Protection de la santé (June, 2011), <https://www.suva.ch/materiel/documentation/connaissez-vous-le-potentiel-des-phenomenes-dangereux-dans-votre-entreprise-le-66105.f-25527-25526>
511. S.L. Mendola, *FCC performance-based safety design – A proposal for a methodology founded on the SFPE guideline* Internal presentation (CERN, June, 2017), <https://edms.cern.ch/document/1770088>
512. International Electrotechnical Commission, *IEC 60812:2018 – Failure modes and effects analysis (FMEA and FMECA)*, 3rd edn., (International Standard. IEC, Geneva, Switzerland, August 10, 2018), <https://cds.cern.ch/record/436804/files/CM-B00042459.pdf>
513. O. Rios, A. Arnalich, *Quantitative Assessment of Fire Hazard for FCC-hh (and FCC-ee)* Internal report (CERN, June, 2018), <https://edms.cern.ch/document/1975602>
514. A. Henriques, *Private communication* (CERN, Geneva, Switzerland, April, 2018)
515. STUVA e.V. society, *Security and Workplace Safety Concepts for the Construction, Installation and Operation of the XFEL Research Facility* European XFEL project documentation, European XFEL GmbH (August, 2005), Project internal, Not public
516. K. McGrattan, S. Hostikka, R. McDermott, J. Floyd, M. Vanella, *Fire Dynamics Simulator User's Guide* special publication, National Institute of Standards and Technology (June, 2018), <https://pages.nist.gov/fds-smv/>; https://github.com/firemodels/fds/releases/download/FDS6.7.0/FDS_User_Guide.pdf
517. T. Otto, *Release of Gaseous Helium in Tunnels* EDMS 1853419 (CERN, Geneva, Switzerland, October, 2017), <https://edms.cern.ch/document/1853419>
518. La République française, *Article L1333-1 to L1333-25*, Code de la santé publique (2018), https://www.legifrance.gouv.fr/telecharger_pdf.do?cidTexte=LEGITEXT000006072665
519. L'Assemblée fédérale de la Confédération suisse, *Loi sur la radioprotection (LRaP)*, Recueil officiel du droit fédéral (RO) (2017), <https://www.admin.ch/opc/fr/classified-compilation/19910045/index.html>
520. L. Bruno, M. Magistris, *Radioactive Waste Management at CERN*, Technical Note EDMS 1453489 (2017)
521. Energy for Sustainable Science at Research Infrastructures, *4th Workshop in Măgurele, Bucharest, Romania* (November 23–24, 2017)
522. *EuCard2 (Enhanced European Coordination for Accelerator Research and Development)*, website: <http://eucard2.web.cern.ch/>
523. *EuCard2 Work Package 3*, Website: <https://www.psi.ch/en/inefficient/>
524. *ARIES (Accelerator Research and Innovation for European Science and Society)*, website: <https://aries.web.cern.ch/>
525. M. Seidel, Energy efficiency of accelerators in the European Programs EuCard2 and ARIES, *November 23–24, 2017, 4th Workshop Energy for Sustainable Science at Research Infrastructures, Măgurele, Bucharest, Romania* (2017)
526. S. Aull, M. Benedikt, D. Bozzini, O. Brunner, J.-P. Burnet, A. Butterworth, R. Calaga, E. Jensen, V. Mertens, A. Milanese, M. Nonis, K. Oide, N. Schweg, L. Tavian, J. Wenninger, F. Zimmermann, L. Rinolfi, A. Blondel, M. Koratzinos, S. Gorgi Zadeh, *Electrical Power Budget for FCC-ee in Proceedings of the IPAC'16, Busan, Korea* (2016), <http://jacow.org/ipac2016/papers/thpor024.pdf>
527. S. Aull, O. Brunner, A. Butterworth, N. Schweg, *Material Options for the Superconducting RF System of the Future Circular Collider* CERN-ACC-2018-0019 (CERN, Geneva, Switzerland, 2018), <http://cds.cern.ch/record/2625126>

528. J.P. Delahaye, *Muon Colliders vs other technologies based Colliders* (ARIES Muon Collider Workshop, Padova, 2–3 July 2018)
529. A. Grosjean, *Tout un quartier chauffé grâce au CERN* (Tribune de Genève, 2018), <https://www.tdg.ch/geneve/actu-genevoise/Tout-un-quartier-chauffe-grce-au-CERN/story/28974479>
530. K. Biesheuvel, R. de Boer, S. Smeding, Waste Heat recovery in industrial batch processes: analysis of combines heat storage and heat pump application in *Proceedings of the 12th IEA Heat Pump Conference* (HPC, IEA Rotterdam, The Netherlands, June, 2017) Vol. 12, <http://hpc2017.org/wp-content/uploads/2017/05/O.3.8.1-Waste-Heat-recovery-in-industrial-batch-processes-analysis-of-combined-heat-storage.pdf>
531. F. Campana, M. Bianchi, L. Branchini, A. De Pascale, A. Peretto, M. Baresi, A. Fermi, N. Rossetti, R. Vescovob, *Energ. Convers. Manage.* **76**, 244 (2013)
532. P. Colonna, E. Casati, C. Trapp, T. Mathijissen, J. Larjola, T. Turunen-Saaresti, A. Uusitalo, *J. Eng. Gas Turbines Power* **137**, 19 (2015)
533. *Accord entre le Gouvernement de la République française et l'Organisation européenne pour la Recherche nucléaire relatif au statut juridique de ladite Organisation en France* (CERN, Geneva, Switzerland, 1973), <https://cds.cern.ch/record/436804>
534. *Convention entre le Conseil fédéral de la Confédération suisse et le Gouvernement de la République française relative à l'extension en territoire français du domaine de l'Organisation européenne pour la recherche nucléaire*, Le Conseil fédéral, Chancellerie fédérale, Palais fédéral ouest, 3003 Berne, Switzerland (September 13, 1965), <https://www.admin.ch/opc/fr/classified-compilation/19650161>
535. A. Poiron, M. Zahnd, *FCC Layout Review in Switzerland* deliverable report contract ca 3797383, Ecotec (December, 2017), <https://edms.cern.ch/document/1838912>
536. Le Conseil fédéral suisse, *Ordonnance relative à l'étude de l'impact sur l'environnement 814.011 (UVPV)*, Recueil officiel du droit fédéral (RO) (2016), <https://www.admin.ch/opc/fr/classified-compilation/19880226/index.html>
537. Office fédéral de l'environnement OFEV, *Directive de la Confédération sur l'étude de l'impact sur l'environnement (Manuel EIE)*, Serie L'environnement pratique (2009), <https://www.bafu.admin.ch/bafu/fr/home/themes/eie/publications/manuel-eie.html>
538. Le Président de la République, *Code de l'environnement*, Journal officiel de la République française (2018), <https://www.legifrance.gouv.fr/affichCode.do?cidTexte=LEGITEXT000006074220&dateTexte=20180924>
539. UNECE, *Convention on environmental impact assessment in a transboundary context* Convention ECE/MP.EIA/21/Amend.1, United Nations, Avenue de la Paix 8, 1202 Genève, Suisse (October, 2017), http://www.unece.org/env/eia/about/eia_text.html
540. M. Hofert, L. Moritz, G.R. Stevenson, *Radiological impact of the LHC project on the environment* (1997), <https://cds.cern.ch/record/325861>, CERN-TIS-97-006-RP, CERN-TIS-97-06-RP, CERN-TIS-97-6-RP
541. M. Silari, L. Ulrici, *Nucl. Instr. Meth. A* **526**, 510 (2004)
542. A. Bibet-Chevalier, D. Chanal, *Étude de sensibilité du scénario d'implantation du project FCC en France et de ses opportunités* Rapport d'étude du Cerema FCC-INF-RPT-040 and EDMS 1853668 (CEREMA, April 26, 2018), <https://edms.cern.ch/document/1853668>
543. Le Conseil fédéral suisse, *Ordonnance sur l'aménagement du territoire (OAT) 700.1*, Recueil officiel du droit fédéral (RO) (2016), <https://www.admin.ch/opc/fr/classified-compilation/national.html>
544. *GeniLac*, website: http://www.citedelenergie.ch/fileadmin/user_upload/Energiestadt/de/Dateien/Instrumente/6_Kommunikation/6_5_2_GeniLa.pdf
545. M. Magistris, H. Vincke, M. Widorski, *Radioactive Waste estimates for the FCC project* EDMS 1992036 (CERN, Geneva, Switzerland, 2018), <https://cds.cern.ch/record/1992036>

546. Département du Rhône-Métropole de Lyon, *Plan de prévention et de gestion des déchets non dangereux du Rhône et de la Métropole de Lyon* version définitive, Département du Rhône-Métropole de Lyon (June, 2015), <http://www.sindra.org/wp-content/uploads/2017/01/Plan-dC3A9chets-non-dangereux-RhC3B4ne-MC3A9tropole-de-Lyon.pdf>
547. Le Président de la République, Journal officiel de la République française, **14263** (2018), <https://www.legifrance.gouv.fr/affichTexte.do?cidTexte=JORFTEXT000031044385>
548. République et Canton de Genève, *Genève – Plan directeur cantonal 2030* première mise à jour, Direction de la planification directrice cantonale et régionale, service du plan directeur cantonal (February, 2017), <https://www.ge.ch/consulter-plans-amenagement-adoptes/plan-directeur-cantonal>
549. P. Joxe, Journal officiel de la République française **33** (2018) 2064, <https://www.legifrance.gouv.fr/affichTexte.do?cidTexte=JORFTEXT000000722113&dateTexte=20180201>
550. Le Président de la République, Journal officiel de la République française **75**, 5568 (2003), <https://www.legifrance.gouv.fr/affichTexte.do?cidTexte=JORFTEXT000000722113&dateTexte=20180201>
551. UNECE, Treaty Ser. **2161**, 447 (1998), https://treaties.un.org/Pages/src-IND-mtdsg_no-XXVII-13-chapter-27-lang-_en-PageView.aspx
552. CEREMA, *Rapport d'études sur les impacts pour l'État en matière de procédures et d'engagements financiers* report, Secrétariat Général pour les Affaires Régionales d'Auvergne-Rhône-Alpes (April, 2018), This report is for government-internal purposes only
553. Le Président de la République, Journal officiel de la République française (JORF) **248** (2002), <https://www.legifrance.gouv.fr/affichTexte.do?cidTexte=JORFTEXT000000232649&categorieLien=id>
554. Le Président de la République, Journal officiel de la République française (JORF), **0181** (2016), <https://www.legifrance.gouv.fr/affichTexte.do?cidTexte=JORFTEXT000032966723&categorieLien=id>
555. Commission nationale du débat public, *Comment ça marche ?* site internet de l'institution, Commission nationale du débat public, 244 boulevard Saint-Germain 75007 Paris France (October, 2002), <https://www.debatpublic.fr/comment-ca-marche>
556. Journal officiel de la République française (JORF), Journal officiel de la République française, **0261** (2014), https://www.legifrance.gouv.fr/affichTexte.do;jsessionid=62A9EC171A12674F234586C187CE51F1.tplgr24s_3?cidTexte=JORFTEXT000029730657&dateTexte=20141111
557. Le Président de la République, Journal officiel de la République française (2018), <https://www.legifrance.gouv.fr/affichTexte.do?cidTexte=JORFTEXT000033926976>
558. Le Président de la République, Journal officiel de la République française **0128**, 10339 (2018), <https://www.legifrance.gouv.fr/affichTexte.do?cidTexte=JORFTEXT000022308227>
559. Direction de l'ARE, *Surfaces d'assolement selon le plan sectoriel SA* Modèle de géodonnées minimal. Documentation sur le modèle. 68, Office fédéral du développement territorial ARE, Worblenstrasse 66, CH-3063 Ittigen, Schweiz (November, 2015), <https://www.are.admin.ch/are/fr/home/developpement-et-amenagement-du-territoire/strategie-et-planification/conceptions-et-plans-sectoriels/plans-sectoriels-de-la-confederation/sda.html>
560. Conseil d'Etat de la République et canton de Genève, *Surfaces d'assolement selon le plan sectoriel SA* Législation K 1 70.13, État de Genève, 2, rue Henri-Fazy, case postale 3964, 1211 Genève 3 (January, 2008) https://www.ge.ch/legislation/rsg/f/s/rsg_k1_70p13.html

561. G. Catalano et al., Guide to Cost-Benefit Analysis of Investment Projects, *Regional and Urban Policy* (European Union, December, 2014), pp. 321–333
562. *Questionnaire for submission of proposals for roadmap 2018* (September, 2016), website: https://ec.europa.eu/research/infrastructures/pdf/esfri/esfri_roadmap/esfri_rd2018_questionnaire.pdf
563. *RI impact pathways H2020 INFRASUPP project 777563, January 2018 to June 2020* (September, 2018), website: https://cordis.europa.eu/project/rcn/212964_en.html
564. M. Florio, E. Sirtori, Forecast. Soc. Change **112**, 65 (2016), <https://econpapers.repec.org/RePEc:eee:tefoso:v:112:y:2016:i:c:p:65-78>
565. M. Florio, S. Forte, E. Sirtori, *Forecasting the Socio-Economic Impact of the Large Hadron Collider: a Cost-Benefit Analysis to 2025 and Beyond* report, Università di Milano, Milano, Italy, Dipartimento di Economia, Management e Metodi Quantitativi, Università di Milano, via Conservatorio 7, I-20122 Milano, Italy (March, 2016), [arXiv:1603.00886](https://arxiv.org/abs/1603.00886) [physics.soc-ph]
566. M. Florio, S. Forte, C. Pancotti, E. Sirtori, S. Vignetti, *Exploring Cost-Benefit Analysis of Research, Development and Innovation Infrastructures: An Evaluation Framework* working paper 01/2016, CSIL Centre for Industrial Studies, Corso Monforte, 15, 20122 Milano MI, Italy (March, 2016), [arXiv:1603.03654](https://arxiv.org/abs/1603.03654) [physics.soc-ph]
567. *United Nations Statistical Commission, System of National Accounts 2008* (2008) website: <https://unstats.un.org/unsd/nationalaccount/sna2008.asp>
568. P. Johansson, B. Kriström, *Cost-Benefit Analysis for Project Appraisal* (Cambridge University Press, October, 2015)
569. P. Herson, L. McNeil, Phys. Today **70**, 39 (2017)
570. T. Camporesi, G. Catalano, M. Florio, F. Giffoni, Eur. J. Phys. **38**, 22 (2017)
571. G. Catalano, M. Florio, V. Morretta, T. Portaluri, *The Value of Human Capital Formation at CERN* CERN-ACC-2018-0025 (CERN, Geneva, Switzerland, August 22, 2018), <https://cds.cern.ch/record/2635864>
572. Economisti Associati, *Marie Curie researchers and their long-term career development: A comparative study*, Final report, European Union, Publications Office of the European Union (March, 2014), http://ec.europa.eu/research/fp7/pdf/mca/marie_curie_researchers_and_their_long-term_career_development.pdf
573. A. Bibet-Chevalier, D. Chanal, *Étude des impacts pour l'État du projet de future collisionneur circulaire du CERN en matière de procédures et d'engagements financiers* Rapport d'étude du Cerema pour le SGAR Auvergne-Rhône-Alpes EDMS 1959547 V1.0 (CEREMA, March, 2018), <https://edms.cern.ch/document/1959547/1.0>, Access to the report is subject to an NDA
574. *European Advances Superconductor Innovation and Training Network* (2018), website: <http://easitrain.web.cern.ch>
575. CEBR, Executive summary report of the centre for economics and business research in *The importance of physics to the economics of Europe* (European Physical Society, 68200 Mulhouse, France, January, 2013), http://www.eps.org/?page=policy_economy
576. M. Bianchi-Streit, N.F. Blackburne, R. Buude, H. Reitz, B. Sagnell, H. Schmied, B. Schorr, *Economic utility resulting from CERN contracts (second study)*, CERN Yellow Reports: Monographs (CERN, Geneva, Switzerland, 1984) <https://cds.cern.ch/record/156911>
577. P. Castelnovo, M. Florio, S. Forte, L. Rossi, E. Sirtori, Res. Policy **47**, 1853 (2018)
578. M. Florio, F. Giffoni, A. Giunta, E. Sirtori, Ind. Corp. Change **27**, 915 (2018)
579. A. Bastianin, M. Florio, *Industrial Spillovers from the LHC/HL-LHC Programme at CERN* CERN-ACC-2018-0026 (CERN, Geneva, Switzerland, August 23, 2018), <https://cds.cern.ch/record/2635876>
580. P. Seidel, *Applied Superconductivity: Handbook on Devices and Applications*, The Art of Computer Programming (Wiley, February, 2015), p. 1238
581. P. Lebrun, Mater. Sci. Eng. **171**, 012001 (2017)

582. E. Autio, M. Bianchi-Streit, A.P. Hameri, *Technology transfer and technological learning through CERN's procurement activity*, CERN Yellow Reports: Monographs (CERN, Geneva, Switzerland, 2003), <https://cds.cern.ch/record/680242>
583. *Le Grand Paris des déblais dévoile ses lauréats* (2008), website: <http://www.batiweb.com/actualites/vie-des-societes/le-grand-paris-des-deblais-devoile-ses-laureats-30-03-2017-30184.html>
584. C. Benna, *Telt-Politecnico, master e dottorandi nel cantiere della Torino-Lione* (Corriere della Sera, 2017), http://torino.corriere.it/cronaca/17_dicembre_15/accordo-telt-politecnico-master-dottorandi-cantiere-torino-lione-ba0f2874-e1e7-11e7-980c-flb8f0b331b7.shtml
585. *Sept projets innovants pour les déblais du Grand Paris* (2017) website: <https://www.usinenouvelle.com/article/sept-projets-innovants-pour-les-deblais-du-grand-paris.N520469>
586. T.B. Lee, M. Fischetti, *Weaving the Web: The Original Design and Ultimate Destiny of the World Wide Web by Its Inventor*, Harper Business, 1 ed. (November, 2000)
587. L. Mascetti, H. Gonzalez Labrador, M. Lamanna, J.T. Moscicki, A.J. Peters, J. Phys.: Conf. Ser. **664**, 062037 (2015)
588. J. Gutleber, A. Niemi, J.P. Penttinen, *An Open Modelling Approach for Availability and Reliability of Systems – OpenMARS* CERN-ACC-2018-0006 (CERN, Geneva, Switzerland, January, 2018), <https://cds.cern.ch/record/2302387>
589. E. Coatanéa et al., Reliab. Eng. Syst. Saf. **183**, 387 (2019), <http://www.sciencedirect.com/science/article/pii/S0951832018307634>
590. A. Alberini, A. Longo, J. Cult. Econ. **30**, 287 (2006)
591. R.C. Bishop, N.W. Bouwes, P.P. Caulkins, Am. J. Agricult. Econ. **68**, 291 (1986)
592. J.P. Poor, J.M. Smith, J. Cult. Econ. **28**, 217 (2004)
593. M. Florio, S. Forte, E. Sirtori, Technol. Forecast. Soc. Change **112**, 38 (2016)
594. C. Risen, J. Am. Inst. Archit. (2018), https://www.architectmagazine.com/awards/studio-prize/studio-prize-the-new-grand-tour-a-new-visitors-center-for-cern_o
595. G. Catalano, I.C. Garido, *Cultural Effects at CERN* CERN-ACC-2018-0048 (CERN, Geneva, Switzerland, November, 2018) <https://cds.cern.ch/record/2649022>
596. R.D. Cabana (Director), J.E. Petro (Master Plan Steering Group Chair), *Kennedy Space Center. Future Development Concept* KSC center master plan 2012–2031 (NASA, John F. Kennedy Space Center, FL 32899, USA, 2012), https://www.nasa.gov/centers/kennedy/pdf/634026main_future-concept.pdf
597. A.J. Barr, A. Haas, C. Kalderon, “That looks weird” = evaluating citizen scientists’ ability to detect unusual features in ATLAS images of collisions at the Large Hadron Collider Report no:ATL-COM-OREACH-2016-017 (University of Oxford, UK and New York University, USA and University of Lund, Sweden, 2017) [arXiv:1610.02214](https://arxiv.org/abs/1610.02214) [physics.soc-ph], <https://arxiv.org/pdf/1610.02214.pdf>
598. *The Zooniverse project: publications* (2016), website: <https://www.zooniverse.org/about/publications>
599. *EXTREME – alla ricerca delle particelle. Museo Nazionale Scienza e Tecnologia Leonardo Da Vinci, Milano, Italia* (2016), website: <http://www.museoscienza.org/extreme>
600. *Anfang – Wie alles begann. Von Galaxien, Quarks und Kollisionen. Naturhistorisches Museum Wien, Austria* (2016), website: <http://www.nhm-wien.ac.at/anfang>
601. F. Giffoni, F. Massimo, *Scientific Research at CERN as a Public Good: A Survey to French Citizens* CERN-ACC-2018-0024 (CERN, Geneva, Switzerland, August, 2018), <https://cds.cern.ch/record/2635861>
602. M. Cabriol, *La France booste le budget du CNES en 2017* (2017), La Tribune newspaper website <https://www.latribune.fr/entreprises-finance/industrie/aeronautique-defense/la-france-booste-le-budget-du-cnes-en-2017-629755.html>

- 603. A. Augier, B. Gindre, *Préparation de l'accompagnement stratégie en concertation socio-territoriale dans le cadre de l'étude FCC* Final project report EDMS 1745888, iddest – Institut durable de développement économique, social & territorial (January, 2017) Access to the report is subject to a NDA
- 604. M. Sauvain, *Rapport d'étude relatif aux procédures administratives sur le territoire suisse* Rapport de la Structure de Concertation Permanente EDMS 20258995 V1.0, Latitude Durable (November, 2018), <https://edms.cern.ch/document/2025895>, Access to the report is subject to an NDA
- 605. European Strategy Forum on Research Infrastructures, *Strategy Report on Research Infrastructures, Roadmap 2018* Roadmap 2018, ESFRI (August, 2018), <http://roadmap2018.esfri.eu/media/1066/esfri-roadmap-2018.pdf>
- 606. European Strategy Forum on Research Infrastructures, *Public Roadmap 2018 Guide* Guide 2018, ESFRI (December, 2016), https://ec.europa.eu/research/infrastructures/pdf/esfri/esfri_roadmap/esfri_rd2018_guide_for_applicants.pdf